

NATIONAL AERONAUTICS AND SPACE ADMINISTRATION

*Space Programs Summary 37-41, Vol. IV*

*Supporting Research and Advanced Development*

For the Period August 1 to September 30, 1966

FACILITY FORM 602	N67-15701	N67-15764
	(ACCESSION NUMBER)	(THRU)
	314	1
	(PAGES)	(CODE)
	CR 81201	11
	(NASA CR OR TMX OR AD NUMBER)	(CATEGORY)

GPO PRICE \$ \_\_\_\_\_

CFSTI PRICE(S) \$ \_\_\_\_\_

Hard copy (HC) 3.00

Microfiche (MF) 1.75

ff 653 July 65

JET PROPULSION LABORATORY  
CALIFORNIA INSTITUTE OF TECHNOLOGY  
PASADENA, CALIFORNIA

October 31, 1966

NATIONAL AERONAUTICS AND SPACE ADMINISTRATION

*Space Programs Summary 37-41, Vol. IV*

*Supporting Research and Advanced Development*

For the Period August 1 to September 30, 1966

JET PROPULSION LABORATORY  
CALIFORNIA INSTITUTE OF TECHNOLOGY  
PASADENA, CALIFORNIA

October 31, 1966

**Space Programs Summary 37-41, Vol. IV**

**Copyright © 1966**

**Jet Propulsion Laboratory  
California Institute of Technology**

**Prepared Under Contract No. NAS 7-100  
National Aeronautics & Space Administration**

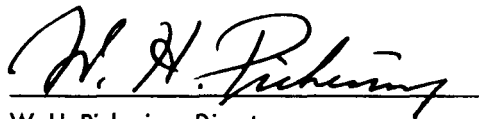
## Preface

The Space Programs Summary is a six-volume bimonthly publication designed to report on JPL space exploration programs and related supporting research and advanced development projects. The titles of all volumes of the Space Programs Summary are:

- Vol. I. *The Lunar Program* (Confidential)
- Vol. II. *The Planetary-Interplanetary Program* (Confidential)
- Vol. III. *The Deep Space Network* (Unclassified)
- Vol. IV. *Supporting Research and Advanced Development* (Unclassified)
- Vol. V. *Supporting Research and Advanced Development* (Confidential)
- Vol. VI. *Space Exploration Programs and Space Sciences* (Unclassified)

The Space Programs Summary, Vol. VI, consists of: an unclassified digest of appropriate material from Vols. I, II, and III; an original presentation of the JPL quality assurance and reliability efforts, and the environmental- and dynamic-testing facility-development activities; and a reprint of the space science instrumentation studies of Vols. I and II.

Approved by:



W. H. Pickering, Director

Jet Propulsion Laboratory

**Page intentionally left blank**

## Contents

### SYSTEMS DIVISION

<b>I. Systems Analysis</b>	1
A. Comparison of the Newtonian and General Relativistic Orbits of a Point Mass in an Inverse Square Law Force Field	1
NASA Code 129-04-01-01, C. B. Solloway and H. Lass	1 ✓

### PROJECT ENGINEERING DIVISION

<b>II. Environmental Requirements</b>	7
A. Microbiological Survey of Environmentally Controlled Areas	7
NASA Code 189-58-23-02, W. W. Paik, M. R. Christensen, and J. A. Stern	7 ✓
References	16

### GUIDANCE AND CONTROL DIVISION

<b>III. Spacecraft Power</b>	17
A. Power System Configuration Study	17
NASA Code 120-33-05-01, E. C. Jazwa	17 ✓
B. Sterilizable Battery	18
NASA Code 120-34-01-03, R. Lutwack	18 ✓
<b>IV. Spacecraft Control</b>	20
A. Propulsive Lander Control System	20
NASA Code 186-68-02-24, R. J. Mankovitz	20 ✓
B. Solar Pressure Effect on Spacecraft Attitude After Gas System Depletion	27
NASA Code 125-19-04-01, E. H. Kopf, Jr.	27 ✓
C. Advanced Scan Platform	32
NASA Code 186-68-02-24, P. Presser	32 ✓
Reference	37
<b>V. Guidance and Control Research</b>	38
A. Variation of Current With Voltage at the Onset of Punch-Through for Thin-Base Solid-State Diodes	38
NASA Code 129-02-05-09, A. Shumka	38 ✓
B. Recent Progress In CdS Photoconductors	41
NASA Code 129-02-05-01, R. J. Stirn	41 ✓
C. Performance of an Electric Gun	46
NASA Code 129-02-01-07, K. Shimoda	46 ✓
References	49

## Contents (contd)

### ENGINEERING MECHANICS DIVISION

<b>VI. Materials</b>	51	
A. Char Reflectances and Planetary Entry Heat Shields		
NASA Code 124-08-03-02, R. G. Nagler	51	✓
B. Carbon and Graphite		
NASA Code 129-03-04-02, D. B. Fischbach	54	✓
C. Ceramic Research		
NASA Code 129-03-04-01, E. C. de Wys and M. H. Leipold	58	✓
References	60	
<b>VII. Applied Mechanics</b>	62	
A. Touchdown Stability Study		
NASA Code 186-68-09-03, J. A. Garba	62	✓
References	64	

### ENVIRONMENTAL SIMULATION DIVISION

<b>VIII. Aerodynamic Facilities</b>	65	
A. Wind Tunnels		
NASA Code 124-07-04-01, B. Walker, P. Jaffe, and R. Weaver;		
124-07-04-02, R. Weaver and C. Klose	65	✓
B. Hypervelocity Laboratory		
NASA Code 124-07-01-04, F. Livingston, G. Stickford, and J. Williard	72	✓
References	82	

### PROPULSION DIVISION

<b>IX. Solid Propellant Engineering</b>	85	
A. Low-Pressure Combustion Studies		
NASA Code 128-32-06-01, L. Strand	85	✓
B. Applications Technology Satellite Motor Development		
NASA Code 630-01-00-00, D. R. Frank and R. G. Anderson	91	✓
References	95	
<b>X. Polymer Research</b>	97	
A. Mechanical Behavior of SBR-Glass Bead Composites		
NASA Code 128-32-05-02, R. F. Fedors and R. F. Landel	97	✓
B. A Preliminary Report on the Suitability of Thermoplastic Rubbers as a Binder for Composite Solid Propellant		
NASA Code 128-32-05-02, B. G. Moser, H. Broyles, and R. F. Landel	107	✓

## Contents (contd)

C. Voltage Endurance Tests for Closed-Cell Foams		
NASA Code 186-68-13-03, J. Moacanin and J. Farrar	109	✓
D. Studies of Sterilizable Elastomers		
NASA Code 186-68-13-03, E. F. Cuddihy and J. Moacanin	111	✓
E. The Reactions of Carboxyl-Terminated Prepolymers with Polyepoxides and Polyaziridines		
NASA Code 129-03-11-04, S. H. Kalfayan and B. A. Campbell	113	✓
F. Sterilization Studies		
NASA Code 186-58-13-02, S. H. Kalfayan, B. A. Campbell, and J. K. Hoffman	115	✓
References	116	
<b>XI. Research and Advanced Concepts</b>	118	
A. 50-kw(e) Thermionic Reactor Study		
NASA Code 120-27-06-02, J. P. Davis	118	✓
B. Thermionic Reactor Stability Studies		
NASA Code 120-27-06-02, H. Gronroos and J. Shapiro	119	✓
C. Liquid Magnetohydrodynamic (MHD) Power Conversion		
NASA Code 129-27-06-03, D. Elliott, D. Cerini, and L. Hays	124	✓
D. An Addition to the Radiator System Computer Program		
NASA Code 120-26-08-01, J. J. Volkoff	132	✓
References	133	
<b>XII. Liquid Propulsion</b>	134	
A. Resonant Combustion		
NASA Code 128-31-06-01, R. M. Clayton, J. W. Woodward, and J. G. Sotter	134	✓
B. Sterilizable Liquid Propulsion System Development		
NASA Code 186-58-08-02, T. A. Groude	151	✓
C. Injector Development: Investigation of Propellant Sheets		
NASA Code 731-12-03-02, R. W. Riebling	156	✓
References	166	

## SPACE SCIENCES DIVISION

<b>XIII. Space Instrument Systems</b>	167	
A. Generation of Horizontal Jitter Requirements in an Analog-Scan Video System		
NASA Code 125-23-02-01, F. C. Billingsley	167	✓
References	169	
<b>XIV. Bioscience</b>	170	
A. Fluorometric Determination of Nucleic Acids.		
I. Deoxyribose Assay of Biological Material		
NASA Code 189-55-02-02, J. H. Rho and J. R. Thompson	170	✓
References	173	

## Contents (contd)

### XV. Physics . . . . . 174

- A. The Interaction of a Nonpolar Atom or Molecule With  
an Inhomogeneous Surface Electric Field  
NASA Code 129-02-03-06, D. P. Merrifield and J. King, Jr. . . . . 174 ✓
- B. New Expressions for the Energy Density and Momentum  
Flux of an Electromagnetic Field  
NASA Code 129-02-07-02, M. M. Saffren . . . . . 177 ✓
- C. Field Stabilization of NMR Spectrometers by Means of  
Samples Coaxial and External to the Receiver Coil  
NASA Code 129-03-11-06, D. D. Elleman and S. L. Manatt . . . . . 179 ✓
- D. The Signs of Fluorine-Phosphorus Coupling Constants  
NASA Code 129-03-11-06, S. L. Manatt, D. D. Elleman, A. H. Cowley, and A. B. Burg . . . . . 180 ✓
- E. Analysis of Mariner II Alfvén Waves  
NASA Code 129-02-07-02, T. W. Unti and M. Neugebauer . . . . . 181 ✓
- F. Junction Conditions in General Relativity  
NASA Code 129-02-07-02, F. B. Estabrook and H. D. Wahlquist . . . . . 189 ✓
- G. Molar Extinction Coefficients of Hydrogen Iodide  
in the Schumann Region  
NASA Code 129-02-03-02, O. F. Raper and W. B. DeMore . . . . . 189 ✓
- H. Four-Fermion Interaction Lagrangians  
NASA Code 129-02-07-02, J. S. Zmuidzinas . . . . . 192 ✓
- References . . . . . 194

### XVI. Fluid Physics . . . . . 196

- A. Rotational Temperature Measurement in a Free Jet  
and in a Static Gas  
NASA Code 129-01-05-03, H. Ashkenas . . . . . 196 ✓
- B. The Scale Depth of the Main Ocean Thermocline  
NASA Code 129-01-09-05, R. C. Alexander . . . . . 200 ✓
- References . . . . . 205

## TELECOMMUNICATIONS DIVISION

### XVII. Communications Elements Research . . . . . 207

- A. Multipactor Effects: Secondary Electron Emission  
NASA Code 125-22-02-01, H. Erpenbach . . . . . 207 ✓
- B. Optical Communications Elements: Simulated Atmosphere  
NASA Code 125-22-02-01, W. H. Wells . . . . . 209 ✓

### XVIII. Spacecraft Telemetry and Command . . . . . 213

- A. A Hybrid Microelectronic Analog to Digital Converter  
NASA Code 125-25-04-01, D. M. Bergens . . . . . 213 ✓
- B. Effects of Thermal Sterilization on Tape Recorder  
Components  
NASA Code 125-23-02-07, J. K. Hoffman, S. H. Kalfayan and B. A. Campbell . . . . . 216 ✓

## Contents (contd)

<b>XIX. Spacecraft Radio</b>	225	
A. Radar Altimeter and Doppler Velocity Sensor Frequency Discriminator Analysis		
NASA Code 186-68-02-14, R. L. Horttor	225	✓
B. Electron Tube Filament Study		
NASA Code 186-68-04-09, L. J. Derr	228	✓
C. Approximate Analysis of a Frequency-Shift Keyed System with Uncertainty in the Carrier Frequency		
NASA Code 186-68-04-11, D. W. Boyd	233	✓
D. High Impact Antenna Study: Cavity-Backed Spiral Antenna		
NASA Code 125-22-01-02, K. Woo	239	✓
E. Experimental Study of Multipacting Between Coaxial Electrodes		
NASA Code 125-22-01-02, R. Woo	242	✓
References	247	
<b>XX. Communications System Research</b>	248	
A. Combinatorial Communications: The Target Lemma		
NASA Code 125-21-01-01, E. Rodemich	248	✓
B. Combinatorial Communications: Primitive Trinomials of High Degree		
NASA Code 125-21-01-01, E. Rodemich and Howard Rumsey, Jr.	250	✓
C. Combinatorial Communications: Note on Existence Criteria for Cyclic Difference Sets		
NASA Code 125-21-01-01, L. D. Baumert and Howard Rumsey, Jr.	251	✓
D. Propagation Studies: On Decision-Directed Subcarrier Phase Estimation		
NASA Code 150-22-11-08, J. W. Layland	254	✓
E. Information Processing: A Class of Two-Weight Codes		
NASA Code 150-22-11-09, R. J. McEliece	264	✓
F. Information Processing: Tri-Weight Cyclic Codes		
NASA Code 150-22-11-09, G. Solomon	266	✓
G. Digital Communications and Tracking: Limit Cycles in Passive-Filter Phase-Locked Loops		
NASA Code 150-22-12-03, R. C. Tausworthe	268	✓
H. Digital Communications and Tracking: The Mean-Square Approximation to the Optimum Cross-Correlation Function		
NASA Code 150-22-12-03, J. J. Stiffler	270	✓
I. Data Compression Development: A Comparison of Two Floating-Aperture Data Compression Schemes		
NASA Code 155-22-15-14, J. C. Wilson	273	✓
J. Digital Devices Development: Integrated Circuits-Delay Line Interface Circuitry		
NASA Code 150-22-15-10, R. A. Winklestein and E. Lutz	278	✓
References	283	

## Contents (contd)

### ADVANCED STUDIES OFFICE

<b>XXI. Future Projects . . . . .</b>	<b>285</b>
A. Venus Capsule Science	
<i>NASA Code 684-30-01-10, R. G. Brereton, R. W. Davies, and C. E. Giffen . . . . .</i>	<i>285</i> ✓
References . . . . .	289

# I. Systems Analysis

SYSTEMS DIVISION

N67-15702

## A) Comparison of the Newtonian and General Relativistic Orbits of a Point Mass in an Inverse Square Law Force Field, C. B. Solloway and H. Lass

### 1. Introduction

The inherent accuracy capability of the combined JPL Deep Space Network Tracking Facility and Orbit Determination Program has led to the consideration of whether or not the small differences between the orbits of two spacecraft operating, respectively, in worlds governed by Newtonian and relativistic mechanics would be observable and measurable with present day equipment.

As a first step in the investigation of this question, we have compared the orbits of a point mass moving in both these regimes. The precise problem statement is given in Sect. 2. The basic results obtained are summarized in Sect. 3, and some conclusions and comments are given in Sect. 4. The details of the analysis are omitted for sake of brevity.

### 2. The Problem

Let a point mass particle move in a planar elliptic orbit under the influence of a central inverse square law force field due to a fixed mass at the origin (one-body prob-

lem). Let a second point mass particle move along a geodesic due to the Schwarzschild line element of general relativity theory in a plane coincident with our Newtonian frame with the same fixed mass at the common origin of both systems. We assume that coordinate time is the same in both systems and that both particles have the same initial conditions (position and velocity) at the periapsis of the Newtonian orbit.

We wish to find at any time analytic expressions for the differences in the radial and transverse components of position and velocity (which are physical observables).

### 3. Development and Results

If  $\rho$  and  $\phi$  are the classical polar coordinates of the (Newtonian) particle measured from the center of force and  $v = \rho^{-1}$ , the classical orbit is given by

$$v(\phi) = \frac{GM}{h^2} (1 + \epsilon \cos \phi) \quad (1)$$

if  $\phi$  is measured from periapsis;  $G$ ,  $M$ ,  $\epsilon$  and  $h$  are constants,  $G$  the universal gravitational constant,  $M$  the mass

of the body fixed at the origin,  $\epsilon$  the eccentricity ( $<1$ ) of the orbit and

$$\rho^2 \frac{d\phi}{dt} = \rho_0^2 \left( \frac{d\phi}{dt} \right)_0 = h = \text{angular momentum} \quad (2)$$

an integral of the motion. Subscripts denote initial values.

The Schwarzschild line element is given by

$$ds^2 = c^2 \left( 1 - \frac{2GM}{c^2 r} \right) dt^2 - \left( 1 - \frac{2GM}{c^2 r} \right)^{-1} dr^2 - r^2 d\theta^2 \quad (3)$$

where  $c$  is the speed of light (assumed constant), and  $r$  and  $\theta$  are position coordinates of the point mass particle in

the relativistic frame, analogous to  $\rho$  and  $\phi$ . If  $u = r^{-1}$  the equations of motion of the particle become

$$u'' + u = \frac{GM}{h_0^2} + \frac{3GM}{c^2} u^2 \quad (4)$$

with prime denoting  $d/d\theta$ . The quantities  $c$ ,  $G$ ,  $M$  are the constants already mentioned and  $h_0$  and  $k$  are given by

$$r^2 \frac{d\theta}{ds} = \left( r^2 \frac{d\theta}{ds} \right)_0 = \frac{h_0}{c} \quad (5)$$

$$\left( 1 - \frac{2GM}{c^2 r} \right) \frac{dt}{ds} = \frac{k}{c} \quad (6)$$

as integrals of the motion (analogous to Eq. 2).

Since both particles start from the Newtonian periapsis at  $t = 0$  with the same initial conditions we have

$$r_0 = \rho_0, \phi_0 = \theta_0 = 0, u'(0) = v'(0) = 0 \text{ and } \left( \frac{d\phi}{dt} \right)_0 = \left( \frac{d\theta}{dt} \right)_0 = 0 \quad (7)$$

here and subsequently  $v' = dv/d\phi$ , and all equations henceforth are correct to order  $c^{-2}$  (i.e., we neglect  $c^{-3}$  and higher order infinitesimals).

Using the Krylov-Bogoliubov improved first approximation form to solve the (non-linear) Eq. (4) we obtain

$$u(\theta) = \frac{GM}{h_0^2} + A \cos \left[ \left( 1 - \frac{3G^2 M^2}{c^2 h_0^2} \right) \theta \right] + \frac{3GM}{c^2} \left[ \frac{G^2 M^2}{h_0^4} + \frac{A^2}{2} \right] - \frac{3GM}{c^2} \frac{A^2}{6} \cos \left[ 2 \left( 1 - \frac{3G^2 M^2}{c^2 h_0^2} \right) \theta \right] \quad (8)$$

with  $A$  a constant of integration. Using the relations in Eqs. (2), (3), (5), (6) and (7) we find

$$k = 1 - \frac{GM}{c^2 r_0} + \frac{h_0^2}{2c^2 r_0^2} = 1 - \frac{G^2 M^2}{c^2 h^2} (1 + \epsilon) + \frac{G^2 M^2}{2c^2 h^2} (1 + \epsilon)^2 \quad (9)$$

$$h_0 = \left[ 1 + \frac{GM}{c^2 r_0} + \frac{h^2}{2c^2 r_0^2} \right] h = \left[ 1 + \frac{G^2 M^2}{c^2 h^2} (1 + \epsilon) + \frac{G^2 M^2}{2c^2 h^2} (1 + \epsilon)^2 \right] h \quad (10)$$

$$\frac{h_0}{kh} = 1 + \frac{2GM}{c^2 r_0} = 1 + \frac{2G^2 M^2}{c^2 h^2} (1 + \epsilon) \quad (11)$$

and

$$A = \frac{GM\epsilon}{h^2} \left( 1 + \frac{4G^2 M^2}{c^2 h^2} \right) \quad (12)$$

and with the aid of these equations we can write

$$u(\theta) = \frac{GM}{h^2} \left[ 1 + \varepsilon \cos \left( 1 - \frac{3G^2 M^2}{c^2 h^2} \right) \theta \right] + \frac{G^3 M^3 \varepsilon}{c^2 h^4} \left[ -4 + \frac{\varepsilon}{2} + 4 \cos \left( 1 - \frac{3G^2 M^2}{c^2 h^2} \right) \theta - \frac{\varepsilon}{2} \cos 2 \left( 1 - \frac{3G^2 M^2}{c^2 h^2} \right) \theta \right] \quad (13)$$

From Eqs. (2), (5), (6) and (11) we obtain

$$r^2 \left( 1 + \frac{2GM}{c^2 r} \right) d\theta = \left[ 1 + \frac{2G^2 M^2}{c^2 h^2} (1 + \varepsilon) \right] \rho^2 d\psi \quad (14)$$

which can be expressed with the aid of Eqs. (1) and (13) as

$$\begin{aligned} \frac{d\phi}{(1 + \varepsilon \cos \phi)^2} - \frac{d\psi}{(1 + \varepsilon \cos \psi)^2} &= \frac{G^2 M^2}{c^2 h^2} \frac{2(1 + \varepsilon)}{(1 + \varepsilon \cos \psi)^2} d\psi \\ &- \frac{G^2 M^2}{c^2 h^2} \left[ \frac{3}{(1 + \varepsilon \cos \phi)^2} - 2\varepsilon \left( -4 + \frac{\varepsilon}{2} + 4 \cos \phi - \frac{\varepsilon}{2} \cos 2\phi \right) + \frac{2}{1 + \varepsilon \cos \phi} \right] d\phi \end{aligned} \quad (15)$$

with

$$\phi = \left( 1 - \frac{3G^2 M^2}{c^2 h^2} \right) \theta.$$

It follows on integrating that  $\phi = \psi + \alpha$  with

$$\begin{aligned} \alpha &= \frac{G^2 M^2}{c^2 h^2} (1 + \varepsilon \cos \psi)^2 \int_0^\psi \left[ -\frac{2}{1 + \varepsilon \cos \psi} + \frac{2\varepsilon - 1}{(1 + \varepsilon \cos \psi)^2} + \frac{2\varepsilon \left( -4 + \frac{\varepsilon}{2} + 4 \cos \psi - \frac{\varepsilon}{2} \cos 2\psi \right)}{(1 + \varepsilon \cos \psi)^3} \right] d\psi \\ &= -\frac{G^2 M^2}{c^2 h^2} (1 + \varepsilon \cos \psi)^2 g(\psi) \end{aligned} \quad (16)$$

with

$$\begin{aligned} g(\psi) &= \int_0^\psi \left\{ \frac{2}{1 + \varepsilon \cos \psi} - \frac{2\varepsilon - 1}{(1 + \varepsilon \cos \psi)^2} - \frac{2\varepsilon \left( -4 + \frac{\varepsilon}{2} + 4 \cos \psi - \frac{\varepsilon}{2} \cos 2\psi \right)}{(1 + \varepsilon \cos \psi)^3} \right. \\ &= \frac{6(1 + \varepsilon)^2 (1 + \varepsilon^2)}{(1 - \varepsilon^2)^{5/2}} \tan^{-1} \left[ \left( \frac{1 - \varepsilon}{1 + \varepsilon} \right)^{1/2} \tan \frac{\psi}{2} \right] - \frac{4\varepsilon (1 + \varepsilon)^2 (2 + \varepsilon)}{(1 - \varepsilon^2)^2} \frac{\tan \psi/2}{\left[ (1 + \varepsilon) + (1 - \varepsilon) \tan^2 \frac{\psi}{2} \right]} \\ &\quad \left. - \frac{2\varepsilon (5 - \varepsilon) (1 + \varepsilon)}{(1 - \varepsilon^2)} \frac{\tan \frac{\psi}{2} \sec^2 \frac{\psi}{2}}{\left[ (1 + \varepsilon) + (1 - \varepsilon) \tan^2 \frac{\psi}{2} \right]^2} \right\} \end{aligned} \quad (17)$$

We are now in a position to calculate the desired observables for any time  $t$ . It is more natural to give these as a function of the Newtonian angle  $\psi$  which is related to  $t$  by means of Kepler's equation. We obtain the following results:

**a. Radial deviation, position.**

$$\Delta r = \rho(\psi) - r(\theta) = \frac{\epsilon GM}{c^2} \sin \psi g(\psi) - \frac{\left(4 - \frac{\epsilon}{2} - 4 \cos \psi + \frac{\epsilon}{2} \cos 2\psi\right)}{(1 + \epsilon \cos \psi)^2} \quad (18)$$

**b. Transverse deviation, position.**

$$\rho \Delta \theta = \rho(\psi - \theta) = + \frac{GM}{c^2} \left[ (1 + \epsilon \cos \psi) g(\psi) - \frac{3\psi}{1 + \epsilon \cos \psi} \right] \quad (19)$$

**c. Radial deviation, velocity.**

$$\dot{\Delta r} = \dot{\rho}(\psi) - \dot{r}(\theta) = - \frac{G^3 M^3 \epsilon}{c^2 h^3} \{ [(1 + \epsilon \cos \psi)^2 \cos \psi g(\psi) - \sin \psi [1 + 2\epsilon(1 - 2 \cos \psi)]] \} \quad (20)$$

**d. Transverse deviation, velocity.**

$$\Delta(\rho \dot{\psi}) = \rho \frac{d\psi}{dt} - r \frac{d\theta}{dt} = \frac{G^3 M^3}{c^2 h^2} \epsilon \left\{ (1 + \epsilon \cos \psi)^2 \sin \psi g(\psi) + \frac{3\epsilon}{2} (1 - \cos 2\psi) - 2(1 - \cos \psi - \epsilon \cos \psi) \right\} \quad (21)$$

#### 4. Comments and Conclusions

The expressions for Eqs. (18) to (21) were applied to the case of a fixed body equal to the mass of the Sun and a point mass with  $\epsilon \approx 0.8226$  (corresponding to the asteroid Icarus) and the results plotted. They are shown in

Figs. 1(a) to 4(a), inclusive. The (b) figures are enlargements of the (a) figures in the range  $0 \leq \psi \leq 160^\circ$  in order to obtain details of the growth. Note the characteristic signatures of these perturbations over long time ( $\psi$ ) intervals. In the two revolutions plotted they are quite distinctive, particularly the velocity components, and certainly within the observable ability of our present day radar instruments.

Perhaps even of more significance is the fact that the results of the numerical case calculated by this method were also obtained by Dr. W. G. Melbourne using an entirely different technique but with *identical* results. In his method, the relativistic effects were treated as perturbative forces acting on the classical orbital elements, and the time variation of these elements was obtained by integrating numerically on an IBM 7094 the perturbation equations with time as the independent variable. These perturbations were then converted to coordinate and velocity deviations between the two orbits and plotted. (For comparison the plots were constructed using the angle as the independent variable, although time was the independent variable in all the computations). The plots when superimposed were *identical* in all cases including the fine structure graphs! Of course the numerical answers were also checked and found to agree, thus giving not only confidence in the results but effectively demonstrating the power of the K-B method as an analytic tool for finding approximate solutions to non-linear equations.

These studies have been extended to the case where the particles have the same initial conditions at an arbitrary point on the Keplerian orbit, with corresponding results and agreement with Dr. Melbourne's work. A relativistic analogue of Kepler's equation has also been obtained.

The next step in the investigation is to consider the  $N$ -body problem and the practical application to the solar system. Unless the uncertainties in the current ephemerides of the basic bodies can be resolved, the relativistic perturbations, if they exist, may be masked by these uncertainties. There are also many unresolved theoretical questions to be considered such as the meaning of coordinates in general relativity theory and their relation to the observable physical world.

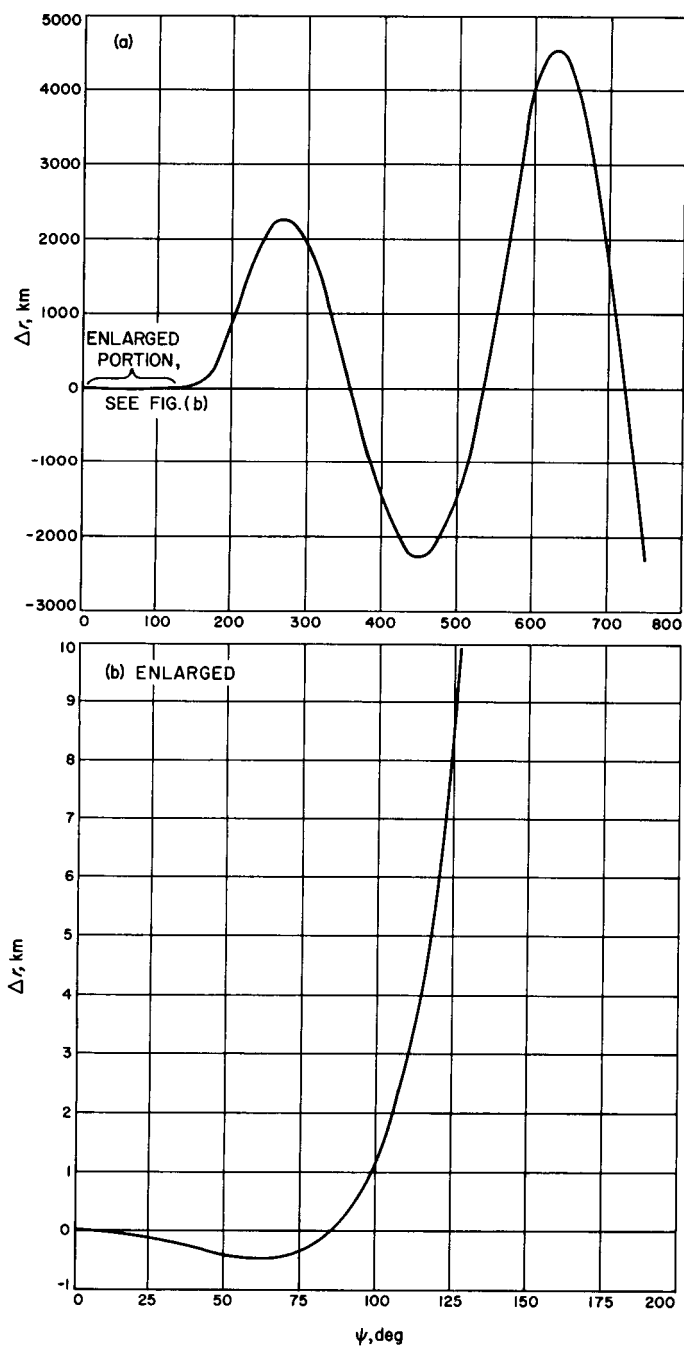


Fig. 1. Radial component of range perturbation

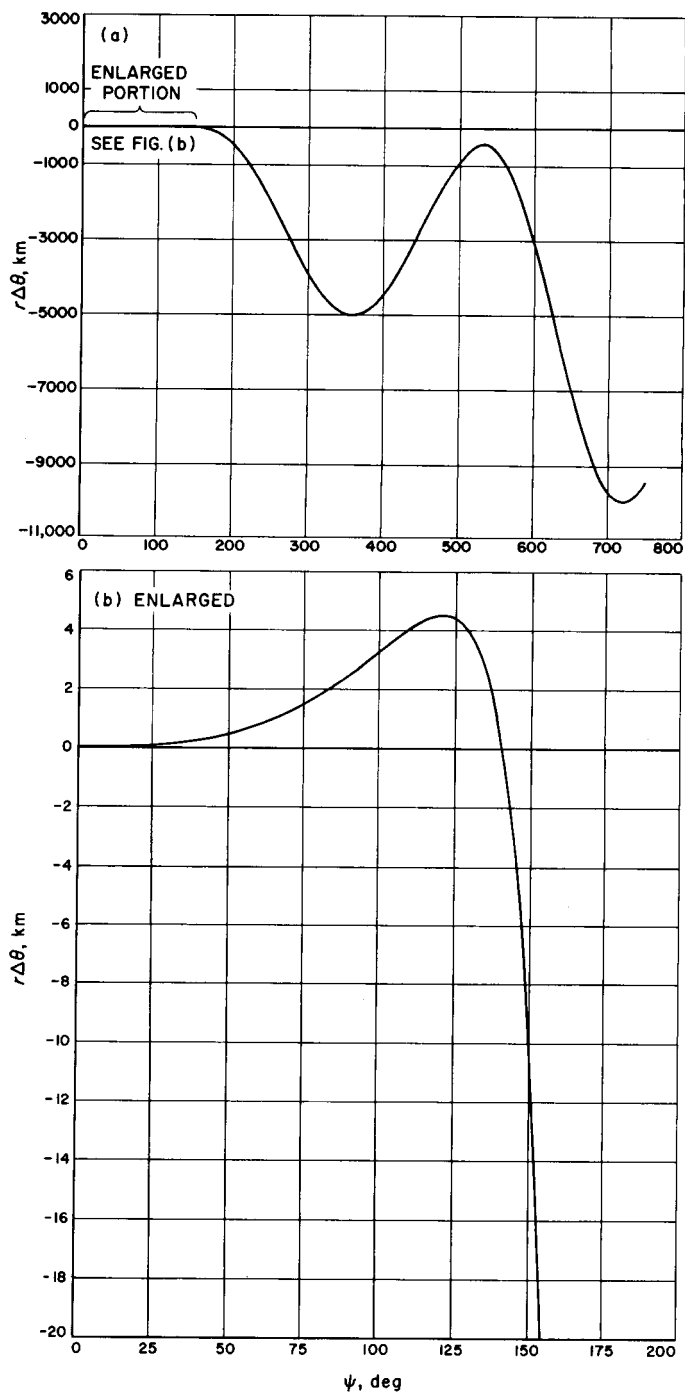


Fig. 2 Transverse component of range perturbation

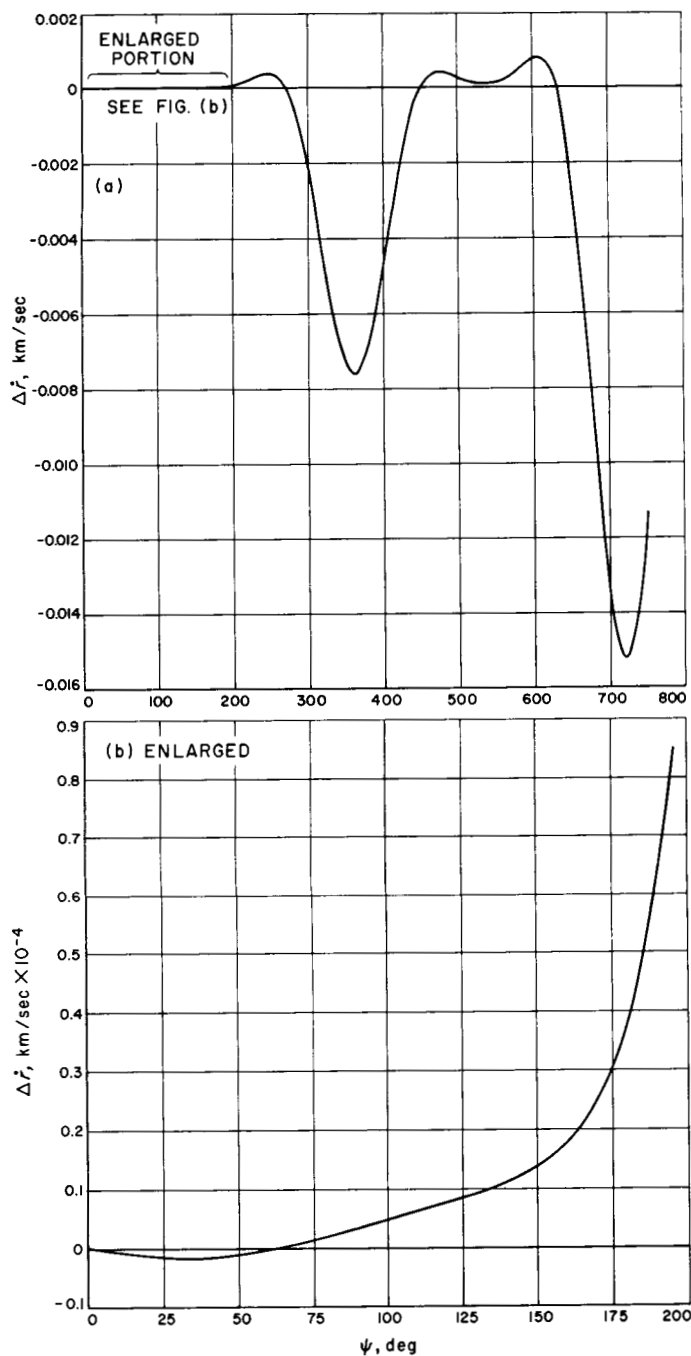


Fig. 3. Radial component of range rate perturbation

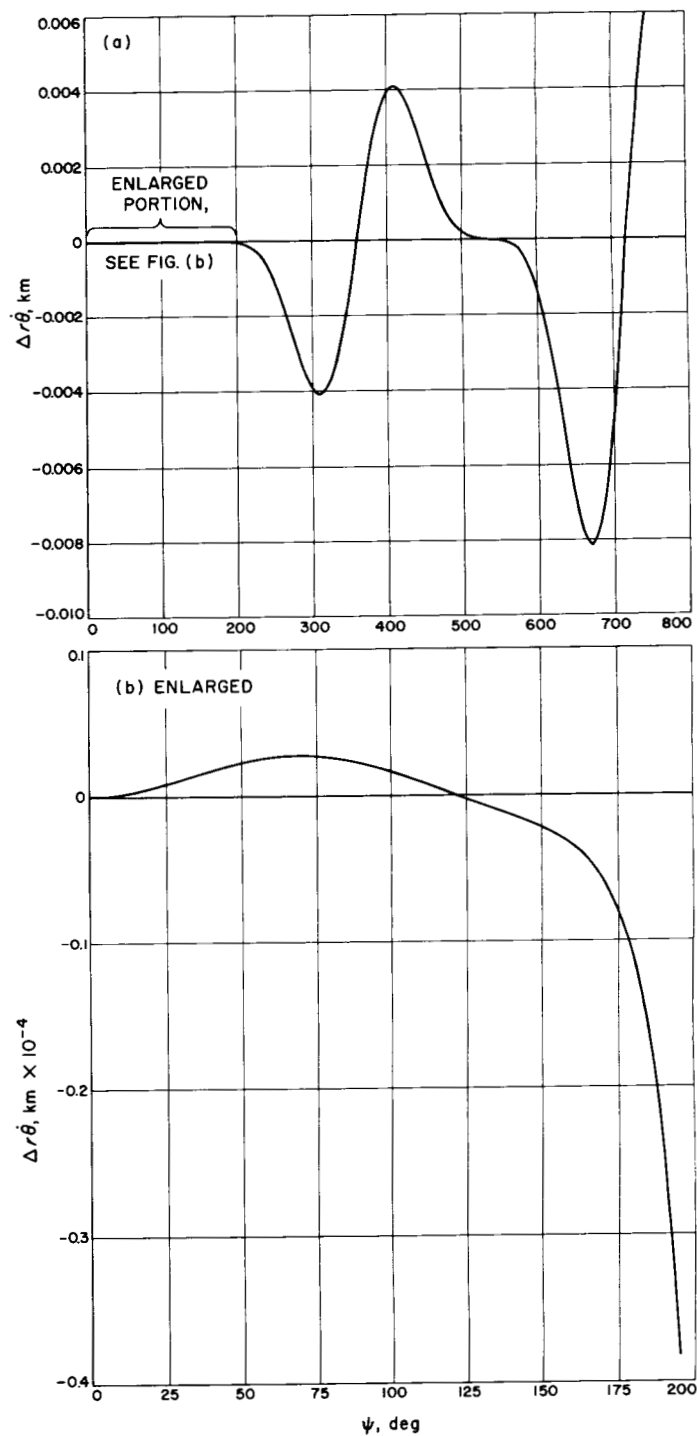


Fig. 4. Transverse component of range rate perturbation

## II. Environmental Requirements

PROJECT ENGINEERING DIVISION

167-15703

**A) Microbiological Survey of Environmentally Controlled Areas**, W. W. Paik, M. R. Christensen, and J. A. Stern

### 1. Introduction

The studies being reported here represent a continuing effort to determine the microbial populations present within environmentally controlled areas. While some of the data has been reported previously (SPS 37-34, Vol. IV, pp. 30-36), the purpose of this report is to present a comprehensive review of all work performed. Part of this investigation was concerned with a sampling program conducted in JPL facilities; including the Experimental Assembly and Sterilization Laboratory (EASL), the Spacecraft Assembly Facility (SAF), and the Structural Test Laboratory. The remainder of the survey was conducted in industrial clean rooms (Douglas Aircraft Company). The study encompassed the range of controlled environments being considered for use in future spacecraft assembly operations.

Since sterilization time-temperature relationships are derived in part by the level of microbial contamination present on the test item, it may be desirable to reduce this load to a relatively low level. Conventional and laminar-flow clean rooms reduce particulate contamination, and

this reduction of particulate matter lowers the level of microbial contamination found within the area. The objective of this study was to quantitatively define the levels of microbial contamination found within these areas. This information may then be used to assess the value of clean rooms as future spacecraft assembly and test areas.

### 2. Experimental

*a. Survey areas.* The survey included the SAF, a Class II, Class III, and Class IV clean room (Douglas Aircraft Company), the Structural Test Laboratory, and a Class 100 vertical laminar air flow clean room (EASL). The studies performed at Douglas were monitoring activities supplementing work accomplished under JPL Contract No. 950920 (Ref. 1). Table 1 contains a summary of the areas sampled microbiologically (air and surface), and the degree of environmental control (physical and personnel) imposed on each area.

#### *b. Materials and methods*

*Air sampling.* Volumetric air samples were collected with slit samplers (Reyniers and Sons, Chicago, Illinois). The samplers were equipped with a 1-hr clock motor, and each sampler was calibrated to operate at an air sampling velocity of 1 ft<sup>3</sup>/min.

Table 1. Clean room description

Building sampled	Personnel occupancy	Physical dimensions, ft <sup>2</sup>	Site(s) sampled (both air and surface samples collected)	Degree of environmental control	Filtration
Spacecraft Assembly Facility (SAF)	5-40	7600	(1) Periphery of access control point (2) Within Ranger PTM area (3) Within Mariner OSE area (4) Within Mariner OSE area (sites 2, 3, and 4 inside high bay area of this building)	Full-length smocks, caps, and gloves Shoe cleaner	HP 2 filters
Structural Test Lab	1-3	300	(1) Structural Test Lab corridor (2) Structural Test Lab "clean area"	Full length smocks, caps, and shoe covers Clothes vacuum	HP 200 filters
Experimental Assembly and Sterilization Lab (EASL)	1-4	600	(1) Hardware Assembly Area (Vertical laminar flow)	Protective suits, hoods, booties, gloves and masks Shoe cleaner, scrub down, air shower	HEPA high efficiency
Class II	20-60	6600	(1) Outer room adjoining the clean room (2) Clean room proper	Full-length smocks and caps Shoe cleaner	Aerosol 45 Aerosol 95
Class III	1-4	390	(1) Corridor outside the clean room (2) Clean room proper	Protective suits, caps, booties Clothes vacuum sticky mat	Cambridge absolute ultra-high efficiency
Class IV	2-6	770	(1) Corridor outside the clean room (2) clean room proper	Full length smocks, caps, shoe covers, gloves for certain work, air shower	10 micron Farr and 0.3 micron Cambridge

**Surface sampling.** Stainless steel strips ( $1.0 \times 3.0 \times 0.016$  in.) were used as microbial fallout sampling surfaces. The strips were arranged as a monolayer on stainless steel sheets ( $10.5 \times 14.5$  in.). Strips were assayed at predetermined time intervals.

**Assay methods.** Detailed methods of air and surface sampling and assay techniques are described in previous reports (Ref. 2 and SPS 37-34). All samples were incubated at 32°C for 72 hr.

### 3. Results

#### a. Air sampling

**Douglas Aircraft Company.** The results from the Class II, III, and IV clean rooms and adjacent corridors are presented in Figs. 1, 2, and 3. The Class II room had the highest range of airborne viable particles; Class II range was 1.5 to 9.5, Class III was 0.0 to 0.5, and Class IV had 0.5 to 1.0 viable particle per cubic foot of air sampled.

**SAF.** The air sampling results for this area are found in Fig. 4. *Ranger* test area results were very similar to those obtained in the *Mariner* test and support areas. The number of airborne viable particles recovered within the high-bay area ranged from 1.0 to 5.8 viable particles per cubic foot of air sampled as opposed to a range of 6.2 to 19.8 for the adjacent outer corridor.

**Structural Test Laboratory.** The air sampling results for the hardware assembly area (non-laminar flow), and the

adjacent outer corridor are found in Fig. 5. Viable particle counts ranged from 0.2 to 1.6 per cubic foot of sampled air in the hardware assembly area and from 1.9 to 8.2 per cubic foot of sampled air in the adjacent corridor.

**EASL.** The air sampling results for the hardware assembly area (vertical laminar flow) are found in Fig. 5. The level of airborne viable particles remained at an extremely

Table 2. Results of surface sampling studies done in three classes of clean rooms

Exposure time, weeks	Number viable aerobic mesophiles recovered per square foot of surface					
	Class II room		Class III room		Class IV room	
	Average <sup>a</sup>	Range	Average	Range	Average	Range
1	4240	1560-11160	220	0-360	180	0-480
4	7980	4320-19440	160	0-360	140	0-240
7	8040	4800-16320	140	0-360	240	0-360
10	9672	5640-16800	340	0-600	180	0-480
13	13200	11280-15720	140	0-360	140	0-360
16	11670	8880-16680	180	0-360	200	0-360
19	10080	7440-15600	160	0-360	240	120-480
22	21456	12720-29760	80	0-240	460	240-840
25	15380	13440-17280	80	0-240	420	360-720
28	18480	10920-40440	180	0-600	460	240-840
31 <sup>b</sup>	9320	5520-12600	120	0-480	340	240-480
34	6880	4560-11760	160	0-360	540	120-1320
37	6460	3120-11280	100	0-240	420	120-720
40	5151	5020-8880	200	120-360	400	120-720

<sup>a</sup>Six strips assayed to form each average.

<sup>b</sup>The beginning of more stringent operational procedures within the Class II clean room.

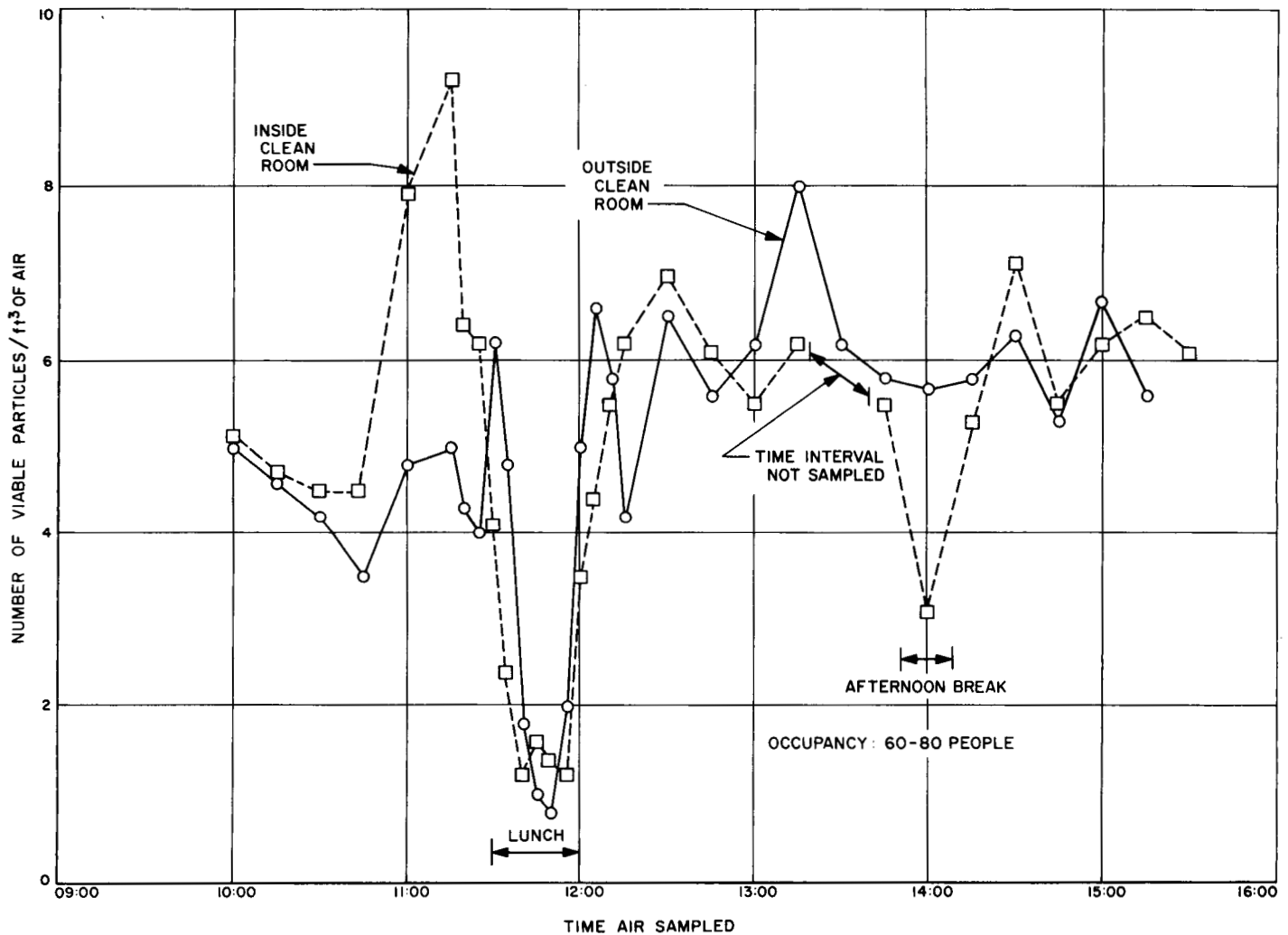


Fig. 1. Microbial contamination found in air samples from the Class II clean room

low level. The range varied from 0.00 to 0.01 viable particle per cubic foot of air sampled.

#### b. Surface sampling

*Douglas Aircraft Company.* Table 2 contains the results of a 40-week surface sampling study carried out in the Class II, III, and IV clean rooms; stainless steel strips were used to measure the microbial accumulation. Both the average value and the range are expressed as viable aerobic mesophiles recovered per square foot of surface.

*SAF.* Fig. 6, 7, and 8 contain the surface sampling data obtained during a 13-week sampling period. Three types of materials (stainless steel, glass, and Lucite) were used to measure the microbial accumulation. Significant differences in accumulation rates were not noted between the materials.

*Structural Test Laboratory.* A summary of the results of microbial surface accumulation on stainless steel strips within the hardware assembly area (non-laminar flow) is found in Table 3. It appears that the early accumulation rates closely resemble those found in a Class IV clean room.

*EASL.* A summary of the results of microbial surface accumulation on stainless steel strips within the hardware assembly area (vertical laminar flow) is found in Table 3. Accumulation rates in this area are extremely low, and a more extensive study is now being conducted.

#### 4. Discussion

This study utilized Reyniers slit samplers for detection of airborne microbial populations. The results of Reyniers air sampling are based on the supposition that the

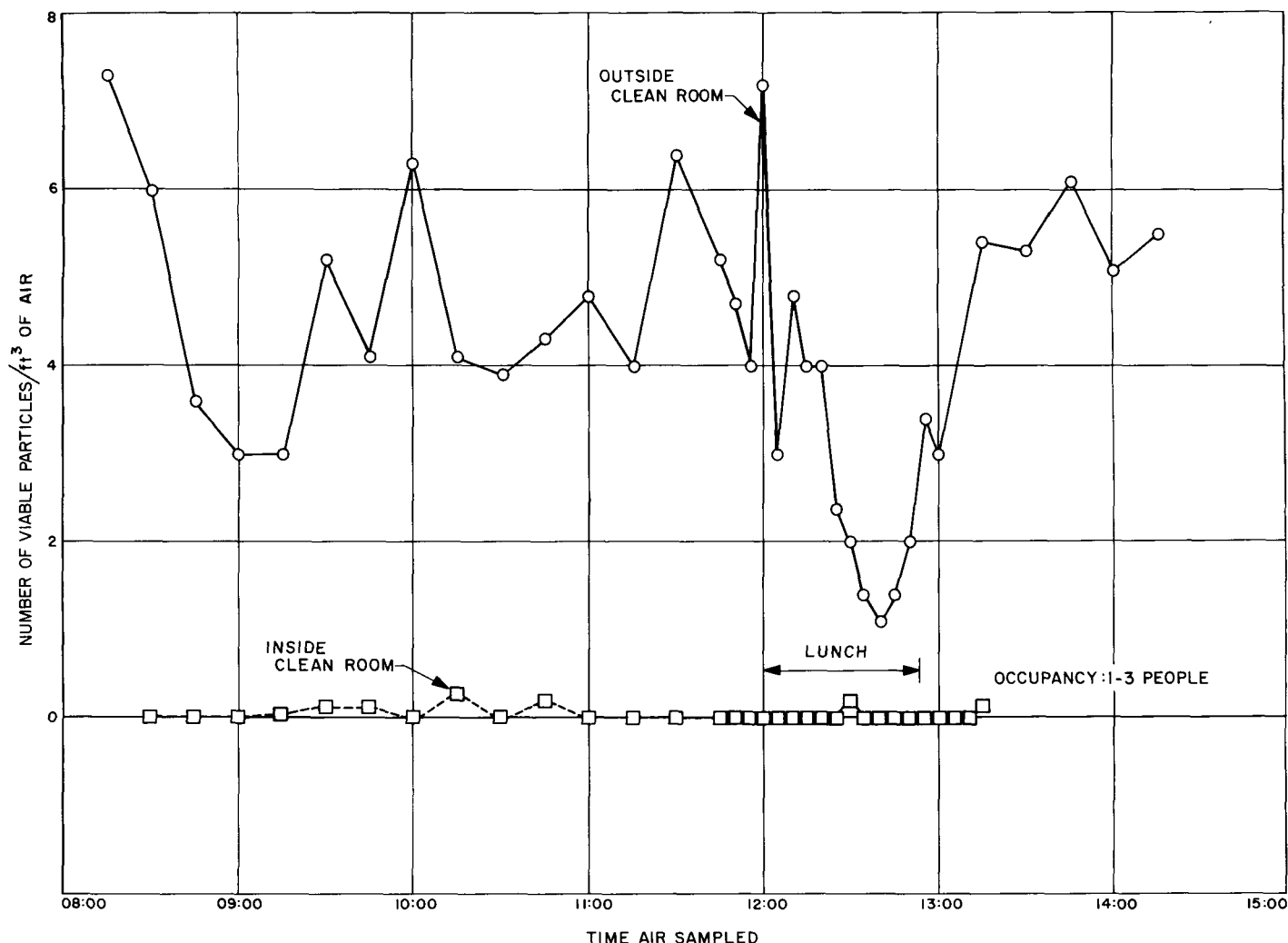


Fig. 2. Microbial contamination found in air samples from the Class III clean room

impingement of a viable particle will yield an individual colony. While this is true, it is well known that a single dust particle may act as a carrier for numerous micro-

Table 3. Surface sampling studies done in Structural Test Laboratory and the Experimental Assembly and Sterilization Laboratory

Exposure time, hr	Number of viable aerobic mesophiles recovered per square foot of surface			
	Structural Test Laboratory "clean" area		EASL vertical laminar flow assembly area	
	Average <sup>a</sup>	Range	Average <sup>b</sup>	Range
24	184	96-288	2.6	0-48
48	304	96-432	2.6	0-48
72	302	144-864	5.3	0-48
168	280	96-528	5.3	0-48

<sup>a</sup>Six stainless steel strips assay to form each average.  
<sup>b</sup>Average based on six samples from each of three sites per interval (total of 18 stainless steel strips assayed to form each average).

organisms. The impingement of this dust particle would be recorded as a single event. Investigators in this field have failed to develop a statistical method to account for this inherent error. In vertical laminar downflow clean rooms (i.e., EASL) air sampling techniques are even less reliable. Airborne microbial contamination will be detected only if the initiating event occurs in the immediate vicinity of the sampling orifice. Presently, the air sampling "state-of-the-art" is not capable of obtaining a representative airborne microbial profile of this type of clean room.

A more reliable method for assessing airborne microbial contamination is the use of stainless steel collecting strips. This method is relatively sensitive in detecting low levels of microbial contamination accumulating on the exposed surfaces. When the surfaces are environmentally exposed, the level of microbial contamination on the strips will increase to a maximum and then remain relatively

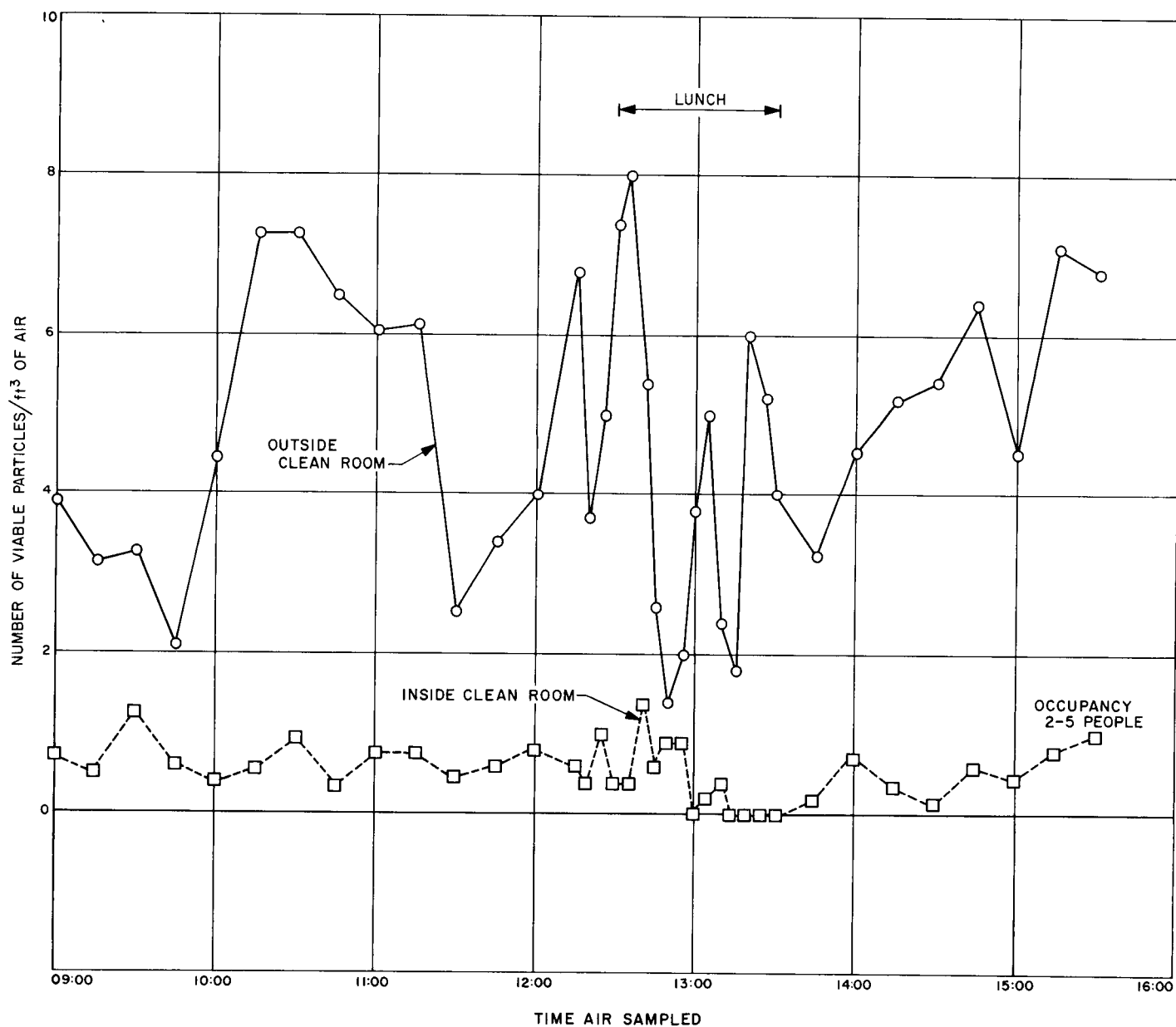


**Fig. 3. Microbial contamination found in air samples from the Class IV clean room**

constant over the remainder of the exposure period. This observation is noted in the majority of the test areas.

This phenomenon has been noted by other investigators and has been termed "plateau" (Refs. 3, 4). This plateau was observed in the Class II room (Table 2) in the 13th week of the study. At this time, the accumulation level had risen to the  $10^4$  range (10,000 to 99,000 microorganisms per square foot of surface). The plateau varied from 11,000 to 21,000 microorganisms from the 13th through the 28th week. After the 28th week, efforts were made to decrease contamination levels by the enforcement of strin-

gent personnel entry and operational procedures. These efforts resulted in a significant decline in the level of microbial surface contamination.

The Class III and IV clean rooms (Table 2) appeared to plateau very early in the study in the  $10^2$  range (100 to 999 microorganisms per square foot of surface). This level was obtained within a few weeks and persisted throughout the 40-week exposure period.

A plateau was also noted in the Spacecraft Assembly Facility (Figs. 6, 7, 8) between the 4th and 7th week. The

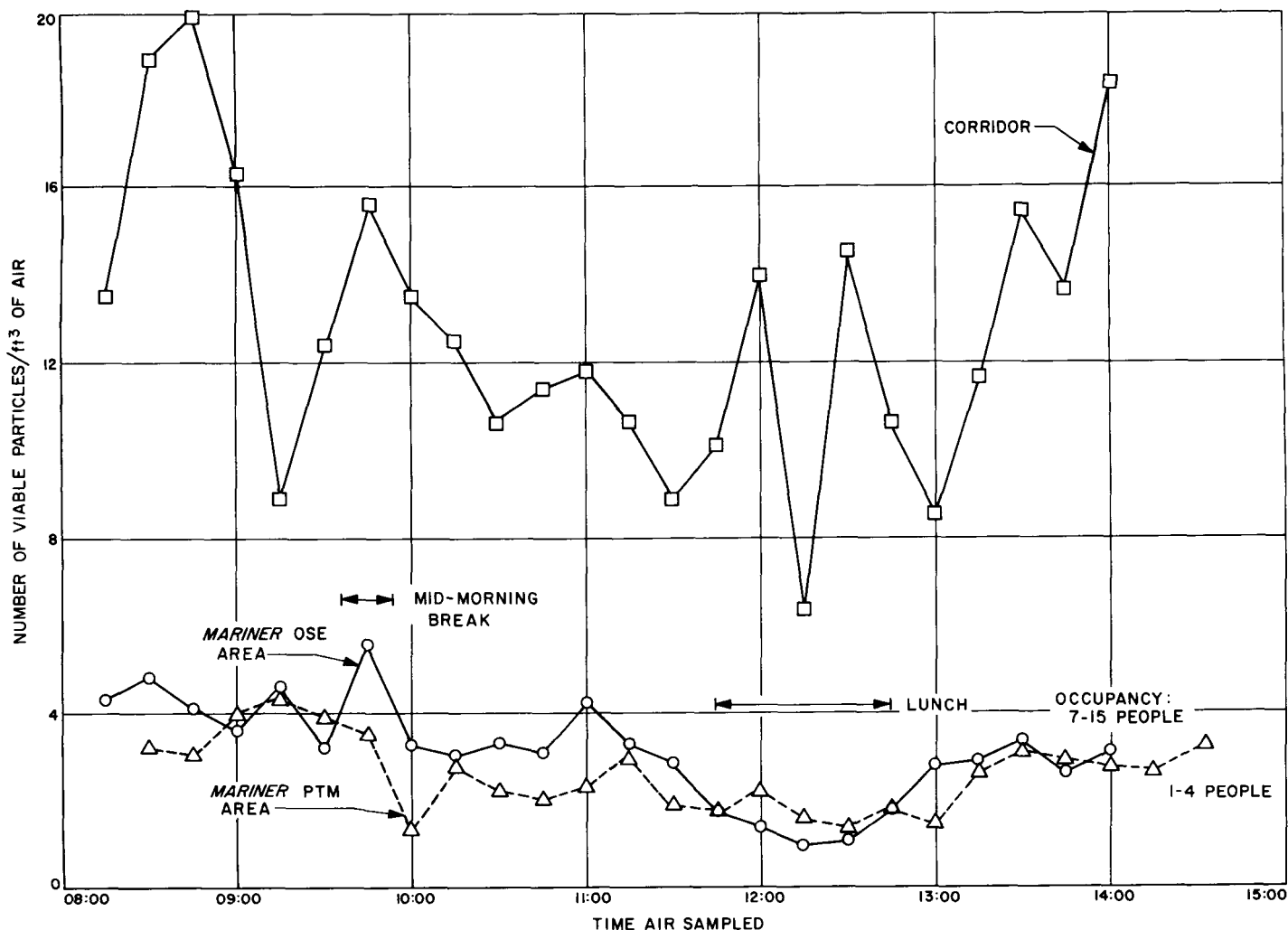


Fig. 4. Microbial contamination found in air samples from the Spacecraft Assembly Facility

accumulation level at this time was in the  $10^3$  range (1000 to 9999 microorganisms per square foot of surface).

The duration of the studies in the EASL as well as the Structural Test Laboratory (Table 3) was not sufficient to establish a plateau. Studies are presently under way in an attempt to delineate these plateau levels, and results will be given at a later date.

The most accepted theory of plateau formation is that the number of microorganisms deposited on or surviving on surfaces is balanced by the number of microorganisms dying on the same surface. Although it is emphasized that the plateau phenomenon is a result of a dynamic rather than a static system, it must be remembered that the plateaus are reached on horizontal surfaces that are not physically moved, nor subjected to maintenance proce-

dures that other surfaces in the room may undergo. Therefore, it should not be assumed that any one square foot of the tested room will contain the population of microorganisms found on the strip unless that square foot has been subjected to the identical conditions of the settling strips, and for the same duration of time.

The results of the study demonstrate a correlation between the level of airborne microbial contamination and (1) the number of personnel in the area, (2) their activity level, (3) the clothing restriction, and (4) the degree of environmental control imposed upon the personnel and the work area. These relationships have been noted by other investigators (Refs. 2, 3).

In general, as personnel numbers and activity increase, the levels of airborne microbial contamination increase.

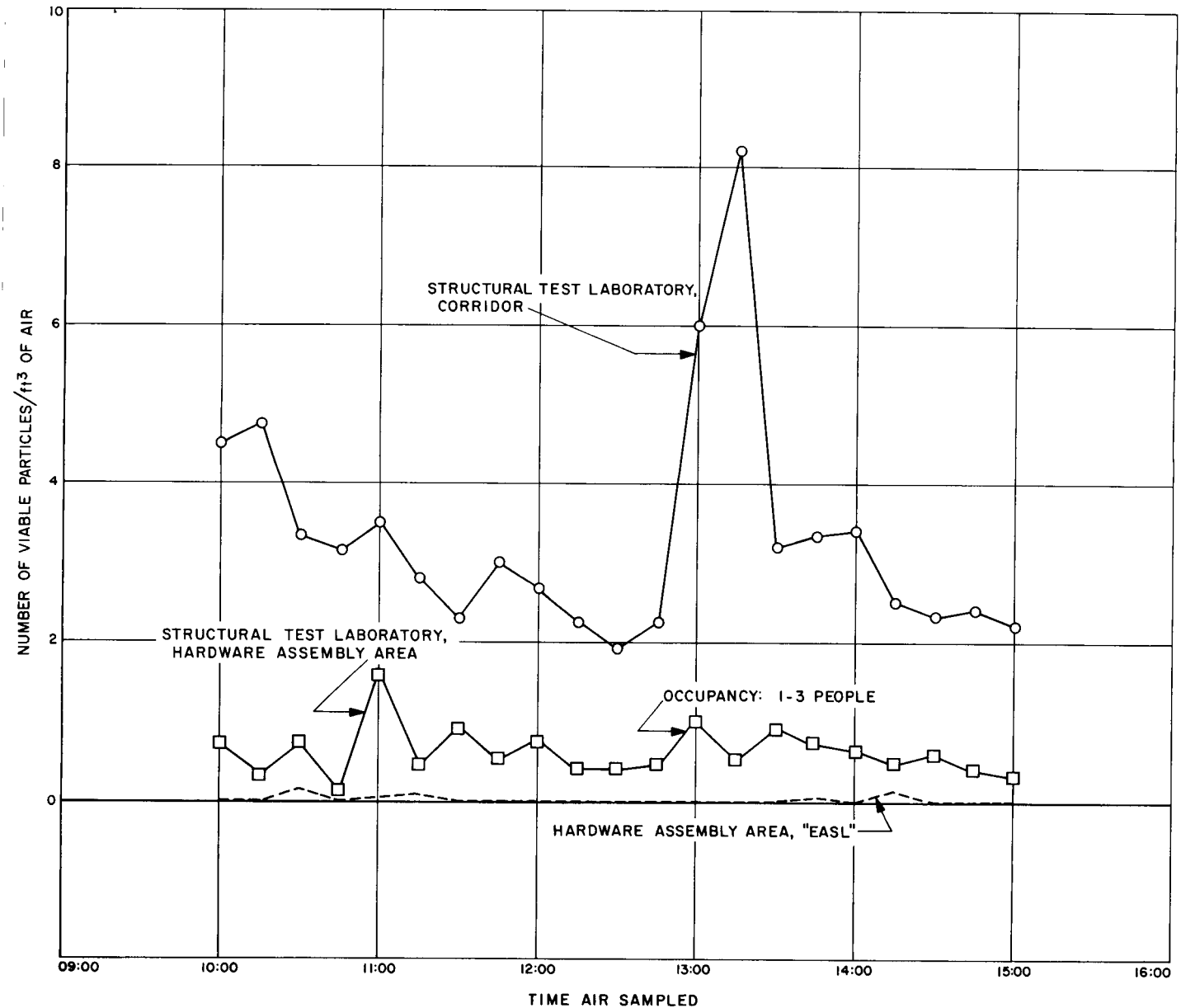


**Fig. 5. Microbial contamination found in air samples from the Structural Test Laboratory**

In the Class II (Fig. 1) and the SAF (Fig. 4) it is noted that airborne microbial counts peak at a rather high level just before lunch as activity increases in preparation for exit. (This might suggest that personnel exit in groups of two or three for lunch and break periods, in order to keep the airborne contamination level stable.) It also becomes evident from the same figures that a significant decrease in airborne counts results once exit is completed and personnel numbers and activity are minimal. At the end of the lunch period, the levels again increase with the re-entry of the personnel and the resumption of their tasks. A simi-

lar relationship is noted in the Class IV room (Fig. 3), but is not as noticeable in the Class III (Fig. 2), the Structural Test Laboratory (Fig. 5), or the EASL (Fig. 5). This observation may be attributed to the fact that the Class IV room appeared to have less restrictive procedures and a greater level of activity than either the Class III, Structural Test Laboratory or the EASL, where airborne microbial levels are normally low and personnel numbers are minimal.

Activity levels play an important part in the number of airborne organisms that may be found in a given area. Of

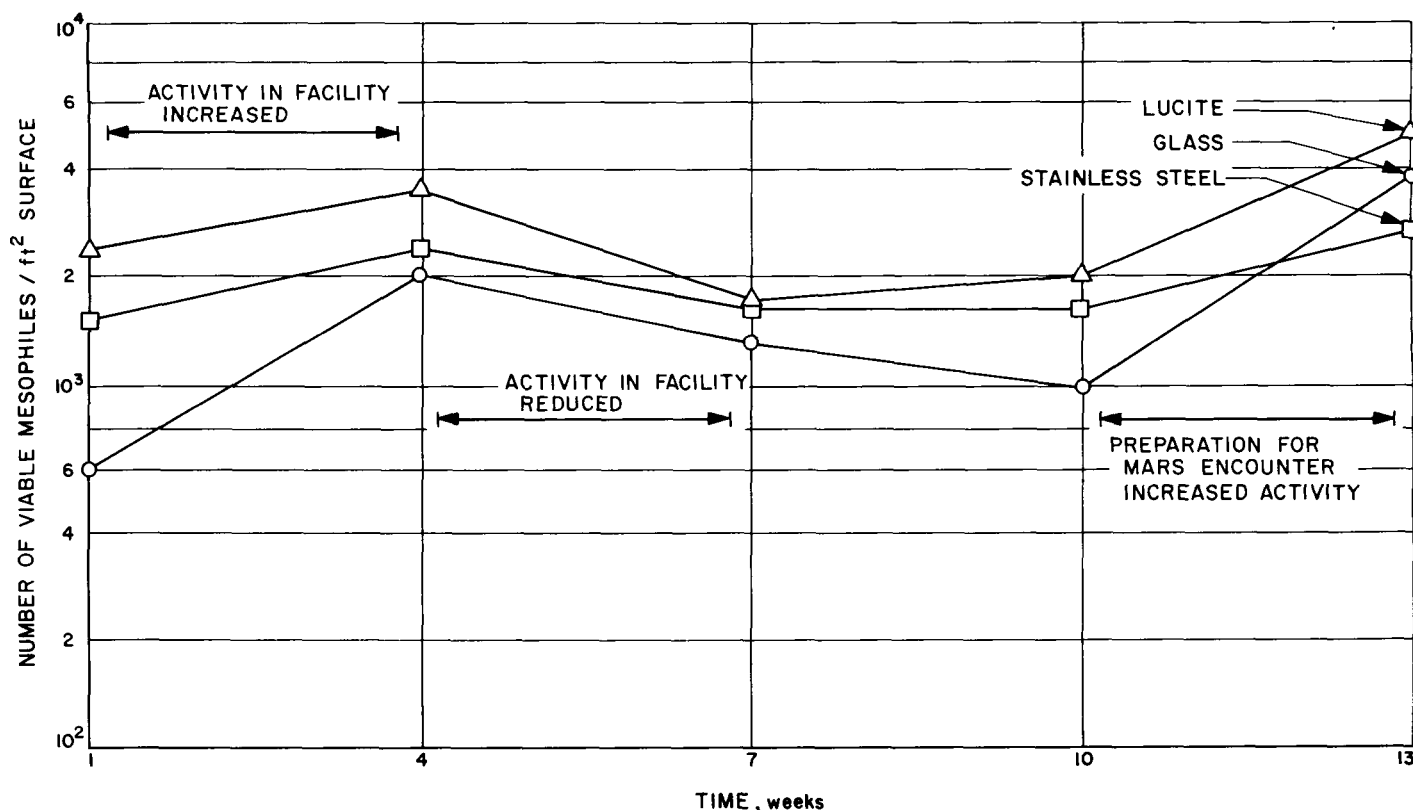


Fig. 6. Microbial fallout found on stainless steel sampling surfaces in the Ranger systems test area of the Spacecraft Assembly Facility

all the clean areas studied, the Class II clean room (Fig. 1) had the greatest number of personnel within the area, and correspondingly, had the highest level of airborne contamination. An interesting observation can be made here in that the clean room personnel would exit into a general processing area where parts were prepared for entry into the clean room proper. This processing room was utilized by the personnel as a lunch site. Approximately thirty to forty people would remain in this area for lunch, (reading, talking, and playing cards) and movement was minimal since the majority sat at tables stationed along the walls. In this example, we have a large number of personnel but virtually no activity; and as noted in (Fig. 1), the airborne viable count remains low throughout the lunch period. This strongly suggests that airborne microbial counts may be held relatively low in those clean areas where it is necessary for a large number of personnel to work together if personnel movement and activity can be held to a minimum.

The full importance of clothing restrictions has not been investigated. In general the dissemination of microorgan-

isms from personnel is relatively high where clothing restrictions are minimal. For example, the clothing restrictions in the Class III room (Table 1) were more extensive than those in the Class IV room, (Table 1) and the levels of airborne contamination detected in the Class III (Fig. 2) were less than those found in the Class IV (Fig. 3). While clothing restrictions were an important factor, it was noted that the Class III entry, exit and operational procedures were under constant supervision while those in the Class IV were not.

This implies that the degree of control imposed upon the personnel greatly influences the levels of microbial populations found within the clean room.

The importance of the implementation of rigid environmental and personnel control is again emphasized by results obtained in the Class II clean room (Table 2). The level of microbial surface contamination within the clean room had increased steadily for 28 weeks until the settling strips (when assayed) indicated approximately 18,000 microorganisms per square foot of surface. At this time,

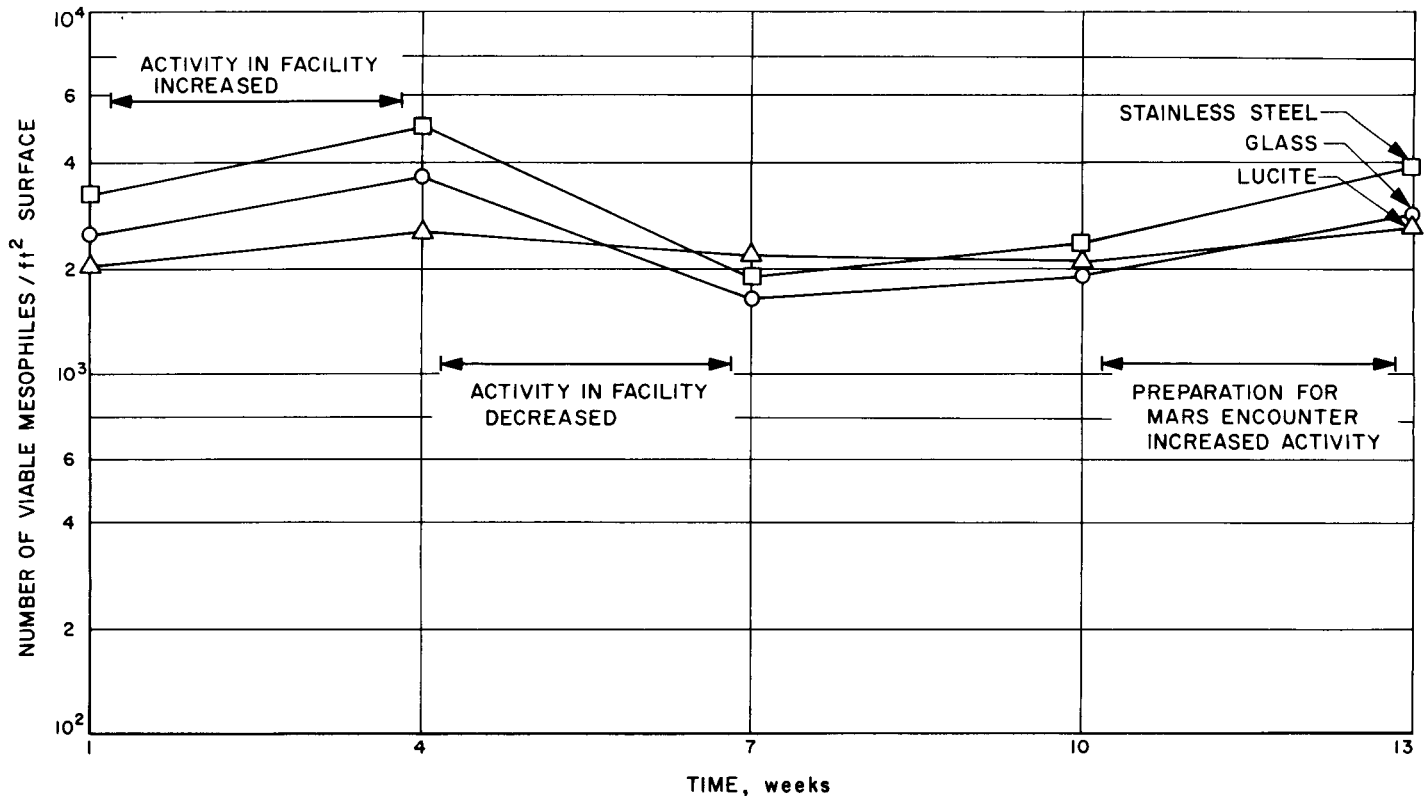


Fig. 7. Microbial fallout found on stainless steel sampling surfaces in the Mariner systems test area of the Spacecraft Assembly Facility

management initiated and enforced stringent entry, exit, and operational procedures. Within 3 weeks, the level of surface contamination had decreased significantly and lower contamination levels were noted throughout the remainder of the study.

In summation, the SAF, under prevailing test conditions, had a microbial population less than the Class II clean room, but greater than the Class III or Class IV. Although SAF and the Class II are similar in area, the Class II had a greater density of personnel and a higher level of activity, and this is reflected in the microbial population level found within the clean area. Of the six environmentally controlled areas studied, the Class II had the highest level of contamination. Although the duration of the study in the Structural Test Laboratory was limited, on a comparative time basis, the microbial population level within the Structural Test Laboratory clean area was similar to those found in the Class III and Class IV clean rooms. The lowest level of microbial contamination detected in this study was found in the EASL, where environmental control and personnel constraints were the most stringent.

## 5. Conclusions

- (1) The level of microbial contamination within a clean room facility is correlated with the number of personnel in the area, their activity level, and the degree of environmental control imposed upon the area. It appears that personnel control factors are as important as the environmental control of the room, and as personnel constraints increase or decrease, contamination levels will increase or decrease.
- (2) Under the prevailing test conditions, the JPL Spacecraft Assembly Facility is comparable in microbiological loading to an industrial Class II conventional clean room, and the JPL Structural Test Laboratory clean area is similarly comparable to an industrial Class III conventional clean room.
- (3) Additional work is necessary in order to delineate the casual effects, and the significance of the plateau. The application of these data in establishing the microbiological profile of any environment must also be critically evaluated.

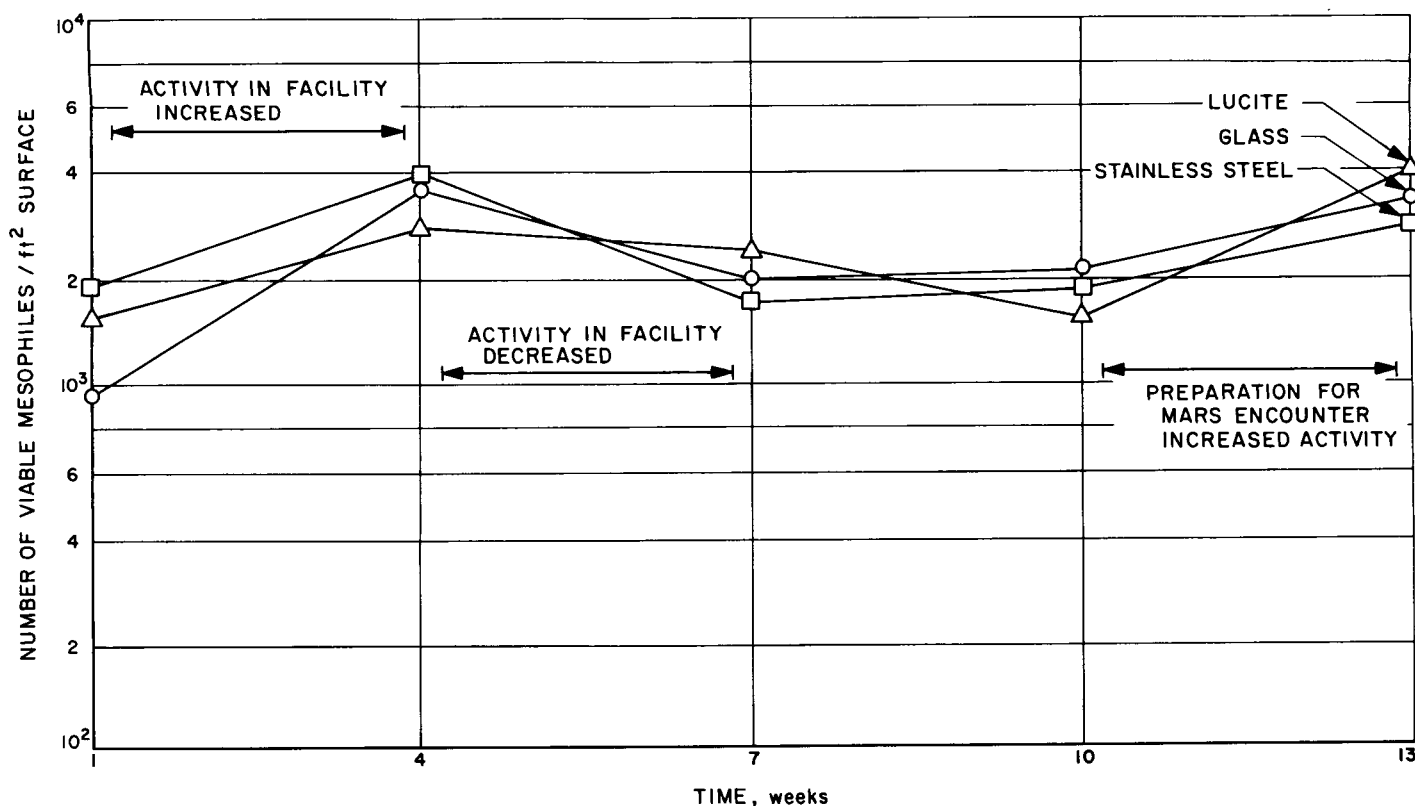


Fig. 8. Microbial fallout found on stainless steel sampling surfaces in the *Mariner* GSE and OSE test complex area of the Spacecraft Assembly Facility

## References

1. *The Microbiological Profile of Clean Rooms*, Final Report, Jet Propulsion Laboratory Contract 950920, Douglas Aircraft Company, Santa Monica, California, 1966.
2. McDade, J. J., Favero, M. S., and Michaelson, G. S., "Environmental Microbiology and the Control of Microbial Contamination," *Procedures of National Conference on Spacecraft Sterilization Technology*, NASA, Washington, D. C., 1966.
3. Favero, M. S., Puleo, J. R., Marshall, J. H., and Oxborrow, G. S., "Comparative Levels and Types of Microbial Contamination Detected in Industrial Clean Rooms," *Applied Microbiology*, vol. 14, pp. 539-551, 1966.
4. Portner, D. M., Hoffman, R. K., and Phillips, C. R., "Microbial Control in Assembly Areas Needed for Spacecraft Sterilization," *Air Engineering*, vol. 7, pp. 46-49, 1965.

### III. Spacecraft Power

GUIDANCE AND CONTROL DIVISION

N67-15704

#### **(A) Power System Configuration Study, E. C. Jazwa**

##### **1. Introduction**

In July, a contract was initiated with TRW Systems covering a 12-month "Power System Configuration Study and Reliability Analysis Program." The primary objective of this study is to determine optimum power system configurations for planetary spacecraft probes operating at 0.3 and 5.2 AU Sun-probe distances and Mars, Jupiter, and Venus orbiters. Effort is directed toward determining the problems associated with implementing electrical power systems for these spacecraft and missions and providing reliable overall system operation through the use of redundancy, failure detection and fault clearing, and the development of optimum in-flight monitoring techniques.

##### **2. Discussion**

The study approach is to synthesize and analyze model power systems for each mission and spacecraft configuration and to recommend an optimum mechanization on the basis of maximum reliability for minimum weight. Each model power system studied will include a photovoltaic power source, batteries for energy storage, and power

conditioning, distribution and control equipment. The analysis will cover various power distribution methods, including AC, DC and combined AC/DC distribution, and various voltage regulation techniques. A failure analysis will be performed for each power system mechanization to determine the most effective use of redundancy, failure detection methods and functional element switching.

The assumptions, data, and design tradeoffs will be summarized and presented in a "Spacecraft Power System Configuration Reference Manual" at the completion of the study. The manual is intended as a design reference to determine optimum solar array/battery power system mechanizations for spacecraft performing missions in the 0.3 to 5.2 AU region at power levels in the range of 100 to 4000 watts.

To date the following progress has been made. Seven spacecraft configurations have been generated to perform the five basic missions shown in Table 1. These provide the basis for the conceptual design of baseline and alternate power supply configurations. Mission profiles and electrical load profiles for each basic mission and spacecraft configuration have been generated, and typical load

Table 1. Model spacecraft characteristics

Mission	0.3-AU probe	Venus orbiter		Mars orbiter	5.2-AU probe	Jupiter orbiter	
Spacecraft	Mariner class	Mariner class	Voyager with entry probe	Voyager with lander	APP class (spin stabilized)	APP class	Voyager class (with probes)
Launch vehicle	Atlas/Centaur /HEKS or Titan III C/Centaur	Atlas/Centaur	Saturn IB/ Centaur or 2/1 Saturn V	Saturn V (2/1)	Atlas/Centaur /TE-364 or Atlas/Centaur /HEKS	Saturn IB/ Centaur/HEKS	Saturn V
Spacecraft injected weight, lb	900	1500	9000	20500	650	2800	16000
Gross power capability at target, watts	350	300	1000	600	200	300	600
Spacecraft science payload, lb	60	50	250	400	50	250	500

equipment and input power characteristics have been defined. Solar array current-voltage characteristics have been computed for each mission, and design points established by comparing solar array power capability as a function of mission time with the model spacecraft load profiles.

The next phase of the study will be concerned primarily with the synthesis of baseline power system configurations and alternate mechanizations based on improved reliability.

N67-15705

## B. Sterilizable Battery, R. Lutwack

### 1. Development of Separators for Sterilizable Batteries

The development program for a separator for the Ag-Zn battery comprises research and development contracts with the Narmco Division, Whittaker Corporation, Monsanto Research Corporation, and Westinghouse Electric Corporation and a continued evaluation of separator materials produced by the RAI Research Corporation under a JPL contract.

*a. JPL Contract 951091 with Narmco Division, Whittaker Corporation.* This effort has been centered on producing films of poly-2,2'-(hexamethylene)-5,5'-bis (1- $\beta$ -cyanoethyl) benzimidazole. Films have been prepared which have satisfactory resistivity and Ag diffusion properties. The immediate aim is to develop the technique required to produce uniform film in quantities sufficient for evaluation in the Ag-Zn cell.

*b. JPL Contract 951524 with Monsanto Research Corporation.* The objective of this program is to investigate ligand-containing polymers for use as separators in the

Ag-Zn battery. In the initial phase polystyrenes, polyacetals, and 1-1 copolymers containing a ligand group in each polymer unit were synthesized and tested for stability at 135°C in an N<sub>2</sub> atmosphere and in a 40% KOH solution. These conclusions have been obtained: (1) Styrene polymers containing 8-hydroxyquinoline and salicylic acid as ligand units coupled with an azo linkage had poor stability. Scission occurred at the azo linkage, and no further azo-type polymers will be made. (2) Copolymers of 2-vinylpyridine and acrylic or methacrylic acid are very resistant to KOH at 135°C, but the films have been brittle. (3) The stabilities of polyacetals are so limited, decreasing with increasing hydroxyl content, that they are not acceptable. (4) The stabilities of polymers prepared by substituting ligands on polystyrene through a methylene linkage seem to be limited by the stability of the particular ligand. (5) The polymers which seem to be sufficiently resistant to KOH are styrene-acrylonitrile copolymers, polystyrenes with amino and sulfonic acid substituents, poly [vinylbenzyl-1-( $\beta$ -amino ethyl)-2-methyl-2-imidazoline] and poly [vinylbenzyl-1-(2-pyridylmethylamine)]. The present phase continues with polymer syntheses, stability tests, and preparation of membranes.

*c. JPL Contract 951525 With Westinghouse Electric Corporation.* The major effort of this program is the investigation of composite membranes as separators for Ag-Zn batteries. A composite membrane is composed of: (1) an organic matrix with adequate resistance to KOH at 135°C and with the necessary flexibility and strength properties and (2) an inorganic phase which provides the selectivity for necessary diffusion and ionic conductivity properties. The candidate materials for the matrix which have been shown to have high stability are polypropylene, Teflon and other fluorocarbons, polyphenyleneoxide, and polysulfone. The inorganic filler substances with the necessary limited solubility in 40% KOH at 135°C are Zr(OH)<sub>4</sub>,

MgO, CaO, and ThO<sub>2</sub>. A number of membranes were fabricated from various combinations of base, binder, and filler, and resistivity and alkali diffusion measurements have been made. It has been shown that membranes with resistivity and diffusion values comparable to cellophane can be made.

A secondary effort is the investigation of the incorporation of chelating groups into the structure of an organic polymer for the purpose of imparting selective permeability characteristics. The effort has been centered on the preparation of intermediate compounds which contain the active chelating moiety characteristics of 8-hydroxyquinoline. A side chain secondary amino group at the 7-position allows the incorporation of these compounds into epoxy resin structures. These modified polymers will then either be cast into films or impregnated on a flexible matrix.

*d. Separator material from JPL Contract 951015 with RAI Research Corporation.* The Electric Storage Battery Company and JPL are continuing to evaluate RAI-116 separator material for uniformity and performance in sterilized Ag-Zn cells. Cells made with four layers fail after 15 cycles of 100% depth of discharge. During cycling, the material is progressively loaded with Ag and in this aspect is similar to cellophane. An evaluation on RAI-110 is being done concurrently; no cycle data are available.

## **2. Research and Development of the Heat Sterilizable Battery**

The contract with the Electric Storage Battery Company, Yardley, Pennsylvania, is for a research and development program for sealed Ag-Zn and Ag-Cd cells capable of providing satisfactory electrical performance after heat sterilization in the uncharged condition and high impact resistance after charging.

*a. Electrochemistry task.* The results of several of the studies which comprise this task are: (1) There is a weak temperature dependence of the dissolution of ZnO in 35, 40, and 46% KOH for the range of 10 to 145°C. (2) Sterilization causes severe losses in cell capacity if HgO is pres-

ent in the negative plate; as little as 2% HgO results in a loss of 50% capacity. (3) PbO cannot be used as an additive in the Zn plate to prevent gassing, since it recrystallizes throughout the cell on cooling after sterilization, causing short circuits. (4) Absorbers made from EM 476 polypropylene do not affect the Ag plate capacity. (5) Gassing of a non-uniform Zn plate proceeds as if uniform sections, having different Tafel overvoltages, are connected together; the section with the lowest Tafel overvoltage gases first. This emphasizes the importance of fabricating Zn plates from well-blended mixes.

*b. Cell case task.* Preliminary studies of cell case materials had been directed toward the qualification of polyphenylene oxide (PPO) and polysulfone (PS), these two having been shown to be the best of the available materials. No further work with PS is planned because of a severe surface crazing problem, which is also a problem with some PPO grades. Extensive tests have been conducted with different grades of PPO to determine the structural, molding, sealing, and sterilization properties. It has been shown that grade 531-801 has the most of the properties required for a sterilizable case material, although some problems remain. For example, the sealing technique is not completely defined; a procedure using a combination of hot gas welding and epoxy bonding seems to be satisfactory. If the present conclusion is substantiated that surface crazing of PPO grade 531-801 can be eliminated by carefully controlling the molding, then it will be selected for the case material.

*c. Cell fabrication and test task.* Three types of cells, varying in plate thickness and structure, have been fabricated and tested. Impact testing was done at JPL at an averaged shock load of 6000 g, and failure analyses showed that: (1) the PPO 531-801 case suffered corner breaks, attributable to poor molding; (2) the epoxy bonding was ruptured in some cases; (3) breakage of the subcovers indicated a need for a redesign to strengthen this part; (4) the thickest Ag plate had the greatest damage; and (5) the damage was dependent upon the direction of the cell impact, as was expected. The cell now includes redesigned plate struts and separator supports. Cycling data are being obtained for this cell.

## IV. Spacecraft Control

### GUIDANCE AND CONTROL DIVISION

N67-15706

#### **A. Propulsive Lander Control System, R. J. Mankovitz**

##### **1. Introduction**

The following report presents a description of a "nominal" control system designed to meet most of the lander performance requirements. In subsequent reports, the detailed problem areas will be discussed, along with the special control modes required to handle them.

The basic performance requirements for the system are to "land" with a vertical velocity of less than 25 ft/sec, a horizontal velocity of less than 5 ft/sec, and an attitude within 10 deg of local vertical.

As a tool for the investigation of the systems, a three-degree-of-freedom (motion in a plane) digital simulation program was written, using DSL/90 (Ref. 1) and the IBM 7094.

##### **2. Description of Nominal Landing**

The three major assumptions for the nominal landing are that the ignition is started by a 20,000-ft slant range mark from the radar system, and that at least 3 of the 4 radar beams remain locked throughout the flight. Thirdly, it is assumed that no staging of the aeroshell is performed.

The following is a nominal case using the VM-8 atmosphere model with worst case continuous winds.

Prior to light-up, the craft is undergoing aerodynamic oscillations about a zero attack angle (Fig. 1). These are on the order of 10 deg, as shown in Fig. 2 (curve 1). The primary cause is poor aerodynamic damping in the transonic region, coupled with a 0.1-ft CG offset.

At a slant range mark of 20,000 ft, as indicated by the radar system, the control system is activated. In the case of VM-8, this occurs at an altitude of 11,000 ft, and at an attitude angle (with respect to local horizontal) of 36 deg, corresponding to the atmospheric path angle.

For the initial 2 sec after ignition, the system is in the stabilization mode. In this mode, the craft's attitude is inertially stabilized, counteracting the thrust offset and aerodynamic torques on the craft. As shown in Fig. 3, this mode consists of wide-angle position gyros (which are uncaged at shutoff), and rate gyros for compensation. This rate-plus-position signal is used to differentially throttle the engines, producing the necessary corrective torques. During the stabilization period, a constant acceleration is commanded, nominally 26 ft/sec<sup>2</sup>. From Fig. 2 (curve 1),

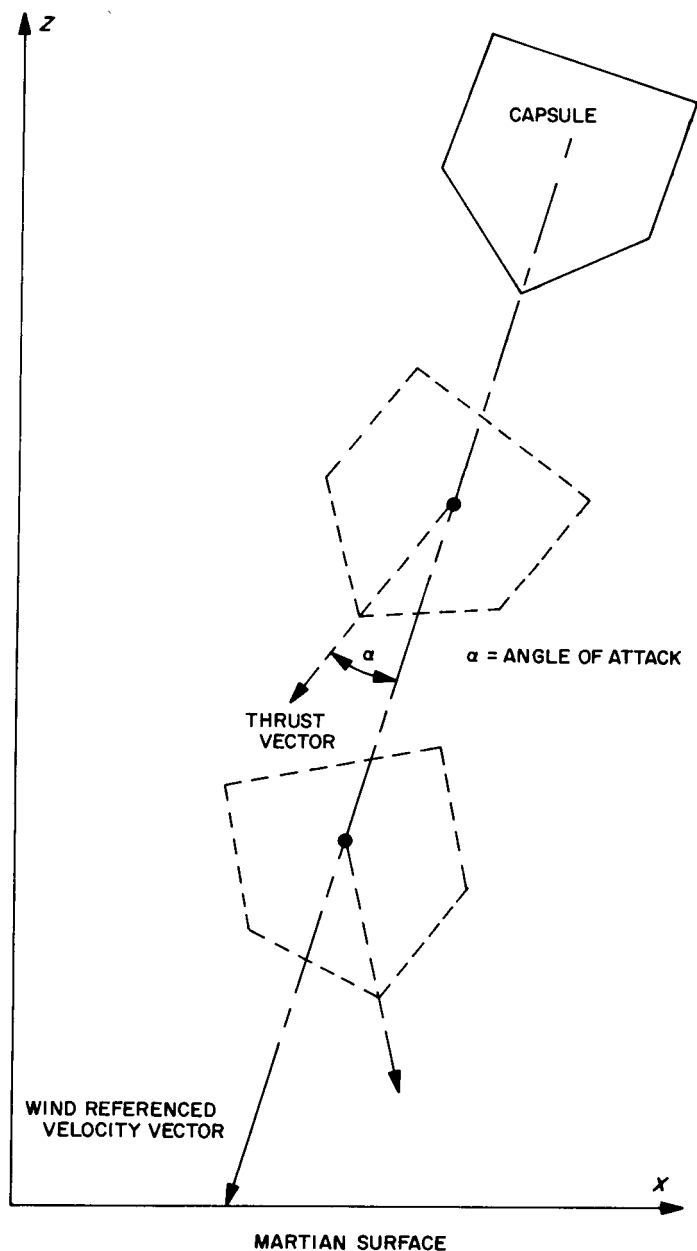


Fig. 1. Lander aerodynamic oscillations

it can be seen that the craft's attitude is stabilized during this period with typically less than 0.1 deg change in attitude. This figure is from a typical three-degrees-of-freedom run.

Almost immediately after ignition, the exhaust gases from the engines interfere with the normal aerodynamic flow. This causes a general reduction in aerodynamic forces, by a factor of 4.

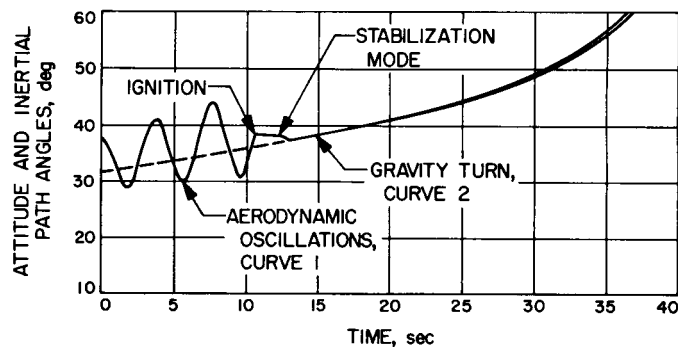


Fig. 2. Typical three-degree-of-freedom data for gravity turn

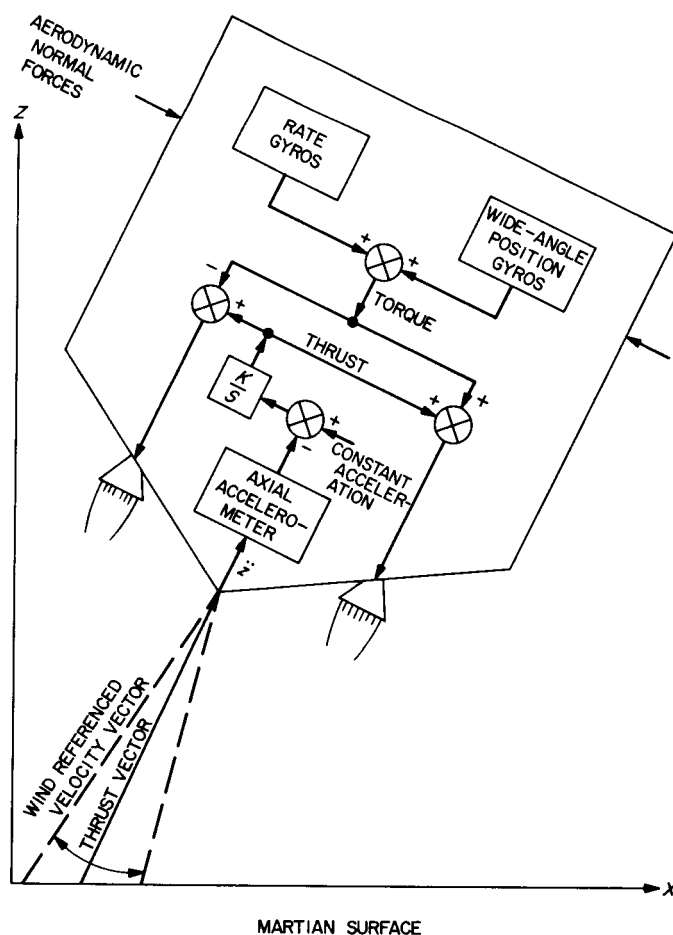


Fig. 3. Lander stabilization mode

At the completion of the stabilization mode, the gravity turn is initiated. During this mode, the craft's attitude must be such that the thrust vector is aligned with the inertial velocity vector. Considering the worst case wind direction, the inertial path angle is initially at 32 deg, as shown in Fig. 2, curve 2. To ensure following a gravity

turn, the ratio of transverse to total velocity, as measured by radar, is used to torque the gyros (see Fig. 4). This velocity ratio is a measure of the gravity turn angular error which is reduced to near zero by the engine torquing system. From Fig. 2, this gravity turn "acquisition" can be seen to occur from 12.6 to 13 sec, at which time the roll axis is aligned to the inertial path angle. The craft maintains this attitude until terminal mode is initiated.

During the gravity turn mode, using the range,  $R$ , and velocity,  $V$ , data from the radar system, the instantaneous axial acceleration,  $A$ , required to land with zero vertical velocity is computed from the equation:

$$A = g_m + \frac{V^2}{2R} \quad (1)$$

where  $g_m$  = Martian gravity. The actual capsule axial acceleration,  $\ddot{z}$ , as sensed by an accelerometer, is compared

with  $A$ , and the integral of the error is used to set the thrust level (see Fig. 4). Eq. (1) is the required acceleration for zero velocity at zero range. To permit the use of a terminal mode, the radar range signal is biased by 28 ft, to force a "landing" at this altitude, at which time the system is switched into the terminal mode.

At an altitude of 30 ft, the control system removes the torquing signals from the gyros, thus locking the craft's attitude in an inertial hold. The computed acceleration,  $A$ , signal is removed from the thrust loop, and a constant velocity of 5 ft/sec is commanded (see Fig. 5). This constant velocity can be seen in curve 1 of Fig. 6, where the terminal mode was initiated at 30 ft. When the craft reaches an altitude of 10 ft, the engines are shut off, and the capsule drops to the surface. Typical terminal conditions are: a vertical velocity of 18 ft/sec, a horizontal velocity of 2 ft/sec, and an attitude angle of 85 deg with respect to horizontal. A typical range curve, showing the capsule trajectory, is in Fig. 7.

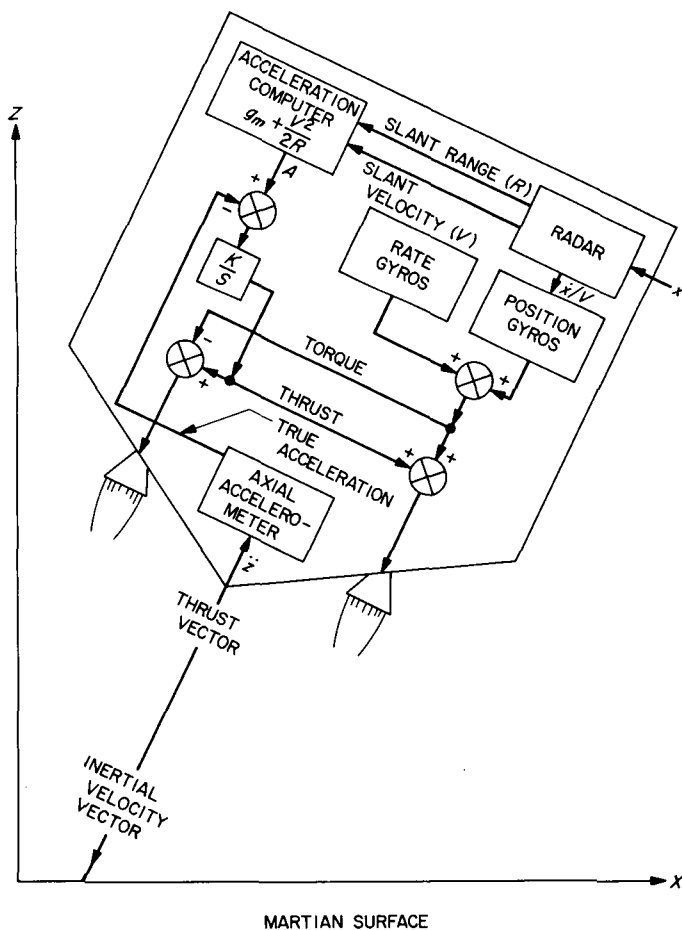


Fig. 4. Lander gravity turn mode

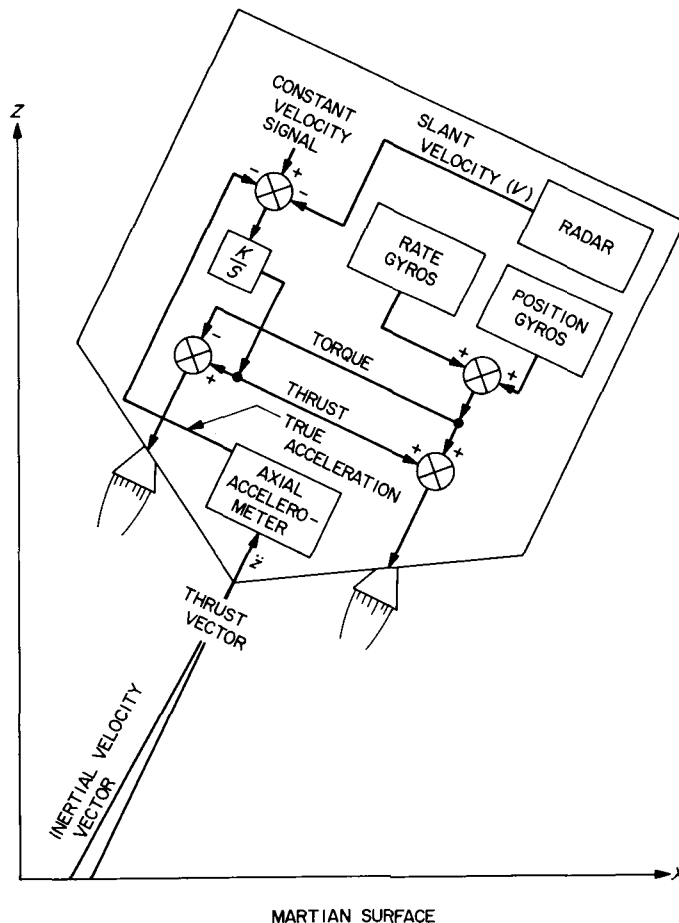


Fig. 5. Lander terminal mode

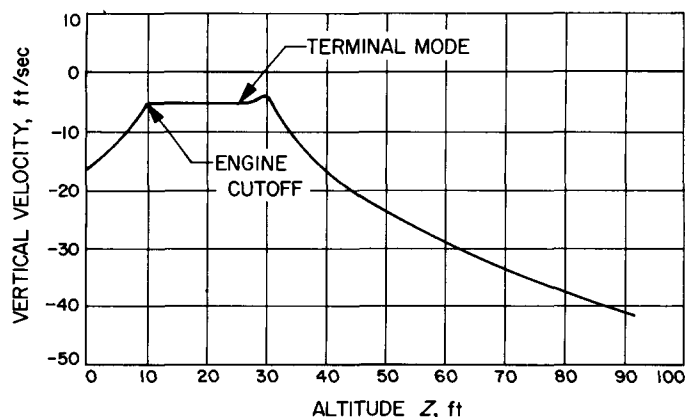


Fig. 6. Lander vertical velocity in terminal mode

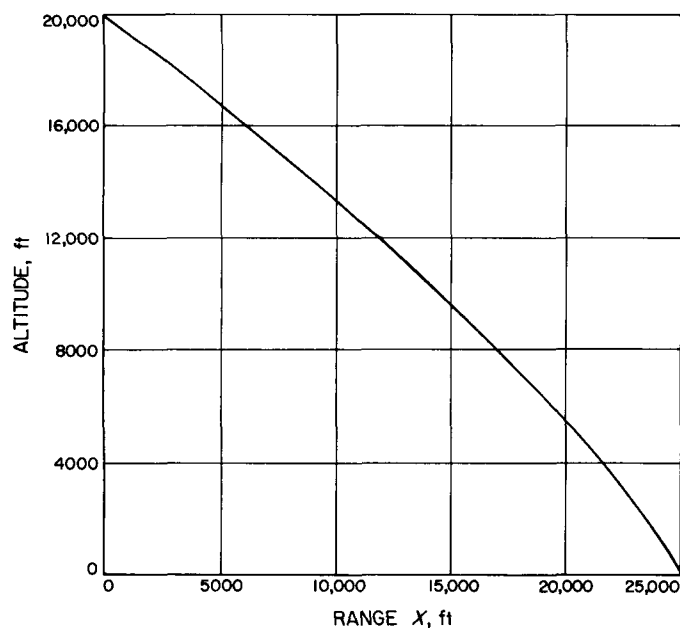


Fig. 7. Lander range curve

### 3. Description of Control Modes

**a. Motor ignition.** For this study, the criterion for ignition was a slant range mark, nominally 20,000 ft, which is not a completely desirable method from a control viewpoint. This is because in the less dense atmospheres, where the propulsion system must take out the most  $\Delta V$ , the path angles are shallow and the actual altitude is much less than the slant range. In the more dense atmospheres the path angles are steep and the altitude is almost equal to the slant range. A system which ignites soon enough to land in a light atmosphere ignites much too soon in a heavy atmosphere possibly requiring special modes to land without expending all the fuel.

A better method of ignition would be an omnidirectional altitude marking radar, but such a radar would be difficult to implement and would require large amounts of power. Possibly a compromise could be effected if the doppler and range descent radar were turned on and the minimum of the operational beams used to mark ignition. This will always be less than the slant range and thus help minimize the ignition altitude spread.

**b. Stabilization mode.** The purpose of the 2-sec stabilization period is to inertially stabilize the craft permitting radar system lock. During this radar acquisition period, it is required that the rates of change of velocity be less than 80 ft/sec<sup>2</sup>, and the rate of change of slant range be less than 4000 ft/sec. After radar has acquired, 10 times the above values are allowable before the tracking capability is lost.

If no stabilization mode were included, the capsule attitude would be attempting to null the attack angle (i.e., align with the atmospheric referenced velocity). Due to the random wind gusts, however, the atmospheric path angle varies rapidly, causing large random changes in capsule attitude; employing the inertial-hold mode makes the capsule insensitive to these atmospheric variations.

Fig. 8 is the block diagram of the torquing system. The wide-angle gyros are uncaged at ignition, and their output (proportional to angular error) is used to provide torquing signals to the engines. The rate gyros provide the necessary damping for the loop. The three sources of torque which must be nulled by the pitch-yaw attitude system are aerodynamic torques, thrust-offset torques, and fuel-slosh torques. In the case of the heavy (VM-10) atmosphere with wind gusts, the aerodynamic torques can

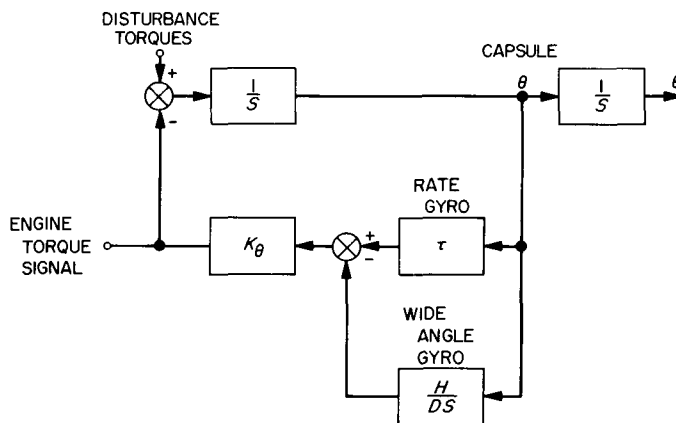


Fig. 8. Attitude stabilization control loop

be on the order of 500 ft-lbs. Another disturbance torque is created by the thrust offsets (i.e., differences in engine moment arms). For the offset value used (0.1 ft), a torque as great as 300 ft-lb can occur when operating at a maximum thrust. A third disturbing torque is that created by fuel slosh. Fig. 9 shows a profile of slosh torque for a VM-10 atmosphere case.

In the roll axis, attitude is maintained by having jet vanes in each engine. The control loop is basically the

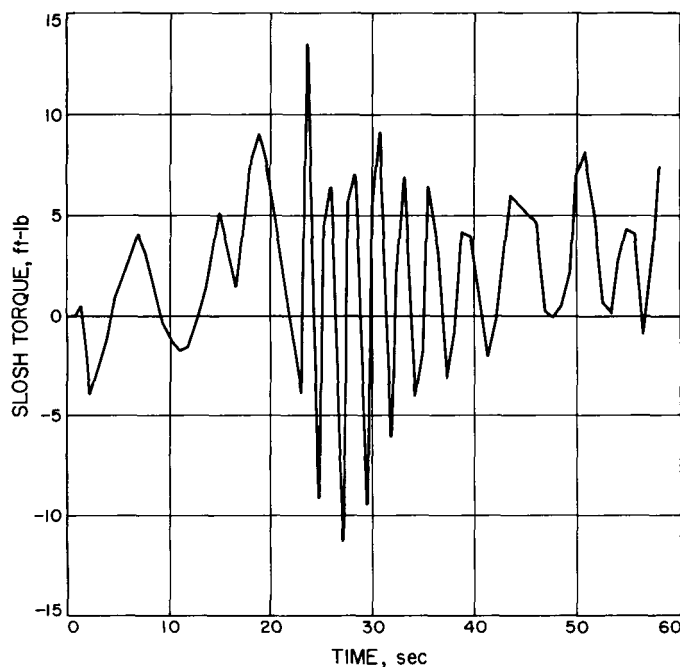


Fig. 9. Slosh torque in VM-10

same as the pitch-yaw configuration, requiring wide-angle and rate gyros. The major sources of torque disturbance in the roll axis are thrust misalignment (e.g., a 1-deg misalignment can generate more than 300 ft-lb of roll torque), and unsymmetrical ablation of the aeroshell. Presently, little is known about the magnitudes of the latter effect.

Since no radar information is available until acquisition, a constant acceleration level is commanded. This level is chosen so that the engine thrust level will be nominally mid-range, allowing large margins for the differential torque signals to operate. An axial accelerometer senses the true craft acceleration, including the drag force, and is used to close the loop around the commanded acceleration. A 26 ft/sec<sup>2</sup> level results in approximately 2000 lb of total thrust during this mode.

### c. Gravity turn mode.

**Computed thrust.** After the stabilization is completed and at least three radar beams are acquired, the system begins a gravity turn. The acceleration computer is started and fed into the thrust control system. Using the law  $A = V^2/2R + g_m$ , as explained for Eq. (1), the capsule begins the turn. If the calculated acceleration is below about 25 ft/sec<sup>2</sup>, a retarded thrust mode is initiated, as explained below. Assuming this is not the case, the gravity turn begins with the calculated acceleration going into the thrust control loop whose simplified block diagram is shown in Fig. 10. The engine's total thrust can slew at a rate of 7000 lb/sec with this loop. The thrust saturation signal represents feedback from either chamber pressures or actuator positions, and is used to prevent the possibility

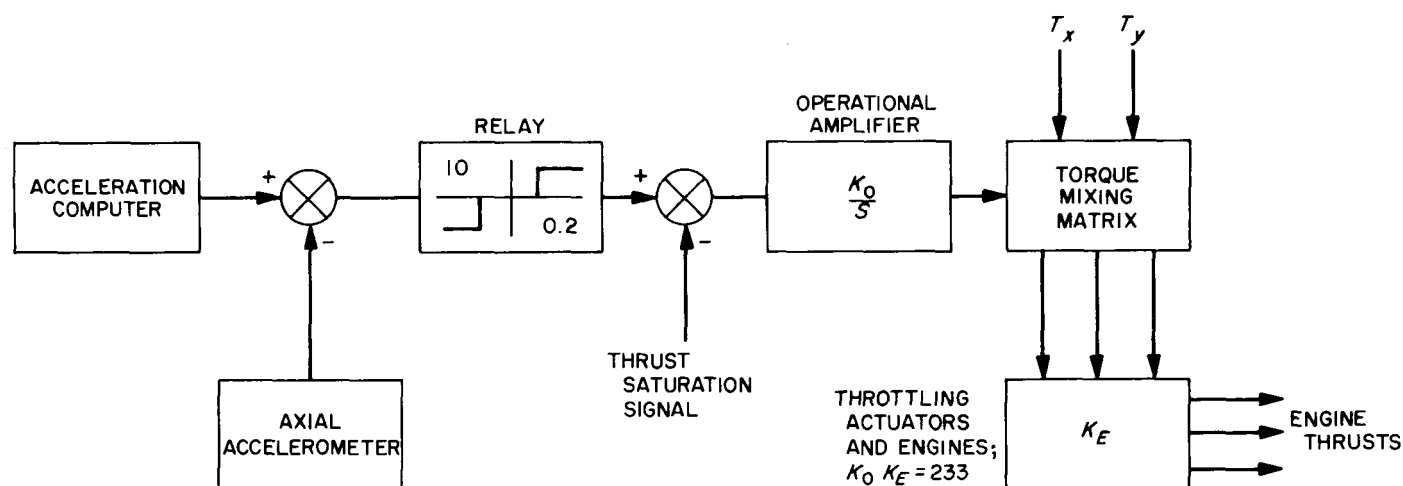


Fig. 10. Simplified gravity turn thrust control loop

of the engines all being at maximum or minimum at the same time, thus preventing torque generation. If, for example, nearly maximum thrust and large differentials for torquing purposes are needed simultaneously, the acceleration requirement is sacrificed for attitude stability.

One of the most important aspects of a gravity turn is that the thrust should be aligned exactly opposite to the velocity vector. Failure to do this results in a degradation of the terminal conditions. During the stabilization period, the original atmosphere-referenced attitude is held by the gyros; now, the gyros must be torqued to bring the attitude into coincidence with the planet-referenced velocity. The doppler radar measures velocity in the body-coordinate system, and, if the attitude were correct, only the body roll component would be non-zero. Fig. 11 shows the pitch and yaw control loops when in the gravity turn mode.

Typical wide-angle gyro parameters assumed for the study were  $K_r/H$  of 360 deg/hr/ma, and  $H/D$  of 0.4. The gyro torque amplifiers were set to saturate at 100 ma.

Referring back to Fig. 2, curve 1, one can see at 12.6 sec the gravity turn was initiated and its gyros were torqued until, at about 13 sec, the attitude angle coincided with the planet-referenced velocity vector.

*Retarded thrust.* As discussed under *Motor Ignition*, the use of slant range for a shutoff criterion has the disadvantage of causing high ignition altitudes for the heavy atmospheres. This condition leads to the possibility that the heavy VM-10 atmosphere may require more fuel than the high velocity VM-7 case. This is due to the fact that long descent times would be required in the heavy atmosphere, because of high ignition altitude and low velocities.

In an effort to optimize the fuel consumption by requiring VM-7 to determine the maximum propellant required, a retarded thrust mode is introduced.

At the completion of the stabilization burn, the craft is oriented in a gravity turn. At this time, if the acceleration computer is requesting less than a 2.1 thrust-to-weight

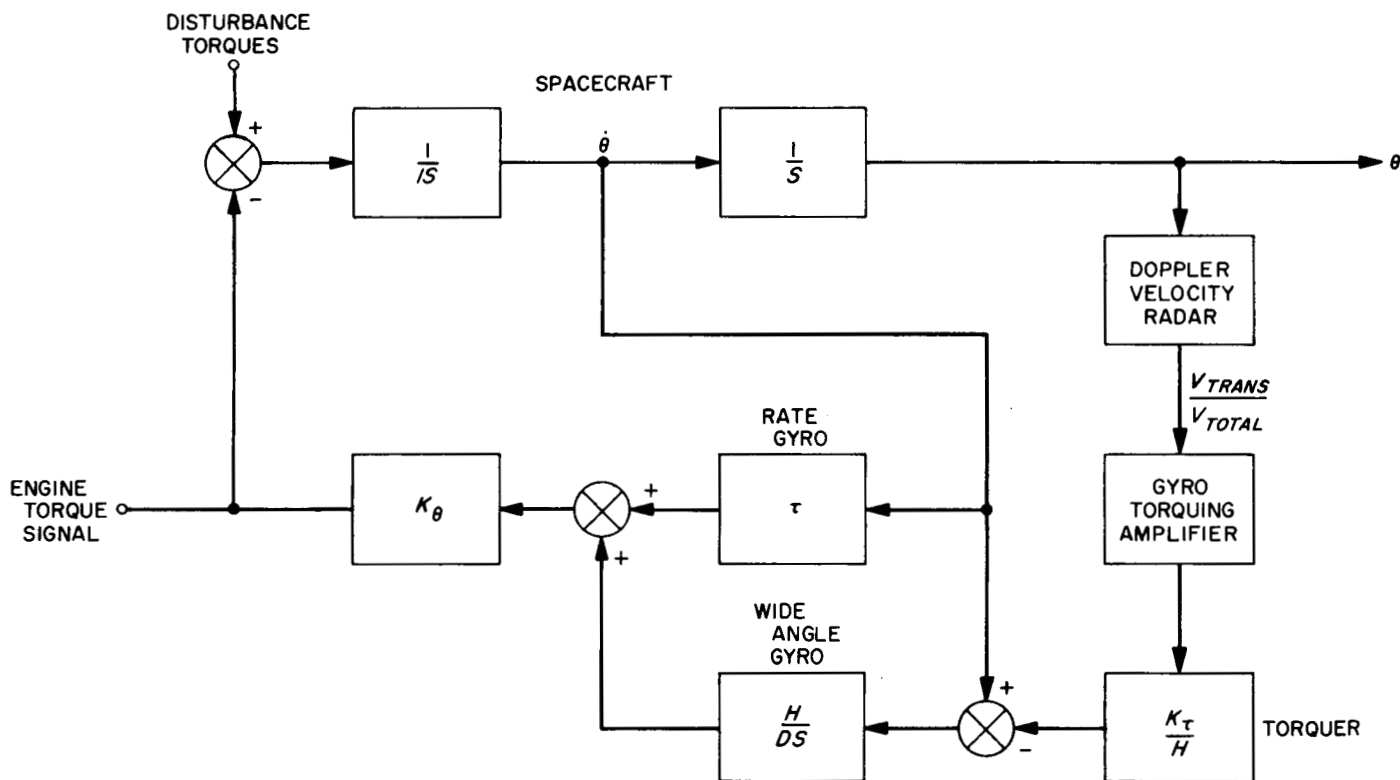


Fig. 11. Pitch and yaw control loop for gravity turn

ratio (25.9 ft/sec<sup>2</sup>), the engines are throttled to their minimum setting. The craft's velocity will increase or decrease in an effort to reach terminal velocity.

The control system remains in this mode until the acceleration computer requests at least a 2.1 thrust/weight ratio, at which time the acceleration computer output is switched into the loop and used to thrust the engines. During the retarded thrust mode, the thrust control loop is identical to that used in the stabilization mode, except that the constant acceleration commanded is not a nominal level, but a minimum level.

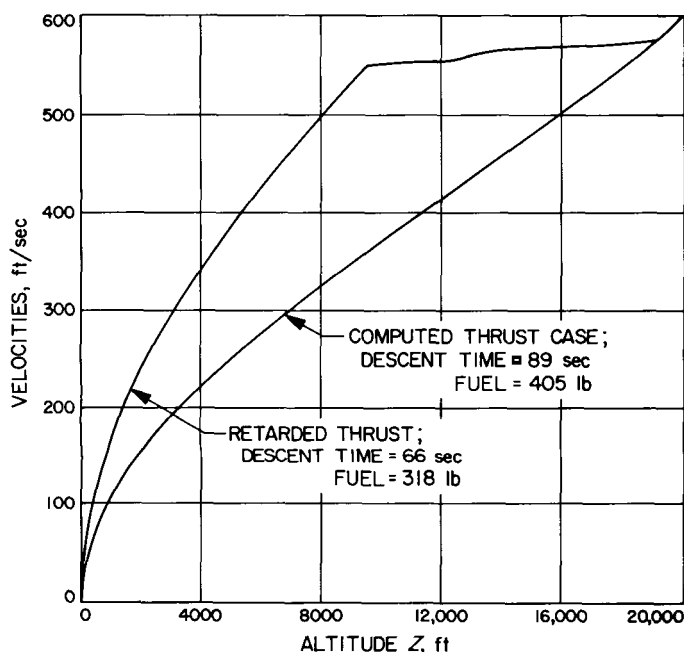


Fig. 12. Retarded thrust comparison VM-10

Fig. 12 shows a comparison of the velocity versus altitude curves for a retarded thrust and a computed thrust case in the heaviest (VM-10) atmosphere. From the curve it can be seen that the retarded thrust mode lasted from stabilization to 9500 ft, at which time the computed acceleration mode was switched in. The figure also indicates the flight times and fuel consumed for these cases. It can be seen that considerable fuel can be saved in the retarded thrust case.

As a second example, a case is presented in Fig. 13 for the lightest atmosphere in which the retarded thrust mode

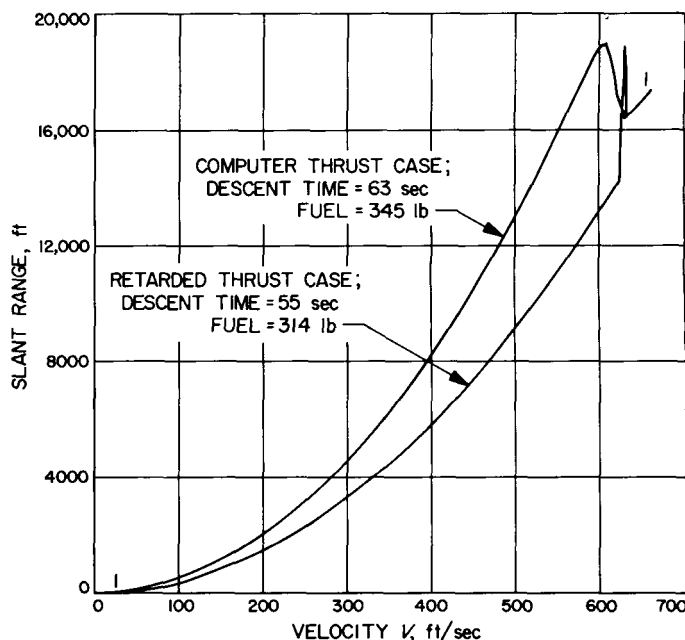


Fig. 13. Retarded thrust comparison VM-4

would be used (i.e., the thrust/weight ratio commanded would initially be less than 2.1). In case shown (VM-4) the retarded thrust mode begins at stabilization and ends at a slant range of 14,000 ft. Again, fuel is conserved by using this mode.

**d. Terminal modes.** There are two possible terminal modes after the completion of the gravity turn at 30 ft. In either case the craft's attitude is inertially held by removing the gyro torquing signals. This retains the nearly vertical alignment which results from a gravity turn. The attitude loop used here is identical to that shown in Fig. 8. The two options are available in the manner of thrust control. One method is to command a constant velocity descent, nominally 5 ft/sec, with the loop shown in Fig. 14. Radar-derived velocity is compared with the commanded value and the error used to drive the standard acceleration

Table 1. Equipment required for the capsule

No.	Equipment	Weight, lb
3	Wide-angle gyros with electronics and heaters	A/C <sup>a</sup>
1	Axial accelerometers with electronics	1.0
3	Rate gyros with electronics	3.0
1	Thrust level estimation and logic control computer	13.0
1	Autopilot and coordinate conversion electronics	10.0
3	Roll control jet vane actuators	9.0
1/2	Wiring harness (shared with A/C) <sup>a</sup>	0.5
Total		36.5

<sup>a</sup>A/C means weight is included in the attitude control system.

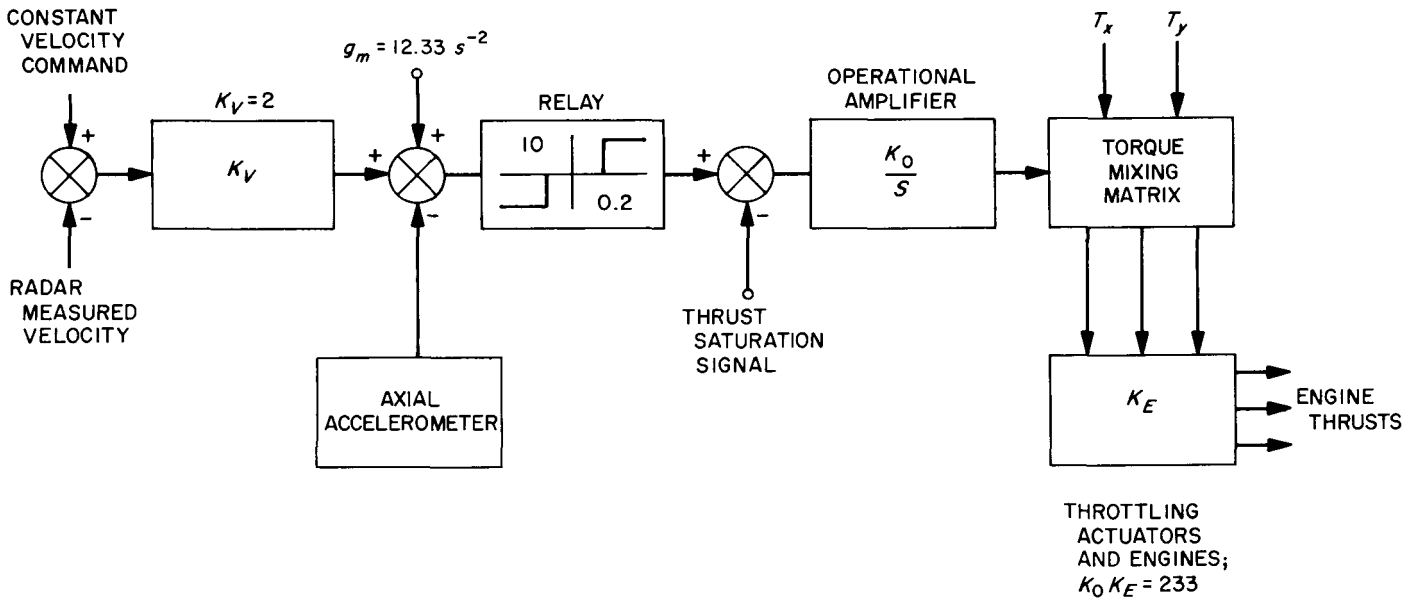


Fig. 14. Constant velocity loop for terminal mode

Table 2. Flight description

VM atmosphere	Control system type	Descent time, sec	Vertical velocity (final), ft/sec	Horizontal velocity (final), ft/sec	Final attitude (WRTH), deg	Fuel, lb
4	Gravity turn	63	15	.2	91.5	346
4	Gravity turn and retarded thrust	55	14	.2	91.8	314
7	Gravity turn	42	14	10	82	404
8	Gravity turn	37	13	9	80	345
10	Gravity turn	89	14	2	96	404
10	Gravity turn and retarded thrust	66	15	2	92	318

loop. The other method is to command a constant acceleration level, less than one martian  $g$ , with a loop identical to the stabilization mode. With this option, the 30-ft point is not rigid, but velocities of less than 5 ft/sec must be achieved before the mode is initiated. This mode can produce slightly greater touchdown velocities. However, it is independent of the radar, after initiation. At 10 ft, the engines are shut down and the craft free-falls to the surface.

Table 1 shows a preliminary equipment list for the lander control system, and Table 2 is a summary of the terminal conditions for several of the cases considered.

**N67-15707**

## B. Solar Pressure Effect on Spacecraft Attitude After Gas System Depletion, E. H. Kopf, Jr.

### 1. Introduction

It was desired to determine whether a *Mariner*-type spacecraft would continue to hold Sun line orientation

after depletion of the Attitude Control gas or a quiescent gas system failure. With no control torques available, the spacecraft slowly begins to spin about the roll axis due to the "propeller" action of solar pressure. Telemetry has shown that this torque, dependent upon solar panel alignment, is typically about 5 dyne-cm. During the spin-up, it would be possible to transmit via the omniantenna, and information could be recovered if Sun line control were maintained.

Since the equations describing this motion could not be solved analytically and no suitable approximations could be made, it was decided to simulate this system on the IBM 7094 via numerical integration. This article describes the modeling procedure and some results obtained from the digital program.

### 2. Solar Torque Model

There are two primary ways in which solar pressure acts on a spacecraft. The first is due to photons absorbed

by the solar panels. Since the solar vanes are highly reflective very little radiation is absorbed by them. The model shown in Fig. 15 was used, where *CP* is the center of pressure, *CG* is the center of gravity, and *x, y, z* are the body coordinates. Define

$A_p$  = total area of solar panels

$F_A$  = force acting at the *CP* due to absorbed photons

$\rho_p$  = reflectivity of solar panels

$P_0$  = photon pressure constant

$\hat{S}$  = Sun pointing unit vector

$l$  = distance *CP* to *CG*

$N_a$  = torque due to absorbed radiation

Then

$$dF_A = -(1 - \rho_p) P_0 S_z dA$$

$$F_A = -(1 - \rho_p) P_0 S_z A_p$$

and the resulting torque is

$$N_a = -(1 - \rho_p) P_0 l S_z \begin{bmatrix} -S_y \\ S_x \\ 0 \end{bmatrix}$$

The second source of torque is due to reflected photons. Assuming that the solar panels are very nearly aligned with the *x, y* plane, no reflective torques are generated by them. This is because the angle of incidence equals the angle of reflection and the resulting momentum change

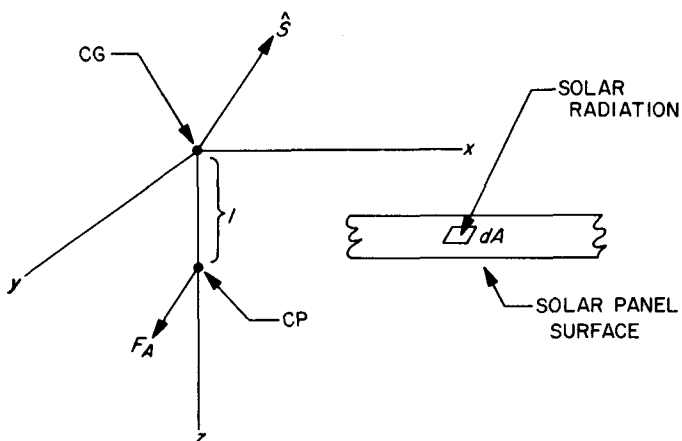


Fig. 15. Solar torque model

is parallel to the roll axis at all times. Considering the solar vanes alone, yields the coordinates of Fig. 16.

Let all vanes be set at an angle  $\gamma$ , and use a subscript system where *PPV* refers to positive pitch vane and  $S_{PPV}$  is the unit Sun pointing vector as resolved in the coordinate system erected at the *CP* of that vane.

$$S_{PPV} = \begin{bmatrix} S_x \cos \gamma + S_z \sin \gamma \\ S_y \\ S_z \cos \gamma - S_x \sin \gamma \end{bmatrix}$$

$$S_{PYV} = \begin{bmatrix} S_x \\ S_y \cos \gamma + S_z \sin \gamma \\ S_z \cos \gamma - S_y \sin \gamma \end{bmatrix}$$

$$S_{NPV} = \begin{bmatrix} S_x \cos \gamma - S_z \sin \gamma \\ S_y \\ S_z \cos \gamma + S_x \sin \gamma \end{bmatrix}$$

$$S_{NYV} = \begin{bmatrix} S_x \\ S_y \cos & - S_z \sin \\ S_z \cos & + S_y \sin \end{bmatrix}$$

Let  $F_v$  be the reflected radiation force on a vane,

$$F_v = 2\rho_v P_0 A_v S_{zV}^2$$

where  $A_v$  is the area of one vane. Let  $L$  be the perpendicular distance from *CG* to line of action of  $F_v$ . Then the reflective torques are

$$N_x = L(F_{PYV} - F_{NYV}) = 2\rho_v P_0 A_v L (S_{zPYV}^2 - S_{zNYV}^2)$$

$$N_x = 8\rho_v P_0 A_v L \sin \gamma \cos \gamma S_z S_y$$

$$N_y = + 8\rho_v P_0 A_v L \sin \gamma \cos \gamma S_z S_x$$

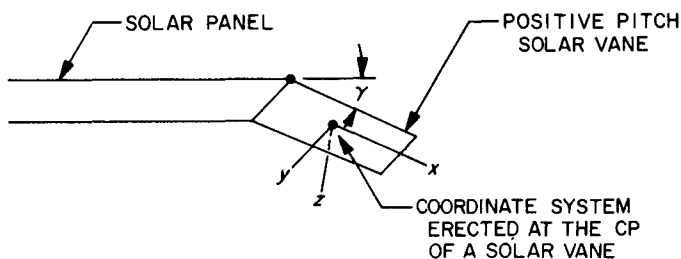


Fig. 16. Solar panel coordinates

Since the roll torque is mainly a function of solar panel alignment, it cannot be determined beforehand. A simple model was used where the torque is proportional to the cosine of the angle offset from the Sun line.

$$N_z = -KS_z$$

where  $K$  is selected around the typical 5 dyne-cm value.

The total spacecraft solar torque is then:

$$N_x = -A_1 S_z S_y$$

$$N_y = -A_1 S_z S_x$$

$$N_z = -KS_z$$

$$A_1 = \underbrace{A_p(1 - \rho_p)P_0 l}_{\text{Spacecraft solar panels}} + \underbrace{8\rho_v P_0 A_v L \sin \gamma \cos \gamma}_{\text{Solar vanes}}$$

A typical spacecraft model is shown in Fig. 17, and the associated parameters are given in Table 3.

A method for introducing unbalanced solar torques is to consider the distance to the line of action of the force on one solar vane to be different from that to the other. This gives rise to the pitch and yaw offset torques

$$N_{x0} = U_x(S_z^2 + S_y^2)$$

$$N_{y0} = U_y(S_z^2 + S_x^2)$$

where  $U_x$  and  $U_y$  are the unbalances observed when the spacecraft is oriented along the Sun line. These are often around 10 dyne-dm.

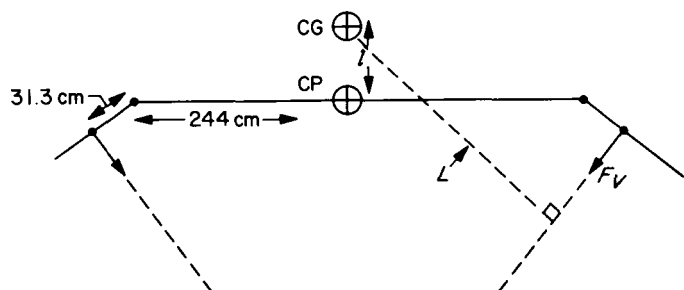


Fig. 17. Typical spacecraft torque model

### 3. Inertial Coordinate System

An inertial coordinate system  $X, Y, Z$  is defined at the position of the spacecraft at  $t = 0$ , the time of gas system failure. As shown in Fig. 18, the definition is such that the inertial  $X$  is along the velocity vector of the vehicle with the  $XZ$ -plane coincident with the plane of the orbit. The orbit itself is modeled as locally circular with  $d\alpha/dt$  being in the order of  $2 \times 10^{-7}$  rad/sec.

The position description of the body system in the inertial system was accomplished by Hamilton-Cayley-Klein (HCK) parameters. These were chosen over the usual Euler angles for two reasons. First, their derivatives do not possess singularities, and second, they are better from a computer viewpoint since no trigonometric functions are involved in their integration. In the HCK parameters used,  $P_0$  through  $P_3$  are considered to rotate the inertial system through an angle  $\phi$  about the vector  $\hat{n}$ . Where  $n_1, n_2, n_3$  are the direction cosines of  $\hat{n}$  as represented in the inertial system.

Using these HCK parameters:

$T \triangleq$  transformation, inertial to body. If we let  $V$  be represented in the body system by

$$v = \begin{bmatrix} v_1 \\ v_2 \\ v_3 \end{bmatrix}$$

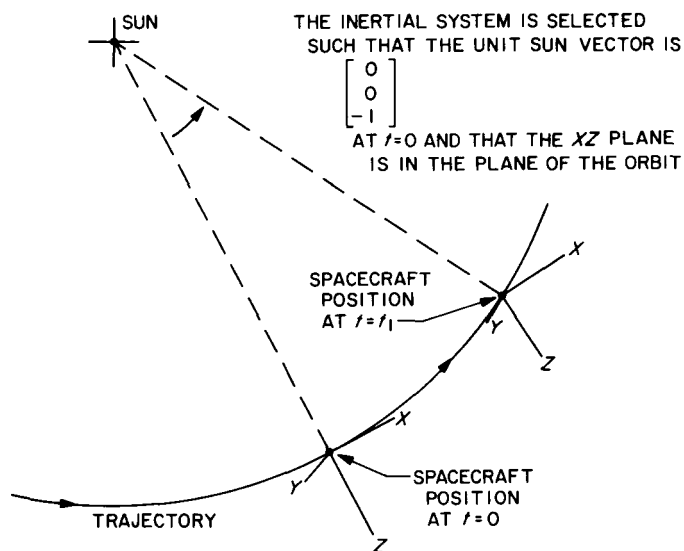


Fig. 18. Inertial system showing Sun line motion

**Table 3. Parameters**

$A_P = 69677.6 \text{ cm}^2$
$A_V = 6503.3 \text{ cm}^2$
$= 22.86 \text{ cm}$
$P_0 = 4.65 \times 10^{-5} \text{ dynes/cm}^2$
$P = 0.75 \text{ (numeric)}$
$V = 1.0 \text{ (numeric)}$
$I_{xx} = 1.14 \times 10^9 \text{ dyne-cm sec}^2$
$I_{yy} = 1.14 \times 10^9 \text{ dyne-cm sec}^2$
$I_{zz} = 1.8 \times 10^9 \text{ dyne-cm sec}^2$
$I_{xy} = 3.97 \times 10^7 \text{ dyne-cm sec}^2$
$I_{xz} = -2.14 \times 10^7 \text{ dyne-cm sec}^2$
$I_{yz} = 1.02 \times 10^7 \text{ dyne-cm sec}^2$
$A_1 = 18.5 + 254.9 = 273.4 \text{ dyne-cm}$
$K = 5 \text{ dyne-cm}$

and in the inertial system by

$$\mathbf{V} = \begin{bmatrix} V_1 \\ V_2 \\ V_3 \end{bmatrix}$$

Then

$$\mathbf{v} = \mathbf{T} \cdot \mathbf{V}$$

$$\mathbf{T} = 2 \begin{bmatrix} P_0^2 + P_1^2 - \frac{1}{2} P_1 P_2 + P_0 P_3 P_1 P_3 + P_0 P_2 \\ P_1 P_2 - P_0 P_3 P_0^2 + P_2^2 - \frac{1}{2} P_0 P_3 + P_0 P_1 \\ P_1 P_3 - P_0 P_3 P_2 P_3 - P_0 P_1 P_0^2 + P_3^2 - \frac{1}{2} \end{bmatrix}$$

#### 4. Differential Equations

Let  $\mathbf{S}$  be the unit Sun pointing vector.  $\mathbf{S}$  is represented in the body system as

$$\mathbf{S} = \begin{pmatrix} S_x \\ S_y \\ S_z \end{pmatrix}$$

and in the inertial system as

$$\mathbf{SI} = \begin{pmatrix} SI_x \\ SI_y \\ SI_z \end{pmatrix}$$

Then according to the assumed trajectory

$$\mathbf{SI} = \begin{bmatrix} -\sin(ct) \\ 0 \\ -\cos(ct) \end{bmatrix}$$

where  $c$  — constant (approx  $2 \times 10^{-7}$ ) and

$$\mathbf{S} = \mathbf{T} \cdot \mathbf{SI}$$

and the torques are

$$N_x = -A_1 S_x S_y + U_x (S_y^2 + S_z^2)$$

$$N_y = A_1 S_x S_x + U_y (S_x^2 + S_z^2)$$

$$N_z = K S_z$$

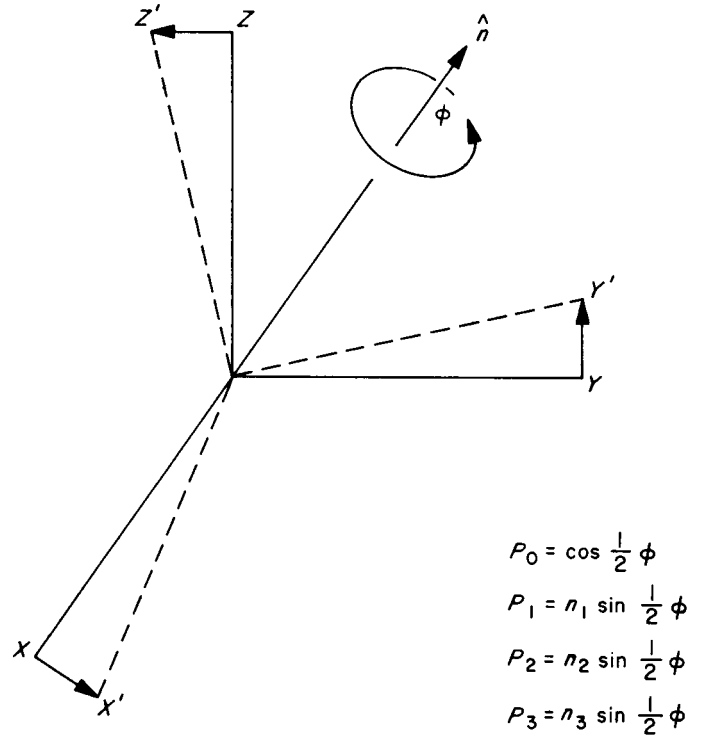


**Fig. 19. Illustration of the Hamilton-Cayley-Klein parameters**

The angular momentum vector  $L$  is

$$L = I \cdot \omega = \begin{bmatrix} L_1 \\ L_2 \\ L_3 \end{bmatrix}$$

where  $I$  is the inertia tensor of the spacecraft. Knowing that  $dL/dt = N$ , the equations for  $\dot{\omega}$  can be written. Combining these with the equations for  $\dot{P}$  yields the system of differential equations which must be integrated

$$\begin{bmatrix} \dot{P}_0 \\ \dot{P}_1 \\ \dot{P}_2 \\ \dot{P}_3 \end{bmatrix} = \frac{1}{2} \begin{bmatrix} 0 & -\omega_x & -\omega_y & -\omega_z \\ \omega_x & 0 & \omega_z & -\omega_y \\ \omega_y & -\omega_z & 0 & \omega_x \\ \omega_z & \omega_y & -\omega_x & 0 \end{bmatrix} \begin{bmatrix} P_0 \\ P_1 \\ P_2 \\ P_3 \end{bmatrix}$$

$$\dot{\omega}_x = \frac{\begin{vmatrix} (N_x + \omega_z L_2 - \omega_y L_3) I_{xx} I_{xz} \\ (N_y + \omega_x L_3 - \omega_z L_1) I_{yy} I_{yz} \\ (N_z + \omega_y L_1 - \omega_x L_2) I_{zz} I_{xz} \end{vmatrix}}{dET(I)}$$

$$\dot{\omega}_y = \frac{\begin{vmatrix} I_{xx} (N_x + \omega_z L_2 - \omega_y L_3) I_{xz} \\ I_{yy} (N_y + \omega_x L_3 - \omega_z L_1) I_{yz} \\ I_{zz} (N_z + \omega_y L_1 - \omega_x L_2) I_{xz} \end{vmatrix}}{dET(I)}$$

$$\dot{\omega}_z = \frac{\begin{vmatrix} I_{xx} I_{yy} (N_x + \omega_z L_2 - \omega_y L_3) \\ I_{xy} I_{yy} (N_y + \omega_x L_3 - \omega_z L_1) \\ I_{xz} I_{yy} (N_z + \omega_y L_1 - \omega_x L_2) \end{vmatrix}}{dET(I)}$$

### 5. Simulation Results

The parameters of the spacecraft of Fig. 19 were used as input, and numerical integration was performed on

the IBM 7094. The numerical method used was Adams/Moulton predictor corrector with adaptive step size. The order was  $h^4$  for both. Fig. 20 shows the input data where there are no offset torques and

$$A_1 \overset{\Delta}{=} A_2$$

$$K \overset{\Delta}{=} A_3$$

INITIAL POSITION			
HAMILTON CAYLEY KLEIN PARAMETERS			
P0	P1	P2	P3
0.0000E-38	0.3000E-02	0.0000E-38	0.1000E-01
INITIAL RATES			
W1	W2	W3	
0.5000E-05	0.2000E-04	0.3000E-05	
SUN MOVES IN THE INERTIAL SYSTEM			
AT A RATE OF 0.202E-06 RADIANS/SEC			
INERTIA TENSOR			
0.1140E 10	0.3970E 08	-0.2140E 08	
0.3970E 08	0.1140E 10	0.1020E 08	
-0.2140E 08	0.1020E 08	0.1800E 10	
SOLAR PRESSURE CONSTANTS			
A1	A2	A3	
0.2734E 03	0.2734E 03	0.5000E 01	

Fig. 20. Input data

Fig. 21 shows the angular momentum and cone angle versus time in days. Cone angle is the angular deviation from the Sun line. Note that although the cone angle oscillates rapidly it just exceeds 50 mrad at maximum even though the craft is spinning at almost 5 mrad/sec at the end of 20 days. This shows that the Sun line control is very good.

In summary, for a variety of runs it has been found that spacecraft of the type in the example hold Sun line control for usually over 40 days even with unbalanced solar torques.

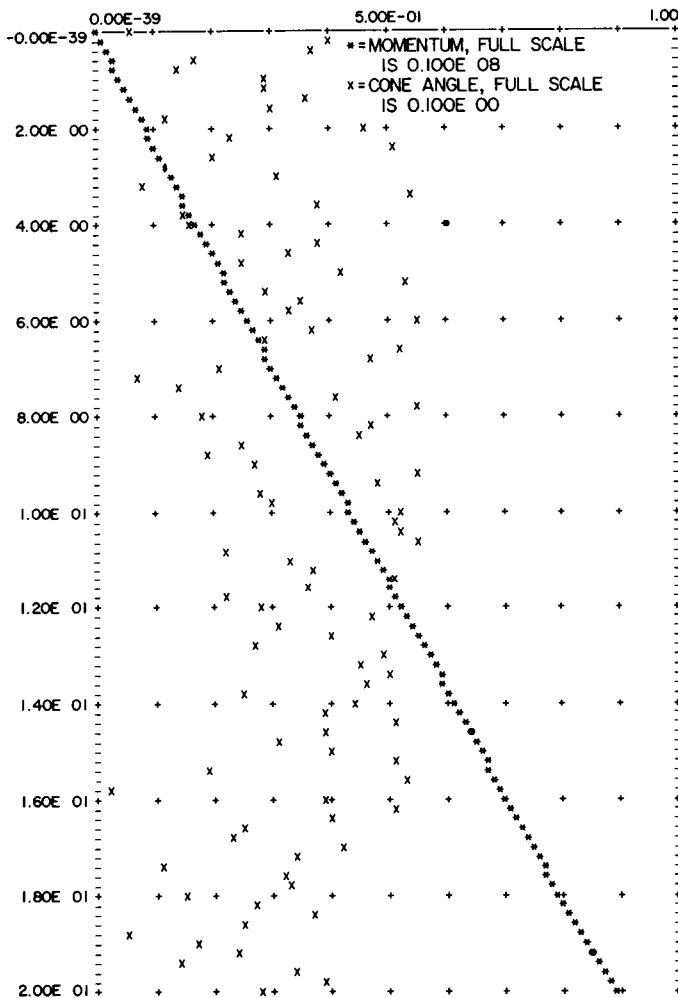


Fig. 21. Angular momentum and cone angle versus time in days

N67-15708

© Advanced Scan Platform, P. Presser

## 1. Introduction

This report presents the conclusion of the analytical effort expended and the start of hardware mechanization of the advanced scan platform. The previous analytical work has been summarized in SPS 37-35, Vol. IV, pp. 33-35, and SPS 37-39, Vol. IV, pp. 33-40.

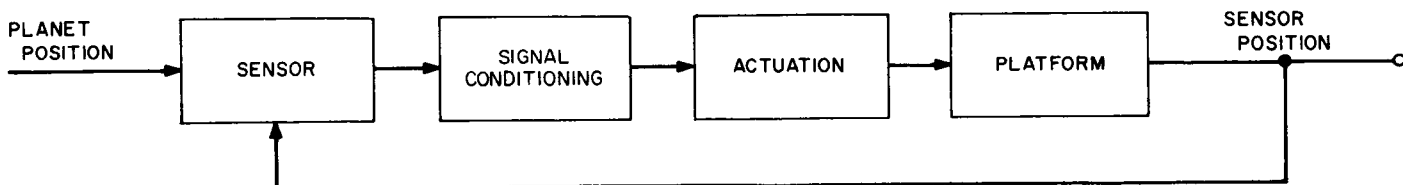


Fig. 22. Block diagram of advanced scan platform

This study was concerned with linear and non-linear sensor representation and open- and closed-loop actuation. The investigation resulted in the following conclusions:

- (1) No shaping, smoothing or other computation is required in the scan platform electronics; sufficient smoothing is provided by the actuator.
- (2) System performance is better without position feedback around the actuator.

A system was designed, and some hardware was tested. Scan platform drive electronics development continues.

## 2. Analysis and Simulation

The advanced scan platform may be represented as shown in the block diagram, Fig. 22. In order to assess the performance of the loop, the characteristics of each block must be identified.

Investigation has shown that for reasonable inputs the platform structure behaved in a linear fashion with a resonant frequency of slightly greater than 2 cps and essentially zero damping. This can be expressed in transfer function form as

$$\frac{\theta_H}{\theta_M} = \frac{15.2^2}{S^2 + 15.2^2}$$

Two configurations of the actuator were studied. One was without position feedback. This configuration yields an output rotational rate proportional to the input. The frequency response of this configuration is characterized by a single first-order break. This configuration can have a non-zero position output with no input.

The other configuration utilized position feedback. This configuration had a frequency response characterized by a critically damped second-order break. A zero input will cause this configuration to have a zero output.

The actuator, when loaded, is assumed to have a break frequency of about 5 cps. This can be tailored using tach and position feedback as shown in root locus form by Fig. 23.

The sensor has a pulse width modulated output. The pulse repetition frequency is 3.5 cps. The resolution of the sensor is 1 deg. Sensor characteristics are illustrated in Fig. 24.

It should be noted that the output of the sensor is not only *not* a continuous function of time, but it is also non-

linear. The non-linearity has the characteristics of a series of bang-bang devices with deadband.

When studying the loop, it becomes apparent that the problem is one of controlling the position of a horizon sensor using an actuator which is at the opposite end of a subtle boom from the horizon sensor. As a prelude to studying the system, functional specifications must be established.

- (1) The scan platform shall point to the center of the subject planet within  $\pm \alpha$  deg.

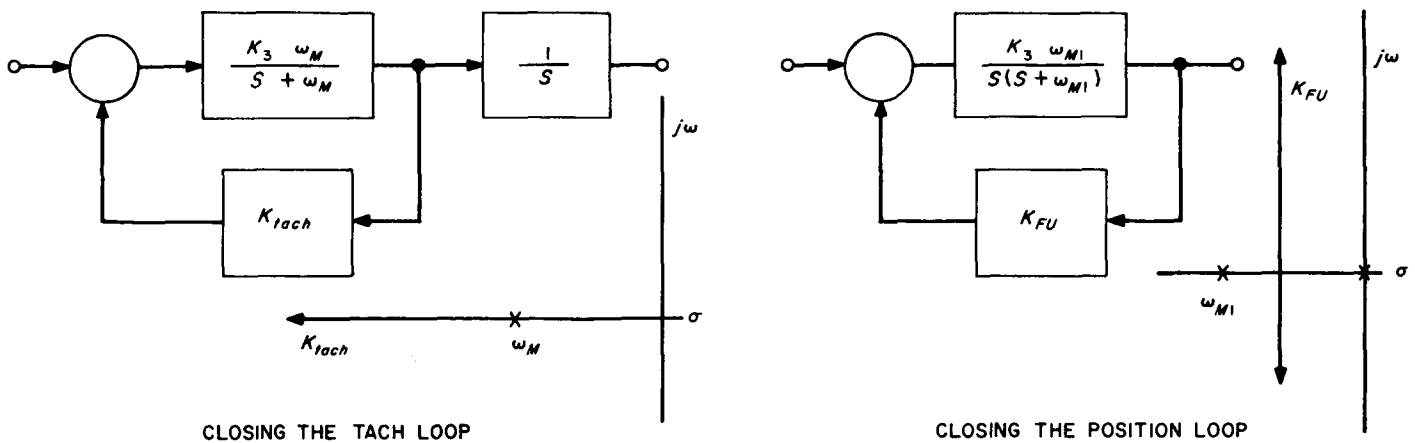


Fig. 23. Actuator characteristics as a function of loop gain

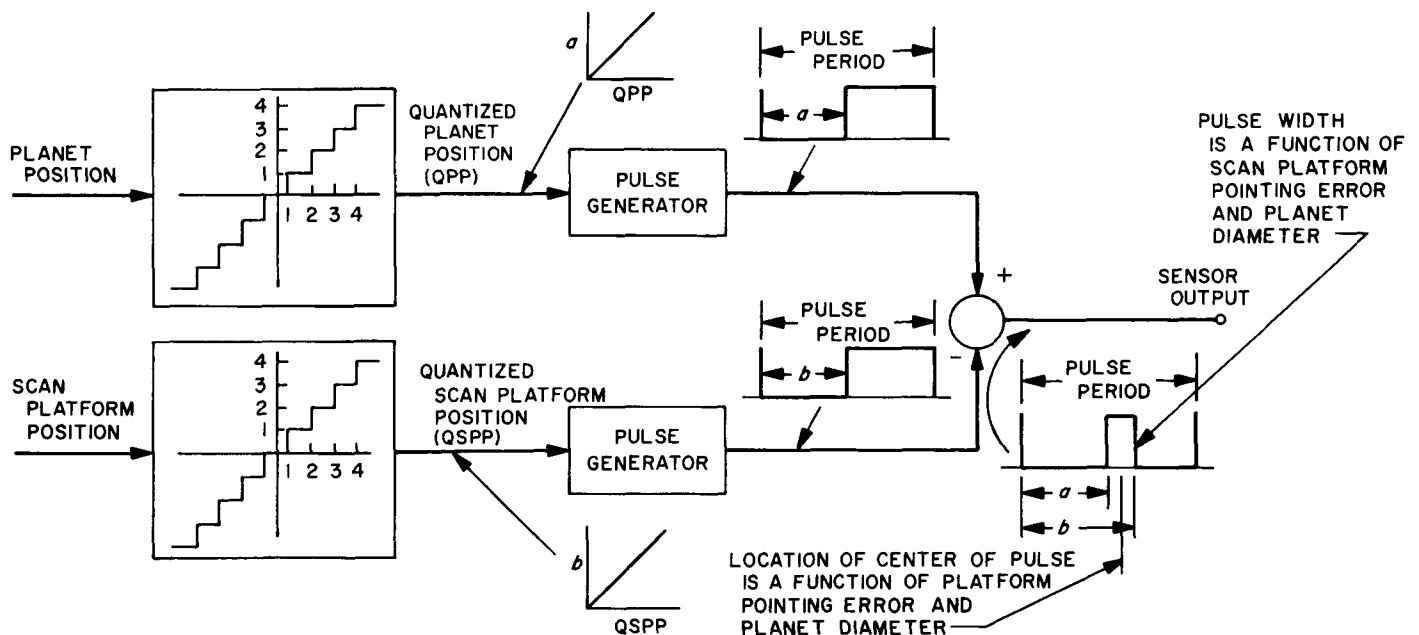


Fig. 24. Sensor characteristics

- (2) The scan platform jitter rates shall be such that TV operation is not deteriorated. This is interpreted such that the TV camera does not move one line width during an exposure. The angular displacement between lines can be considered as  $\beta$  deg. A conservative estimate of the jitter velocity is  $\beta/\tau = \gamma$  deg/sec where  $\tau$  is the exposure time. It should be noted, however, that the limiting specification is

$$\beta \cong \int_t^{t+\tau} (\text{platform rate}) dt.$$

- (3) The platform should be capable of slewing at a rate equal to  $\delta$  deg/sec.

These specifications were used as guidelines more than as firm and fast rules. Values used were  $\alpha = 0.5$  deg/sec,  $\beta = 0.75 \times 10^{-3}$  deg,  $\tau = 0.1$  sec,  $\gamma = 7.5 \times 10^{-3}$  deg/sec, and  $\delta = 1$  deg/sec. The specification which was used in evaluating system performance almost to the exclusion of the others was Spec. (2).

Two methods of assessing system performance were used, simulation and analysis. Simulation was used to investigate whether there was a jitter component in the platform motion. Analysis was used to obtain limiting values of loop gain, and to assess error sensitivity. Loop gains in line with those found acceptable in the analysis were used in the simulation.

In the course of simulation, various models were used to represent the sensor. These were, in the order of their deleterious effect on system performance:

- Linear sensor (least deleterious).
- Sensor with pulse width modulated output (Fig. 24).
- Sensor with dead zone.
- Sensor with bang-bang characteristics and deadband.
- Sensor represented by sampler and zero-order hold.

During the course of system simulation, several qualitative parametric relationships became apparent. These were:

- The stiffer the platform structure, the less the jitter.
- The lower the actuator break frequency, the less the jitter.
- The higher the sampling rate, the less the jitter.

No attempt at system optimization was made during the simulation effort, but it became apparent that the jitter specification could easily be met if the sensor model was as shown in Fig. 24. Although no formal attempt was made to meet the pointing error specification, it is felt that this could also be met.

Fig. 25 shows a plot of platform position as a function of time. The sensor model used in this particular simulation is that of Fig. 24. For this run, the spacecraft is assumed to be moving relative to the planet at a constant rate.

During analysis the system was linearized initially. As mentioned above, the platform is essentially linear. Thus the only departure from a nearly exact representation of the loop was in the sensor. The sensor was represented as a summing point and a gain. The analysis of the linearized system indicates that the error for a rate input to the system with position feedback in steady state is unbounded:

Enclosed loop actuator =

$$\lim_{s \rightarrow 0} \frac{(S^2 + 2\zeta\omega S + \omega^2)(S^2 + 2\zeta_M\omega_M S + \omega_M^2)}{S(S^4 + A_1S^3 + B_1S^2 + C_1S + D_1)} = \infty$$

The system which includes an actuator without position feedback will have an angular error inversely proportional to loop gain

Open loop actuator =

$$\lim_{s \rightarrow 0} \frac{(S + \omega_M)(S^2 + 2\zeta\omega S + \omega^2)}{S^4 + A_1S^3 + B_1S^2 + C_1S + D_1} = \frac{\omega_M\omega^2}{D_1} = \frac{1}{KK_s}$$

and equal to 5.33% of the input rate if loop gain is set for marginal stability.

Analysis of a system utilizing pulse width modulation proved elusive. The literature yielded no analytical methods applicable to this type of system. The author could find no closed form expression useful in this regard. Thus simulation was used as the primary tool to investigate system performance when the sensor was represented as having an output of this format.

The sensor characteristics differ from linear characteristics in three ways. First, the sensor output is discontinuous in time. Second, the sensor output is discontinuous

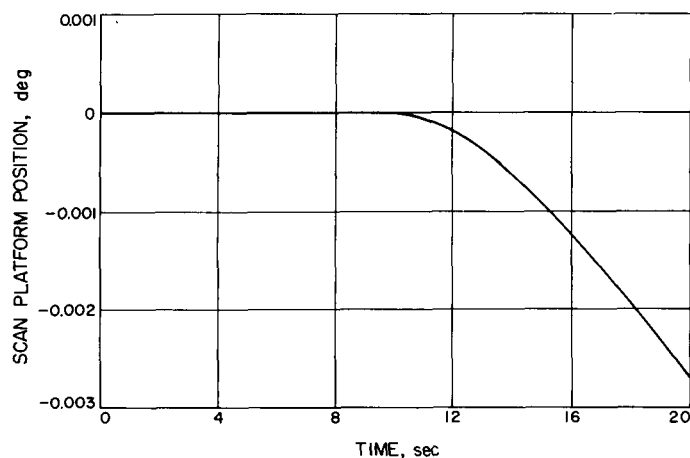


Fig. 25. Plot of scan platform position as a function of time

in amplitude. Thirdly, the sensor exhibits deadzone characteristics. In lieu of direct analysis, the sensor was treated as (1) dead zone, (2) bang-bang, with and without dead zone, and (3) as sampler and zero-order hold with and without the previous non-linearities.

During the non-linear analysis, it was found that for the deadzone and for bang-bangs with  $a/M \leq 0.638$ , as defined in Fig. 26, limit cycle operation, for stable systems, is impossible. Since  $a/M$  for the system is equal to one,

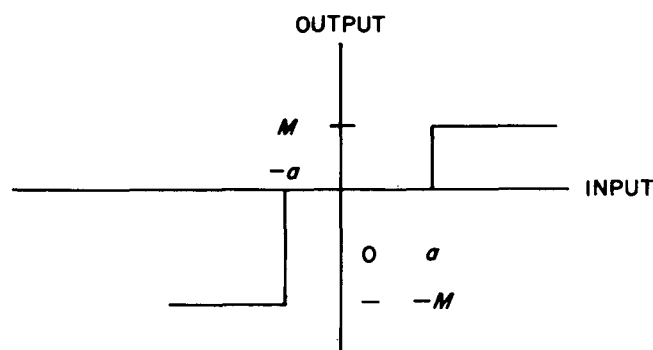


Fig. 26. Definition of deadzone parameters

limit cycle should be no problem if this sensor representation is correct. Gains which might be used for linear system operation will not cause limit cycling if the sensor is represented as a dead zone.

A sampled data analysis was performed. The analysis showed that stable, limit cycle free system operation could be obtained.

Previous analysis showed that the actuator without feedback was superior in performance when compared with the actuator with feedback. Thus sampled data analysis was performed only on the system with the open loop actuator. The block diagram used in this analysis is shown in Fig. 27.

The system was studied for  $0 \leq T \leq 0.5$ . Root loci showed that some portion of the locus for  $T = 0$  always lies outside the unit circle. For  $T = 0.1$ , the singularities outside the unit circle nearly cancel. Except for this, the loci for  $T \geq 0.1$  lie within the unit circle.

The limitations on non-linearities for the temporally continuous system hold for the sampled data system.

### 3. Control System Mechanization

The control system mechanization is shown in Fig. 28. Effort is presently being expended in developing servo drive electronics.

The particular mechanization features precise control of the timing and non-linearity of the simulated sensor. Provision is made for tach feedback to allow for varying the motor break frequency. Shunt FET switches are used as synchronous modulators.

Pulse repetition frequency is varied by changing the frequency of the free-running multivibrator. The step size of the quantizer is varied by changing the bias on the divider network.

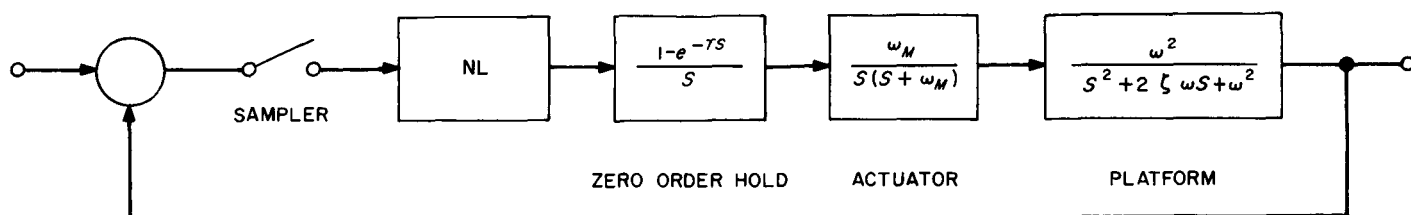


Fig. 27. System block diagram for sampled data analysis

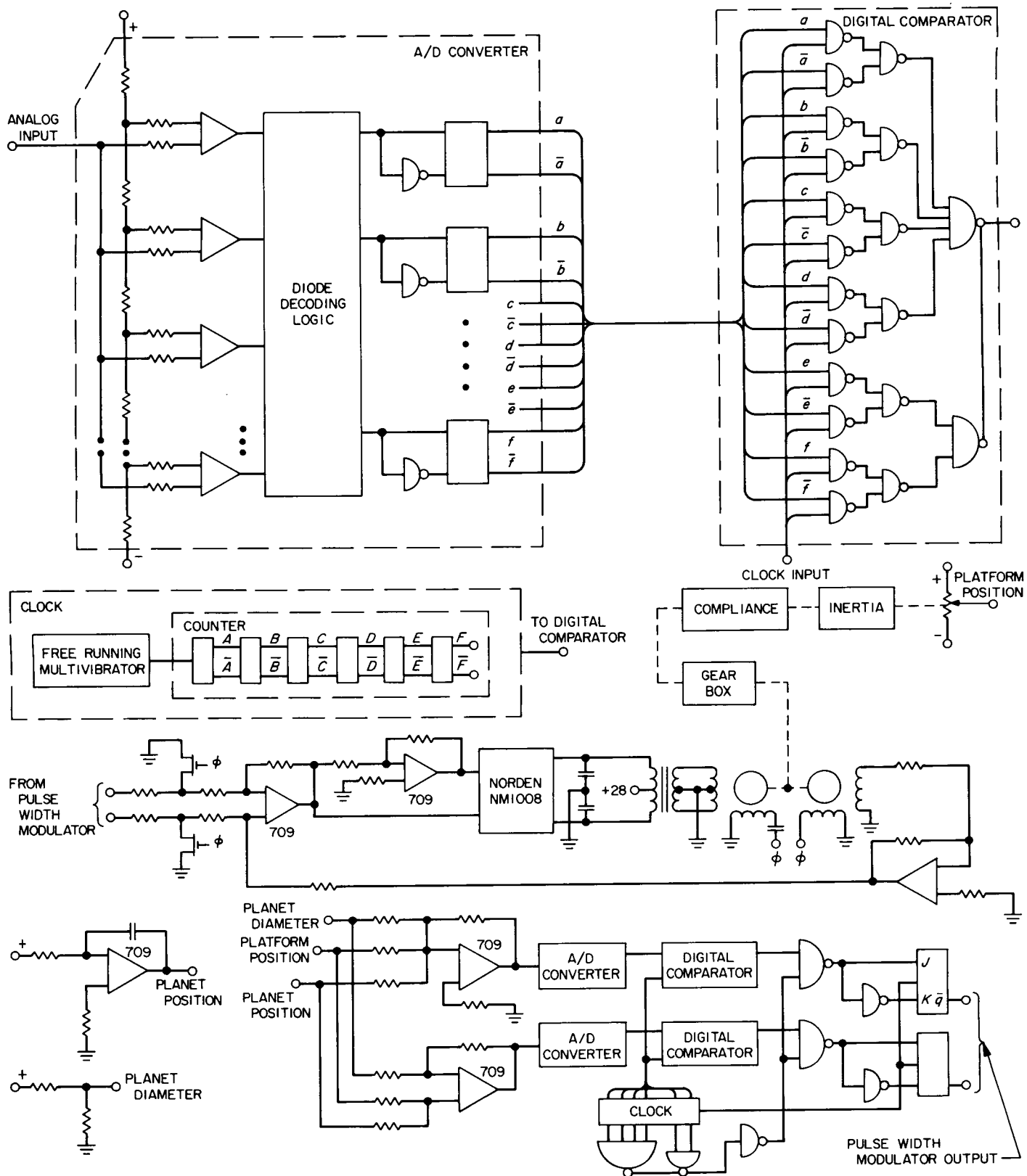


Fig. 28. Control system mechanization for advanced scan platform

Present plans call for using a Norden NM1008 integrated servo amplifier to drive the servo motor. The output transformer is used to decouple the dc bias from the motor. Differential input for the servo amplifier is provided by using Fairchild  $\mu$ a 709 amplifier.

Another amplifier is used to buffer the tach. This signal is summed with the two pulse width modulated signals.

The pulse width modulators operate by first converting the analog error signal to a digital signal. The complement of the digital error signal is compared with the clock. A

flip-flop is gated on when these two are identical. The flip-flop remains on for the remainder of the pulse period, yielding a pulse-width modulated signal. Changing the clock rate changes the pulse period.

The A/D converter is of standard design. The use of a digital signal automatically provides signal quantization. The size of the steps can be adjusted by changing the bias to the comparators.

When work on the servo amplifier is completed, development will be initiated on the pulse-width modulator.

## Reference

1. Syn, W. M., and Wyman, D. G., *Digital Simulation Language, DSL/90*, Technical Report 02.355, International Business Machines Corporation, San Jose, California, July 1, 1965.

## V. Guidance and Control Research

### GUIDANCE AND CONTROL DIVISION

N67-15709

**A. Variation of Current with Voltage at the Onset of Punch-Through for Thin-Base Solid-State Diodes, A. Shumka**

#### 1. Introduction

Deviations observed between the  $I$ - $V$  characteristics of the actual solid-state diodes and the characteristics predicted by the theoretical model for the solid-state diodes in the low current range for the thinner base samples indicated that probably the assumptions of a fixed base width and a zero voltage drop across the emitter were not valid. Theoretical calculations were performed, and the results clearly show the influence of the emitter junction on the  $I$ - $V$  characteristics to be appreciable in the low current range when the width of the transition region is comparable to that of the base. The modified theory is in good agreement with the experiment.

#### 2. Experimental Results

Space-charge-limited (scl) electron and hole currents have been investigated in fabricated  $n^+pn^+$  and  $p^+vp^+$  germanium solid-state diodes, respectively, of various base widths (Ref. 1 and SPS 37-39, Vol. IV, pp. 49-50). An analysis indicated that the theoretical model of Dacey

(Ref. 2) was in excellent agreement with experimental results for the samples of thicker base. However, for thinner base samples ( $<20\mu$ ), the theory was found to be inadequate to explain the experimental results in the low current range (Fig. 1). A new theoretical model had to be constructed to predict the behavior of the solid-state diode in the low current range.

Two  $p^+vp^+$  germanium solid-state diodes of base width less than  $20\mu$  were fabricated. Their  $I$ - $V$  characteristics in the low current range were accurately determined by making dc measurements. These samples had been immersed in a liquid nitrogen bath to minimize the effect of saturation currents (Ref. 1). A metallurgical cross-section (SPS 37-35, Vol. IV, pp. 49-52) was made on only one sample to determine the separation distance between its two alloyed  $p^+$  contacts. The separation distance was  $18\mu$ . The  $I$ - $V$  characteristics for this sample are shown in Fig. 1.

#### 3. Theory

Two important features of the theoretical model considered which differ from the original model are that the base width is dependent on the applied voltage,  $V$ , and that the voltage drop,  $V_j$ , across the emitter junction is non-zero. The active regions in a thin-base  $p^+vp^+$  solid-state

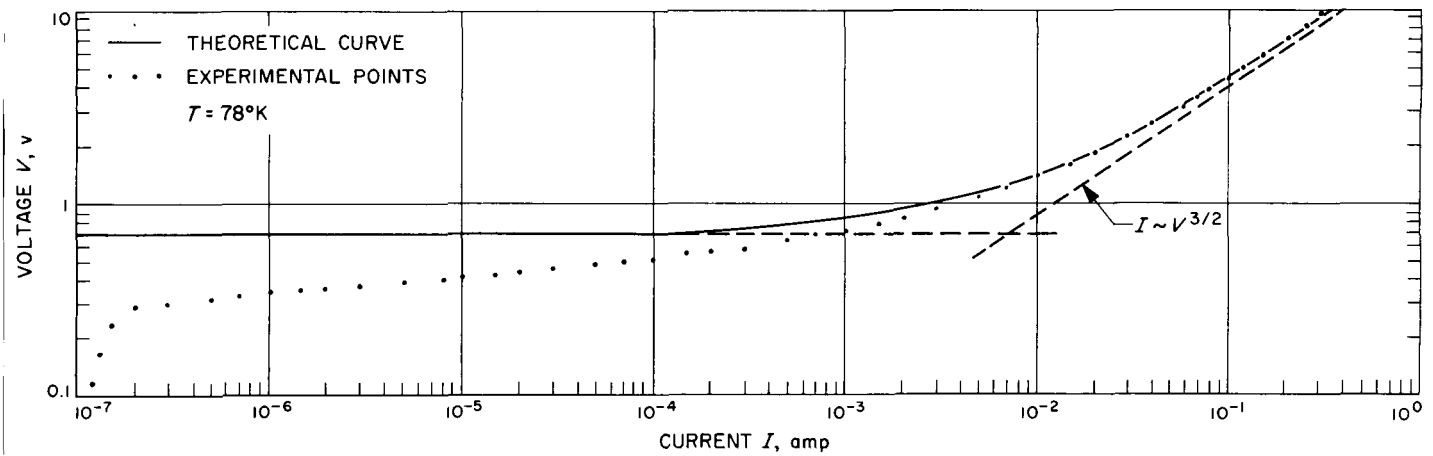


Fig. 1.  $I$ - $V$  characteristic for a thin-base  $p^+vp^+$  germanium solid-state diode; separation distance between  $p^+$  contacts is  $18\ \mu$ .

diode are sketched in Fig. 2. The separation distance between the two  $p^+$  contacts is  $W + W_t$ , where  $W_t$  is the width of the emitter junction transition region at thermal equilibrium and may be several microns wide for a low doped base. When an applied voltage  $V$  is greater than the punch-through voltage  $V_B$ , there will be a voltage drop  $V_J$  across the emitter junction. This voltage  $V_J$  forward-biases the emitter junction and also decreases the width of the transition region by  $\delta$ . Consequently, the effective width of the base has been increased from  $W$  to  $W + \delta$ , and the voltage drop across the active base region becomes  $V - V_J$ . A theoretical calculation is performed which includes these two important features.

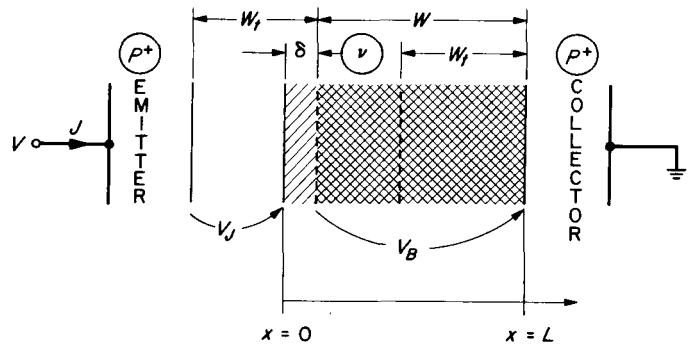


Fig. 2. A sketch of the active regions in a thin-base  $p^+vp^+$  solid-state diode

Equations for describing the one-dimensional hole charge transport in the active base region are

$$J = q \mu_p p E - q D_p \frac{dp}{dx} \quad (1)$$

and

$$\frac{dE}{dx} = \frac{q N_D}{\epsilon \epsilon_0} + \frac{qp}{\epsilon \epsilon_0} \quad (2)$$

where  $J$  is the hole current density,  $q$  the electronic charge,  $p$  the injected hole density in the base,  $E$  the electric field,  $N_D$  the ionized donor density in the base,  $\mu_p$  and  $D_p$  the hole mobility and diffusion constant, respectively, and  $\epsilon \epsilon_0$  the dielectric constant. The sign convention is that given in Fig. 2. In the low current range the injected hole density

is everywhere less than  $N_D$ ; that is,  $p \ll N_D$  and, consequently, Poisson's equation can be expressed as

$$E = \frac{q N_D}{\epsilon \epsilon_0} x \quad (3)$$

where  $E = 0$  at  $x = 0$ . Eqs. (1) and (3) are combined to obtain

$$\frac{J}{q D_p} = 2 \beta^2 p x - \frac{dp}{dx} \quad (4)$$

where

$$\beta^2 = \frac{q N_D}{2 \epsilon \epsilon_0 V_T} \quad \text{and} \quad V_T = \frac{kT}{q}.$$

The general solution for the injected hole density in the base is

$$p(x) = \left\{ p(L) e^{-\beta^2 L^2} + \frac{J}{(2)^{1/2} q \beta D_p} \int_{(2)^{1/2} \beta x}^{(2)^{1/2} \beta L} e^{-y^2/2} dy \right\} e^{\beta^2 x^2} \quad (5)$$

where  $p(L)$  is the hole density at the collector contact.

The injected hole density at the emitter contact (at  $x = 0$ ) is

$$p(0) = p(L) e^{-\beta^2 L^2} + \frac{J}{(2)^{1/2} q \beta D_p} \int_0^{(2)^{1/2} \beta L} e^{-y^2/2} dy. \quad (6)$$

Eq. (6) can be simplified as follows:

$$L \gtrsim \left( \frac{2 \epsilon \epsilon_0 V_B}{q N_D} \right)^{1/2}$$

where  $V_B$  is voltage drop across the depletion region. Thus,

$$(2)^{1/2} \beta L \gtrsim (2)^{1/2} \left( \frac{q V}{k T} \right)^{1/2}$$

and is much greater than unity since we are considering samples in which the punch-through voltage is much greater than  $kT/q$ . For  $(2)^{1/2} \beta L \gg 1$ ,

$$\int_0^{(2)^{1/2} \beta L} e^{-y^2/2} dy \simeq \int_0^\infty e^{-y^2/2} dy = \left( \frac{\pi}{2} \right)^{1/2}$$

and  $p(0) \gg p(L) e^{-\beta^2 L^2}$  since  $p(0) > p(L)$ . Hence, Eq. (6) can be expressed

$$J = \frac{2 q \beta D_p}{\pi^{1/2}} p(0). \quad (7)$$

From junction theory, the injected charge is

$$p(0) = p_v (e^{V_J/V_T} - 1)$$

where  $p_v$  is the thermal equilibrium hole density in the base. In order to find the dependence of current on voltage, it is necessary to express  $V_J$  in terms of the applied potential. Let

$$V_J = V - V_B - \Delta V \quad (8)$$

where  $V_B$  is the voltage drop across the base when the depletion region extends the distance  $W$ . From the abrupt junction theory

$$W^2 = \frac{2 \epsilon \epsilon_0 (V_B + V_D)}{q N_D} \quad (9)$$

$$L^2 = (W + \delta)^2 = \frac{2 \epsilon \epsilon_0 (V_B + \Delta V + V_D)}{q N_D} \quad (10)$$

and

$$W_i^2 = \frac{2 \epsilon \epsilon_0 V_D}{q N_D} \quad (11)$$

where  $V_D$  is the built-in junction diffusion potential, and  $\delta$  is the incremental increase in the base width. Eqs. (8), (9), (10) and (11) are combined to obtain

$$V_J = V - V_B - \frac{\delta (2W + \delta)}{W_i^2}. \quad (12)$$

At the emitter junction

$$V_D - V_J = \left( \frac{W_t - \delta}{W_t} \right)^2 V_D. \quad (13)$$

From Eqs. (12) and (13),

$$\delta = \frac{V - V_B}{2 V_D} \frac{W_i^2}{W + W_t} \quad (14)$$

and

$$V_J = (V - V_B) \frac{W_t}{W + W_t} \left[ 1 - \frac{W_t}{W + W_t} \cdot \frac{V - V_B}{4 V_D} \right]. \quad (15)$$

The theoretical  $I$ - $V$  relationship for the low current range becomes

$$J = \frac{qD_p}{\pi^{1/2}} \left( \frac{2\epsilon\epsilon_0 V_T}{qV_D} \right)^{1/2} p_v \left[ \exp \left\{ \frac{V - V_B}{V_T} \frac{W_t}{W + W_t} \left[ 1 - \frac{W_t}{W + W_t} \frac{V - V_B}{4V_D} \right] \right\} - 1 \right]. \quad (16)$$

From Eq. (14) it is evident that the incremental increase in the base width can be appreciable if the junction transition region width  $W_t$  is comparable to separation distance between the  $p^+$  contacts. A similar dependence is observed for the voltage drop across the emitter junction in Eq. (15).

Two interesting results are obtained from Eq. (16). For

$$\frac{V - V_B}{V_T} \cdot \frac{W_t}{W + W_t} \ll 1, \quad (17)$$

$$J = \frac{qD_p}{\pi^{1/2}} \left( \frac{2\epsilon\epsilon_0 V_T}{qN_D} \right)^{1/2} p_v \frac{V - V_B}{V_T} \cdot \frac{W_t}{W + W_t}.$$

Here the initial rise of current just beyond punch-through is an ohmic current. For the more typical case, where

$$\frac{V - V_B}{4V_D} \frac{W_t}{W + W_t} \ll 1, \quad \text{and} \quad \frac{V - V_B}{4V_T} \frac{W_t}{W + W_t} > 1,$$

$$J = \frac{qD_p}{\pi^{1/2}} \left( \frac{2\epsilon\epsilon_0 V_T}{qN_D} \right)^{1/2} p_v e^{+\frac{W_t}{W + W_t} \frac{V - V_B}{V_T}}. \quad (18)$$

In Eq. (18) the current is exponentially dependent on the applied voltage  $V$ , on the separation distance  $(W + W_t)$  between the contacts and on the width of the junction transition region  $(W_t)$ .

#### 4. Theory and Experiment

The low current range of the  $I$ - $V$  characteristic in Fig. 1 is replotted in Fig. 3, with  $\log I$  as a function of  $V$ . From Fig. 3 it is evident that a linear relationship exists between  $\log I$  and  $V$  as is anticipated from Eq. (17). The slope of the line is 14.3 (volts) $^{-1}$  and should be equal to

$$\frac{W_t}{W + W_t} \frac{\log e}{V_T}.$$

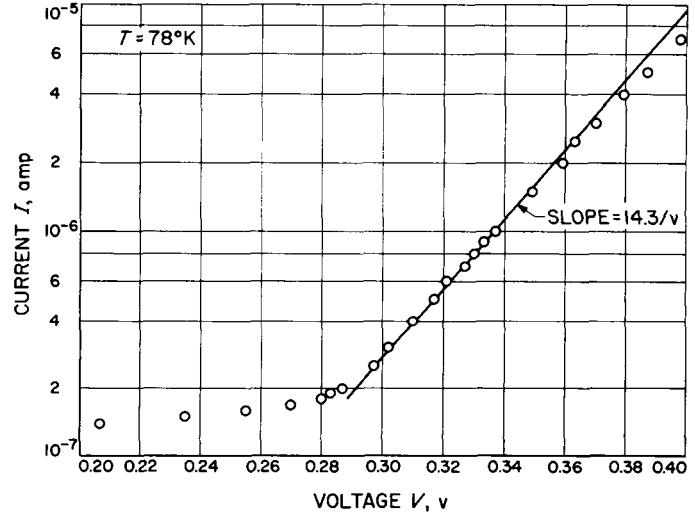


Fig. 3. Low current  $I$ - $V$  characteristics for the same sample as in Fig. 1

Since  $W + W_t = 18 \mu$ , then the value of  $W_t$  must be  $4 \mu$ , which appears to be reasonable for the  $p^+v$  junction where  $N_D = 10^{13}$  donors/cm $^3$ . In Fig. 3, departures from linearity are observed; however, they are in the range where the limits of Eq. (18) are exceeded.

The theoretical calculations clearly showed the influence of the emitter junction to be appreciable if  $W_t$  is comparable to  $W$ . Furthermore, the theory predicted a linear relationship between  $\log I$  and  $V$  which is observed, and also gave a quantitative result of  $W_t$  which could not be checked out directly, but whose value is very reasonable. This theoretical treatment makes it possible to explain the deviations observed between the experiment and the original theory, and it also makes it possible to give a lower limit of applicability to the original theory.

**N67-15710**  
**(B) Recent Progress in CdS Photoconductors, R. J. Stirn**

#### 1. Introduction

In the interest of reducing the size, weight, and power requirements of space navigational components, it is desirable to utilize solid state photodetectors in place of the vacuum tube type.

Commercially available, sintered cadmium sulfide (CdS) photoconductor cells are presently being used on spacecraft for several applications (Ref. 3), though there are certain difficulties which preclude their use in future, more sophisticated applications. Among these problems are: (1) large degradation or outright failure of cells during sterilization, (2) long term changes in the photoconductive properties, (3) insufficient sensitivity, and (4) excessively long response times under weak illumination.

Since the single crystal form of CdS is not useful for optimizing photodetector parameters, an extremely large amount of work on evaporated layers has been reported. Many of the published results are inconsistent, because of the strong influence of vacuum conditions, starting materials and dopants, and substrate-source temperatures and geometries. Improvement over the sintered layers had not been realized either, because of unreliable contacts, very large trap densities, and chemisorption-desorption of gases from the surfaces.

Various investigators have reported improved evaporated layers of CdS using the process of recrystallization (Refs. 4-8). These investigations were mainly concerned with increasing the Hall mobility to values comparable to those of the bulk (about 300 cm<sup>2</sup>/V-sec), by lowering the number of grain boundaries, etc., as much as possible. These layers were generally not sensitive as photoconductors. A recent publication by Böer, et al. (Ref. 9), reported high mobility CdS layers that were also highly photoconducting and had remarkably low trap densities.

In the following sections, we shall review the major features of these improved layers and recent important findings on single-crystal CdS, which may be pertinent to further improvements in evaporated photoconducting CdS cells.

## 2. Some Basic Concepts of Photoconductors

**a. Intrinsic photoconductivity.** Generally, photoconduction is an increase in the electrical conductivity of a solid, when electrons are raised to higher energy levels by the process of light absorption. When the transition occurs between the valence and conduction bands, the photoconductivity is said to be intrinsic, and its maximum occurs at the photon wave length which corresponds to the energy width of the forbidden gap. When an electric field is applied and one of the contacts is non-ohmic (blocking), the maximum gain is unity, i.e., one carrier generated for each photon absorbed. Since a potential is built up across the blocking contact, this is a photovoltaic process. When both contacts are ohmic, the photoexcited carrier leaves

the photoconductor while another enters from the other electrode in order to maintain charge conservation. This process occurs continuously during the lifetime of the carriers, and hence gains of millions are possible. Thus, photoconductive type detectors are inherently much more sensitive than the photovoltaic type.<sup>1</sup> We will now indicate quantitatively, some of the parameters involved.

**b. Photoconductive gain and electron lifetime.** For a trap-free insulator of unit cross-section exposed to a uniform area excitation which generates free electrons at the *total* rate of  $F$  per second, the *total* number of electrons in the steady state is

$$N = F\tau, \quad (1)$$

where  $\tau$  is the electron lifetime. The photocurrent is

$$I_p = Ne/T_r, \quad (2)$$

where  $T_r$  is the transit time from the cathode to the anode. For an electrode separation  $L$ , applied field  $E$ , and photoconductor with thermal velocity  $v$  and mobility  $\mu$ , the transit time is given by

$$T_r = \frac{L}{v} = \frac{L}{\mu E} = \frac{L^2}{V\mu}. \quad (3)$$

Thus,

$$I_p = eFG = \frac{eF\mu\tau}{L^2} V, \quad (4)$$

where the photoconductive gain  $G$  is given by

$$G = \frac{\tau}{T_r} = \frac{\mu\tau}{L^2} V. \quad (5)$$

Higher gains (sensitivity) can be obtained by increasing the applied voltage  $V$  or decreasing the electrode separation, and by improving the material so that the mobility and electron lifetime are increased. The first two methods are, of course, limited by space-charge-limited currents, dielectric breakdown, and electron multiplication by such processes as impact ionization.

The electron lifetime is the time required for an electron to trace out a volume equal to that associated with one hole and equals  $(vSN)^{-1}$ , where  $S$  is the capture cross section of a hole for an electron, and  $N$  is the number of free

<sup>1</sup>In applications where speed of response is of prime importance, sensitivity must be sacrificed and photovoltaic detection is superior.

electrons per cubic centimeter. Eq. (1) can be rewritten as

$$f = n/\tau = vSn^2, \quad (6)$$

where  $f$  is light excitation rate per  $\text{cm}^3$ . Thus, we have

$$I_p = \frac{e\mu VF}{L^2 (vSf)^{1/2}}, \quad (7)$$

from which the photocurrent should be proportional to the square root of the light intensity. However, it is usually observed experimentally, that  $I_p \propto F^x$  ( $0.5 < x < 1.0$ ). Indeed, sometimes  $x$  is greater than one (supra-linearity). The explanation for this phenomenon and others not to be discussed, lies in the presence of traps, i.e., centers which temporarily capture free electrons until they are thermally freed, and recombination centers which allow a free electron to combine with a hole (Ref. 10).

**c. Recombination processes.** Infinite gains are not observed because the lifetime  $\tau$  is limited by various recombination processes. The most probable process is that of recombination near the middle of the band gap, with centers that have a large electron capture cross-section. The lifetime  $\tau$  is now given by

$$\tau = (vS_r N_r)^{-1}, \quad (8)$$

where  $S_r$  is the electron capture cross-section of the recombination centers, and  $N_r$  is their density.

Photoconductors are sensitized, i.e., lifetimes increased, by intentionally doping so as to introduce additional centers which readily capture holes as they are formed, but then have a low capture cross-section for electrons. Lifetimes in sensitized crystals of CdS are about  $10^{-2}$  to  $10^{-3}$  sec as compared to values of  $10^{-6}$  to  $10^{-8}$  sec in pure crystals.

**d. Response time.** The time required for the conductivity to change with changes in light intensity would be determined by the free carrier lifetime (Eq. 8) if there were only recombination centers present. In practice though, particularly for low light levels, trapping centers located near the band edges lengthen the decay time by thermally releasing trapped carriers after the excitation is terminated. In the case of low-intensity excitation, the density of trapped carriers may greatly exceed the density of free carriers, so that the decay time is determined by the time needed to free a carrier from a trap, rather than by the free lifetime determined by recombination. A similar situation holds for the rise time.

The exact form of the expression for the observed decay time  $\tau_0$  depends on the trap distribution in energy. In general, for a uniform quasi-continuous distribution,  $\tau_0$  will be given by the number of electrons  $n_t(kT)$ , trapped in approximately a  $kT$ -wide portion of the gap in the vicinity of the Fermi level, divided by the rate of recombination. Thus,

$$\tau = \frac{n_t(kT)}{rS_r N_r n} = \frac{n_t(kT)}{n} \tau. \quad (9)$$

The relationship can also be seen from the fact that doubling the number of free carriers causes a doubling of the number of trapped electrons (for  $n_t > n$ ). The Fermi level must drop in energy by about  $kT$ , in order for the density of free electrons to decay to  $1/e$  of their original value at the beginning of the decay.

### 3. Recent Developments Applicable to CdS Photodetectors

#### a. Properties of recrystallized evaporated CdS layers.

It had been pointed out above that, recently, methods for obtaining greatly improved photoconducting CdS layers have been reported in the literature (Ref. 9). Evaporated layers of about  $1\text{-}\mu$  thickness are heat-treated in an environment containing  $N_2$ ,  $O_2$ ,  $HCl$ ,  $Cu$ , and  $CdS$  at  $630^\circ\text{C}$ . The copper, present as a layer of 320-mesh powder, is necessary to enhance the recrystallization (Ref. 4). It and the chlorine atoms also act as dopants to sensitize the CdS (Part c of Sect. 2). It is not known what role the small amount of  $O_2$  (0.25% of the  $N_2$  amount) serves, but it appears to be necessary for good recrystallization. The excess CdS vapor, transported by the  $N_2$  gas, prevents the formation of sulfur vacancies. The latter innovation is crucial for obtaining high photoconductivity, since Cd ions act as recombination centers, which greatly reduce the free electron lifetime.

In general, maintaining stoichiometry is a problem with II-VI compounds, unlike the case for III-V compounds. The excess of one of the two components forms single and associated defects, which greatly affect the conduction and photo-conduction processes. Associated defects are complex formations composed of vacancy and impurity or lattice defects. In addition, foreign impurities tend to be interstitial rather than substitutional in II-VI compounds. These defects set up microstresses in the crystal lattice, enhancing the diffusion of intrinsic defects, which enables complicated associate defects to be formed even at temperatures near room temperature. This can lead to irreversible changes in the physical properties upon heating to higher temperatures. Investigations by Böer, et al.

(Ref. 11) on the production and annealing of X-rays and thermal damage in CdS single crystals appear to be shedding some light on these problems.

The recrystallized layers of Böer (Ref. 9) show crystallite sizes of several mm<sup>2</sup> and Hall mobilities at 140 to 230 cm<sup>2</sup>/V-sec. They exhibit photoconductivities of 10<sup>-3</sup> to 2 × 10<sup>-1</sup> ohm<sup>-1</sup> cm<sup>-1</sup> at 750 ft-c (2600°K white light) with light-to-dark-current ratios of 10<sup>8</sup> to 10<sup>9</sup>. Decay times at 100 ft-c are as low as 0.3 msec. This compares to decay times of 1 msec in Clairex type "5H" sintered cells and 8 msec in Vactec "VT series" evaporated cells.

More importantly, the parameters listed above for Böer's layers can be varied over a wide range depending on slight changes of the recrystallization procedure (Ref. 12), e.g., O<sub>2</sub> or HCl partial pressure, treatment temperature, and contents of the Cu layer. For example, layers were purposely grown to show an unusually high sensitivity for modulated light excitation (up to 250 kHz) with a very low noise spectrum (Ref. 12). This was accomplished by reducing the trap density around 0.35 eV (to < 3 × 10<sup>11</sup> eV<sup>-1</sup> cm<sup>-3</sup>), so that with a bias illumination 5 ft-c and with 0.5 ft-c modulation, the rise and decay times are about 5 μsec at room temperature (Ref. 13). This was accomplished at the expense of having higher trap densities (≲ 4 × 10<sup>17</sup> cm<sup>-3</sup>) around 0.65 eV than occur in the layers discussed in Ref. 9 and, consequently, lower sensitivity (τ = 30 μsec). However, when the temperature is decreased to 170°K or lower, the electron lifetime increases to 20 msec and a maximum gain factor of 10<sup>8</sup> with a useful photo-to-dark current ratio of at least 10<sup>7</sup> at 100 ft-c illumination is obtained.

The decay time of these layers is an order of magnitude shorter at room temperature than for single crystals of the same sensitivity, and *five* orders of magnitude shorter at dry ice temperatures of 245°K (Ref. 13).

The fact that trap densities in the re-crystallized layers are significantly lower than even those in pure crystals grown from the vapor phase, is due to the much lower temperatures involved (630°C as compared to at least 1100°C required for crystal growing) in the heat treatment.

**b. Electrical contacts.** The retention of stable electrodes on II-VI compounds at temperatures above 100°C is very difficult. Ever-present oxygen on the surface reacts with the metal electrode forming rectifying barriers. Also, diffusion of the metal (usually In or Ga) into the bulk at

higher temperatures modifies the electrical properties. An exception to the latter phenomena occurs with the use of Al as a contacting material. However, because of the oxygen on the CdS surface, it is very difficult to obtain ohmic contacts initially. The breakdown of photoconducting cells during the sterilization procedure (135°C) can be attributed in large part to this contacting problem.

Good electrical contacts to CdS that retain their ohmic properties up to 350°C have been developed in Böer's group recently (Ref. 14). The general technique uses multi-layer contacts. A monolayer of preparative metal, which enhances impurity desorption from the CdS surface, is deposited by evaporation in a high vacuum. This is followed by a thin film of the active metal which forms the ohmic contact. Finally, a covering metal is used which supplies the electrons to the bulk and acts as a sink for the diffusion of any excess active metal.

It was found (Ref. 14) that the best results were obtained using titanium (< 15 Å thick) as the preparatory metal, since it has a higher affinity for O<sub>2</sub> than Al. The active metal, aluminum, then makes an intimate contact with the CdS. It is necessary for these two layers to be deposited in a vacuum of at least 10<sup>-6</sup> mm Hg. More consistent results were obtained, if in addition, the vacuum system is flushed with nitrogen or argon gas. The final covering layer can be any stable metal such as gold, silver, or platinum.

**c. Oxygen and water vapor chemisorption.** It has long been known that the photoconductive properties of sensitized CdS are greatly affected by water vapor. Photoconducting layers or crystals degrade irreversibly when operated in a humid atmosphere, showing a greatly reduced dark resistance, and hence, photoconduction. This problem is easily avoided by placing the photodetector in a hermetically sealed case. Some commercial cells are covered with some type of plastic coating, but this is undesirable for reasons to be discussed in Part d.

Interestingly enough, there have been several samples of recrystallized evaporated layers that show no effect whatsoever when stored at 40°C in an atmosphere with 100% relative humidity for periods up to 1 year (Ref. 13). The mechanism for this behavior is not understood, but apparently some unknown dopants or special combination of dopants is fixing the Fermi level in a way that causes water vapor molecules to be repelled from the surface. The effect is analogous to the conversion of iron to stainless steel, and the latter's passivity to oxygen.

Of much greater concern, because of the difficulty in controlling it, is the influence of chemisorption and desorption of oxygen from the surface of CdS. Oxygen creates acceptors, which can act as recombination centers at the surface and influence the dark- and photo-conductance. The effects would be expected to be the most pronounced for thin crystals or layers. It is only recently though, that the real significance of  $O_2$  is being appreciated.

Measurements (Ref. 15) on crystals of pure CdS, CdS:Cl:Cu, and CdS:Cu which were exposed to flowing atmospheres of helium, oxygen, and air at temperatures ranging from 80°K to 430°K, indicate that decreases in dark conductivity of about  $10^6$  to  $10^8$  and increases in electron lifetimes of  $10^3$  can occur. Such changes would occur when the material was taken from an atmosphere of  $O_2$  and heated to temperatures of 125 to 150°C in *any* atmosphere. The desorption of  $O_2$  from CdS at these temperatures was confirmed by recent measurements in an ultra-high vacuum of  $10^{-10}$  torr (Ref. 16). In the latter, the evolved  $O_2$  was detected directly by a mass spectrograph set for a mass number of 16. The crystal was exposed to oxygen initially, cooled to  $-180^\circ\text{C}$  and then heated in the vacuum.

Bube (Ref. 15) discovered that all CdS (and CdSe) crystals had about the same electron lifetime ( $10^{-3}$  to  $10^{-4}$  sec) once they were free of oxygen, *regardless of the kind of impurity incorporation, if any*. Since long lifetimes indicate high photosensitivity, it appears that intrinsic defects such as cadmium vacancies are the sensitizers, and that the halogen principally serves as a source of electrons to reduce the effects of absorbed oxygen. Earlier, Woods (Ref. 17) had obtained qualitative results that are in agreement with Bube's.

Consideration of the barrier layer thickness associated with chemisorbed oxygen indicates that the oxygen sensitivity should be large for thicknesses of pure CdS crystals less than about  $240\ \mu$  (Ref. 15). In principle, it would appear that photosensitive evaporated layers could be grown without doping. However, the problem of maintaining a surface free of adsorbed oxygen could nullify any advantages of such layers. In any case, copper doping is required to aid recrystallization, which gives layers having values of mobility, and thus gain (see Eq. 5), up to 100 times larger than conventional evaporated CdS.

It should be pointed out, however, that high mobility layers have recently been grown without recrystallization (Ref. 18). This was accomplished by using special puri-

fication procedures for the starting material, and by performing the evaporation in an ultra-high vacuum system of about  $10^{-10}$  torr pressure. No measurements of photo-conductance were made, nor was any attempt made to desorb oxygen.

Even if it proved practical to sensitize *pure* CdS layers by desorption of  $O_2$ , the question would remain as to whether response times, i.e., trap densities (see Eq. 9), would be as low as those reported for the recrystallized layers (Refs. 9, 12).

**d. Protective coatings.** The area of protective coatings for CdS photodetectors is not covered very well in the open literature. The type of coating needed will depend heavily on the reason(s) for which it is desired. All applications require that the CdS be protected from water vapor. This can be accomplished easily by hermetically sealing the device or by any number of plastic type coatings. However, when direct application of a plastic type covering is used, it is often found that long-term changes occur in the electrical properties—probably due to diffusion of impurities.

One form of a plastic-like covering (Ref. 19) is a monomer (allyl diglycol carbonate) that polymerizes in the presence of a catalyst such as 1–2% benzoyl peroxide. A slide glass could be “glued” to the CdS layer with the monomer before the necessary heat treatment at 160°F for additional protection. The glass would also serve as a filter for ultraviolet light, which may cause darkening of the coating.

A study by Harshaw Chemical Company for NASA on the development of optical coatings for CdS thin film solar cells (Ref. 20) found that no one technique of the ones investigated was entirely suitable for applying coatings. However, the requirement for the case of photovoltaic devices, (1) to maximize the amount of light in the region of spectral sensitivity, (2) to reflect the remainder as much as possible, (3) to have high thermal emittance, as well as (4) to provide protection from the environment, are more stringent than those required for photoconductive devices.

A group at Allen-Bradley Co. has developed an evaporative multi-layer technique to protect the recrystallized layers developed by Böer. They observe (Ref. 21) an initial degradation of 20 to 50%, but complete stability thereafter. It should be remembered that these are the same CdS layers that have on occasion, shown absolute insensitivity to water vapor without undergoing extra treatment. Should

this mechanism be understood, coatings would not be required except as protection against radiation and handling.

Radiation (X-ray, electron, and proton) causes irreversible damage by forming Frenkel-type defects, which then combine with vacancies—increasing the number of recombination centers. Because of the differences in gain between photoconductive and photovoltaic devices, radiation damage is much more serious a problem in the latter. To the author's knowledge, no results of an investigation of radiation damage on CdS photoconducting cells have been published.

A new means of increasing the radiation damage resistance of silicon solar cells by as much as 50 times has been reported (Ref. 22). The technique involves using lithium as a dopant. Because of its small ionic radius (0.7 Å), the lithium is very mobile and substitutes freely for Si ions that have been removed from their lattice sites. Lithium has no significant detrimental effect on the electrical properties of silicon solar cells while it is interstitial. However, this does not necessarily follow for lithium in CdS. The lithium ions may form associate defects that are deleterious to the photoconductive properties, or may even *prevent* the formation of such defects. The actual effect to be found may be different for the recrystallized layers of CdS as compared to single crystal photoconducting CdS. Experiments along these lines would be very useful and interesting.

**N67-15711**

**C. Performance of an Electron Gun, K. Shimada**

## 1. Introduction

Electron bombardment is widely used for heating electron emitters of thermionic energy converters. Usually, a filament is placed in close proximity of the emitter ( $\frac{1}{16}$  in.) and a high accelerating (bombardment) voltage is applied. The bombardment current between filament and emitter results in emitter heating. There are certain disadvantages in using this bombardment method. The most serious problem is the definition of heat received by the emitter from the filament of the bombarder. There are also structural constraints imposed by the necessity of placing a filament in the proximity of the emitter. In order to permit application of an external magnetic field to the emitter region of our research diode, an electron gun was designed and assembled in our laboratory. The gun produces a pencil-sized electron beam which originates at a filament located over 4 in. from the target (emitter). The electron gun has semispherical electrodes and has operated

successfully at a beam power of approximately 300 w. At this power level, a beam efficiency of 85% was recorded.

## 2. Gun Design

An axially symmetrical electron gun was designed by using two semispherical electrodes. The cathode is stainless steel and machined to form a dish of radius 1.5 in. A hole with a diameter of 0.657 in. was drilled in the center of the cathode to permit installation of a counter-wound gun filament. The accelerating anode is a semi-spherical dome of radius 0.737 in. The anode material is molybdenum. A hole with a diameter of 0.358 in. was drilled through the dome-shaped anode, for beam emergence after acceleration. The cathode and the anode are placed concentrically, so that a converging electrostatic lens is formed. The two electrodes are independently movable with respect to the gun filament by means of threaded mounts.

The cone angle formed by the cathode hole and geometrical focus point equals 13.9 deg. Using the previously defined cathode and anode dish radii, and a cone angle of 13.9 deg, a gun perviance of  $0.54 \times 10^{-6} a/v^{1.5}$  is calculated. For this perviance, a beam current of 136 ma should be observed when an accelerating voltage of 4 kv is applied. An observed value was 50 ma at 3.8 kv. The reduced beam current results because the gun filament subtends a smaller cone angle than the cathode hole. This decreases the effective perviance, and a reduced beam current results. According to theory (Ref. 23) a beam diameter minimum of 0.18 in. is formed at a distance of 1.73 in. from the cathode hole. Fig. 4 shows the theoretical expectations.

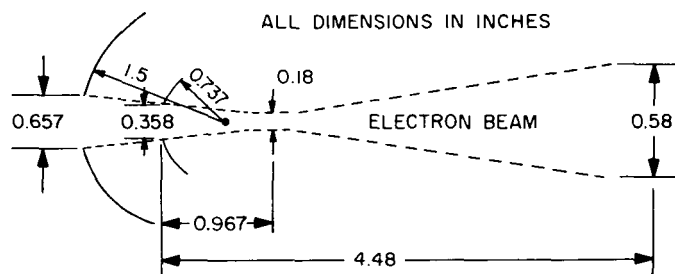


**Fig. 4. Electron beam trajectory**

## 3. Results

The hole in the accelerating anode was 10% larger than the theoretical value in order to pass more than 85% of the electrons emitted from the gun filament through the anode hole.

The beam efficiency which is the ratio between the target current and cathode current, was measured as a function of relative separations between the cathode dish and the anode dome. The results indicated that the efficiency peaks at a separation of 7.5% greater than the theoretical value. The beam efficiency, however, was more strongly affected by the location of the gun filament with respect to the cathode hole. It was found that the plane of the gun filament must be recessed inside the cathode opening by 70 to 80 mils in order to achieve a maximum value. When the gun filament was located flush with the cathode opening, the efficiency was approxi-

mately 50%. This low efficiency may be caused by the deformation of the electric field near the electron-emitting bombardment filament. An aluminum foil was used as a target plate at a distance of 4.48 in. from the anode hole. At this distance, the target size was observed to vary between 0.75 and 1 in. depending on the configuration. The beam size which was calculated from dimensions of the gun was 0.58 in. Part of the reason for the discrepancy may be attributed to heat conduction along the foil. This heat conduction would tend to spread the observed beam size.

Further study of the gun showed that better performance can be achieved by post-accelerating the electron beam after it leaves the anode hole. Consequently the present gun is connected as shown in Fig. 5. This arrangement improves the focusing effect of the gun in such a way that the spreading of the beam is minimized. This is particularly true at higher bombardment currents.

The beam efficiency is shown as a function of the total beam power in Fig. 6. For example, with a cathode current of 52 ma, a target current of 46.7 ma and a beam efficiency of 0.9 were obtained for  $R = 220,000 \Omega$ . The target beam power at this point was 257 w, and the total beam input power was 286 w. The gun filament was

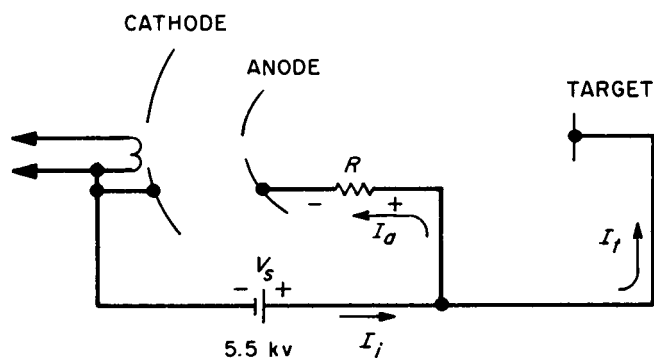


Fig. 5. Electron gun circuit

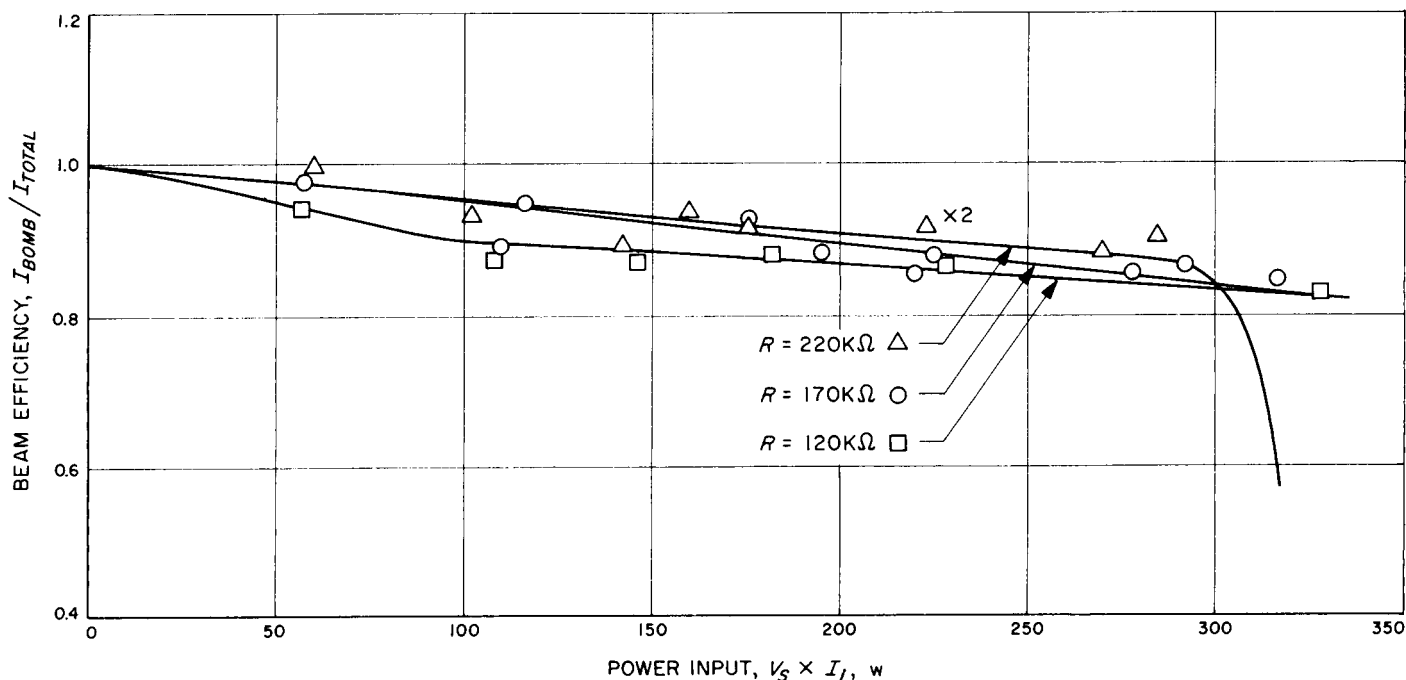


Fig. 6. Beam efficiency versus beam power

wound by using 40-mil tantalum wire. A filament current of 35.7 a was required to obtain the correct beam current for an applied voltage of 5.5 kv.

The gun was used to heat a research converter, TEECO P-VI-S, having a tantalum emitter. Observed emitter temperatures are plotted in Fig. 7 as a function of cathode beam power. The preliminary test of the research diode is now being conducted by using this gun.

#### 4. Conclusion

Use of an electron gun having a large focal length is advantageous for heating thermionic converters because (1) the heating power arriving at the target surface can be determined directly from the beam power, and (2) the target region can be free of other structures (i.e., gun filaments) so the entire target is optically accessible. This gun was operated successfully with our research converter and produced emitter temperatures up to 2100°K.

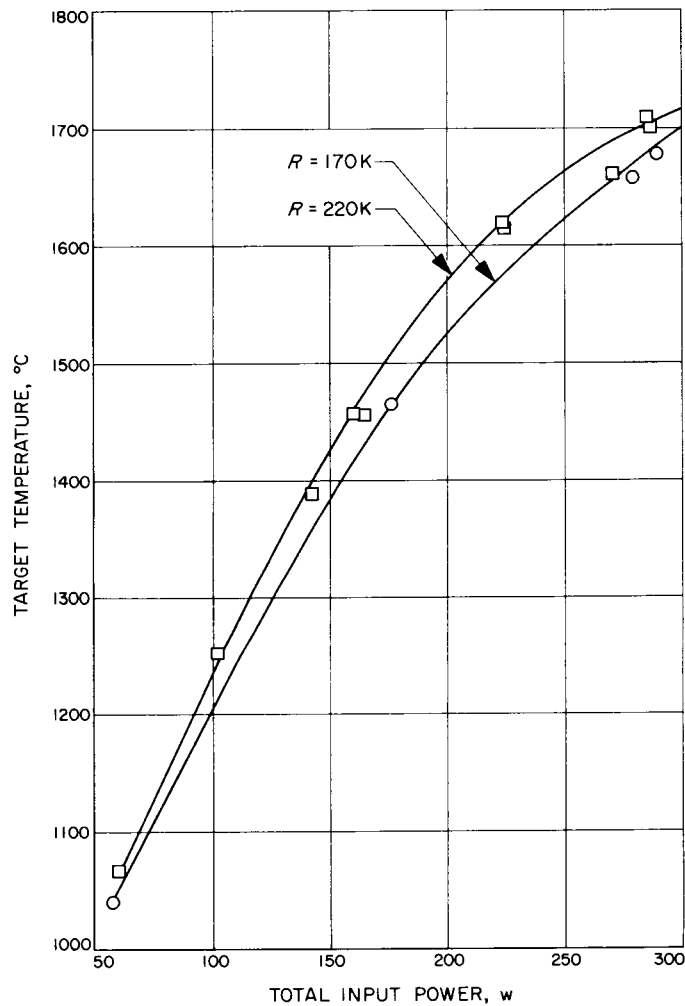


Fig. 7. Target temperature versus input power

## References

1. Shumka, A., *Space-Charge-Limited Current in Germanium*, p. 43, Division of Engineering and Applied Science Report, California Institute of Technology, Pasadena, California, 1966.
2. Dacey, G. C., *Phys. Rev.*, Vol. 90, pp. 759-764, 1953.
3. *Photoconductor Cells*, Clairex Corporation, 8 West 30th Street, New York, N. Y., 1966.
4. Gilles, J. M., and Van Cakenberghe, J., *Nature*, Vol. 182, p. 862, 1958.
5. Dressner, J., and Shallcross, F. V., *Solid-State Electronics*, Vol. 5, p. 205, 1962.
6. Dressner, J., and Shallcross, F. V., *J. Appl. Phys.*, Vol. 34, p. 2390, 1963.
7. Addiss, R. R., Jr., *Trans Am. Vac. Soc. Symp.*, p. 354, 1963.
8. Vecht, A., and Apling, A., *Phys. Stat. Solidi*, Vol. 3, p. 1238, 1963.
9. Böer, K. W., Esbitt, A. S., and Kaufman, W. M., *J. Appl. Phys.*, Vol. 37, p. 2664, 1966.
10. Bube, R. H., *Photoconductivity of Solids*, p. 303, John Wiley & Sons, Inc., New York, 1960.
11. Böer, K. W., O'Connell, J. C., and Kennedy, C. A., Technical Report No. 2, NASA Contract NSG-573, University of Delaware, Newark, Del., Feb., 1966.
12. Böer, K. W., Feitknecht, J. W., and Kannenberg, D. G., *Phys. Stat. Solidi*, Vol. 16, p. 697, 1966.
13. Böer, K. W., *private communication*, 1966.
14. Hall, R. B., Master's Thesis submitted to University of Delaware, Newark, Del., June, 1966.
15. Bube, R. H., *J. Electrochem. Soc.*, Vol. 113, p. 793, 1966.
16. Schubert, R., *Phys. Stat. Solidi*, Vol. 16, K157, 1966.
17. Woods, J., *J. Electronics & Control*, Vol. 5, p. 417, 1958.
18. Hudock, P., *AIME Conference*, unpublished, Boston, 1966.
19. Willardson, R. K., Bell & Howell Research Center, Pasadena, Calif., *private communication*. Their photo-detectors are used in camera light metering and punch card read-out, and have not necessarily been tested for stability at sterilization temperatures.
20. Schaeffer, J. C., and Hill, E. R., "Development of Optical Coatings for CdS Thin Film Solar Cells," NASA CR-54965, Harshaw Chemical Co., Cleveland, Ohio, 1965.
21. Feitknecht, J. W., *private communication*, the materials and method used are proprietary, Allen-Bradley Co., Milwaukee, Wis., 1966.

### References (contd)

22. Vavilov, U. S., Smirnova, I. V., and Chapnin, V. A., *Soviet Physics—Solid State*, Vol. 4, p. 2469, 1962.
23. Pierce, J. R., *Theory and Design of Electron Beams*, D. Van Nostrand Co., Inc., New York, 1949.

## VI. Materials

### ENGINEERING MECHANICS DIVISION

N67-15712

#### **(A) Char Reflectances and Planetary Entry Heat Shields, R. G. Nagler**

##### **1. Introduction**

With the prospect of entering into planets other than Earth where the probability of a significant carbon dioxide content in the atmosphere is high, the optical properties of ablating or nonablating heat shield surfaces take on new importance. Instead of the radiant heat rejection being limited to the emitted energy from the surface at its characteristic temperature and wavelength, a second radiant heat-rejection mechanism, reflection of shock layer radiation back into the atmosphere, begins making a significant contribution (Ref. 1). For the entry cases in which radiative energy inputs from the shock layer are large, precise determination of this reflectance property becomes very important to any realistic analysis of the heat-shield requirements necessary for capsule survival.

##### **2. Apparatus**

Recently Arthur D. Little, Inc., assembled an apparatus and made measurements for JPL on the reflectance of pyrolytic graphite and of typical phenolic nylon chars

(Ref. 2). An optical schematic of the system is shown in Fig. 1. A three-dimensional gimbal arrangement was used to allow angles of incidence between 33 and 72 deg from the perpendicular and hemispherical collection by a stepwise summation of overlapping spherical polygons. This goniometric technique is an absolute method requiring no reflectance standard. It has the advantages of relative simplicity and of errors easily identified and estimated. Its major drawback is that the measurement itself is a

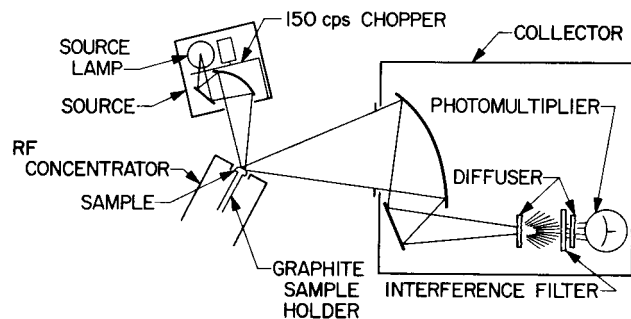


**Fig. 1. Optical schematic of reflectance measuring device**

time-consuming process (approximately 1 hr per reflectance determination). A reference comparison was made on a standard spacecraft grade black-paint specimen furnished by JPL. The Arthur D. Little reflectance measurement was well within the normally acceptable tolerance for the reflectance of this particular black paint ( $5 \pm 1\%$ ).

### 3. Results and Discussion

Aside from testing the capability of the apparatus, three major questions needed to be determined:

- (1) In a typical nonablating radiation heat shield, is the surface truly Lambertian (i.e., reflectance constant in all directions), and if not, what are the consequences?
- (2) Since a typical entry shock layer at temperatures of as much as  $30,000^\circ\text{R}$  emit a major portion of their radiant energy at wavelengths below  $0.3\ \mu$ , are there gross changes in reflectance at wavelengths in this region?
- (3) If the normal variation in surface roughness is bounded for a typical ablative char, how great is the difference in measured reflectance for the two bounds?

The effect of assuming a Lambertian surface when the actual material is not one, has been discussed by Semple and Roshier (Ref. 3) in relation to the thermal balance of satellites. Most materials approach complete reflectance at some glancing angle. How rapidly the reflectance increases with angle of incidence is a function of the material and its effective surface roughness. In the near-perpendicular planetary entry case at initial entry velocities greater than 26,000 ft/sec, radiant heating of thermal protection systems for blunt entry bodies predominates, and an increase of one percentage point in the effective reflectance, due to low angle variations in reflectance, causes a corresponding 1% decrease in the total energy to the body. If this actual effective reflectance is used, rather than the lower perpendicular reflectance value, in determining the portion of the total vehicle weight required for the thermal protection system, the weight estimated will be lower and perhaps more realistic (although there are other factors involved). The additional weight may then be released for scientific payload.

Pyrolytic graphite was used as the sample material. Reflectance data for as-deposited pyrolytic graphite are shown in Fig. 2. A reflectance increase of 5% is seen

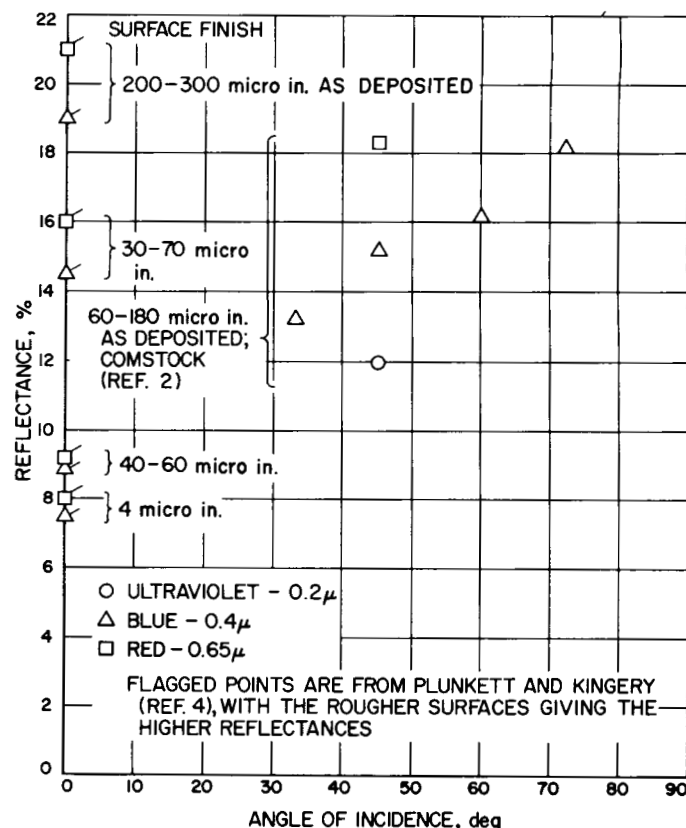


Fig. 2. Reflectance of pyrolytic graphite

from a change in incident angle from 33 to 72 deg. Reflectance also seems to increase with longer wavelengths. The natural variation in pyrolytic graphite samples makes it difficult to compare reflectances from different experimenters. The data of Plunkett and Kingery (Ref. 4) are shown on Fig. 2 for comparison. Their data show the strange progression of reflectance decreasing as the surface roughness decreased. There seems to be fair agreement for equivalent surface finish and a similar trend of higher reflectance at longer wavelengths. Neither set of data agrees particularly with the data of either Null and Lozier (Ref. 5)—24.8% at a 45-deg angle of incidence—or Autio and Scala (Ref. 6)—~27% at normal incidence. Both sets of experimenters considered their specimens to be highly polished and clean, approaching single-crystal graphite. A single crystal would be expected to give a higher reflectance than as-deposited pyrolytic graphite. Plunkett and Kingery's opposing trend is probably due to grinding debris.

In any case, pyrolytic graphite is not Lambertian and increases 38% in reflectance between 33 and 72 deg from the normal. This increase in effective reflectance is partially offset by wavelength effects wherein reflectance is

lower for the shorter wavelengths typical of high-temperature planetary-entry shock layers.

The effect of wavelength on the reflectance of phenolic nylon chars is shown in Fig. 3. The circles and triangles were measured by Comstock (Ref. 2) on chars produced in a 1660°R reducing atmosphere furnace at JPL and heat-treated for a half an hour at 5000°R in an inert atmosphere to achieve graphitization. The samples of Wilson (Ref. 7) were also charred in a furnace at 2000°R and then were heated to approximately 5000°R in an arc imaging furnace during measurement. All of the chars show an apparent drop in reflectance in the blue (around 0.4  $\mu$ ). More data would be needed before any conclusion could be made as to whether or not there is an increase in reflectance in the ultraviolet (below 0.3  $\mu$ ). If there is an increase in reflectance in the ultraviolet, it is probably small, which means there is little benefit from the peak

radiative wavelength of the shock layer being in the ultraviolet.

The variation in reflectance level for different temperatures and for different experimenters is fully explainable from surface characteristics. The two sets of room temperature samples do not show a significant variation in reflectance, in spite of the large difference in macro surface roughness caused by a factor of two differences in the nylon particle size in the original composite. Apparently, the important surface property is the micro-surface roughness, not the macro roughness. Fig. 4 shows how the deterioration of reflectance came about at high temperatures. The deterioration in reflectance corresponds to a change in micro roughness, resulting in a final sample surface with a velvet appearance. This change appears to be brought about by vaporization and oxidation of free atoms at crystallite boundaries. It would appear that it is primarily an oxidation process, since the chars were heat-treated at 5000°R in the absence of oxygen without deterioration but degraded rapidly in elevated temperature tests, due to oxygen retained in the system or carried in as an impurity in argon. The specimens tested by Wilson were similarly oxidized and would thus be expected to show a lower reflectance than the nonoxidized room temperature samples. The important factors to be remembered from Figs. 3 and 4 are that wavelength has only limited effect on char reflectance,

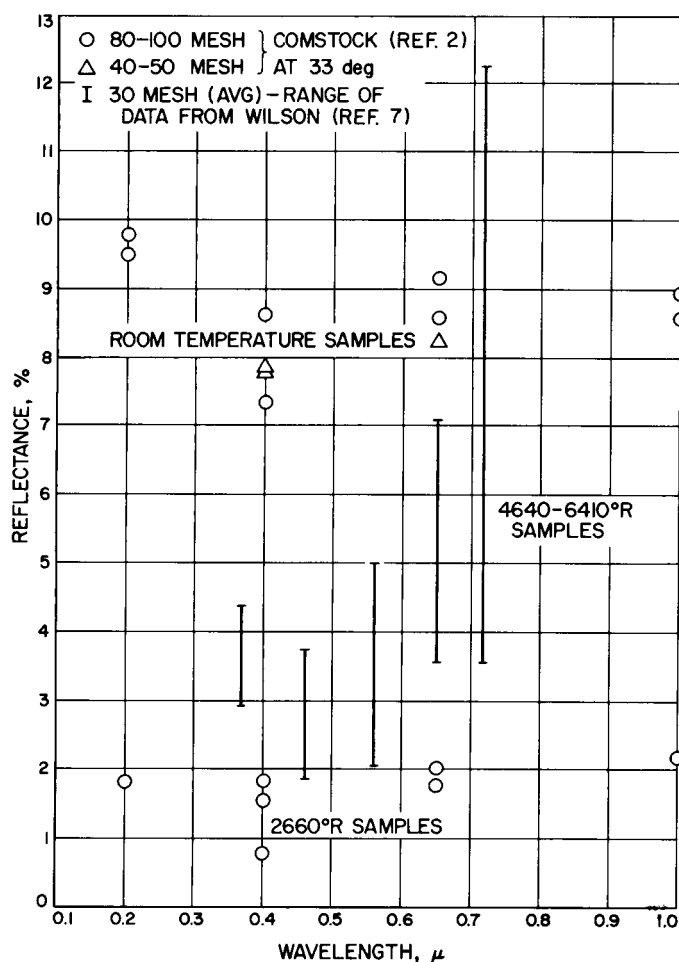


Fig. 3. Effect of wavelength on reflectance of phenolic nylon chars

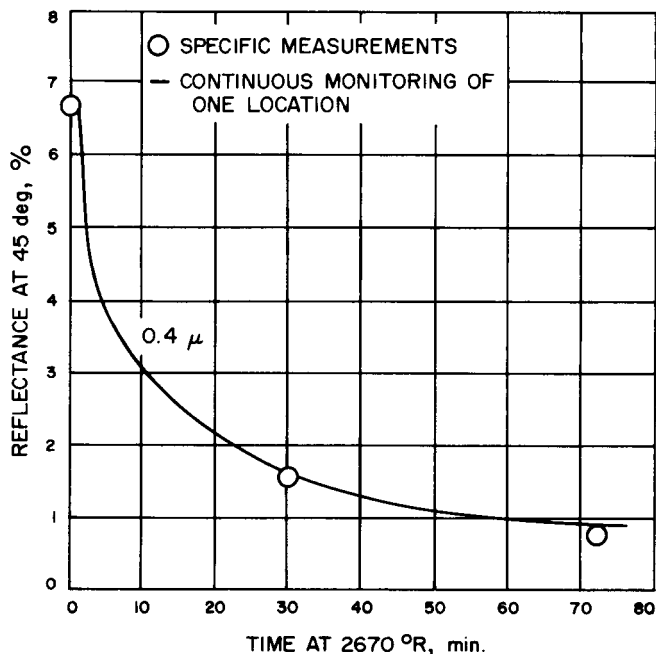


Fig. 4. Effect of time at temperature on reflectance

that the size of the macroscopic pores has little effect on char reflectance, and that the microscopic surface roughness has a large effect on reflectance which is dependent on time, temperature, oxygen availability, graphite crystallite sizes, free carbon availability, etc.

Phenolic nylon, like pyrolytic graphite, may have some angle of incidence effect, but it is not at all obvious from the available data (Fig. 5). The collection technique showed the reflected energy to be double-lobed in distribution with the peak of one lobe at the normal spectral angle and the peak of the second directly back at the incident beam. This is an interesting area which could use further investigation.

The char reflectance measurements can also be compared with char emittance measurements (Ref. 8). Southern Research Institute measured total emittance on phe-

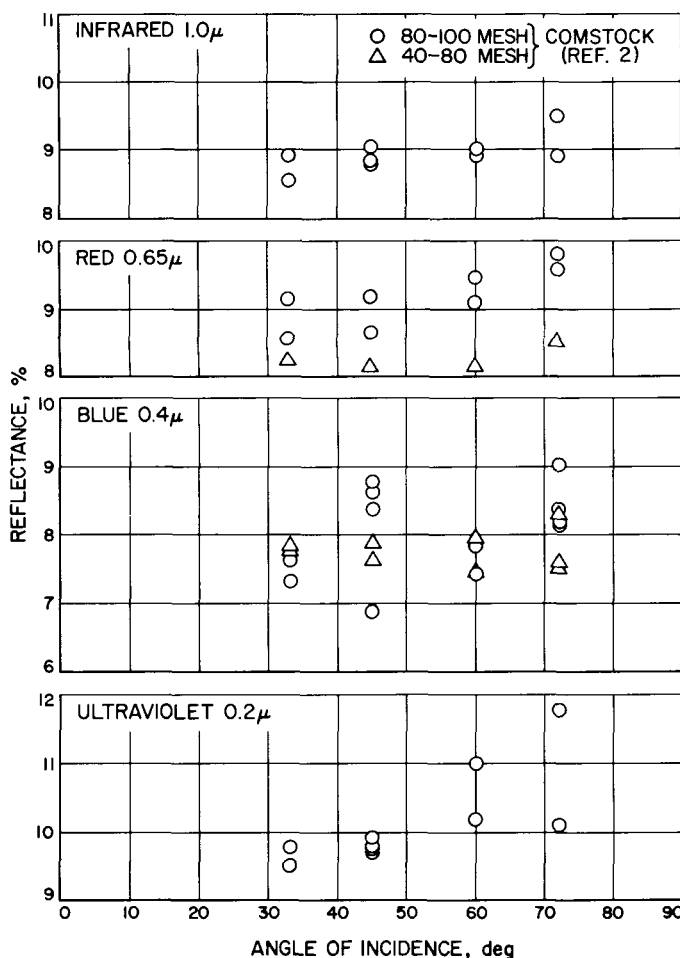


Fig. 5. Effect of angle of incidence on the reflectance of phenolic nylon chars

nolic nylon chars similar to those used by Wilson (Ref. 7). Assuming total reflectance to be one minus total emittance, these reflectances would range between 6 and 38% over temperatures between 2000 and 4500°R. This does not compare at all with the data from reflectance techniques and appears to be of questionable value if it is to be used as a measure of the absorptance of external radiation.

#### 4. Conclusion

The conclusions that might be derived from this work are: (1) Absolute reflectance techniques have great potential for improvement of our high-temperature optical property data. (2) Angle-of-incidence effects should be looked into and may provide a higher effective reflectance. (3) The optical properties of chars are not particularly affected by gross surface roughness, whereas microscopic roughness can vary the reflectance as a function of the environmental history.

#### B. Carbon and Graphite, D. B. Fischbach

##### 1. Dependence of Mechanical Properties on Microstructure

Graphite is very promising as a high-strength, high-modulus, lightweight material. Young's modulus of perfect single-crystal graphite, parallel to the basal (layer) planes, is about  $150 \times 10^6$  psi, and the specific gravity is only 2.26. Furthermore, it is well known that even polycrystalline graphite retains useful mechanical strength to temperatures of about 3000°C. Both the production of large single crystals of graphite and their application to structural engineering requirements are difficult, and neither has been achieved. It is likely that practical graphites will continue to be polycrystalline for some time to come. Experience with other materials indicates that it should be possible to approach theoretical single-crystal mechanical property values in fine polycrystalline fibers, which can be incorporated into fiber-reinforced composites for engineering use. Consequently, there is considerable current interest and activity in the development of high-modulus, high-strength carbon and graphite fibers. The very strong intrinsic anisotropy of the graphite crystal structure makes the properties of polycrystalline carbon and graphite materials, including fine fibers, very sensitive to microstructure. The influence of two microstructural variables, preferred orientation texture and crystallographic perfection, on mechanical properties

has been investigated here, using data obtained on samples of bulk pyrolytic and glassy carbon.

The dependence of the Young's modulus on preferred orientation texture in pyrolytic carbons is very strong, as shown in Fig. 6, where the points indicate experimental results. The preferred orientation texture is expressed in terms of the root-mean-square misorientation angle of the basal planes relative to the substrate plane of the deposit. Preferred orientation was varied by high-temperature plastic deformation. This treatment also resulted in increased layer stacking order and crystallite size. The modulus was measured statically at room temperature. There is a similar strong dependence of tensile strength on preferred orientation at room temperature, but at elevated temperatures the orientation dependence of the strength appears to decrease.

Price (Ref. 9) has shown that the elastic modulus of dense polycrystalline carbons can be calculated from the single-crystal elastic constants and the preferred orientation texture, using a simple constant stress model. The very pronounced orientation dependence of the modulus

can be ascribed primarily to the very low shear modulus parallel to the layer planes. Three curves calculated using Price's theory are shown in Fig. 6. There is evidence from studies on single crystal and very highly oriented polycrystalline graphite that the interlayer shear modulus is a sensitive function of crystallographic perfection (Ref. 10), and curves were calculated for values of shear compliance  $s_{44}$  appropriate to perfect single-crystal graphite, good graphite (annealed pyrolytic carbon) and a very poorly crystalline, nongraphitic carbon (hypothetical). With the exception of the interlayer shear constant, the elastic constants for perfect graphite (Ref. 10) were used for all three curves. It is clear from Fig. 6 that the degree of layer plane orientation required to approach the high intrinsic layer-plane modulus of graphite is very high and increases with increasing structural perfection. Such high degrees of preferred orientation are realized in graphite whiskers (Ref. 11) and might be achievable in pyrolytically deposited fibers by hot stretching. However, such highly oriented graphite fibers would be subject to premature failure by axial shear or delamination, and bonding to the matrix phase in a fiber-reinforced composite would probably be difficult.

Alternatively, if the intrinsic anisotropy could be reduced, for example by introducing cross-link bonds between the layer planes, usefully high modulus values could be achieved with much more modest degrees of preferred orientation (curve for very poor graphite in Fig. 6). Available evidence suggests that this may be the case for nongraphitizing carbons, such as glassy or vitreous carbons. For example, the Young's modulus of isotropic Japanese glassy carbon with a specific gravity of only 1.5 is  $2.5$  to  $3.5 \times 10^6$  psi (Ref. 12), while the modulus of isotropic pyrolytic carbon with a specific gravity of 1.8 is only  $1.5 \times 10^6$  psi (Ref. 9). Furthermore, the strength of isotropic glassy carbon is comparable to that of well-oriented pyrolytic carbon parallel to the substrate plane (Ref. 12). It seems likely that both the modulus and the strength of such nongraphitizing carbons would increase appreciably with preferred orientation, and cross-linked structures should make possible better bonding to the matrix in composite materials. These considerations suggest that nongraphitizing cross-linked forms of carbon offer more promise for the development of desirable fiber properties than do graphitizing carbons. This conclusion seems to be borne out by the high modulus and strength values which have recently been achieved elsewhere in layer-plane oriented nongraphitizing carbon fibers (Refs. 13, 14).

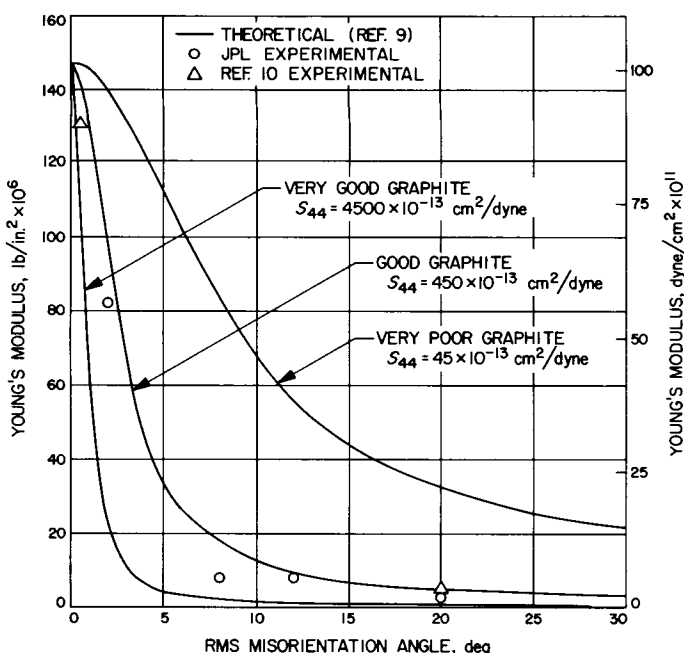


**Fig. 6. Young's modulus (parallel to average layer plane orientation) of polycrystalline carbons and graphite as a function of root mean square layer plane misorientation angle**

## 2. Effect of Plastic Deformation on Graphitization Rate in Pyrolytic Carbon

It has been established that high-temperature tensile deformation parallel to the substrate plane greatly enhances the amount of graphitization (layer stacking order) achieved in pyrolytic carbons for a given heat-treatment time and temperature (SPS 37-36, Vol. IV). A more detailed investigation is currently being made of the influence of stress and deformation on the kinetics of graphitization, using constant-load tensile creep deformation of pyrolytic carbon parallel to the substrate plane. A sample of the same carbon is supported beside the creep specimen in the test apparatus in such a way that it is not stressed but receives the same thermal treatment

as the deformed specimen. The progress of the graphitization is measured by the decrease in interlayer spacing determined from Debye-Scherrer diffraction patterns of powder samples taken from the two specimens as a function of isothermal creep/heat-treatment time.

A series of six successive creep/heat treatment runs at 2600°C and 10,000-psi stress has been completed, using a single pair of specimens (one stressed, one unstressed). The specimens were completely removed from the apparatus for measurement; X-ray samples were filed off following each high-temperature run; and the specimens were then remounted for the next run. The success of this series of tests is proof that the problems associated with

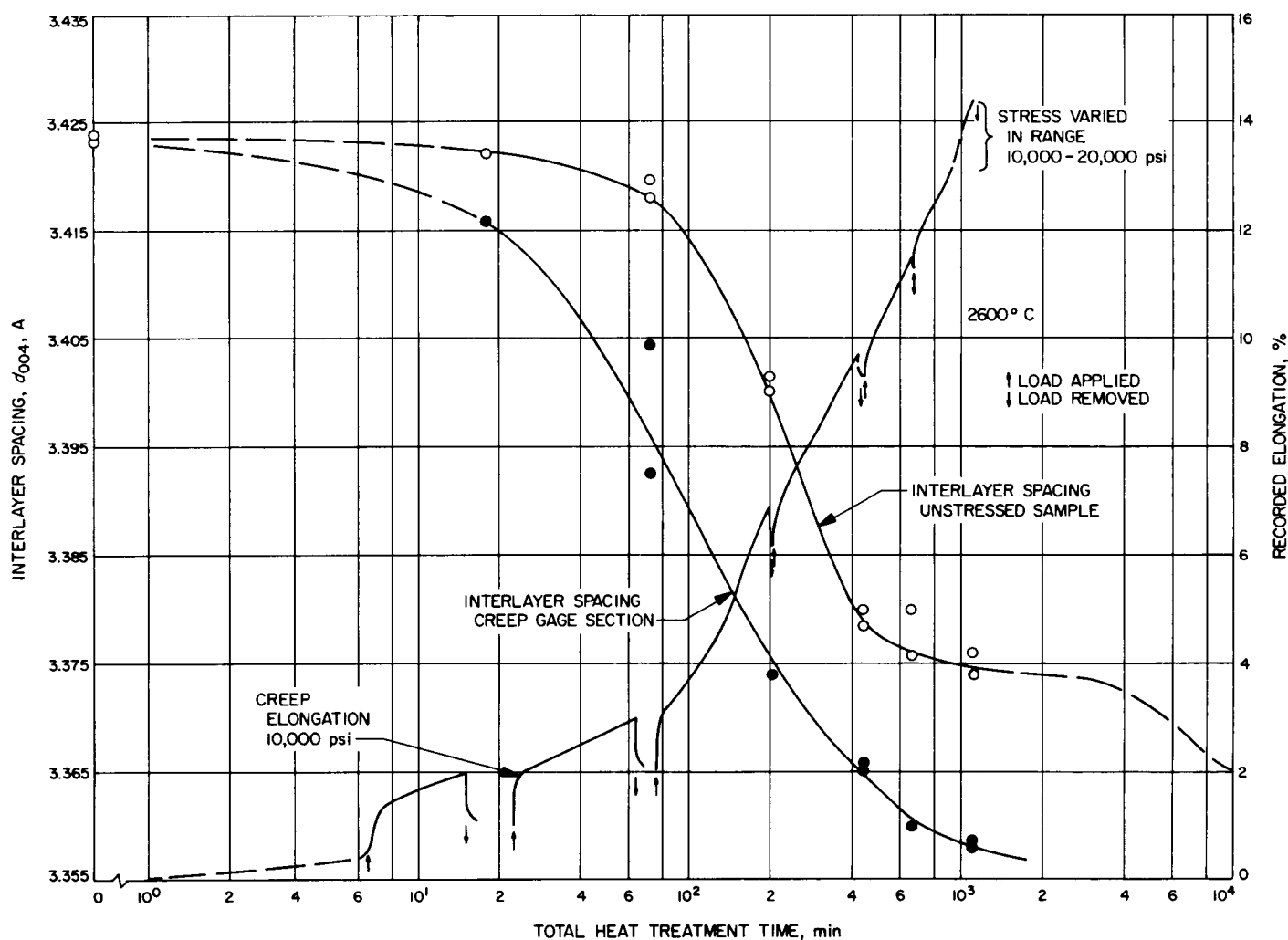


Fig. 7. Interlayer spacing and creep elongation (parallel to substrate) of pyrolytic carbon as a function of time at 2600°C

handling fragile specimens have been largely overcome by the equipment and procedure modifications similar to those reported on earlier for the tensile test apparatus (SPS 37-38, Vol. IV). The results of this test series are shown in Fig. 7, where interlayer spacing and cumulative recorded elongation, expressed as percent of the gage length at the beginning of each run, are plotted against the logarithm of the cumulative time at temperature. Under these experimental conditions there is a definite enhancement of layer ordering after only about 1% elongation (18 min at temperature), and the graphitization of the stressed specimen is greater than that of the unstressed specimen throughout the entire series of treatments. Furthermore, although the unstressed specimen shows the typical two-stage graphitization behavior observed in earlier studies of pyrolytic carbon, the graphitization of the stressed specimen appears to proceed in a single stage. The second stage of graphitization is associated with a pronounced increase in preferred orientation texture and apparent crystallite layer diameter (Ref. 15). Changes in both preferred orientation (SPS 37-33, Vol. IV), (Ref. 16) and crystallite size are greatly accelerated by tensile deformation, and this appears to account for the absence of a second stage in the deformed specimen. Further studies at other stress levels and temperatures are planned to further define the mechanisms involved in the graphitization rate increase.

### 3. Stress-Dependence of Tensile Creep Rate in Highly Oriented Graphite

Among several mechanisms which have been proposed for tensile deformation parallel to the average basal plane orientation in highly oriented graphites, nonbasal dislocation glide and Nabarro-Herring diffusion mass transport seem most promising (Ref. 16). The stress-dependence of the creep rate offers a possible means for distinguishing between these two possibilities. For the Nabarro-Herring mechanism the creep rate increases linearly with stress. For a dislocation climb mechanism, such as operates in metals, the creep rate is expected to increase as the fourth (or higher) power of the stress. An initial test of this technique was made using the creep specimen employed in the deformation-enhanced graphitization study discussed above. This test was made during the last half of the final creep run shown in Fig. 6. The specimen had undergone a total elongation of about 13% and had a high degree of layer stacking order (interlayer spacing was about 3.358 Å, Fig. 6) and preferred orientation. The high preferred orientation was confirmed qualitatively after the test by examining the microstructure. The stress was alternately increased and decreased in the

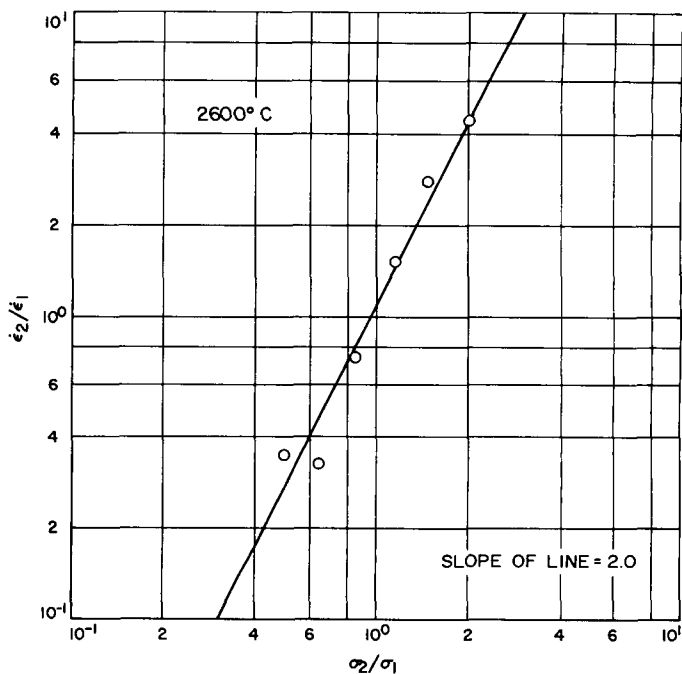


Fig. 8. Dependence of creep rate on stress at 2600°C for a pyrolytic carbon specimen prestrained 13%; tension parallel to substrate plane

range 10,000 to 20,000 psi and the effect on the creep rate measured. The results are shown in Fig. 8 where the logarithm of  $\dot{\epsilon}_2/\dot{\epsilon}_1$ , the ratio of the creep rate before a stress change to that after the change, is plotted against the logarithm of the ratio of the two stress values ( $\sigma_2/\sigma_1$ ). It was found that the creep rate was proportional to the stress squared.

This second-power stress dependence is much lower than the 5.5 to 6.5 power stress dependence which has been reported recently for commercial coke-pitch graphite (Ref. 17) and a special uranium-loaded graphite (Ref. 18). Therefore, it appears that a different creep mechanism operates in well-oriented, graphitized pyrolytic carbons than in coke-pitch graphite. The exact meaning of the observed second-power dependence is not yet clear, however. It could result from a combination of Nabarro-Herring and dislocation mechanisms operating simultaneously. It might also be influenced by systematic experimental errors resulting from deformation of the specimen grips and other features of the equipment and technique used. These errors should tend to increase the apparent stress dependence. Further studies are planned, using improved experimental techniques, to investigate the influence of temperature and specimen pretreatment on the stress dependence.

## 1. Introduction

The research program to determine the role of grain boundaries and their associated impurities on the mechanical behavior of polycrystalline ceramics continues. Present research is being continued on magnesium oxide (MgO). This portion of the work emphasizes a detailed study of the atomic structure of grain boundaries.

## 2. Recent Development of Grain Structure

At this time the study has been limited to the use of X-ray topographic techniques. A survey of such methods is available in the literature (Ref. 19). The use of X-ray diffraction micrography, whereby the diffraction image is intersected by a sheet of high resolution film a few mm from the sample surface, revealed grain structural data indicated below. The data (Figs. 9 and 10) was obtained from pressure-sintered polycrystalline MgO by rocking the depicted grains in the X-ray beam.

The data indicate that the two grains separated by the Grain Boundary No. 1 have 1.0.0. planes which have an

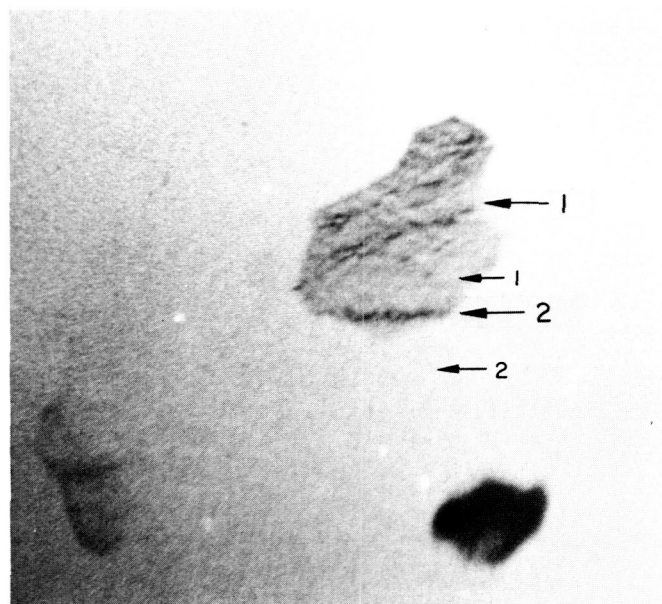
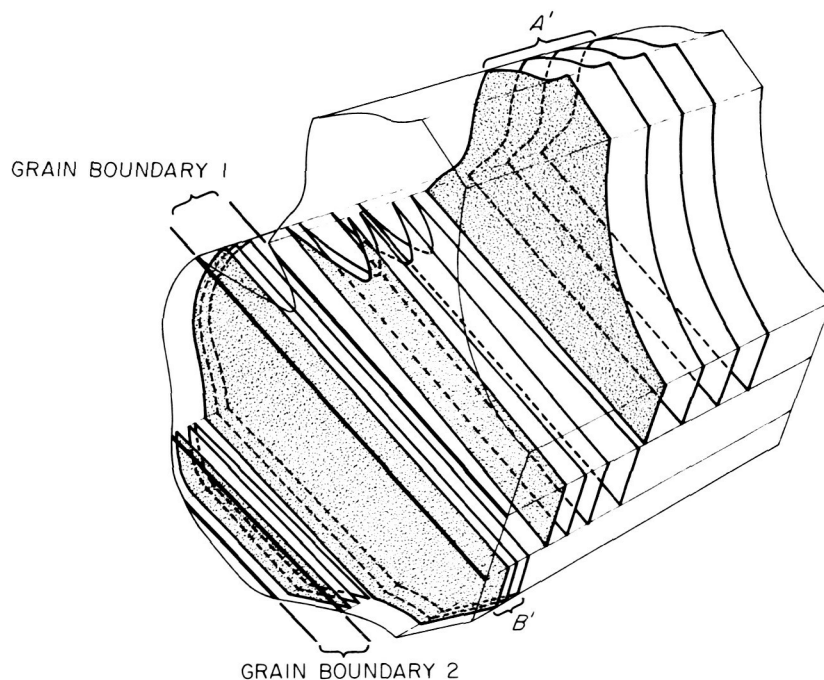


Fig. 10. X-ray diffraction micrograph of 2 MgO grains



$A' < B' = 7.5$  MINUTES OF ARC  
 PLANAR ANGLES WITHIN GRAIN BOUNDARY 1 = 5 MINUTES OF ARC  
 PLANAR ANGLES WITHIN GRAIN BOUNDARY 2 = 9 MINUTES OF ARC

Fig. 9. Schematic of 1.0.0. planes located within grain depicted in Fig. 10: (a) schematic of Fig. 10 with associated regions, (b) side view of grain, revealing disturbed boundary regions

angle of approximately 7.5 minutes of arc with one another. The Boundary Region No. 1, which must be crystalline by its associated strong diffraction signal, appears to contain a disturbed mosaic crystalline region the 1.0.0. planes of which make a maximum angle of 5 minutes of arc with another. The basic resolution of this technique is within seconds of arc. The Boundary Region No. 2 appears to be similar to No. 1, except that the related angle is 9 minutes of arc.

Figs. 11 and 12 show mosaics of a polycrystalline MgO region taken with reflected light microscopy and diffracted X-ray microscopy, respectively. The similar regions are bounded by a dark line. The X-ray topograph was assembled by associating physically the diffracted images which appeared in unrelated areas of the X-ray film, due to slight angular misalignments of the grains themselves. A normal photograph was then made of the pasted grain assembly. Grains 1, 3 and 5 clearly show glide planes and dislocation loops in Fig. 12. The Grains 2 and 4 apparently responded to the stresses by polygonizing into parallel substructural regions. The 1.0.0. X-ray topograph

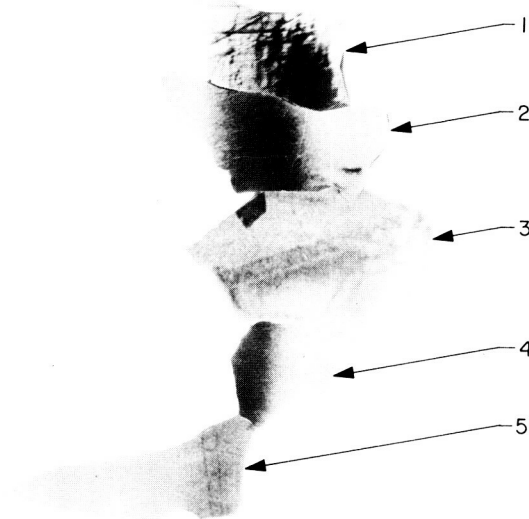


**Fig. 12. X-ray micrograph of a polycrystalline MgO region indicated in Fig. 11**

which reveals a number of adjacent grains with similar orientation, substantiates the preferred orientation data published in *SPS 37-40*, Vol. IV, p. 25.

Fig. 13 shows the results obtained by a more careful angular orientation of Grain No. 3. The slip lines, as well



**Fig. 11. Reflected light microscopic image of polycrystalline MgO**

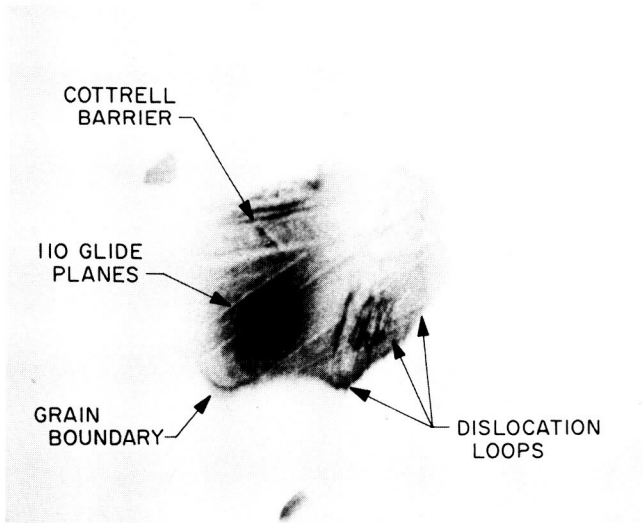


**Fig. 13. Detailed X-ray micrographic image of Grain No. 3 indicated in Fig. 12**

as the dislocation loops and the Cottrell barriers (where two slip lines appear to cross causing a blocking of one of them), are clearly visible. The strongly diffracting grain boundary appears at the bottom of the grain image. The diffraction image and presence of the numerous dislocations at the grain boundary again tend to indicate a highly disturbed crystalline region in that area.

At this time attempts are under way to obtain improved images of the boundary region by means of critical crys-

tal rocking techniques and the use of very high-resolution spectroscopic plates.

The data obtained at this time are too preliminary to be more definitive concerning the description of the grain boundaries. This of course is the primary purpose of this program. However, the results do indicate the presence of large amounts of substructure and disorder in a pure, annealed polycrystalline ceramic. Such results would not be expected.

## References

1. Nagler, R. G., "Preliminary Analysis of the Importance of Material Properties and Thermal Inputs on Heat Shields for Mars Entry," *Journal of Spacecraft and Rockets*, Vol. 3, No. 5, May 1966, pp. 693-699.
2. Comstock, D. F., "Measured Directional Reflectances of Chars in the UV, Visible, and Near Infrared," Final Report on JPL Contract 950867 by Arthur D. Little, Inc., March, 1966.
3. Semple, E. C., and Roshier, K. H., "Deviations from Lambert's Law in the Absorptance of Metallic and Non-Metallic Surfaces and the Effect of These on the Thermal Balance of Satellites," Royal Aircraft Establishment Technical Memo., No. Space 53, January 1965.
4. Plunkett, J. D., and Kingery, W. D., "The Spectral and Integrated Emissivity of Carbon and Graphite," *Proceedings of Fourth Conference on Carbon*, Pergamon Press, New York, N. Y., 1960, pp. 457-481.
5. Null, M. R., and Lozier, W. W., "Research and Development on Advanced Graphite Materials, Vol. XXI, Carbon Arc Image Furnace Studies of Graphite," WADC-TR-61-72, November 1963.
6. Autio, G. W., and Scala, E., "The Normal Emissivity of Isotropic and Anisotropic Materials," AIAA 6th Structures and Materials Conference, Palm Springs, California, April 5-7, 1965.
7. Wilson, R. Gale, "Hemispherical Spectral Emittance of Ablation Chars, Carbon and Zirconia to 3700°K," NASA TN D-2704, Langley Research Center, March, 1965. (See also "Symposium on Thermal Radiation of Solids," San Francisco, California, March 4-6, 1964, NASA SP-55, Air Force ML-TDR-64-159.)
8. Wilson, R. Gale (compiler), "Thermophysical Properties of Six Charring Ablators from 140° to 700°K and Two Chars from 800° to 3000°K," NASA TN D-2991, Langley Research Center, October 1965.
9. Price, R. J., "Young's Modulus of Pyrolytic Carbon in Relation to Preferred Orientation," *Philosophical Magazine*, Vol. 12, p. 561, 1965.

## References (cont d)

10. Meers, J. T., et al., "Effects of Neutron Damage on the Mechanical Properties of Pyrolytic and Single Crystal Graphite," Semiannual Report (July-December 1965), Union Carbide Corporation, Carbon Products Division, AT-(40-1)-3237, February 25, 1966.
11. Bacon, R., "Growth, Structure and Properties of Graphite Whiskers," *Journal of Applied Physics*, Vol. 31, p. 284, 1960.
12. Kotlensky, W. V., and Fischbach, D. B., "Tensile and Structural Properties of Glassy Carbon," Technical Report 32-842, November 15, 1965.
13. Bacon, R., Pallozzi, A. A., and Slosamik, S. E., "Carbon Filament Reinforced Composites," paper presented at 21st Annual Meeting of the Reinforced Plastic Division, Society of the Plastics Industry, Inc., Chicago, February 8 to 10, 1966.
14. Standage, A. E., and Prescott, R., "High Elastic Modulus Carbon Fibre," *Nature*, Vol. 211, p. 169, 1966.
15. Fischbach, D. B., "Kinetics of Graphitization. I. The High Temperature Structural Transformation in Pyrolytic Carbons," Technical Report 32-532, February 1, 1966.
16. Fischbach, D. B., and Kotlensky, W. V., "On the Mechanisms of High Temperature Plastic Deformation in Pyrolytic Carbons," Paper No. 72, Symposium in Graphite, Electrochemical Society, Cleveland, Ohio, May 1-5, 1966 (to be published in *Electrochemical Technology*).
17. Green, W. V., and Zukas, E. G., "The Stress Dependence of the Creep Rate of Two Commercial Graphites," Paper No. 71, Symposium on Graphite, Electrochemical Society, Cleveland, Ohio, May 1 to 5, 1966.
18. Green, W. V., "The Stress Dependence of the Creep Rate of a Uranium-Loaded Graphite," *Carbon*, Vol. 4, p. 81, 1966.
19. Newkirk, J. B., "Observation of Dislocations and Other Imperfections by X-ray Extinction Contrast," *Transactions of the Metallurgical Society of the AIME*, Vol. 215, pp. 483 to 497, June 1959.

## VII. Applied Mechanics

### ENGINEERING MECHANICS DIVISION

N67-15715

#### **A. Touchdown Stability Study, J. A. Garba**

##### **1. Introduction**

Some early work performed in the area of dynamic stability of a three-legged vehicle, such as *Surveyor*, indicated that a two-dimensional landing (i.e., the vehicle CG moving in a plane normal to the landing surface) is most critical from the stability standpoint (Ref. 1). Later, NASA's Langley Research Center undertook concurrent analysis and tests of a four-legged vehicle, modeled to simulate the lunar module (LM) configuration (Ref. 2), which showed that for a four-legged vehicle the above finding is not valid. While this work was conclusive for a four-legged vehicle, no extrapolations to a three-legged vehicle could be made. At that time there were no computer programs available to study the dynamics of a three-legged vehicle in other than planar landings.

In March 1965, JPL initiated a three-dimensional lunar touchdown stability study. The task took the form of an outside procurement. A contract was awarded to the Bendix Corporation, Aerospace Division, in July 1965, who had at that time just completed a similar study for LM.

##### **2. Study Phases I and II**

This study was divided into two phases: Phase I consisted of the development and checkout of a computer

program suitable for establishing stability boundaries as a function of 11 parameters. These are: 9 initial conditions of the spacecraft, the surface slope, and the coefficient of friction. In Phase II the checked-out computer program was used to study the effect of three-dimensional parameters on the stability boundaries of the *Surveyor* spacecraft.

The *Surveyor* vehicle landing system consists of three inverted tripod legs and three body blocks mounted under the frame symmetrically about the roll axis of the vehicle. One strut of each leg contains a compressible shock absorber. The shock absorber characteristics are described by a hydraulic spring in parallel with a viscous damper and a coulomb friction mechanism. Thus, the force opposing displacement and velocity has nonlinear characteristics. Attached to the apex of each tripod is a pivoting footpad made of aluminum honeycomb having a force characteristic which is a function of the angle of the applied load, the contact area, and the crushing displacement.

The force-displacement characteristics of the blocks are similar to those of the footpads. The location of these blocks on the vehicle is such that the honeycomb is crushed only after an appreciable deflection of the legs has taken place.

In the formulation of the equations of motion twelve degrees of freedom are considered. These are: the six degrees of freedom describing the motion of the vehicle; one degree of freedom describing the angular position of each leg with respect to the vehicle main body; and one degree of freedom describing the angular orientation of each footpad with respect to the lower leg struts.

The forcing functions acting on the CG are determined from the external forces and the geometry of the vehicle.

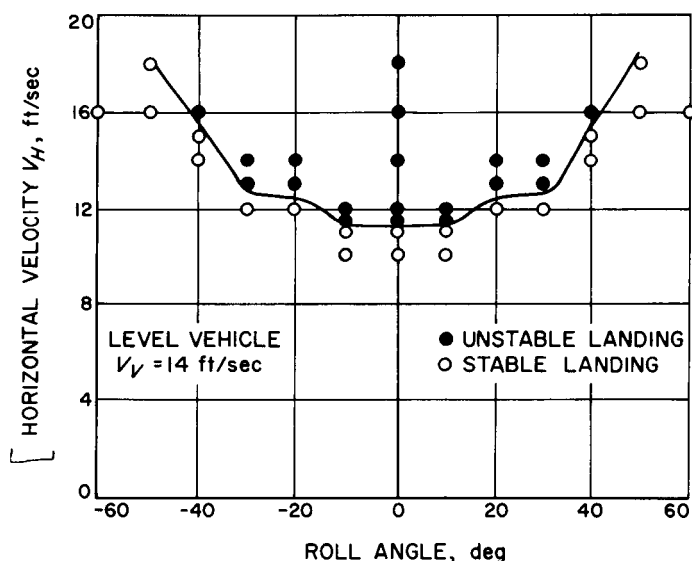


Fig. 1. Horizontal velocity versus roll angle stability profile

The equations are then integrated, using a fourth-order Runge-Kutta integration routine with a variable step size. The step size is controlled by the permissible truncation error on any one of the 12 variables and their derivatives. A new geometry is then determined, and the forcing functions are upgraded for the next integration step.

The approach taken in Phase II was to first establish stability boundaries for two-dimensional or "planar" base cases, then introduce three-dimensional parameters such as roll orientation and cross-slope velocity to study the change in stability boundary.

### 3 Results

It was found that for a level vehicle the stability margin increased with the introduction of three-dimensional effects. Fig. 1 shows a typical stability profile, of roll angle versus horizontal velocity, for a level vehicle and a constant vertical velocity of 14 ft/sec. A roll angle of zero indicates a planar downhill landing. It can be seen that a higher horizontal velocity is required to topple the spacecraft as it is rolled out of the planar configuration.

For a vehicle having its roll axis tipped from the vertical by 5 deg, it was found that a slight degradation of stability exists at certain combinations of roll angle and cross slope angle. The results of this investigation are shown in Fig. 2. Here  $\nu$  denotes the amount the vehicle roll axis is tipped from the vertical, and  $\Gamma$  denotes the

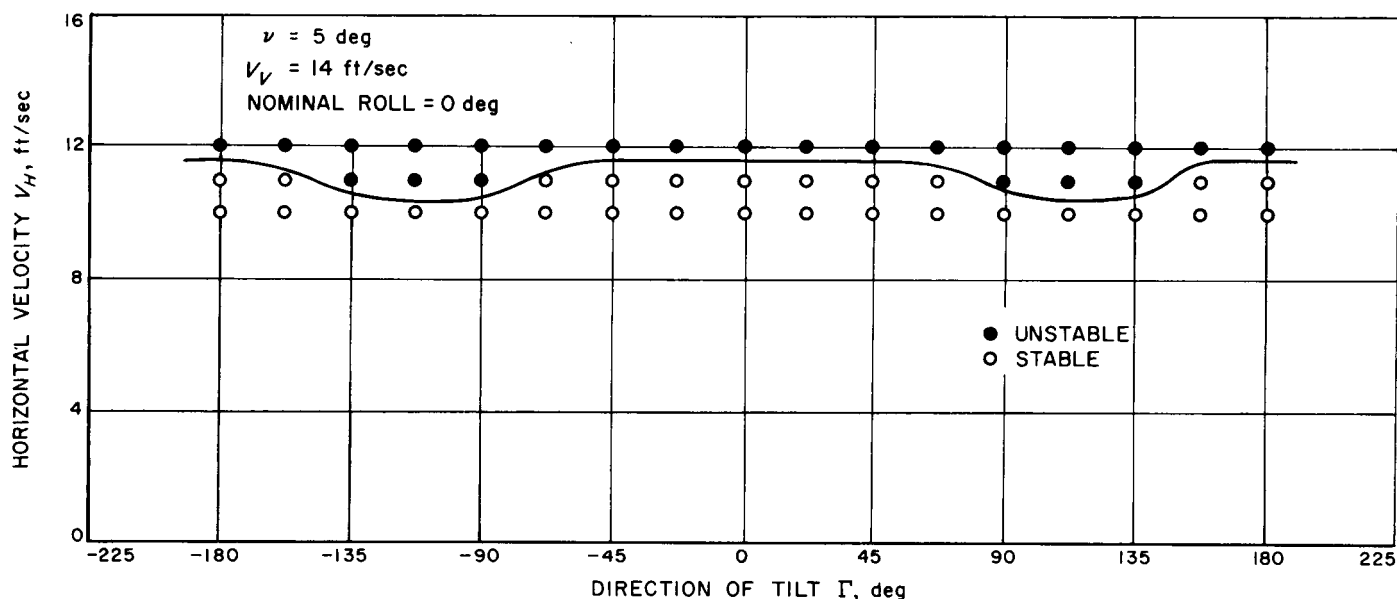


Fig. 2. Horizontal velocity versus direction of tilt stability profile

direction of this tilt.  $\Gamma$  equal to zero indicates a planar downhill landing. It can be seen that for a nonlevel vehicle, there are three-dimensional landings more critical than the corresponding planar cases. However, the stability degradation is so slight that it is of little practical consequence, particularly for *Surveyor*, since all stability boundaries were found to be far outside the required range of landing velocities.

The study tends to indicate that the amount of stability degradation due to three-dimensional effects is not a function of the number of legs only. It is also a function of the particular vehicle geometry; namely, the ratio of the center of gravity location above the base polygon, formed by the tips of the landing legs, to the critical overturning radius. The critical overturning radius is defined as the smallest distance from the projection of the

center of gravity onto the base polygon to any of the edges of the polygon.

It appears, however, that the stability of a four-legged vehicle is more sensitive to three-dimensional effects as compared to a three-legged vehicle with the same minimum overturning radius and the same center of gravity location.

Results of the study are documented in Ref. 3. This report has been prepared by the contractor and will be released by JPL in the near future, pending minor corrections and modifications.

Computer predictions using the above program have been compared to a full-scale drop test. The results of this investigation are to be published in a JPL Technical Report.

## References

1. Cappelli, A. P., "Dynamic Analysis for Lunar Alightment," *AIAA Journal*, Vol. 1, No. 5, pp. 1119-1125, May 1963.
2. Walton, Jr., W. C., Herr, R. W., and Leonard, H. W., "Studies of Touchdown Stability for Lunar Landing Vehicles," *Journal of Spacecraft*, Vol. 1, No. 5, pp. 552-556, September-October 1964.
3. Alderson, R. G., and Wells, D. A., "Final Report on *Surveyor* Lunar Touchdown Stability Study," Report No. MM-66-19, Bendix Products, Aerospace Division, South Bend, Indiana, July 8, 1966.

## VIII. Aerodynamic Facilities

### ENVIRONMENTAL SIMULATION DIVISION

N67-15716

**Wind Tunnels,** B. Walker, P. Jaffe, R. Weaver, and C. Klose

#### 1. Variable Stability Test, B. Walker

Wind Tunnel Test 20-630 of the Army Missile Command (Redstone Arsenal, Alabama) variable stability model, was performed in the JPL 20-in. Supersonic Wind Tunnel in order to determine the static stability characteristics of various fin configurations in the presence of a missile-like body. Approximate aerodynamic parameters for the test were Mach numbers 1.48, 1.65, 1.84, 2.02, and 2.22 and Reynolds number/in. from  $0.03 \times 10^6$  to  $0.53 \times 10^6$ . The angle of attack was varied from  $-4$  to  $+8$  deg.

A six-component internal strain gage balance was used to measure the aerodynamic forces. Force and moment data were reduced to body axis coefficients. The center-of-pressure positions along the longitudinal axis of the body were calculated and base pressure measurements were also recorded.

The model is shown in Fig. 1 with one set of fins attached. The grit band on the nose was used to artificially trip the boundary layer. The model was designed so that

only the afterbody loads (essentially the loads on the fins) were measured by the balance. The ogive nose and centerbody were part of the sting and therefore nonmetric.

#### 2. Vehicular Limit Cycle Motion, P. Jaffe

The angle-of-attack envelope of a body flying through a medium will diverge or converge according to the sign of the effective decay factor,

$$\left[ C_D - C_{L_\alpha} + \frac{md^2}{I} (C_{m_q} + C_{m_{\dot{\alpha}}}) \right]$$

$C_D$ ,  $C_{L_\alpha}$  and  $(C_{m_q} + C_{m_{\dot{\alpha}}})$  are the aerodynamic coefficients of drag, lift curve slope, and dynamic stability, and  $md^2/I$  is the square of the ratio of body diameter to radius of gyration, the mass distribution parameter. If the factor is positive, the body is dynamically unstable and the envelope will diverge; if the factor is negative, the body is dynamically stable and the envelope will converge.

The linearized method of flight analysis, such as that used in ballistic ranges, assumes that the aerodynamic coefficients are constant and, consequently, the decay

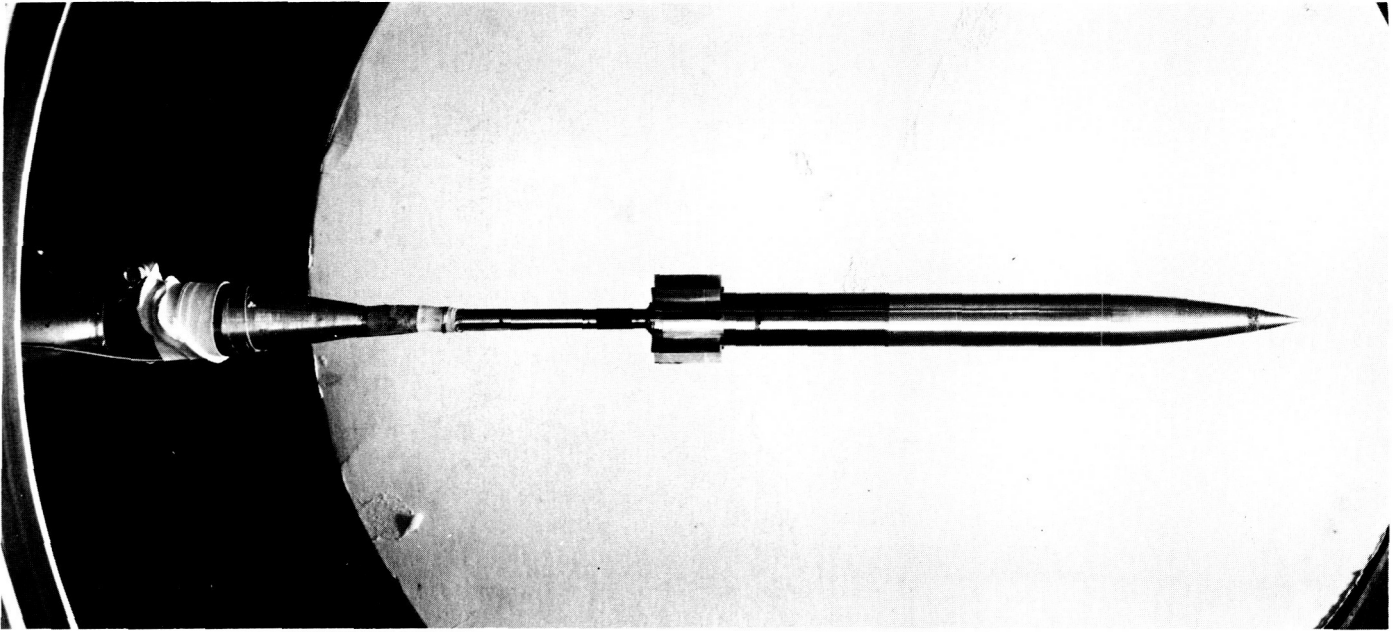


Fig. 1. Model installation in 20-in. Supersonic Wind Tunnel

factor is constant. Accordingly, a body will diverge, remain at the initial angle-of-attack envelope, or converge depending on whether the decay factor is positive, zero, or negative, respectively. In actual situations the aerodynamic coefficients are functions of the angle of attack and the effective decay factor will be a function of the angle-of-attack envelope. When this factor changes signs from positive to negative as the envelope increases, the body will exhibit an asymptotic angle-of-attack envelope or, as commonly called, a "limit cycle." For instance, consider a planar oscillating body which has lift and drag coefficients of the following form:

$$C_L = C_{L\alpha} \alpha + C_1 \alpha^3 \quad (1)$$

$$C_D = C_{D_0} + C_2 \alpha^2 \quad (2)$$

For a class of blunt bodies and moderate angles of attack this is a decent representation; typical values of the constants are

$$C_L = 1.0\alpha + 2.0\alpha^3$$

$$C_D = 1.4 - 1.0\alpha^2 \quad (\alpha \text{ is in radians})$$

Employing the energy-integral method of dynamic stability flight analysis (Ref. 1) the effective decay factor is

determined to be

$$(C_{D_0} + \frac{1}{4}C_2\alpha_0^2) - (C_{L\alpha} + \frac{3}{4}C_1\alpha_0^2) + \frac{md^2}{I}(C_{m\dot{q}} + C_{m\ddot{\alpha}}) \quad (3)$$

For the example taken, it is

$$+ 1.4 - 0.25\alpha_0^2 + 1.0 - 1.5\alpha_0^2 + \frac{md^2}{I}(C_{m\dot{q}} + C_{m\ddot{\alpha}})$$

where  $\alpha_0$  is the amplitude of oscillation or the angle-of-attack envelope. If we take  $(C_{m\dot{q}} + C_{m\ddot{\alpha}})$  to be  $-0.1$  and  $md^2/I$  to be  $(4.5)^2$  (which are representative values), the effective decay factor is  $0.375 - 1.75\alpha_0^2$ . This factor becomes zero when  $\alpha_0 = 26.5$  deg. Therefore, if the body is in flight at an amplitude greater than  $26.5$  deg, the decay factor being negative will tend to make the body converge to this angle; and, if it is at an amplitude less than  $26.5$  deg, the positive decay factor will make it diverge. To verify this, the amplitude motion of the body at initial amplitudes of  $25.0$  and  $28.0$  deg was determined with a 6 degrees-of-freedom computer program. Curves A and B of Fig. 2 show the results of these two computer runs as a function of the distance traveled by the vehicle. The computer results confirm the above.

This simple analysis brings out an extremely important point: one must be careful when drawing qualitative conclusions from flight data. Consider what would happen if

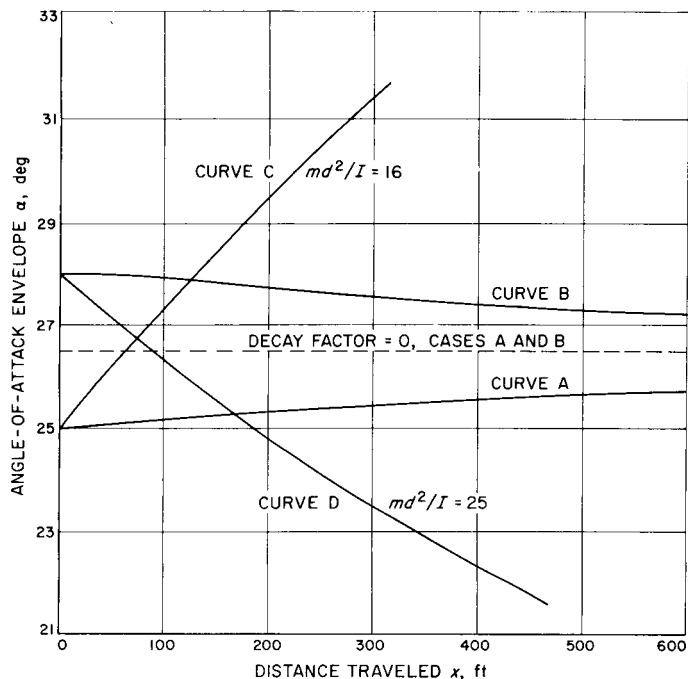


Fig. 2. Angle-of-attack envelope as a function of the mass distribution parameter

the radius of gyration were changed *slightly* from  $1/4.5$  to  $1/4$  and  $1/5$   $d$  ( $d$  = model diameter). Eq. (3) predicts that in the case of the  $1/4$  radius of gyration, the body would be dynamically unstable and diverge until it reached an amplitude of 68 deg and, in the case of the  $1/5$ - $d$  radius of gyration, the body would always be dynamically stable; the corresponding computer runs are depicted as cases C and D, respectively. In ballistic ranges the radii of gyration are usually higher than those of wind tunnel free-flight tests because of the severe model integrity problem in ranges. It is quite possible, consequently, that equally valid data from both a ballistic range test and a wind tunnel free-flight test will, qualitatively, show two completely different things. Therefore, to qualitatively apply test data to predict the motion of a full-scale vehicle could, for the same reasons, be completely erroneous. By the same token, if the data from both tests are properly reduced they will both predict the same full-scale vehicular motion.

### 3. Aerodynamic Drag Characteristics of a Blunt Body in a Retrorocket Exhaust Plume, R. Weaver

Future plans for planetary exploration include survivable landings on other planets. Many systems for landing have been proposed but few have been practically demonstrated. One system that has been tested on Earth

and used successfully in a lunar landing is the *Surveyor I* retro system.

When the Mars survivable landing missions are planned, the *Surveyor I* system will most certainly be considered. There is, however, a significant difference between a lunar landing and a landing on a planet which supports an atmosphere. The presence of an atmosphere requires an understanding of the aerodynamic characteristics of the entry body involved. The aerodynamics of candidate entry shapes have been, or are being, obtained at JPL and elsewhere. However, the effect of retrorocket exhaust on entry body aerodynamics has not previously been examined.

To investigate these effects, a wind tunnel test was conducted in the JPL 20-in. Supersonic Wind Tunnel. The model used was a 4-in. diameter, 60-deg, spherically blunted rounded edge cone with 3 simulated retrorockets. Figs. 3 and 4 show the model, mounted in the tunnel, on a six-component internal strain gage balance. The rockets were simulated by three brass tubes that were internally contoured to produce a rocket plume shape which approximated that of the full-scale rockets being considered (Fig. 5). The tubes were connected to a plenum chamber that surrounded the balance.

The model was mounted on the balance in such a manner that the rockets could be fired forward, but the thrust would not be recorded by the balance. Only the aerodynamic forces were measured. Fig. 6 shows drag retro on (drag  $R$ ) over drag retro off (drag  $\infty$ ) versus thrust over drag retro on. These data confirm the general trend noted in Ref. 2; i.e., as the thrust level increases, the effective aerodynamic drag decreases. The data presented in Fig. 6 are for a Mach number of 0.70 (except the one point, as noted on the figure). Because of the limited amount of data obtained, the fairing shown in Fig. 5 may not be accurate in the thrust-to-drag region from 0 to 0.8. The thrust was calculated using the equation

$$\text{Thrust} = C_f P_c A_T$$

where

$$C_f = \text{a thrust coefficient } (\approx 1.61)$$

$$P_c = \text{rocket plenum chamber pressure}$$

$$A_T = \text{the area of the rocket throat.}$$

All drag values are based on measured data.

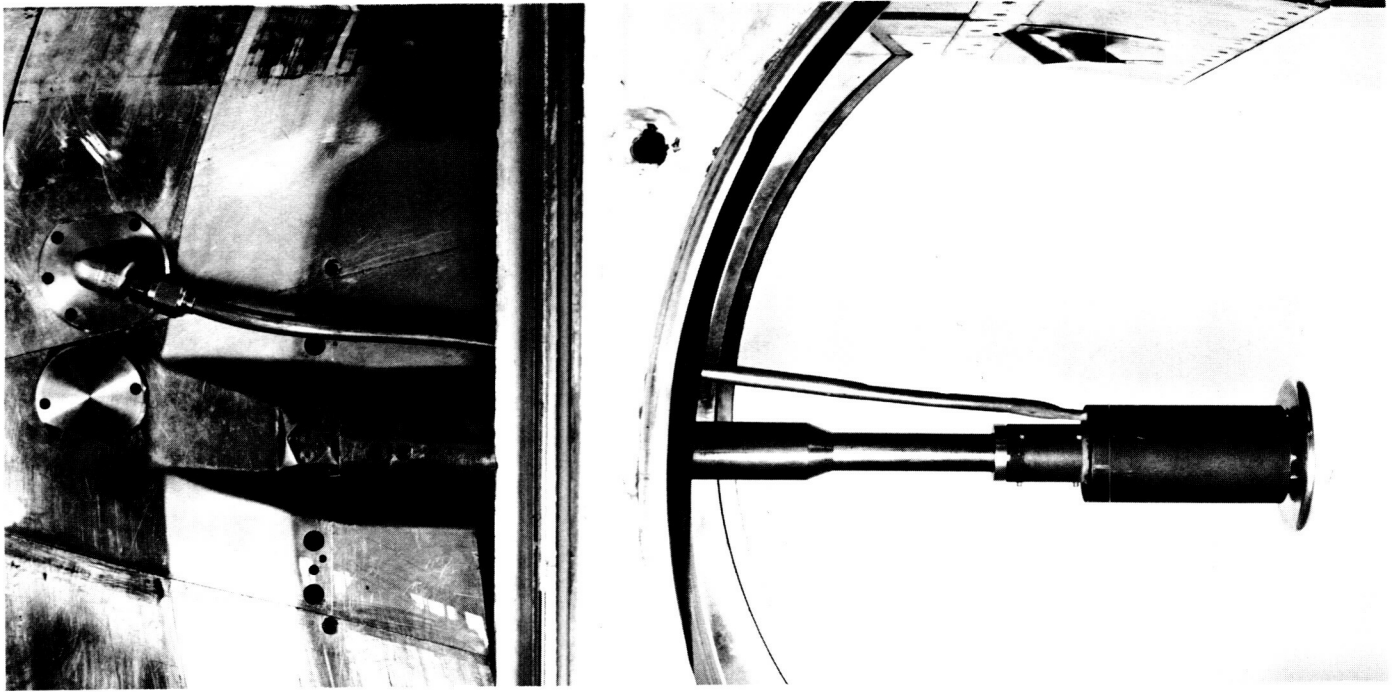


Fig. 3. Side view of model in tunnel, showing plenum chamber

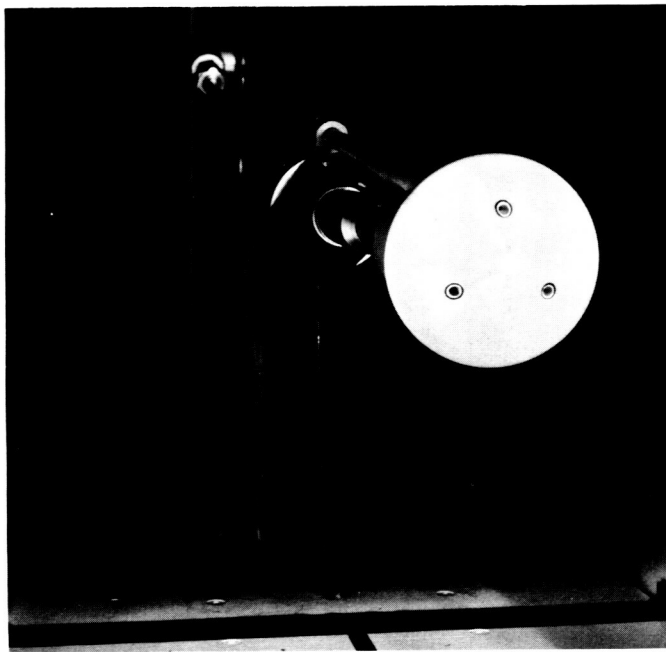


Fig. 4. Front view of model in tunnel, showing simulated rockets

The parameters that were varied during the test are: rocket chamber pressure; tunnel stagnation pressure; and, to the extent possible, Mach number. The data for Mach

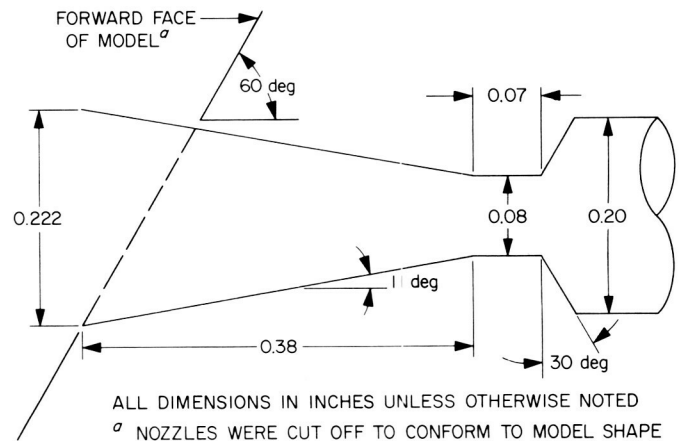


Fig. 5. Nozzle contour

numbers other than 0.7 were invalid except for two runs made at  $M = 2.6$ .

The tunnel used is basically supersonic, but by opening the nozzle throat it can run subsonic. However, due to the size of the model and the tunnel test section area and design, the data can only be considered relative. Absolute values are not considered reliable.

The data obtained in this test are preliminary but nevertheless are indicative of the retrorocket effects. Future

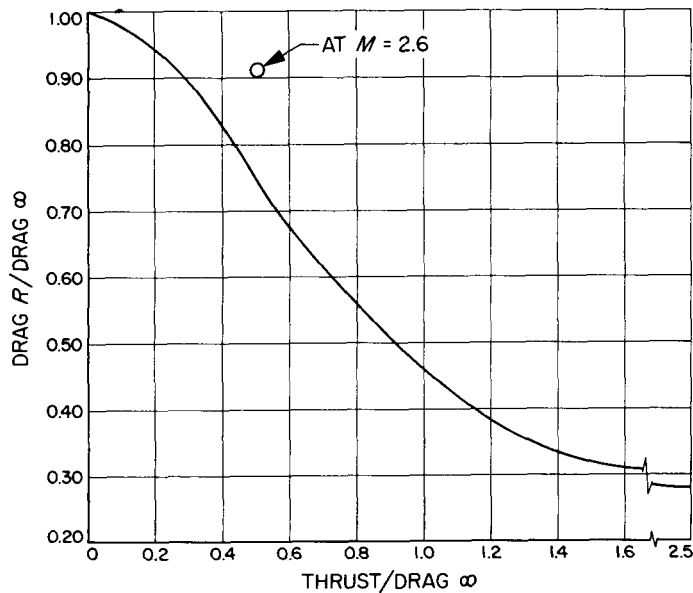


Fig. 6. Drag ratios versus thrust-to-drag ratio

plans include a further evaluation of these data and further testing.

#### 4. Reconstruction of a Density Profile for an Unknown Atmosphere, R. Weaver and C. Klose

The future exploration of the planet Mars will require the soft landing of instrument packages. To insure that such packages survive the descent and landing, some information about the atmosphere must be known as far in advance as possible. In view of this requirement, a study has been initiated to investigate the least complex instrumentation package on a probe-type capsule capable of producing useful information about the atmosphere.

The least complex package would probably be a transmitter and the only data would be the time from separation to impact. This system would require two capsules of different ballistic coefficients. The difference in time to impact between the two capsules could give some indication of the atmospheric characteristics. Some problems are apparent: (1) two successful entries are required, (2) entry conditions must be identical for both capsules, and (3) the impacts must occur at the same surface elevation. Since acquiring knowledge about these conditions necessitates additional instrumentation, the difference in time scheme does not seem practical.

As a second phase in this study, an accelerometer package is being investigated. Using time versus acceleration along the flight path for 90-deg entry angles, density versus

time can be computed using the classical  $F = MA$  equation. Using both the 3 and 6 degrees-of-freedom computer programs to generate the acceleration versus time data, variations of the resulting equations were tried. These variations are

Variation 1:

$$V_1 = \frac{2(a_s^2 + a_s g \sin \theta)}{da_s/dt} \quad (1)$$

$$\rho_1 = \frac{2 \Delta a_s}{V_1^2} \quad (2)$$

where the subscript 1 refers to Variation 1.

Variation 2:

$$V_2 = \frac{2\Delta(a_s^2 + a_s g \sin \theta)}{a_s \Delta + \frac{V_1^2}{2} \frac{d\rho_1}{dt}} \quad (3)$$

$$\rho_2 = \frac{2\Delta a_s}{V_2^2} \quad (4)$$

Variation 1 proved to be inadequate when the acceleration curve had a steep slope. The error arises because of the invalid assumption that the density variation between data points is small. Thus, Variation 2 was derived. This variation is iterated by replacing the  $V_1$  and  $\rho_1$  in Eqs. (3) and (4) by the new values found for  $V_2$  and  $\rho_2$  until successive values repeat within tolerable bounds.

Variation 2 has also proved to be inadequate. The problem lies in finding the value of  $d\rho/dt$  in the equation for velocity. A small error in reading acceleration as a function of time is magnified when the density is computed. In this method, the computed densities and the measured times are used to plot  $\rho$  as a function of time. This is not a smooth curve because of the above mentioned errors and any value of  $d\rho/dt$  chosen is arbitrary. If an incompatible value is chosen (one that is not accurate to within a few percent), the velocity computed in the next iteration will be in error. These errors have been as high as 50%. In view of what this error does to the density value calculated, this variation was also abandoned.

Both of these variations find the altitude by integrating from impact backward to any time,  $t$ .

A third variation has been developed in an attempt to overcome the deficiencies of the first two.

From accelerometer readings, the instantaneous capsule velocity can be determined at any point by numerically integrating the following equation:

$$V = V_E + \int (g \sin \theta - a_s) dt \quad (5)$$

Altitude can be calculated by starting at the surface of the planet and numerically integrating velocity until time zero is reached. The equation below defines the process:

$$h = \int V \sin \theta dt \quad (6)$$

To demonstrate the feasibility of using numerical integration as a method for determining velocity and altitude, a 3 degrees-of-freedom flight trajectory was used. The outputs [time, acceleration in the direction of velocity vector  $AP$ , and the angle between the local horizontal and the velocity vector  $GAMMA$ , (Fig. 7)] from the 3 degrees-of-freedom program were used as inputs for a computer program that numerically integrated Eqs. (5) and (6) to find velocity and altitude, respectively. The results obtained are shown in Table 1, which also contains the 3 degrees-of-freedom computed values.

The entry angle for the example shown in Table 1 was  $-90$  deg. Data for a run with an entry angle of  $-45$  deg is now being prepared for computation.

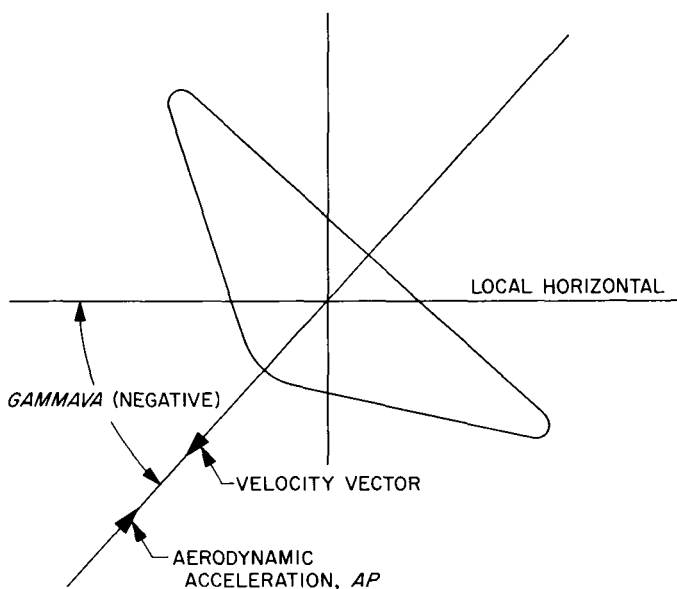


Fig. 7. Reference system

Table 1. Comparison of results using constant gravity factor

Time, sec	Velocity (numerical integration), ft/sec	Velocity (3 degrees of freedom), ft/sec	Altitude, (numerical integration), ft	Altitude (3 degrees of freedom), ft
0.700	23,023.9	23,023.9	780,219	783,897
10.30	23,141.9	23,128.3	563,378	562,524
20.30	23,265.0	23,241.4	331,497	330,833
30.30	22,820.5	22,791.8	98,807	98,397
32.70	15,428.8	15,399.1	50,471	50,075
35.50	5,975.9	5,945.8	22,790	22,521
40.30	2,149.2	2,118.8	5,793	5,688
43.679	1,380.0	1,349.3	0	0

In Eq. (5), a constant value of  $g$  was used. Actually,  $g$  varies considerably from the approximate starting altitude of 800,000 ft to impact. The equation that gives  $g$  as a function of altitude is

$$G(h) = \left( \frac{R_e}{R_e + h} \right)^2 g \quad (7)$$

Eq. (5) can now be rewritten as follows:

$$V = V_E + \int g \left( \frac{R_e}{R_e + h} \right)^2 (\sin \theta - a_s) dt \quad (8)$$

Eq. (8) can be solved by using the values of  $h$  calculated from Eq. (6). Altitude can be recalculated using Eq. (6) and the corrected velocities from Eq. (8). A comparison of the improved computed and reference values is given in Table 2, which also shows that numerical integration yields results that are within 0.1% of the 3 degrees-of-freedom program results.

Table 2. Comparison of results using variable gravity factor

Time, sec	Velocity (numerical integration), ft/sec	Velocity (3 degrees of freedom), ft/sec	Altitude (numerical integration), ft	Altitude (3 degrees of freedom), ft
0.700	23,023.9	23,023.9	783,944	783,897
10.30	23,128.8	23,128.3	562,568	562,524
20.30	23,242.4	23,241.4	330,870	330,833
30.30	22,793.3	22,791.8	98,423	98,397
32.70	15,401.1	15,399.1	50,096	50,075
35.50	5,948.0	5,945.8	22,537	22,521
40.30	2,121.1	2,118.8	5,695	5,688
43.679	1,351.5	1,349.3	0	0

Acceleration measurements will lead to instantaneous values of drag force, which, when combined with the instantaneous velocities computed in Eq. (8), yield instantaneous ambient densities. The fundamental equation for density is

$$\rho = 2 \left( \frac{M}{C_D A} \right) \left( \frac{a_s}{V^2} \right) \quad (9)$$

For a first approximation, ambient density was computed using a constant drag coefficient. Table 3 gives the values of density computed in this manner as a function of altitude. The 3 degrees-of-freedom values of density are included in Table 3 for reference.

In summary, it can be seen that this variation yields good results (all values are within 1.0% of the 3 degrees-of-freedom values). A preliminary error analysis indicates that small random errors of  $\pm 3.0\%$  of true value effect the final accuracy by less than 0.5%. However, a biased error of 1.0% may be intolerable because this type of error is accumulative in a numerical integration process. Future plans call for further error analysis.

The only possible disadvantages of using this variation lie in not knowing the flight path entry angle, or when the angle varies greatly during the entry.

Ambient pressure can be defined as the weight of a column of gas acting on a unit area. The pressure can, in principle, be found at any altitude by integrating densities down from the top of the atmosphere to the desired altitude

$$P = \int_{h \text{ any point}}^{h \text{ top}} \rho G dh \quad (10)$$

To further illustrate the possibility of using numerical integrating, the first approximations of density, as computed by Eq. (9), were numerically integrated from the top of the atmosphere to impact, using Eq. (10). The above computed values of pressure are shown in Table 4 as a function of altitude. The 3 degrees-of-freedom values of pressure are also included in Table 4.

The ratio of specific heats  $\gamma$  for the Martian atmosphere will probably lie between 1.35 and 1.45. An approximate

Table 3. Comparison of density results

Altitude, ft	Density (numerical integration program), slugs/ft <sup>3</sup>	Density (3 degrees of freedom), slugs/ft
0	0.2643E-04 <sup>a</sup>	0.2560E-04
2,020	0.2550E-04	0.2447E-04
6,339	0.2231E-04	0.2215E-04
21,649	0.1537E-04	0.1510E-04
62,076	0.3819E-05	0.3732E-05
128,389	0.7304E-07	0.7137E-07
219,211	0.3488E-09	0.3408E-09
300,629	0.3115E-11	0.3042E-11
451,454	0.5928E-15	0.5791E-15
783,897	0.8036E-23	0.7850E-23
<sup>a</sup> 0.2643E-04 = 0.2643 $\times 10^{-4}$ = 0.00002643		

Table 4. Comparison of pressure results

Altitude, ft	Pressure (numerical integration), lb/ft <sup>2</sup>	Pressure (3 degrees of freedom), lb/ft <sup>2</sup>
0	0.1055E 02	0.1042E 02
2,020	0.9849E 01	0.9790E 01
6,339	0.8630E 01	0.8545E 01
21,649	0.5144E 01	0.5052E 01
62,076	0.7751E 00	0.7593E 00
128,389	0.1482E -01	0.1452E -01
219,212	0.7078E -04	0.6932E -04
300,629	0.6317E -06	0.6188E -06
451,454	0.1203E -09	0.1341E -09
783,897	0	0.1597E -17

instantaneous Mach number can be calculated by means of the equation:

$$M = \frac{V}{C} = \frac{V}{[\gamma(P/\rho)]^{1/2}} \quad (11)$$

The coefficient of drag for a high drag, conic entry capsule is relatively independent of Reynolds number, gas composition, and angle of attack for small angles (Ref. 4). In the supersonic and transonic regions,  $C_D$  becomes a function of Mach number which can be determined from wind tunnel tests for a specific entry configuration.

Using wind tunnel data and Eq. (11), instantaneous values of  $C_D$  can be calculated. Density and pressure can now be recalculated using instantaneous values of  $C_D$ , and Eqs. (9) and (10), respectively. The results from this

**Table 5. Comparison of pressure and density results using variable gravity factor**

Altitude, ft	Density (numerical integration program), slugs/ft <sup>3</sup>	Density (3 degrees of freedom), slugs/ft <sup>3</sup>	Pressure (numerical integration), lb/ft <sup>2</sup>	Pressure (3 degrees of freedom), lb/ft <sup>2</sup>
0	0.2552E -04	0.2560E -04	0.1036E 02	0.1042E 02
2,020	0.2441E -04	0.2447E -04	0.9735E 01	0.9790E 01
6,339	0.2211E -04	0.2215E -04	0.8500E 01	0.8545E 01
21,649	0.1510E -04	0.1510E -04	0.5028E 01	0.5052E 01
62,076	0.3733E -05	0.3732E -05	0.7576E 00	0.7593E 00
128,389	0.7138E -07	0.7137E -07	0.1449E -01	0.1452E -01
219,212	0.3408E -09	0.3408E -09	0.6919E -04	0.6932E -04
300,629	0.3042E -11	0.3042E -11	0.6174E -06	0.6188E -06
451,454	0.5792E -15	0.5791E -15	0.1175E -09	0.1341E -09
783,897	0.7852E -23	0.7850E -23	0.0000E -38	0.1597E -17

approximation are summarized in Table 5. The 3 degrees-of-freedom computed values are also shown.

#### Definition of symbols

- A reference area
- $a_s$  measured acceleration of the body
- C local speed of sound
- $C_D$  aerodynamic drag coefficient
- G acceleration due to gravity at any altitude  $h$
- $g$  acceleration due to gravity at the planet surface
- $h$  altitude at any time  $t$
- M Mach number
- $m$  mass of the entry body
- $P$  pressure at any altitude  $h$
- $R_e$  planet reference radius
- $t$  time
- $V$  velocity of the body at any time  $t$
- $V_E$  entry velocity at time zero
- $\gamma$  ratio of specific heats
- $\Delta$  ballistic coefficient
- $\theta$  flight path angle
- $\rho$  density

**N67-15717**

**B. Hypervelocity Laboratory**, F. Livingston, G. Stickford, and J. Williard

#### 1. Pitot Pressure and Heat Transfer Measurements in the 43-in. Shock Tunnel, F. Livingston, and G. Stickford

**a. Pitot pressure distribution.** One method of measuring the performance of a nozzle is to survey the test sec-

tion with a pitot pressure probe. The standard technique for measuring pressure by a manometer-type gage, however, is ineffective when applied to the shock tunnel because of the short test duration available. It is necessary therefore to use a transducer-type gage which has a high-frequency response. The pitot pressure probe designed and used for the present measurements is shown in Fig. 8. A Kistler Model 701A quartz transducer was used as the sensing element. This gage is capable of measuring pressures from 0.01 to 30 psi with 0.01 psi resolution, with a nominal sensitivity of 5 picocoulombs/psi. Coupled with the Model 566 charge amplifier, the maximum sensitivity is 0.5 v/psi.

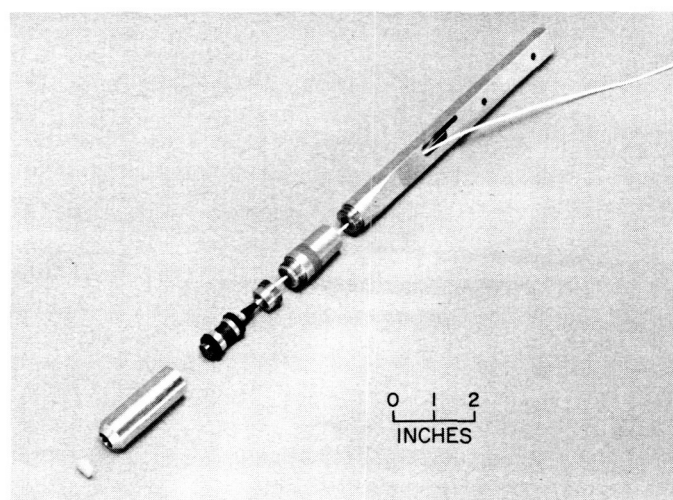


**Fig. 8. Pitot pressure probe and transducer**

The transducer is soft-mounted with O-rings in the pitot probe head; the head is then isolated from the main body of the rake assembly by 0.25 in. of RTV<sup>1</sup> rubber. The vibration transmission from the rake to the gage was found to be small in the frequency range of interest.

Initial tests in the shock tunnel have been conducted using nitrogen as the driven gas. In the shock tube, nitrogen tailors with hydrogen driver gas at a Mach number of 6.4 or shock speed of 7400 ft/sec. Using nitrogen at an initial pressure of 75 mm Hg results in a reflected shock condition of (1) measured pressure equal to 500 psia, (2) calculated (Ref. 5) enthalpy of 2500 Btu/lb, and (3) calculated temperature of 4500°K.

The vertical distribution of pitot pressure has been made at the exit of the 43-in.-diameter nozzle, as shown

<sup>1</sup>Room temperature vulcanizing.

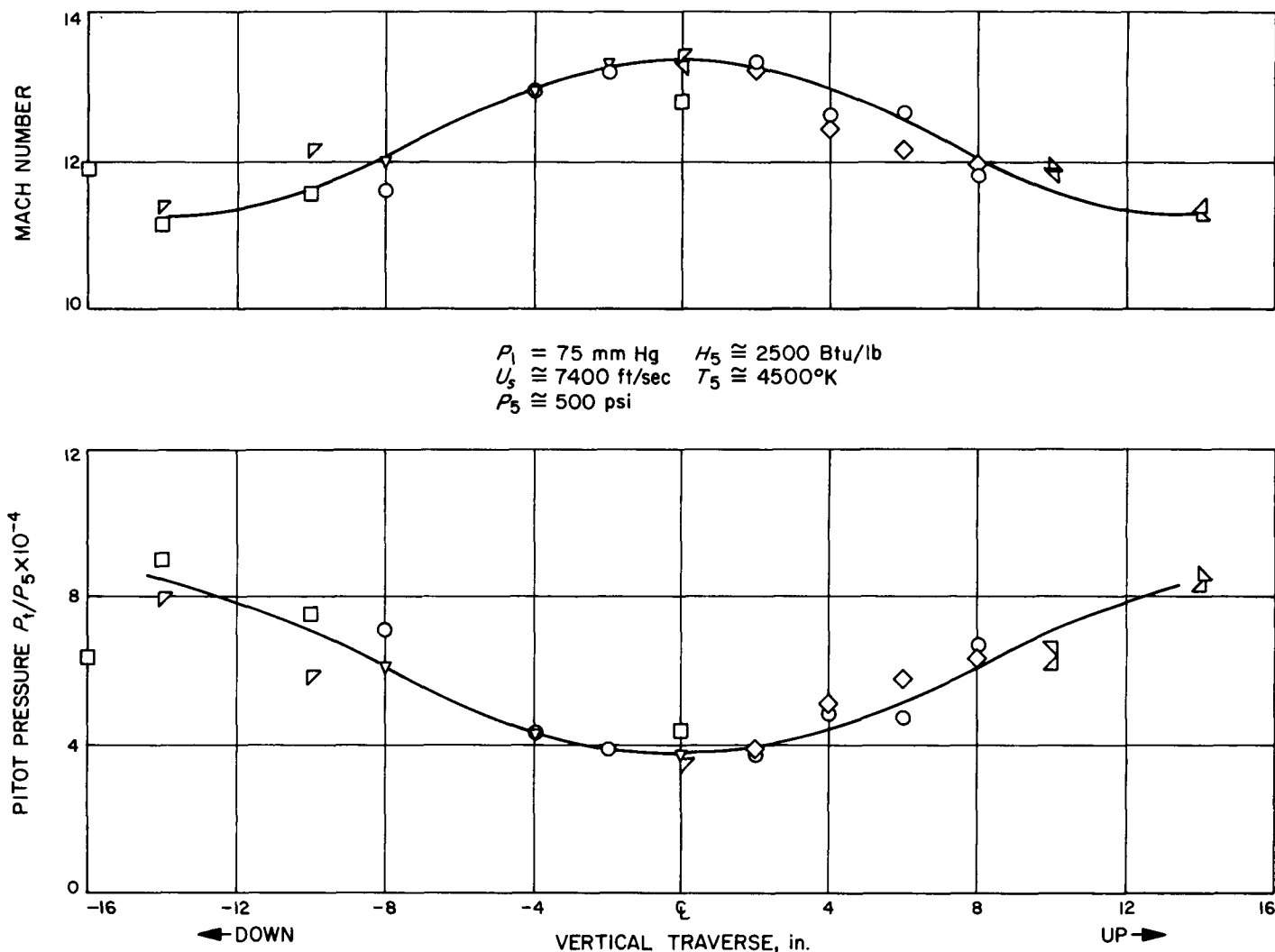


Fig. 9. Nozzle exit vertical flow distribution employing nitrogen

in Fig. 9. The pitot pressure ratio varies in a smooth manner from a value of approximately  $4 \times 10^{-4}$  on the centerline to approximately  $8 \times 10^{-4}$  at a location 14 in. above and below the centerline. Measurements indicate the edge of the boundary layer to be approximately 14 in. off the centerline, or 7.5 in. from the nozzle wall. The Mach number distribution of Fig. 9 corresponds to the measured pitot pressure data for equilibrium nitrogen (Ref. 6). The data indicate a centerline Mach number of approximately 13.3 with a smooth reduction to 11.3 at the boundary layer edge. Aerodynamic models of up to 6-in. diameter may be used in the tunnel without making corrections for a nonuniform test section flow field. Pitot pressure measurements made at stations up to 30 in. aft of the nozzle exit show little variation from those shown. The pitot pressures depicted in Fig. 9 are those existing

at a time of approximately 1 msec after the starting shock moves out of the nozzle.

Fig. 10 is an oscillogram of the output of the crystal transducer. The pressure pulse is seen (1) to take approximately 1 msec to reach a maximum, (2) to hold a constant pressure for approximately 0.5 msec before decaying as hydrogen appears at the pitot rake, and (3) to then abruptly drop as the reflected shock from the dump tank passes over the pitot head. These events are also confirmed by heat transfer measurements made in the tunnel.

**b. Heat transfer rate measurements.** Methods of measuring the aerodynamic heating to models in hypersonic shock tunnels is well documented (Refs. 7 and 8). The most common method used in these short-flow duration

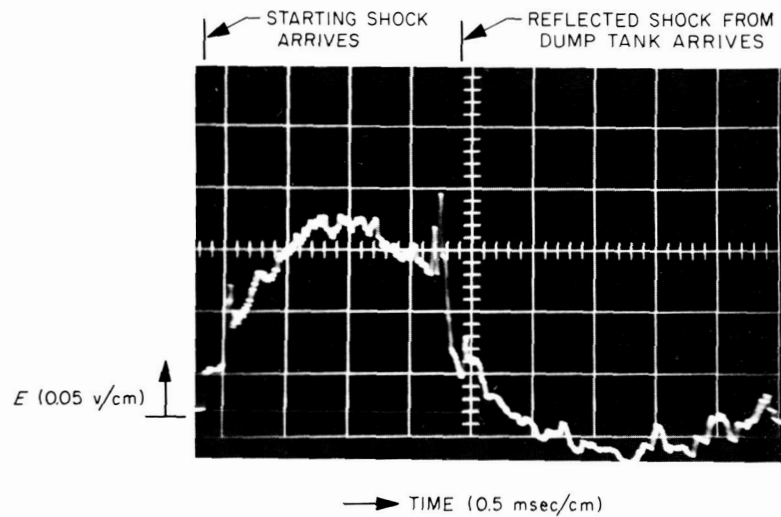


Fig. 10. Oscillograph of output of pitot pressure transducer located 6 in. above the centerline

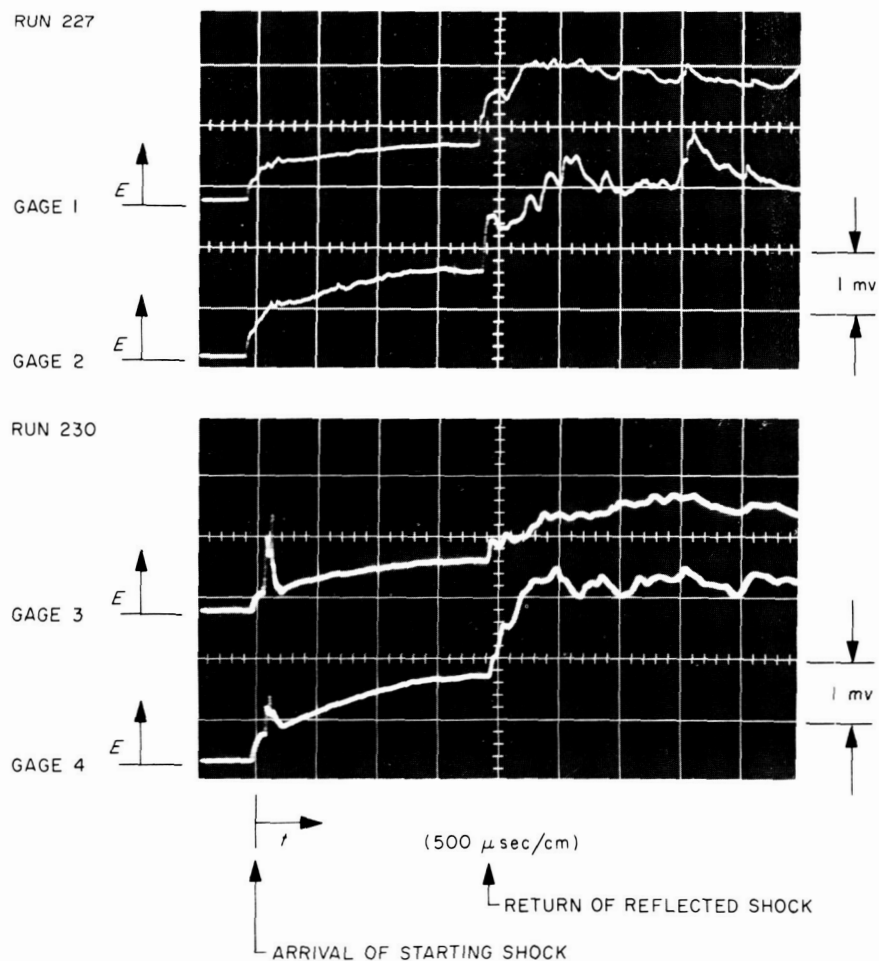
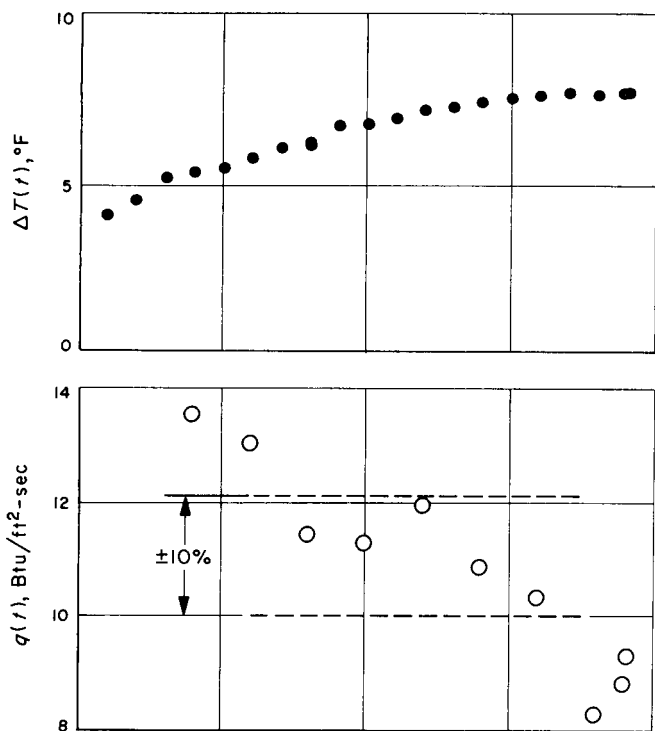


Fig. 11. Thin-film heat transfer gage oscillograms

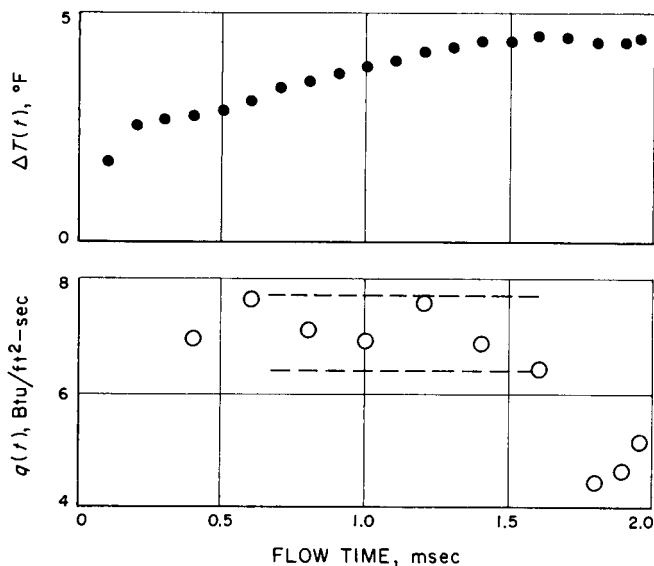
facilities utilizes the resistance thermometer gage technique. These gages can be used to measure very small heating rates ( $q < 1 \text{ Btu/ft}^2 \text{ sec}$ ) and have a response time on the order of  $1 \mu\text{sec}$ . Thus, they are ideally suited to shock tunnel applications.

The resistance thermometer gage consists of a semi-infinite slab of insulator with a thin layer of temperature-sensitive conductor bonded to the surface of the insulator. The average temperature of the conductor is approximately equal to the ideal surface temperature of the

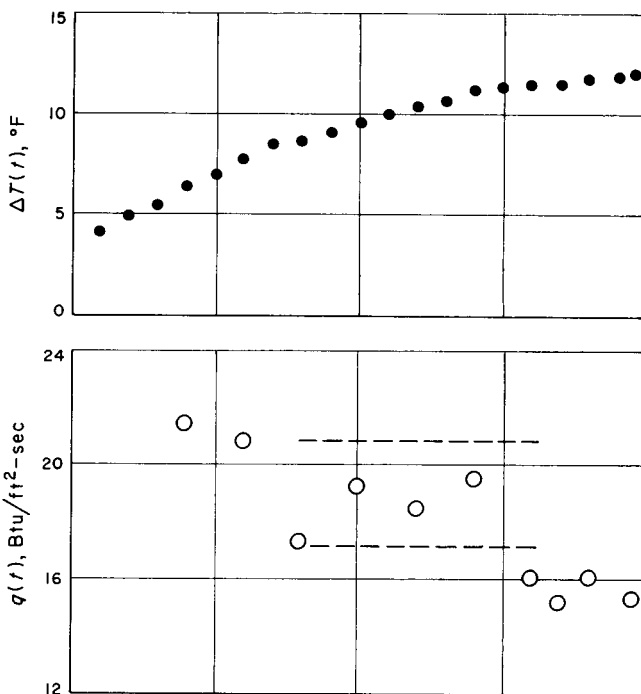
RUN 227, GAGE 1



RUN 227, GAGE 2



RUN 230, GAGE 3



RUN 230, GAGE 4

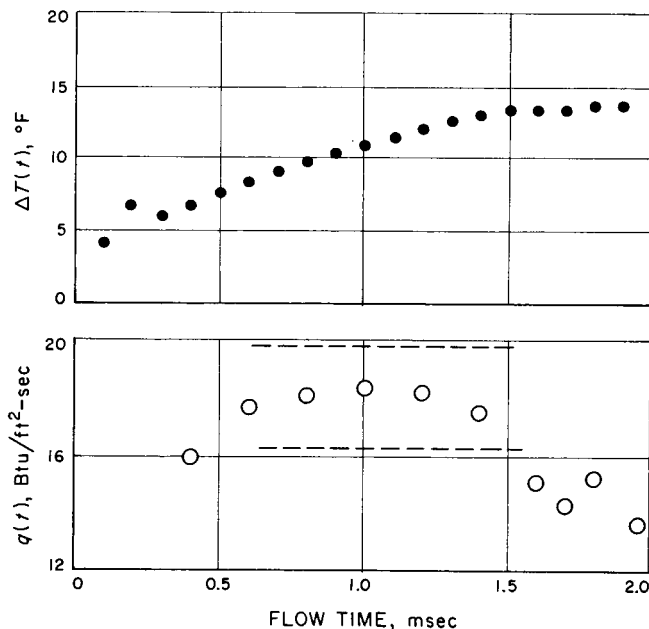


Fig. 12. Temperature and heat transfer rate time history

insulator. The surface temperature of the insulator is related to the heat transfer rate to the surface by solving the one-dimensional, time-dependent heat conduction equation,

$$\frac{dT}{dt} = k \frac{d^2T}{dy^2} \quad (1)$$

A useful solution to Eq. (1) is (Ref. 9):

$$q(t) = \frac{k\rho C_p^{1/2}}{\pi} \left[ \frac{T(t)}{t} + \frac{1}{2} \int_0^t \frac{T(t) - T(\tau) d\tau}{(t - \tau)^{1.5}} \right] \quad (2)$$

where  $k$ ,  $\rho$ , and  $C_p$  are the properties of the insulator, and  $T(t)$  is the temperature of the surface as a function of time ( $\tau$  is a dummy variable).

Shown in Fig. 11 are the voltage output oscillograms of two shock tunnel runs. The voltage is converted to temperature by the expression

$$\Delta T = \frac{\Delta E}{\alpha R_0 I} \quad (3)$$

where  $R_0$  is the initial resistance of the gage,  $I$  is the gage current during the test, and  $\alpha$  is the temperature coefficient of resistivity of the gage. Calibration of each gage is necessary to determine  $\alpha$ .

Eq. (2) can be solved for the particular temperature distribution by using a method outlined in Ref. 10. The heat transfer rates obtained by applying this method to the data in Fig. 11 are shown in Fig. 12. The scatter in the heat transfer rate distribution is due to the slight fluctuations in the temperature distribution, which are caused by electrical noise in the signal and inaccuracies in reading the photos.

The data shown are convective heating measurements obtained on a flat plate model. The gages were located approximately 0.75 cm from the leading edge. The leading edge thickness was approximately 0.2 cm. The measurements were obtained primarily to detect the arrival of the hydrogen driver gas at the test section of the nozzle. The heat transfer rate to a body with hydrogen as the free-stream gas is approximately half as great as the rate with nitrogen as the free-stream gas, assuming all other conditions are identical. Thus, the presence of hydrogen in the free-stream should result in a reduction in the heating rate, the magnitude of the reduction being proportional to the concentration of hydrogen.

As shown in Fig. 12, the heat transfer rate drops significantly at a flow time of approximately 1.5 msec. Therefore, the usable test time for this nozzle is terminated at 1.5 msec, on the average. It is deduced from the heat transfer rate time history that equilibrium in the free-stream flow does exist for approximately 0.75 to 1 msec. This is ample time for the flow field about the body, and the viscous flow near the body, to reach equilibrium.

#### Definition of symbols

$C_p$	specific heat
$E$	voltage
$H_s$	total enthalpy
$I$	current
$K$	conductivity
$P_1$	initial shock tube pressure
$P_s$	stagnation pressure
$P_t$	pitot pressure
$q$	heat transfer rate per unit area
$R$	resistance
$t$	time
$T, \Delta T$	temperature, temperature change
$\alpha$	coefficient of resistivity
$\mu$	viscosity
$\rho$	density

## 2. Performance Evaluation of a 12-in.-Diameter Free-Piston Shock Tube, J. W. Williard

A free-piston shock tube (Fig. 13) is now being evaluated in the JPL Hypervelocity Laboratory. A 12-in.-diameter piston is used to develop the high temperature and pressure driving gas necessary for production of strong shock waves. The piston tube driver chamber combination (Fig. 14) is filled with the driver gas He, at low pressure. The reservoir is filled with the piston driving gas  $N_2$ , at high pressure, while the piston is held by a mechanical release device. When the piston is released it accelerates forward, compressing the driver gas ahead of it. The initial pressure ratio across the piston can be adjusted to a value which will allow the piston to just reach the face of the driver chamber. At that instant a sting, mounted on the face of the piston, pierces the diaphragm and initiates the shock tube flow.

Current performance evaluation tests of the free-piston shock tube have produced highly successful and encouraging (for future performance) results. An outstanding factor

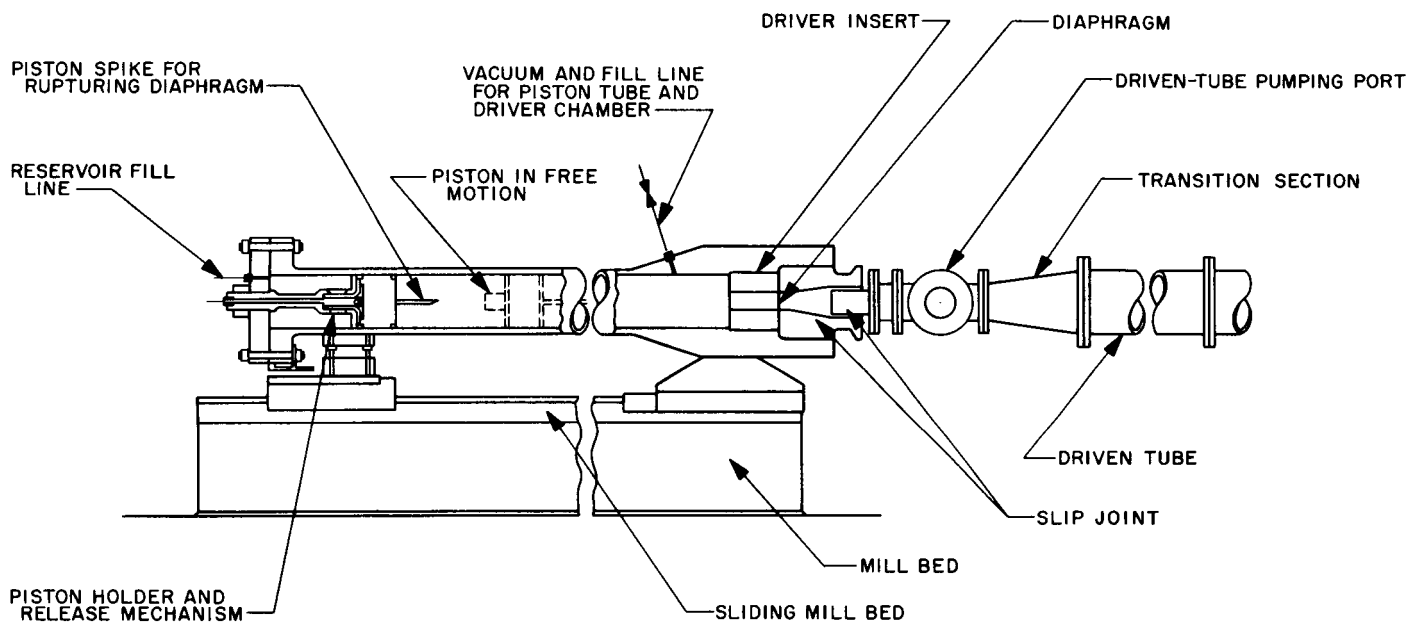
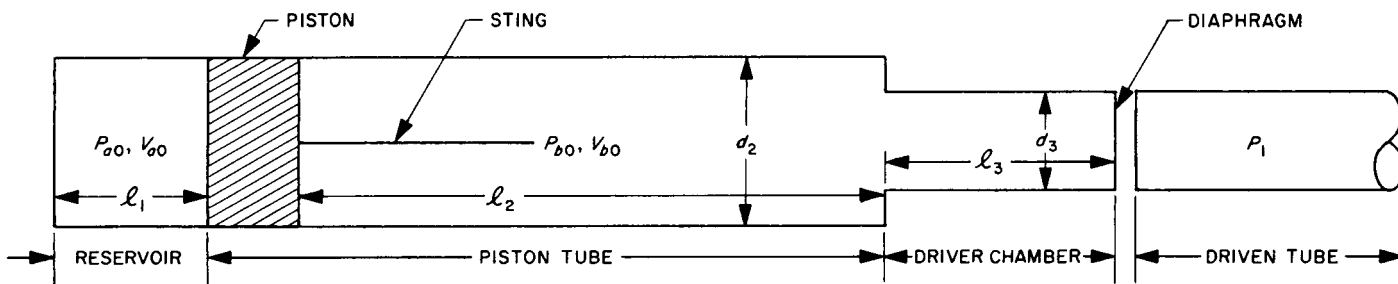
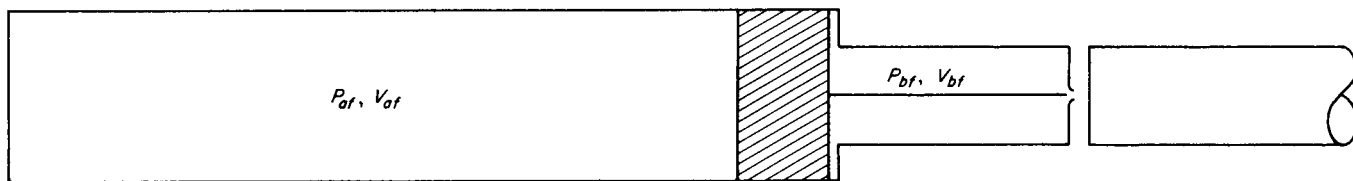


Fig. 13. Free-piston shock tube



(a) INITIAL CONFIGURATION OF FREE-PISTON DRIVER



(b) INSTANT OF DIAPHRAGM BURST

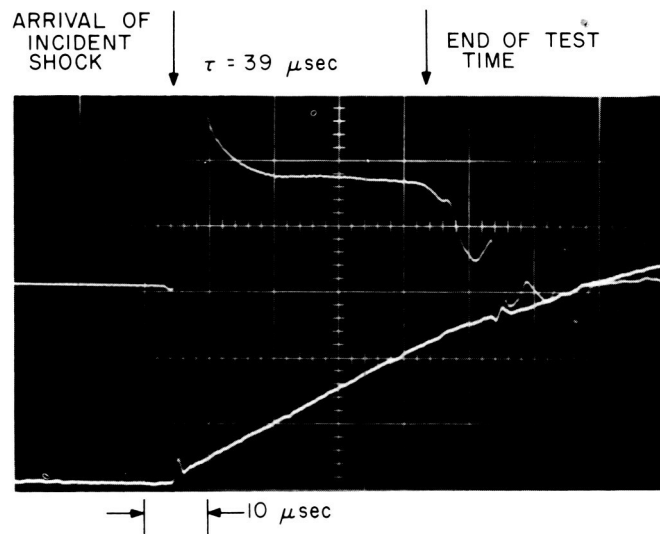
Fig. 14. Schematic of free-piston driver operation

has been the performance of a new Teflon piston. Original piston designs incorporated an aluminum or steel body with a thin layer of spray-coated Teflon. This piston concept was inadequate since heat and friction effects on the thin Teflon layer reduced the operating life of the piston to 20–30 shots. The rapid deterioration of this coating caused increased piston friction, in addition to introducing contaminants into the driver gas. The so-called “Teflon piston” now in use consists of an aluminum core with a 0.375-in.-thick Teflon sheath molded over it, eliminating the frequent need for spray coating, and reducing significantly the addition of contaminants to the driver gas. This piston was fabricated to closer tolerances than previous pistons and fits tightly into the piston tube, eliminating gas leakage across the piston.

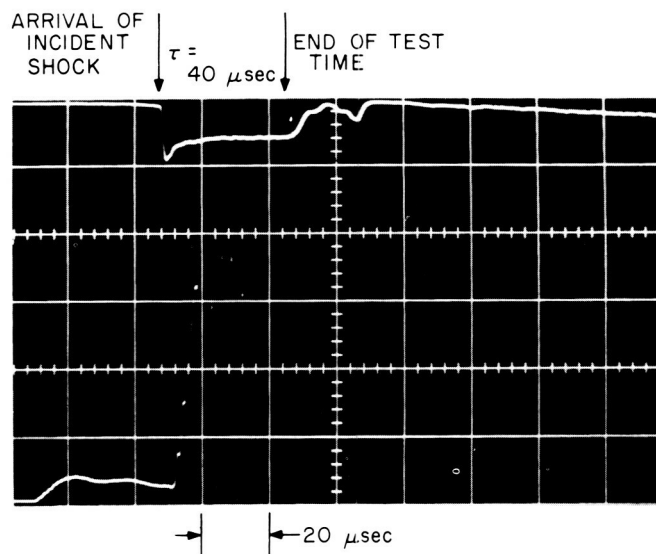
Initial tests of the Teflon piston, although eliminating gas leakage, showed some form of dynamic friction which caused erratic performance. The increased driving pressure required to overcome this friction, coupled with the erratic behavior of the piston, necessitated a slight reduction of the piston diameter. Since this operation, the performance of the piston has greatly improved. It was also determined that high temperatures in the tube, near the limit of piston travel, burn the grease in this area, resulting in increased friction. Frequent cleaning and reapplication of grease in this area have further increased the piston performance.

One of the most interesting objectives of the present series of tests was to determine how well the diaphragm rupture technique would work, especially as the thickness of the diaphragms approached 0.25 in. The spike will burst the scribed diaphragms if the pressure difference between the burst pressure of the diaphragm and the driver pressure is between 200 and 500 psia. No serious preruptures have occurred; a good knowledge of diaphragm rupture pressure is important to avoid prerupture. So far, 0.130-in.-thick diaphragms have been successfully opened at final driver pressures up to 5100 psia. An attempt to open a 0.200-in.-thick diaphragm at a pressure of 7600 psia was only partially successful. It is believed that by utilizing pressures closer to the static burst pressure of the diaphragm, and an improved spike mechanism, these thicker diaphragms can be opened.

Data were taken in air at three initial pressures: 250, 100, and 50 $\mu$ . For each test, shock speed, test time, and convective heat transfer, measurements were taken; oscilloscope traces are shown in Figs. 15 and 16. Two measurements of test time were made. In Fig. 15(a), the potential of a calorimeter gage with respect to ground was used



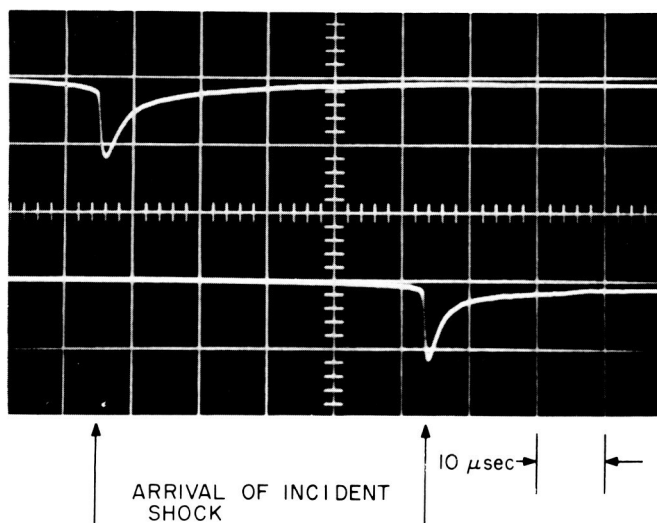
(a) POTENTIAL LEVEL OF A CALORIMETER GAGE WITH RESPECT TO GROUND (UPPER TRACE), AND STAGNATION POINT CALORIMETER GAGE SIGNAL (LOWER TRACE)  $U_s = 20,600$  ft/sec



(b) PHOTOMULTIPLIER VIEWING STAGNATION REGION OF THE MODEL (UPPER TRACE). LOWER TRACE IS A PRESSURE MEASUREMENT WHICH WENT OFF SCALE.  $U_s = 20,600$  ft/sec

**Fig. 15. Oscilloscope trace of calorimeter gage outputs**

for defining the length of the test slug. This technique was used by General Electric Co. (Ref. 11) and is probably dependent upon the response of the gage to ionized (test slug) flow and nonionized (driver gas) flow. When this



$$U_s = 20,600 \text{ ft/sec}$$

**Fig. 16. Oscilloscope trace of two photomultiplier responses to the arrival of the incident shock at stations 1 ft apart**

measurement is compared with that of a photomultiplier viewing the stagnation region of the model [Fig. 15(b)], excellent agreement is found. Another measure of the test time, although much less sensitive than the other two, is the change in slope of the heat transfer gage upon the arrival of the driver gas. In Fig. 15(a), such a change in slope occurs at the arrival of the driver gas, although it is not always so apparent. The test time data obtained are plotted in Figs. 17–19 and compared with the laminar

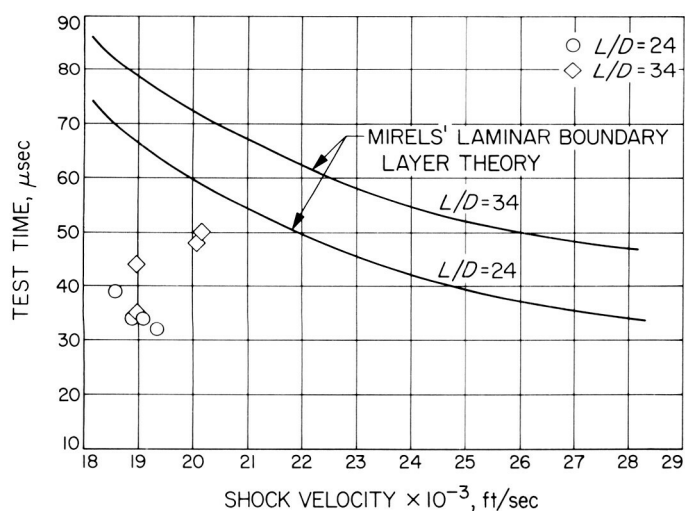


**Fig. 17. Test time in air as a function of shock velocity and driven-tube length for an initial pressure of 0.250 mm Hg**

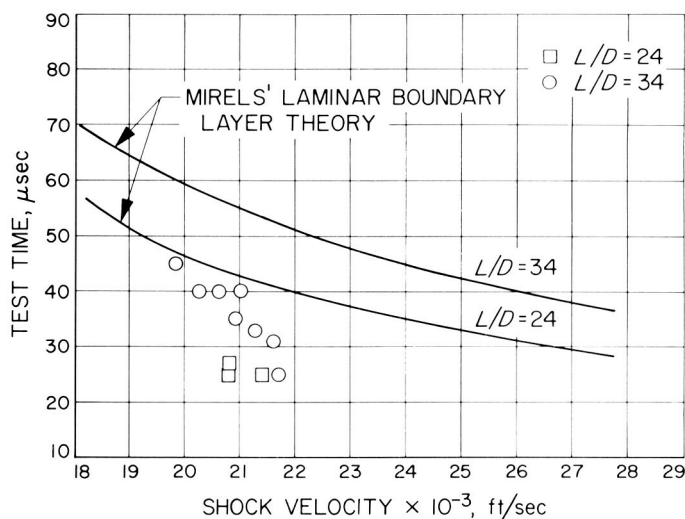


**Fig. 18. Test time in air as a function of shock velocity and driven-tube length for an initial pressure of 0.100 mm Hg**

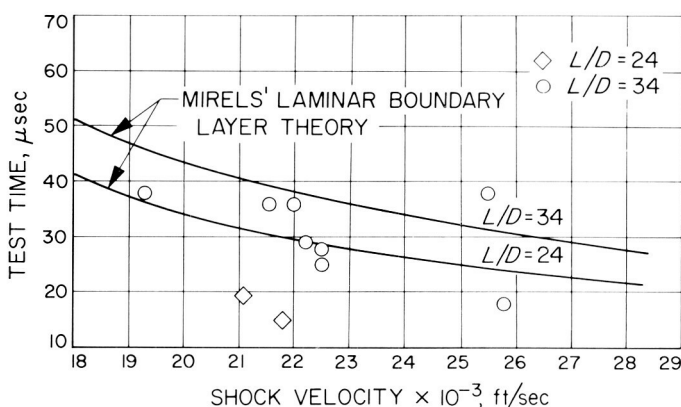


**Fig. 19. Test time in air as a function of shock velocity and driven-tube length for an initial pressure of 0.050 mm Hg**

boundary layer theory of Mirels. In Fig. 17, the test time data for an  $L/D$  of 34 seem to indicate that the test time is limited. Calculations of driver tube length (Ref. 12) needed for noninterference from the expansion wave indicated marginal conditions at a shock speed of 19,000 ft/sec into 0.25 mm Hg of air at an  $L/D$  of 34.

Shock velocities were measured, using pairs of photomultipliers spaced 1 ft apart. Typical responses of such a pair to the luminous shock front are shown in Fig. 16. Noteworthy is the absence of the strong visible radiation emitted by the driver gas, as experienced in arc discharge facilities. In this facility the driver gas is relatively free of contaminants and is cold at the contact surface.

One of the advantages of the free-piston shock tube is that knowledge of the driver conditions permits the accurate prediction of the expected shock speed from known shock tube theory. Shock velocities obtained in this series of tests were predicted to within 3% or better and are presented in Fig. 20. The driver pressure  $P_4$  was taken as the measured pressure obtained in bomb shots. The data representing different driver volumetric ratios  $V_{b0}/V_{bf}$ , are actually points of different speed-of-sound ratios  $a_4/a_1$ , as is usually presented in this type of plot. The calibrated conditions from which these shock speeds were produced are presented in Figs. 21 and 22. Pressure data were measured in "bomb" shots (firing the piston with a plug in the place of a diaphragm) in which the maximum stroke of the piston was measured and the temperature calculated from knowledge of the final pressure and volume. At present, these are the only calibrated driver conditions for which shock speed data are available. However any combination of piston-driving pressure  $P_{a0}$ , piston tube pressure  $P_{b0}$ , and volumetric compression ratio which is within design limits, can be calibrated.

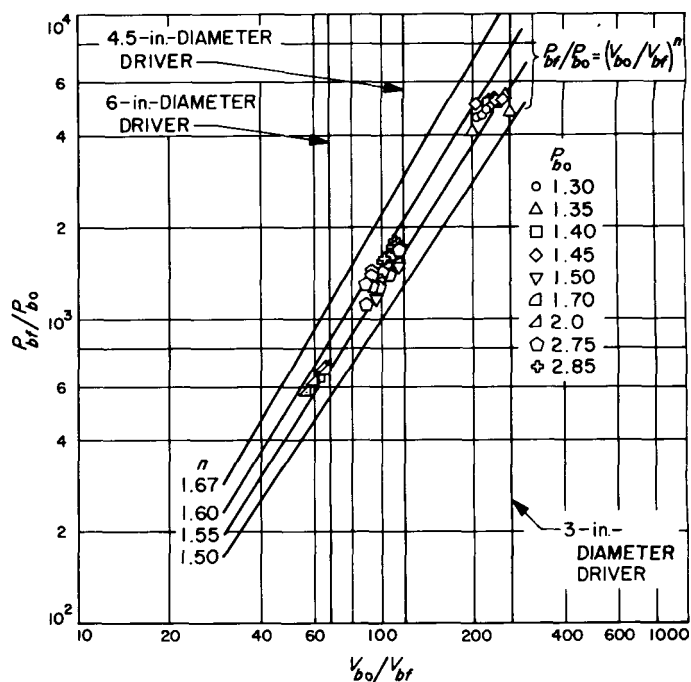


Fig. 21. Final driver pressure as a function of volumetric compression ratio

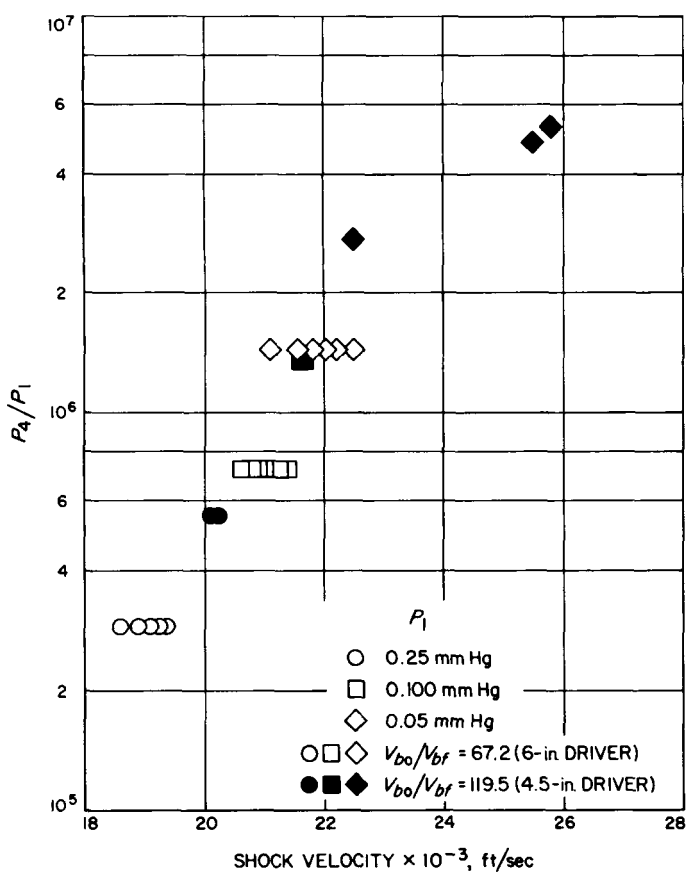


Fig. 20. Shock velocity as a function of pressure ratio across the diaphragm

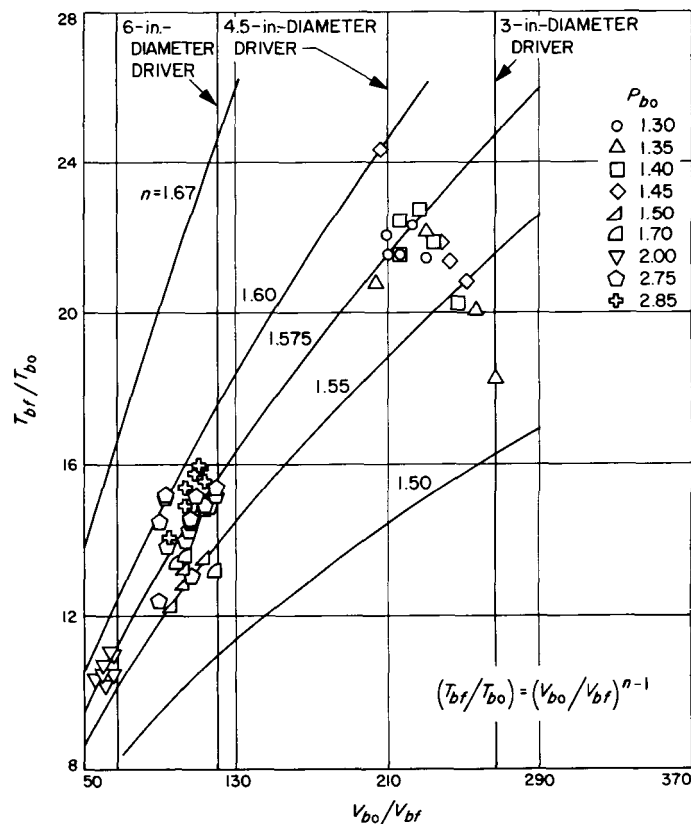


Fig. 22. Final driver temperature as a function of volumetric compression ratio

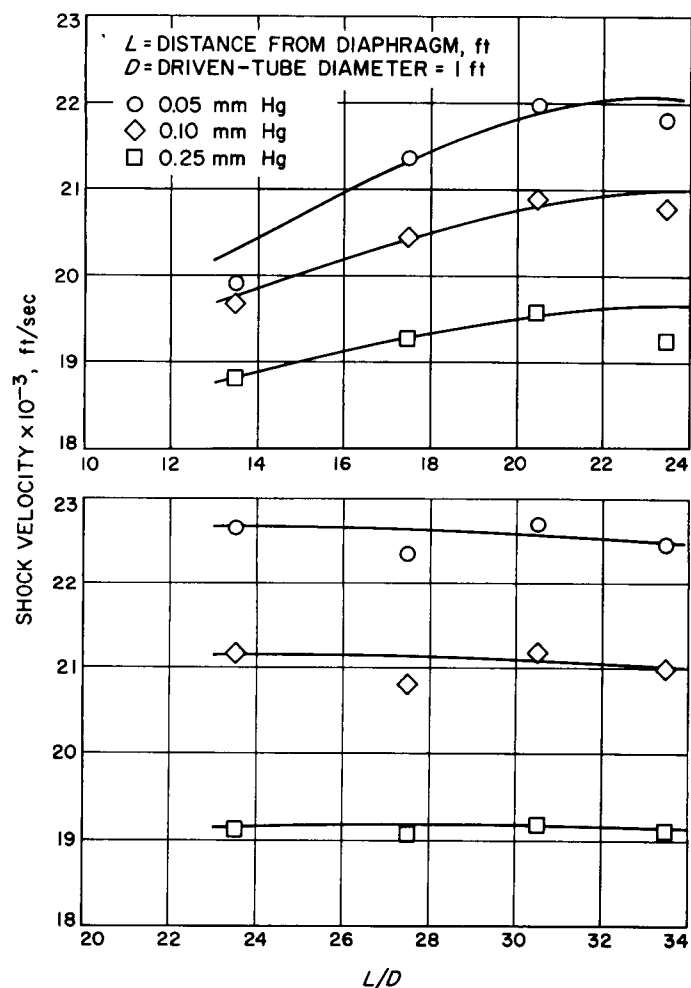


Fig. 23. Shock velocity variation along the driven tube for constant driven length of 8.75 in. and the 6-in.-diameter driver

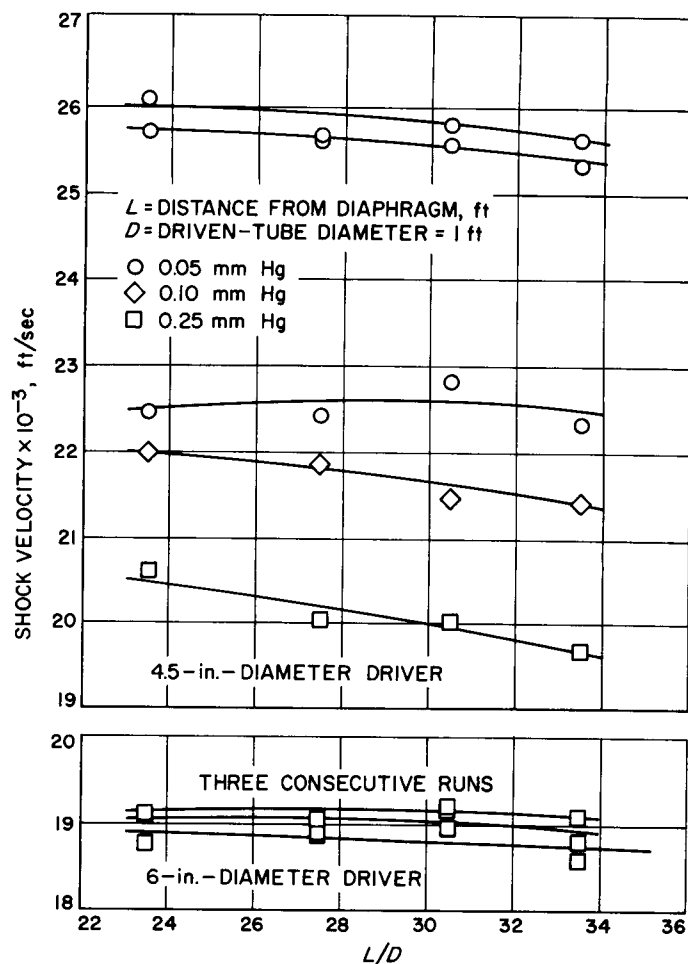


Fig. 24. Shock velocity variation along the driven tube for constant driver length of 8.75 in.

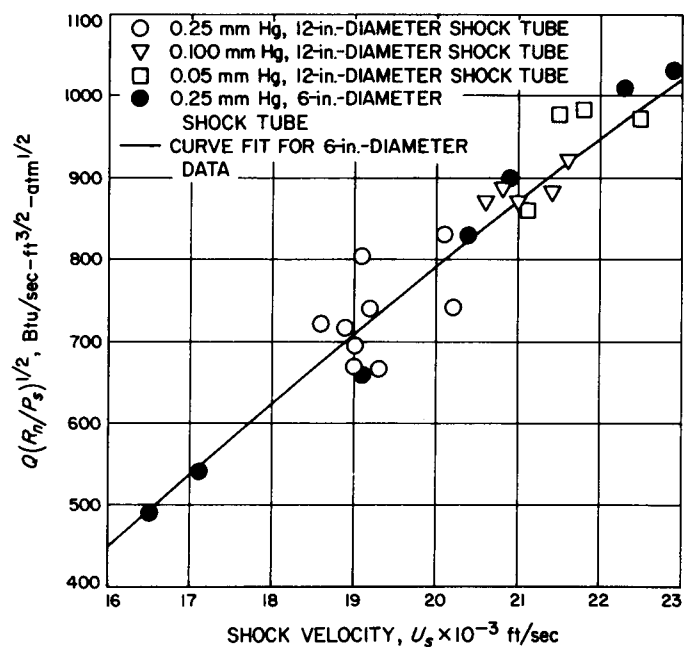


Fig. 25. Comparison of convection data from 12- and 6-in.-diameter shock tubes

The variation of shock velocity with driven-tube length is shown in Figs. 23 and 24. With a total driven-tube length of 24 ft, the shock wave is accelerating up to the test station. With a driven-tube length of 34 ft, the shock speed is remarkably constant over the last 10 ft with very little attenuation. In fact, the attenuation is negligible compared to other facilities at this speed.

The capability of the free-piston shock tube to reproduce shock velocities is indicated in Fig. 18 and in the lower plot of Fig. 24. The maximum deviation holding  $P_4/P_1$  constant is seen to be 5% or better.

Convective heat transfer data obtained in the free-piston shock tube are compared with recently published data from Horton and Babineaux (Ref. 13) in Fig. 25. Considering that the data from the 12-in. facility were obtained as a by-product of test time measurements, the agreement is excellent. Data points at velocities of 25,000 ft/sec were obtained, but could not be used because of a damaged model. Because of the excellent shock velocity

repeatability of the free-piston facility and the long test times available, the quality of the data was much better and more repeatable than similar data obtained in the arc-heated facility.

---

#### Definition of symbols

---

$V$	volume
$P$	absolute pressure
$T$	absolute temperature
$n$	polytropic exponent

#### Subscripts

$a0$	conditions behind piston before it is released
$af$	conditions behind piston after it is released
$b0$	conditions ahead of piston before it is released
$bf$	conditions ahead of piston after it is released
1	driven-tube initial pressure
4	pressure on piston side of diaphragm at instant of diaphragm rupture

---

## References

1. Jaffe, P. *A Generalized Approach to Dynamic Stability Flight Analysis*, Technical Report No. 32-757, Jet Propulsion Laboratory, Pasadena, California, July 1, 1965.
2. Peterson, V. L., and McKenzie, R. L., "Effects of Simulated Retrorockets on the Aerodynamic Characteristics of a Body of Revolution at Mach Numbers from 0.25 to 1.90," TN D-1300, NASA Ames Research Center, Moffett Field, California, May 1962.
3. Seiff, A., "Some Possibilities of Determining the Characteristics of the Atmosphere of Mars and Venus from Gas-Dynamics Behavior of a Probe Vehicle," TN D-1170, NASA Ames Research Center, Moffett Field, California, April 1963.
4. Seiff, A., and Reese, D. E., "Use of Entry Vehicle Responses to Define the Properties of the Mars Atmosphere," Symposium, Unmanned Exploration of the Solar System, *American Astronautical Society* Preprint No. 65-24, February 1965.
5. Lewis, C. H., and Burgess, E. G., III, "Charts of Normal Shock Wave Properties in Imperfect Nitrogen," AEDC-TDR-64-104, Arnold Engineering Development Center, Tullahoma, Tennessee, May 1964.

## References (contd)

6. Berstein, L., "Equilibrium Real-Gas Performance Charts for a Hypersonic Shock-Tube Wind-Tunnel Employing Nitrogen," A.R.C. 23,232, Hyp. 217, Aeronautical Research Council, National Physical Laboratory, Teddington, England, September 26, 1961.
7. Hall, G. J., Hertzberg, A., "Recent Advances in Transient Surface Temperature Thermometry," *Jet Propulsion*, Vol. 28, No. 11, 1958.
8. Vidal, R. J., "Model Instrumentation Techniques for Heat Transfer and Force Measurements in a Hypersonic Shock Tunnel," C.A.L. Report AD-917-A-1, Cornell Aeronautical Laboratory, New York, February 1956.
9. Hartunian, R. A., and Varwig, R. L., "A Correction to Thin-Film Heat Transfer Measurements," Aerospace Corp. Report No. TDR-594 (1217-01) El Segundo, California, TN-2, May 1961.
10. Cook, W. J., and Felderman, E. J., "Reduction of Data from Thin Film Heat-Transfer Gages, *AIAA Journal* TN, 4, 3, p. 561, March 1966.
11. Gruszczynski, J. S., and Rogers, D. A., "Shock Tube Instrumentation Techniques for Study of Hypervelocity Entry Problems," Technical Information Series, R64SD67, Space Sciences Laboratory, Missile and Space Division, General Electric Co., King of Prussia, Pennsylvania, 1964.
12. Lobb, R. K., "On the Length of a Shock Tube," U.T.I.A. Report No. 4, Institute of Aerophysics, University of Toronto, Canada, July 1950.
13. Horton, T. E., and Babineaux, T. L., "Experimental Assessment of the Effect of Large Amounts of Argon in a Planetary Atmosphere on Stagnation-Point Convective Heating," *AIAA Paper* No. 66-29, presented at the 3rd Aerospace Sciences Meeting, New York, New York, January 24-26, 1966.

**Page intentionally left blank**

## IX. Solid Propellant Engineering

### PROPULSION DIVISION

N67-15718

#### **(A) Low-Pressure Combustion Studies, L. Strand**

As has been reported in Refs. 1-5, low-pressure instability and extinguishment data for a number of composite solid propellants have been acquired during the past several years, using both threaded and flanged versions of a small 3-in. ID test motor (flanged version shown in Figs. 1 and 2) and regressive burning cylindrical propellant charges of the type shown in Fig. 3 (2½-in. D by 4- to 4½-in. length, inhibited on the head end only). The motor  $L^*$  (motor free volume to throat area) and chamber pressure ( $P_c$ ) were varied by varying both the motor chamber length (4½ to 12½ in.) and nozzle throat diameter. Propellant variables have included aluminum/oxidizer concentration ratio, aluminum particle size, ammonium perchlorate oxidizer particle size, and binder type (only a small amount of testing with latter two). Polyurethane has been the standard binder used.

As was reported in Ref. 3, in the low-pressure combustion tests the propellant charges were ignited in the stable-operating-pressure region, burned regressively with decreasing pressure into the unstable pressure region, and ultimately ceased burning (extinguished). For

a majority of the test data records, low-frequency, low-amplitude oscillations in pressure appeared to occur prior to extinction of combustion. The information that has previously been obtained from the low-pressure instability and extinguishment test data records has included the mean chamber pressure, motor  $L^*$ , and frequency of pressure oscillations (where measurable) at combustion extinction. Further reduction and analysis of the data for the propellant variables shown in Table 1 has

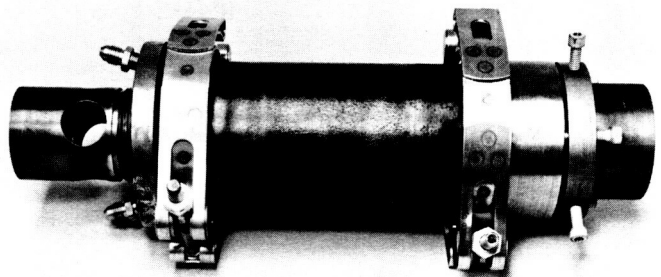


Fig. 1. 3-in. ID test motor, assembled

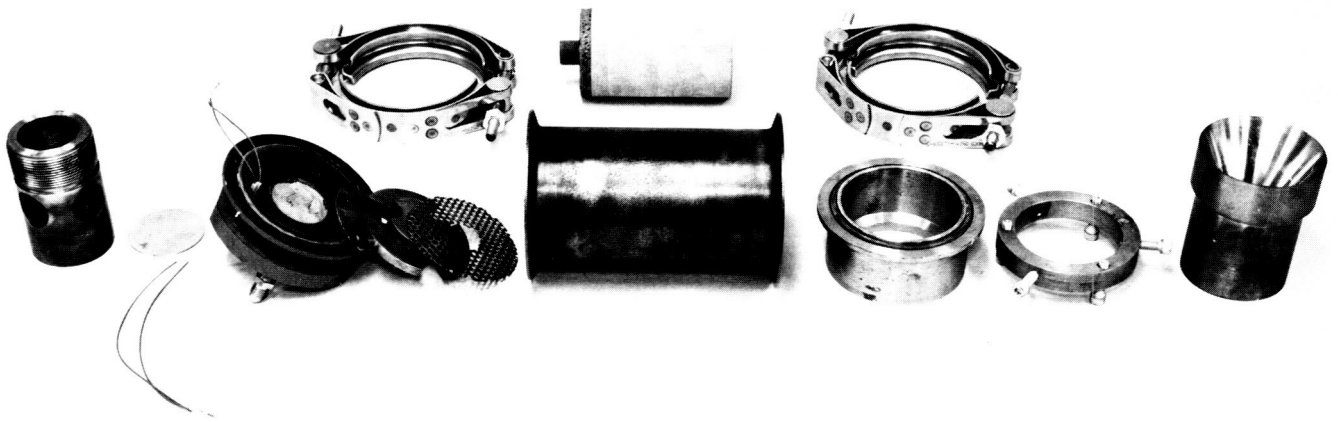


Fig. 2. 3-in. ID test motor, disassembled

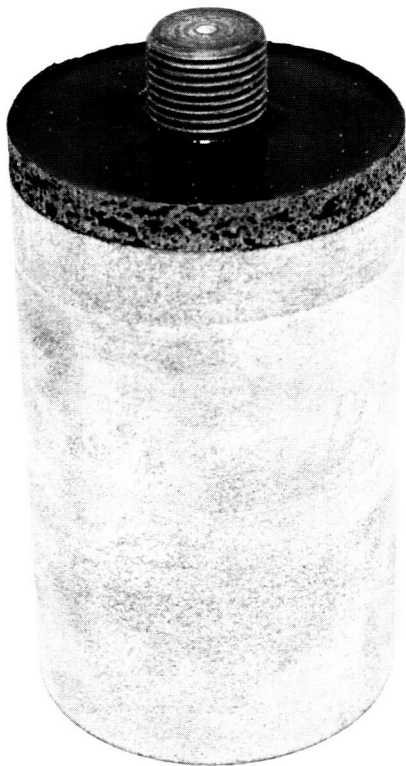


Fig. 3. Propellant charge, 2½ by 4 in.

Table 1. Experimental propellants

Propellant	Aluminum, %	Average aluminum particle diameter	Aluminum/oxidizer concentration ratio
JPL 534	2	7	Decreased
JPL 540	16	7	Standard
JPL 540 Mod A	0	—	0
JPL 540 Mod B	8	7	Decreased
JPL 540 Mod 1	16	31	Standard
JPL 540 Mod 2	16	15–17	Standard

aluminum/oxidizer concentration ratio.) This additional information is being used to attempt to gain new insight into the actual mechanisms of these phenomena.

### 1. Onset of Instability

The motor  $L^*$  and chamber pressure at the onset of instability (OI) have been determined for the first four propellants shown in Table 1. The onset point is defined as the point of initiation of the chamber pressure oscillations that continue to increase in amplitude until combustion extinction occurs. Figs. 4 and 5 show the indicated onset of instability point on oscillograph pressure-time trace reproductions for tests with the 2 and 16% aluminized propellants, respectively. The  $P_c$  values were measured from the oscillograph traces. The  $L^*$  values were obtained by: (1) determining the propellant burning area at OI from  $K_n$  (burning area to throat area ratio)— $P_c$

been pursued. (The Mod A and Mod B propellant formulations were obtained by replacing all and half, respectively, of the aluminum in the standard JPL 540 propellant with oxidizer, resulting in a decreased

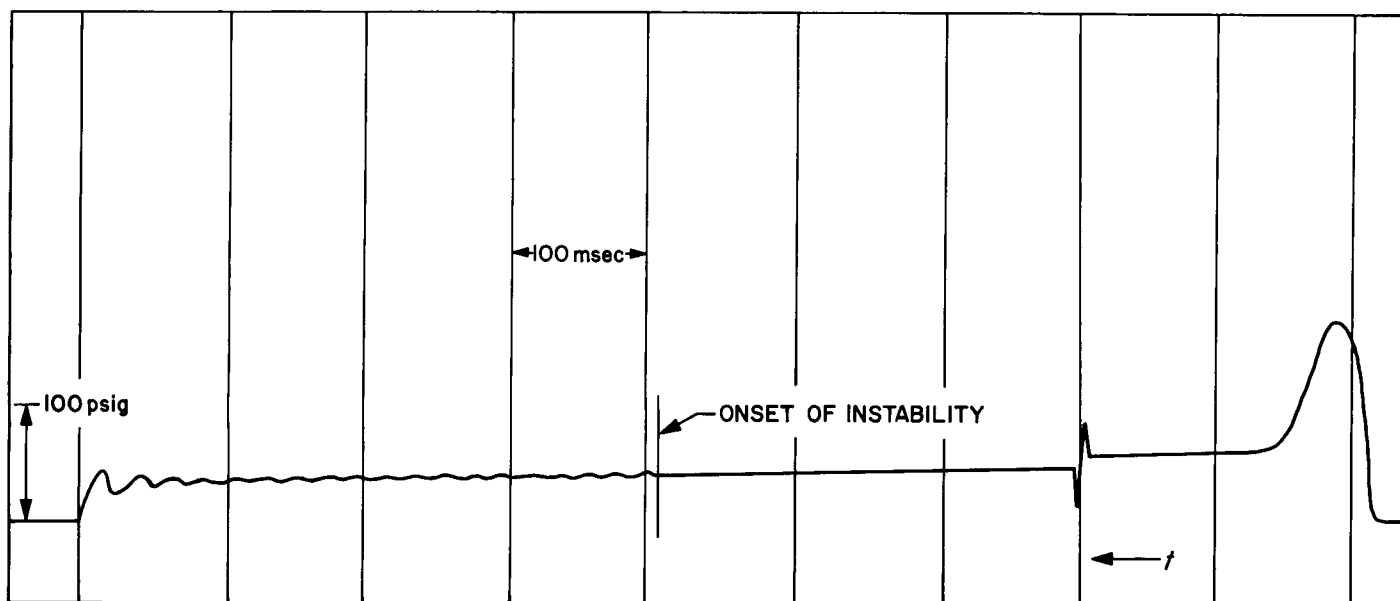


Fig. 4. Pressure-time trace for Run No. 1468, JPL 534 propellant

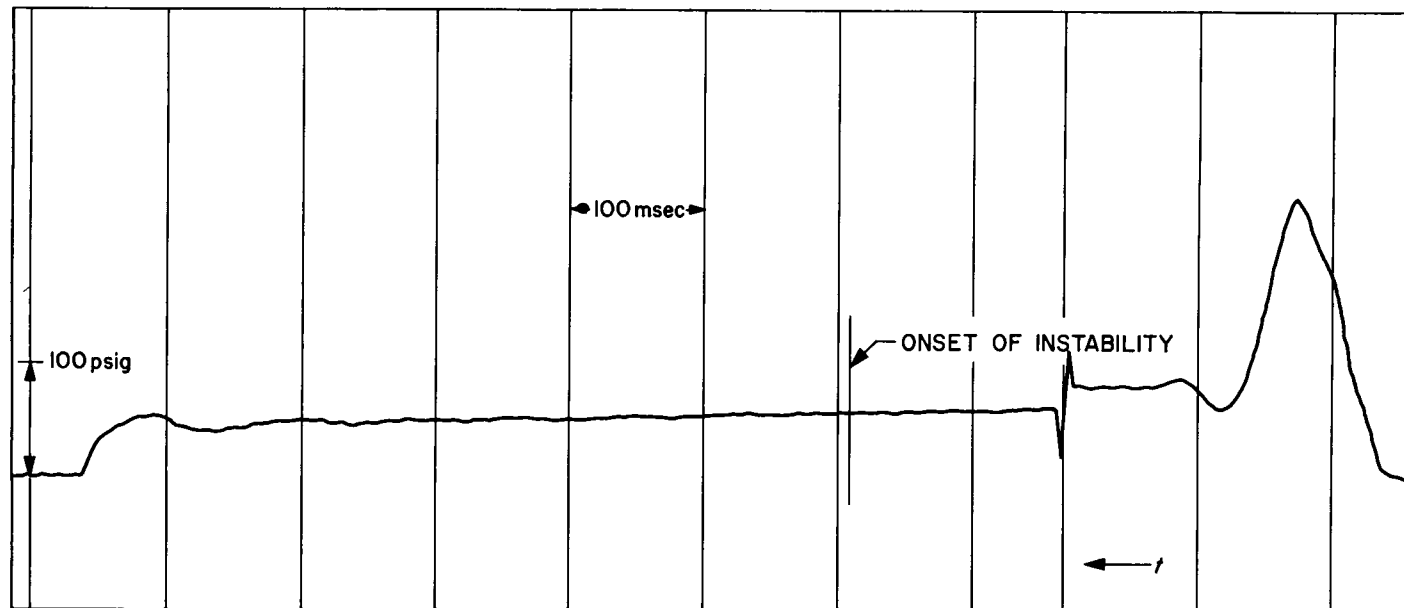


Fig. 5. Pressure-time trace for Run No. 1476, JPL 540 propellant

graphs (Fig. 6), (2) calculating the propellant charge dimensions at OI by back-calculating from the measurements taken at extinction, and (3) calculating the propellant volume and, consequently, motor  $L^*$ . For all propellants tested the OI boundary, plotted on a  $L^*-P_c$  log-log graph, lies approximately parallel to and to the right (higher pressure regime) of the extinction boundary, as expected from test experience. Figs. 7 to 10 show the

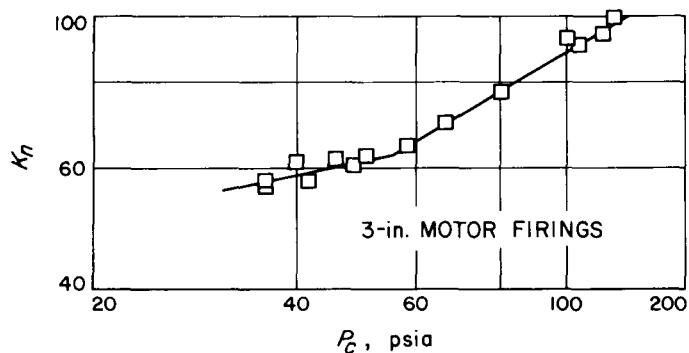


Fig. 6.  $K_n$  versus chamber pressure, JPL 540-Mod B propellant

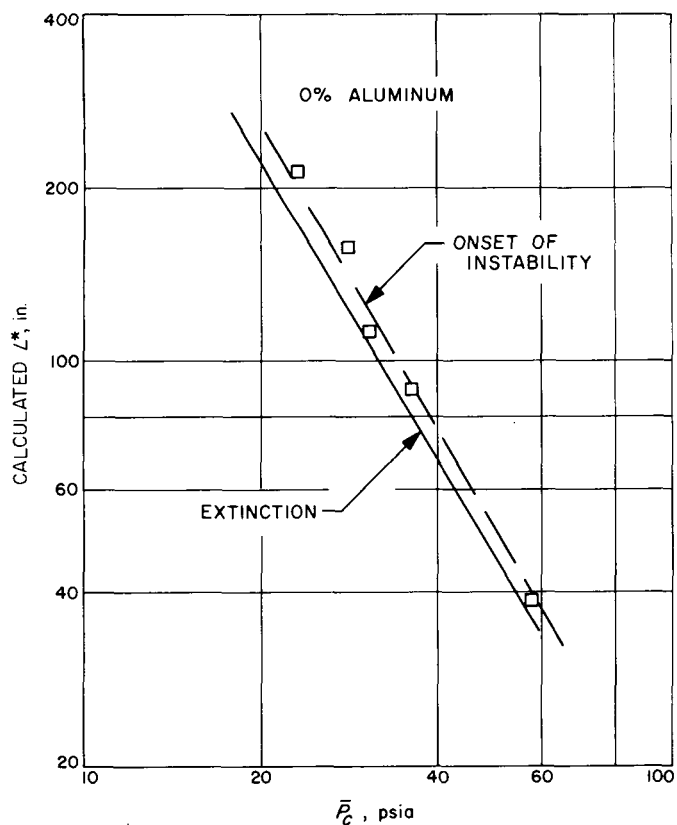


Fig. 7.  $L^*$  versus chamber pressure at onset of instability, JPL 540-Mod A propellant

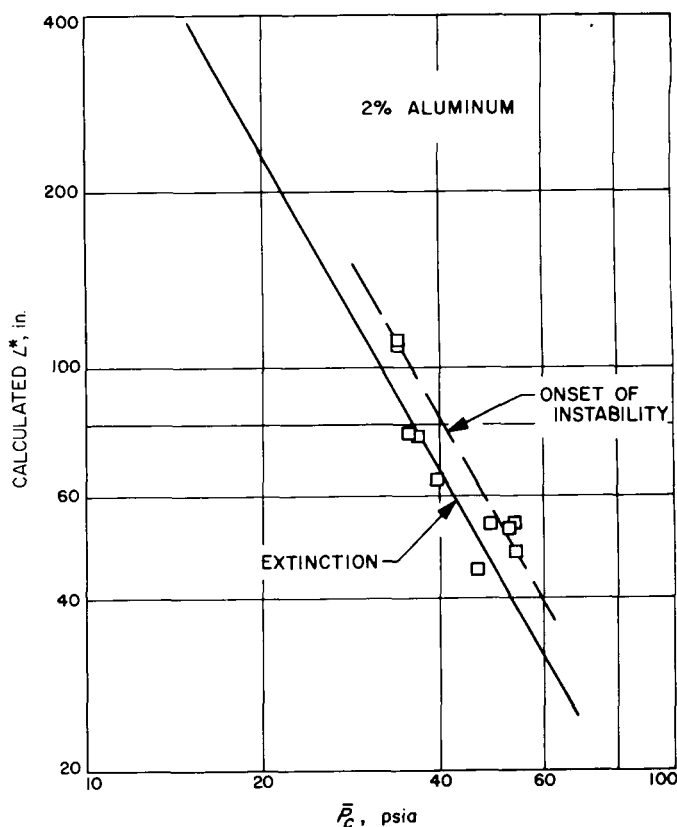


Fig. 8.  $L^*$  versus chamber pressure at onset of instability, JPL 534 propellant

onset of instability and extinction boundaries for the 0, 2, 8, and 16% aluminum propellants, respectively. The OI boundary approaches the extinction boundary as the propellant aluminum/oxidizer concentration ratio is reduced.

## 2. Pressure Oscillation Rate of Depressurization

It has been observed that, as a result of the increasing amplitude of pressure oscillations following the onset of instability, the rate of depressurization of the oscillations increases up to the point of extinction. From the oscillograph data the negative slope of the last pressure oscillation at, or immediately prior to, the onset of extinction was therefore measured (at best a very approximate measurement) for JPL 540 propellant and its modification formulations, as shown in Figs. 11 and 12. Although there is great amount of scatter in the data, a definite correlation between the rate of depressurization ( $dP/dt$ )<sub>e</sub> and the mean chamber pressure prior to extinction was found for each propellant (Fig. 13). Further analysis is being pursued to determine if this rate of depressurization-pressure correlation is significant in itself, or is merely

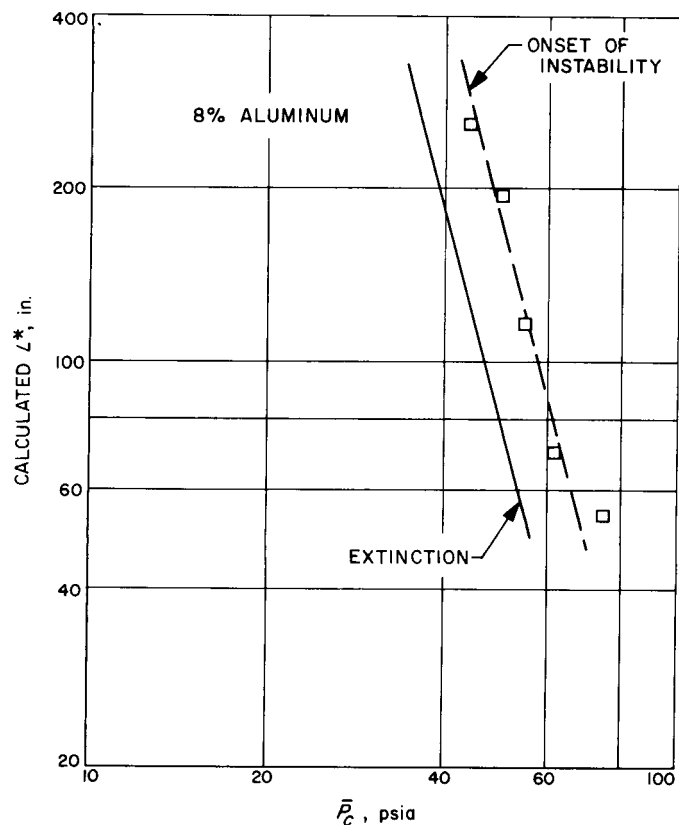


Fig. 9.  $L^*$  versus chamber pressure at onset of instability, JPL 540-Mod B propellant

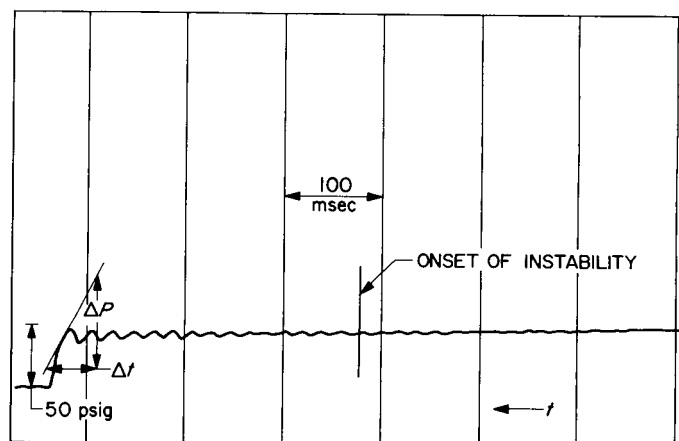


Fig. 11. Pressure-time trace for Run No. 1430, JPL 540-Mod A propellant

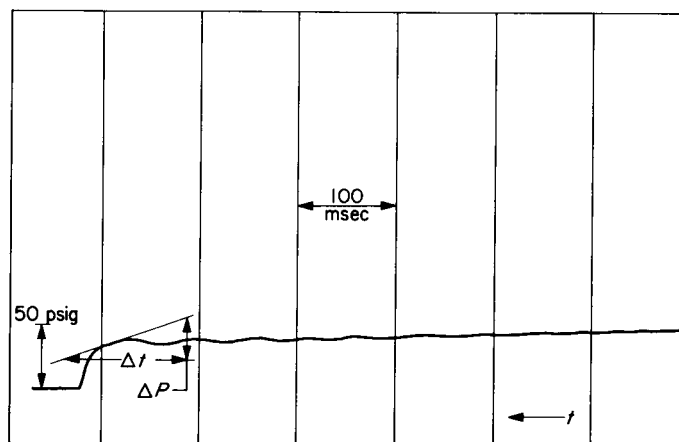
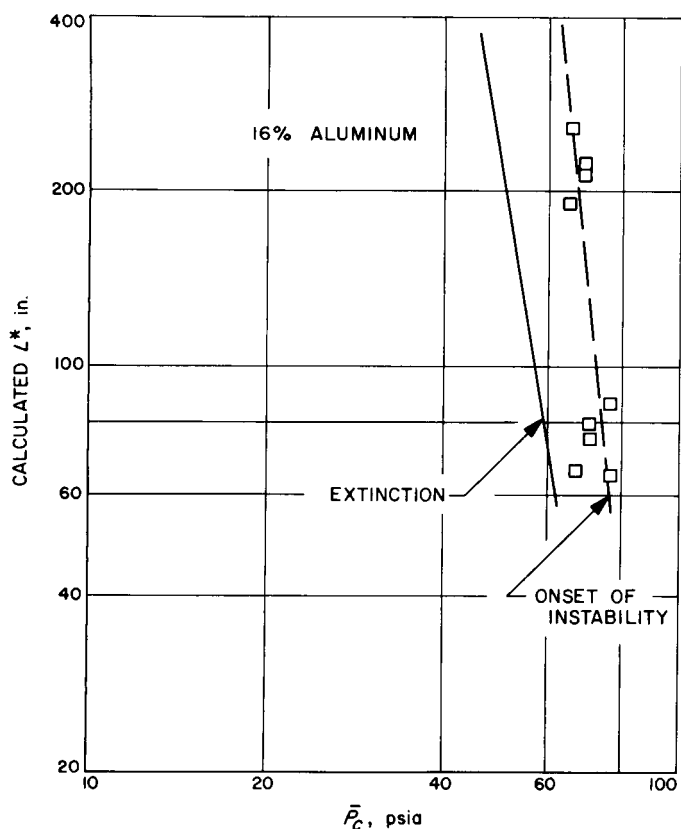
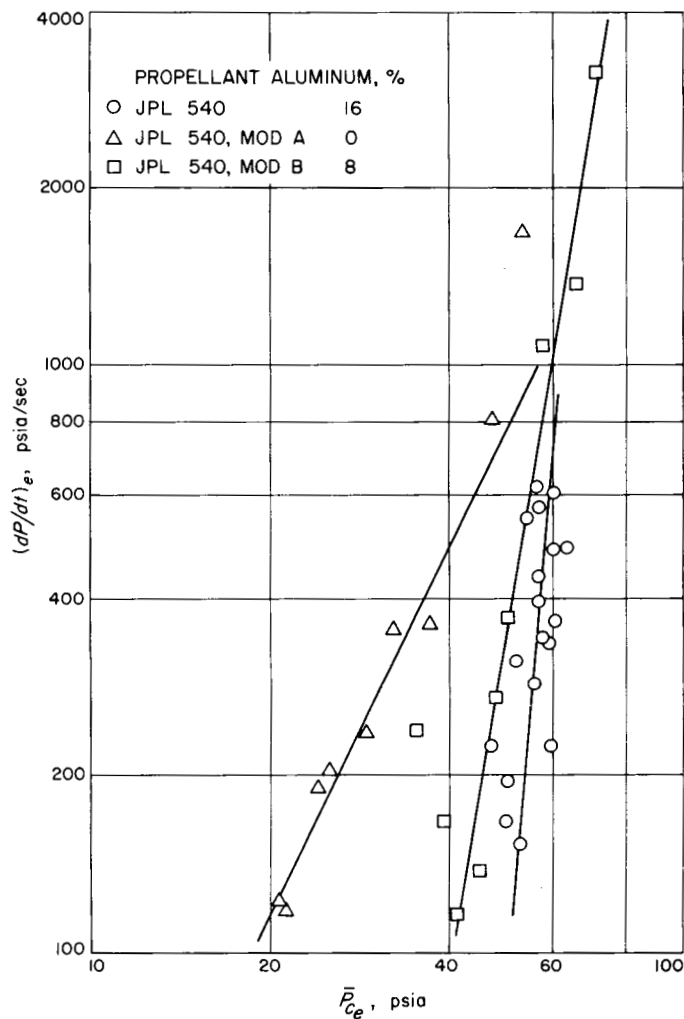


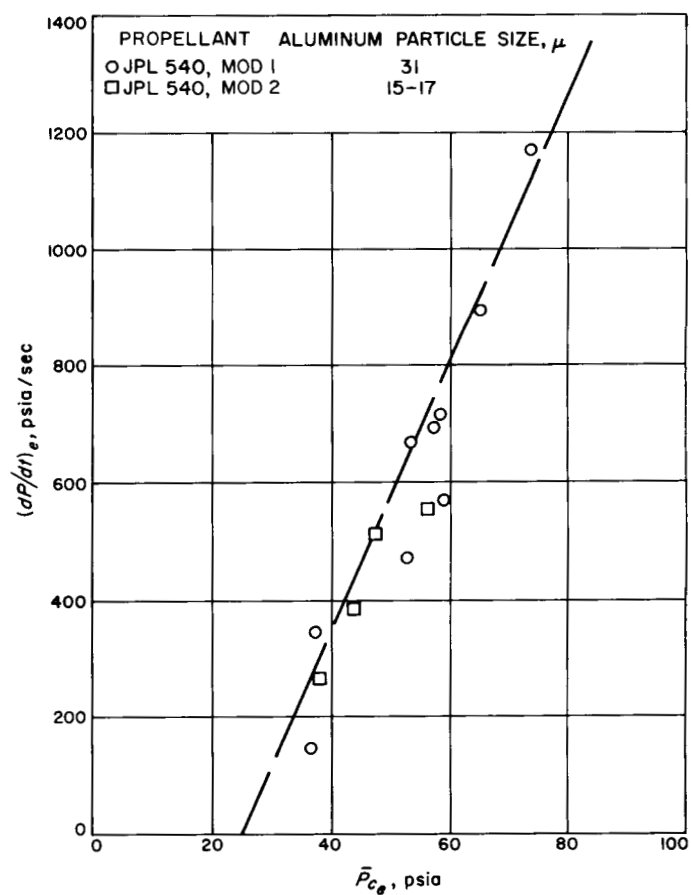
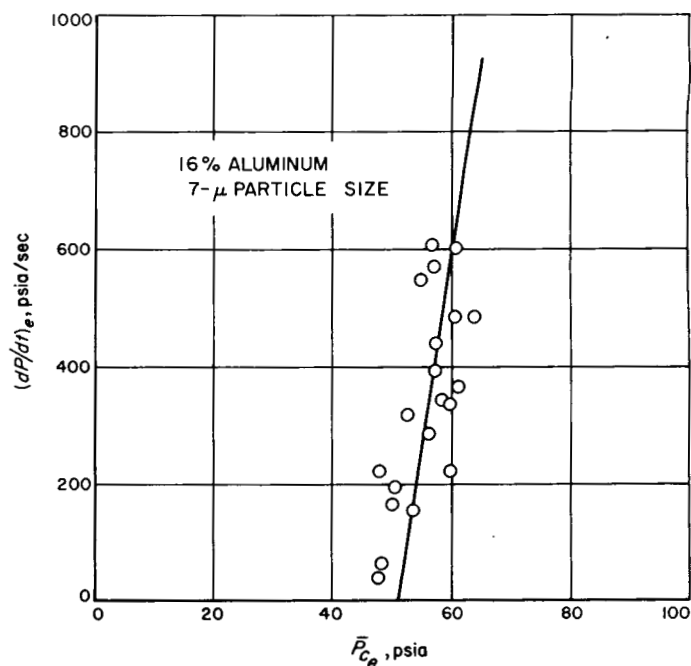
Fig. 12. Pressure-time for Run No. 1437, JPL 540-Mod B propellant

Fig. 10.  $L^*$  versus chamber pressure at onset of instability, JPL 540 propellant

**Fig. 14. Rate of chamber depressurization versus mean chamber pressure at combustion extinction, JPL 540 propellant**



**Fig. 13. Rate of chamber depressurization versus mean chamber pressure at combustion extinction, log-log plot**



**Fig. 15. Rate of chamber depressurization versus mean chamber pressure at combustion extinction, JPL 540-Mod 1 and Mod 2 propellants**

due to the frequency-pressure correlation at extinction (Refs. 2 and 3). For each propellant the correlation curve crosses the pressure coordinate  $(dP/dt)_e = 0$  at a pressure significantly greater than the propellant's measured deflagration limit (Figs. 14 and 15), indicating the existence of a minimum pressure, below which stable combustion within a motor cannot occur. This minimum pressure increases with increasing aluminum/oxidizer concentration ratio.

### 3. Motion-Picture-Oscillograph Pressure Data Correlation

Transparent motor  $L^*$  instability and extinguishment studies, described in detail in Refs. 6-7, have been conducted using the motor shown in Fig. 16, which is basically the motor of Fig. 1 with a 6-in. long, 1/4-in. wall thickness Lucite chamber substituted for the steel one. The tests were designed so that low-pressure extinction occurred about 2 to 4 sec following ignition, within the visual and structural lifetime of the Lucite. Motion picture film and oscillograph pressure data from tests with several different propellant formulations have been correlated. Common characteristics of the motion picture films and pressure data have given an indication of the series of events leading to complete combustion extinction. These events consist of: (1) the onset of extinction, (2) a rapid decrease in propellant gasification, (3) extinction, and (4) chamber venting. The location of these events on a typical oscillograph pressure-time trace is shown in Fig. 17. On the film the onset of extinction  $B$

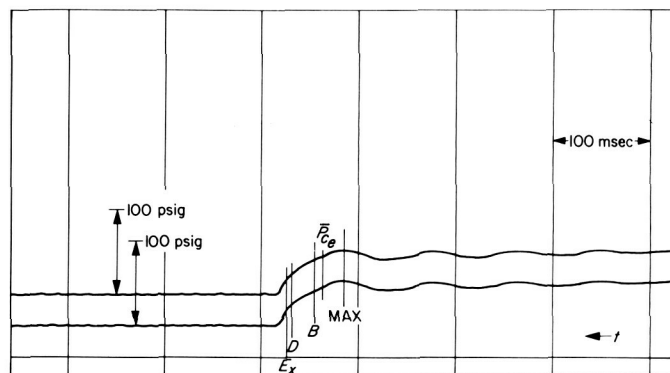


Fig. 17. Pressure-time trace for Run No. 1491, JPL 540-Mod 1 propellant

is a break and rapid decrease in the light intensity; at Point D, gasification appears to begin to decrease, with darkening of frames; and at extinction ( $E_x$ ) gasification appears to have largely ceased.

**N67-15719**

**(B) Applications Technology Satellite Motor Development, D. R. Frank and R. G. Anderson**

#### 1. Introduction

In January 1963 the Jet Propulsion Laboratory initiated a development program to provide a solid propellant apogee motor for a second-generation *Syncom* satellite. This program, under the management of the Goddard Space Flight Center, was designated *Advanced Syncom*. It was to result in a spin-stabilized, active repeater communications satellite weighing about 750 lb, operating at synchronous altitude (22,300 mi), which would handle voice communications, teletype, and monochrome and color television signals.

In January 1964 the *Advanced Syncom* communication program was redirected to include a number of experimental instruments in addition to the original communication instruments. This expanded program is the Applications Technology Satellite (ATS) program and will result in a general purpose satellite capable of operation at synchronous altitude with experimental instruments in the areas of meteorology, communications, radiation, navigation, gravity gradient stabilization and various engineering experiments. In order to place those satellites in synchronous orbit, JPL will provide a solid propellant rocket motor to provide final required velocity increment at the apogee of the elliptical transfer orbit. This rocket motor is designated the JPL SR-28-1 (steel chamber) or JPL SR-28-3 unit will be delivered for flight use.

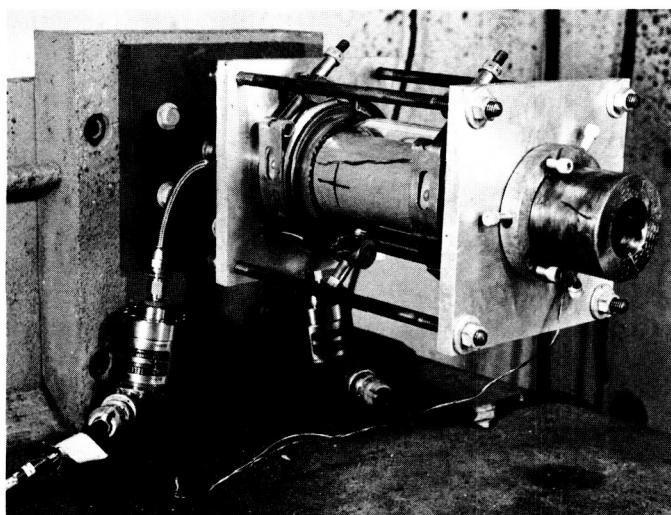


Fig. 16. Transparent motor with dummy charge mounted on test stand

Previous reports of progress on the development of this motor have been published in SPS 37-20 to 37-33, Vol. V (Confidential) and SPS 37-34 to 37-40, Vol. IV.

## 2. Program Status Summary

The motor development program calls for static firing of four heavywall motors and 25 flightweight motors, including two with flight-design titanium chambers, prior to conducting an 8-motor qualification program. To date, the 4 heavywall motors plus 22 flightweight motors have been static-fired, 4 of which were under simulated high-altitude conditions at Arnold Engineering Development Center (AEDC), Tullahoma, Tennessee. All of the flightweight motors tested to date have been with Type 410 chromium steel chambers, with the exception of Dev. G-8T, G-9T and E-3T, which used titanium chambers. In addition, 8 motors have been tested at AEDC while conducting a motor-qualification program.

## 3. ATS Storage Units

The three storage units, cast during September, 1965, are presently in storage. During the week of August 8, 1966, these units were removed after approximately nine months of storage and given critical visual and physical inspections. For these inspections the units were essentially weighed, visually inspected and subjected to a propellant and motor assembly alignment inspection. No detrimental effects due to the nine months of storage were observed.

One unit will be stored for 1 yr before it is statically tested. The remaining units will be stored for 2 yr before they are tested. The next inspection time will occur after the units have been stored for 1 yr.

## 4. ATS Qualification Tests

In July and August of this year the ATS apogee motor qualification tests were conducted at AEDC. The 8 apogee motor firings were performed in test cell T-3 of the Rocket Test Facility (RTF). In general, the purpose of the qualification program was to establish a performance-temperature history to be used for flight input information and to demonstrate the acceptability of the motor hardware for flight use. During each test the motor was spun at 100 rpm. The first 4 motors were fired following a complete motor temperature conditioning at 100°F. The remaining 4 motors were temperature-conditioned at 40°F before ignition. In Table 2 are listed all the motor component S/N's used in the qualification program.

Motor preparation at AEDC began with a visual inspection of each apogee motor after opening its shipping container. Detail X-ray inspections were performed on each motor to verify its acceptability for a static test. Results of the X-ray inspections indicated that all motors were acceptable for static testing.

While the motors were being X-rayed the inspection and preparation of the igniter assembly was being performed. The igniter assembly consists of a safe/arm device with two Hi-Shear PC-37 squibs supplied by the Harry Diamond Laboratory (HDL) and the igniter basket supplied by JPL. Leak checks were performed to evaluate all O-rings used in the safe/arm device. Once the igniter assembly had been installed in the apogee motor a final leak check was made of the completed unit.

Once a motor was completed, it was placed in its respective temperature-conditioning box. All motors remained in the temperature conditioning box at least 72 hr prior to removing it for a test. The motors were removed from their conditioning box anywhere from 24 to 12 hr prior to ignition. The test cell was also temperature-conditioned at the desired test temperature so that each motor was out of its test temperature environment only during the time it was transported from the RTF preparation area to the test cell, which was approximately 45 min.

Prior to installing the motor in the test cell, all test stand hardware was statically balanced. Once the motor was installed it was necessary only to align the motor about the spin axis to complete the motor installation. Prior to evacuating the test cell the safe/arm device was armed remotely from the blockhouse. Equivalent pressure altitudes of approximately 120,000 ft were maintained at ignition. During a test the minimum pressure altitude maintained was approximately 105,000 ft, with the exception of that portion of the test following flow breakdown in the diffuser section.

The data presented in Table 3 gives some of the important performance parameters. For particular analysis the vacuum specific impulse has been plotted as a function of motor conditioning temperature in Fig. 18. All values of  $I_{sp(vac)}$  are within 0.3% of the average at each temperature, which is the stated accuracy of the thrust integral recording system at AEDC. During two of the qualification tests temperatures on the external surface of the motor chamber and nozzle were recorded. This data will be presented in a future SPS.

**Table 2. S/N's of components used in ATS apogee motor qualification program**

Firing order	Dev. code	Chamber	Nozzle	Safe/arm	Igniter basket	Squib 1	Squib 2
1	Q-8T	T-14	F-39	16	94	37929	37890
2	Q-6T	T-12	F-41	17	76	37918	37924
3	Q-2T	T-8	F-34	13	89	37910	37905
4	Q-4T	T-10	F-44	15	87	37926	37884
5	Q-5T	T-11	F-32	18	85	37896	37919
6	Q-7T	T-13	F-43	10	67	37920	37923
7	Q-1T	T-7	F-31	11	72	37886	37889
8	Q-3T	T-9	F-38	14	81	37915	37891

**Table 3. Apogee motor weight and performance data**

Test conditions								
Motor firing order	1	2	3	4	5	6	7	8
JPL code	Q-8T	Q-6T	Q-2T	Q-4T	Q-5T	Q-7T	Q-1T	Q-3T
Test date	7-29-66	8-3-66	8-5-66	8-9-66	8-15-66	8-18-66	8-19-66	8-23-66
Average test altitude, ft	104,000	106,000	105,000	104,000	104,000	103,000	104,000	107,000
Motor condition temperature, °F	100	100	100	100	40	40	40	40
Weight data								
JPL loaded propellant weight, lbm	760.0	759.5	759.7	760.0	758.9	759.4	759.2	760.8
AEDC pre- and post-fire weight difference, lbm	769.0	769.1	768.9	769.2	767.4	768.7	768.1	769.5
Inerts expelled, lbm	9.0	9.6	9.2	9.2	8.5	9.3	8.9	8.7
Time data								
Igniter delay time, msec	2.5	2.5	3.0	2.5	2.5	3.0	3.0	4.0
Motor delay time, msec	28.0	23.0	28.0	23.0	25.0	25.0	33.0	28.0
Motor action time, sec	41.92	41.85	42.35	42.02	43.33	43.03	43.27	43.61
Pressure data								
Motor chamber starting pressure, psia	101	101	100	100	102	101	101	100
Motor chamber run peak pressure, psia	264.2	262.2	259.8	262.8	251.6	255.7	250.5	248.2
Chamber pressure integral, psia-sec	8909.6	8904.5	8925.8	8924.5	8891.1	8900.1	8876.6	8897.1
Characteristic velocity, $\bar{W}^*$ , ft/sec	4974.3	4986.0	4983.4	4985.2	4965.5	4967.3	4955.4	4960.2
Thrust data								
Run peak vacuum thrust, lbf	6397	6362	6279	6355	6074	6180	6065	6012
Vacuum total impulse, lbf-sec	213,957	214,119	213,860	214,021	213,087	213,533	213,189	213,797
Vacuum specific impulse (JPL loaded propellant weight), lbf-sec/lbm	281.5	281.9	281.5	281.6	280.8	281.2	280.8	281.0
See Table 5 for parameter definitions.								

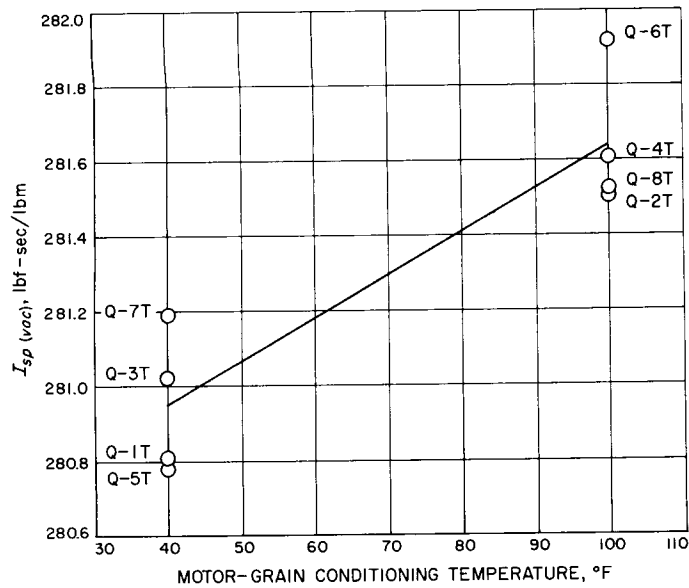


Fig. 18. Apogee motor vacuum specific impulse based on loaded JPL propellant weight

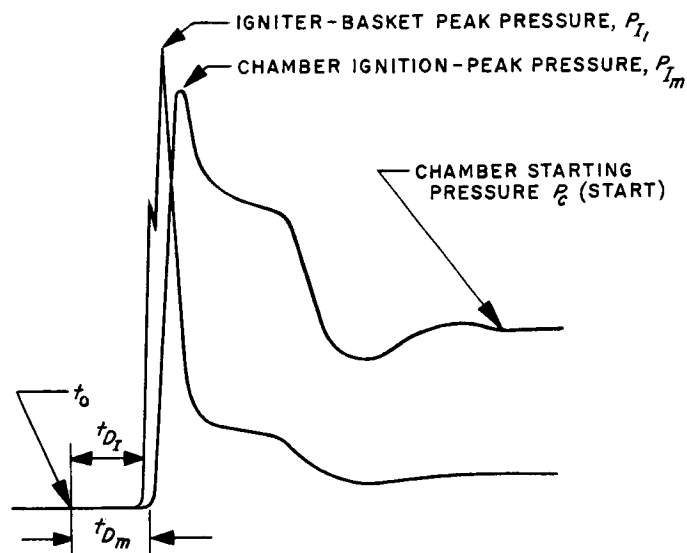


Fig. 19. Measurements made during ignition phase of motor operation

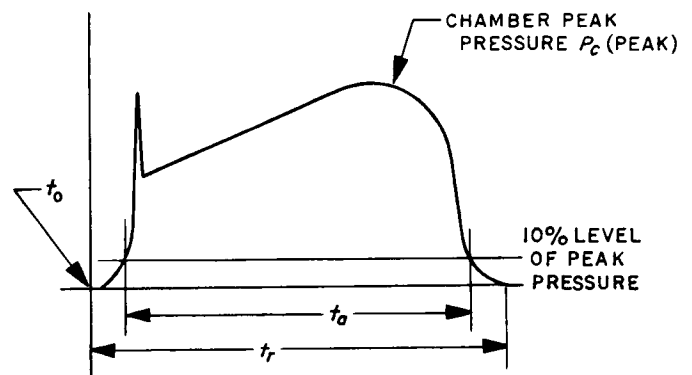


Fig. 20. Measurements made over the entire motor test

**Table 4. Parameter definitions used in ATS performance data summary**

$$(1) \overline{W^*}, \text{ ft/sec}, \frac{g_0 A_t \int_{t_0}^{t_r} P_c dt}{W_p}$$

where

$g_0$  = gravitational constant (32.14 lbf-ft/lbf-sec<sup>2</sup>)

$A_t$  = average nozzle-throat area (based on the average of the prefire and postfire measurements)

$W_p$  = loaded propellant weight

$t_r$  = run time (Item 9)

$t_0$  = zero time (Item 5)

(2) Chamber-pressure integral, psia-sec,

$$\int_{t_0}^{t_r} P_c dt$$

(3) Chamber-starting pressure, psia,  $P_c$  (start) (Fig. 19)

(4) Chamber peak pressure, psia,  $P_c$  (peak) (Fig. 20)

(5) Zero time, sec,  $t_0$ ,  $t_0$  is the instant electrical current is supplied to the squib (Fig. 19)

(6) Igniter delay time, msec,  $t_{D_I}$ ,  $t_{D_I}$  is the time period between the application of electrical current to the squib until the first indication of igniter pressure (Fig. 19)

(7) Motor delay time, msec,  $t_{D_M}$ ,  $t_{D_M}$  is the time period between the application of electrical current to the squib until the first indication of motor chamber pressure (Fig. 19)

(8) Action time, sec,  $t_a$ ,  $t_a$  is the time period between the time the motor-chamber pressure has reached 10% of its run peak value at ignition until it has decreased to 10% of the run peak value during motor tailoff (Fig. 20)

(9) Run time, sec,  $t_r$ ,  $t_r$  is the time period between the application of electrical current to the squib until the motor chamber pressure has returned to ambient conditions following motor tailoff (Fig. 20)

(10) Peak vacuum thrust, lbf,  $F_{vac}$  (peak), measured at the same time as the chamber peak pressure value (Fig. 20)

(11) Vacuum total impulse, lbf-sec,

$$I_{sp, vac} = \int_{t_0}^{t_r} F_{vac} dt$$

(12) Vacuum specific impulse, lbf-sec/lbm

$$I_{sp(vac)} = \frac{\int_{t_0}^{t_r} F_{vac} dt}{W_p}$$

## References

1. Anderson, F. A., Strand, L. D., and Strehlow, R. A., "An Experimental Investigation of the Low-Pressure Combustion Limits of Some Solid Propellants," Technical Memorandum No. 33-134, Jet Propulsion Laboratory, Pasadena, California, June 3, 1963 (Confidential).
2. Anderson, F. A., and Strand, L. D., "Low Pressure Combustion Studies," SPS No. 37-22, Vol. V, pp. 13-15, Jet Propulsion Laboratory, Pasadena, California, August 31, 1964 (Confidential).
3. Strand, L. D., "Low-Pressure Combustion Studies," SPS 37-27, Vol. IV, pp. 49-52, Jet Propulsion Laboratory, Pasadena, California, June 30, 1964.
4. Strand, L., "Low-Pressure Combustion Studies," SPS 37-29, Vol. IV, p. 78, Jet Propulsion Laboratory, Pasadena, California, October 31, 1964.
5. Sehgal, R., and Strand, L., "Low-Pressure Combustion," SPS 37-22, Vol. IV, pp. 109-112, Jet Propulsion Laboratory, Pasadena, California, April 30, 1965.

### **References (contd)**

6. Strand, L., "Studies of Unstable Combustion in a Transparent Solid Rocket Motor," *SPS 37-23*, Vol. V, pp. 4-6, Jet Propulsion Laboratory, Pasadena, California, October 31, 1963 (Confidential).
7. Strand, L., "Studies of Unstable Combustion in a Transparent Solid Rocket Motor," *SPS 37-25*, Vol. IV, pp. 60-63, Jet Propulsion Laboratory, Pasadena, California, February 29, 1964.

## X. Polymer Research

### PROPULSION DIVISION

N67-15720

#### **A Mechanical Behavior of SBR-Glass Bead Composites, R. F. Fedors and R. F. Landel**

##### **1. Theoretical Considerations**

In preceding reports, certain aspects of the mechanical behavior of a well-characterized composite system based on styrene-butadiene rubber filled with varying amounts of glass beads and cured by means of dicumyl peroxide were discussed. Thus, Refs. 1 and 2 are concerned with the preparation and characterization and Ref. 3 with a preliminary survey of the mechanical behavior of the composites in uniaxial tension, including the ultimate properties, as a function of test rate and test temperature. A more recent study of the stress-strain behavior of these composites, including an investigation of strain-induced particle-binder dewetting, has been reported in Ref. 4. In this part, a theoretical model will be proposed which attempts to predict both the dependence of the isothermal volume dilatation and the form of the stress-strain relationship on both the magnitude of the strain and the concentration of filler. In Sects. 2 and 3, the theoretical relationships for both volume dilatation and stress-strain response will be compared to experimental data.

*a. Small strains.* There have been several attempts to derive theoretical relationships for the dependence of the ratio  $E/E_0$  on the volume fraction of filler  $\phi_0$ , where  $E$  and  $E_0$  are the moduli of the composite and unfilled binder, respectively, at small strains. One such equation is the Guth-Gold expression (Ref. 5):

$$\frac{E}{E_0} = 1 + 2.5\phi_0 + 14.1\phi_0^2 + \dots \quad (1)$$

which is based on the Einstein viscosity equation, but modified so as to take into account interaction between filler particles. The equation is useful at low  $\phi$  values only (Ref. 6).

Also, using the Einstein viscosity equation as a starting point, and considering the effect of adding particles one at a time to a fixed volume of slurry, Roscoe (Ref. 7) derived a viscosity expression, whose modulus analog may be written as

$$E/E_0 = \left( \frac{\phi_m}{\phi_m - \phi_0} \right)^n \quad (2)$$

where  $n$  has the value 2.5 and  $\phi_m$  is the maximum value which  $\phi_0$  can attain, i.e.,  $\phi_m$  represents the maximum

volume fraction of filler which the fluid can accept without having to introduce voids in order to satisfy volume packing requirements. Roscoe took  $\phi_m$  to be unity. Eilers (Ref. 8) proposed an empirical viscosity expression whose modulus analog can be written approximately in the same form as Eq. (2), except that  $n$  has the value 2. He assumed the value of about 0.78 for  $\phi_m$ .

Landel, et al. (Ref. 9) have shown that Eq. (2) with  $n = 2.5$  provided an excellent representation of the dependence of viscosity of slurries on  $\phi_0$  at low shear rates. Further, they were able to show that  $\phi_m$  predicted by the fit of the equation to their experimental data was in excellent agreement with the  $\phi_m$  value measured experimentally. Landel (Ref. 10) has shown that Eq. (2) with  $n = 2$  was applicable to unvulcanized polyisobutylene-glass bead composites, and Landel and Smith (Ref. 11) later showed that the same equation provided a good representation for  $E/E_0$  versus  $\phi_0$  over a wide range of  $\phi_0$  for several highly filled composites.

Certain conditions, i.e., the assumption that the fluid completely wets the particle surface, are implicit for the validity of Eqs. (1) and (2). Hence, the equations cannot be expected to remain valid at large strains, because the binder phase can be expected to become detached from the particle surface, with resultant formation of voids.

**b. The model.** However, if it is assumed that Eqs. (1) and (2) will remain valid even at large strains *provided* that this detachment or dewetting is taken into account, then, as will now be shown, the dependence of both the volume dilatation and the stress on the strain and  $\phi_0$  can be calculated.

Fig. 1(a) shows an individual spherical filler particle imbedded in a binder matrix. Assume that the binder wets the entire surface of the filler; therefore, for strains small enough so that the surface remains wetted, Eqs. (1) and (2) should remain valid. As the strain is increased still further, however, the binder will eventually pull away from the particle surface and dewetting will occur. The strain at which dewetting becomes a significant determinant in the behavior of the composite depends on factors such as the magnitude of the binder-filler interaction and binder properties such as degree of crosslinking. In addition, for large binder-filler interaction, there may exist a threshold strain required to initiate dewetting.

Fig. 1(b) shows a particle which has dewetted; it is evident that only a portion of the particle surface is de-

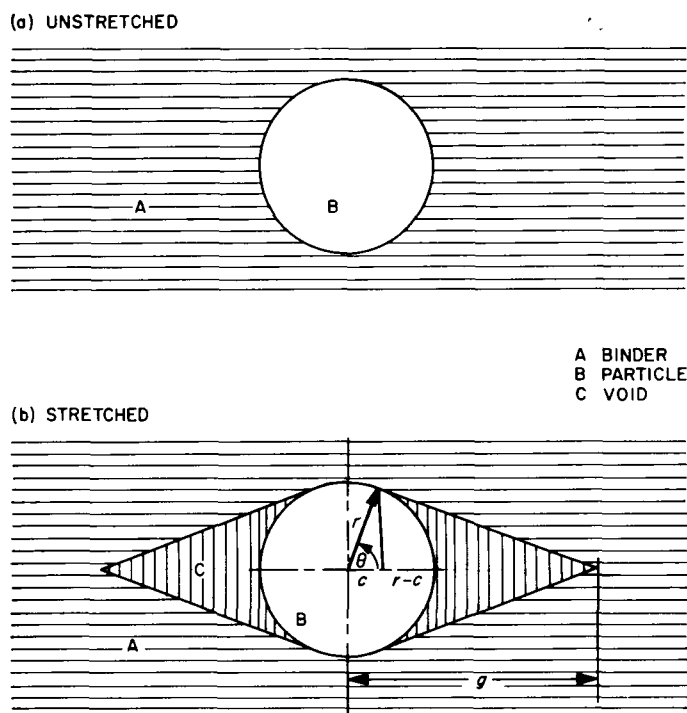


Fig. 1. Schematic representation of a spherical filler particle imbedded in an elastomeric binder

wetted at a given strain, and, furthermore, that the portion dewetted will increase with increase in strain. As shown in Fig. 1(b), the void formed is assumed to be conical in shape (Ref. 12). When the specimen has undergone a strain  $\epsilon$ , the height of the conical void is taken as  $g - c$ , where  $c = r \cos \theta$ ,  $r$  is the particle radius, and  $\theta$  is defined in Fig. 1(b). The fraction of particle surface still in contact with the binder  $S_a$ , can be shown to be

$$S_a = \cos \theta \quad (3)$$

Since only the filler which is in contact with the rubber can affect the mechanical properties of the composite, the initial volumetric loading before dewetting has occurred,  $\phi_0$  is, in effect, reduced according to the fractional surface area lost due to the pulling away of the binder from the particle surface. Hence the volume fraction of the active or effective filler after dewetting  $\phi_{eff}$  is assumed to be

$$\phi_{eff} = \phi_0 \cos \theta \quad (4)$$

The quantity  $(g - r)$ , the distance from the apex of the cone to the particle surface, is taken to be directly proportional to the particle radius and to the strain. The latter is assumed to be the difference between the "internal" strain  $\epsilon_i$  and the threshold value of the internal

strain required to initiate dewetting,  $\epsilon_{i0}$ . Thus,

$$(g - r) = kr(\epsilon_i - \epsilon_{i0}) = \frac{r(1 - \cos \theta)}{\cos \theta} \quad (5)$$

where  $k$  is a parameter independent of the  $\theta$ , which is expected to depend on factors such as the extent of filler-binder interaction and binder properties such as degree of crosslinking. The final equality simply expresses  $g - r$  in terms of  $r$  and  $\theta$ . Eq. (5) expresses the known fact that dewetting occurs preferentially at the larger particles (Ref. 12), presumably due to a stress concentration effect. The "internal" strain  $\epsilon_i$ , is the strain experienced by the binder when an external or overall strain  $\epsilon$  is imposed on the composite specimen. Following Bueche (Ref. 13), the relationship between  $\epsilon$  and  $\epsilon_i$  is taken to be

$$\epsilon_i = \frac{\epsilon}{1 - \phi_0^{1/3}} \quad (6)$$

Using the results shown in Eqs. (5) and (6), Eq. (4) can be written as

$$\phi_{eff} = \frac{\phi_0}{1 + \frac{k(\epsilon - \epsilon_0)}{(1 - \phi_0^{1/3})}} = \frac{\phi_0}{1 + k\epsilon_{eff}} \quad (7)$$

which provides a relationship for the effective volume fraction of filler as a function of the volume fraction present initially, before dewetting has occurred, and the strain.

**c. Volume dilatation.** Based on the model shown in Fig. 1(b), an expression for the volume dilatation to be expected from the formation and growth of voids as a function of the uniaxial strain may also be developed. If the void volume is taken to be that occupied by the conical cavity having a spherical segment as the base, then the relative increase in volume for particles far enough apart so that they do not interact can be written as

$$\frac{\Delta V}{V_0} = \frac{\sum_{i=1}^N \frac{2n_i r_i^3}{3} \left[ \frac{k^2 \epsilon_{eff}^2}{1 + k\epsilon_{eff}} \right]}{V_0} \quad (8)$$

where  $n_i$  is the number of particles of radius  $r_i$  and  $N$  is the total number of particles the threshold strain,  $\epsilon_0$  may be a function of both particle size and  $k$ . On the assumption that it is independent of both, Eq. (8) can be rewritten as:

$$\frac{\Delta V}{V_0} = \frac{\phi_0 k^2 \epsilon_{eff}^2}{2(1 + k\epsilon_{eff})} \quad (9)$$

Hence according to Eq. (9) estimates for both  $k$  and  $\epsilon_0$  can be conveniently obtained from measurements of  $\Delta V/V_0$  as a function of both  $\epsilon$  and  $\phi_0$ .

**d. Large strain response.** Returning to the relationship for the dependence of  $E/E_0$  on both  $\phi$  and  $\phi_m$ , Eq. (2), the relationships developed in Eqs. (3) to (9) will now be employed to generalize Eq. (2) so that it can be applied to situations where dewetting has occurred. Substitution of Eq. (7) into Eq. (2) yields an expression for the modulus of a composite in terms of the modulus of the binder and the total strain

$$E = E_0 \left[ \frac{\phi_m \{(1 - \phi_0^{1/3}) + k(\epsilon - \epsilon_0)\}}{\phi_m \{(1 - \phi_0^{1/3}) + k(\epsilon - \epsilon_0)\} - \phi_0(1 - \phi_0^{1/3})} \right]^n \quad (10)$$

The term in square brackets may be referred to as the modulus amplification factor, since it represents the modulus of the composite in terms of  $E_0$  and a multiplying factor which depends on strain and  $\phi_0$ .

If the stress-strain relation for a binder is taken to be

$$\sigma = E_0 f(\epsilon) \quad (11)$$

where  $\sigma$  is the stress based on the initial cross-sectional area and  $f(\epsilon)$  is a function of the strain alone, then the stress-strain response for a composite can be expressed as

$\sigma =$

$$E_0 \left[ \frac{\phi_m \{(1 - \phi_0^{1/3}) + k(\epsilon - \epsilon_0)\}}{\phi_m \{(1 - \phi_0^{1/3}) + k(\epsilon - \epsilon_0)\} - \phi_0(1 - \phi_0^{1/3})} \right]^n f(\epsilon) \quad (12)$$

It is expected that both Eq. (9) for the volume dilatation and Eq. (12) for the stress-strain response will not be applicable at very large strains or very high loadings, because under these conditions the model breaks down, i.e., the cavities around the particles are no longer conical and independent of one another. Thus mutual interference between neighboring particles will cause the actual  $\Delta V/V_0$  to be lower than that predicted by Eq. (9). For the same reason, it might be expected that individual voids would coalesce, thereby increasing the fraction of dewetted surface area. This factor would cause Eq. (12) to overestimate  $\sigma$  for a given  $\epsilon$ .

A second mechanism which can lead to failure of Eq. (12) is that of rupture in the binder as the initial site of void formation rather than dewetting at the surface. In the latter case  $\phi_0$  is calculated, as just shown, simply by assuming no volume change on mixing the filler with the binder. However in the former, as a first approximation, the appropriate value of  $\phi_0$  may be calculated by replacing the filler particle by a substitute having a radius

$r + a$ , where  $r$  is the particle radius and  $a$  is the effective thickness of the binder shell surrounding the particle. Clearly, the value of  $\phi_0$  calculated on the basis of the filler alone will always be less than  $\phi_0$ , calculated on the basis of the filler + binder shell.

The two mechanisms are readily separated, however, since in the case of rupture in the binder there will be permanent damage and irrecoverable softening. That is, if the stress is removed and then reapplied after a rest period, there would be no recovery, and the samples would appear to be softer in the second loading cycle. In the case of dewetting at the particle surface the rubber would be expected to readhere and the initial properties would be recovered.

A third instance in which the simple model may not be appropriate and may require modification is that in which agglomerates are present. If these are stable, symmetrical, and do not change the effective particle size distribution, there will be no effect on the final results. On the other hand, if the agglomerates break down during stretching, there will be particle-particle interference within the region of the agglomerates, leading to a smaller  $\Delta V/V_0$  and  $\sigma$  with  $\epsilon$  than would be predicted from Eqs. (9) and (12). Asymmetrical particles will affect the size and size distribution of the voids according to their axial ratio and orientation. If the particle size distribution changes, then  $\phi_m$  will have to be evaluated for that distribution. Normally the value of  $\phi_m$ , although dependent on such factors as particle size, particle-size distribution, and both filler-polymer and filler-filler interaction, should be essentially a constant for a given binder-filler system.

Some consequences of the model and the validity of the proposed equations will be investigated in Sects. 2 and 3. First,  $\Delta V/V_0$  versus  $\epsilon$  data will be used to determine the applicability of Eq. (9), and to determine the values of the parameters  $k$  and  $\epsilon_0$ . Then, these parameters will be used in conjunction with Eq. (12) to provide theoretical stress-strain curves for comparison with experimental data.

## 2. Dependence of Isothermal Volume Dilatation on Uniaxial Strain and Filler Loading

In Sect. 1 a model was proposed which provided theoretical relationships for the dependence of both isothermal volume dilatation and the uniaxial stress-strain response on both the magnitude of the strain and on the filler loading. In this section, experimentally measured volume dilatation behavior for 8 composites with  $\phi_0$  varying from 0.0922 to 0.339 at two temperatures, 23 and 0°C, will be

reported and compared to the theoretical relationships derived on the basis of the model.

**a. Experimental.** The procedure employed for assessing volume dilatation is based on the hydrostatic weighing technique. A stainless steel rig was made on which six to eight ring specimens (1% in. ID and 1% in. OD and about 0.080 in. thick) could be stretched simultaneously under water in 1/2-in. increments. The totally immersed rig, with specimens, was suspended by means of a 10-mil platinum wire from one side of the beam of an analytic balance having a capacity of 200 g. A totally immersed counterweight of approximately the same weight as the rig was suspended from the other side of the beam by the same size wire. By this technique, surface tension contributions to the apparent weight were effectively eliminated. A small amount of surface active agent was added to the bath, primarily to minimize the dampening action of the surface tension. No special effort to thermostat the bath was taken, since periodic temperature measurements indicated that the water temperature did not vary by more than 0.2°C during any given run. For the experiments conducted at 0°C, a portion of the bath water was replaced by ice sufficient to maintain an excess of ice at all times during a given run. A stainless steel wire cage was placed around both the rig and counterweight in order to keep them clear of ice. The bath was stirred for a few minutes about 15 min before a reading was taken. The water temperature was maintained at  $0.2 \pm 0.1^\circ\text{C}$ .

In practice, the rings were stretched in 1/2-in. increments until either all rings had broken, or the run was terminated for other reasons. Generally, rings broke one at a time and at various extensions, as expected (Refs. 14, 15). Preliminary experiments had shown that the dilatation at fixed strain depended on time as well as on  $\phi_0$ . Fig. 2 shows the results obtained with the most highly filled composite containing 33.9 vol % glass at two strains,  $\epsilon = 12$  and 63% as a function of  $t^{1/3}$ . The figure indicates that the cube root time relationship is a satisfactory representation for these data. The slope for the lower strain is  $0.14 \text{ sec}^{-1/3}$ , while that for the higher strain is approximately  $0.1 \text{ sec}^{-1/3}$ . On the basis of the cube root time dependence, it is proposed that the small increase in  $\Delta V/V_0$  with time is due to slow creep of the binder itself, which causes additional dewetting and, hence, an increase in the size of the void. On this basis, it would be expected that the value of the slope, for data such as that depicted in Fig. 2, would be independent of strain for small strains but dependent on  $\phi_0$ . This latter dependence was indirectly observed in that it was noted

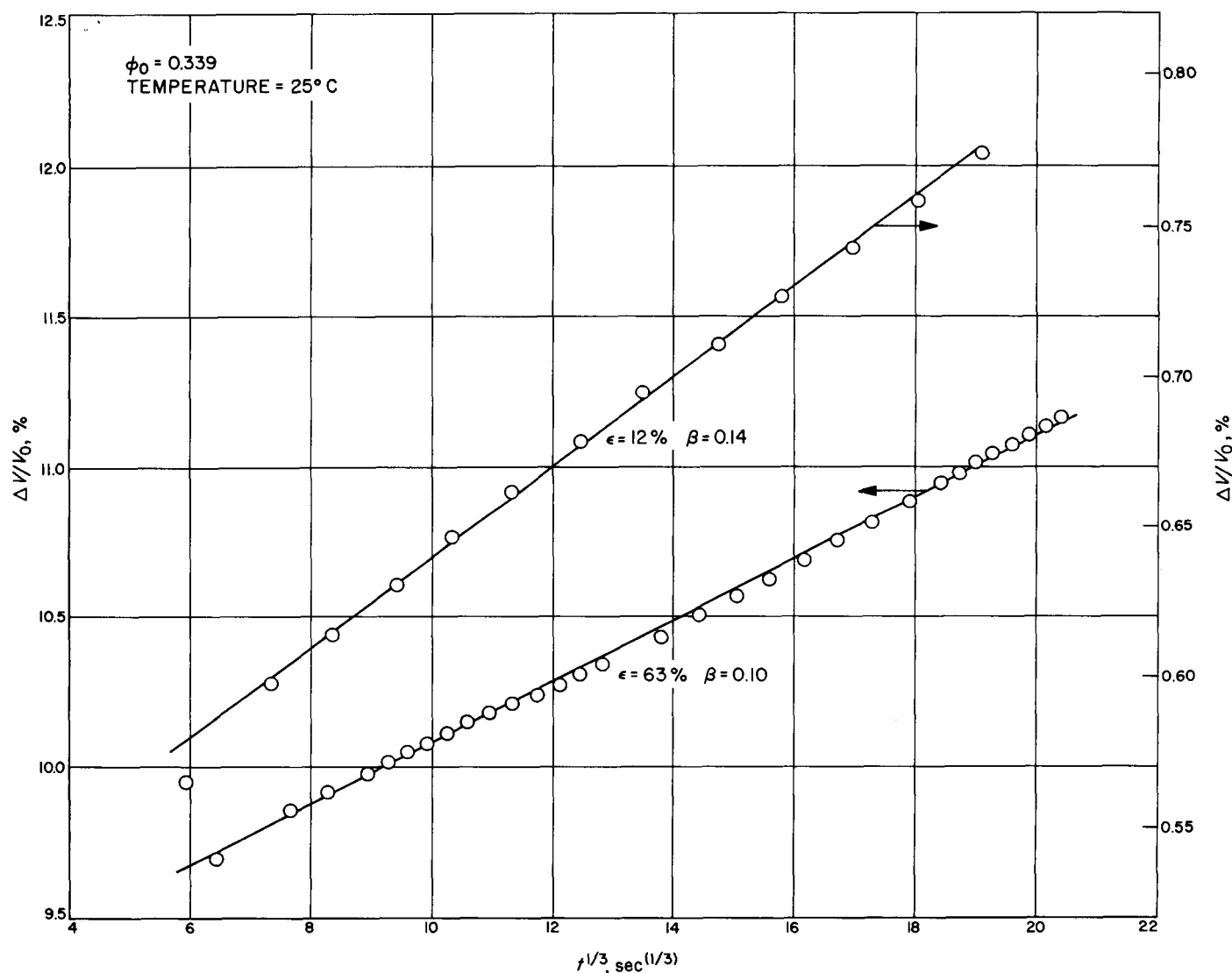


Fig. 2. Time dependence of the relative volume change at two strains,  $\epsilon = 12\%$  and  $\epsilon = 63\%$  for a composite containing 33.9 vol % glass beads. The values of  $\beta$  indicated are the calculated slopes

that the weight of the rings (volume) did not vary appreciably with time for the composites having the lower filler concentration. Ideally, the  $\Delta V/V_0$  versus time data should be collected at each strain value and these results used to obtain the value of  $\Delta V/V_0$  extrapolated to zero time. However, in view of the need to acquire data, it was arbitrarily decided to use the value of  $\Delta V/V_0$  obtained 20 min after the specimens were stretched.

**b. Results.** The results obtained at 23°C are shown in Fig. 3 for eight composites with  $\phi_0$  varying from 0.0922 to 0.339. The volume change measurements were continued for each composite until all specimens had broken. Thus, the data shown represent the dilatation of these com-

posites essentially to break. The data are depicted as the coded circles and the full curves shown are the fit of the equation derived in Part 1:

$$\frac{\Delta V}{V_0} = \frac{\phi_0 k^2 \epsilon_{eff}^2}{2(1 + k\epsilon_{eff})} \quad (13)$$

using  $k = 0.52$  and assuming  $\epsilon_0$  to be zero. It is evident that the equation provides a satisfactory one-parameter fit to the volume data over the entire range of  $\phi_0$ . Eq. (13) can fit the data rather more precisely if  $k$  is allowed to vary slightly, i.e., from  $k = 0.48$  for  $\phi_0 = 0.0922$  to  $k = 0.52$  for  $\phi_0 = 0.339$ . Since the value of  $k$  is expected to vary with degree of crosslinking in the binder phase, slight variations in the value of this parameter

may be expected on this account. In addition, small variations in the value of  $k$  with  $\phi_0$  may also be due to the time dependence of  $\Delta V/V_0$  as mentioned earlier. Since the time dependence is apparently a function of  $\phi_0$ , being essentially zero for the lowest loading and increasing with increase in  $\phi_0$ , the fact that a 20-min time interval was used to obtain the  $\Delta V/V_0$  values shown in Fig. 3 means that volume dilatation at high  $\phi_0$  has been overestimated compared to that obtained at low  $\phi_0$ . In any event, the differences are small and setting  $k = 0.52$  for the whole range in  $\phi_0$  provides a satisfactory fit to the experimental data.

In Fig. 4 are shown the results obtained at 0°C for some of the same composites used at 23°C. The full curves represent the fit of Eq. (13) with  $\epsilon_0 = 0$  and  $k = 0.56$ . Here, as at 23°C, a better fit to the data can be obtained by letting  $k$  vary slightly.

The fact that  $k$  is essentially independent of temperature, at least in the range 0 to 23°C, implies that no substantial amount of energy is required to break the glass-binder interface. It also indirectly supports the contention that the threshold strain is zero for this composite

system, for an  $\epsilon_0 > 0$  would imply that the interface could store energy or that a finite amount of work was required to break the interfacial adhesion. An appreciable energy requirement for this process would imply a temperature dependent  $k$ .

A study of Figs. 3 and 4, especially Fig. 3, indicates that the experimental data fall below the theoretical curves at large strains, i.e., the actual  $\Delta V/V_0$  is less than the predicted value at large strains. In addition, the strains at which the differences become appreciable decrease with increased  $\phi_0$ . These deviations are probably due to breakdown of the model used to obtain Eq. (13). The latter assumes that each particle acts independently of all others and further that the conical voids associated with one particle do not affect the formation and growth of voids associated with a neighboring particle. Clearly this simplification must break down at large strains and high  $\phi_0$  values. If interference occurs between neighbors, this will lead to smaller  $\Delta V/V_0$  values than would be predicted on the basis of Eq. (13). Further, although satisfactory agreement with experiment has been observed for  $\phi_0$  values up to about 0.34, it is clear that Eq. (13) must break down as  $\phi_0$  approaches  $\phi_{0m}$ .

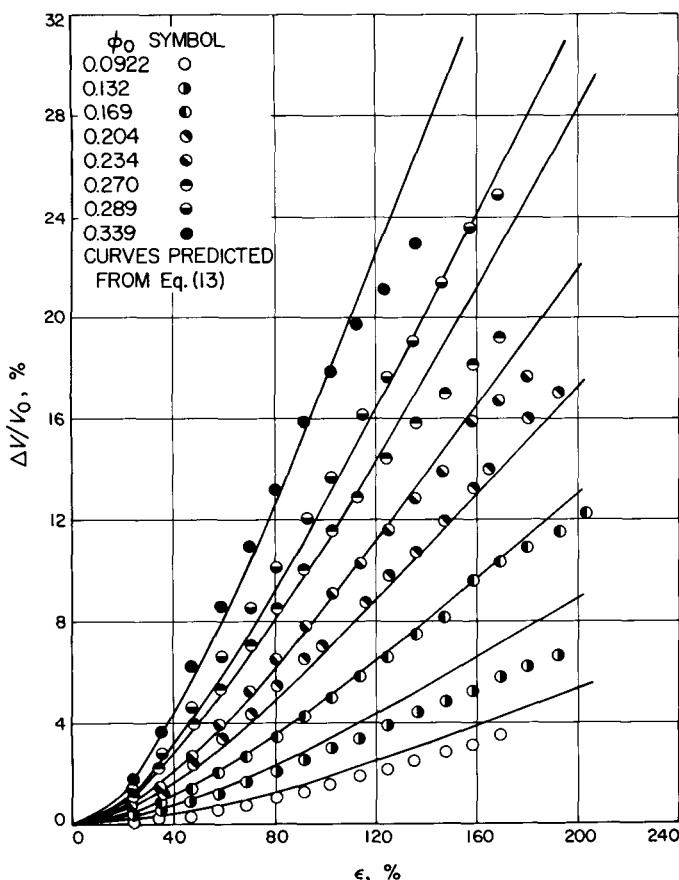


Fig. 3. Isothermal volume dilatation for SBR-glass bead composites as a function of strain at 23°C

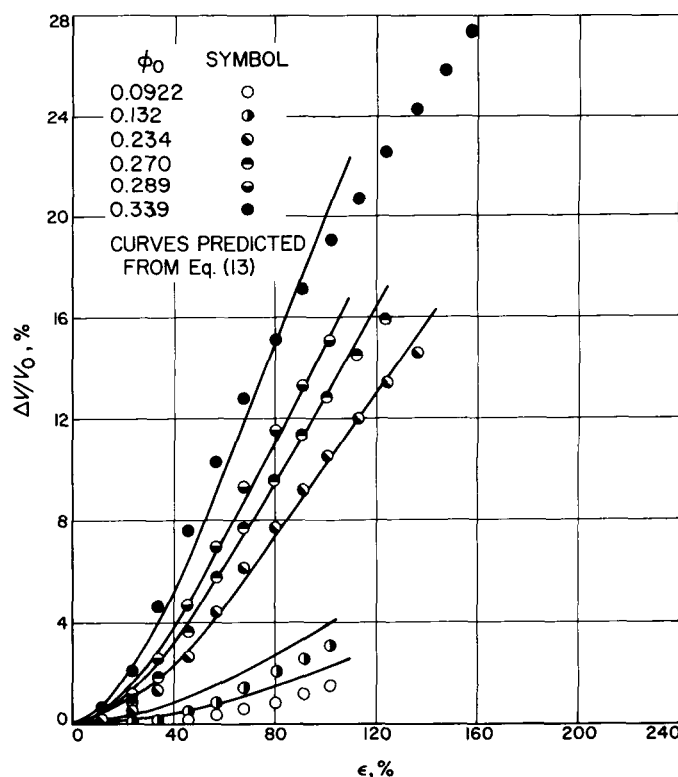


Fig. 4. Isothermal volume dilatations for SBR-glass bead composites as a function of strain at 0°C

### 3. Stress-Strain Behavior and Stress Softening Effects

In Sect. 1, a model was proposed for relating the uniaxial volume dilatation and stress-strain response of composites to both the strain level and the filler content. In Sect. 2, it was demonstrated that the dependence of the volume dilatation on both strain and filler content was satisfactorily described in terms of the model. In this part, the model will be further tested to determine how well it predicts the uniaxial stress-strain response.

**a. Experimental.** Ring specimens having an inside diameter of 0.750 in. and an outside diameter of 0.875 in. were cut from molded sheets, using a specially designed four-blade cutter mounted in a high-speed mill. The rings were tested on an Instron testing machine at three rates, 0.17, 4.25 and 17.0 per minute and at temperatures between  $-40$  and  $+60^\circ\text{C}$  using ungreased hooks 0.25 in. in diameter. The strain was calculated from the crosshead displacement  $\Delta L$ , as  $\epsilon = 2 \Delta L / \pi D_i$ . The stress was calculated as the ratio of the load to the original cross-sectional area of the ring.

In the work concerned with stress softening effects, ring specimens of the composites were studied at both  $-20$  and  $25^\circ\text{C}$  at a strain rate of  $0.85 \text{ min}^{-1}$ . The rings were subjected to repeated loading-unloading cycles. In the steady test mode a time interval of a few seconds elapsed before the subsequent loading cycle was begun, although this interval was not precisely controlled. In the intermittent test mode, the specimens were allowed to rest after each load-unload cycle. One day at room temperature was arbitrarily selected as the rest period, since the specimens seemed to regain essentially their initial dimensions after this time period. The strain was calculated from the crosshead displacement  $\Delta L$ , as indicated previously. The fact that the inside diameter varied slightly, due to set, was not taken into account; at most the set amounted to a few percent and, variations of this order would show up primarily in the low strain region of the stress-strain response.

#### b. Results

**First-stretch response.** Typical results for the effect of temperature and  $\phi_0$  on the stress strain response at  $0.85 \text{ min}^{-1}$  are shown in Figs. 5 and 6, as the unfilled circles, for values of  $\phi_0 = 0, 0.169, 0.289$ , and  $0.339$  and for temperatures of  $25$  and  $-20^\circ\text{C}$ , respectively. These data show in general that for small strains, the stress at a given strain level (at constant temperature) increases as expected with increase in  $\phi$ ; further, at a fixed  $\phi$  value,

the corresponding values of the stress increase as the temperature is decreased. In the small strain region the stress-strain response is approximately linear, but the slope is less than unity for strains down to about 10% (except possibly for the unfilled binder). Unfortunately, the use of ring specimens did not allow meaningful stress-strain data to be obtained for strains less than about 10% for the particular ring sizes used in the present study. It is apparent that the strain region in which Hooke's law is obeyed must be less than 10% for these composites; thus, even for strains as low as 10% it is not possible to define a unique modulus and hence, the present data cannot be employed in conjunction with equations of the form

$$\frac{E}{E_0} = \left( \frac{\phi_m}{\phi_m - \phi_0} \right)^n \quad (14)$$

(Sect. 1) to define a unique value for  $\phi_m$ .  $E$  and  $E_0$  are the moduli of the composite and unfilled binder respectively,  $\phi_0$  is the volume fraction of filler present before dewetting has occurred,  $\phi_m$  is the maximum value  $\phi_0$  can attain, and  $n$  is a parameter with a value of 2 for the Eilers-van Dijk (Ref. 16) equation and 2.5 for the Roscoe (Ref. 17) equation.

As the strain is increased to intermediate values, the data in Figs. 5 and 6 (unfilled circles) indicate that the slopes of the stress-strain response decrease monotonically and at a rate which increases with increase in  $\phi_0$ , i.e., the stress-strain curves for the composites converge to the response shown by the unfilled gum. In addition, at  $-20^\circ\text{C}$ , the slopes for both the filled and unfilled materials increase again at higher strains; however, the response of the composites continues to converge to that of the gum.

In Sect. 1 of this series, based on a model which related the dependence of volume dilatation and stress-strain response on both strain level and filler content to the fraction of filler surface dewetted, the following relationship for the dependence of the stress-strain response of a composite was proposed

$$\sigma = E_0 \left[ \frac{\phi_m \{ (1 - \phi_0^{1/3}) + k(\epsilon - \epsilon_0) \}}{\phi_m \{ (1 - \phi_0^{1/3}) + k(\epsilon - \epsilon_0) \} - \phi_0 (1 - \phi_0^{1/3})} \right]^n f(\epsilon) \quad (15)$$

where  $k$  is a parameter,  $\epsilon_0$  is the threshold value of the strain required to initiate dewetting, and  $f(\epsilon)$ , a function

of the strain alone, is the strain function characteristic of the unfilled binder. Thus, when  $\phi_0 = 0$ , the equation reduces to  $\sigma = E_0 f(\epsilon)$ , the stress-strain response of the gum. Values for both  $k$  and  $\epsilon_0$  were evaluated in Sect. 2 from experimental data on volume dilatation studies. It was found that  $\epsilon_0 = 0$  and  $k = 0.52$  at  $23^\circ\text{C}$  and  $\epsilon_0 = 0$  and  $k = 0.56$  at  $0^\circ\text{C}$ . Thus for this composite system, there is no threshold strain required to initiate dewetting; further, the value of  $k$  is essentially temperature-independent.

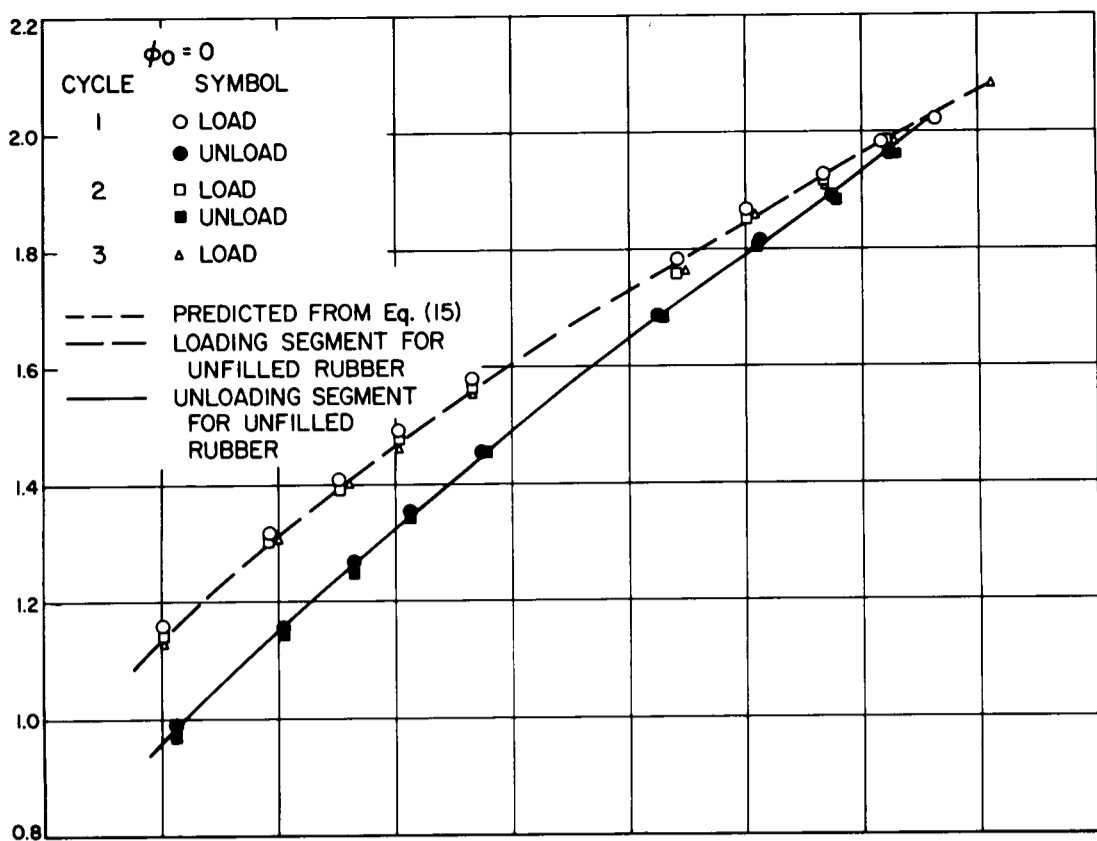
In Figs. 5 and 6, the predicted stress-strain curves based on Eq. (15) are shown as the dotted lines, and these curves are to be compared with the experimental stress-strain response denoted by the unfilled circles. The calculated curves were obtained by assuming  $n = 2$  in Eq. (15) (Eilers-van Dijk exponent) and then using the experimental points to arrive at a value of  $\phi_m$ . The best value of  $\phi_m$  appears to be 0.63, which is the value obtained experimentally by measuring  $\phi_m$  for the same glass case beads in mineral oil (Ref. 18). The data could equally well be fit using  $n = 2.5$  (Roscoe exponent), but in this case a value of  $\phi_m = 0.74$  was required. For the stress-strain data obtained at  $-20^\circ\text{C}$ , it was assumed that  $k = 0.60$ , a value obtained by linear extrapolation of the values of this parameter obtained at  $23^\circ\text{C}$  ( $k = 0.52$ ) and  $0^\circ\text{C}$  ( $k = 0.54$ ). Unfortunately, Eq. (15) is rather insensitive to the precise value of  $k$  used and the differences obtained using  $k = 0.52$  and  $k = 0.60$  are apparent only at high strains where the larger value of  $k$  predicts a few percent lower value of  $\sigma$ , at a given strain level. It is evident from the figures that Eq. (15) provides a satisfactory representation of the stress-strain response in the low and intermediate strain region. At higher strains, in Fig. 5, Eq. (15) predicts a higher stress at a given strain than that observed experimentally. Further, the strains at which the divergence becomes apparent decrease with increase in  $\phi_0$ , which is identical to the effect observed in the volume dilatation experiments. Break-down of the validity of the model employed, as discussed in Sect. 1, is responsible for the observed discrepancies for both the stress strain and the volume dilatation responses.

In the case of volume dilatation, the volume increases more slowly than the equations would predict, while in the case of the stress-strain response the stress decreases more rapidly than Eq. (15) predicts. These two effects are related to the fact that at both large strain and high  $\phi_0$  value, the growth of voids (and hence volume increase) about individual particles will be impeded by interference from neighboring particles.

*Stress softening effects.* The unfilled circles represent data obtained on the initial stretch. Experiments were also carried out to ascertain the effects on subsequent response of various prior stress-strain histories. In the experiments conducted at  $25^\circ\text{C}$  (Fig. 5) specimens of each composite were strained to about 170% at a rate of 0.85 per minute; they were then immediately unloaded by reversing the direction of the crosshead of the testing machine. This cyclic procedure was repeated several times. For the two most highly filled composites, the maximum strain was 165% rather than 170%. The unfilled symbols represent the stress-strain response on the loading portion of each cycle and the filled symbols denote the corresponding behavior during unloading. Fig. 5 shows the results obtained for several composites which were carried through  $2\frac{1}{2}$  cycles; during the third loading portion (last  $\frac{1}{2}$  cycle) the specimens were strained to break. In one case, the composite was carried through  $4\frac{1}{2}$  cycles. It is evident that the stress-strain behavior for the gum specimen, Fig. 5a, is reproducible both during the loading and unloading portions of each cycle. For the composites, however, the initial loading curves are *unique*; while the initial unloading and all subsequent load-unloading curves are reproducible. Furthermore, these latter curves essentially reproduce the stress-strain response shown by the gum, except in the neighborhood of the maximum strain used in the experiment. For ease of comparison, the dashed curve and the solid curve in both Figs. 5 and 6 represent the response of the gum vulcanizate.

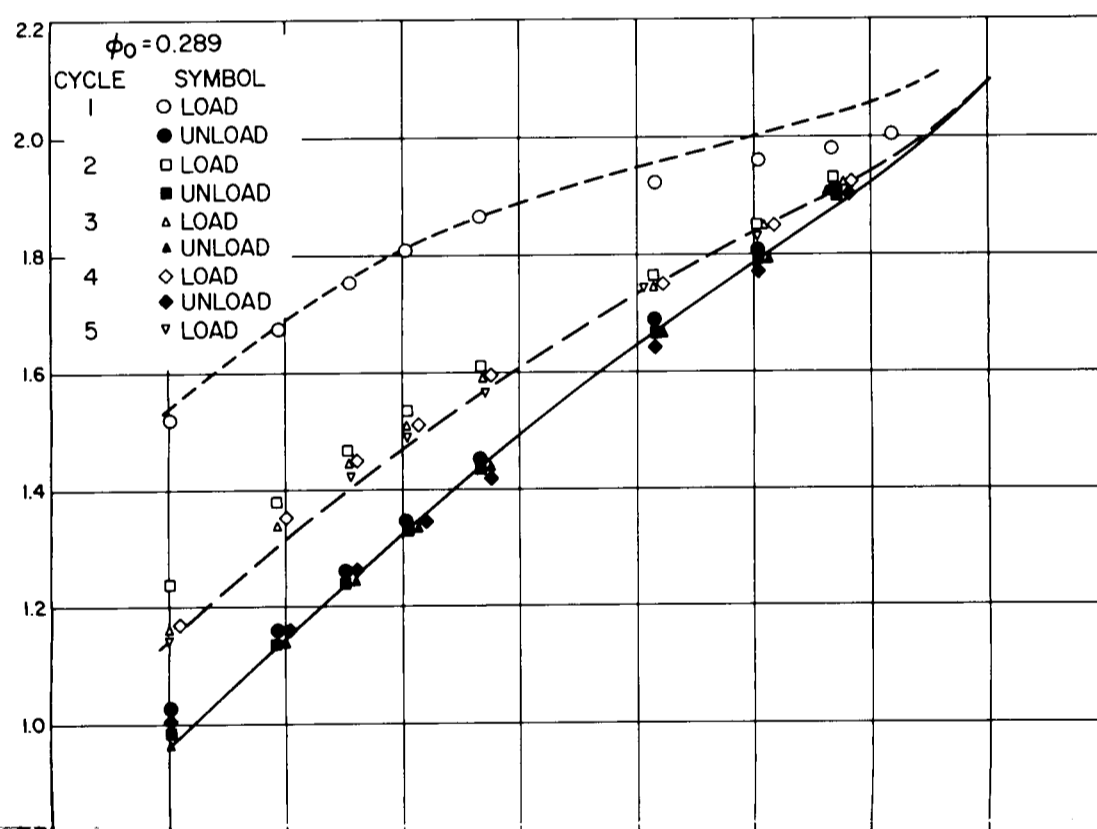
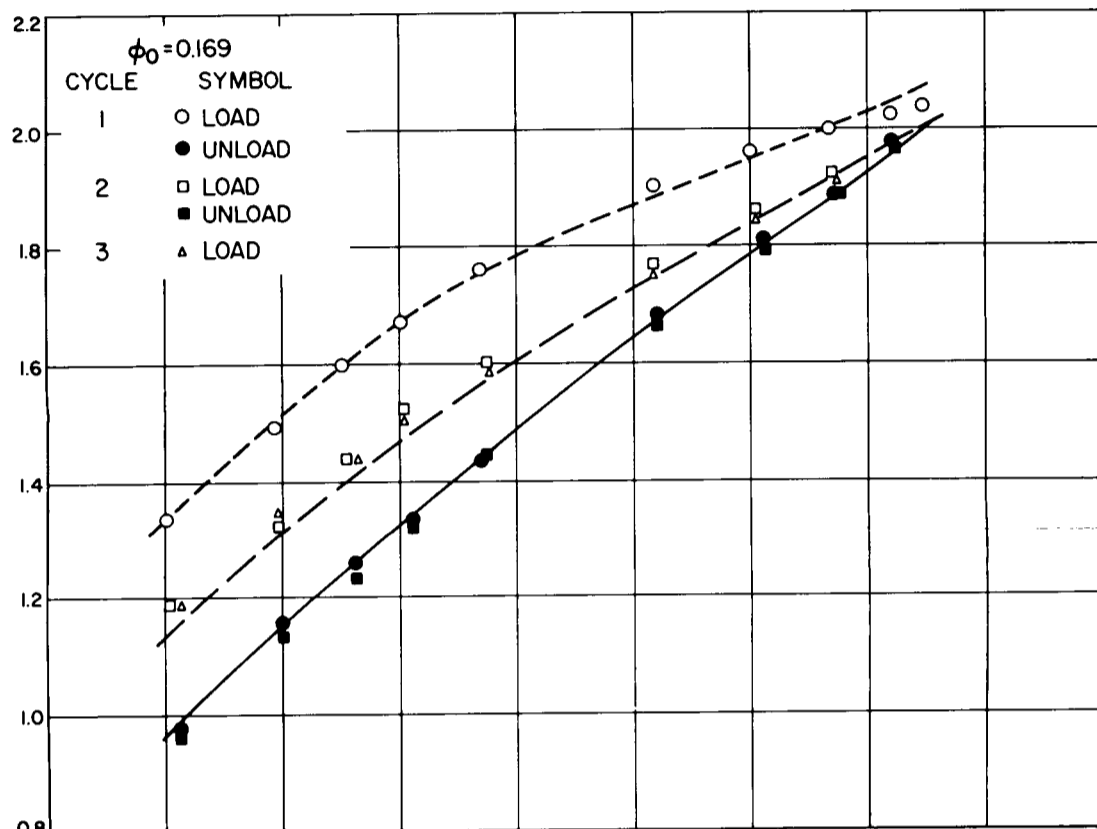
For the experiments conducted at  $-20^\circ\text{C}$ , after each load-unload cycle, the specimens were allowed to rest at room temperature for about a day before subsequent testing. This procedure was required in order to reduce the larger set of the specimens after being stretched; after this rest period at room temperature contraction occurred and the set was essentially recovered. At  $-20^\circ\text{C}$ , all stress-strain curves for the composites for both loading and unloading segments of each cycle were reproducible as may be seen in Fig. 6. It is evident that for all composites the unloading curves are essentially the same as the corresponding curve generated by the gum. This behavior is similar to that observed at  $25^\circ\text{C}$ . However, the stress-strain response of the composites on the initial loading as well as on subsequent loading positions are all reproducible, contrary to the results obtained at  $25^\circ\text{C}$ . This effect is presumably due to the fact that the specimens were allowed to rest between each cycle. The rest period was evidently sufficiently long to allow the specimens to heal or to revert to their original condition.

105-1



LOG  $\sigma$ , psi

105-2



105-3

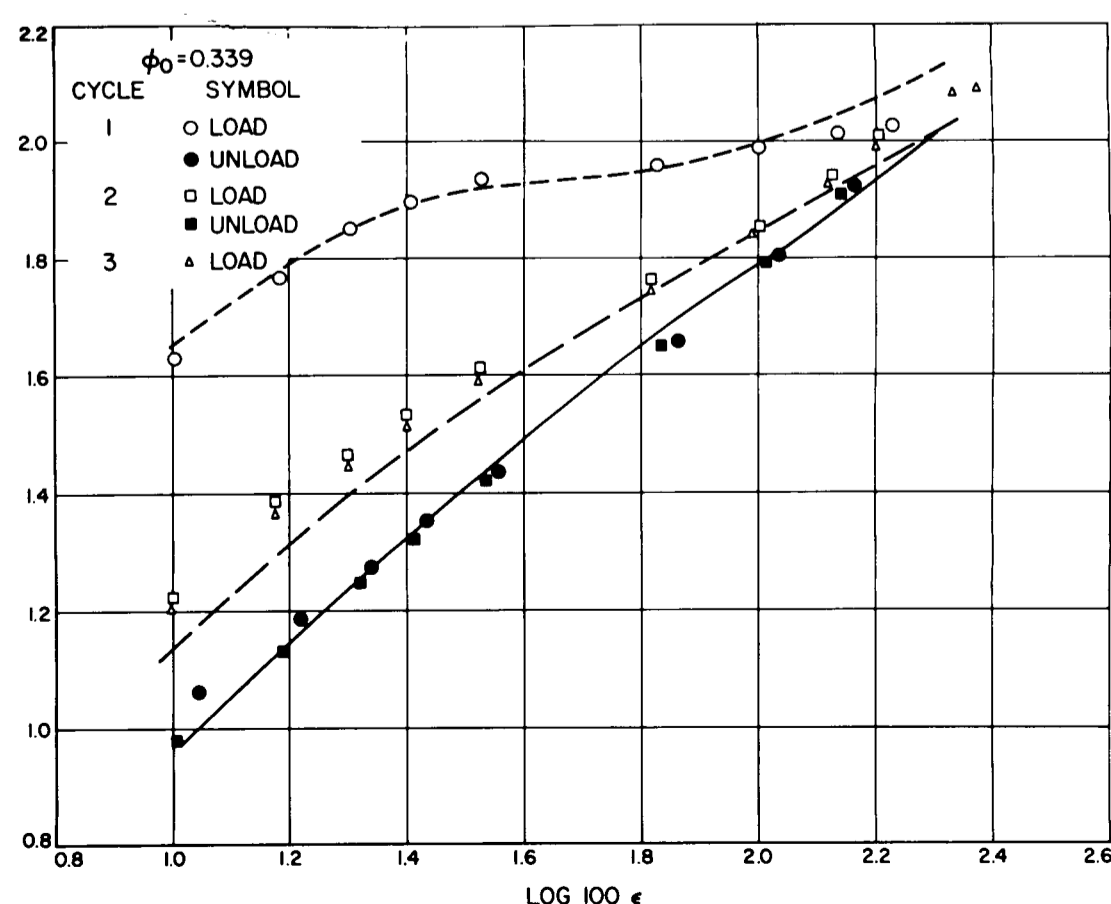
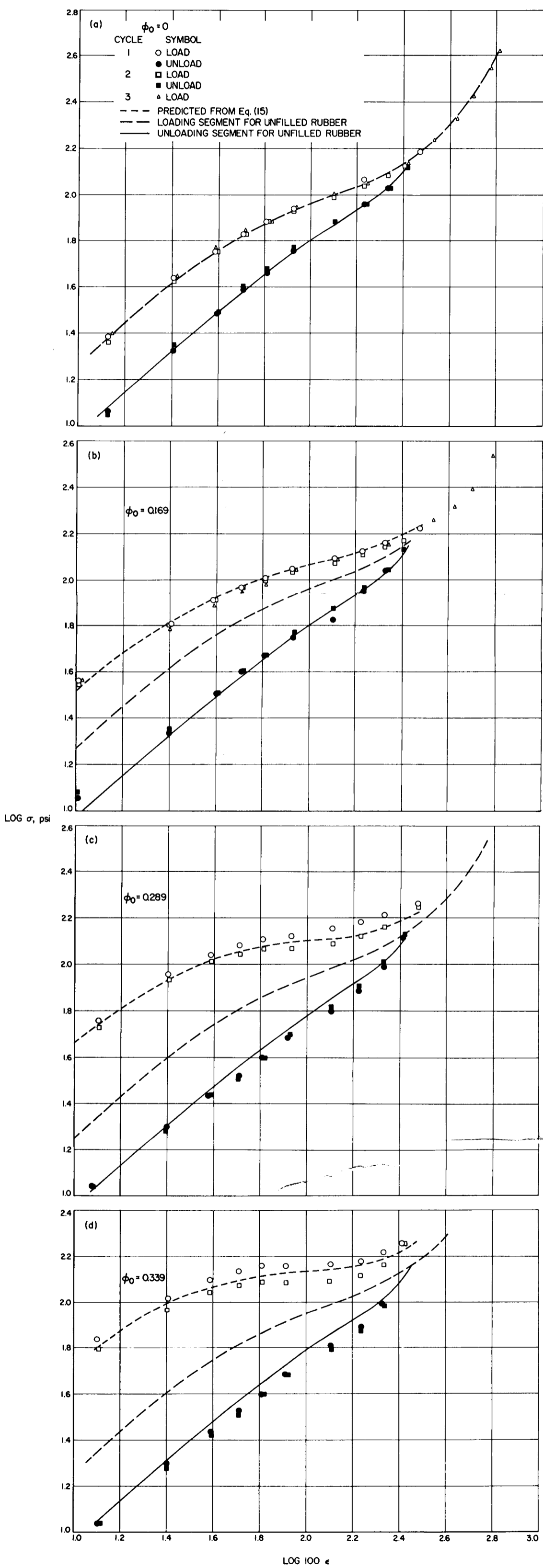


Fig. 5. Stress-strain response of selected SBR-glass bead composites to cyclic loading-unloading tests conducted at 25°C at a strain rate of 0.85 per minute



106-3

106-2

Fig. 6. Stress-strain response of selected SBR-glass bead composites to cyclic loading-unloading tests conducted at  $-20^{\circ}\text{C}$  at a strain rate of 0.85 per minute

Eq. (15) provides a plausible explanation for the behavior observed in cyclic loading experiments as exemplified in Figs. 5 and 6. For example, if a composite is strained to  $\epsilon^*$  and then allowed to retract, the subsequent stress-strain response for strains less than  $\epsilon^*$  will be given by Eq. (15) with  $\epsilon$  replaced by  $\epsilon^*$ . That is, the fraction of filler surface dewetted when the specimen was strained to  $\epsilon^*$  will no longer be active in subsequent stress-strain responses for  $\epsilon$  less than  $\epsilon^*$ , provided that no time is allowed for rewetting to occur. Hence, the composite will appear to have softened. If, on the other hand, sufficient time is allowed for the binder to rewet the particle surface, the initial stress-strain response will be reproduced.

Other, more complete, stress softening effects have been studied and will appear in future reports.

**B. A Preliminary Report on the Suitability of Thermoplastic Rubbers as a Binder for Composite Solid Propellant, B. G. Moser, H. Broyles, and R. F. Landel**

**1. Introduction**

The present investigation of thermoplastic rubbers as a candidate for composite solid propellant was undertaken for two reasons. First, the mechanical properties of the rubbers are quite good, and if the rubbers prove to be suitable for a binder, the resultant propellants might have improved mechanical properties. The second and more important reason is related to previous work at JPL (SPS 37-35, Vol. IV) which showed that the burning rate of composite solid propellant is in some measure controlled by the degree of dispersion of the oxidizer particles in the binder matrix. It is postulated that the thermoplastic rubbers will result in rather poor dispersion because there are no polar groups on the polymer chains to cause them to act as surface active agents. Such poor dispersion should result in higher burning rates than those found with propellants made from castable and curable rubbers, which necessarily contain reactive and, hence polar, end groups. It is further suggested that this poor dispersion and attendant higher burning rate can be enhanced by plasticising the rubber system with inert (non-surface-active) mineral oil, because it was shown in SPS 37-35, Vol. IV, that the burning rate of propellant slurries made with USP mineral oil and ammonium perchlorate reached values in excess of 60 in./sec.

The lack of castability of the thermoplastic rubber is the chief drawback in a solid propellant application and

was initially one of the largest obstacles in sample preparation. A new freeze-drying technique has been employed to overcome this obstacle.

**2. Sample Preparation**

Three types of thermoplastic rubber were used in these experiments. All were manufactured by Shell Chemical Company and are designated as Kraton 101, Kraton 102, and Thermolastic 125. All are styrene-butadiene elastomers which can be molded by conventional plastic forming techniques, such as injection molding and extrusion, rather than curing in a hot mold under pressure as with normal elastomers. Sheet specimens can also be formed by evaporation of solvent from solutions of the rubber. Either benzene or toluene make excellent solvents.

Milling of the oxidizer particles into the binder with a conventional rubber mill has been tried elsewhere with poor results.<sup>1</sup> Therefore, an attempt was made to prepare specimens by dissolving the rubber, making a suspension with the AP, and then evaporating the solvent. Benzene was used to make 20% solutions of the three rubbers mentioned above. The viscosities of the solutions were not sufficiently high to prevent sedimentation of the oxidizer before evaporation could take place. The literature accompanying the rubber suggested the use of Cab-O-Sil to jell the system to prevent this sedimentation. This was tried but was not at all satisfactory. Fig. 7 is a picture of a biscuit of propellant jelled with Cab-O-Sil to prevent sedimentation during evaporation (Thermolastic 125 with 80% by weight 30/70 bimodal ammonium perchlorate). As can be clearly noted in the picture, the shrinkage upon evaporation resulted in severe cracking of the grain.

<sup>1</sup>Blatz, P. J., California Institute of Technology, private communication.



**Fig. 7. Grain cracking in thermoplastic propellant based on Thermolastic 125 and ammonium perchlorate prepared by evaporating from benzene**

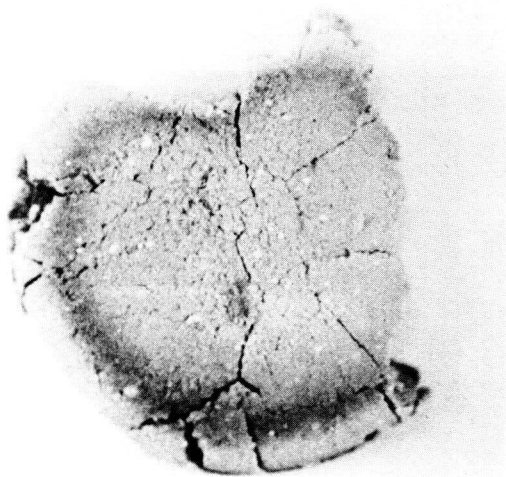


**Fig. 8. Grain cracking in thermoplastic propellant based on Thermolastic 125 pregelled with Cab-O-Sil and evaporated from benzene**

Fig. 8 is the same 80% bimodal ammonium perchlorate-Thermolastic 125 material without Cab-O-Sil. The slurry was stirred by hand during evaporation until it had become sufficiently viscous to prevent sedimentation when the stirring was stopped and the evaporation completed. This system also cracked rather badly, although not so badly as the Cab-O-Sil loaded system.

Freeze-drying was ultimately utilized to prepare specimens without sedimentation. The technique was to load the benzene-rubber solution with oxidizer and mix thoroughly by kneading in a plastic bag. The bag was then dropped into a shallow tray of liquid nitrogen and retrieved as soon as it was solidly frozen. The bag was quickly cut away, and the frozen suspension was placed in a vacuum chamber. The benzene sublimates, and its heat of vaporization is such that the suspension remains frozen without external cooling.

After the freeze-drying was complete, the dry and porous mass of propellant was molded in a Teflon-coated mold at  $\sim 175^{\circ}\text{C}$  and  $\sim 150$  psi. For future tests the temperature will be dropped and the pressure increased. This molding technique resulted in a flat sheet of propellant of uniform thickness ( $\sim 0.10$  in.) and a bulk density which indicates that there is essentially no porosity. Sheets were prepared from both the gum rubber and from the rubber plasticized with 25% USP mineral oil (this resulted in a mixture of 80% oxidizer, 15% thermoplastic rubber, and 5% mineral oil). The oil was mixed in during the initial slurring and, of course, has

a very low vapor pressure, especially when the rubber is frozen. Consequently, there was no oil loss during freeze-drying. There was no attempt to carefully work out the stoichiometry of oxidation at this time, and the propellant was simply loaded to 80% with bimodal oxidizer, 30%  $12\mu$ , and 70%  $100\mu$ .

Tensile specimens were rings approximately  $1\frac{1}{2}$  in. in diameter with a wall thickness of approximately 0.125 in., although they varied slightly from specimen to specimen. Burning rate strands were cut with a razor blade, the sharp corners sanded, the ignition and clock wires placed in the usual manner, and the strands burned in the Crawford Bomb in  $\text{N}_2$  at 1000 psi. From the soot accumulated in the burning rate bomb (especially in the mineral oil systems) and from a general knowledge of the chemistry of the systems, they are probably under-oxidized by 5 to 10%. Further tests will be made at 85% oxidation, if possible.

### 3. Results

The tensile test results of the ring specimens are shown in Table 1. Nominal maximum stress based on the initial cross-sectional area and the maximum strain based on the internal circumference of the ring are given. It turned out for all the systems studied that the maximum stress and strain are also stress and strain at break. There is no maximum in the curve as there is for a typical propellant. We see this illustrated in the representative stress-strain curves illustrated in Fig. 9, which is discussed below.

The values given in Table 1 are an average taken from at least three specimens and were run at a strain rate of 0.42 per minute and at room temperature. In the case of the Thermolastic 125 and the Kraton 102, the addition of mineral oil resulted in a decreased strain at break. In the case of the Kraton 101, the opposite effect is observed—there is an increase in the strain from 291 to 368%. However, there is no similar anomaly in the stress at break; it is decreased by roughly half in all the systems. Obviously the above strain anomaly must be accounted for by the chemistry of the systems and will be studied further.

Fig. 9 shows representative stress-strain curves of Thermolastic 125 propellant, both plasticized and un-plasticized. As can be seen, the general shape of the curves remains more or less unchanged by the addition of mineral oil, there is simply a vertical shift downward, which corresponds exactly to that expected according to

**Table 1. Maximum stress and strain of thermoplastic propellants (80 % ammonium perchlorate) at room temperature and a strain rate of 0.42 per min**

Propellant	Stress at break $\sigma_m$ , psi (avg)	Strain at break $\epsilon_b$ , % (avg)
Kraton 101	97	291
Kraton 101 plasticized with 5% USP mineral oil	67	368
Kraton 102	86	358
Kraton 102 plasticized with 5% USP mineral oil	38	54
Thermolastic 125	64	347
Thermolastic 125 plasticized with 5% USP mineral oil	29	103

**Table 2. Burning rates of thermoplastic propellants, unplasticized and plasticized, with 5 % mineral oil at 1000 psi**

Binder	Burning rate, in./sec
Kraton 101	0.495
Kraton 101 plasticized with 5% mineral oil	0.463
Kraton 102	0.574
Kraton 102 plasticized with 5% USP mineral oil	0.490
Thermolastic 125	0.476
Thermolastic 125 plasticized with 5% mineral oil	0.960
Kraton 101 with 0.15% asolectin	0.642

underoxidation. This would result in a decreased burning rate in spite of poorer dispersion tending to increase the rate. This view is supported by an experiment designed to improve the dispersion. Asolectin, a phospholipid surface-active agent, was used to treat the oxidizer particles (0.15 wt % asolectin) in another batch of Kraton 101. As can be seen in Table 2, this resulted in an even more striking decrease than in the mineral oil plasticized system. In this case, of course, the decrease is exclusively due to better dispersion (SPS 37-35, Vol. IV).

In contrast to the Kratons, Thermolastic 125 exhibited the predicted increase in burning rate with the addition of mineral oil. This increase is quite striking and amounts to around 100%. Work is continuing to separate the combustion from the dispersion effects when adding the mineral oil and/or the asolectin for all the above systems. Data is also being collected at various pressures in order to assess the effects on the pressure exponent and will be reported later.

**N67-15722**

**(C) Voltage Endurance Tests for Closed-Cell Foams, J. Moacanin and J. Farrar**

**1. Introduction**

Previously, results of short-time electrical breakdown tests have provided information on the high-voltage strength of plastic foams of varying densities (SPS 37-39, Vol. IV). However, in considering foams for encapsulant applications, it is the prediction of long-time behavior which is of interest. Endurance tests at a constant voltage simulating operating conditions are impractical for the purpose of screening materials, because they are inherently time consuming. Moreover, a statistical analysis based on relatively few test results is difficult because

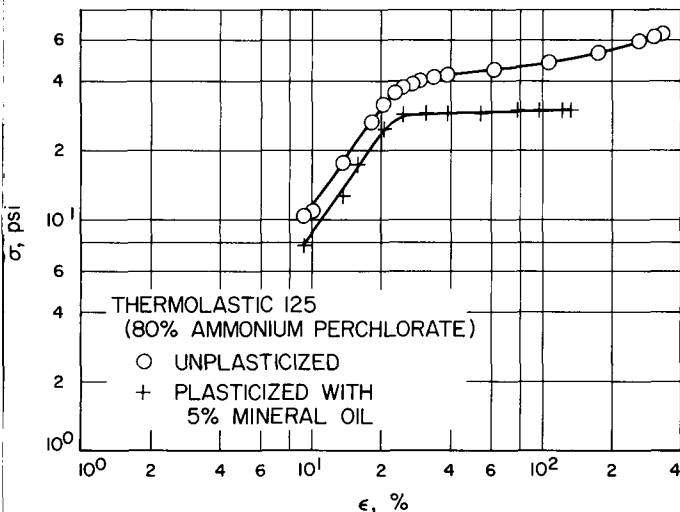


**Fig. 9. Representative stress-strain curves typifying plasticized and unplasticized thermoplastic propellant based on Thermolastic 125**

the decrease in rubber content. The stress-strain curve of the unfilled rubbers has not yet been determined and will be reported for comparative purposes later.

The burning rates of the thermoplastic rubbers were presumed to be the most interesting data, and indeed this turned out to be the case. Table 2 is the tabulation of the rates measured thus far. In the case of the Kraton 101 and 102, contrary to our prediction, addition of mineral oil to the system resulted in a decreased burning rate. One explanation which could be advanced at this time is that the addition of mineral oil results in even greater

of the following peculiarities common to this type of test: Occasionally, specimens fail while the voltage is being brought to the test value, whereas others may last several orders of magnitude longer than the mean lifetime.

It turns out, however, that considerable information can be obtained by carrying out tests applying the voltage at varying rates, since the rate dependency of failure time is directly related to the failure time at constant voltage. These problems have been considered extensively in studies of electrical insulators (Ref. 19).

The purpose of this report is to present the general relationships for correlating failure times to rate, and to discuss parameters characterizing foams which are expected to be critical in determining their high-voltage endurance.

## 2. Theory

The basic assumption underlying the following development (Ref. 19) is that the extent of damage imparted to a dielectric during a time interval is only a function of voltage  $V$ , which is in excess of the discharge inception voltage,  $V_i$ . In addition, the total damage necessary to result in failure is a constant  $k$ , for a given material. These physical conditions can be expressed as

$$\int_0^\tau 1(V - V_i) f(V - V_i) d\xi = k \quad (1)$$

where  $\tau$  is failure time. The unit step function is:

$$1(V - V_i) = \begin{cases} 0 & \text{for } V < V_i \\ 1 & \text{for } V \geq V_i \end{cases}$$

For any time  $t < \tau$ , the extent of damage  $D$ , is given by:

$$\int_0^t 1(V - V_i) f(V - V_i) d\xi = kD \quad (2)$$

Clearly for  $V < V_i$  no damage will occur.

For constant voltage,  $f(V_c - V_i)$  is a constant and Eq. (1) becomes:

$$1(V_c - V_i) f(V_c - V_i) \tau_c = k \quad (3)$$

where  $\tau_c$  is the failure time at constant voltage. For solid insulators or dielectric specimens with flaws or manufactured voids, several investigators have found the following relation to hold for test results at constant voltage (Refs. 19-24):

$$(V_c - V_i)^n \tau_c = k \quad (4)$$

In view of the above assumption, the same functional form should hold for variable voltage.

For voltage applied at a constant rate  $\lambda$ , the voltage  $V$ , will be given by:

$$V = \lambda t \quad (5)$$

Hence, substituting in Eq. (2) we have:

$$\int_0^t 1(\lambda\xi - V_i) (\lambda\xi - V_i)^n d\xi = kD \quad (6)$$

Carrying out the integration between 0 and the failure time for rate  $\lambda$ ,  $\tau_\lambda$ , the result is

$$k = \frac{1}{\lambda(n+1)} (\lambda, \tau_\lambda - V_i)^{n+1} \quad (7)$$

Thus, from test results at several rates  $\lambda$ , one can determine  $k$  and the exponent  $n$ . If the initial assumptions are correct, then the same parameters are applicable for constant voltage; and hence, the lifetime of the dielectric can be predicted for any condition.

For solid dielectrics, it is pretty well accepted that discharges are initiated preferentially in gases in voids or flaws. Inasmuch as a closed-cell foam is a medium with a dispersion of voids, it is reasonable to expect that discharge will initiate in the gas phase within a void. From previous studies, it has been established that  $V_i$  for a single void in a solid dielectric medium is proportional to the breakdown strength for the gas  $E$ , entrapped in the void.  $E$  depends on the nature of the gas, pressure, and on the size and geometry of the void. To a lesser extent,  $V_i$  will depend on the permittivity of the surrounding dielectric. In general,  $E$  increases with decreasing void size.

In view of these considerations, it appears plausible that in a foam, discharges will initiate preferentially in larger voids, i.e., where  $V_i$  is lowest. Once a cell wall is ruptured, the void increases in size,  $V_i$  will further decrease, and by an avalanche effect failure will rapidly ensue. On the basis of this reasoning, we propose to pursue this investigation by assuming that to predict initiation of failure we have to consider only what occurs in a single void. It is of interest to note that an equation similar to Eq. (4) was derived by applying extreme value statistics to the problem of dielectric breakdown (Ref. 23). Since the distribution of large voids in a foam should also follow the same statistics, this observation suggests a reasonable approach to a theoretical analysis of the problem at hand. The validity of this hypothesis is to be ascertained by extensive experimentation.

### 3. Experiments and Results

Closed cell polyurethane foams (Eccofoam SH, Emerson and Cummings Co.) with nominal bulk densities of 2, 4, 6, 8, 10 lb/ft<sup>3</sup> were purchased in the form of sheets 12- × 25- × 1-in. thick. These were cut into test specimens 4 × 4 in. The test was carried out with a Dielectric Strength Tester, Model PDA-1 from Industrial Instruments Co., using 60-cycle mode. The higher rates could be set on the tester, however, the very low rates were increased in steps of approximately 5-min intervals over a 2- to 3-hr period.

Fig. 10 shows a plot of  $\log (V - V_i)$  versus  $\log \lambda$  for the 2 lb/ft<sup>3</sup> foam where  $\lambda$  is the rate of voltage application. The value of 10 kv used for this plot is that for  $V_i$  in CO<sub>2</sub> at atmospheric pressure and a 1-in. gap (SPS 37-39, Vol. IV). This should be the lower limit to  $V_i$ , in view of the small dimension of the cell in a foam. The upper limit must be below 19 kv, the lowest breakdown voltage observed for the slow rates. The plot in Fig. 10 along with Eq. (7) yields  $n = 9$  and  $k = 3.2 \times 10^6$ . Using these values for the parameters along with Eq. (4), we

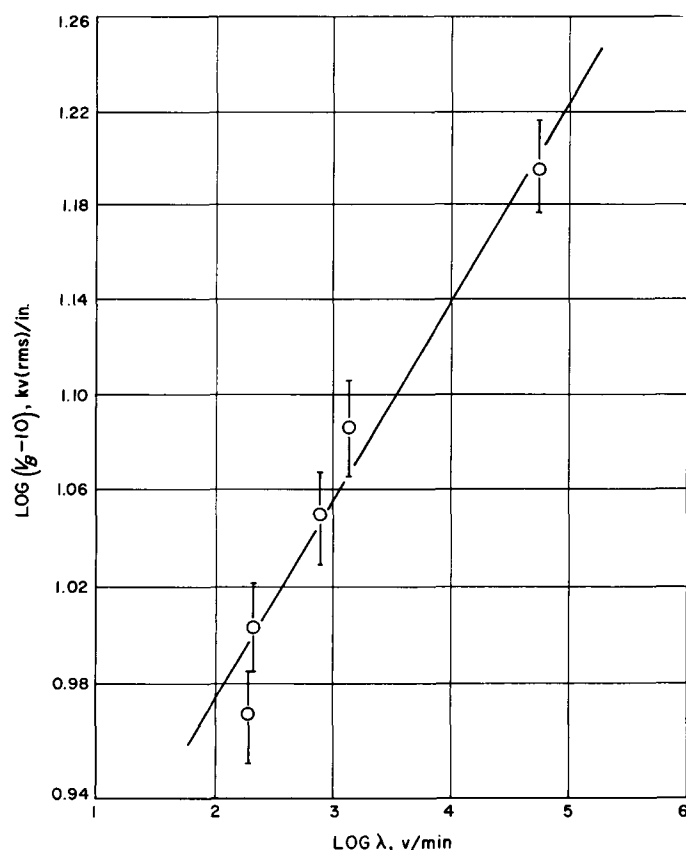


Fig. 10. Dependence of electrical strength on rate of voltage application

estimate a failure time at constant voltage of about 5 days for  $V - V_i = 2$ , and about 2,000 days for  $V - V_i = 1$ . These calculations demonstrate dramatically the necessity of determining  $V_i$  accurately in order to make reasonable estimates of failure time.

The main emphasis for the next phase of this investigation will be to study rate effects in foams of fixed density, but varying cell size. Also, experimental determinations of  $V_i$  will be attempted.

In conclusion, it should be added that the interrelation between constant and variable voltage tests may break down for materials in which significant chemical degradation is induced by means of corona. The latter would be more significant in constant voltage, long-time tests.

### **N67-15723** Studies of Sterilizable Elastomers, E. F. Cuddihy and J. Moacanin

The development of a sterilizable polybutadiene elastomer has been previously reported (SPS 37-40, Vol. IV). This elastomer is prepared from a commercial liquid carboxyl-terminated polybutadiene (HC-434) and a commercially available aziridine curative HX-740, made by the Minnesota Mining and Mfg. Co. (Fig. 11). This elastomer can only be cured at extremely high temperatures (ca. 146°C) at which the material also undergoes sterilization. Other elastomers usually require a low-temperature cure (ca. 70–100°C) and degrade rapidly upon exposure to high temperatures.

Studies on the chemistry of the reaction between carboxyl and aziridine groups have been reported by S. H. Kalfayan and B. A. Campbell (SPS 37-39) who

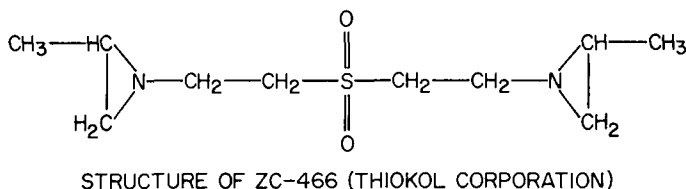
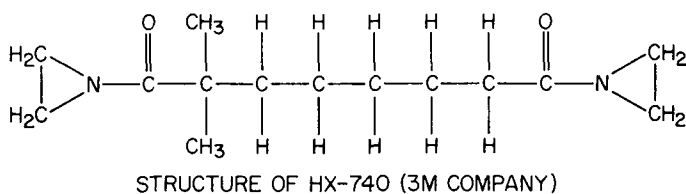


Fig. 11. Structures of aziridine curatives

found that at elevated temperatures in an acid medium aziridine groups can self-react. This suggests that cure with an excess of aziridine could lead to the formation of a polyaziridine in addition to the polybutadiene network.

A sensitive method for determining the network structure of an elastomer is the measurement of the temperature dependence of the dynamic mechanical properties. For this study, a torsion pendulum constructed according to a previously reported design (Ref. 25) was employed to obtain the damping constant for the elastomer over the temperature range from  $-196^{\circ}\text{C}$  to room temperature. Two sets of elastomers were prepared, one containing stoichiometric amounts of HC-434 and HX-740 (1.00 imine/carboxyl ratio) and the other containing a 10% excess of the diaziridine HX-740 (1.10 imine/carboxyl ratio). One-half of each elastomer was cured in air at  $146^{\circ}\text{C}$ , and the other half first degassed at room temperature and then cured at  $146^{\circ}\text{C}$  under a high vacuum (ca.  $10^{-4}$  mmHg). Test specimens were removed from the curing ovens after 8, 16, 64, 96, and 136 hr, the latter three corresponding to three consecutive sterilization cycles at  $146^{\circ}\text{C}$  following an initial cure period of 16 hr. For comparison, elastomers were also prepared from HC-434 and another diaziridine ZC-466, made by the Thiokol Corp. (Fig. 11). In contrast to the HX-740 system, the ZC-466 elastomers cure almost completely in one hour at  $146^{\circ}\text{C}$ , thus reducing significantly the exposure time to high temperatures and the opportunity for self-polymerization of the aziridines.

The damping constant curves for the two diaziridine curatives, HX-740 and ZC-466, are shown in Fig. 12. ZC-466 is a low molecular weight compound which exhibits a damping curve characteristic of an amorphous material. Its principal transition temperature is  $-57^{\circ}\text{C}$ , and it exhibits three additional minor transitions at  $-66$ ,  $-122$ , and  $-170^{\circ}\text{C}$ . HX-740 is a crystalline substance (melting point about  $-10^{\circ}\text{C}$ ) and its principal transition, which occurs at  $-78^{\circ}\text{C}$ , is therefore correspondingly less intense than that observed for the ZC-466. HX-740 exhibits two additional minor transitions at  $-130$  and  $-170^{\circ}\text{C}$ . The  $-122^{\circ}\text{C}$  (ZC-466) and the  $-130^{\circ}\text{C}$  (HX-740) transitions are similar to that in polyethylene (Ref. 26). The ZC-466 probably requires a higher temperature for the transition because of the greater steric hindrance of the centrally located sulfur group. The common transition of  $-170^{\circ}\text{C}$  can be attributed to the aziridine group, the only group common to the two curatives. The  $-66^{\circ}\text{C}$  transition observed for ZC-466 may result from the sulfur group.

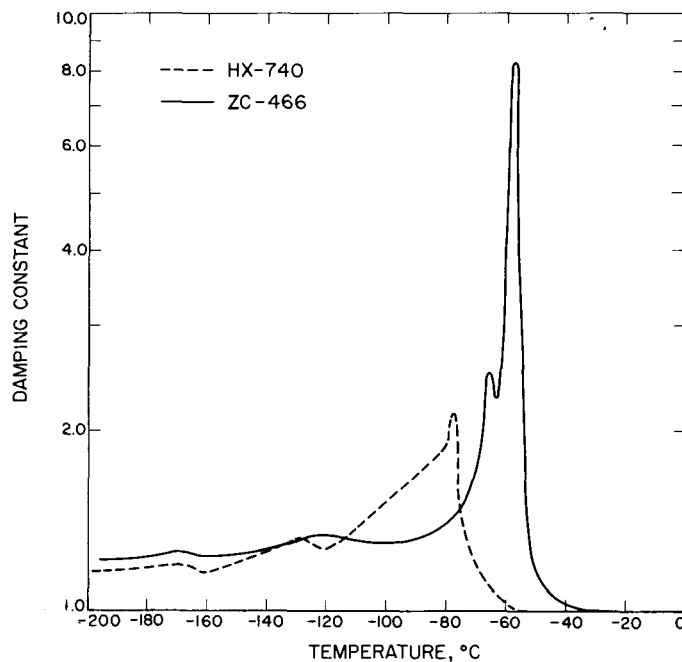


Fig. 12. Damping constant versus temperature for diaziridine curatives

The damping constant curves for the vacuum-cured HX-740/HC-434 elastomer containing the 10% excess of aziridine are shown as a function of increasing cure time in Fig. 13. Also included and shown as curve A is the damping constant curve for HC-434. This liquid prepolymer has its principal transition located at  $-84^{\circ}\text{C}$  and further exhibits a broad minor transition having a peak near  $-140^{\circ}\text{C}$ .

Curves B, C, D, and E were obtained after a cure of 8, 16, 64, and 96 hr with excess HX-740 at  $146^{\circ}\text{C}$ . The principal transition for curve B is located at  $-79^{\circ}\text{C}$ , an increase of  $5^{\circ}$  from  $-84^{\circ}\text{C}$ . This shift is undoubtedly caused by the increase in the molecular weight of the polymer. Curve B also exhibits a transition at  $-170^{\circ}\text{C}$ , indicating the presence of unreacted aziridine rings. With increasing reaction time, all the aziridine is reacted as indicated by the absence of the  $-170^{\circ}\text{C}$  transition in curves C, D, and E.

After 16 hr of cure at  $146^{\circ}\text{C}$ , two transitions appear at  $-70^{\circ}$  and  $-79^{\circ}\text{C}$ . With increasing cure time, the intensity of the  $-79^{\circ}\text{C}$  transition gradually diminishes and disappears, while the location of the  $-70^{\circ}\text{C}$  transition shifts slightly down temperature. Finally, after 96 hr only a single transition remains at  $-72^{\circ}\text{C}$ . For the same elastomer cured in air, a single transition was observed resembling curve E and which also slowly shifted with increasing cure time from  $-70$  to  $-72^{\circ}\text{C}$ . For both the

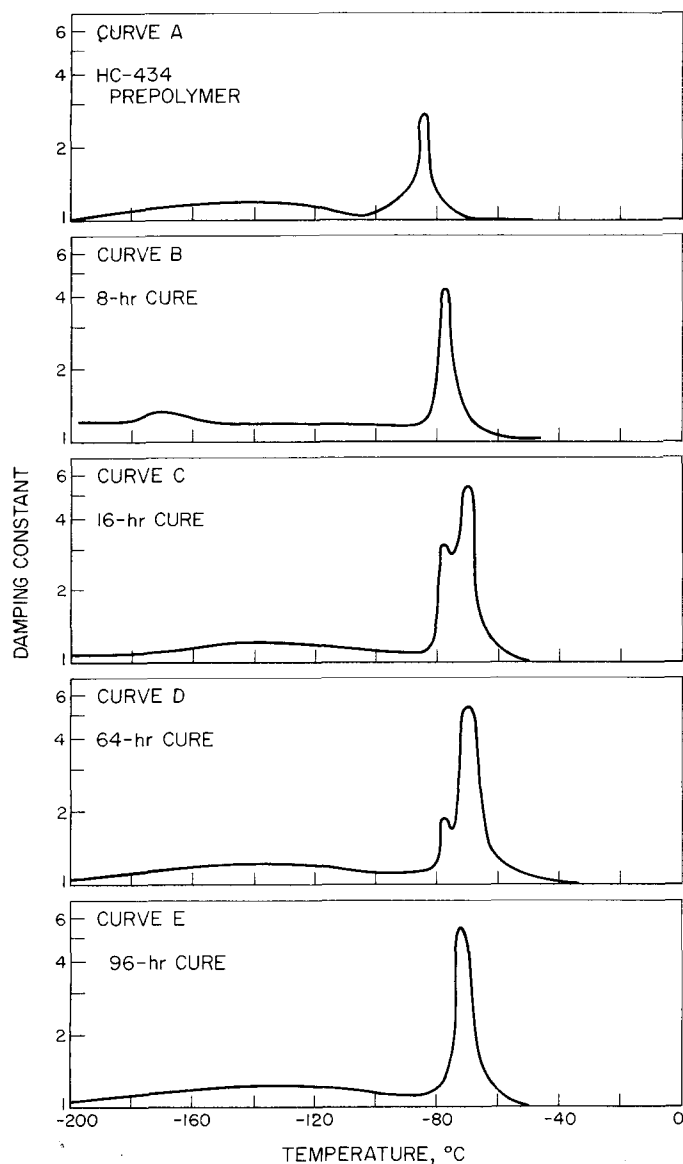


Fig. 13. Damping constant versus temperature for various cure times at 146°C for a vacuum-cured elastomer of HC-434 and HX-740 (1.10 imine/carboxyl ratio)

air- and vacuum-cured elastomers which contained the stoichiometric amount of HX-740, the damping curves resembled curve E and had a single transition at  $-78^{\circ}\text{C}$ . Thus the double transition was observed only for the vacuum-cured elastomer which contained the excess aziridine.

The foregoing results can be explained by assuming that a block-copolymer of polybutadiene and polyaziridine is found in the vacuum-cured system. Chemical evidence for the ability of HX-740 to homopolymerize

was presented previously (SPS 37-39, Vol. IV). The  $-70$  to  $-72^{\circ}\text{C}$  transition corresponds to the polybutadiene while the  $-79^{\circ}\text{C}$  corresponds to the polyaziridine. The disappearance of the  $-79^{\circ}\text{C}$  transition indicates that at  $146^{\circ}\text{C}$  the polyaziridine undergoes degradation and after 96 hr, the vacuum-cured elastomer becomes identical to the air-cured elastomer.

The reason for the apparent failure of the excess aziridine to polymerize in the air-cured elastomer is not clear but it can be speculated that oxygen may serve to tie up the slightly positive nitrogen, and thus prevent ring opening of the aziridine group which is necessary for polymerization.

Elastomers prepared with ZC-466 did not exhibit a double transition, but in this case cure of the elastomer proceeds so rapidly (ca. 1 hr) at  $146^{\circ}\text{C}$  that not enough time is allowed for polymerization. Further, Kalfayan and Campbell found that ZC-466 polymerizes much slower than HX-740.

This study concentrated on the changes of the dynamic-mechanical properties of a sterilizable polybutadiene elastomer during exposure to a temperature of  $146^{\circ}\text{C}$ . With an excess of aziridine curative and in the absence of air, a block copolymer of polybutadiene and a polyaziridine was formed. Continuous exposure to  $146^{\circ}\text{C}$  resulted in the eventual degradation of the polyaziridine and the retention of only the polybutadiene. Elastomers cured in air failed to form block copolymers, indicating that some constituent of the atmosphere, probably oxygen, inhibited the polymerization of the excess aziridine.

**N67-15724**

**E. The Reactions of Carboxyl-Terminated Prepolymers with Polyepoxides and Polyaziridines, S. H. Kalfayan and B. A. Campbell**

**1. Introduction**

In previous reports (Refs. 27 and 28) it was indicated that, after cure, carboxyl-ending prepolymers with unsaturated hydrocarbon backbones aged on thermal exposure, resulting in hardening and embrittlement at the exposed surface. No such behavior was shown by carboxyl and amino-ending poly(propylene oxides). Aging, therefore, was ascribed to the oxidation and/or crosslinking at the sites of unsaturation.

Saturating the hydrocarbon backbone of the carboxyl-ending poly(butadienes) by hydrogenation gives waxy products, which are inconvenient to use as propellant

binders. Recently, (Ref. 29) a carboxyl-terminated liquid saturated aliphatic hydrocarbon polymer with a molecular weight of about 2000 has been available. This, at the present, is being evaluated at JPL.

The unsaturation in the cured polymer can also be reduced by blending the poly(butadiene)-backboned prepolymers with appropriate liquid, saturated polybasic acids. Studies using this approach are reported presently, as well as other related problems.

## 2. Experimental

Materials used, which were not described previously are: (1) Empol 1010, made by Emery Industries, de-

**Table 3. Curing of Empol 1010 with epoxides and aziridines**

Curing agent	Gel time		Shore A hardness	
	At 100°C	At 150°C	48 hr at 100°C	22 hr at 150°C
DER 732	>48 hr	>7 hr <22 hr	Fluid	Soft <sup>b</sup>
DER 736	>48 hr	>7 hr <22 hr	Fluid	31(31) <sup>a</sup>
Epon 828	>48 hr	>7 hr <22 hr	Soft <sup>b</sup>	50(50) <sup>a</sup>
ERL 0510	>48 hr	1 ½ hr	Partial gelling	51(51) <sup>a</sup>
Shell X 801	>48 hr	3 ½ hr	Soft <sup>b</sup>	66(66) <sup>a</sup>
HX-740	22 min	<22 hr	Soft, tacky <sup>b</sup>	
ZC-466	16 min	<16 min	20	
MAPO	½ hr	<7 min	31	54

<sup>a</sup> Values in parenthesis indicate hardnesses of the interior of the sample.  
<sup>b</sup> Not measurable on the Shore A scale.

scribed as a C<sub>36</sub> dibasic acid, containing 3.5% C<sub>54</sub> tri-basic acid (neutralization equivalent 285 and iodine value less than 15, indicating a low amount of unsaturation); (2) DER 732 and DER 736, made by Dow Chemical Co., which are epoxy-terminated poly (alkylene oxides) with epoxide values of approximately 320 and 190, respectively.

Reactants were always used in stoichiometric amounts.

## 3. Results

*a. Reaction of Empol 1010 with epoxides and aziridines.* Empol 1010, by itself, cured slowly with the epoxides of this study. Gelation did not take place at 100°C after two days. At 150°C, however, mixtures gelled faster with the triepoxides ERL 0510 and Shell X-801 than with the diepoxides DER 732, DER 736, and Epon 828 (Table 3). The surface and interior hardnesses of the products were the same. However, mechanical properties obtained were poor.

Gelation with aziridines was relatively fast at 100°C. Products obtained with the two diaziridines, HX-740 and ZC 466, were soft and tacky, or became so after exposure to higher temperatures. MAPO gave a product which would melt below 150°C.

*b. Reaction of a blend of Telagen CT and Empol 1010 with epoxides and aziridines.* Table 4 gives some of the results obtained with a blend made in the ratio of 1 equivalent of Telagen CT and 3 equivalents of Empol 1010 (750 g Telagen CT and 213 g Empol 1010). The noteworthy result here is that the products obtained by curing the blend with ERL 0510 and MAPO did not

**Table 4. Reaction of a blend of Telagen CT and Empol 1010 with epoxides and aziridines**

Curing agent	Catalyst	Gel time at 100°C	Shore A hardness			
			After 24 hr at 100°C	After 48 hr at 100°C	After 48 hr at 100°C plus 18 hr at 150°C	After thermal cycling
Epoxides						
ERL 0510	None	2 ¼ hr	32(32) <sup>a</sup>	37(37) <sup>a</sup>	—	41(41) <sup>a</sup>
Shell X-801	None	>28 hr <40 hr	Fluid	Soft, tacky	70(35) <sup>a</sup>	—
Shell X-801	(CH <sub>3</sub> ) <sub>2</sub> NCl	>3 hr <18 hr	Soft, tacky	Soft, tacky	62(36) <sup>a</sup>	—
Aziridines						
HX-740		19 min	Soft <sup>b</sup>	Soft <sup>b</sup>	10(8) <sup>a</sup>	—
MAPO		43 min	15(14) <sup>a</sup>	—	—	37(35) <sup>a</sup>

<sup>a</sup> Values in parenthesis indicate hardnesses of the interior of the sample.  
<sup>b</sup> Not measurable on the Shore A scale.

show much difference between surface and interior hardnesses noticeable with products obtained with Telagen CT and the same curing agents after they, too, were thermally cycled in nitrogen at 145°C. With Shell X 801 and HX 740, the blend gave poorly cured products after 48 hr at 100°C. These products were not thermally cycled. They would cure after exposure to 150°C in air to relatively hard products.

**c. Reaction of carboxyl-ending poly(butadienes) with epoxide-aziridine mixtures.** Results of reaction between three carboxyl-ending poly(butadienes) and two epoxide-aziridine mixtures, namely, Epon 828-HX-740 and Shell X-801-HX-740 are given in Table 5. For purposes of comparison, results previously obtained (Refs. 27, 28) with HX-740, Epon 828, and Shell Z 801 alone are also included in the same table.

Gel times and rates of cure with the epoxide-aziridine mixtures were intermediate between the epoxide and the aziridine cures. No synergistic effects were noticed.

**N67-15725**

**F. Sterilization Studies,** S. H. Kalfayan, B. A. Campbell, and J. K. Hoffman

The Polymer Research Section supports other elements of the Laboratory in problems related to polymer science and technology. One of the most active areas is that of sterilizable polymers and sterilization effects. Recently (SPS 37-40, Vol. IV) an automatic ethylene oxide decontamination system was described. In this past bimonthly period, a study of the effects of thermal sterilization on the REL Tape Recorder was completed. The results are reported more fully in the present SPS as part of the report by the Telecommunications Division.

**Table 5. Reaction of carboxyl-ending poly(butadienes) with epoxide-aziridine mixtures**

Prepolymer	Curing agent	Gel time at 100°C	Shore A hardness			
			After 24 hr at 100°C	After 48 hr at 100°C	After 48 hr at 100°C plus 18 hr at 150°C	After thermal cycling
Telagen CT	Epon 828	>48 hr	Fluid	Fluid	12	53(35) <sup>a</sup>
	HX-740	22 min	4	4	—	15(5) <sup>a</sup>
	Epon 828 + HX-740	20 hr	Soft <sup>b</sup>	Soft <sup>b</sup>	45(41) <sup>a</sup>	—
	Shell X-801	>48 hr	Fluid	Fluid	23	56(37) <sup>a</sup>
	Shell X-801 + HX-740	20 hr	Soft, tacky <sup>b</sup>	Soft <sup>b</sup>	39(12) <sup>a</sup>	—
Butarez CTL	Epon 828	>48 hr	Fluid	Soft	60(37) <sup>a</sup>	71(49) <sup>a</sup>
	HX-740	12 min	21	23	—	34(21) <sup>a</sup>
	Epon 828 + HX-740	>5 hr <20 hr	Soft <sup>b</sup>	18(13) <sup>a</sup>	50(45) <sup>a</sup>	—
	Shell X-801	>6 hr <21 hr	Soft <sup>b</sup>	3	—	64(46) <sup>a</sup>
	Shell X-801 + HX-740	>5 hr <20 hr	Soft <sup>b</sup>	18(13) <sup>a</sup>	60(45) <sup>a</sup>	—
HC 434	Epon 828	>48 hr	Fluid	Fluid	34(29) <sup>a</sup>	57(43) <sup>a</sup>
	HX-740	29 min	5	5	—	15(15) <sup>a</sup>
	Epon 828 + HX-740	20 hr	Soft <sup>b</sup>	Soft <sup>b</sup>	64(36) <sup>a</sup>	—
	Shell X-801	>48 hr	Fluid	Fluid	37	52(45) <sup>a</sup>
	Shell X-801 + HX-740	20 hr	Soft, tacky <sup>b</sup>	Soft <sup>b</sup>	28(24) <sup>a</sup>	—

<sup>a</sup>Values in parentheses indicate hardnesses of the interior of the sample.  
<sup>b</sup>Not measurable on the Shore A scale.

## References

1. Fedors, R. F., and Landel, R. F., "Mechanical Behavior of Styrene-Butadiene Rubber Filled With Glass Beads," *SPS 37-32*, Vol. IV, p. 120, Jet Propulsion Laboratory, Pasadena, California, August 31, 1965.
2. Fedors, R. F., and Landel, R. F., "Degree of Crosslinking of SBR-Glass Bead Composites," *SPS 37-40*, Vol. IV, pp. 80-83, Jet Propulsion Laboratory, Pasadena, California, August 31, 1966.
3. Fedors, R. F., and Landel, R. F., "Mechanical Behavior of Styrene-Butadiene Rubber Filled With Glass Beads," *SPS 37-35*, Vol. IV, p. 93, Jet Propulsion Laboratory, Pasadena, California, October 31, 1965.
4. Fedors, R. F., and Landel, R. F., "The Reduced Failure Envelope for Filled Elastomers, II." Paper presented at the 40th National Colloid Symposium, American Chemical Society, Madison, Wisconsin, June 1966.
5. Guth, E., and Gold, O., *Physical Review*, Vol. 53, p. 322, 1938.
6. Payne, A. R., *Journal of Applied Polymer Science*, Vol. 6, p. 57, 1962.
7. Roscoe, R., *British Journal of Applied Physics*, Vol. 3, p. 267, 1952.
8. Eilers, H., *Kolloid-Zeitschrift*, Vol. 97, p. 313, 1941.
9. Landel, R. F., Moser, B. G., and Bauman, A. J., Proceedings of the Fourth International Congress on Rheology, Brown University, Providence, Rhode Island, E. H. Lee, Ed., Interscience Publishers, New York, N. Y., Vol. 2, p. 663, 1965.
10. Landel, R. F., "The Dynamic Mechanical Properties of a Model Filled System: Polyisobutylene-Glass Beads II. Long Time Studies," paper presented before the Division of High Polymer Physics, American Physical Society, Boston, March 1959.
11. Landel, R. F., and Smith, T. L., *ARS Journal*, Vol. 31, p. 599, 1961.
12. Jones, H. C., and Yiengst, H. A., *Ind. Eng. Chem.*, Vol. 32, p. 1354, 1940.
13. Bueche, F., *Journal of Applied Polymer Science*, Vol. 4, p. 107, 1960.
14. Fedors, R. F., and Landel, R. F., *Transactions of the Society of Rheology*, Vol. 9, p. 195, 1965.
15. Smith, T. L., and Stedry, P. J., *Journal of Applied Physics*, Vol. 31, p. 1892, 1960.
16. Eilers, H., *Kolloid-Zeitschrift*, Vol. 97, p. 313, 1941.
17. Roscoe, R., *British Journal of Applied Physics*, Vol. 3, p. 267, 1952.
18. Moser, B. G., Wiech, R. E., Jr., Landel, R. F., "A Theory of the Sedimentation Volume for Monodisperse Spheres," paper presented at the 4th National Colloid Symposium, Madison, Wisconsin, June 1966.
19. Starr, W., and Endicott, H., *AIEE Transactions on Power Apparatus and Systems*, Vol. 80, Pt. III, p. 515, August 1961.

## References (contd)

20. Moses, G. L., *AIEE Transactions*, Vol. 70, Pt. 1, pp. 763-769, 1951.
21. Montsinger, V. M., *AIEE Transactions*, Vol. 54, pp. 1300-1301, December 1935.
22. Parkman, N., Report L/T 364, The British Electrical and Allied Industries Research Association, Leatherhead, England, 1957.
23. Epstein, B., *Journal of Applied Physics*, Vol. 19, p. 544, 1948.
24. Parkman, N., "The Electrical Properties of High Polymers," in *Physics of Plastics*, P. D. Ritchie, Ed., D. Von Nostrand Co., Inc., Princeton, N. J., p. 285, 1965.
25. Koppelman, V. J., *Kolloid-Zeitschrift*, Vol. 144, p. 12, 1955.
26. Schatzki, T. F., *Polymer Preprints*, American Chemical Society, Vol. 6, No. 2, p. 646, September 1965.
27. Kalfayan, S. H., and Campbell, B. A., "The Reaction of Carboxyl- and Amino-Terminated Prepolymers with Polyaziridines," *SPS 37-39*, Vol. IV, pp. 103-106, June 30, 1966.
28. Kalfayan, S. H., and Campbell, B. A., "The Reaction of Carboxyl- and Amino-Terminated Prepolymers with Polyepoxides," *SPS 37-40*, Vol. IV, August 31, 1966.
29. General Tire and Rubber Company, Product Bulletin, "Telagen S," June 1, 1966.

## XI. Research and Advanced Concepts

### PROPULSION DIVISION

N67-15726

**(A) 50-kw(e) Thermionic Reactor Study, J. P. Davis**

Previous mission studies at JPL have shown that a nuclear-powered electric-propulsion system in the specific weight range of 40 to 60 lb/kw(e) with a  $10^4$ -hr (full-power) operating life, delivering 50 kw(e) to an ion engine, is a system of high potential interest for unmanned spacecraft application. However, the possibility of achieving this specific weight range at this relatively low power level in a realistic design is rather uncertain. A study was therefore initiated to analyze the potential of nuclear systems to attain this goal; in particular, it was desired to compare the various nuclear-cycle concepts as applied to this power range with regard to reactor, shielding, conversion machinery, radiator, and power conditioning requirements. Initial calculations have been made for a "minimum"-power thermionic reactor utilizing NaK-78 coolant and operating at temperatures permitting the use of stainless steel for the fluid circuit. The reactor characteristics are given in Table 1.

The system chosen for this study is one which, with the exception of the reactor, is well within the realm of current technology. The choice of NaK coolant and a stainless-steel system results in a very minor weight

penalty, as compared to that for a higher-temperature lithium refractory metal system in this power range. The advantages of the lower-temperature system from development, cost, testing, and space startup considerations are apparent. In both systems, the thermionic reactor represents the major unknown with respect to performance and reliability.

In the thermionic reactor, several barriers exist between fission products in the fuel and the fluid system. For the system to be contaminated, fission products must pass through the diode emitter, interelectrode gap, collector, insulator, and fluid containment tube. Considering the much smaller relative danger of system contamination (as compared to that for a non-thermionic reactor), the desirability of incorporating a separate radiator loop for this reason alone is not apparent. At power levels of 50 to 100 kw(e), the radiator armor requirement is sufficiently small that trade-off against a separate loop and a redundant radiator system does not yield any weight advantage. In fact, in the externally fueled arrangement, it is possible to segregate the coolant to groups of diodes and maintain independent fluid paths to the radiator without using a separate loop. Therefore, this study was based on a single-loop concept.

**Table 1. Design characteristics of a 50-kw(e) thermionic reactor**

Item	Description
Configuration	Externally fueled full-core-length diode
Equivalent core	11-in. right circular cylinder plus 2.5-in. BeO reflector
Fuel	UC-ZrC (90-10), 10 <sup>4</sup> -hr burnup: 0.3 atom %
Fuel volume fraction in core	0.60
Coolant	NaK-78
Core temperature rise, °F	
Inlet	1200
Outlet	1350
System material of construction	Stainless steel
Thermal power, kw (t)	620
Gross electric power, kw (e)	
No failures	81
20% diode failures	65
Efficiency, %	
Conditioning loss	15
Auxiliaries	10
Net electric	8
Diode performance	
Total number of diodes	160
Number of working diodes	128
Single diode net output	
w	507
v	0.635
amp	800
Single diode area, cm <sup>2</sup>	82.6
Average power density, w/cm <sup>2</sup>	6.1

Major weight elements were taken as: reactor, shield (10<sup>13</sup> nvt, 10<sup>9</sup> rad), power conditioning, armored radiator [ $P(0) = 0.95$ ], plumbing and controls, ion engine, and structure. The weight breakdown is shown in Fig. 1. Since these are relatively crude estimates, the associated uncertainty is perhaps a factor of 1.5. Weights were calculated in each category at 50 kw(e) and were scaled to higher powers by the following approximate relationships, where  $W$  = weight, lb, and  $P$  = power, kw(e):

$$W_{\text{reactor}} = 1000 \left[ 0.5 + 0.5 \left( \frac{P}{50} \right)^{0.33} \right]^3 \quad (1)$$

$$W_{\text{shield}} = 1000 \left[ 0.5 + 0.5 \left( \frac{P}{50} \right)^{0.33} \right]^2 \quad (2)$$

$$W_{\text{radiator}} = 75 \left[ \frac{P}{50} + \left( \frac{P}{50} \right)^{1.33} \right] \quad (3)$$

$$W_{\text{conditioning}} = 250 \left( \frac{P}{50} \right) \quad (4)$$

$$W_{\text{plumbing and controls}} = 100 \left( 1 + \frac{P}{50} \right) \quad (5)$$

$$W_{\text{engine}} = 150 \left( 1 + \frac{P}{50} \right) \quad (6)$$

$$W_{\text{structure}} = 0.1 \Sigma W \quad (7)$$

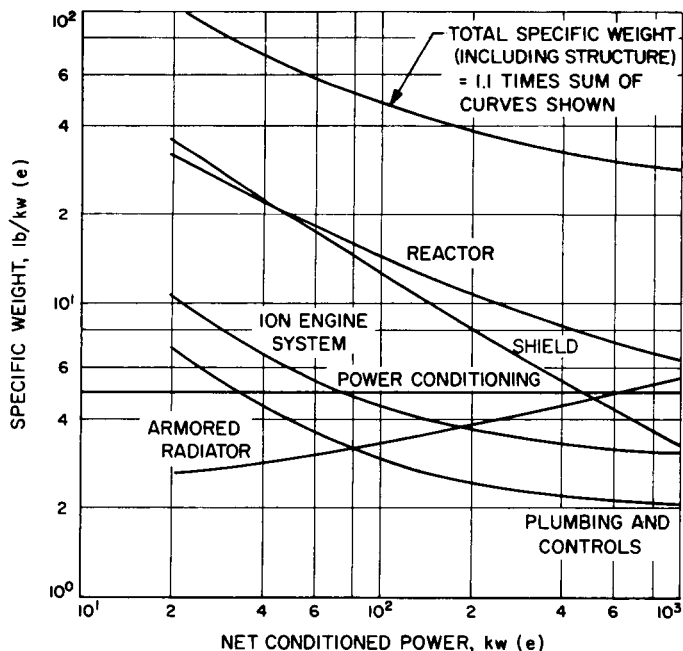


**Fig. 1. Specific weight vs net conditioned power for a thermionic-reactor/electrostatic-thruster NaK-cooled stainless-steel system**

**N67-15727**

**B. Thermionic Reactor Stability Studies,**  
H. Gronroos and J. Shapiro

**1. Introduction**

The thermionic reactor stability studies reported in earlier SPS articles (SPS 37-35, Vol. IV, pp. 180-188; and SPS 37-39, Vol. IV, pp. 121-125) are continuing. Briefly restated, the aim is to delineate the problems of the stability and control of a space in-pile thermionic reactor power plant. The stability problems are related to positive doppler coefficients associated with the highly enriched fuel needed in small fast reactors. Control may be a problem because the thermionic system has a narrow acceptable region of operation.

Concurrent with direct simulation of system models on an analog computer, analytical work has been carried out to interpret the measured responses and to derive stability criteria. Fig. 2 shows schematically the simulated "lumped" parameter model. Nonlinear elements are introduced by the neutron kinetics, the diode current-voltage ( $I$ - $V$ ) characteristics, and the energy transfer in the inter-electrode gap. The model was developed for normal operating conditions, and is not suited for investigation of open or short circuits, startup, large reactivity insertions, or other hazardous conditions.

The analytical complexities associated with the nonlinear elements have prompted investigations of the effect of linearization of the system equations. Individual nonlinear elements in the analog simulation were linearized, and the changes in the responses were observed. Some results of these studies and those from linear stability analysis shall be discussed herein.

Considerable effort has also been spent on development of power-plant design data and on doppler coefficient evaluations. If the results of the most recent doppler coefficient measurements<sup>1</sup> are valid, it may be necessary

<sup>1</sup>Brehm, R. L., *Estimates of Doppler Coefficients for In-Pile Thermionic Reactor Materials*, Technical Report, Jet Propulsion Laboratory, Pasadena, California (to be published).

that measures be taken to guarantee stability for small reactors [i.e.,  $\lesssim 200$  kw(e)]. The necessary high enrichment in the fissile isotope may lead to a positive doppler coefficient for the fuel. If this is not properly accounted for in the design, the negative contributions from the other reactor core components may not provide adequate stabilization. Even in those cases where stability exists, the magnitude of the reactor excursions to small perturbations in load or reactivity must be examined and control parameters established to ensure satisfactory performance.

## 2. Analog Simulation Results

To check out the analog simulation setup, many runs were made using only one or two temperature coefficients of reactivity. It is a simple process to predict the new equilibrium temperature for that region which has been assigned a temperature coefficient if: (1) no other regions give feedback effects to the neutron kinetics, and (2) the size of the reactivity or electric load perturbation is prescribed. Similarly, the largest value of

positive temperature coefficient in one region  
negative temperature coefficient in one region

for zero-frequency asymptotic stability may be uniquely determined from a simple expression given in the next

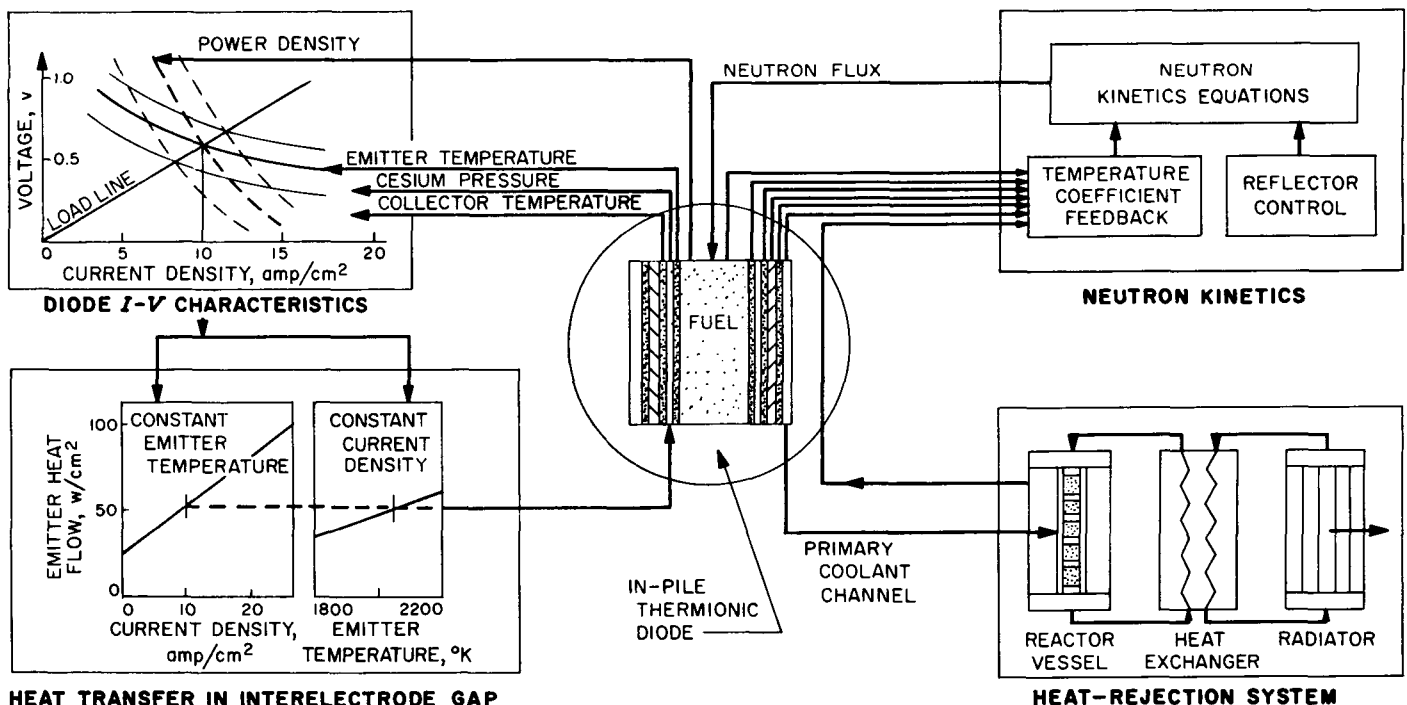


Fig. 2. Simulated thermionic reactor power-plant model

section. Analog simulation results using the general non-linear model for electric load perturbation runs are reported in Ref. 1. Here, the responses to reactivity perturbations and temperature coefficient stability ratios will be considered.

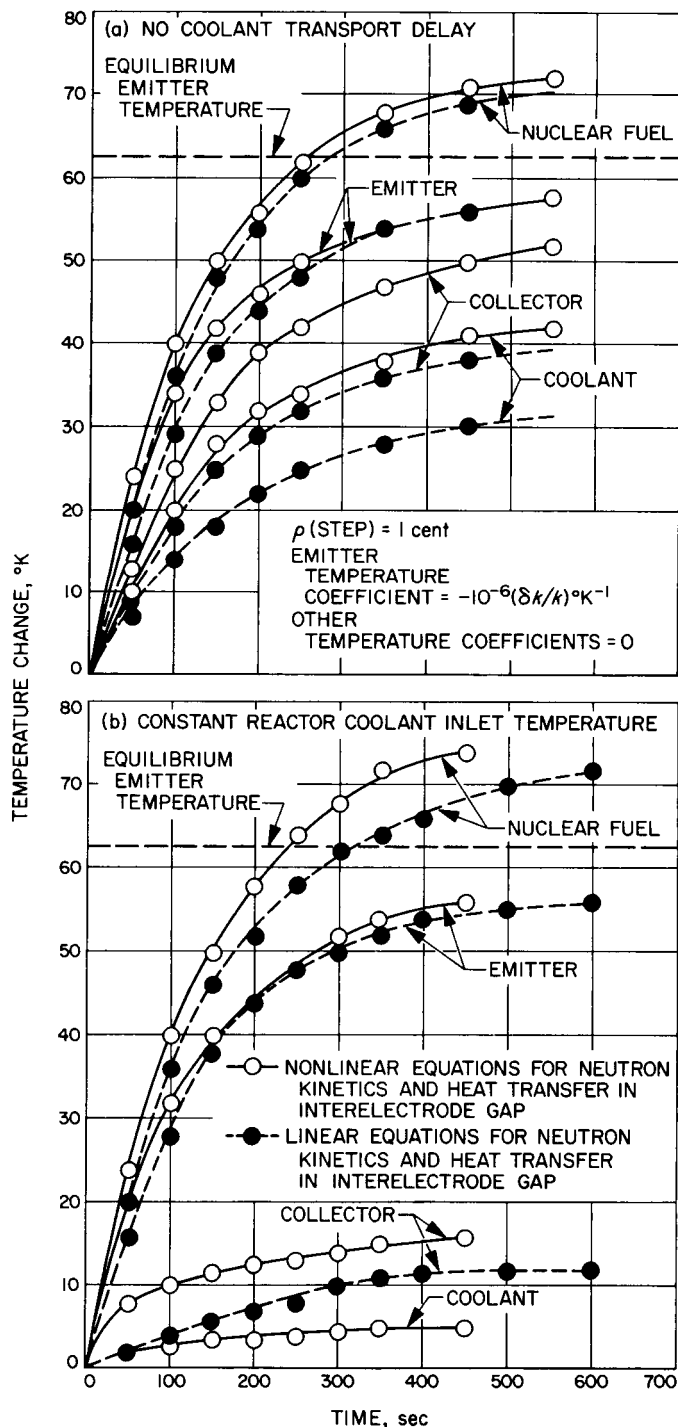
**a. Comparisons between linear and non-linear models.**

Fig. 3(a) shows the response to a +1-cent step reactivity insertion when there is no coolant transport delay. The emitter temperature coefficient is  $-10^{-6}(\delta k/k)^{\circ}\text{K}^{-1}$ , which implies that the new equilibrium lies at a 65°K higher emitter temperature. (All other coefficients are taken as zero.) The broken lines indicate the trajectories for linearized neutron kinetics and heat transfer in the interelectrode gap equations. As can be seen in Fig. 3(a), the emitter and fuel temperatures follow closely the same trajectories for the linear and nonlinear models. This is as expected, since the linearization at such a small reactivity change does not introduce a significant error. The spread is within the accuracy and reproducibility of individual analog computer runs. There is marked difference, however, between the collector temperature trajectories for the linear and nonlinear models. This correspondingly introduces a change between the coolant temperature trajectories. Obviously, a first-order Taylor expansion of the equation for the energy transfer in the interelectrode gap poorly approximates the true relationship. This poor approximation exists, despite the small relative temperature change: 1300°K at time zero to about 1350°K at the new equilibrium. In Fig. 3(b), the reactor coolant inlet temperature is held constant (infinite coolant time delay); otherwise, the conditions are the same as those in Fig. 3(a). As expected, the change in collector temperature is smaller, and the general effect of linearization remains the same.

The diode current-voltage characteristic equations were not linearized in any run. However, when operating on a constant load line, the current versus emitter temperature plots were closely linear for relatively large ( $\sim \pm 150^{\circ}\text{K}$ ) perturbations. Thus, it was not considered necessary to mathematically linearize this equation in the simulation setup.

**b. Zero-frequency stability.** From the preceding, one would deduce that linearization of the systems equations would give conservative estimates of stability criteria. However, the value of

$$\frac{\text{positive nuclear fuel temperature coefficient}}{\text{negative emitter temperature coefficient}}$$



**Fig. 3. Temperature response to a step reactivity change for linear and nonlinear thermionic reactor power-plant models**

for zero-frequency stability should be approximately the same for the linear and nonlinear version due to the close agreement of the two models for those regions. Also, since the nuclear fuel and the emitter respond most

promptly, the emitter carries more stabilizing importance if all negative temperature coefficients are approximately equal for the non-fuel regions. Thus, a model that considers only the fuel and emitter in the determination of the necessary temperature coefficient ratio for zero-frequency stability is most conservative and, in fact, may be too restrictive. If, in addition, the collector region is considered, the use of the linear equations would correspond to the use of a safety margin, even if the coolant transport delay is taken to be zero. Additional margin is

**Table 2. Comparison of the analog-computer-measured and calculated values of the largest stability ratio for zero-frequency asymptotic stability**

Region	Positive nuclear fuel temperature coefficient Negative structure region temperature coefficient			
	Measured		Calculated	
	No coolant transport time delay			Infinite delay
	Nonlinear	Linear	Linear	Linear
Emitter	$0.84 \pm 0.08$	$0.80 \pm 0.08$	0.865	0.718
Collector	$0.62 \pm 0.06$	$0.64 \pm 0.06$	0.629	0.339
Insulator	$0.52 \pm 0.06$	$0.60 \pm 0.06$	0.566	0.212
Cladding	$0.50 \pm 0.05$	$0.60 \pm 0.05$	0.511	0.099
Coolant	$0.46 \pm 0.05$	$0.50 \pm 0.05$	0.500	0.075

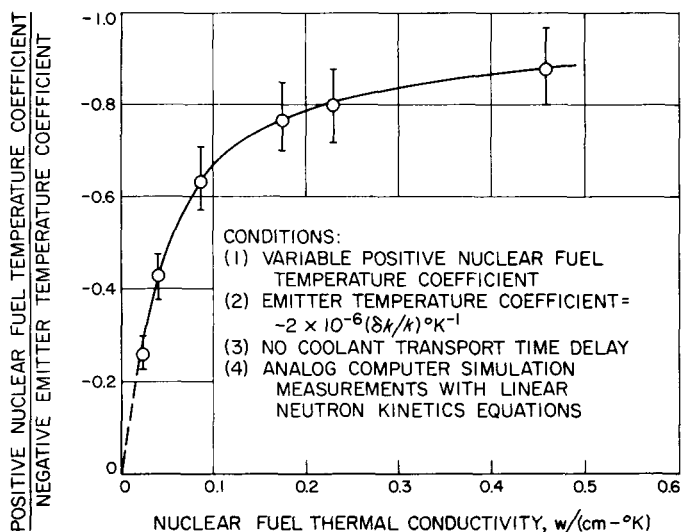


**Fig. 4. Nuclear fuel thermal conductivity vs (positive nuclear fuel temperature coefficient)/(negative emitter temperature coefficient) for zero-frequency asymptotic stability**

introduced by considering the constant reactor coolant inlet temperature case.

The above conjectures were tested on an analog computer in a qualitative way. The zero-frequency "perturbation" was approximated by selecting a stabilizing region, giving it a plausible negative temperature coefficient, and by momentarily introducing a reactivity perturbation. The positive temperature coefficient of the fuel was varied to bracket the narrowest band outside which the perturbation leads either to a return to the initial conditions or to no return. Table 2 compares the results of the machine estimates and the results from a linear analysis. The correlation is well within the estimated error bands. For Fig. 4, the effect of variation of the fuel thermal conductivity is shown. Obviously, the highest possible thermal conductivity would be beneficial.

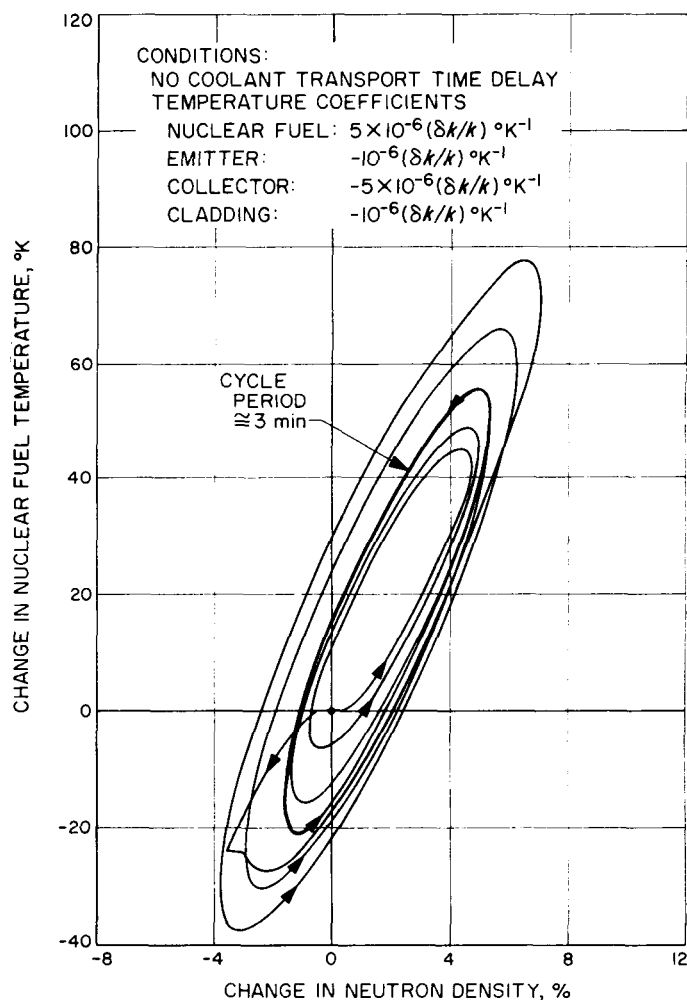


**Fig. 5. Phase-plane trajectories of limit-cycle conditions for a thermionic-reactor power-plant model**

**c. Oscillatory instabilities.** It was found that, in general, an unstable condition led to an exponentially increasing or decreasing trajectory. Also, no coolant transport delay resonances have been found thus far. Oscillatory modes of operation could be induced only by postulating an unrealistically high positive fuel temperature coefficient and corresponding large negative temperature coefficients in the collector, insulator, cladding, or coolant regions. Furthermore, the heat-rejection system must be coupled to the reactor core for this to occur. Fig. 5 illustrates a limit cycle solution applicable to the completely non-linear simulation model. It was obtained by superimposing two analog computer runs, one with no perturbation introduced and the other with a momentarily inserted reactivity step, such that an initial amplitude larger than the limit cycles was given. If the systems equations are linearized, the oscillatory region still exists, but the oscillations are the center type; i.e., their amplitude depends on the initial perturbation.

**d. Phase and gain versus frequency response.** Some phase and gain versus frequency responses have been measured by coupling a Solartron transfer function analyzer to the simulation setup. Although this work is

still in process, some results are available. Fig. 6 illustrates the responses obtained for a model with emitter temperature feedback to the linearized neutron kinetics equations. The transfer function looks very much like those of other reactor power plants with small temperature coefficients. The identification of the various portions of the curve with system components has not yet been carried out.

### 3. Linearized Stability Analysis

Although the linearized equations are of little value in describing transients, they are useful for describing stability criteria. Previously (SPS 37-39, Vol. IV, pp. 124, 125), a general formulation was developed for examining linear stability, which would indicate that unstable conditions could appear at any frequency. To keep this problem of manageable size, it was necessary to reduce the number of regions in the diode from six to two.

Prior to performing the final numerical work on that model, it was observed both on the simulator and analytically for some simplified models that, for the magnitudes of temperature coefficients conceivable in this system,

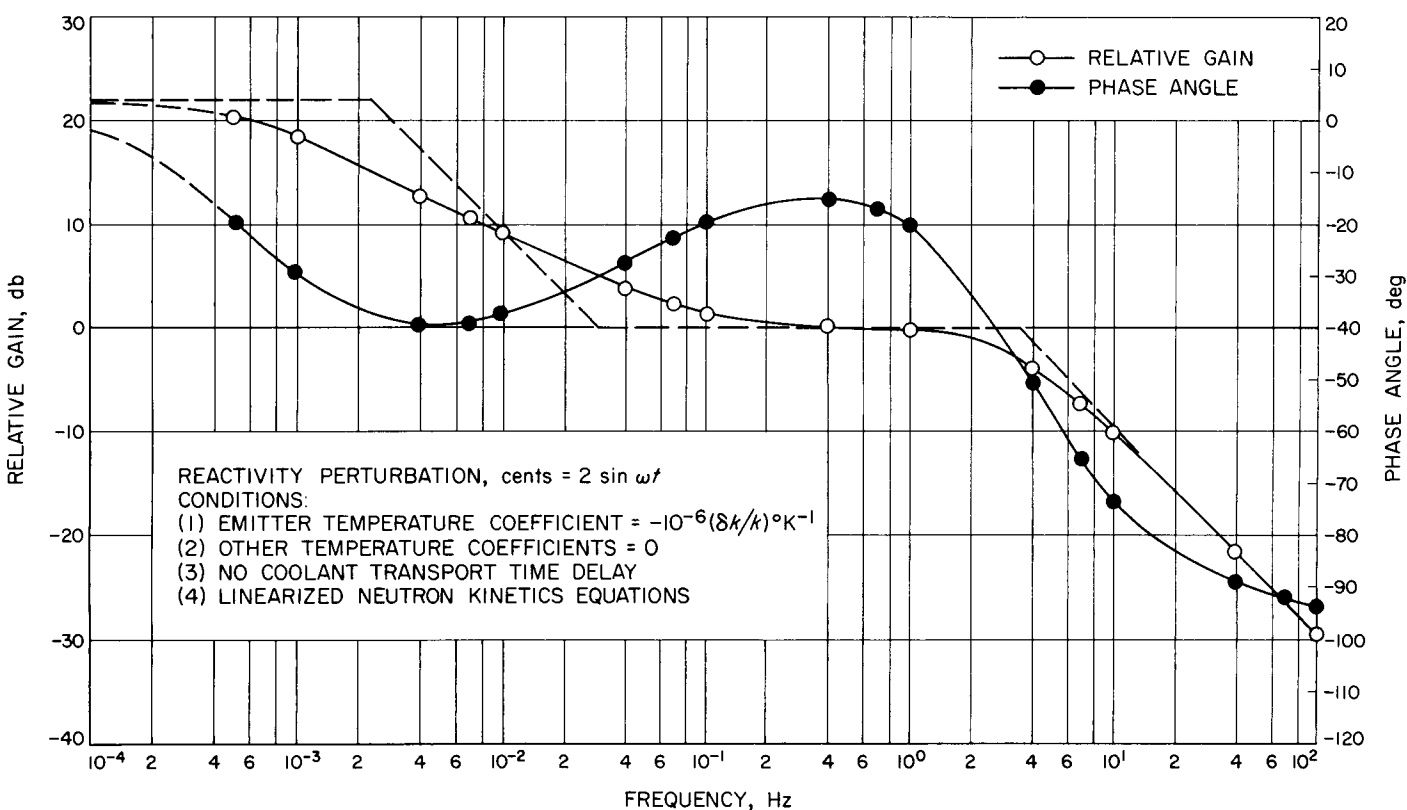


Fig. 6. Measured gain and phase angle vs frequency for a thermionic-reactor power-plant model

the zero-frequency instability was the only type observed. Only by increasing the size of the coefficients by factors of 10 or more (Fig. 5) could oscillatory instabilities be induced.

The zero-frequency (i.e., equilibrium) instability conditions have therefore been examined analytically for the model shown in Fig. 2 and described in SPS 37-35. The technique is simply to set the time derivatives to zero; differentiate the coupled systems equations with respect to the power  $n$ ; and require for stability that

$$\sum_i \alpha_i \frac{dT_i}{dn} < 0,$$

where  $\alpha$  is the temperature coefficient of reactivity,  $T$  is the temperature, and the subscript  $i$  refers to a structural region in the reactor core. This method is equivalent to the application of the Routh-Hurwitz criterion to the zeroth-order coefficients only. The results of this analysis are shown in Table 3 for the same parameters as those used in the analog simulation.

These results show that, while the ratio  $dT_1/dT_2$  is not strongly affected by simplification in the model, the ratio  $dT_1/dT_3$  is very sensitive to such changes. Since region 3 (the collector) may have a large negative doppler coefficient if it is made of niobium, it is obviously desirable to use a model which treats the temperature variations properly.

It also appears that, for  $\alpha_1$  positive, the ratio of  $-\alpha_1/\alpha_2$  does not have to be much less than unity to achieve stability, even if  $\alpha_3 \rightarrow \alpha_6$  were neglected. This is the case, provided the fuel thermal conductivity is reasonably high (Fig. 4).

The parameters used in this calculation were based on the assumption of perfect thermal contact between the

fuel and the emitter. The effect of a poorer thermal contact is easily examined in the linearized equilibrium model. If it is assumed that a certain  $\Delta T$ , °K, exists across the interface and that the fuel region temperature is then  $T_1 + \Delta T$ , the factor  $\Delta T/10$  may be added to the  $dT_1/dn$  in Table 3. It follows that even a drop of 100°K across the fuel-emitter interface will not affect the stability ratio requirements by more than 10 to 15%. It should be noted that a contact resistance temperature drop does not have the same quantitative effect as a lower fuel conductivity.

N67-15728

### C. Liquid Magnetohydrodynamic (MHD) Power Conversion, D. Elliott, D. Cerini, and L. Hays

The long lifetimes required of electric-propulsion powerplants make cycles without rotating components attractive. Such a cycle under investigation at JPL is the liquid-metal MHD system shown schematically in Fig. 14, p. 63, of SPS 37-40, Vol. IV. In this cycle, a fluid such as cesium circulates in the vapor loop and causes a liquid metal such as lithium to circulate through an MHD generator in the liquid loop. The cesium leaves the radiator (or radiator-loop condenser) as condensate, flows through an electromagnetic pump and regenerative heat exchanger to the nozzle, separates from the lithium in the separator, and returns to the radiator through the regenerative heat exchanger. The lithium leaves the separator at high velocity (typically 500 ft/sec), decelerates through the production of electric power on the MHD generator, and leaves the generator with sufficient velocity (typically 300 ft/sec) to return through a diffuser to the reactor (or reactor-loop heat exchanger) where it is reheated.

#### 1. AC Generator

As described in SPS 37-40, Vol. IV, pp. 63-72, the second AC generator delivered 185 w of power at 900 cps before a short occurred between phases. Additional tests

Table 3. Equilibrium variation of temperature with power ( $dT_i/dn$ ) using the linearized model (all units are relative)

Region	Model				
	No coolant delay	Infinite coolant delay	$\frac{dT_1}{dn} = 0$	$\frac{dT_2}{dn} = 0$	$\frac{dT_3}{dn} = 0$
1 (Fuel)	93.4	63.1	61.1	57.1	53.4
2 (Emitter)	83.9	53.6	51.6	47.6	43.9
3 (Collector)	43.0	9.9	7.7	3.7	0
4 (Insulator)	39.0	6.1	4.0	0	—
5 (Cladding)	35.6	2.9	0.7	—	—
6 (Coolant)	34.8	2.2	0	—	—

Table 4. Compatibility of insulators and candidate separator materials with lithium at 2000°F

Specimen (number tested)	Compatibility <sup>a</sup> at 2000°F for indicated duration, hr					Comments		
	100	500	1000	2000	3000			
Static tests								
BeO (2)		Poor				Partially dissolved; lithium penetration into ceramic		
CaO (2)		Poor / Unusable				Poor / Unusable	Disintegration of 500-hr sample and significant mass transfer for 1000-hr sample; may be due to impurities	
Sm <sub>2</sub> O <sub>3</sub> (2)		Fair				Poor	Moderate mass transfer at 500 hr; dissolution and partial reduction at 1000 hr	
ThO <sub>2</sub> (2)		Fair				Fair	Relatively unaffected; some dissolution at one cor- ner; some cracking due to poor thermal stress resistance	
Y <sub>2</sub> O <sub>3</sub> (7)		Fair				Fair	Fair / Poor	Very minor dissolution at 500 to 1000 hr; signifi- cant mass transfer at 3000 hr from lower part of specimen; upper part of specimen unaffected
5% Y <sub>2</sub> O <sub>3</sub> , 95% ThO <sub>2</sub> (3)						Fair	Fair / Poor	Very minor dissolution at 500 to 1000 hr; signifi- cant mass transfer at 3000 hr from lower part of specimen; upper part of specimen unaffected
10% Y <sub>2</sub> O <sub>3</sub> , 90% ThO <sub>2</sub> (3)						Fair	Fair / Poor	Very minor dissolution at 500 to 1000 hr; signifi- cant mass transfer at 3000 hr from lower part of specimen
TiC (1)							Fair	Some cracking observed
ZrC (1)							Fair	Some cracking observed
CaZrO <sub>3</sub> (1)		Unusable						Very deep cracking and flaking
BaZrO <sub>3</sub> (1)		Unusable						Very deep cracking and flaking
AlN (3)						Poor	Poor	Heavy cracking
AlB <sub>12</sub> (4)						Unusable		Completely disintegrated
BN (1)		Unusable						Completely disintegrated
MgO (1)		Unusable						Completely disintegrated
MgO • Al <sub>2</sub> O <sub>3</sub> (1)	Unusable		Completely disintegrated					
High-velocity (100- to 150-ft/sec) tests								
Cb-1% Zr (1)	Good					Slight wearing of tool marks; otherwise unaffected		
W-2% ThO <sub>2</sub> (1)	Fair / Poor					Loss of ~60 mils of material from tip		
TiC (1)	Unusable					Severe cracking; loss of ~30 mils of material from tip		
ZrC (1)	Unusable					Severe cracking; loss of ~1/4 in. of material from tip		
TaC (1)	Unusable					Severe chemical reaction; loss of ~30 mils of ma- terial from tip		
<sup>a</sup> Good: corners sharp and no measurable mass loss or cracking; useful for structural and nonstructural applications. Fair: corners sharp, but a small amount of dissolution, mass transfer, and/or cracking present; useful for nonstructural applications; marginal for structural uses. Poor: significant dissolution and/or cracking present; not useful for most applications. Unusable: heavy dissolution, cracking, and/or chemical reaction.								

were then conducted at increasing NaK feed pressure to measure the compensating pole losses. At 900-psi feed pressure, the epoxy inlet nozzle opened. This caused NaK to enter the micarta housing, which cracked and leaked NaK. The NaK burned and destroyed the generator, cabling, and instrumentation.

The instrumentation and cabling were replaced, and the third generator was strengthened by adding steel sleeves to the epoxy inlet and exit nozzles and replacing the micarta housing with an aluminum housing. The additional power dissipation due to the conducting sleeves and housing was found to be not more than 10%. Testing was then completed, and final results will be available by the next reporting period.

## 2. High-Temperature Tests

A 3000-hr test was completed which determined the static compatibility of four refractory ceramics with 2000°F lithium. The results of this experiment and those of previous static and high-velocity compatibility tests (SPS 37-21 through -40, Vol. IV) with 2000°F lithium show yttrium oxide ( $Y_2O_3$ ) and columbium-1% zirconium (Cb-1%Zr) to be the best combination of readily available electrical insulator and structural material for a ground prototype liquid MHD system. Besides having the best liquid-metal compatibility of the materials tested, both are fabricable and possess good thermal shock resistance, adequate strength, and nearly equal coefficients of thermal expansion. Further tests are being conducted to determine their adequacy for the eventual long-life requirements of a space power system.

Nineteen materials have been tested with 2000°F lithium for periods varying from 100 to 3000 hr. Useful results were obtained for 40 specimens. The non-metallic test pieces were prepared by vacuum hot-pressing high-purity powders. The static tests were conducted with the test material and high-purity lithium in Cb-1% Zr capsules. These capsules were maintained at 2000°F by radiant heating in a getter-ion pumped vacuum system (SPS 37-34, Vol. IV, pp. 163-170). The dynamic tests were carried out in a Cb-1% Zr flow loop (SPS 37-38, Vol. IV, pp. 91-95). Heating to maintain the lithium at 2000°F was provided by induction losses from the electromagnetic pump, which was used to obtain maximum lithium velocities of 150 ft/sec.

The results of all tests conducted thus far are summarized in Table 4. Some interaction between the lithium

and test material was obtained in every case. The reaction ranged from very severe for materials such as  $CaO$ ,  $AlB_{12}$ , and others to very minor for  $Y_2O_3$  and  $ThO_2$ . An example of appreciable lithium attack is shown in Fig. 7, a photomicrograph of  $Sm_2O_3$  after exposure for 1000 hr. Large voids are seen where dissolution of the material occurred. The voids become much smaller toward the interior of the specimen. The attacked zone had a depth of about 50 mils after 1000 hr.

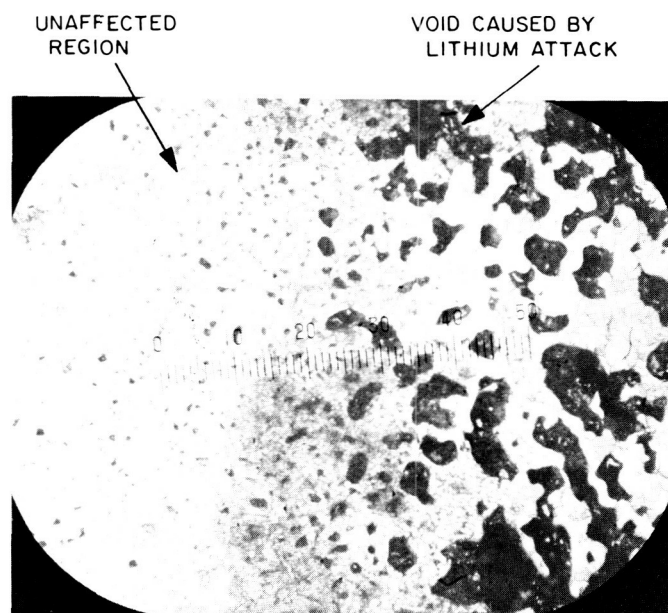
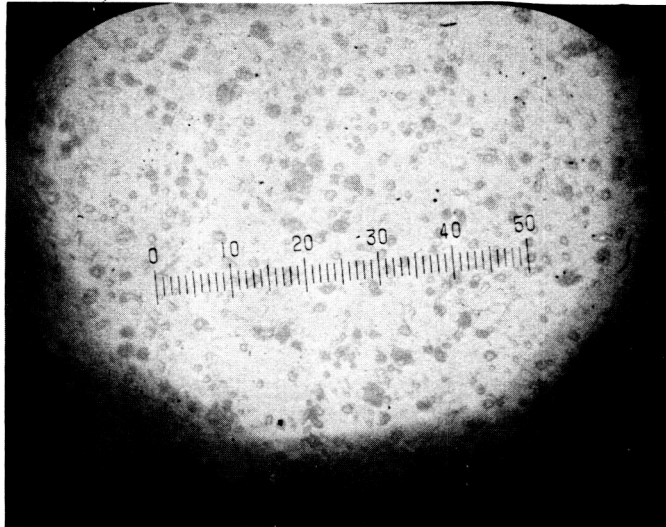


Fig. 7. Samarium oxide ( $SM_2O_3$ ) after exposure to 2000°F static lithium for 1000 hr ( $\times 100$  magnification)

Photomicrographs of  $ThO_2$ , a more resistant material, are shown in Fig. 8. No significant changes in the microstructure, other than a darkening, were apparent after 1000-hr exposure to static lithium at 2000°F. Mechanical properties of the thorium (and yttria) specimens were very similar before and after testing for 1000 hr. However, when the exposure time was increased to 3000 hr, a substantial transfer of mass from the bottom to the top of the specimen was observed. Fig. 9 shows an yttria specimen after 3000-hr exposure. The dashed lines form the original outline of the rectangular specimen before exposure. Although much of the bottom of the specimen had dissolved in the lithium, the original sharp corners remained on the top. Since the application for an electrical insulator in the liquid MHD power system would occur at the coldest part of the lithium circuit, yttria may still be useful for long-term applications. Tests are in progress to determine if this is the case.

a) BEFORE EXPOSURE ( $\times 400$  MAGNIFICATION)



(b) AFTER EXPOSURE ( $\times 400$  MAGNIFICATION)

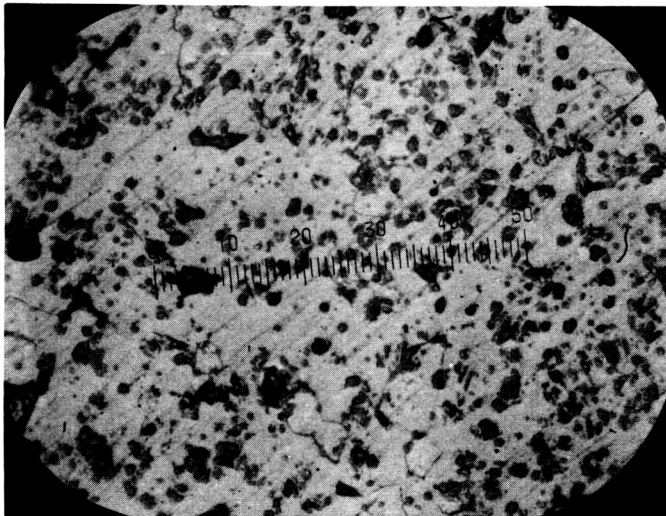


**Fig. 8. Thorium oxide ( $\text{ThO}_2$ ) before and after exposure to 2000°F static lithium for 1000 hr**

The carbides of titanium, tantalum, and zirconium were investigated to determine their usefulness as high-hardness separator materials. Results of the 2000-hr static test appeared to show titanium carbide ( $\text{TiC}$ ) was suitable. However, testing in the high-velocity lithium stream for only 100 hr led to gross cracking and material loss. Subsequent microscopic examination of the static specimens showed lithium penetration similar in nature to that for the dynamic specimens. Figs. 10 and 12 show the microstructure of the  $\text{TiC}$  before and after exposure to lithium. The cracking was attributed to lithium reaction and penetration because of the smoothed edges of

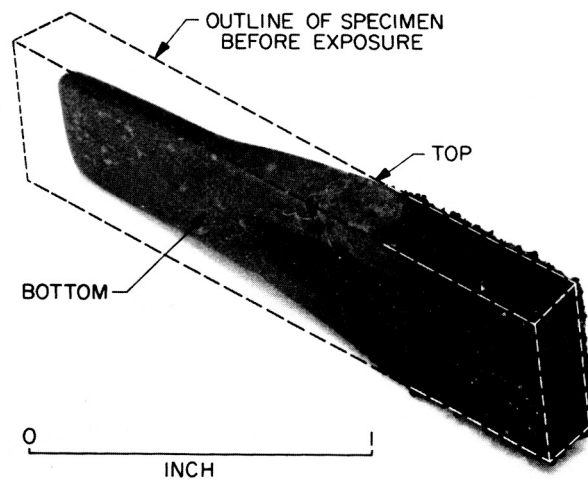


**Fig. 9. Yttrium oxide ( $\text{Y}_2\text{O}_3$ ) after exposure to 2000°F lithium for 3000 hr**

the grain boundaries and because previous experiments had established  $\text{TiC}$  to be very resistant to thermal shock.

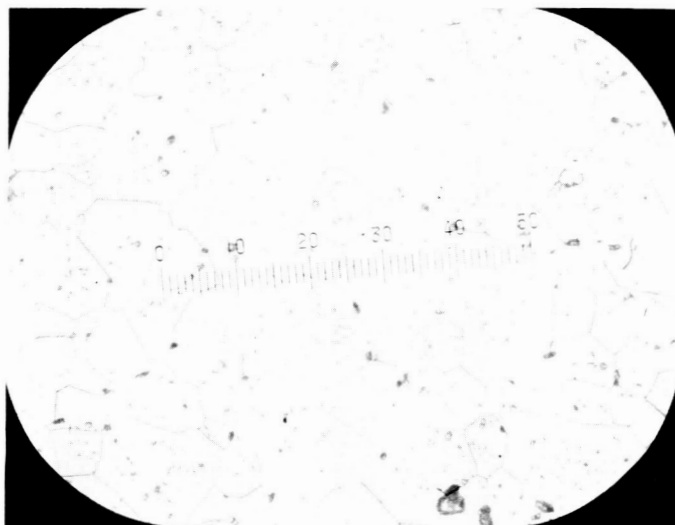
Of all potential separator materials tested thus far,  $\text{Cb-1\%Zr}$  has shown the best resistance in both static and flowing lithium. The apparently accelerated reaction in  $\text{TiC}$  and  $\text{ZrC}$  due to high-velocity flow raises a question as to whether any static test results can determine the suitability of a material for a liquid MHD system. To answer this question,  $\text{Cb-1\%Zr}$  and  $\text{Y}_2\text{O}_3$  will be tested in flowing lithium at 2000°F over a range of velocities to establish the dependency of weight loss upon velocity.

Of the test results shown, only that for  $\text{CaO}$  is felt to be questionable. Difficulties were encountered during the fabrication of the test specimens which may have resulted in moisture absorption and caking. Another means of fabrication discussed in the literature apparently produces better mechanical properties and lessens the severity of the absorption problem (Ref. 2).  $\text{CaO-1\%TiO}_2$  ceramics constructed in this way were reported to be compatible in lithium liquid and vapor to 900°C. Several specimens will be fabricated using the reported techniques and will then be tested in 2000°F lithium to determine their suitability for the liquid MHD system.

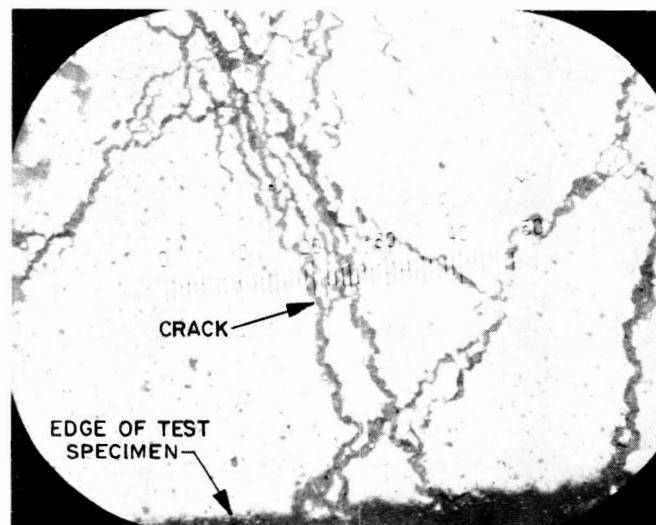
### 3. $\text{NaK-N}_2$ Conversion System

A closed-loop system incorporating all of the components of a liquid-metal MHD conversion system is under

(a) BEFORE EXPOSURE (×400 MAGNIFICATION)



(b) AFTER EXPOSURE (×100 MAGNIFICATION)



(c) AFTER EXPOSURE (×400 MAGNIFICATION)

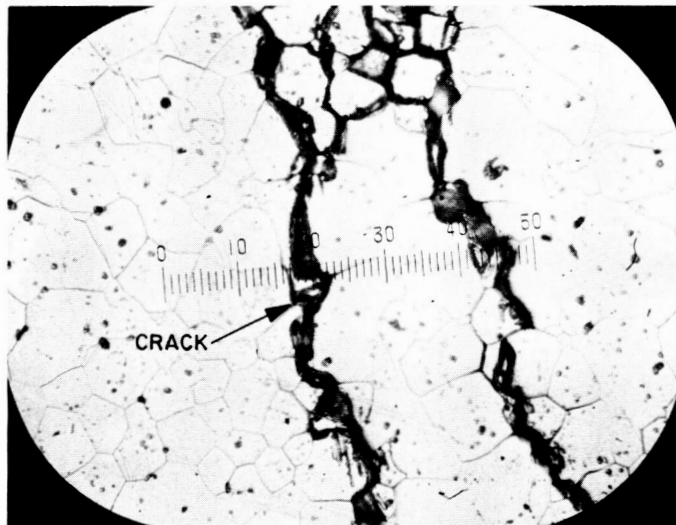


Fig. 10. Titanium carbide (TiC) before and after exposure to 2000°F high-velocity lithium for 100 hr

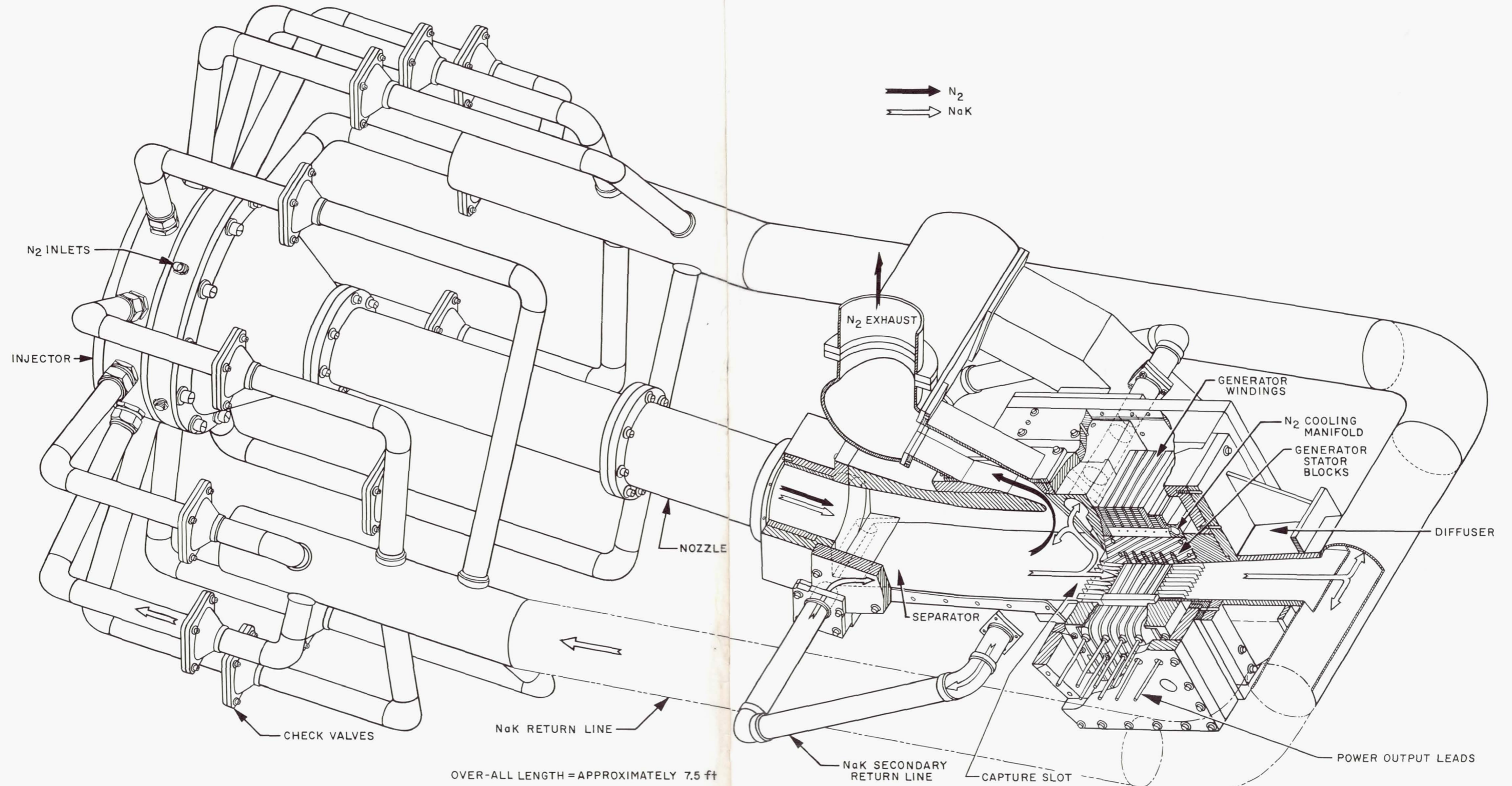
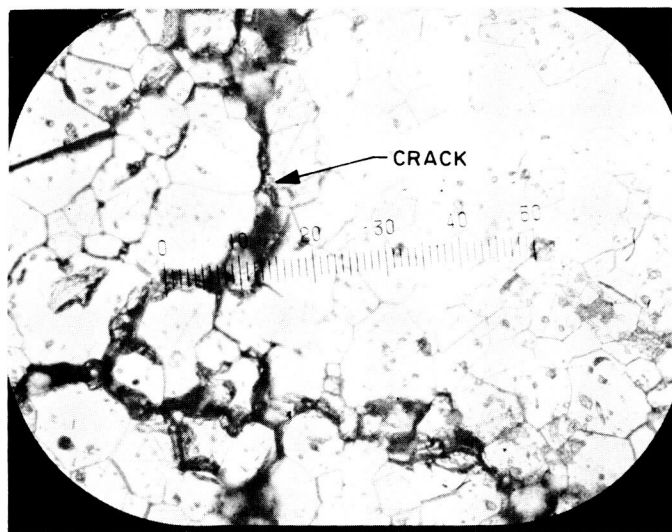


Fig. 11. NaK-N<sub>2</sub> MHD conversion system



**Fig. 12. Titanium carbide (TiC) after exposure to 2000°F static lithium for 2000 hr ( $\times 400$  magnification)**

construction for testing with NaK (representing the lithium) and  $N_2$  (representing the cesium vapor). The NaK circulates in a closed loop, and the  $N_2$  flows in an open loop from a bottle bank to the atmosphere to provide a 15-min test duration. The system operates at ambient temperature. The purposes of the NaK- $N_2$  system are to verify the present performance calculations based on component tests and to serve as a prototype of a subsequent high-temperature system.

Fig. 11 shows the NaK- $N_2$  conversion system. At calculated operating conditions, 185 lb/sec of NaK and 6 lb/sec of  $N_2$  are injected with low velocity into the nozzle inlet at 230 psia—the vapor pressure of cesium at 2000°F—and are expanded through the nozzle to 22 psia, reaching a velocity of 385 ft/sec. The NaK impinges on the 6-in.-wide inclined-plate separator and decelerates to 330 ft/sec because of friction; the  $N_2$ , with about 1 lb/sec of entrained NaK, exhausts to an external entrainment separator and then to the atmosphere.

The 0.6-in. capture slot collects 95% of the NaK and an equal volume of  $N_2$ . The remaining NaK enters a second slot and decelerates to provide 5-psi pressure rise for returning the NaK to an injection slot at the separator inlet. The collected NaK- $N_2$  mixture undergoes three simultaneous processes in the 1.8-in. section following the capture slot: (1) The mixture is pressurized to 94 psia by contraction of the channel to 0.4 in., making the generator exit flow subsonic for good diffuser efficiency; (2) the stream is subjected to a 4800-gauss, 575-cps, compensating AC magnetic field to cancel end

effects in the traveling-wave region of the generator; and (3) the flow is divided into multiple streams by insulating vanes to block the eddy currents induced by the compensating magnetic field. The NaK is slowed to 270 ft/sec by pressure rise, friction, and electrical drag in this region.

The channel is then stepped outward to a 0.52-in. gap to provide an approximation to free-jet conditions for minimizing friction. The gap remains constant through the 4.3-in. length of the traveling-wave region. The traveling magnetic field has an 8000-gauss amplitude and a velocity of 227 ft/sec at the inlet and 189 ft/sec at the exit. The NaK decelerates from 270 to 210 ft/sec. The deceleration extracts 112 kw of power from the fluid; of this, 19 kw is dissipated in friction, 12 kw in fluid ohmic loss, and 25 kw in winding loss (including compensating-winding loss), leaving 56 kw of net output power. The output is 600 v, 575 cps, 6-phase.

The windings are cooled by  $N_2$  gas fed at 150 psia to the generator housing. Part of the  $N_2$  flows through the winding slots into the NaK, and the other part flows past the outside turns and exhausts to the atmosphere.

After leaving the generator, the NaK enters the diffuser, which diverges at a 3.75-deg half-angle to 4 times the inlet area. The diffuser inlet projects between the 2.0-in downstream compensating poles, and vanes are again used to block the eddy currents. The NaK leaves the diffuser at 250 psia and enters two 5.0-in.-ID return lines. These lines connect to the 12 1.5-in. lines and check valves employed in the previous closed-loop tests (SPS 37-34).

To obtain a rough measure of the equivalent over-all efficiency of the NaK- $N_2$  system, it can be noted that room-temperature  $N_2$  has the same density as 2000°F cesium. Therefore, the equivalent cesium flow rate is the same: 6 lb/sec. The equivalent heat input, using the cesium latent heat of 220 Btu/lb, is  $6 \times 220 = 1320$  kw. The equivalent cycle efficiency is  $56/1320 = 4.2\%$ , a satisfactory approach to the 6 to 7% level attainable at 300 kw with cesium and lithium.

Fabrication of the separator and the generator housing has been completed. Flow models of the capture slot and generator inlet have been fabricated for water testing; included is an inlet with gas injection to replace the main length of the vanes and possibly reduce friction. The nozzle, start tank, and NaK supply system are available

from the previous tests. The laminations (Hiperco-50) for the generator have been cut and heat-treated in preparation for bonding and machining. A copper-bar heat-transfer model of one coil has been prepared for testing to determine required cooling flow.

**N67-15729**

**D. An Addition to the Radiator System Computer Program, J. J. Volkoff**

In the design of an all-liquid heat-rejection radiator system, consideration must be given to the various elements comprising the system, the feasibility of the process and design constraints established, and the resulting weights of the system. When optimizing the radiator system weight for a spacecraft, the radiator system weight without coolant and the weight of the coolant it can carry are both important parameters. Previously, the JPL computer program M091 (SPS 37-36, Vol. IV, pp. 93-97) was designed to compute the radiator system weight without coolant. The computer program has now been changed to include the computation for the coolant weight required. These program changes and their effect on the optimum radiator design are described here.

Previously, the fluid velocity in the supply and return headers (SPS 37-36) were read in as inputs to the program and remained constant for all computed runs. The program now designates the fluid velocity in the header as a fraction  $f$  of the fluid velocity in the tube. This fraction is selected to ensure a nearly uniform flow distribution throughout the tubular array in the panel system. The program reads in:

$$V_h = f \cdot V_t \quad (1)$$

A second change to the program is the computation of the mean tube temperature  $T_0$ . This computation is made using the inlet fluid temperature  $T_3$  and the outlet fluid temperature  $T_4$  of the system as follows:

$$T_0 = \left[ \frac{3T_3^2 T_4}{T_3^2 + T_4^2 + T_3 T_4} \right]^{1/4} \quad (2)$$

Finally, the weights of the coolant in the tubular array, supply header, and return headers are computed to give the combined system weight of the radiator system and total coolant. The resulting weight of the coolant required in the radiator sections is also read out as an output of the program.

As an example, assume that a liquid coolant (NaK-78) is to be cooled from 1350 to 1200°F by a heat-rejection two-panel space radiator system (SPS 37-36). The fluid-flow pressure-drop design value is 5 lb/in.<sup>2</sup>, and the thermal hemispherical emissivity of the radiating surfaces is 0.9. It is assumed that the space radiator is to be used for 833 days on a Jupiter interplanetary mission. The probability of no meteoric penetration damage is assumed to be 0.95. The materials used for the radiator elements are stainless steel for the intube liners and beryllium for

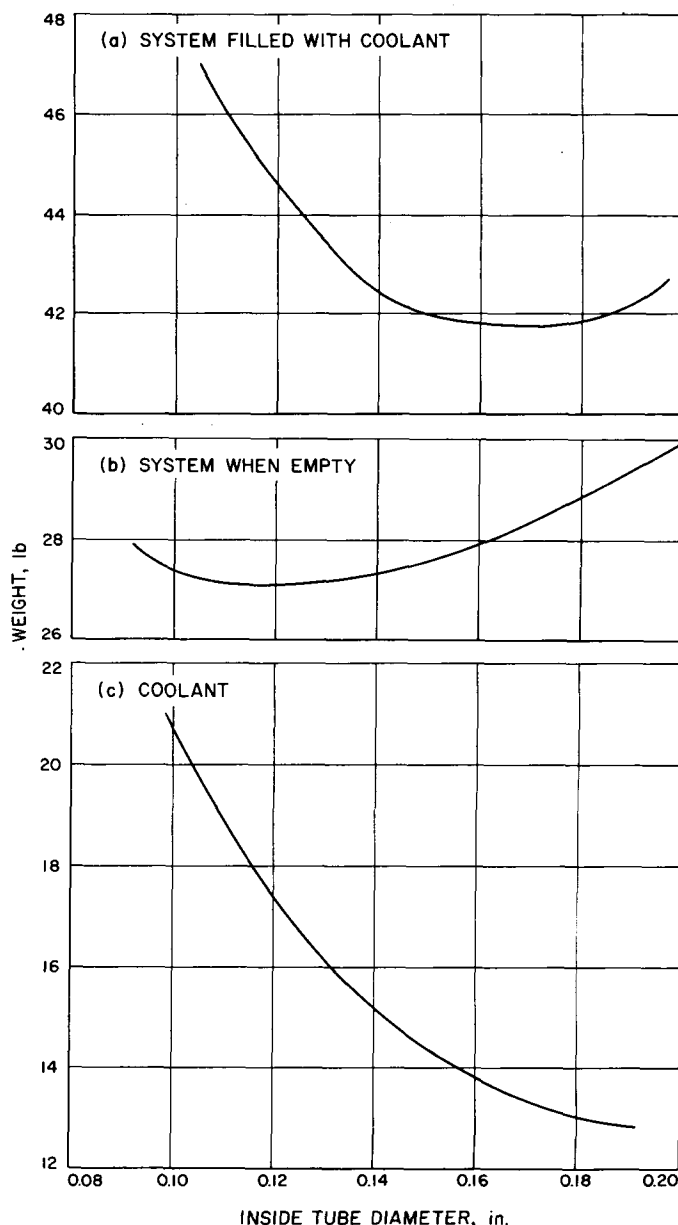


**Fig. 13. Weight vs inside tube diameter for a 10<sup>6</sup>-Btu/hr heat-rejection system**

the tube armor and fins. The total heat-rejection rate for the system is  $10^6$  Btu/hr.

The resulting system weights are presented in Fig. 13 as functions of inside tube diameter for the system both empty and full of coolant. It may be noted that the tube diameter with the minimum weight of the system empty is smaller than that with the minimum weight of the system full of coolant. This is due to the smaller liquid

inventory required in the radiator for the larger tube configurations in the tube-diameter range shown. Thus, if the radiator system with minimum weight when empty were selected, this system full of liquid coolant would be about 8% heavier than a system minimized considering coolant weight. From this, it can be concluded that the weight of the liquid coolant is significant and must be considered in the design of a radiator system if a minimum-weight system is to be obtained.

## References

1. Gronroos, H., "Analog Computer Study of Thermionic Reactor Power Plant Transients," *Transactions of the American Nuclear Society*, Vol. 9, No. 1, 1966.
2. Lukin, Y. S., and Serova, G. A., *Certain Properties of Calcium-Oxide Refractories*, Report No. FTD-TT-65-1396/1 + 2 + 4, Foreign Technology Division, Air Force Systems Command, Wright-Patterson Air Force Base, Ohio, January 20, 1966.

## XII. Liquid Propulsion

### PROPULSION DIVISION

N67-15730

**A. Resonant Combustion**, R. M. Clayton,  
J. W. Woodward, and J. G. Sotter

**2. Circumferential Variations in the Resonant Pressure Wave**, R. M. Clayton

#### 1. Introduction

The resonant combustion program is currently involved in the verification of a "rotating detonation-like wave" concept to explain the steep-fronted, high-amplitude pressure disturbances associated with the destructive oscillatory modes of liquid rocket combustion. The work comprises both experimental and analytical studies, concentrating on three relatively large scale research engines which exhibit this combustion phenomenon. Recent efforts have been directed toward:

- (1) Conducting a series of experiments to determine the variations in the behavior of the pressure wave during its rotation about the chamber circumference.
- (2) Developing diagnostic techniques for examining the combustion processes (under resonant conditions) within the chamber volume.
- (3) Investigating the hydrodynamic response of the injection scheme to high amplitude chamber pressure oscillations.

Some results of these efforts will be discussed here.

In the course of obtaining the boundary pressure distribution exhibited by one of the 11-in. diameter, 20,000-lb thrust research engines during the resonant mode, certain variations in the time-history of the pressure disturbance were noted as the wave swept past different locations on the chamber circumference. This behavior was interpreted as variations in wave amplitude and velocity due to local variations in the combustion media through which the wave passed. Those observations and the experiments leading to them are summarized in *SPS 37-36*, Vol. IV, pp. 163-173.

In order to further define the extent of such wave variations, an additional series of experiments was conducted utilizing a more extensive array of pressure tap locations on the wall of the chamber. These later firings also utilized RMIR Injector 7 using  $N_2O_4 + 50/50$  (UDMH/ $N_2H_4$ ) propellants.

*a. Experimental procedure.* The instrumentation equipment and techniques used for the high-response measurements of these experiments have been previously described in Ref. 1. The major components consisted of ablatively

protected, vibration isolated, model 603A Kistler transducers; Kistler charge amplifiers; a 14-channel Consolidated Electrodynamics Corporation (CEC) VR 2600 tape recorder and a CEC oscillograph. In summary, the measurement scheme provided an over-all rise time of  $\sim 6 \mu\text{sec}$  in response to a step change in pressure (e.g., shock tube end shot), and a final time resolution on the oscillograph record of the type playbacks of  $\sim 100 \mu\text{sec/in.}$  of display length.

The array of transducer locations on the chamber wall is depicted in Fig. 1. At a station located 2.57 in. from the injector face, a "set" of six transducers was installed with individual transducers placed circumferentially at 0, 20, 135, 155, 250, and 270 deg, respectively, clockwise from the chamber reference mark. Additional locations were also available (but not shown) at 0.43, 3.73, and 5.23 in. from the face.

A clamped-flange arrangement for joining the chamber to the injector allowed the chamber and its transducer array to be affixed to the injector at any circumferential orientation with the injection scheme. Thus, a set of six simultaneously recorded measurements for the 2.57-in. station could be made per firing. Rotating the chamber to new positions prior to subsequent firings provided analogous sets of measurements for new circumferential locations.

Gross combustion conditions were maintained nearly constant for each of the firings. A nominal mixture ratio of 1.27 was used in order to conform to the uniformity mixture ratio (Ref. 2) for the injector with  $\text{N}_2\text{O}_4 + 50/50$  propellants. Total flow rates provided a nominal chamber pressure of 300 psia during the steady state portion of each run. Variations from these nominal conditions were within  $\pm 0.08$  mixture ratio units and  $\pm 25$  psi, respectively.

Each run commenced with approximately 400 msec of nonoscillatory combustion, during which time flow rates were established. Near-steady values of the nominal operating conditions were attained by the end of this period. A 13.5-grain high-explosive bomb (Ref. 1) was fired near the wall of the chamber at this time and a transition to the sustained resonant mode always occurred within less than 10 msec. The run was terminated after approximately 100 msec of resonance.

There was provision for only one bomb location on the chamber (Fig. 1). Thus, while the bomb's distance from the face and its radial position from the wall were invari-

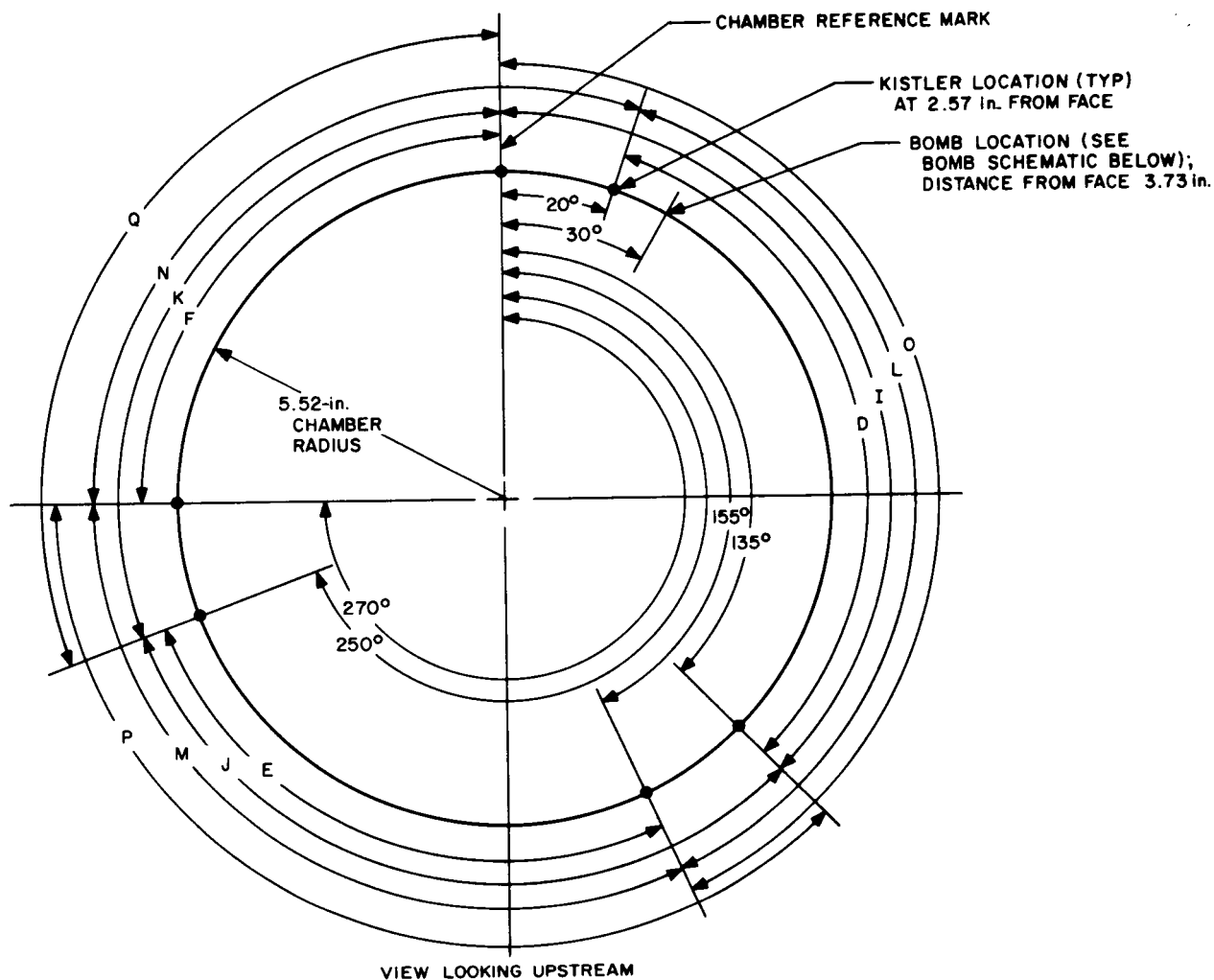
ant, the different chamber orientations for the individual runs resulted in different bomb orientations relative to the injector.

**b. Results.** Since it was known that the direction of rotation for the sustained resonant mode for this engine varied in accordance with the bomb orientation with the injector, it was decided to obtain the circumferential measurements for both wave travel directions. Portions of typical pressure versus time records for clockwise (CW) and counterclockwise (CCW) wave travel are shown in Figs. 2 and 3, respectively. (Note that travel direction is always referenced to a view looking upstream.) These figures are intended to illustrate the changing waveform of the disturbance-to-boundary intersection as the wave sweeps about the chamber periphery; therefore, no meaningful phase relationship between traces is shown. Note also that the amplitude sensitivity for each record varies somewhat and must be taken into account when comparing traces.

The measurement locations are shown superimposed upon a representation of the injection scheme, which is based on the mass distribution produced by the individual unlike impinging doublet elements when flowed with nonreacting fluids at the uniformity mixture ratio. The plane of the distribution depicted here is 3.11 in. downstream from the face and hence is not far removed from the 2.57 in. plane of the pressure measurements. The mass flux distribution is viewed in the upstream direction.

We observe that for either direction of rotation, two sectors about the periphery of the injection pattern appear wherein the rise time of the gross disturbance becomes generally less steep — this effect being most obvious for the CCW wave case (Fig. 3). Confining our attention to those injector elements which lie in proximity to the chamber wall, we also note that the spatial aspect which the individual spray patterns present to the wave motion is essentially identical in each sector of flattened waveform. That is, in each such case the pressure wave approaches the individual spray patterns from a "quarterly" direction and toward the side of the spray opposite to the adjacent wall. This again suggests, as was mentioned in the earlier experiments reported in SPS 37-36, that there is a close coupling between the properties of the pressure wave and the local conditions in its path, even though an explicit quantitative relationship has not been determined.

From the sets of 6 simultaneously recorded pressure measurements mentioned earlier, it was possible to obtain for each firing the average wave tangential velocity across



MEASUREMENT SECTORS	
SECTOR	SIZE, deg
D	115
I	135
L	135
O	155
E	95
J	115
M	115
P	135
F	90
K	110
N	110
Q	130

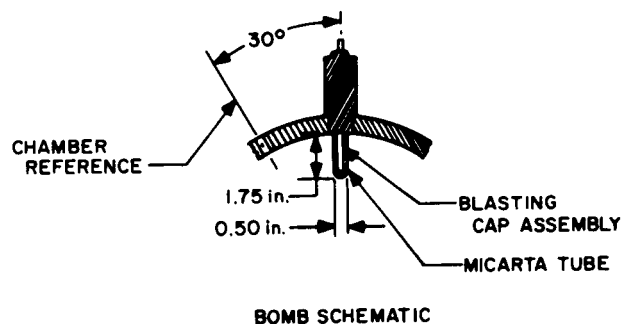


Fig. 1. Transducer and bomb locations on wall of chamber used for circumferential variation study

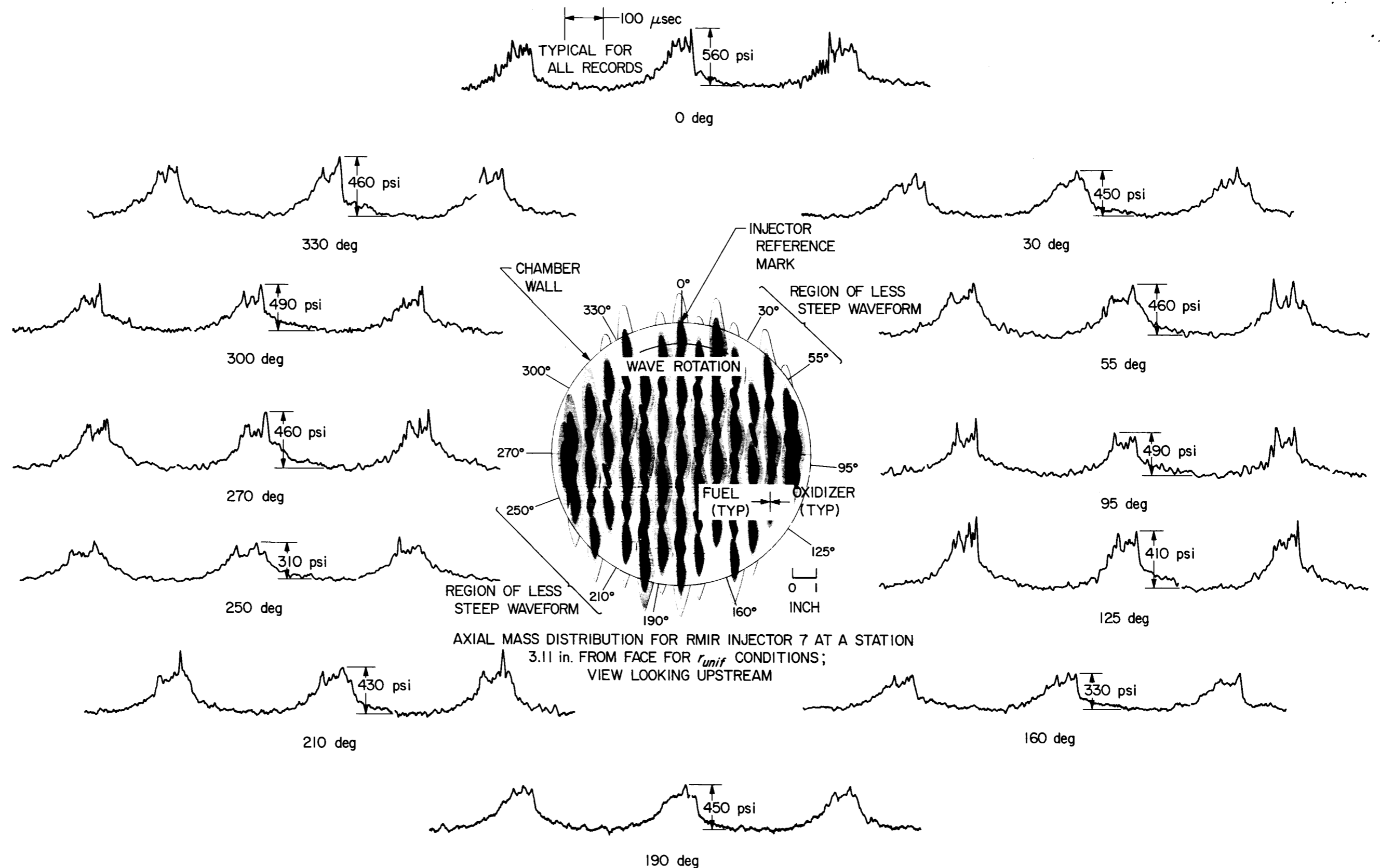


Fig. 2. Typical waveforms around chamber circumference at 2.57 in. from injector face; clockwise wave direction. RMIR Injector 7 with  $N_2O_4 + 50/50$  (UDMH/ $N_2H_4$ )

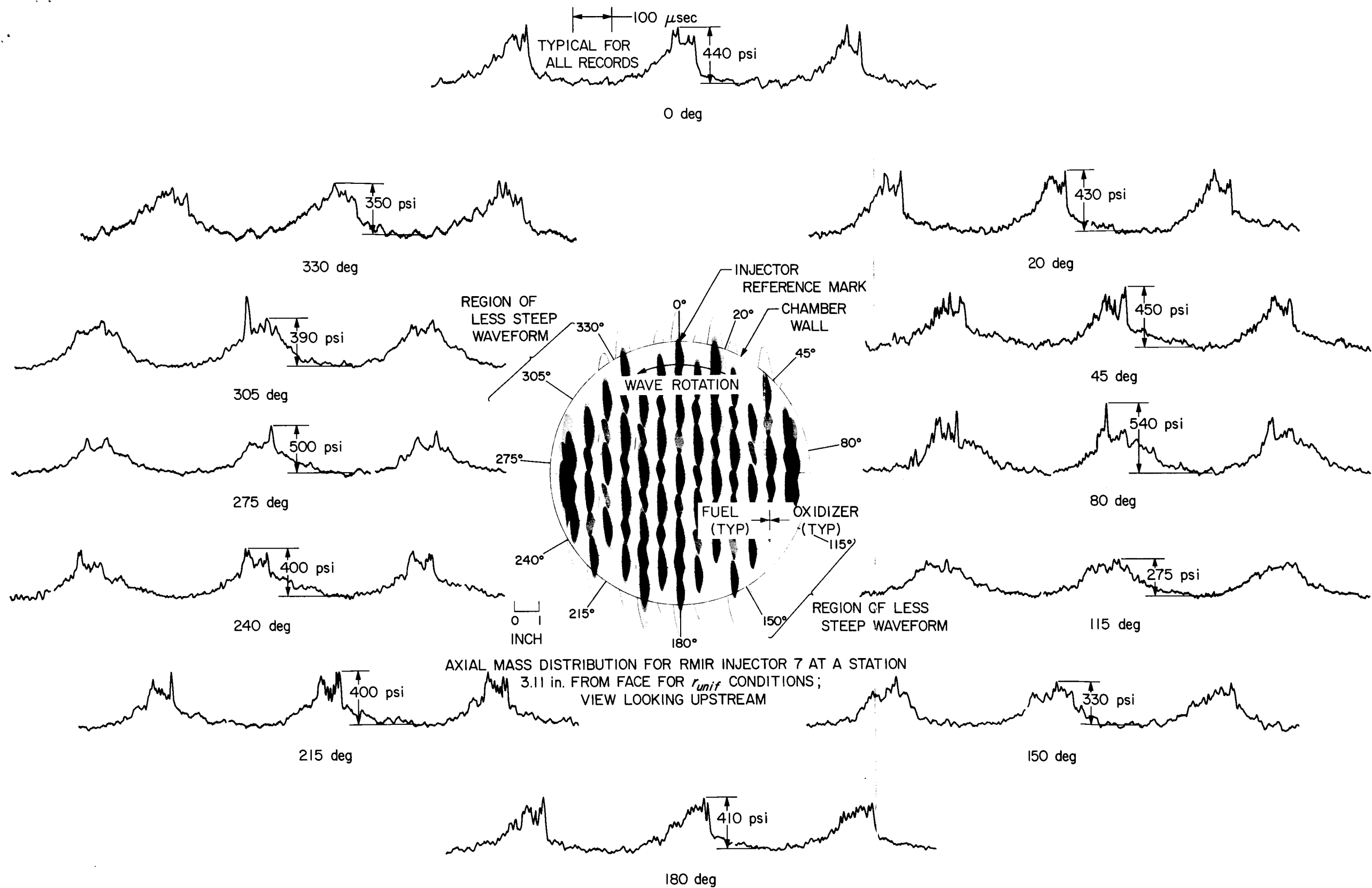


Fig. 3. Typical waveforms around chamber circumference at 2.57 in. from injector face; counterclockwise wave direction. RMIR Injector 7 with  $N_2O_4 + 50/50$  (UDMH/ $N_2H_4$ )

12 different sectors of the combustion chamber periphery. These measurement sectors are identified in Fig. 1, where it can be seen that they can be divided into three groups of four sectors each. The position of the sectors of each group is considered to be nearly coincident; therefore, the computation of average velocity from the various combinations of measurement channels forming the end points of the sectors provided four almost independently derived velocities for each group of sectors.

These results for the entire series of firings are shown in Figs. 4 and 5 for CW and CCW wave rotation, respectively. The ratio of sector tangential velocity  $v_{sec}$  to the average velocity for a complete wave rotation  $v_T$  is plotted

versus the sector median position relative to the injector reference mark. The letter symbols identify the particular measurement sectors from which the data were derived.

The mean curves drawn through the data on Figs. 4 and 5 have been replotted on the polar coordinates in Fig. 6 in order to show more graphically the geometrical orientation of the velocity variations with the injection distribution. The dominant features of this comparison are:

- (1) The sectors exhibiting maximum average velocity appear near those regions of the injection distribution where propellant impingement on the wall is

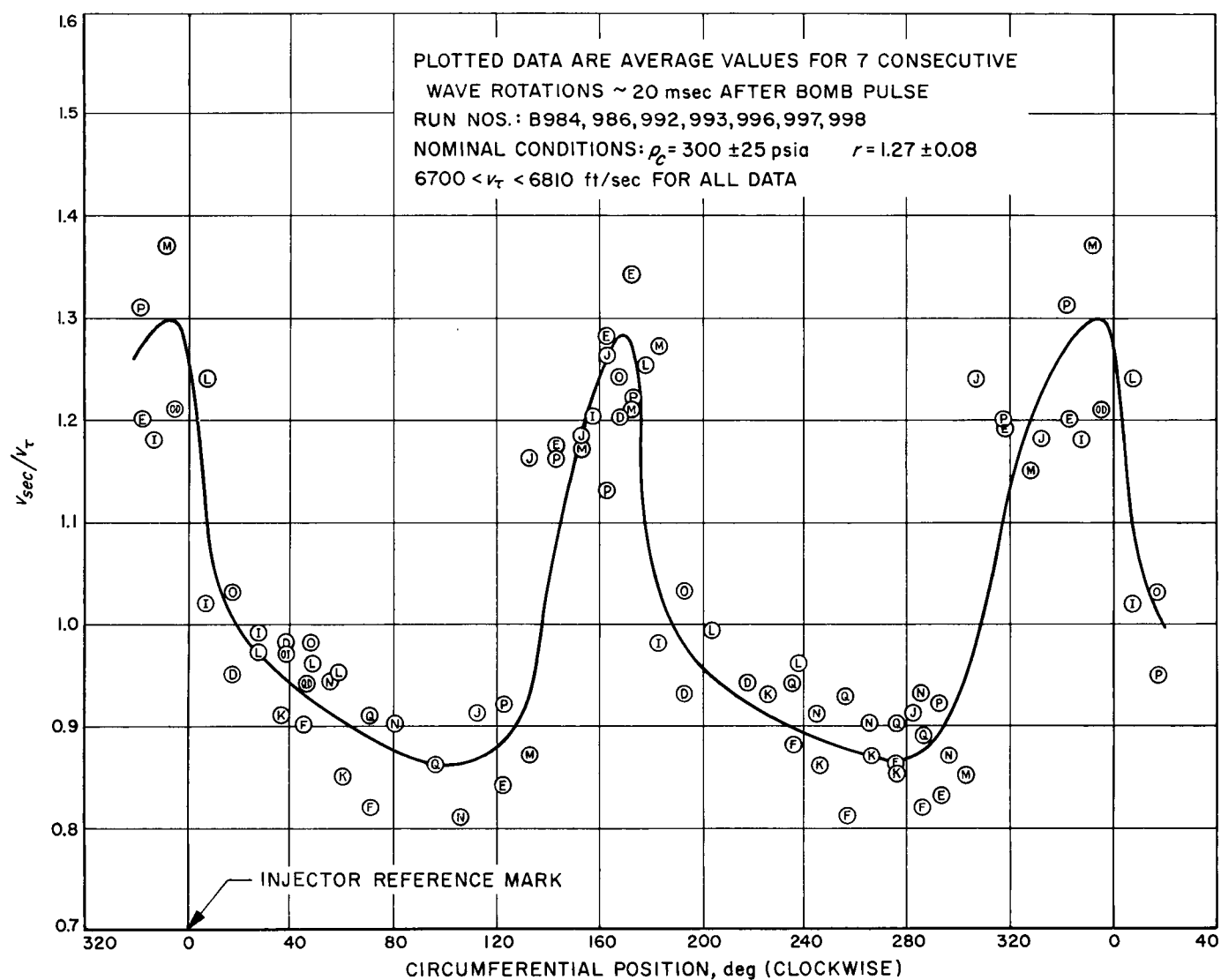
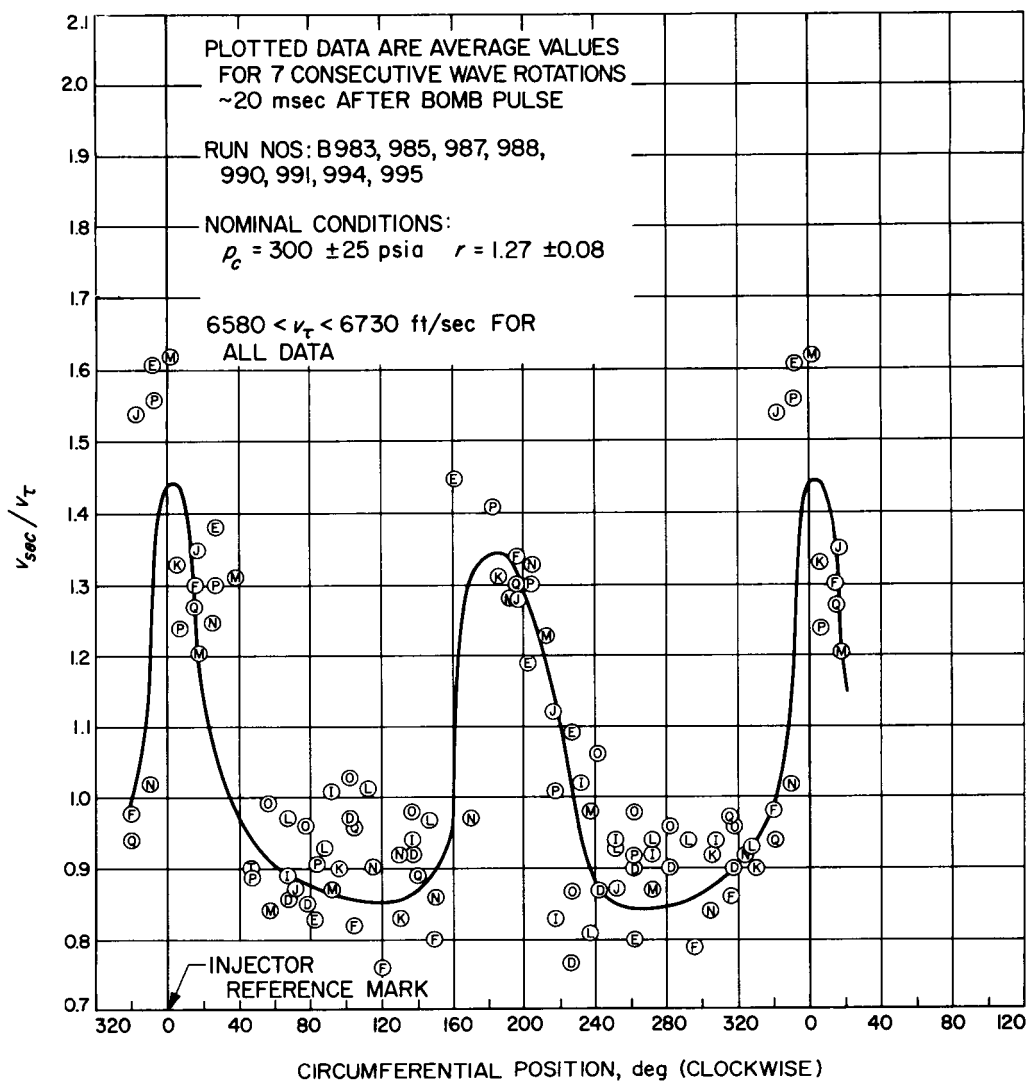


Fig. 4. Variation in tangential velocity around chamber circumference at 2.57 in. from injector face; clockwise wave direction. RMIR Injector 7 with  $N_2O_4 + 50/50$  (UDMH/ $N_2H_4$ )



**Fig. 5. Variation in tangential velocity around chamber circumference at 2.57 in. from injector face; counterclockwise wave direction. RMIR Injector 7 with  $N_2O_4 + 50/50$  (UDMH/ $N_2H_4$ )**

greatest and where the tangential wave motion is nearly broadside to the element spray patterns. The relative importance of these effects is not known.

- (2) The greatest velocity variation appears for the CCW direction of motion.
- (3) Except for magnitude of variation, the velocity profiles for the respective directions of motion are nearly mirror images of each other. This is believed to be related to the waveform variations previously shown in Figs. 2 and 3.

Also included on Fig. 6 is a summary of the rotational direction of the sustained pressure wave relative to the

initiating bomb location. Note that the direction of rotation seems to coincide with the direction from the bomb to the nearest high-velocity region. For example, a bomb pulse in the region of either the 45- or 225-deg locations precipitates a CCW wave since the nearest high-velocity regions lay in that direction. In a similar manner, a CW wave would result from a bomb pulse originating near the 135- or 315-deg regions.

The  $\tilde{p}_{min}$  to  $\tilde{p}_{pk}$  amplitudes observed around the circumference of the 2.57-in. station during these fringes are shown in Fig. 7. Almost no pattern of variation can be discerned; however, the pressures for the CW direction generally exhibit some 25% greater amplitude. The fact

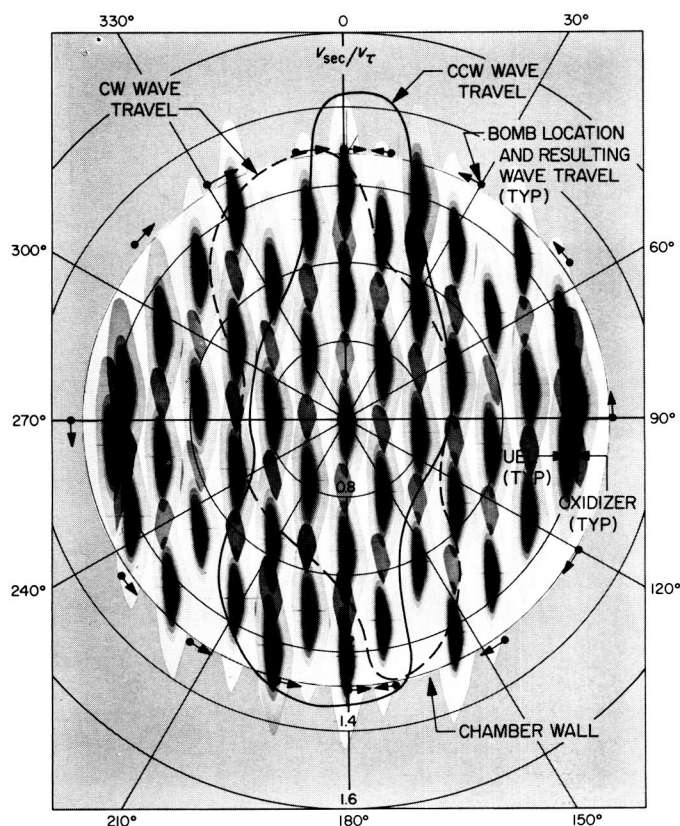


**Fig. 6. Comparison of circumferential velocity variation with injection scheme and bomb position with sustained wave travel direction. RMIR Injector 7 with  $N_2O_4 + 50/50$  (UDMH/ $N_2H_4$ )**

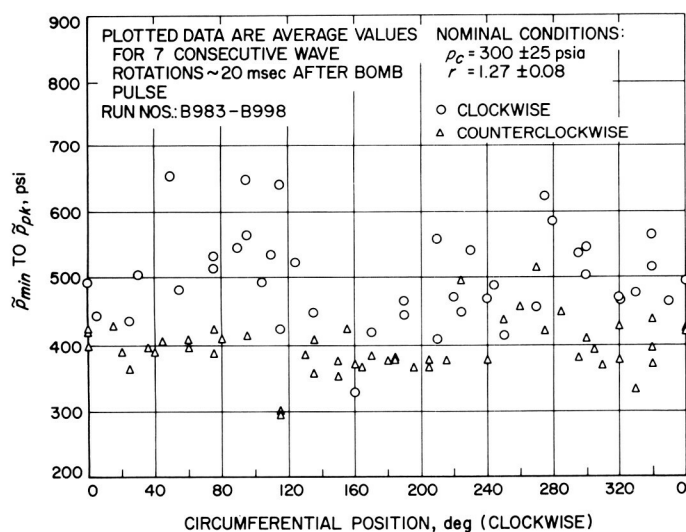


**Fig. 7. Disturbance amplitude versus position around chamber circumference at 2.57 in. from injector face. RMIR Injector 7 with  $N_2O_4 + 50/50$  (UDMH/ $N_2H_4$ )**

that consistent amplitude variations were not readily correlated with the velocity variations may in part be attributed to instrumentation limitations. However, the possibility that a more fundamental process is involved should not be discounted. These studies are continuing.

### 3. Development of Diagnostic Techniques, J. G. Sotter and R. M. Clayton

For practical reasons, combustion chamber instrumentation provisions in flight engine design are usually kept to a bare minimum; yet, later in the development stage, knowledge of combustion behavior sometimes becomes vitally important. The purpose of this section is to describe two relatively simple and inexpensive methods, developed during the resonant combustion study, which could be used to monitor the combustion process in some flight engines, with no permanent design changes. These methods were proven under extremely severe resonant burning conditions in two 11-in. engines, each of which produces approximately 20,000 lb of thrust for optimum expansion. Tests had to be restricted to approximately 0.5-sec duration to prevent destruction of the engine, and since only combustion chamber phenomena were under investigation, the exhaust jet was allowed to be highly underexpanded; however, conceptually at least, these restrictions are not necessary.

**a. Photographic technique.** A camera housing was constructed of 0.25-in. steel plate, and is shown in Fig. 8. Two tubular legs support its weight, and a third is anchored to a block normally used for bracing the hydraulic jack used in thrust calibration. A 3-in.-ID pipe (only the protruding end of which shows in Fig. 8), about 18 in. long, leads from the camera housing to a steel flange to which is bolted a single thickness of 1-in. plexiglass. The pipe also serves as support for a steel wedge (0.75-in. plate) which deflects the exhaust gases from the camera box itself. Since the wedge is not directly attached to the box, post-run heat conduction to the box from the wedge is minimized. A small nitrogen bleed is maintained into the box, to help prevent entry of combustion gases. The surfaces of the wedge and box could be protected by sheets of Teflon, Micarta, or any other convenient opaque ablative material having low thermal conductivity; and a water spray on the ablative surface would help to minimize heat-soak. However, for short-duration firings (< 1 sec), an uncooled steel surface has proved to be satisfactory.

Fluid dynamic processes in the combustion chamber itself are unaffected by conditions downstream of the



Fig. 8. Camera housing mounted aft of 11-in. engine

throat, since disturbances cannot propagate upstream against the supersonic jet; therefore, the expansion cone normally used with the engine was removed for these experiments in order to place the apparatus as close as possible to the chamber. A short diverging section remains, however, to insure supersonic flow at the exit.

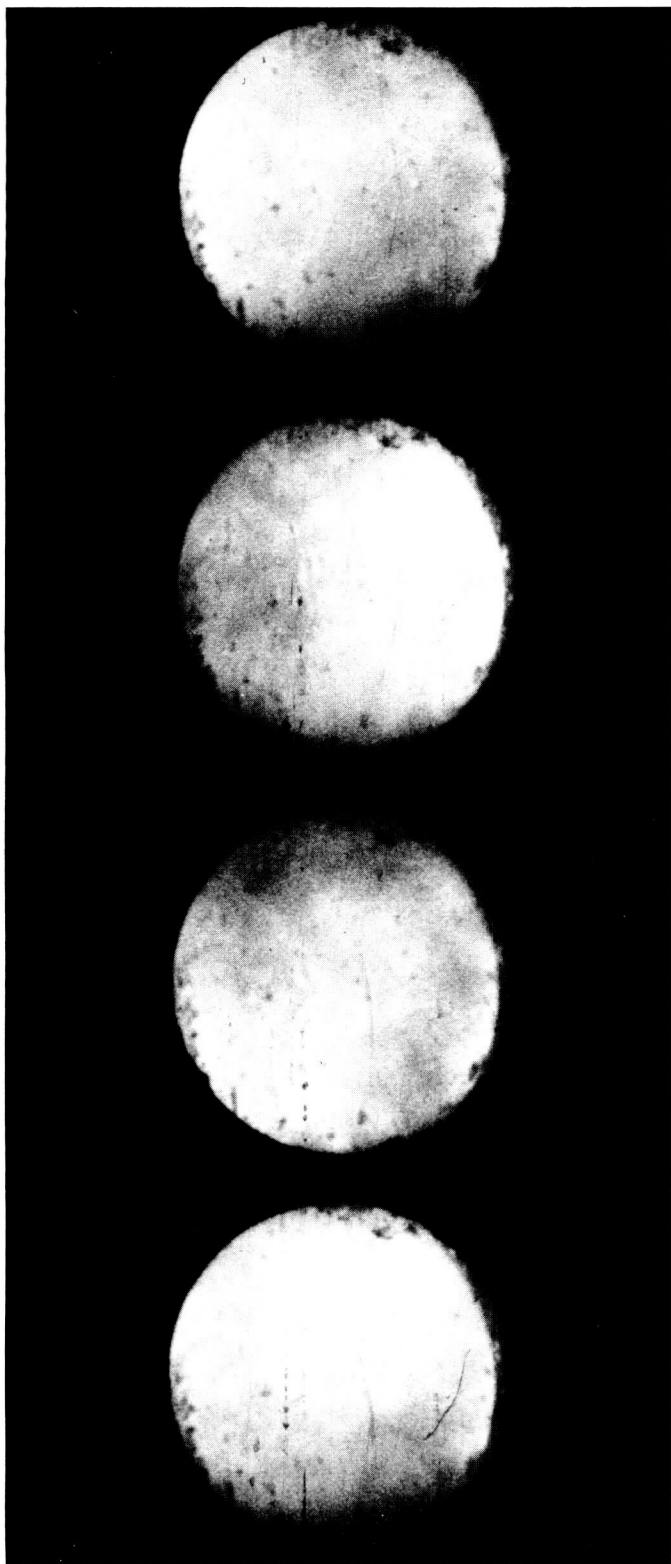
The box is able to hold either a Fairchild HS101, a Wollensak Fastax, or a Beckmann-Whitley Dynafax camera. Using the Fastax with an 8-mm framing device, frame rates up to 16,000 pps have been used successfully.

Fig. 9 shows some 16-mm photographs taken with the Fastax camera at 8,000 pps. These pictures show a single cycle of the rotating detonation-like wave. The window is located upstream of the point where the first shock would normally occur in the free jet. Impingement of the jet on the window produces a shock, with gas temperature

rising as high as its stagnation value (which is greater than 5000°F); but the thickness of this region is small, and visually the presence of the shock is not obvious as viewed by the camera inside the box.

**b. High-frequency pressure measurements.** An ablatively-cooled probe was designed to obtain high-frequency pressure measurements within the combustion chamber at locations removed from the chamber boundaries. This probe, 1 in. in diameter at the transducer location, is shown in Fig. 10. It is introduced through the nozzle (Fig. 11) and braced from the downstream end, being positioned laterally by means of a housing supported by three ablatively-cooled struts. The transducer used was the Kistler 603A, protected by an 0.080-in.-thick layer of RTV-580 silastic rubber.<sup>1</sup> In the probe configuration, shock-tube tests have

<sup>1</sup> Manufactured by General Electric Silicone Products Department, Waterford, New York.



**Fig. 9. High-speed movies of 11-in. combustion chamber as seen from the camera housing: consecutive frames during resonant combustion. The detonation-like wave (bright zone) is seen sweeping clockwise**

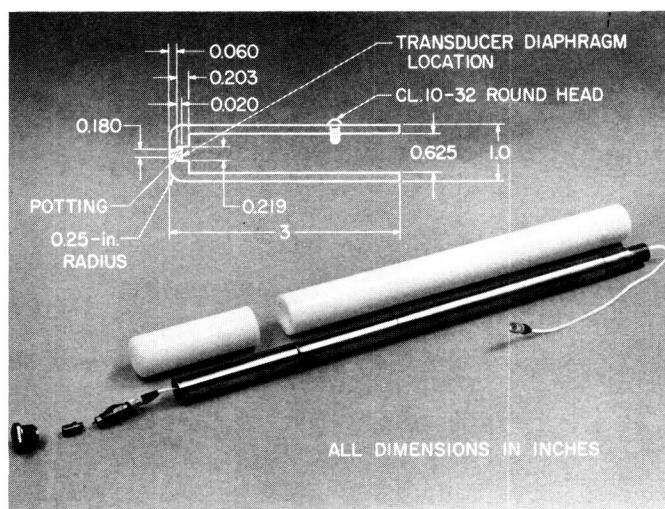


**Fig. 10. Exploded view of pressure probe. Inset: details of ablative cap**

shown the Kistler to have a rise time of 4 to 5  $\mu$ sec, accompanied by an overshoot of approximately 100% for an *end*-impinging shock.

Teflon was chosen as the ablative for the probe because it is durable and opaque, and has low thermal conductivity. A heat-transfer study by Parisse (Ref. 3) shows that in an ablative body of low conductivity, at high rates of heat input, the heated zone extends only a very short distance below the surface. This has been confirmed for the probe in a firing in which a thermocouple was placed at what is normally the location of the transducer diaphragm. Heat-soak after the run was minimized by introducing a generous water purge to the fuel and oxidizer manifolds, one at a time. The end of the probe was positioned at the nozzle entrance plane. The thermocouple, housed in Teflon and protected from the 5000-deg gases by 0.080 in. (or less) of silastic compound, reached a maximum temperature of 200°F.

Fig. 12 shows results obtained using an actual transducer in the probe, and a comparison with traces from an identical transducer located nearby on the chamber wall. Both of the transducers are located 13.5 in. from the injector face, and are separated in space by a distance of 2.3 in. They are both located on the same radial line in the chamber. Phase measurements show that the "inner" part of the wave (which passes the probe position) leads the "outer" part (where it intersects with the chamber wall) by approximately 26 deg. Qualitatively, this agrees with corresponding measurements at the injector face (Ref. 1), which also show that the inner part leads the intersection with the curved wall of the chamber.

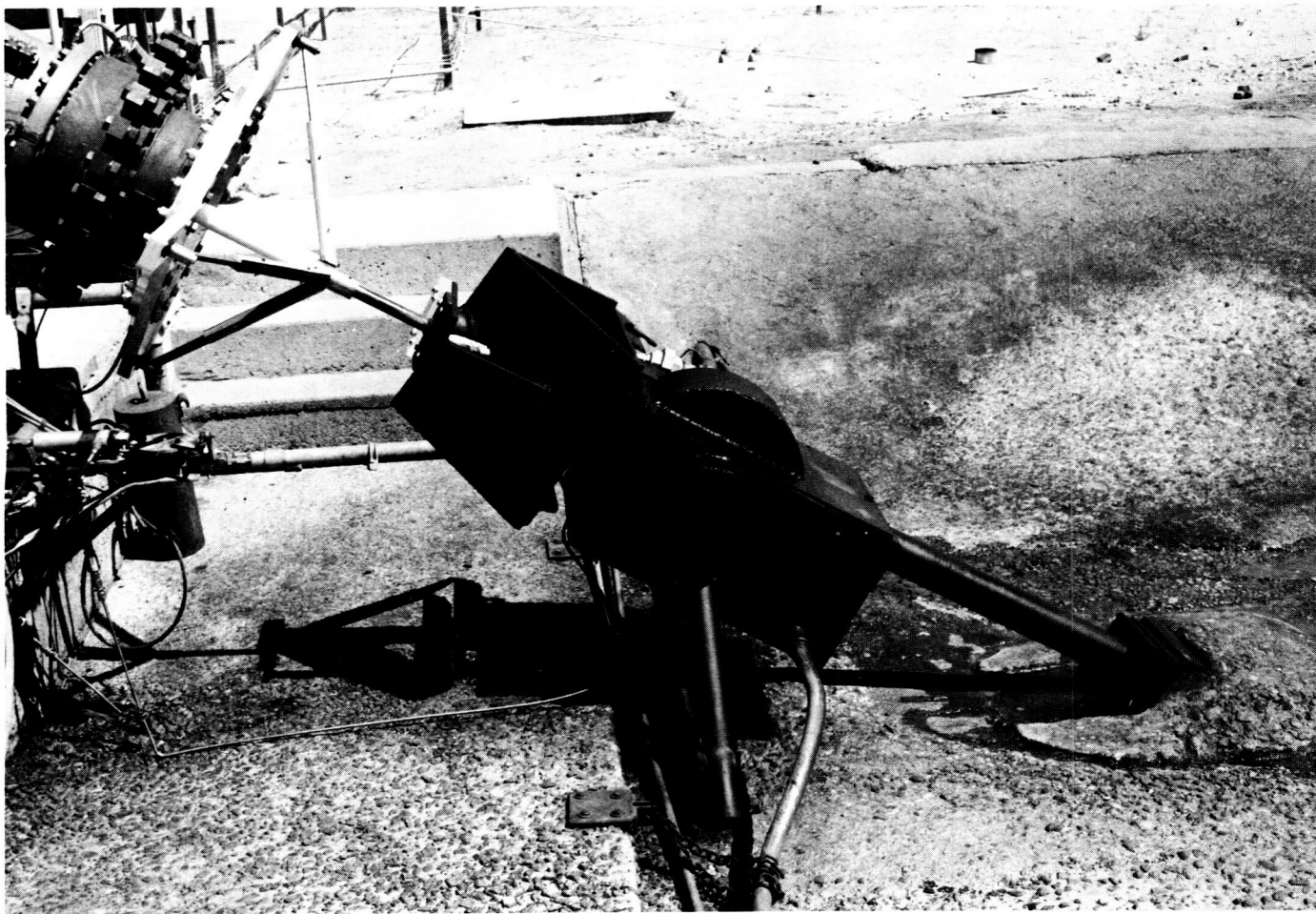


Fig. 11. Pressure probe mounted in off-center position on 11-in. engine

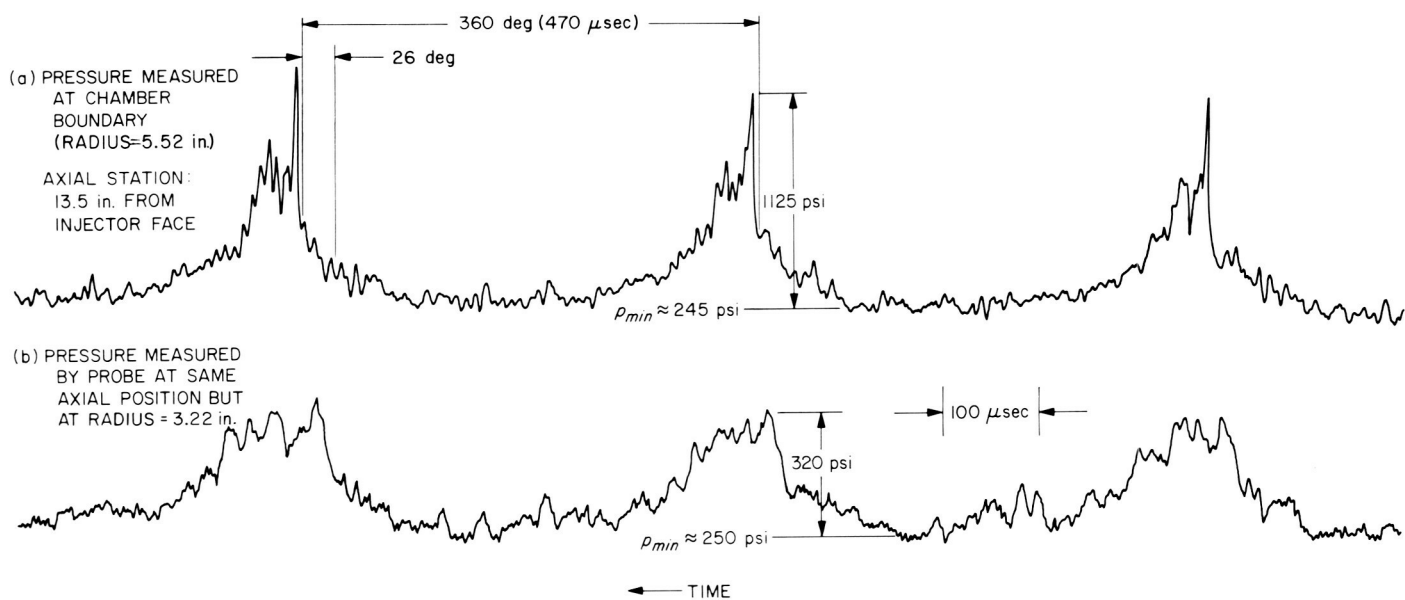


Fig. 12. High-frequency pressure records from probe, and from another Kistler transducer, during the same run

#### 4. Response of Injectors to High-Amplitude Oscillations,

J. W. Woodward and J. G. Solter

When a bomb is detonated in a liquid propellant rocket engine, or high-amplitude waves occur within the combustion chamber for any other reason, almost every conceivable complication arises. In particular, the combustion process is apt to be triggered into a transition to an oscillatory mode which is characterized by steady, high-amplitude pressure waves within the cavity. To understand the mechanism which allows the waves to be sustained, we naturally wish to know how the waves affect their environment and/or boundary conditions. One possibility is that the rapidly varying chamber pressure may have an important effect on the injection process. In the 11-in. engine, RMIR Injector 5, the rotating detonation-like wave gave transient local pressures (at the injector face) of several times the propellant feed pressure. When this occurs, the momentum of the propellant in the feed system is important in helping to keep the injection rate relatively steady.

The coupling of *infinitesimal* sinusoidal pressure oscillations and propellant feed line response has been studied a number of times in connection with low-frequency oscillations, or "chugging." In Summerfield's analysis (Ref. 4), the liquid was considered incompressible, but later studies (e.g., Refs. 5 and 6) by other authors included the effects of wave propagation in the (compressible) liquid propellant itself. Reardon and Waugh (Ref. 7) extended this type of study to medium- and high-frequency oscillations.

Recent developments in high-frequency pressure measurement and in stability rating techniques now make it desirable to investigate feed system response under pressure variations of very high amplitude.

**a. The model.** For the present analysis, a simple model was formulated in order to obtain a qualitative idea of how the flow in the JPL resonant combustion experimental engines, and other engines, might be affected by high-amplitude, or "nonlinear" oscillations. The element type considered was the unlike impinging doublet. The geometry used for individual orifices is shown in Fig. 13. The following assumptions were made: the fluid comes from a manifold of infinite cross-sectional area, and is fed at a constant manifold pressure,  $P_0$ ; changes in the potential energy of the fluid (e.g., due to the acceleration of gravity) are negligible; the velocity of the fluid is uniform at all points on a given cross section ("flat" velocity profile); viscous effects can be computed using standard empirical

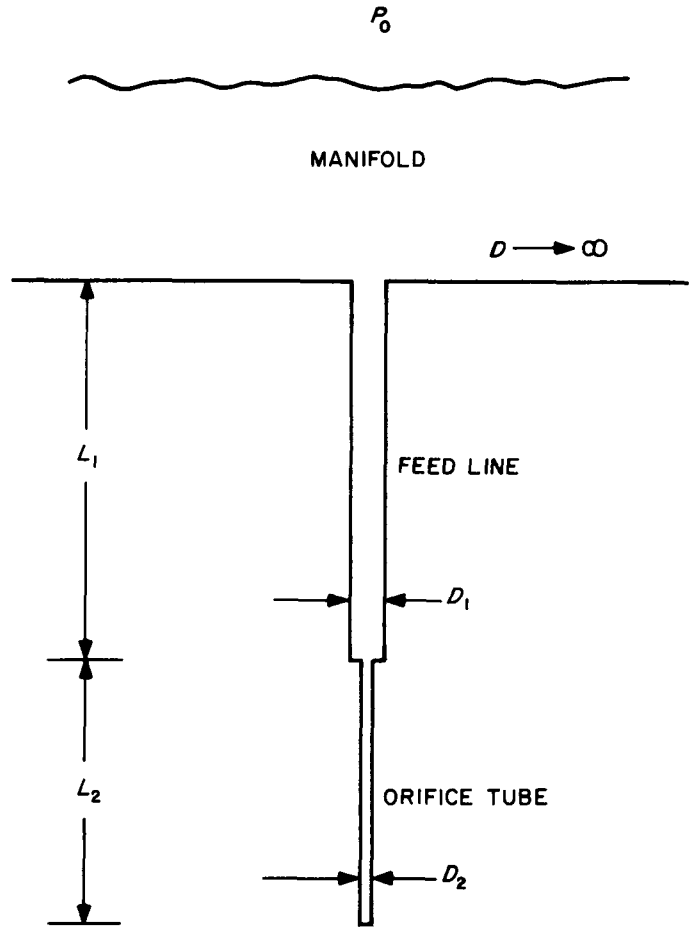


Fig. 13. Feed-system model for a single orifice

laws applying to steady flow in smooth-walled tubes; and, the downstream pressure controlling orifice flow is the pressure measured by a transducer at the same radius on the injector face.

The kinetic energy content of a given volume element is then a result of input by convection, pressure work, and viscous losses. The rate of change of the total kinetic energy,  $K_{tot}$ , in the system is given (Ref. 8) by

$$\frac{d}{dt}(K_{tot}) = -\Delta \left[ \left( \frac{1}{2} v^2 + \frac{p}{\rho} \right) w \right] - E_r \quad (1)$$

where

$t$  = time

$v$  = flow velocity

$p$  = pressure

$\rho$  = the liquid density (taken to be constant)

$w$  = the mass rate of flow

$E_v$  = the rate of viscous loss

$\Delta$  = exit value minus entrance value

As shown in Fig. 13, subscript 1 refers to the feed tube (a flexible hose on the JPL engines, but considered rigid here), and subscript 2 refers to the orifice tube.

$K_{tot}$ ,  $w$ , and  $v_1$  are given by

$$K_{tot} = \int_V \frac{1}{2} \rho v^2 dV \quad (2)$$

$$w = \rho v_2 \frac{\pi}{4} D_2^2 \quad (3)$$

$$v_1 = \left( \frac{D_2}{D_1} \right)^2 v_2 \quad (4)$$

where  $V$  is the total volume of the fluid. Neglecting contraction effects on local velocities, Eq. (2) is written as

$$K_{tot} = \frac{\rho}{2} \left( v_1^2 \frac{\pi}{4} D_1^2 L_1 + v_2^2 \frac{\pi}{4} D_2^2 L_2 \right)$$

where  $D$  is diameter, and  $L$  is length.

Using Eq. (4), then simplifying, we have

$$K_{tot} = \frac{\pi}{8} \rho v_2^2 D_2^2 \left[ \left( \frac{D_2}{D_1} \right)^2 L_1 + L_2 \right]$$

Differentiation gives

$$\frac{d}{dt}(K_{tot}) = \frac{\pi}{4} \rho D_2^2 \left[ \left( \frac{D_2}{D_1} \right)^2 L_1 + L_2 \right] v_2 \frac{dv_2}{dt} \quad (5)$$

as the left-hand side of Eq. (1). Now we consider the right-hand side. The work done by the pressure difference is

$$-\Delta \left( \frac{P}{\rho} \right) = \frac{P_0 - P_2(t)}{\rho} \quad (6)$$

where  $P_2(t)$  is the time-dependent chamber pressure, and is taken directly from experimental measurements.

For the viscous loss  $E_v$  in Eq. (1), four terms are included, treating losses in the straight sections of the feed tube and orifice tube, and at the entrances to the feed and orifice tubes:

$$E_v = |w| \left\{ 2v_1^2 \frac{L_1}{D_1} f_1 + 2v_2^2 \frac{L_2}{D_2} f_2 + \frac{1}{2} v_1^2 f_c + \frac{1}{2} v_2^2 f_c \right. \\ \left. \times \left[ 1 - K \left( \frac{D_2}{D_1} \right)^2 \right] \right\} \quad (7)$$

The friction factors  $f_i$  ( $i = 1, 2$ ) are functions of the Reynolds number

$$Re_i = \frac{D_i v_i \rho}{\mu}$$

where  $\mu$  is viscosity. For  $Re_i > 2100$ , an expression applying to hydraulically smooth tubes is used (Ref. 9)

$$f_i = 0.0791 (Re_i)^{-0.25}$$

If the flow should become so slow as to fall in the laminar flow regime ( $Re < 2100$ ), we arbitrarily use (Ref. 9)

$$f_i = 16 (Re_i)^{-1}$$

[although a flat velocity profile is still assumed for the kinetic energy terms in Eqs. (1) and (2)]. The contraction loss factor in Eq. (7) is (Ref. 10)

$$f_c = 0.05, \text{ with } K = 0, \text{ for a rounded entrance}$$

$$f_c = 0.45, \text{ with } K = 1, \text{ for a sudden contraction. (For this case we must mention an additional assumption: that there is no cavitation at the entrance.)}$$

Eq. (7) can be simplified by using Eq. (4) to eliminate  $v_1$ .

$$E_v = |w| v_2^2 \left\{ 2 \left( \frac{D_2}{D_1} \right)^5 \frac{L_1}{D_2} f_1 + 2 \frac{L_2}{D_2} f_2 + \frac{f_c}{2} \right. \\ \left. \times \left[ 1 - K \left( \frac{D_2}{D_1} \right)^2 + \left( \frac{D_2}{D_1} \right)^4 \right] \right\} \quad (8)$$

After substituting Eqs. (5), (6), and (8) into Eq. (1), we solve for  $dv_2/dt$  and obtain

$$\begin{aligned} \frac{dv_2}{dt} = & \left[ \frac{P_0 - P_2(t)}{\rho} - v_2^2 \left\{ \frac{1}{2} + \frac{f_c}{2} \right. \right. \\ & \times \left[ 1 - K \left( \frac{D_2}{D_1} \right)^2 + \left( \frac{D_2}{D_1} \right)^4 \right] + 2 \left( \frac{D_2}{D_1} \right)^5 \frac{L_1}{D_2} f_1 \\ & \left. \left. + 2 \left( \frac{L_2}{D_2} \right) f_2 \right\} \right] \left[ \left( \frac{D_2}{D_1} \right)^2 L_1 + L_2 \right]^{-1} \end{aligned} \tag{9}$$

The appropriate value of the reservoir pressure  $P_0$  is obtained by setting the left-hand side of Eq. (9) equal to zero and using the steady-state value of  $v_2$  to solve for  $P_0$ .

Eq. (9) is integrated using the fourth-order process of Runge-Kutta-Gill (Ref. 11).  $P_2(t)$  is represented by 50 values taken from experimental measurements for a single cycle. Linear interpolation is used to obtain a pressure at the midpoint of each interval. For convenience, the 50 experimental values are considered to be representative of the entire resonant period, and are used repetitiously for the desired number of cycles. For an injector with no feed tube, we simply set  $D_2/D_1$  equal to zero.

Table 1 gives the engine parameters used in the calculations for all cases, and Table 2 gives the calculated pressure drops for the three injectors studied.

**b. Results.** Since the orifice exit pressure  $P_2(t)$  in the model is arbitrary, it was possible to use numerical pressure values obtained from actual experiments on RMIR Injector 5. A single cycle was chosen, as representative of the entire resonant period, for each of two different positions on the injector face (since the wave characteristics vary radially). The "typical" cycle was imposed

Table 2. Calculated injector pressure drops

Oxidizer			
Orifice type	Orifice length, in.	$D_2/D_1$	$P_{\text{manifold}} - P_{\text{chamber}}$
100 D	17.3	0.693	238
20 D	3.5	0	107
3 D sharp entry	0.52	0	116
Fuel			
Orifice type	Orifice length, in.	$D_2/D_1$	$P_{\text{manifold}} - P_{\text{chamber}}$
100 D	9.9	0.527	528
20 D	2.0	0	211
3 D sharp entry	0.29	0	207

repeatedly on the orifice exits up to 200 times, simulating the length of the resonant period in the experiments. Note that the analysis differs from most others in that the local chamber pressure is treated as a *known* quantity; we avoid the subject of its own dependence on the feed line's response.

Fig. 14(a) and (b) shows the calculated response of an injector element located at a radius  $R$  of 3.2 in. on the 11-in.-diameter RMIR Injector 5. The pressure history of the typical cycle is shown by the lower graph in Fig. 14(a). The upper graph shows oxidizer injection velocity  $v_{ox}$ . High-frequency response is slight, due to the high total momentum of the fluid in the orifice and feed line; however, the integrated average orifice exit pressure is greater than the steady-state chamber pressure, and the average velocity shows a corresponding drift toward a lower value, to which it has nearly converged after 100 cycles. Fig. 14(b) shows the fuel velocity  $v_f$  (which converges in less than 100 cycles), and the mixture ratio for the doublet. This local mixture ratio is seen to decrease from 2.8 to 2.4.

Near the center of the engine the pressure fluctuations are comparatively small, but the average pressure is *lower* than the preresonant value. This gives an increase in injection rate, as shown in Fig. 15(a) and (b), along with the pressure history and mixture ratio.

We now investigate the effects of the same pressure histories on an injector element having shorter orifices. The RMIR Injector 5 had orifice lengths equal to 100 diameters; leading to these were feed tubes, approximately 2 ft long (the actual figures are given in Table 2). The feed tubes and orifices had smoothly contoured entries.

Table 1. Engine parameters used for all cases

	RFNA	Corporal fuel
Viscosity, cp	1.37	4.76
Density, lb/ft <sup>3</sup>	97.0	66.9
Orifice diameter, in.	.173	.0986
Feed tube length <sup>a</sup> , ft	1.75	2.00
Injection velocity, ft/sec	86.0	137.0
Chamber pressure, psia	332	
Design mixture ratio	2.8	
Frequency of oscillation, cps	2105	
<sup>a</sup> Applicable only for $L = 100 D$ ( $D_2/D_1 \neq 0$ )		

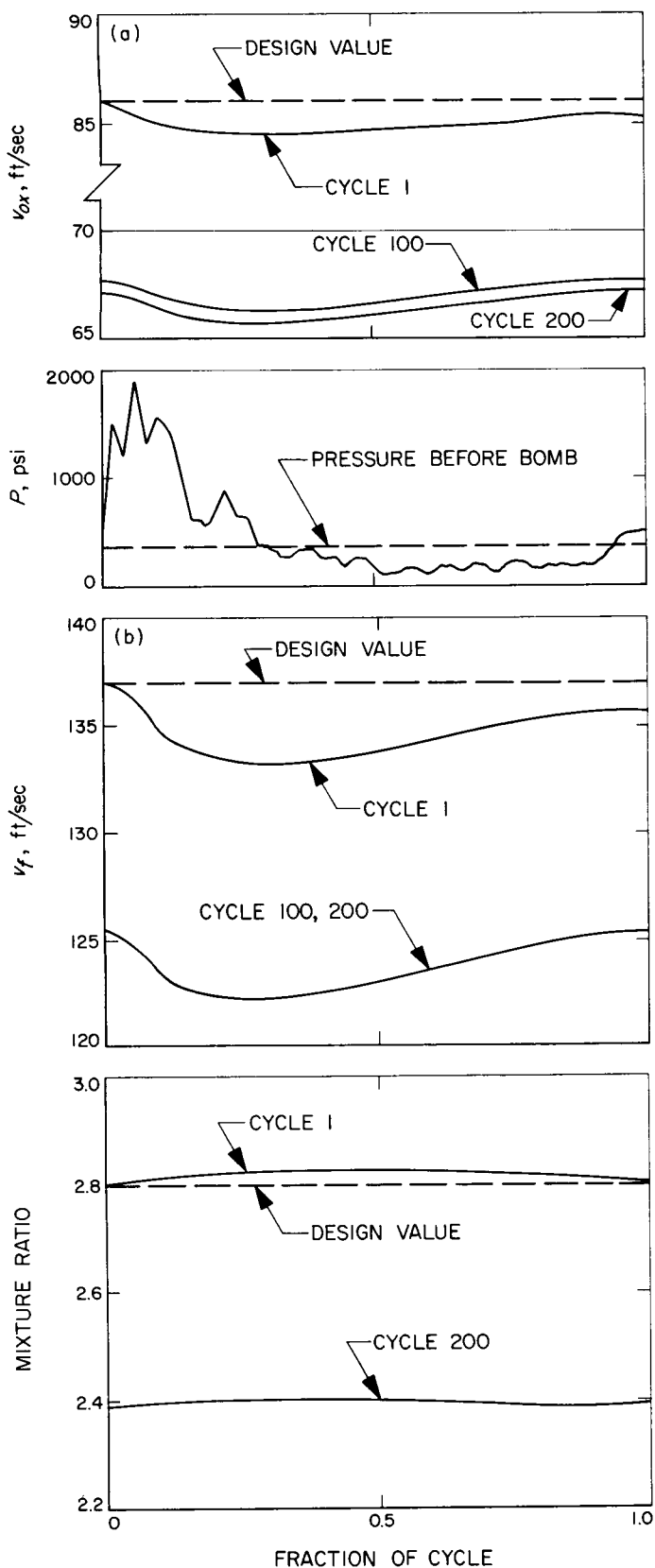


Fig. 14. Injector response at  $R = 3.2$  in.;  $L = 100 D$

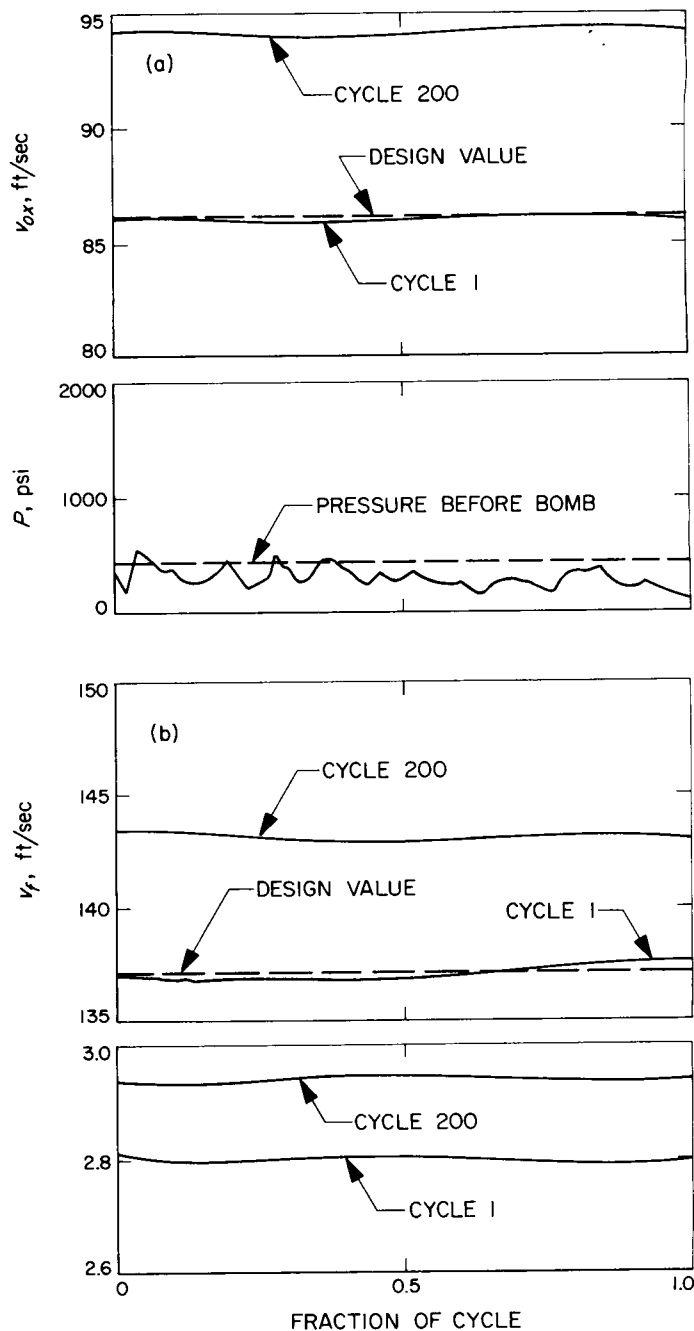


Fig. 15. Injector response at  $R = 0.8$  in.;  $L = 100 D$

We now consider an injector with no feed tubes and with orifices 20 diameters in length, leading from an infinite manifold directly to the chamber. These orifices are assumed to have smoothly contoured entries at the manifold end. Other parameters are kept constant, except for the calculated manifold pressure, which must be lower to give the same design flow rates used in the previous injector.

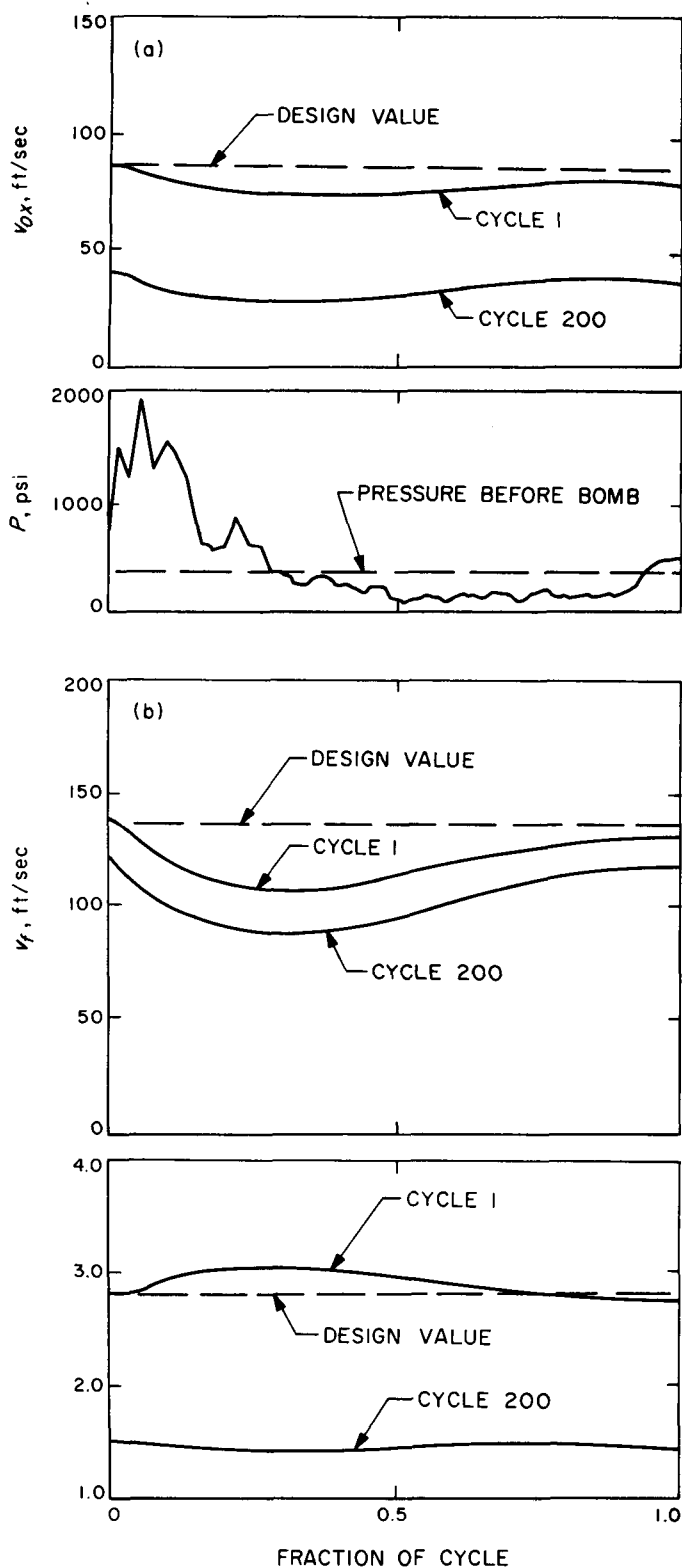


Fig. 16. Injector response at  $R = 3.2$  in.;  $L = 20 D$

Fig. 16(a) and (b) gives the response of the shorter orifices at a radius of 3.2 in. on the injector face. These curves may be compared to Fig. 14(a) and (b); however, note that the velocity scales are different. As expected, the shorter orifices show somewhat larger excursions of velocities and mixture ratio from the design values. The flow rates near the center of the engine (not shown) increase more strongly than those in RMIR Injector 5, so that now there is a more marked radial variation. In general, the calculated response of this injector is appreciable, but not spectacular.

Next we consider orifices which are more representative of current designs for flight-type engines. For this case, we again omit the feed tubes, so that the orifices lead directly from manifolds to chamber. Each orifice has a length equal to three times its diameter, and has a sharp entry. This type of orifice requires approximately the same manifold pressures as the orifices in the previous case, because of the high energy losses associated with sharp entries (as compared to those for contoured entries). *Flow separation is ignored.*

The effect of the pressure oscillations, at  $R = 3.2$  in. is shown in Fig. 17. Early in the first cycle, the fuel velocity changes direction, and the instantaneous mixture ratio becomes infinite. The oxidizer velocity does not change

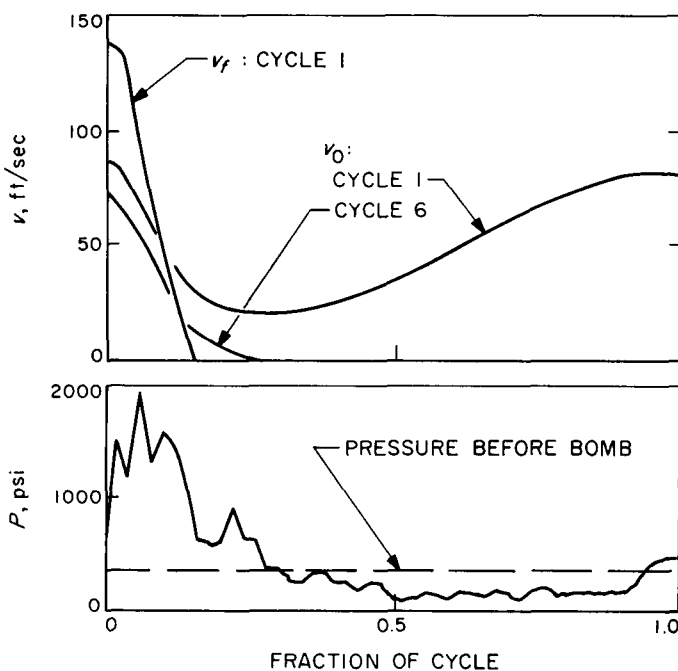


Fig. 17. Injector response at  $R = 3.2$  in.;  $L = 3 D$

sign until the sixth cycle. Beyond this point, the calculation is meaningless, but we may visualize a violent reciprocating motion of the liquids and gases in the orifices for the remainder of the resonant period.

Fig. 18 shows the response of a similar element near the center of the injector face. There is a strong contrast between the behavior of this element and that of the previous element, 2.4 in. farther away from the engine axis.

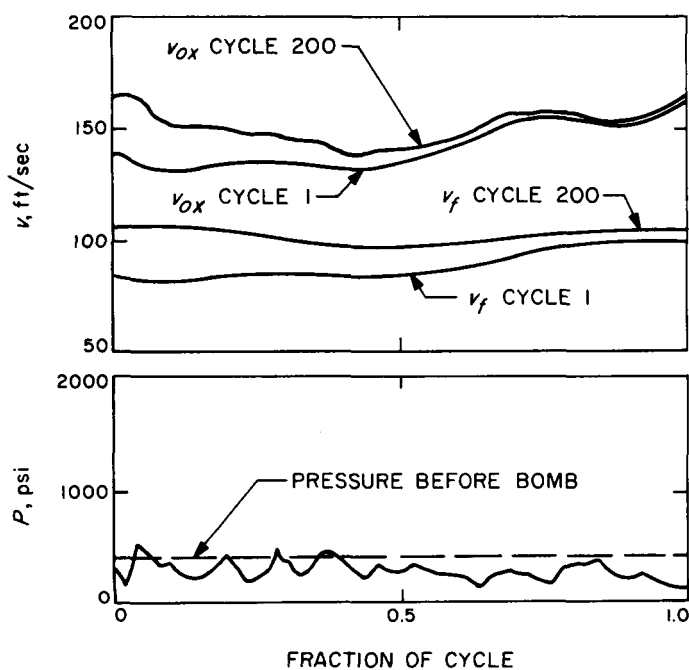


Fig. 18. Injector response at  $R = 0.8$  in.;  $L = 3 D$

Fig. 19 shows the convergence characteristics for most of the cases mentioned above. The velocity at the end of each cycle is plotted versus accumulated number of cycles. The shortest orifices converge quickly to their new average velocities. For the case of  $L/D = 100$  (RMIR Injector 5), convergence is attained after approximately 100 cycles, indicating that the injection process does reach a steady mean (though still oscillatory) value during the experimental firings. Further calculations, not shown, indicated that while the high-frequency response of the orifices (especially the shorter ones) is strongly affected by waveform, the slower drift of average flow rate is determined almost completely by the magnitude of the integrated average pressure, and not by the details of the wave itself.

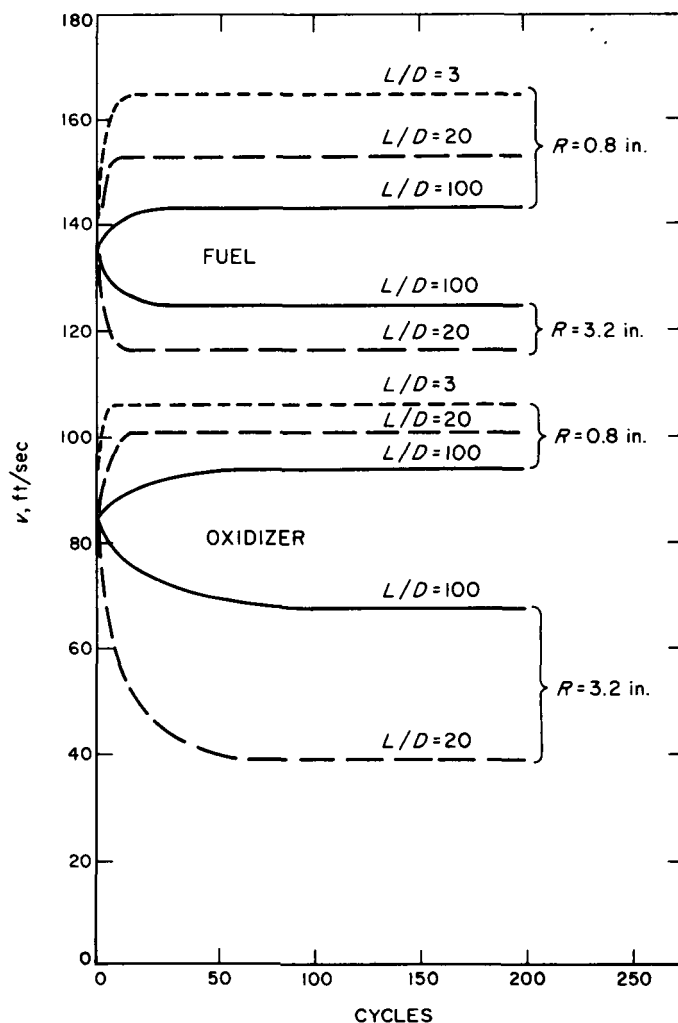


Fig. 19. Velocity at end of cycle

**c. Discussion.** Although the assumptions used severely restrict the drawing of conclusions from the results summarized, it does seem likely that RMIR Injector 5 is only slightly affected by the pressure oscillations, at least over very short intervals of time, provided a feed-system resonance does not exist. When the flow rates have converged to new levels, appreciable radial variations in average mass flow and mixture ratio are indicated; however, in this respect the calculated variations are susceptible to error as resulting from inaccuracies in the experimental determination of chamber pressure. Ignoring the effects of propellant compressibility, then, it seems that to a first approximation the research injector may be fairly well isolated from the high-frequency pressure variations in the combustion chamber. Consideration of boundary layer effects within the long feed passages might indicate even greater suppression of injection rate variations.

For the flight-type orifices, the admittedly crude model gives quite a different picture. We note that the first pressure cycle, which produced flow reversal in the fuel line (Fig. 17) can be likened to a bomb pulse. When the flow reverses, there is a possibility that gases may enter the orifices. The injection process is completely transformed, and this might alter the stability of the combustion process: under the new conditions, the wave may even be self-annihilating. This points out a danger of basing dynamic stability tests on results produced by a large bomb pulse: the initial shock wave, and its many reflections from other surfaces in the chamber, may so alter the injection process that the wave is not sustained, although a smaller bomb might have led to permanent oscillations. Indeed, cases are known in which an engine was stable to a large pulse, but unstable to a smaller one.

The reversal of flow in a short orifice also leads to the possibility that gases may be pumped back into the manifold. A sobering thought is the idea that hot combustion product gases may enter a manifold which contains a monopropellant.

When no monopropellants are involved, the effect might be less obvious, but no less important. If gas bubbles are present in the manifold and a foam is injected into the combustion chamber, the nonlinear oscillations might again be self-annihilating. Few designers would knowingly stake engine stability on the reproducibility of this process; but instances are known in which engines have been flight-qualified or even man-rated, and suddenly, in a routine test, have developed instability and destroyed themselves. Furthermore, even in systematic research studies of flight-engine designs, it is well known that resonance characteristics are not usually reproducible. They can hardly be expected to be, if the injector-end boundary condition varies in a random manner.

It seems advisable that long orifices and feed lines be used for studies of those resonant combustion phenomena which are not believed to be caused by injection-rate variations. We might ask whether the same principles should be applied to flight engines. A slight weight and volume penalty would be involved, but a 1% increase in combustion efficiency, which might be realized by using the more hydraulically stable long orifices, could result in a saving of many tons of propellant for a given large booster mission. Cost-wise, it seems possible that long orifices would be more favorable, because for a number of reasons they increase the stability and reproducibility of the injection process (Ref. 12). Examination of large engine develop-

ment programs shows that a lack of predictable, dependable combustion behavior has been extremely costly.

N67-15731

## B. Sterilizable Liquid Propulsion System<sup>\*</sup>

Development, T. A. Groudie

### 1. Introduction

Monopropellant-hydrazine is a candidate energy source for use in the *Voyager* capsule for such purposes as capsule deflection from orbit, turboalternator power supply, and attitude control during aerodynamic entry. The extensive JPL experience with similar monopropellant propulsion systems during the *Ranger* and *Mariner* programs, and the resulting surplus hardware from these programs, prompted investigations into the heat-sterilizability of this propellant. Some earlier work with small samples and tanks is described in SPS 37-35, Vol. IV, p. 155. The success of this work prompted JPL to assemble and test a complete system using available surplus hardware.

The first system constructed (Figs. 20 and 21) consisted of the following components:

- (1) A heavyweight spherical stainless steel propellant tank with a metal (aluminum) diaphragm clamped at the equator of the tank.

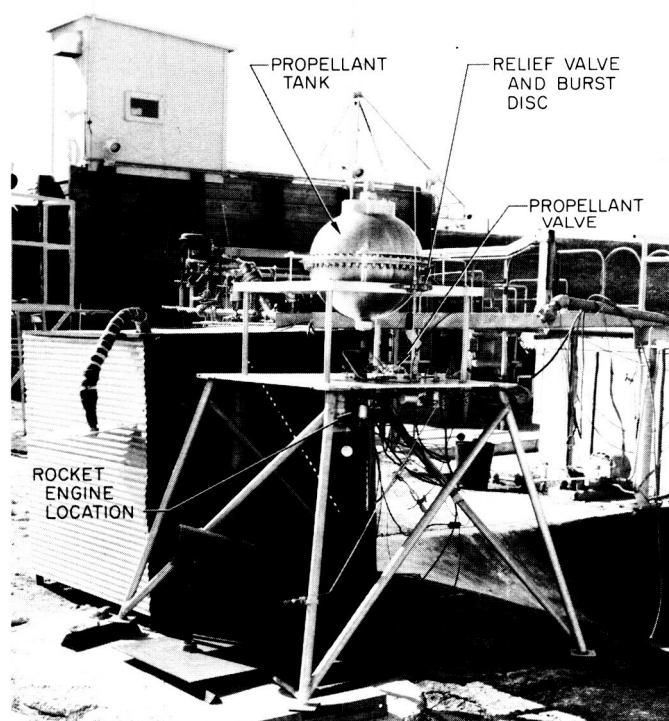
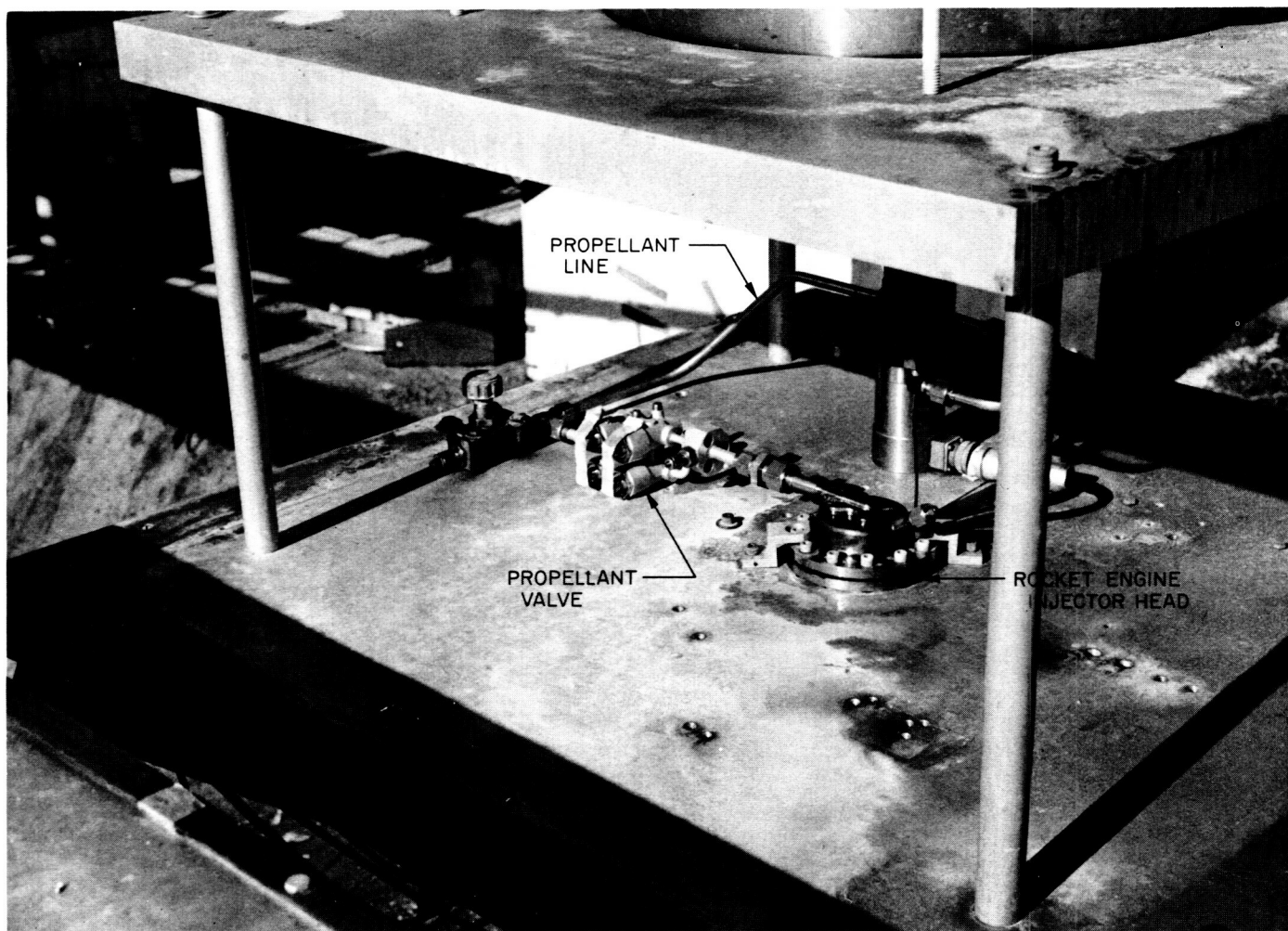


Fig. 20. System configuration



**Fig. 21. Injector valve assembly**

- (2) A *Mariner* Mars 1964-type squib-actuated propellant valve of aluminum construction.
- (3) A 50-lb<sub>f</sub> monopropellant rocket engine with an expansion area ratio  $\epsilon$  of 4:1. The chamber was packed with Shell-405 spontaneous catalyst, as illustrated in Fig. 22.

These individual components were assembled on a convenient structure. After leak-testing, the fuel tank was filled with approximately 50 lb<sub>m</sub> of hydrazine, N<sub>2</sub>H<sub>4</sub> (50% tank ullage), allowed to stand for 20 min and then removed from the tank. This was done in an attempt to remove residual foreign matter that was generated during assembly of the components and to passivate the assembly. The tank was again filled with approximately 50 lb<sub>m</sub> of N<sub>2</sub>H<sub>4</sub>, and then 5 lb<sub>m</sub> was removed to provide an ullage space on the fuel side of the diaphragm since there would be liquid expansion due to increased temperature.

Table 3 lists the heat sterilization cycles used for this test series. In each case the maximum or minimum temperature (275°F or ambient) was considered to be attained after it had stabilized for approximately 1 hr. However, in practice this technique proved to be difficult to maintain, particularly at night, because of the combined effects of an undersized heater and a large ambient temperature gradient. Fig. 23 shows the propulsion system covered with its thermal box, and Fig. 24 is a schematic of the total system and support equipment.

Table 4 lists the instrumentation parameters that were monitored on the system. A continuous temperature and pressure record was kept during and between cycles.

Table 5 summarizes data for Test Series 1. The first line of each cycle indicates the initial conditions and the last line indicates the conditions after return to ambient.

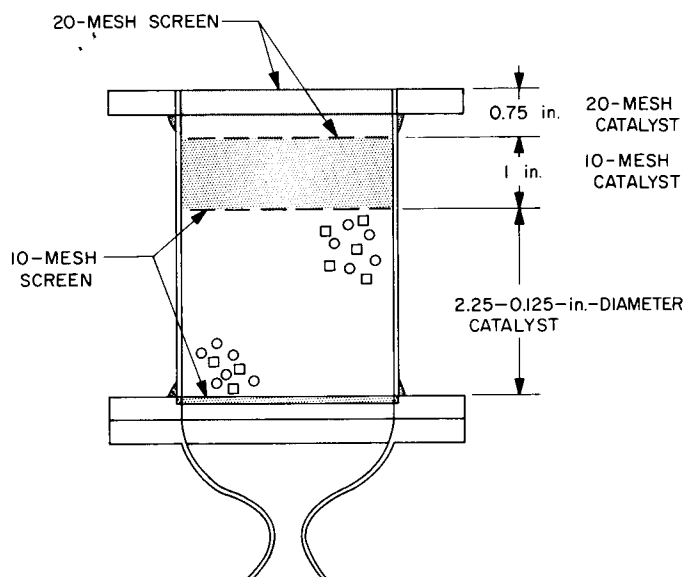


Fig. 22. Rocket engine bed packing configuration

Table 3. Sterilization cycle

Cycle 1 53 hr at  $275 \pm 5^\circ$ , measured from time of steady-state temperature equalization. At the end of 53 hr, temperature cools to ambient.

Repeat for 5 additional cycles (total of 6 cycles).

Note: The system shall not be removed or modified during the 6-cycle period. The system shall be fired in position at the end of the 6th cycle and engine performance ( $c^*$ ) compared with presterilization performance.

Table 4. Instrumentation parameters

Rocket engine chamber pressure ( $p_c$ )  
 Propellant tank pressure ( $P_T$ )  
 Propellant line pressure ( $P_{LF}$ )  
 Rocket engine chamber temperature ( $T_c$ )  
 Propellant tank temperature ( $T_T$ )  
 Propellant line temperature ( $T_{LF}$ )  
 Thermal box temperature ( $T_B$ )

At the end of Cycle 6, the data indicated a very low propellant tank pressure for that particular ambient temperature, and 0 psig propellant line pressure. A visual check was made of the system by removing the thermal box. A white deposit was observed on some of the lower structural members and on the mounting plate near the hand-fill valves in the propellant circuit. The liquid side of the diaphragm was pressurized with  $\text{GN}_2$  to check for leaks. Two GSE fill valve stem packings (Kel-F material) leaked very badly and had, in fact, disintegrated. The packing could not stand the combination of high temperature and

Table 5. Data summary for Test Series 1

Test	Hour	$T_{c_i}$ °F	$T_{LF_i}$ °F	$T_{B_i}$ °F	$T_{T_i}$ °F	$P_{LF_i}$ psig	$P_{T_i}$ psig	Cycle
1	0845	—	—	—	26	—	260	1
4	1600	—	276	294	273	403	403	
5	1630	—	276	—	270	403	404	
6	1415	76	81	86	84	282	—	
6	1500	—	—	—	78	—	282	2
7	0100	—	273	277	—	385	—	
8	0800	219	274	281	259	388	—	
9	0600	—	276	283	—	388	—	
10	0800	—	44	47	41	262	262	3
10	1501	—	66	—	70	293	297	
11	0100	—	272	285	—	420	—	
11	1400	225	280	294	274	402	399	
13	0600	—	279	285	—	—	402	4
14	0600	—	80	—	—	267	—	
14	0600	—	—	—	80	00	267	
14	1800	—	275	285	—	380	—	
15	1350	219	277	289	266	384	382	5
16	1630	229	272	296	278	388	380	
18	0900	51	51	—	57	256	—	
18	0900	—	—	—	51	—	256	
18	1800	—	270	294	—	363	—	6
19	0800	235	272	294	280	369	367	
20	2300	—	45	—	—	—	250	
21	2300	—	40	—	—	—	248	
22	0800	238	2682	294	259	356	357	7
23	1610	233	260	294	277	369	369	
24	0100	AC circuit breaker failed					—	
24	1330	150	126	128	158	282	282	
29	0800	—	102	76	—	—	149	

corrosive action of the hydrazine; thus, the propellant had simply leaked out through both valve stems.

The system was then disassembled and the rocket engine fired under the same conditions as those prior to the sterilization test. The performance measured during this firing was within 3% of the pretest value ( $c^* = 4230$  ft/sec versus 4305 ft/sec previously), and the start transient data did not indicate a significant change in response time.

The diaphragm from the propellant tank was removed and examined. The portion of the diaphragm in contact with liquid  $\text{N}_2\text{H}_4$  appeared uniformly grayed; the nitrogen side appeared unchanged. But the portion in which one would expect  $\text{N}_2\text{H}_4$  vapor to be present had been severely chemically attacked, as was the corresponding tank hemisphere (Fig. 25).



Fig. 23. System with thermal box

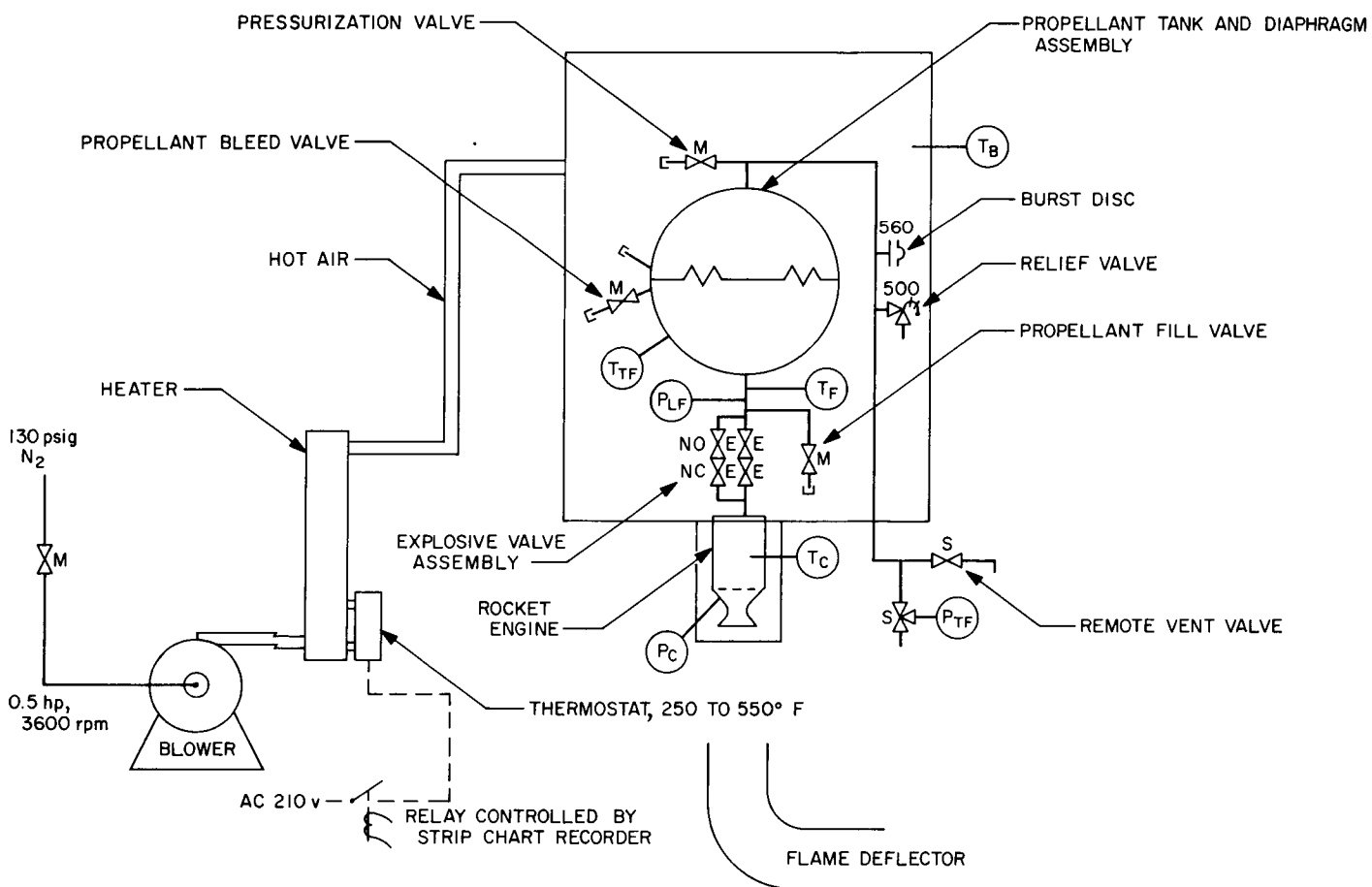


Fig. 24. System schematic

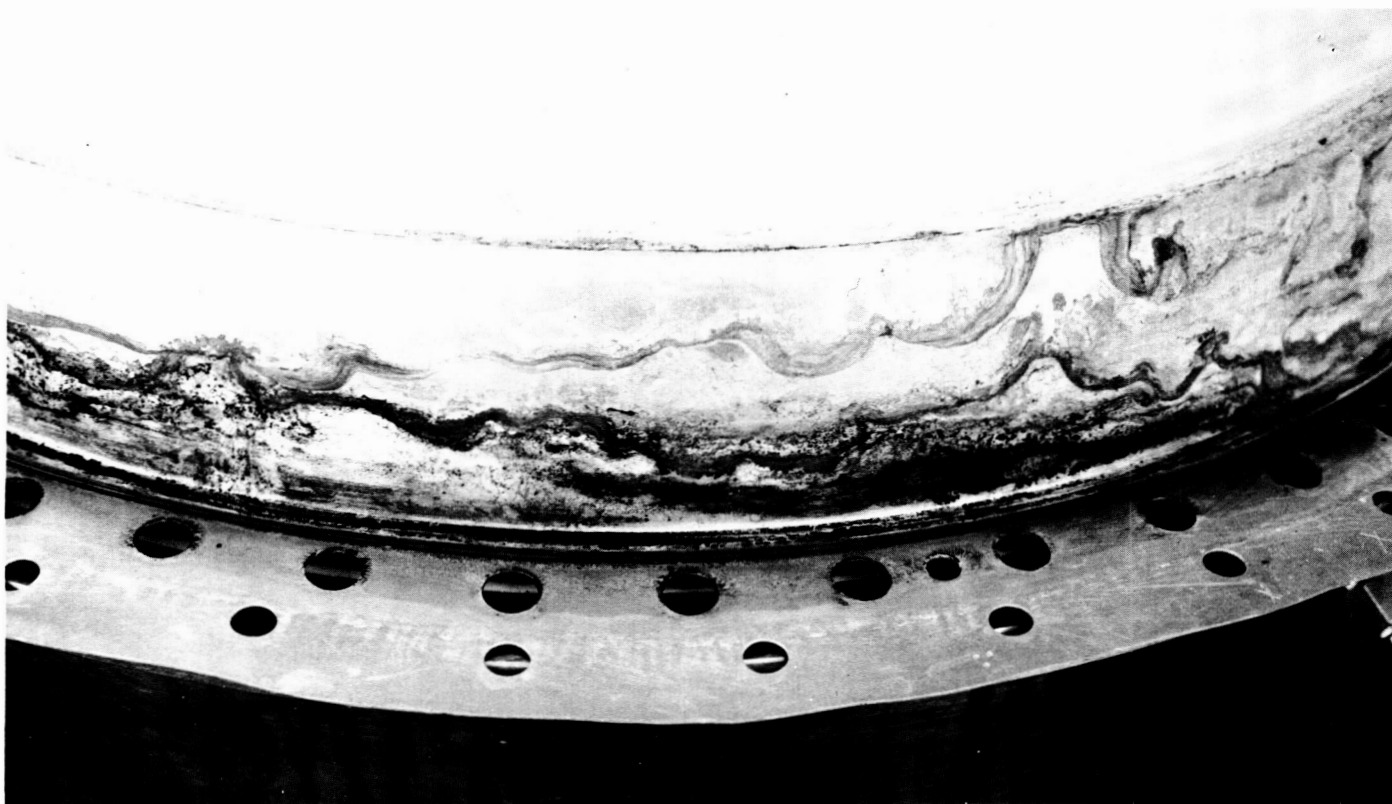


Fig. 25. Propellant diaphragm

In summary, the ability of a monopropellant-hydrazine system to undergo heat cycling was demonstrated, although it was not possible to conduct a post-test system firing because of the failure of two GSE valve assemblies during cool-down from the last thermal cycle. The monopropellant thrust chamber assembly did perform satisfactorily, however. Both stainless steel and aluminum exhibited evidence of a severe chemical attack from the propellant vapor. Further work is now in progress to investigate the problems associated with thermal cycling of liquid propulsion systems, both monopropellant and bipropellant.

N67-15732

## C. Injector Development: Investigation of Propellant Sheets, R. W. Riebling

### 1. Introduction

When a jet of liquid from a circular orifice is directed tangentially against a solid, concave deflector surface, it spreads to form a thin liquid sheet of width  $w$  (Fig. 26). Upon leaving the deflectors, these free sheets spread through an angle  $\beta$  before finally breaking up into drop-lets. However, the sheets do not generally exit tangen-

tially. Rather, the axes of the sheets are deflected through an angle  $\delta$  away from the tangents to the deflector surfaces (Fig. 26).

Injector elements incorporating this effect are being developed at JPL because they offer certain advantages over the more conventional impinging-jet varieties [SPS 37-41, Vol. V, (Confidential)]. An applied research program was conducted to determine the manner in which the dimensions and spatial orientation of such liquid sheets, as well as the velocity and mass distribution within them, vary with deflector geometry, injection velocity, and propellant physical properties. Such information is necessary to the intelligent design of all injector elements based on the thin-sheet concept.

Earlier work (reported in Vol. IV of succeeding SPS's, beginning with SPS 37-37) showed that the sheet dimensions and orientation were essentially independent of the Reynolds and Weber numbers of the flowing liquids (and therefore of fluid velocity, fluid physical properties, and the size of the sheet-formation device). Rather,  $w$ ,  $\beta$ , and  $\delta$  (Fig. 26) were found to depend only on several dimensionless ratios defined by the deflector and orifice geometry, the most useful being the overhang ratio,  $h/d_o$ .

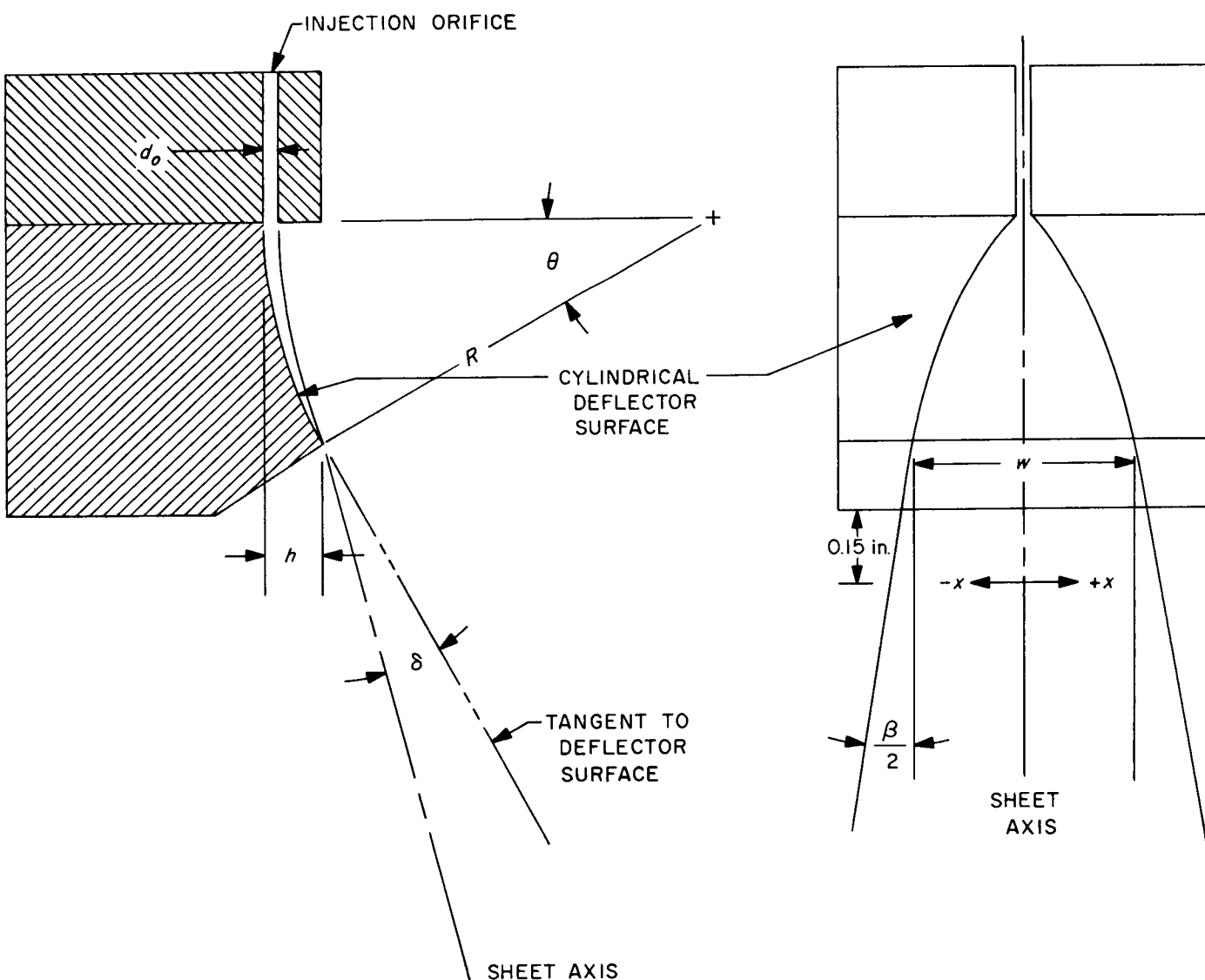


Fig. 26. Schematic of experimental apparatus

Because of the complete geometric and dynamic similarity, it became possible to predict these sheet dimensions for deflectors of nearly any size by means of equations such as those presented in SPS 37-39, Vol. IV, p. 132.

This report presents the results of the final phase of the investigation, in which generalized correlations for the distributions of mass flow rate and fluid velocity across flowing sheets were obtained. From these it was possible to derive the variation of sheet thickness (a dimension not accurately measurable for sheets of the size used in rocket engine injectors) with sheet width.

## 2. Sheet Mass Flow-Rate Distribution

The mass flux per unit width of sheet,  $d\dot{w}/dx$ , may be normalized by dividing it by the fluid density, fluid velocity, and orifice diameter to obtain a dimensionless mass distribution parameter  $\mathcal{M}$ :

$$\mathcal{M} \equiv \frac{d\dot{w}}{dx} \cdot \frac{144}{\rho \bar{V} d_o} \quad (1)$$

From dimensional considerations, it would be expected that  $\mathcal{M}$  should be a function of the velocity and liquid properties, as well as of geometric factors:

$$\mathcal{M} = f \left[ \frac{x}{d_o}, \frac{R}{d_o}, \theta, Re, We \right] \quad (2)$$

However, if Reynolds number  $Re$ , and Weber number  $We$ , effects were negligible over the ranges of variables studied, as was found to be the case for the sheet dimensions (SPS 37-39, Vol. IV), Eq. (2) would reduce to

$$\mathcal{M} \cong f_1 \left[ \frac{x}{d_o}, \frac{R}{d_o}, \theta \right] \quad (3)$$

Since some of the other sheet dimensions were earlier found to be best correlated with the overhang ratio  $h/d_o$ , it was anticipated that the mass flux distribution might also depend on  $h/d_o$  as well as on  $x/d_o$ . If that were true, substitution of

$$\frac{h}{d_o} = \frac{R}{d_o} (1 - \cos \theta) \quad (4)$$

into Eq. (3) would give

$$\mathcal{M} \cong f_2 \left[ \frac{x}{d_o}, \frac{h}{d_o} \right] \quad (5)$$

which would be a reduction from a five- to a two-parameter dependence. Further, at constant  $h/d_o$ ,

$$\mathcal{M} \cong f_3 \left[ \frac{x}{d_o} \right]_{h/d_o} \quad (6)$$

Eq. (6) implied that, if  $Re$  and  $We$  effects were truly negligible, and if  $h/d_o$  were a valid substitution for  $R/d_o$  and  $\theta$  in the functional relationship of Eq. (3), all deflectors with a constant value of  $h/d_o$  would produce dynamically and geometrically similar sheets (regardless of the fluids, velocities, or physical sizes involved), whose mass distributions would be given by a single curve in which  $\mathcal{M}$  were plotted versus  $x/d_o$ . Varying  $h/d_o$  would then be expected to produce a *family* of general mass flux distribution curves.

To verify this contention, the mass flux per unit width of sheet,  $d\dot{w}/dx$ , was measured by traversing the width of the sheets with a small, flattened-end tube which collected liquid over a known time interval at each station. This device is shown schematically in Fig. 27. The probe was positioned as close to the edge of the deflector as possible (0.15 in.) without disturbing the sheet formation process. Most of the sheets studied were formed on "small" deflectors (0.1- to 0.7-in. radii and 0.018- to 0.040-in. orifice diameters), although a few experiments were made on the "large" deflectors (6.45-in. radii and 0.405-in. orifice diameters) to check the scalability of the results. The test fluids were water and trichlorethylene, flowing at injection velocities ranging between 57 and 142 ft/sec. Corresponding Reynolds numbers ranged between  $1.1 \times 10^4$  and  $3.1 \times 10^5$ , while Weber numbers varied from 60 to approximately 360. All orifices used had length-to-diameter ratios of 100, and the deflector angles ranged between 15 and 45 deg.

Numerous mass distribution curves were obtained, some of which were presented earlier in SPS 37-39, Vol. IV. As a check on the experimental accuracy, integration of these curves gave essentially the total flow rates through the orifices. It was subsequently found that the curves could all be condensed into a few completely general correlations by normalizing both  $d\dot{w}/dx$  and the corresponding distance across the sheet into appropriate dimensionless ratios, as anticipated by Eqs. (1) and (5).

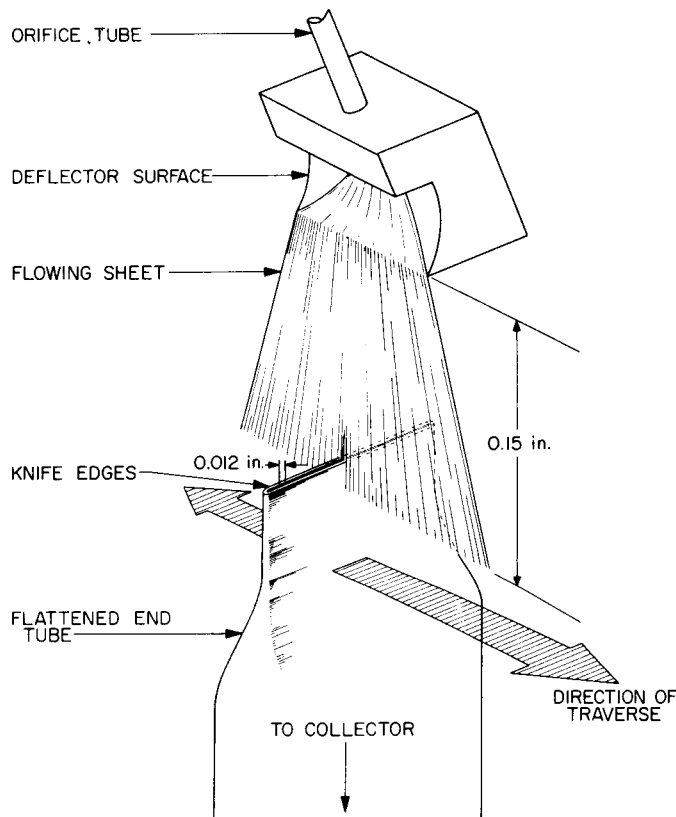


**Fig. 27. Schematic of mass flow rate distribution apparatus**

Some typical normalized mass distribution data are presented in Fig. 28. The ordinate of each curve is the mass distribution parameter  $\mathcal{M}$  (Eq. 1), while the abscissa is  $x/d_o$ , the ratio of distance across the sheet (measured outward from the sheet centerline) to the orifice diameter. Included on each plot is the over-all sheet width-to-diameter ratio at the edge of the deflector. The maximum values of  $x/d_o$  for the distributions of Fig. 28 are greater than those values because they were measured 0.15 in. away from the edges of the deflectors; even in that short distance the sheets spread considerably.

Fig. 28(a) was prepared from data obtained for sheets formed under the widely varying conditions of geometry, Reynolds number, and Weber number already enumerated. The only thing that the six sheets, whose normalized mass distributions are plotted in Fig. 28(a), had in common was their formation by deflector/orifice combinations with an overhang ratio  $h/d_o$  of unity. Similar remarks apply to the plots of Fig. 28(b) and (c), which correlate data for sheets formed by deflectors with  $h/d_o$  values of 2 and 3, respectively. Fig. 28(b) includes data for one of the large deflectors, more than 20 times the size of the

others. These results indicate that the distribution of mass flux across a sheet, when appropriately nondimensionalized, is nearly independent of injection velocity, fluid physical properties, and the scale of the apparatus. The normalized distributions appear to depend primarily on  $h/d_o$ , as predicted by Eq. (5).

### 3. Sheet Velocity Distribution

The fluid velocity  $V_e$  at any point across the width of a free sheet close to the edge of the deflector may likewise be normalized by dividing it by the average exit velocity of the jet from which it was formed, to obtain a dimensionless velocity distribution parameter  $\mathcal{V}$ :

$$\mathcal{V} \equiv \frac{V_e}{\bar{V}} \quad (7)$$

By reasoning similar to that employed in the analysis of mass flow rate distribution, it would be expected that

$$\mathcal{V} \cong f \left[ \frac{x}{d_o}, \frac{h}{d_o} \right] \quad (8)$$

if Reynolds and Weber number effects were again found to be negligible and the geometrical dependencies are reducible. All velocity distributions at constant  $h/d_o$  would then be correlated by a single curve of  $\mathcal{V}$  versus  $x/d_o$ , much as the mass distributions were found to be, and varying  $h/d_o$  would be expected to produce a corresponding family of general velocity distribution curves.

This hypothesis was checked experimentally by measuring dynamic pressure across sheets formed from the same wide variety of deflector/orifice combinations, flowing water and trichlorethylene over Reynolds and Weber number ranges similar to those used in the mass-distribution experiments. A 0.0071-in.-diameter capillary tube probe (Fig. 29), connected to a pressure transducer, measured dynamic pressure across the width of each sheet at a distance of 0.15 in. from the edge of the deflector. At each station along the sheet, the probe was also moved in a direction normal to the sheet width to assure that the maximum pressure (velocity head) at that station was measured. The exit velocity at each position across the sheet was calculated from

$$V_e = \left( \frac{2g_c P_d}{\rho} \right)^{1/2} \quad (9)$$

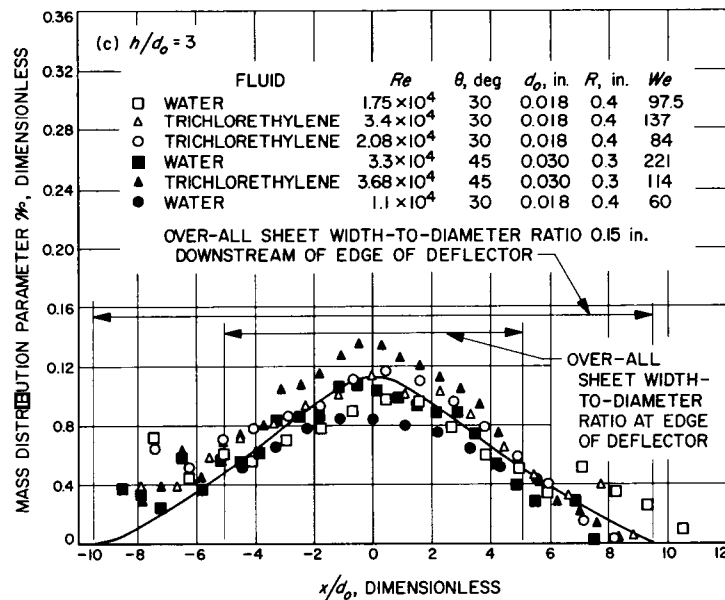
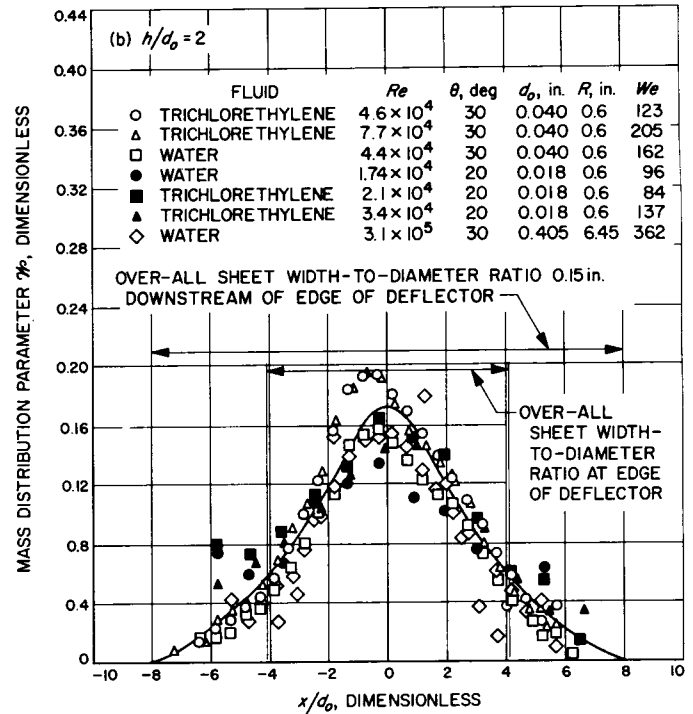
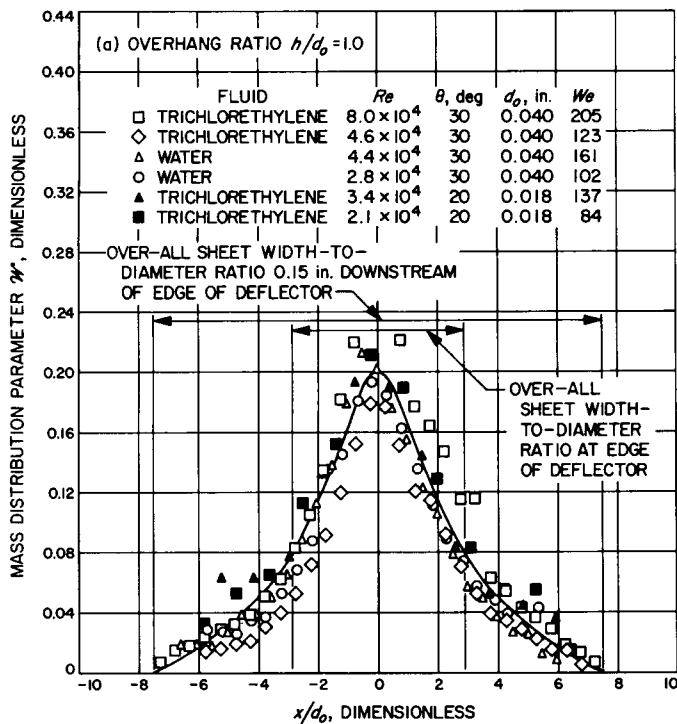


Fig. 28. Generalized mass flow rate distribution in sheets formed on deflectors at a station 0.15 in. downstream of edge of deflector

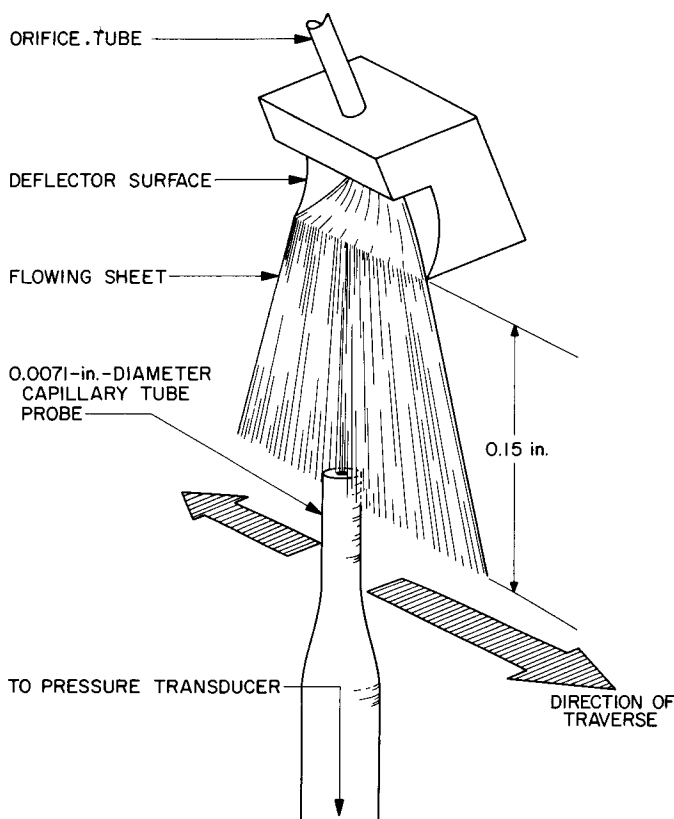


Fig. 29. Apparatus for measuring velocity distribution

The original objective of these experiments was to obtain *comparative* measurements, which would have sufficed to check the validity of Eq. (8). However, since it has been found convenient to use the velocity distribution data in the prediction of sheet thicknesses (Section 4 of this report), some remarks are in order concerning the degree of confidence that can be placed in these velocity data. In the first place, the capillary tube probe, although the smallest that could be used practically, had a diameter of the same order of magnitude as the sheet thicknesses probed. Thus a local "average," rather than a centerline velocity was encountered by the probe at each station across the sheet. Secondly, if some secondary (recirculatory) flow occurred within the probe, the pressure measured might not have indicated the true stagnation value at all. Finally, it was assumed that the velocity was related to the dynamic pressure by Eq. (9), the customary definition of velocity head.

There were no primary standards against which to check the present data because, so far as is known, no previous experiments have ever measured velocities in such exceedingly thin flowing sheets. The variation with free-stream distance of the centerline velocity in *jets* from round orifices had been studied, however. Rupe (Ref. 13) measured centerline stagnation pressures in 0.12-in.-diameter jets, using a so-called flat-plate probe (a flat plate with a hole in it, against which the jets impinged perpendicularly), believed to have several advantages over the more conventional pitot tube approach used in the present experiments. Accordingly, the variation with free-stream distance of the centerline velocity in several jets from the smaller (0.018- to 0.040-in. diameter) orifices used in the present studies was measured with the capillary tube probe, and the results compared (Fig. 30) with those of Rupe.

Fig. 30 shows a fair comparison between Rupe's flat-plate data and the writer's pitot tube results in the region from 3.75 to 7.5 jet diameters downstream of the orifice (where sheet velocities were measured). The amount of scatter from one set of conditions to the next indicates an experimental error of perhaps  $\pm 10\%$  in the capillary tube measurements relative to Rupe's data. However, it is still not possible to assign absolute values of experimental accuracy because of the uncertainties in Rupe's results. The fact that Rupe was unable to reproduce, with the flat-plate probe measurements, either the uniform velocity profile of LeClerc (Ref. 14) or the Prandtl centerline stagnation pressure for fully developed turbulent pipe flow (Ref. 15), shows just how difficult accurate measurements of this type really are. We must concede, with Rupe, that

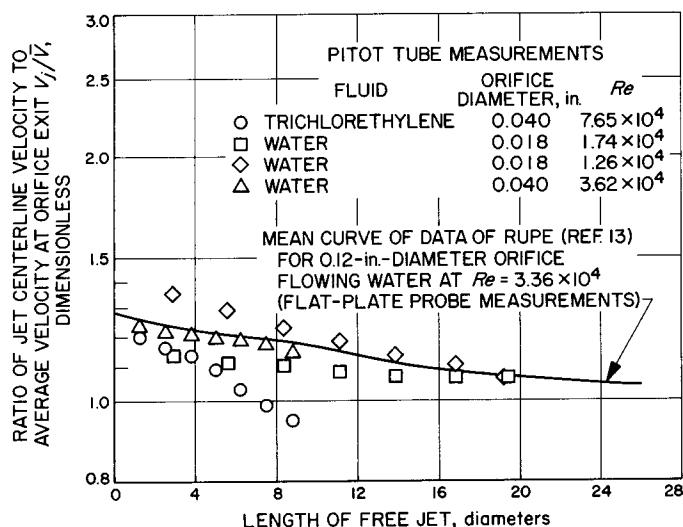


Fig. 30. Comparison of normalized jet centerline velocities measured by two alternative methods

In this manner, many different velocity distribution curves were obtained, some of which were published in SPS 37-38, Vol. IV, p. 116.

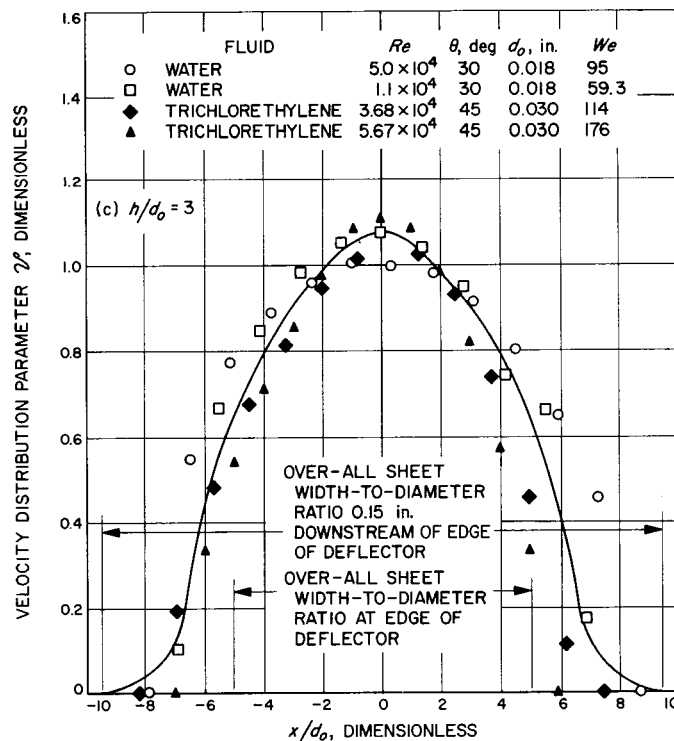
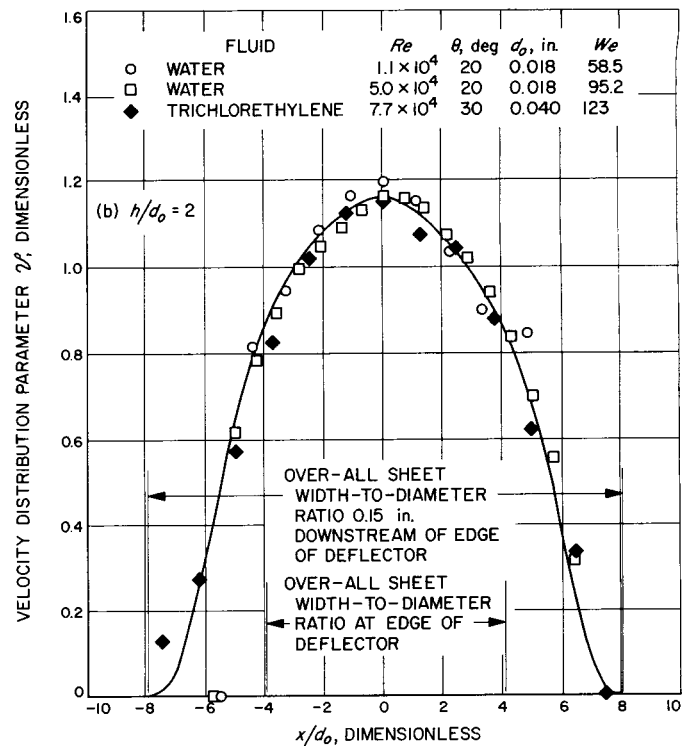
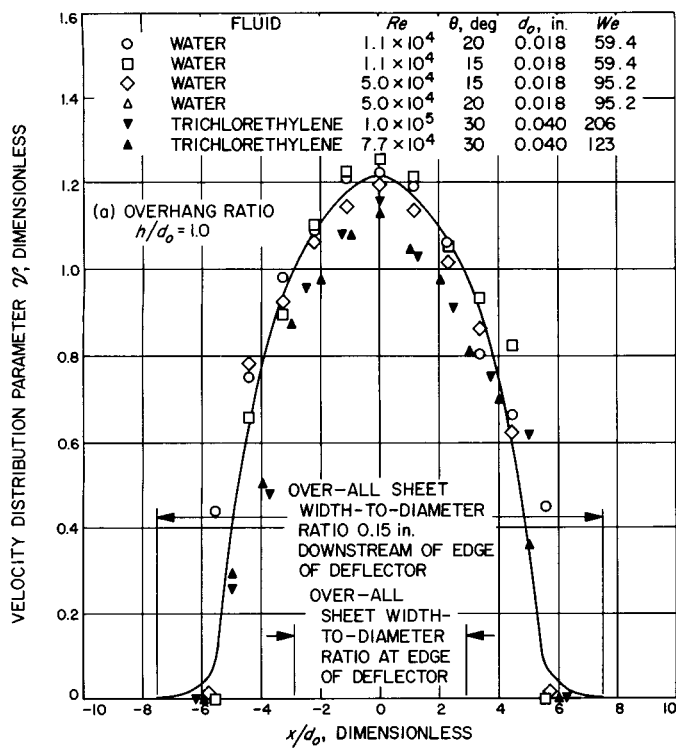


Fig. 31. Dimensionless velocity distribution curve for deflectors at a station 0.15 in. downstream of edge of deflector

“...this technique has the practical disadvantage that the data obtained are primarily comparative,” (Ref. 13).

It was again found that the velocity distribution curves, however comparative they might be, could be condensed into a few completely general correlations by normalizing both  $V_e$  (Eq. 7) and  $x$ . Some typical normalized velocity distribution data are presented in Fig. 31. These results indicate that, like the distribution of mass flux, the sheet velocity distribution, when suitably nondimensionalized, is essentially independent of injection velocity and fluid physical properties. The normalized distributions depend on  $h/d_o$ , as predicted by Eq. (8).

It is not practical to present here the many velocity distribution curves derived from the experimental measurements. However, for these distributions the effect of increasing the overhang ratio is to make them broader and flatter. The manner in which  $\mathcal{V}$  decreases with  $h/d_o$  may be seen in a simplified fashion by examining the variation of only one point (the value of  $\mathcal{V}$  at the sheet centerline) on each curve. This is plotted in Fig. 32.

#### 4. Sheet Thickness Distribution

The last dimension required to fully describe and predict the behavior of sheets of liquid formed on deflectors by tangential impingement of round jets from orifices is the sheet *thickness*—and the manner in which it varies across the width of the sheet. It is virtually impossible to measure sheet thickness accurately, even for sheets formed on the large (6.45-in. radius) deflectors, because the sheets are extremely thin (typically about 0.005-in. thick). With the establishment of the generalized mass and velocity distribution curves, however, it is possible to *estimate* correspondingly general sheet thickness distribution curves. Defining a normalized sheet thickness as

$$\mathcal{T} = \frac{t}{d_o}, \tag{10}$$

it can be shown from the Continuity Principle that, at constant  $x/d_o$  and  $h/d_o$ ,

$$\mathcal{T} = \frac{\mathcal{M}}{\mathcal{V}} \cong f \left[ \frac{x}{d_o}, \frac{h}{d_o} \right] \tag{11}$$

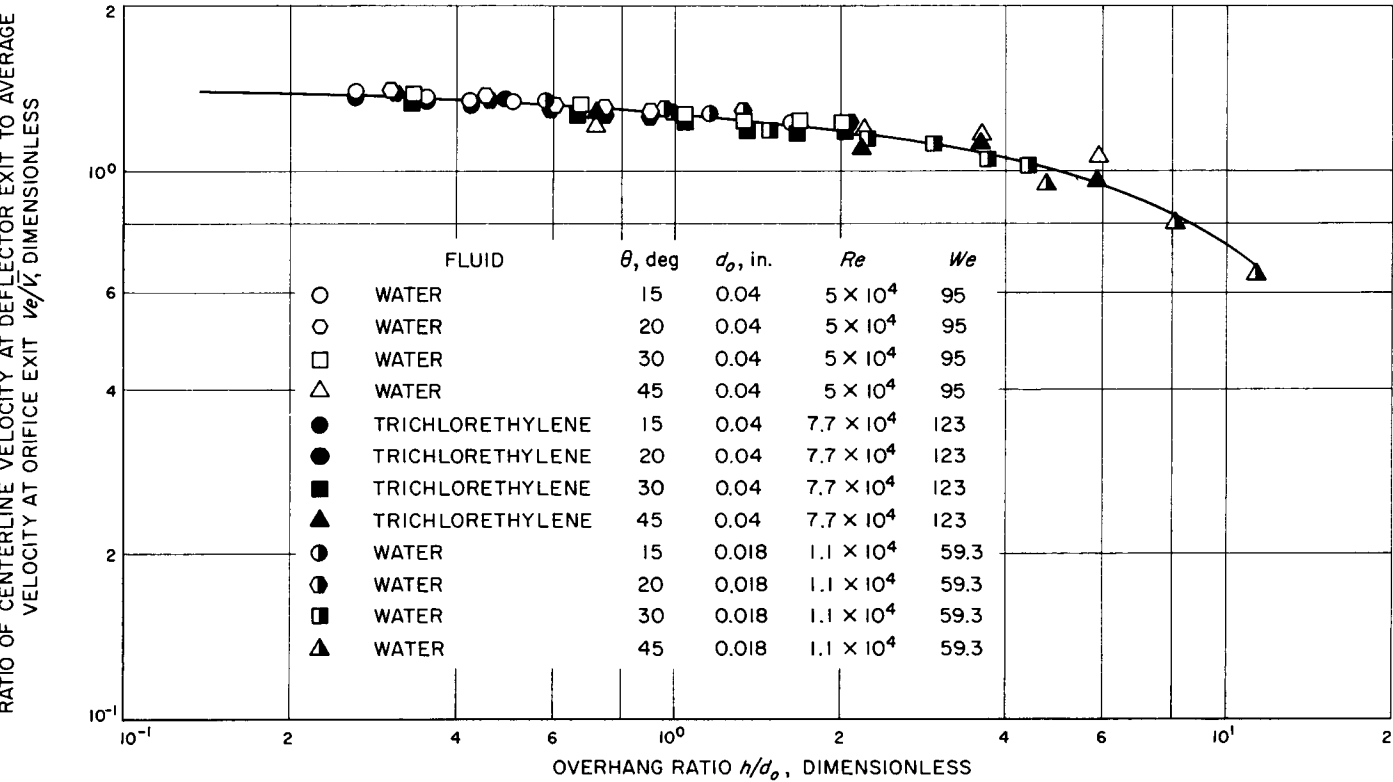
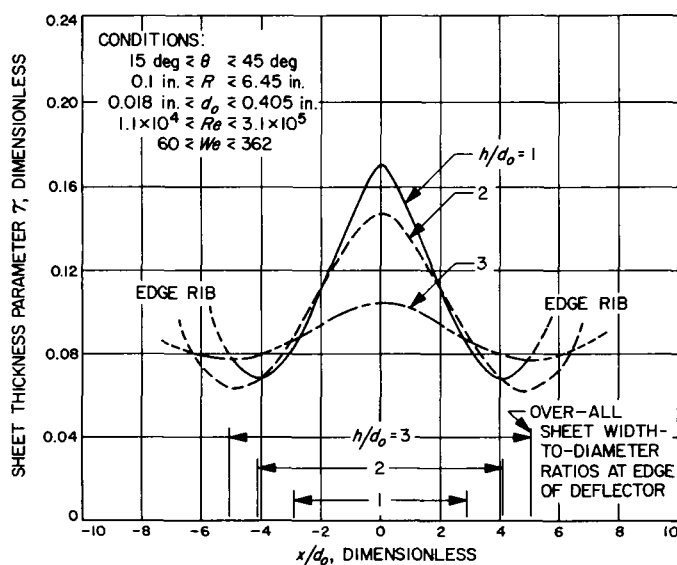


Fig. 32. Effect of deflector overhang ratio on normalized centerline velocity at deflector exit

Generalized thickness distributions calculated from the general mass and velocity curves of Figs. 28 and 31 are shown in Fig. 33, where the increased thickness characteristic of the edge ribs may be seen. The curve for  $h/d_o = 1$ , for example, was obtained by dividing the curve of Fig. 28(a) by that of Fig. 31(a), point by point. Since these curves were derived from measurements taken 0.15 in. from the edge of the deflectors, they strictly apply only in regions that close to the deflector exits. To use Fig. 33 for a specific deflector, it is only necessary to multiply both abscissa and ordinate of the curve, for the proper  $h/d_o$  value, by the orifice diameter. Actual sheet thickness versus actual sheet width is then obtained.



**Fig. 33. Generalized thickness distribution for sheets formed on deflectors with various overhang ratios at a station 0.15 in. down-stream of edge of deflector**

The central curve  $h/d_o = 2$  was used to predict the thickness distribution for one of the large deflectors with that overhang ratio. The thickness in the actual flowing sheet (water, 100 ft/sec) was then measured in a crude manner by inserting a machinist's rule. The predicted and measured values are compared in Table 6. Ranges, rather than discrete values, are given for the measured values to indicate the level of uncertainty. Nevertheless, agreement between the predicted and measured values was excellent across the whole sheet, illustrating the scalability of the generalized thickness distribution curves (derived from data collected for the small deflectors) to flow devices at least 20 times as large in linear dimension. The comparison of Table 6 also increases the confi-

**Table 6. Comparison of predicted and measured sheet thicknesses for large<sup>a</sup> deflector**

Location	Predicted thickness, in.	Measured thickness, in.
Centerline	0.085	0.08–0.09
$x/d_o = 2$	0.063	0.05–0.06
$x/d_o = 4$	0.039	0.03–0.04

<sup>a</sup> $R = 6.45$  in.,  $d_o = 0.405$  in.,  $\theta = 30$  deg,  $V = 100$  ft/sec, water

dence level of the velocity distribution data (discussed in the previous section) from which the thickness curves were derived.

## 5. Summary of Results

The results of the sheet formation studies to date may be summarized as follows:

- (1) Sheet dimensions, such as normalized width  $w/d_o$ , spreading angle  $\beta$ , and deflection angle  $\delta$ , are virtually independent of fluid physical properties, injection velocity, or actual size of the flow device, over a wide range of conditions ( $10^4 \lesssim Re \lesssim 3 \times 10^5$ ). They vary with, and may be correlated in terms of, simple dimensionless geometrical ratios. Sheets formed by the tangential impingement of round jets on concave, cylindrical deflector surfaces exhibit nearly complete *dynamic* and *geometric similarity*, thus permitting accurate prediction, control, and scaling of the key sheet properties.
- (2) The actual distributions of mass flux, velocity, and thickness across the sheets depend upon fluid physical properties, injection velocity, and the scale of the apparatus. However, these may be *normalized* (expressed in terms of certain dimensionless ratios) to yield general correlations which depend only on the dimensionless overhang ratio  $h/d_o$ .
- (3) Orifice length-to-diameter ratio has no effect on the time-averaged properties of flowing sheets. But fully-developed turbulent flow (orifice length-to-diameter ratios of 50 or greater) is necessary to produce stable sheets whose properties do not vary randomly with time about the average values.
- (4) The deflector overhang ratio  $h/d_o$  must be *greater* than 0.75 for true sheets to form; below this critical value, perturbed round jets with ill-defined properties are formed. As  $h/d_o$  is increased above 1, however, energy dissipation due to frictional losses on the deflectors also increases, so that  $h/d_o = 3$

would seem a reasonable upper limit for practical sheet-formation devices. On the other hand, maximum sheet thickness *decreases* as  $h/d_o$  becomes larger, and there may be some applications where the optimum value of  $h/d_o$  would result from trade-offs between thickness and energy utilization considerations.

- (5) The sheet properties are also affected by the wettability of the deflector surfaces on which they are formed. The results of the present program were obtained with clean, degreased surfaces. Experimentation showed, however, that controlled application of coatings not wet by the fluid to the deflector surfaces could significantly alter key sheet properties.

- (6) Sufficient engineering information on the formation and properties of flowing sheets is now available to permit their intelligent application to a wide variety of injection and flow devices.

This report concludes the investigation of the formation and properties of flat sheets on curved deflector surfaces. A formal JPL Technical Report documenting the entire research effort is presently in preparation. Future work will include nonreactive spray studies to determine those conditions necessary for optimum mixing and atomization in impinging-sheet injector elements, as well as a continuation of development effort on liquid propellant spacecraft engine injectors utilizing the impinging-sheet concept. SPS 37-41, Vol. V, reports some preliminary test-firing results.

### Definition of symbols

$d_o$ orifice diameter, in.	$\mathcal{O}$ mass distribution parameter, dimensionless; $\mathcal{O} \equiv (d\dot{w}/dx) \cdot (144/\rho\bar{V}d_o)$
$g_c$ gravitational constant, 32.16 ft lb <sub>m</sub> /lb <sub>f</sub> sec <sup>2</sup>	$We$ Weber number, dimensionless; $We \equiv \bar{V}/12 (\rho d_o/\sigma g_c)^{1/2}$
$h$ deflector overhang, in.; $h = R(1 - \cos \theta)$	$\dot{w}$ mass flow rate, lb <sub>m</sub> /sec
$P_d$ dynamic pressure, lb <sub>f</sub> /ft <sup>2</sup>	$w$ overall sheet width, in. (Fig. 26)
$Re$ Reynolds number, dimensionless; $Re \equiv (d_o\bar{V}\rho)/[\mu(144)]$	$x$ distance across sheet, measured outward from centerline, in. (Fig. 26)
$R$ deflector radius, in. (Fig. 26)	$\beta$ sheet spreading angle, deg (Fig. 26)
$t$ sheet thickness, in.	$\delta$ sheet deflection angle, deg (Fig. 26)
$\mathcal{E}$ sheet thickness parameter, dimensionless; $\mathcal{E} \equiv \mathcal{M}/\mathcal{Q}$	$\rho$ liquid density, lb <sub>m</sub> /ft <sup>3</sup>
$\mathcal{Q}$ velocity distribution parameter, dimensionless; $\mathcal{Q} \equiv V_e/\bar{V}$	$\sigma$ liquid surface tension, lb <sub>f</sub> /in.
$V_e$ local velocity in sheet at deflector exit, ft/sec	$\theta$ deflector angle, deg (Fig. 26)
$\bar{V}$ average exit velocity of orifice, ft/sec	$\mu$ liquid viscosity, lb <sub>m</sub> /in.-sec

## References

1. Clayton, R. M., and Rogero, R. S., "Experimental Measurements on a Rotating Detonation-Like Wave Observed During Liquid Rocket Resonant Combustion," *Technical Report No. 32-788*, Jet Propulsion Laboratory, Pasadena, California, August 15, 1965.
2. Rupe, J. H., "A Correlation Between the Dynamic Properties of a Pair of Impinging Streams and the Uniformity of Mixture Ratio Distribution in the Resulting Spray," *Progress Report 20-209*, Jet Propulsion Laboratory, Pasadena, California, March 28, 1956.
3. Parisse, R. F., "Ablation of a Solid Sphere of a Low Conductivity Material," PIBAL Report No. 683, Polytechnic Institute of Brooklyn, April 1964.
4. Summerfield, M., "A Theory of Unstable Combustion in Liquid Propellant Rocket Systems," *ARS Journal*, Vol. 21, No. 9, pp. 108-114, September 1951.
5. Sabersky, R. H., "Effect of Wave Propagation in Feed Lines on Low-Frequency Rocket Instability," *Jet Propulsion*, Vol. 24, No. 3, pp. 172-174, May-June, 1954.
6. Crocco, L., and Cheng, Sin-I, *Theory of Combustion Instability in Liquid Propellant Rocket Motors*, Butterworths, London, 1956.
7. Reardon, F. H., and Waugh, R. C., "Feed-System Effects in Combustion Instability," (Unclassified Paper) *Bulletin of the 5th LP Symposium*, Vol. II, CPIA Publication #37, pp. 843-862, December 1963 (Confidential).
8. Bird, R. B., Stewart, W. E., and Lightfoot, E. N., *Transport Phenomena*, p. 212, John Wiley & Sons, Inc., New York, 1960.
9. Bird, R. B., Stewart, W. E., and Lightfoot, E. N., *Transport Phenomena*, p. 186, John Wiley & Sons, Inc., New York, 1960.
10. Bird, R. B., Stewart, W. E., and Lightfoot, E. N., *Transport Phenomena*, p. 217, John Wiley & Sons, Inc., New York, 1960.
11. Lapidus, L., *Digital Computation for Chemical Engineers*, p. 90, McGraw-Hill Book Co., Inc., New York, 1962.
12. Rupe, J. H., "On the Dynamic Characteristics of Free-Liquid Jets and a Partial Correlation with Orifice Geometry," *Technical Report No. 32-207*, Jet Propulsion Laboratory, Pasadena, California, January 15, 1962.
13. Rupe, J. H., "On the Dynamic Characteristics of Free-Liquid Jets and a Partial Correlation With Orifice Geometry," *Technical Report No. 32-207*, Jet Propulsion Laboratory, Pasadena, California, January 15, 1962.
14. LeClerc, A., "Deflection of a Liquid Jet by a Perpendicular Boundary," M. S. Thesis, University of Iowa, 1948.
15. Prandtl, L., and Tietjens, O. G., "Applied Hydro- and Aero-Mechanics," McGraw-Hill Book Co., Inc., New York, 1934.

## XIII. Space Instrument Systems

### SPACE SCIENCES DIVISION

N67-15733

#### **A) Generation of Horizontal Jitter Requirements in an Analog-Scan Video System, F. C. Billingsley**

The efforts discussed here are a continuation of the digital video data processing efforts reported earlier (*SPS 37-22*, Vol. IV, pp. 68-71, and *SPS 37-31*, Vol. IV, pp. 22-26). For those unfamiliar with this work, briefly the situation is as follows: We have been developing the techniques for digital processing of the pictures returned from JPL spacecraft. As an adjunct to this effort, we have had to develop and study film conversion techniques to precisely convert an electrical signal to a film image and vice versa. This study is concerned with the problem of the loss of line resolution due to sample timing errors.

**THE PROBLEM:** What happens to the horizontal resolution, i.e., horizontal modulation transfer function (MTF), when there is line synchronization jitter or time base displacement (e.g., wow and flutter of a tape deck)?

**MILIEU:** A line scan system with nominally constant line sweep rates and zero line-start jitter.

**ANALYSIS:** Consider a modulating frequency perfectly synchronized with the line sync pulse, starting at the same

phase on every line. The appearance on the image will be a series of sinusoidally intensity-modulated vertical bars of a width determined by the ratio of sweep speed to frequency. At some inspection point partway across the lines, there will be relative phase errors in the sinusoids on the various lines in a line group, caused by time base instabilities or sync jitter, or both.

Let us examine a number of lines by means of a narrow vertical slit of length  $n$ , where  $n$  is the number of lines covered by the slit. Assume that the slit has zero width compared with the frequencies of interest; in any event, it is relatively simple to compensate for the slit width in a practical situation, if it is not negligible. An *interest function* is defined as a weighting function having a value at each line location proportional to the interest we have in that particular line. For the uniform slit, it has the value unity for  $n$  lines, and zero outside those lines. Note that it need not be uniform; e.g., in detailed examination of a picture, interest is centered on only a few lines, with some, but relatively less, interest on adjacent lines. A nonuniform interest function can be simulated by varying the transmittance of the slit along its length.

The total response of the system is then the summation of the product of the interest function  $I$  times the ampli-

tude of sinusoid  $A$  at the position of the slit taken for each line:

$$\text{Response} = \sum_j (I_j \times A_j)$$

For analysis, let us approach this from the spread function (impulse response) point of view. At some time after the sync pulse for each line (corresponding to the position of the slit), erect a delta function. For example, in writing a film, a single impulse spot is recorded. The line of delta functions so generated will be straight and sharp in the absence of all jitter, or will be wiggly or diffuse in the presence of jitter. Now apply the interest function, and plot the spot position density function versus horizontal position. This function is simply the impulse response of the group of lines within the interest function, taken as a whole. The effective horizontal frequency response for this group of lines is then the one-dimensional Fourier transform of the impulse response (Ref. 1). In general, the horizontal MTF will not be the same for all parts of the picture.

For a sufficiently large number of lines for the distribution to be applicable, it is immaterial whether the impulse response is caused by a static distribution of the delta functions or by one delta function moving in time to give the given distribution function. The latter case corresponds to blur due to image motion (e.g., vibration) in one direction (Ref. 2).

Appropriate jitter distributions must then be determined. It has been shown (Ref. 3) that the probability density function for time base errors is approximately Gaussian for the error in a magnetic tape recorder. For Gaussian jitter,

$$f(x) = e^{(-1/2)(x/\sigma)^2}$$

and, when normalized, the transform is

$$F(\omega) = e^{(-1/2)(\sigma\omega)^2}$$

Letting  $\omega = \frac{2\pi}{P_f}$ , where  $P_f$  is the period of the sinusoid,

$$F(P_f) = e^{-2\pi^2(\sigma/P_f)^2}$$

This is the equation plotted in Fig. 1.

For other than Gaussian jitter, of course, the transform of the appropriate function must be taken. Note that, in

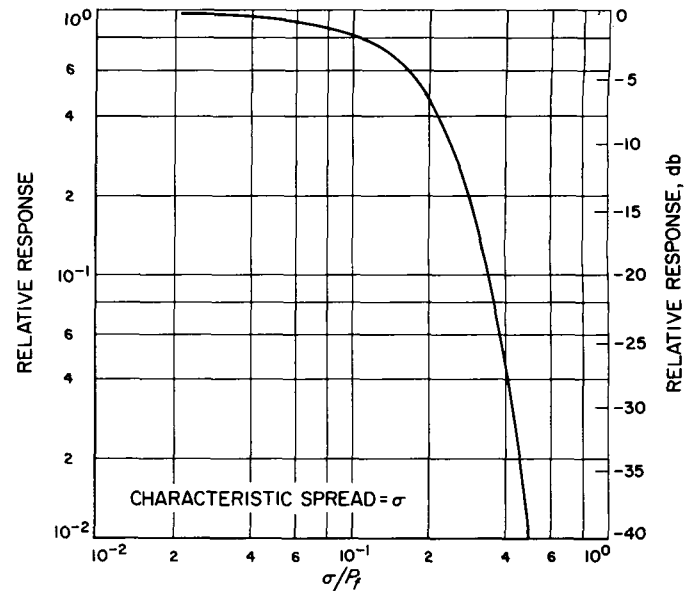


Fig. 1. Loss of high frequency resolution due to Gaussian jitter

general, for the case of a picture reproduced from longitudinal tape, resolution degrades progressively along the scan line as the time base displacement errors accumulate.

The total horizontal frequency response is then the product of the response due to jitter times the response due to a cathode-ray-tube recording spot of half-amplitude diameter  $D$ , given in Fig. 2.

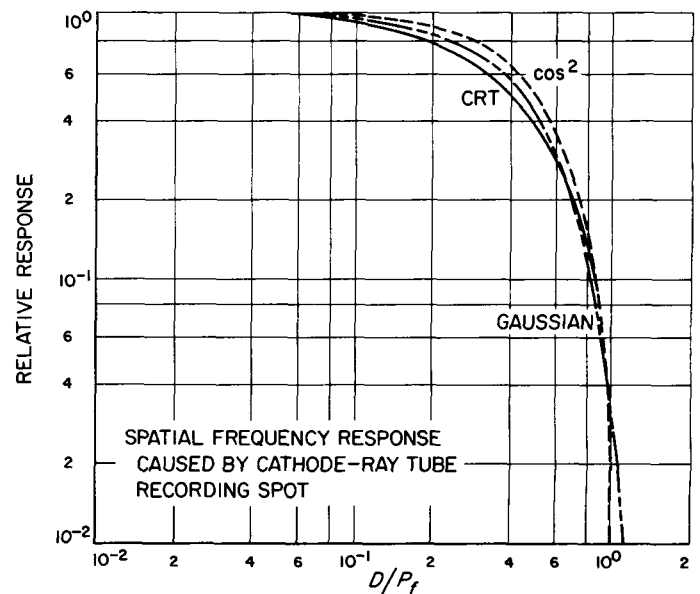


Fig. 2. Spatial frequency response caused by cathode-ray-tube recording spot

## References

1. Harger, R. O., "An Analysis of Recorder Motion Errors in Optical Processing," *Applied Optics*, Vol. 4, No. 4, pp. 383-386, 1965.
2. Myszko, R., "Effect of Vibration on the Photographic Image," *Journal of the Optical Society of America*, Vol. 53, No. 8, pp. 935-940, August 1963.
3. Chao, S. C., "Flutter and Time Errors in Instrumentation Magnetic Recorders," *IEEE Transactions on Aerospace and Electronic Systems*, Vol. AES-2, pp. 214-223, March 1966.

## XIV. Bioscience

### SPACE SCIENCES DIVISION

N67-15734

#### **A. Fluorometric Determination of Nucleic Acids. I. Deoxyribose Assay of Biological Material,**

J. H. Rho and J. R. Thompson

##### **1. Introduction**

Interest in the search for life on other planets has emphasized the need for analytical methods of great sensitivity to determine essential biological compounds in soil samples by means of a fully automated instrument.

The sugar deoxyribose is a unique component of deoxyribonucleic acid (DNA). Many colorimetric and spectrophotometric methods have been devised for estimating nucleic acid on the basis of deoxyribose assay of isolated material. Since Feulgen and Rossenbeck (Ref. 1) introduced the Feulgen-Schiff reaction in 1924, the histochemical technique for DNA has been further improved by use of various Schiff reagents other than fuchsin (Refs. 2, 3, and 4).

The Feulgen reaction depends on the release of aldehyde groups from the deoxyribose sugar of DNA by mild acid hydrolysis with *N* hydrochloric acid (HCl) at 60°C.

The exposed aldehyde groups then react with the Schiff reagent to produce a color reaction at the site of any DNA present. Specificity of this reaction for DNA has been argued (Ref. 5), and its use has been restricted to histochemical techniques where unreacted reagents can be efficiently washed away.

Measurement of DNA in samples of tissue has also been accomplished generally by spectrophotometric determination of the colored product of the reaction between deoxyribose and diphenylamine (Refs. 6 and 7), and by determination of the color produced by the indole reaction (Ref. 8). An ultraviolet chromophore produced under specially defined conditions of acidity, temperature, and time may also be used for an estimation of deoxyribose in the presence of nucleosides (Ref. 9). These methods not only require samples of tissue of the order of 50 to 100 mg but also require reasonably pure chemical systems.

Velluz, et al. (Ref. 10) reported a reaction which is a modification of the Doebuer-Miller quinaldine synthesis, whereby aldehydes of the type  $R-CH_2-CHO$  yield strongly fluorescent products when allowed to react with

3,5-diaminobenzoic acid dihydrochloride (DABA) under rather violent conditions of prolonged heating in concentrated mineral acids. The reaction is a general one, requiring only that the carbon atom in the  $\alpha$ -position to the aldehyde group be unsubstituted. An analytical method for acetaldehyde and deoxyribose has been described (Refs. 11, 12, and 13), and a modification of the analysis for acetaldehyde has been made by reducing volumes and modifying experimental conditions for the measurement of DNA in animal tissues, with special reference to the central nervous system (Ref. 14). This report presents a further modification of the chemical procedure and an application of the method of the estimation of soil microorganisms.

## 2. Materials

**a. *E. coli* B.** This culture was obtained from Dr. Ru-Chi Huang, California Institute of Technology, Pasadena, and was grown in pure culture in an inorganic medium enriched with glucose as the sole carbon source (as described in SPS 37-25, Vol. IV, p. 243).

**b. Soil samples.** Sandy soils collected from the surface ( $\frac{1}{8}$  in.) of the Colorado Desert, Thermal, California, were used, and the ignited soil was prepared by heating the soil at 800°C for 24 hr.

**c. Reagents.** The DNA (ex herring sperm) was obtained from the California Corporation for Biochemical Research, Los Angeles, California; the ribonucleic acid (RNA) from Nutritional Biochemical Corporation, Cleveland, Ohio; and 3,5-diaminobenzoic acid from Aldrich Chemical Company, Milwaukee, Wisconsin. A solution of 0.17 g of 3,5-diaminobenzoic acid in 1 ml of 4.0 N HCl was decolorized with Norit and used as the reagent. Other chemicals were reagent grade.

**d. Spectrophotofluorometer.** Both an Aminco-Bowman spectrophotofluorometer and a Farrand fluorometer having xenon mercury lamps and an RCA IP 28 photomultiplier detector were used. For the determination of fluorescence of trace amounts of sample, a capillary cell with an inside diameter of 1 mm was used, with an adaptor fitted into the Farrand fluorometer.

## 3. Experimental Procedure

Samples consisting of 10 to 100  $\mu$ g of DNA,  $10^6$  to  $10^{10}$  *E. coli* cells, and 25 to 250 mg of the sandy desert soils were placed in centrifuge tubes. The samples were first washed with cold 0.3 N trichloroacetic acid (TCA) to remove possible contamination by acid soluble aldehydes,

and then washed with 0.5 ml of 0.1 N alcoholic potassium acetate to extract any lipid materials present. The samples were again extracted, twice each, with 0.5 ml of absolute alcohol. In the first extraction, the tubes, capped with parafilm, were heated at 60°C for 15 min. After centrifugation, the supernatant fluid was decanted and the precipitates were dried over CaSO<sub>4</sub>. Deoxyribose standards containing 5 to 50  $\mu$ g per 50  $\mu$ l were evaporated to dryness. Beyond this point, nucleic acids, *E. coli* cells, soil samples, and blanks were treated identically.

One-tenth milliliter of freshly prepared M DABA was added, with mixing, to the tubes containing the blanks, the standards, and the dried samples. The tubes were then tightly capped with rubber stoppers and were heated at 60°C for 20 min in a water bath. Each of the tubes was made up to 10 ml with 0.6 N perchloric acid. Fluorescence intensity of these solutions was determined at 510 m $\mu$  with the maximum excitation at 410 m $\mu$ .

## 4. Results and Discussion

**a. Deoxyribose assay of DNA.** The use of strongly acidic DABA accomplished both hydrolysis of DNA and formation of the fluorescent product in a single step.

The fluorescent product of 3,5-diaminobenzoic acid and pure deoxyribose is maximally excited by light at a wavelength of 410 m $\mu$ , and results in a fluorescence with maximal intensity at a wavelength of 510 m $\mu$ , as determined with an Aminco-Bowman spectrophotofluorometer. The products obtained by the reaction of 3,5-diaminobenzoic acid with pure DNA have the same fluorescence properties as those obtained from deoxyribose.

The increase of the fluorescence intensity of the reaction product obtained by allowing DABA to react with DNA was proportional to the amount of DNA over the concentration range 0.5 to 10  $\mu$ g/ml. An equivalent amount of RNA subjected to the same procedure did not show any sign of fluorescence (Fig. 1).

Since the pyrimidine deoxyribosides and pyrimidine deoxynucleotides are known to be quite resistant to the mild acid hydrolysis described, the use of the reaction with 3,5-diaminobenzoic acid appears to measure almost entirely the deoxyribose liberated from purine deoxynucleotides. The fluorescence produced by 10  $\mu$ g of DNA per ml yielded a fluorescence equivalent to approximately 1.6  $\mu$ g of deoxyribose. If we assume that the deoxyribose content of DNA is about 40% by weight and that the

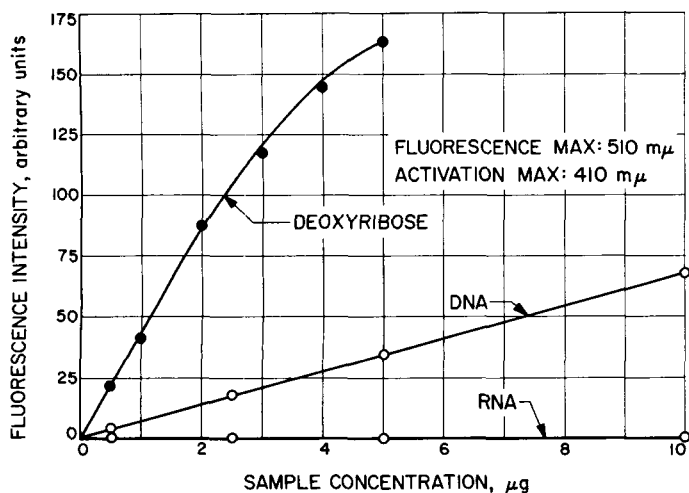


Fig. 1. Deoxyribose assay of nucleic acids

purine deoxynucleotides are about one-half of the total nucleotides of the DNA used, the fluorescence yield obtained in this experiment is about 80%. This yield could be further improved by use of highly purified DNA and by optimizing the reaction conditions with respect to temperature and duration.

**b. Quantitative estimation of deoxyribose in microorganisms and soil samples.** The fluorescence of the reaction products with 3,5-diaminobenzoic acid was determined in samples of the microorganism *E. coli* and sandy desert soil, as shown in Figs. 2 and 3. A good proportionality is observed between intensity of fluorescence and the quantity of pure deoxyribose, DNA, soil samples, and *E. coli*. Twenty-five milligrams of this soil yielded fluorescence equivalent to approximately 0.4 μg of DNA. If 3.72% of the dry weight of *E. coli* is DNA (Ref. 16), assuming that the dry weight of a single cell of *E. coli* is about  $10^{-12}$  g, we estimate that  $10^7$  cells is equivalent to the amount of DNA in 25 mg of the soil tested, or that the amount of DNA in 1 g of soil is equivalent to about  $4 \times 10^8$  cells. We observed, however, that soil invariably decreases the fluorescence yield of the reaction products upon the amount of soil present and also upon the concentration of reaction products. The actual deoxyriboside content of the soil may well be much higher than the level we have detected.

For a study of the quenching effect of various soil components on the fluorescence of the reaction products, it is necessary to accurately determine the content of available deoxyribose in the soil as well as the concentration of the reaction products. The fluorescence produced in the reaction with *E. coli* cells is distinct, even with a

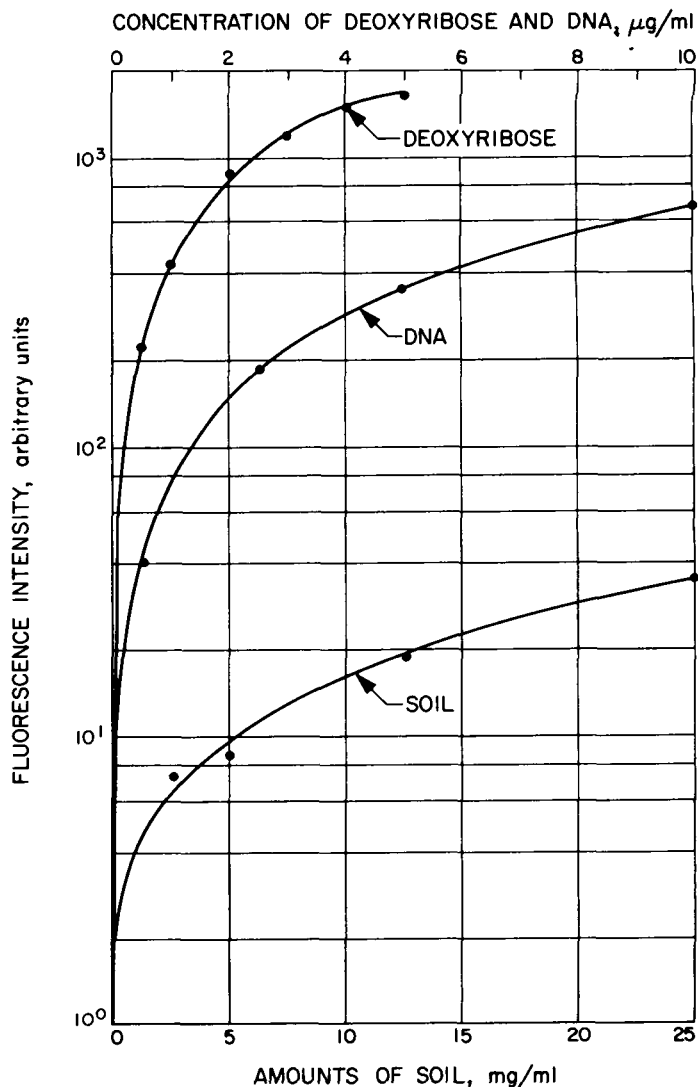


Fig. 2. Fluorometric assay of DNA and soil sample

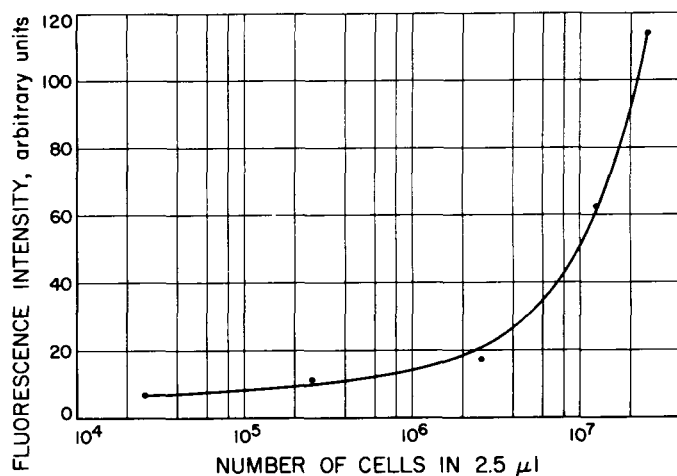


Fig. 3. Deoxyribose assay of *E. coli*

relatively small number of the bacteria (Fig. 3). In accord with the above calculation,  $10^5$  *E. coli* cells would contain about 3.7 ng of DNA, and this will provide a readily detectable level of fluorescence.

### 5. Summary

A fluorometric method for measuring DNA has been modified and applied to the estimation of a bacterial population and of DNA in soil microorganisms. The pro-

cedure is based on the measurement of the fluorescent products of the reaction between 3,5-diaminobenzoic acid in 4 N HCl and deoxyribose. No separation of DNA and RNA is necessary, for the reaction is highly specific for deoxyribose, as opposed to ribose. The method applied to pure DNA and *E. coli* yielded values in close agreement with those based on calculation and permits the determination of as little as  $10^5$  cells of *E. coli* and the microbial population in 5 to 25 mg of sandy desert soil samples.

### References

1. Feulgen, R., and Rossenbeck, H., *Hoppe-Seyler's Zeitschrift für Physiologische Chemie*, Vol. 135, p. 203, 1924.
2. Ostergren, G., *Hereditas*, Vol. 34, p. 510, 1948.
3. Ornstein, L., Manter, W., Davis, B. J., and Tamura, R., *Journal of the Mount Sinai Hospital*, Vol. 24, p. 6, 1957.
4. Culling, C., and Vassar, P., *Archives of Pathology*, Vol. 71, p. 76, 1961.
5. Pearse, A. G. E., *Histochemistry*, J. and A. Churchill, Ltd., London, 1960.
6. Dische, Z., *Microchemie*, Vol. 8, p. 4, 1930.
7. Schneider, W. C., *Journal of Biological Chemistry*, Vol. 161, p. 293, 1945.
8. Schmid, P., Schmid, C., and Brodie, D. C., *Journal of Biological Chemistry*, Vol. 238, p. 1068, 1963.
9. Seydel, J. K., and Garrett, E. R., *Analytical Chemistry*, Vol. 37, p. 271, 1965.
10. Velluz, L., Amiard, G., and Pesez, M., *Bulletin de la Société Chimique de France*, Vol. 15, p. 678, 1948.
11. Velluz, L., Pesez, M., Herbain, M., and Amiard, G., *Bulletin de la Société Chimique de France*, Vol. 15, p. 681, 1948.
12. Velluz, L., Pesez, M., and Amiard, G., *Bulletin de la Société Chimique de France*, Vol. 15, p. 680, 1948.
13. Pesez, M., *Bulletin de la Société de Chimie Biologique*, Vol. 32, p. 701, 1950.
14. Kissane, J. M., and Robins, E., *Journal of Biological Chemistry*, Vol. 233, p. 184, 1958.
15. Vendrely, R., and Lehault, Y., *Comptes Rendus Hebdomadaires des Séances de l'Académie des Sciences*, Vol. 222, p. 1357, 1946.

## XV. Physics

### SPACE SCIENCES DIVISION

N67-15735

#### A. The Interaction of a Nonpolar Atom or Molecule With an Inhomogeneous Surface Electric Field, D. P. Merrifield and J. King, Jr.

The basic assumption in the electrostatic theory of physical adsorption (Ref. 1) is that for some adsorption phenomena the induced dipole moment interacting with the surface fields is the predominant contribution to the energy of interaction. For the electrostatic interaction the potential is taken as

$$\phi = -\frac{1}{2}\alpha\mathcal{E}^2 \quad (1)$$

where  $\alpha$  is the polarizability in the direction of the field and  $\mathcal{E}$  is the electric field strength at the center of the adsorbed atom or molecule. This energy is the second-order term in the perturbation expansion for a neutral atom or molecule in a homogeneous electric field; i.e., the usual Stark effect calculation in which the first-order term vanishes.

In the actual interaction of an atom or molecule with an ionic surface, the field varies strongly over the dimension of the atom or molecule. This field variation necessitates an investigation of the perturbation terms to see if a modified version of Eq. (1) can be derived.

#### 1. Perturbation by the Electric Field

The electric field outside the surface of an adsorbent can be written as

$$\mathcal{E} = \mathcal{E}_0 f(z) \quad (2)$$

where  $z$  is the distance normal to the surface and  $\mathcal{E}_0$ , which may contain  $x$  and  $y$  dependence, is strongly characteristic of the adsorption site. The perturbation to the Hamiltonian of the adsorbate becomes

$$H' = -e \sum_{i=1}^N V(z_i) + Ne V(z_0) \quad (3)$$

where  $V(z)$ , the electric potential at the point  $z$ , is given by  $-\int \mathcal{E}(z) dz = -\mathcal{E}_0 \int f(z) dz$ , and  $N$  and  $e$  have their usual meaning. For the present, only an  $N$ -electron atom with the nucleus at  $z_0$  is being considered.

The unperturbed Hamiltonian  $H$  generates the zero-order wave functions and energies,  $\psi_n^0$  and  $E_n^0$ :

$$H\psi_n^0 = E_n^0\psi_n^0 \quad (4)$$

so that the perturbation in energy, to second order, is given by

$$\Delta E_n = H'_{nn} + \sum'_m \frac{H'_{nm}{}^2}{E_n^0 - E_m^0} \quad (5)$$

where the  $m = n$  term is to be omitted from the sum and

$$H'_{nm} = \int \psi_n^{0*} H' \psi_m^0 d\tau \quad (6)$$

Usually, only perturbations of molecules and atoms in their ground states, i.e., with  $n = 0$ , will be of interest.

In a homogeneous field,  $V(z) = -\mathcal{E}_0 z$  and  $H'_{00}$  vanishes, leaving only second-order and higher perturbations to the energy. But for an inhomogeneous field, the first-order energy perturbation will not vanish, and the second-order contribution will not have the same form.

## 2. An Appropriate Treatment of Second-Order Perturbation

If the sum in Eq. (5) is multiplied by unity in the form

$$1 = \frac{E_m^0}{E_n^0} + \frac{E_n^0 - E_m^0}{E_n^0}$$

the equation becomes

$$\Delta E_n^2 = \frac{1}{E_n^0} \sum'_m (H'_{nm})^2 + \sum'_m \frac{E_m^0}{E_n^0} \frac{(H'_{nm})^2}{E_n^0 - E_m^0} \quad (7)$$

Since the  $\psi_m^0$  form a complete set, the representation

$$H' \psi_n^0 = \sum_m H'_{mn} \psi_m^0$$

can be used. Operating twice with  $H'$  on  $\psi_n^0$  and integrating with  $\psi_n^{0*}$ , we find that

$$\begin{aligned} (H'^2)_{nn} &= \int \psi_n^{0*} H'^2 \psi_n^0 d\tau = \int \psi_n^{0*} H' \left( \sum_m H'_{mn} \psi_m^0 \right) d\tau \\ &= \sum_m H'_{mn} H'_{nn} = \sum_m (H'_{mn})^2 \end{aligned} \quad (8)$$

Thus, after eliminating the term  $m = n$ ,

$$\begin{aligned} \sum'_m (H'_{mn})^2 &= \sum_m (H'_{mn})^2 - (H'_{nn})^2 \\ &= (H'^2)_{nn} - (H'_{nn})^2 \end{aligned} \quad (9)$$

With the help of Eq. (9), Eq. (7) becomes

$$\Delta E_n^2 = \frac{(H'^2)_{nn} - (H'_{nn})^2}{E_n^0} + \sum'_m \frac{E_m^0}{E_n^0} \frac{(H'_{mn})^2}{E_n^0 - E_m^0} \quad (10)$$

The approximation which has often been made in quantum chemistry is based on the assumption that the remaining summation in Eq. (10) can be made small by a judicious choice of the zero from which one measures the energies  $E_m^0$ . By choosing an appropriate zero of energy, some of the differences in the denominators will be positive and some negative, and cancellation can be obtained. Usually, the zero of energy is taken as the singly ionized atom or molecule, the only justification being that the right order of magnitude for the interaction energy or polarizability (or other second-order effect) is obtained with some facility. If we take  $E_n^0$ , then, as the energy to remove one electron (i.e.,  $-I$ ), the first- and second-order perturbations to the ground-state energy are

$$\Delta E_0^1 = H'_{00}$$

and

$$\Delta E_0^2 = - \frac{(H'^2)_{00} - (H'_{00})^2}{I} \quad (11)$$

The next step is to calculate these energies for fields which represent the situation at the surface of an actual solid. In computing these fields outside of an ionic solid, it is assumed that the arrangement of the surface atoms is the same as that found within the solid and the effective charges on the ions are their full valence values. For example,  $\text{CaF}_2$  is taken as  $\text{Ca}^{+2}(\text{F}^{-1})_2$ , a fully ionized solid. The general form of the field, falling off exponentially with  $z$  and modulated periodically in the  $x$  and  $y$  directions, then follows directly from the solution of Laplace's equation outside the solid, with appropriate boundary conditions (Ref. 2). Such a treatment assumes that there is no overlap between the electrons of the solid and those of the adsorbed atom. This would seem to be within the spirit of assuming physical adsorption rather than chemical adsorption and using perturbation theory to calculate the interaction.

## 3. Matrix Elements in Terms of Atomic Orbitals

Since the operator of Eq. (3) is a one-electron operator, and the atomic wave function may be taken as an antisymmetrized product of doubly occupied atomic orbitals  $u_i$ ,  $H_{00}$  can be written as

$$H'_{00} = NeV(z_0) - 2e \sum_{i=1}^{N/2} V_{ii} \quad (12)$$

where  $V_{ii} = \int u_i^* V(z) u_i d\tau$ . If an  $S$  state is not involved, the form will be slightly different. Noting that

$$2e \sum_{i=1}^{N/2} u_i^* u_i$$

is simply the density of electrons  $\rho(\bar{r})$ , and using  $\Delta V(z) = V(z) - V(z_0)$ , we can write

$$H'_{00} = -2e \sum_{i=1}^{N/2} \Delta V_{ii} = - \int \rho(\bar{r}) \Delta V(z) d\tau \quad (13)$$

In order to obtain a form for the  $u_i$ , the matrix element  $(H'^2)_{00}$  must be examined.

If the operator  $H'$  of Eq. (3) is squared, there results

$$H'^2 = N^2 e^2 V(z_0)^2 - 2Ne^2 V(z_0) \sum_{i=1}^N V(z_i) + e^2 \sum_{i=1}^N \sum_{j=1}^N V(z_i) V(z_j) \quad (14)$$

which can be rewritten as

$$H'^2 = e^2 \sum_{i=1}^N \sum_{j=1}^N \Delta V(z_i) \Delta V(z_j) \quad (15)$$

as can be easily seen by using the definition of  $\Delta V(z)$ . For example, the matrix element taken between two antisymmetrized products (with wave function  $\psi_0 = A[u_1(1)d(1)u_1(2)\beta(2)u_2(3)d(3)u_2(4)\beta(4)]$ ) is

$$(H'^2)_{00} = 2e^2 \int (u_1^2 + u_2^2) \Delta V^2 + 2e^2 [(\int u_1^2 \Delta V)^2 + (\int u_2^2 \Delta V)^2] + 4e^2 [2 \int u_1^2 \Delta V \int u_2^2 \Delta V - (\int u_1^* u_2 \Delta V)^2] \quad (16)$$

where the variables of integration [ $z$  for  $\Delta V(z)$  and  $x, y$ , and  $z$  for  $u_i(\bar{r})$ ] have been omitted. If  $\Delta V$  is designated by  $v$ , and numerical subscripts indicate the orbitals averaged over [so that  $(v^2)_1$  is  $\int u_1^2 \Delta V^2$  and  $(v^2)_{12}$  is  $(\int u_1^* u_2 \Delta V)^2$ ], the above matrix element may be written

$$(H'^2)_{00} = 2e^2 \{ (v^2)_1 + (v^2)_2 + (v^2)_1^2 + (v^2)_2^2 + 2[2(v)_1(v)_2 - (v^2)_{12}] \} \quad (17)$$

If we square the matrix element in Eq. (13) for the case of our example,  $N = 4$ , we have, in the same notation as Eq. (17),

$$(H'_{00})^2 = \{ -2e [(v)_1 + (v)_2] \}^2 = 4e^2 [(v)_1^2 + (v)_2^2 + 2(v)_1(v)_2] \quad (18)$$

Thus, the approximate form for the second-order contribution to the interaction energy, from Eq. (11), is

$$\Delta E_0^2 = -\frac{2e^2}{I} \{ [(v^2)_1 - (v^2)_1^2] + [(v^2)_2 - (v^2)_2^2] - 2(v^2)_{12} \} \quad (19)$$

From this simple case, we can easily discover the general form of Eq. (19) for atoms with an even number of electrons, and with a little care, the form for an odd number. However, for our purposes of investigating the dependence of the interaction energy on  $\alpha$  and  $\mathcal{E}(z_0)$  for an inhomogeneous electric field, it will be enough to compute  $\Delta E_0^1 + \Delta E_0^2$  for helium.

#### 4. Integrals of Potential Over Atomic Orbitals for Helium

If we were to represent the atomic orbitals by Slater-type orbitals (STO), the integrals over the exponentially varying field and potential would be easily calculated. As a first step, however, we will consider the case of a constant field, for which  $\Delta V$  or  $v$  is  $-\mathcal{E}_0(z - z_0)$  (where  $\mathcal{E}_0$  is the field strength). Then, for  $1s$  orbitals we will use

$$u_1 = (k^3/\pi)^{1/2} e^{-kr} \quad (20)$$

The matrix elements of  $v$  over these orbitals vanish, and we have only the matrix elements of  $v^2$ . Since the  $z - z_0$  in the potential is equivalent to  $z$  in the atomic system,

$$(v^2)_1 = \mathcal{E}_0^2 \frac{k^3}{\pi} \int z^2 e^{-2kr} d\tau = \mathcal{E}_0^2/k^2 \quad (21)$$

Using the expression from Eq. (19) for only two electrons,  $E_0^2$  becomes

$$E_0^2 = -\frac{2e^2 \mathcal{E}_0^2}{Ik^2} = -\frac{1}{2} \alpha \mathcal{E}_0^2 \quad (22)$$

if  $\alpha$  is taken as  $4e^2/Ik^2$ .

The next step is to calculate the energy for the case of the field  $\mathcal{E}(z) = \mathcal{E}_0 e^{-z/a}$ , where  $z$  is measured from the

atomic center, so that  $\mathcal{E}_0$  contains a dependence on  $z_0$ . Since  $V(z) = a\mathcal{E}_0 e^{-z/a}$ , we have

$$\Delta V = v = V(z) - V(0) = a\mathcal{E}_0 (e^{-z/a} - 1)$$

and

$$v^2 = a^2 \mathcal{E}_0^2 (e^{-2z/a} - 2e^{-z/a} + 1) \quad (23)$$

Of interest then, is the integral

$$\int_0^{2\pi} \int_0^\infty \int_0^\pi e^{-pr} e^{-qr \cos \theta} \sin \theta d\theta r^2 dr d\phi = 8\pi p (q^2 - p^2)^{-2} \quad (24)$$

where we have assumed that the electron distribution of the atom does not extend into the solid. Using the result of Eq. (24) together with the potentials of Eq. (23), we easily obtain

$$(v)_1 = a\mathcal{E}_0 \left[ \frac{1}{(1 - 1/4k^2 a^2)^2} - 1 \right]$$

and

$$(v^2)_1 = a^2 \mathcal{E}_0^2 \left[ \frac{1}{\left(1 - \frac{1}{k^2 a^2}\right)^2} - \frac{2}{\left(1 - \frac{1}{4k^2 a^2}\right)^2} + 1 \right]$$

so that

$$(v^2)_1 - (v)_1^2 = a^2 \mathcal{E}_0^2 \left[ \left(1 - \frac{1}{k^2 a^2}\right)^{-2} - \left(1 - \frac{1}{4k^2 a^2}\right)^{-4} \right] \quad (25)$$

If  $ka$  is large with respect to unity, indicating that the field does not fall off extremely sharply across the atomic dimensions, we can expand Eq. (25), keeping the leading term  $\mathcal{E}_0^2/k^2$ . This is the same result obtained above for the linear case, except for the  $\Delta E_0^1$  term, which now does not vanish. This term is  $-2e(v)_1$  (or  $-\mathcal{E}_0/k^2 a$ ) in the same approximation as the second-order term  $-2e^2 \mathcal{E}_0^2 / Ik^2$  (or  $-\frac{1}{2} \alpha \mathcal{E}_0^2$ ).

To compare the first- and second-order contributions, we need approximate values for the parameters. One calculation for the field outside  $\gamma\text{-Al}_2\text{O}_3$  over a reasonable site gives an  $\mathcal{E}_0$  ( $z_0 = 1.7 \text{ \AA}$ ) of  $6 \times 10^8 \text{ v/cm}$  with  $a = 0.7 \text{ \AA}$ . The value of  $k$  for helium, according to Slater's

rules, is  $1.7/a_0$  or  $3.2 \text{ \AA}^{-1}$ . If  $I$  is about 24 eV, again from Slater's rules, then

$$\frac{\Delta E_0^1}{\Delta E_0^2} = \frac{I}{2e\mathcal{E}_0 a} = \frac{24 \text{ eV}}{(12 \times 10^8 \text{ eV/cm})(0.7 \times 10^{-8} \text{ cm})} = 3 \quad (26)$$

Thus, we must evaluate the contribution of both terms in each case. Much stronger fields would be necessary to decrease the ratio significantly. If we keep the two terms, we can introduce  $\alpha$  into the first, as in Eq. (22); thus,

$$E_0 = \Delta E_0^1 + \Delta E_0^2 = -\alpha I \mathcal{E}_0 / 4ea - \frac{1}{2} \alpha \mathcal{E}_0^2 \quad (27)$$

which shows an  $\alpha$  dependence, provided the  $I$  dependence is not too strong from one atom to the next. These results could explain the observed linear relation between absorption energies and polarizabilities for the rare gases, methane, and even nitrogen (Ref. 3). For example, the effective field could be written as  $\mathcal{E}_0 = \mathcal{E}_0 + I/4ea$ , so that

$$E_0 = -\frac{1}{2} \alpha \mathcal{E}_0^2 + \frac{1}{2} (I/4ea)^2 \quad (28)$$

where the last term might be unimportant and is at least not dependent on  $\alpha$  or on the field strength at  $z_0$ .

Extension of these calculations to other closed-shell atoms and molecules (with the same approximations) is not difficult and is being carried on at present. At the same time, careful comparison with dispersion energies is being undertaken, since these, too, can be dependent mainly on the polarizability of the adsorbed atom for a given surface and for a series of atoms with not too different values of  $I$ .

**N67-15736**

**B. New Expressions for the Energy Density and Momentum Flux of an Electromagnetic Field,**  
M. M. Saffren

In this note we derive what appear to be new expressions for the energy density and momentum flux of an electromagnetic field. These expressions enable us to express the photon momentum flux at a point in space in terms of current-current correlations in the source emitting the radiation.

We proceed by using the theorems given in *SPS* 37-38, Vol. IV, p. 161, to express the components of the photon

stress energy as a function of photon and electron variables. We take the "in" stress-energy tensor to be

$$t_{\lambda\kappa} = f_{\mu\lambda} f_{\kappa}^{\mu} + \frac{1}{4} g_{\lambda\kappa} f_{\mu\nu} f^{\mu\nu} \quad (1)$$

where  $f_{\mu\lambda}$  are the "in" electromagnetic field strengths:

$$f_{\mu\nu} = a_{\mu,\nu} - a_{\nu,\mu} \quad (2)$$

where  $a_{\mu}$  is the "in" 4-potential. From the commutation relations of  $a_{\mu}$ ; namely,

$$\left. \begin{aligned} [a_{\mu}(x), a_{\nu}(y)] &= g_{\mu\nu} D(x-y) \\ D(x) &= \int \frac{[d^3\mathbf{k}]}{|\mathbf{k}|} (e^{ikx} - e^{-ikx}) \end{aligned} \right\} \quad (3)$$

we find that

$$[t_{\lambda\kappa}(x), j_{\nu}(\xi) a^{\nu}(\xi)] = i(h_{\lambda} D_{,\kappa} + h_{\kappa} D_{,\lambda} + g_{\lambda\kappa} h^{\sigma} D_{,\sigma}) \quad (4)$$

where

$$h_{\kappa} = j^{\nu} f_{\nu\kappa} \quad (5)$$

We are now in a position to evaluate Eq. (8) of SPS 37-38, Vol. IV, p. 163, with  $\odot(t) = t_{\kappa\lambda}$  and we find

$$\begin{aligned} T_{\kappa\lambda}(x) &= t_{\kappa\lambda}(x) + \partial_{\lambda} \int_{-\infty}^{x_0} [d^4\xi] h_{\kappa}(\xi) D(\xi - x) \\ &\quad + \partial_{\kappa} \int_{-\infty}^{x_0} [d^4\xi] h_{\lambda}(\xi) D(\xi - x) \\ &\quad + g_{\lambda\kappa} \partial_{\sigma} \int_{-\infty}^{x_0} [d^4\xi] h^{\sigma}(\xi) D(\xi - x) \end{aligned} \quad (6)$$

Letting  $\kappa = 0$ , we find for the photon momentum flux

$$\begin{aligned} \mathbf{E}(x) \times \mathbf{B}(x) &= \mathbf{e}(x) \times \mathbf{b}(x) + \nabla_{\xi} \int [d^3\xi] \frac{\mathbf{J}(\xi, \xi_0) \cdot \mathbf{E}(\xi, \xi_0)}{|\mathbf{x} - \xi|} \Big|_{\xi_0 = x_0 - |\xi - \mathbf{x}|} \\ &\quad - \frac{\partial}{\partial \xi_0} \int [d^3\xi] \frac{\mathbf{J}(\xi, \xi_0) \times \mathbf{B}(\xi, \xi_0)}{|\mathbf{x} - \xi|} \Big|_{\xi_0 = x_0 - |\xi - \mathbf{x}|} \end{aligned} \quad (7)$$

Also, we find for the photon energy density

$$\begin{aligned} \mathbf{E}^2(x) + \mathbf{B}^2(x) &= \mathbf{e}^2(x) + \mathbf{b}^2(x) - \frac{\partial}{\partial \xi_0} \int [d^3\xi] \frac{\mathbf{J}(\xi, \xi_0) \cdot \mathbf{E}(\xi, \xi_0)}{|\mathbf{x} - \xi|} \Big|_{\xi_0 = x_0 - |\xi - \mathbf{x}|} \\ &\quad + \nabla_{\xi} \cdot \int [d^3\xi] \frac{\mathbf{J}(\xi, \xi_0) \times \mathbf{B}(\xi, \xi_0)}{|\mathbf{x} - \xi|} \Big|_{\xi_0 = x_0 - |\xi - \mathbf{x}|} \end{aligned} \quad (8)$$

In differential form, we have

$$\begin{aligned} \left( \nabla_{\mathbf{x}}^2 - \frac{\partial^2}{\partial x_0^2} \right) (\mathbf{E} \times \mathbf{B}) &= \nabla_{\mathbf{x}} (\mathbf{J} \cdot \mathbf{E}) - \frac{\partial}{\partial x_0} (\mathbf{J} \times \mathbf{B}) \\ \left( \nabla_{\mathbf{x}}^2 - \frac{\partial^2}{\partial x_0^2} \right) (\mathbf{E}^2 + \mathbf{B}^2) &= - \frac{\partial}{\partial x_0} (\mathbf{J} \cdot \mathbf{E}) + \nabla_{\mathbf{x}} \cdot (\mathbf{J} \times \mathbf{B}) \end{aligned} \quad (9)$$

so that the right-hand terms are the sources of the photon momentum flux and energy density, respectively.

More importantly, by expressing  $\mathbf{E}$  and  $\mathbf{B}$  in terms of  $\mathbf{J}, J_0$  we obtain an expression for  $\mathbf{E} \times \mathbf{B}$  and  $\mathbf{E}^2 + \mathbf{B}^2$  en-

tirely in terms of the current and charge density. We have for the fields

$$\begin{aligned} \mathbf{E}(x) &= \mathbf{e}(x) - \frac{\partial}{\partial x_0} \int [d^3\xi] \frac{\mathbf{J}(\xi, \xi_0)}{|\xi - \mathbf{x}|} \Big|_{\xi_0 = x_0 - |\xi - \mathbf{x}|} \\ &\quad + \nabla_{\mathbf{x}} \int [d^3\xi] \frac{J_0(\xi, \xi_0)}{|\xi - \mathbf{x}|} \Big|_{\xi_0 = x_0 - |\xi - \mathbf{x}|} \end{aligned}$$

$$\mathbf{B}(x) = \mathbf{b}(x) + \nabla_{\mathbf{x}} \times \int [d^3\xi] \frac{\mathbf{J}(\xi, \xi_0)}{|\xi - \mathbf{x}|} \Big|_{\xi_0 = x_0 - |\xi - \mathbf{x}|}$$

By inserting these values in Eqs. (7) and (8), we obtain the desired expressions. We note that this expression is formally different from the expression obtained by directly evaluating  $1/2[(\mathbf{E} \times \mathbf{B}) - (\mathbf{B} \times \mathbf{E})]$  using the values of  $\mathbf{E}$  and  $\mathbf{B}$  that are given in Eq. (10).

N67-5737

**C. Field Stabilization of NMR Spectrometers by Means of Samples Coaxial and External to the Receiver Coil, D. D. Elleman and S. L. Manatt**

Nuclear stabilized nuclear-magnetic-resonance (NMR) spectrometers for the direct observation of nuclei other than  $^1\text{H}$  and  $^{19}\text{F}$  are few in number and require important instrumentation modifications and additional components which are not available at most NMR spectrometer installations (Ref. 4). A nuclear-stabilized high-resolution spectrometer system for the nuclei  $^2\text{H}$ ,  $^{10}\text{B}$ ,  $^{11}\text{B}$ ,  $^{13}\text{C}$ ,  $^{14}\text{N}$ ,  $^{15}\text{N}$ ,  $^{17}\text{O}$ ,  $^{29}\text{Si}$ ,  $^{31}\text{P}$  (and probably a number of other nuclei), used in conjunction with recently developed time averaging techniques (Refs. 5 and 6), would be practical for investigating numerous chemical systems. Such a system would be especially useful for biological samples, for natural or isotopically labeled molecules, with samples having unfavorable relaxation times, and for magnetic nuclei with low nuclear sensitivities at a constant field relative to  $^1\text{H}$  and  $^{19}\text{F}$ .

We have considered the various aspects of the techniques for achieving nuclear stabilization of NMR spectrometers for nuclei other than  $^1\text{H}$  and  $^{19}\text{F}$ . Nuclear stabilized spectrometers can be divided into two types: (1) those with external control samples (Ref. 4), and (2) those with internal control samples (Ref. 7). Systems of the former type have two receiver coils, two receivers, and, generally, two transmitters; one channel is the control channel and the other is the sample channel. For observation of  $^1\text{H}$ , a water control sample is commonly used. For such a system, only one RF source frequency is necessary. For observation of nuclei other than  $^1\text{H}$ , with this type of system it is common practice to use a water control sample and RF frequency synthesizer techniques in the sample channel to lock the  $^1\text{H}$  control sample frequency to any other frequencies desired (Ref. 4). With this latter method of achieving nuclear stabilization, a resonance line is used in the spectrum to derive a control signal (Ref. 7). In this case, there is only one receiver coil and one RF source. Usually a substance having a sharp single line is added to the mixture or substance to be studied. This technique has been used for some time in the case of  $^1\text{H}$ , and it has been found quite successful for recording  $^{19}\text{F}$  spectra (Refs. 8 and 9).

However, there are certain problems which can arise with this technique. In many cases, one is faced with the difficulty of selecting an appropriate internal reference because of chemical incompatibilities. In the NMR studies of gases, the selection of a reference compound may be difficult. Aqueous solutions also present problems, but we have successfully recorded spectra by means of a reference sample in a coaxial tube or internal capillary (Ref. 9). However, for nuclei with low sensitivities, any reference sample added to a sample to be studied will significantly dilute the number of nuclei of interest in the volume seen by the receiver coil. Another possible solution to the problem was addition of a second receiver coil in the transmitter field in the receiver circuit of commonly available NMR spectrometers. This coil would be wound about a sample of a reference material. This system has been successfully tested<sup>1</sup> for  $^1\text{H}$  and should also work well for  $^{19}\text{F}$ , where a very small sample suffices and maximum signal-to-noise ratio is not critical. With the nuclei  $^{14}\text{N}$ ,  $^{13}\text{C}$ , and  $^{31}\text{P}$ , our tests with an internal-field lock system (Ref. 10), using available 5-mm inserts<sup>2</sup> and 5-mm sample tubes with commonly available RF units and aluminum probes<sup>3</sup>, suggested that the size and disposition of the reference sample required for an extra receiver coil would introduce numerous problems of placement, phase adjustment, homogeneity, tuning, and loss of signal-to-noise ratio<sup>4</sup>. For these reasons, this approach was not investigated further.

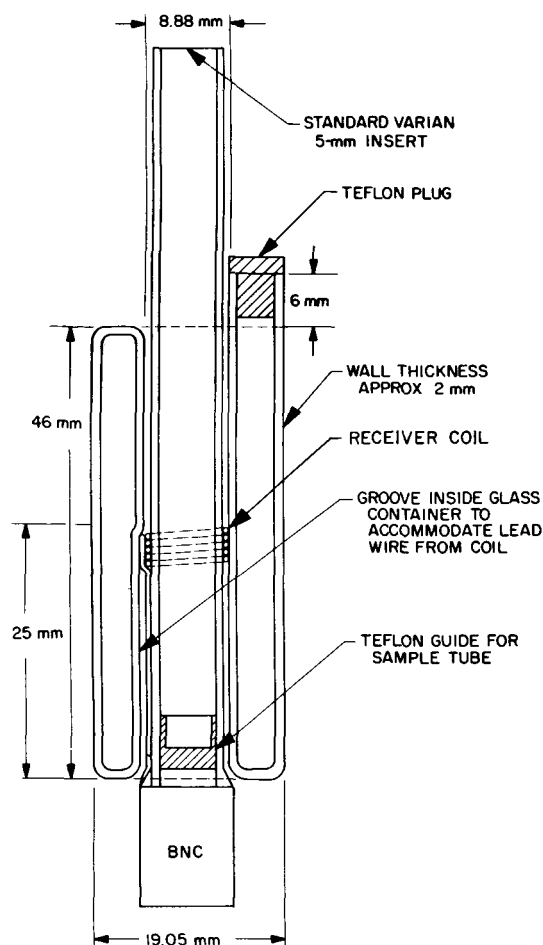
A rather elementary addition to common NMR inserts<sup>2</sup> makes achievement of nuclear stabilization rather simple for nuclei other than  $^1\text{H}$  and  $^{19}\text{F}$ . We have constructed cylindrical sample containers which can be placed coaxially about common 5-mm NMR inserts<sup>2</sup>, as shown in Fig. 1a. We have found that a reference sample in such a container has a field that is sufficiently homogeneous to give a signal suitable for locking the field and frequency of an NMR spectrometer with a simple audio modulation system (Refs. 7 and 10) of the type now in use in a number of laboratories. We have successfully recorded  $^{14}\text{N}$ ,  $^{13}\text{C}$ ,  $^{11}\text{B}$ ,  $^{31}\text{P}$ ,  $^{19}\text{F}$ , and  $^1\text{H}$  spectra when the spectrometer was stabilized on a sample of the corresponding nucleus in such a sample container external to the receiver coil. Resolution of the order of 0.2 to 0.4 cps was achieved for  $^{14}\text{N}$ ,  $^{13}\text{C}$ ,  $^{11}\text{B}$ , and  $^{31}\text{P}$ . The ultimate in design, which would

<sup>1</sup>Private communication from J. D. Baldeschwieler, Stanford University, Stanford, Calif., 1965.

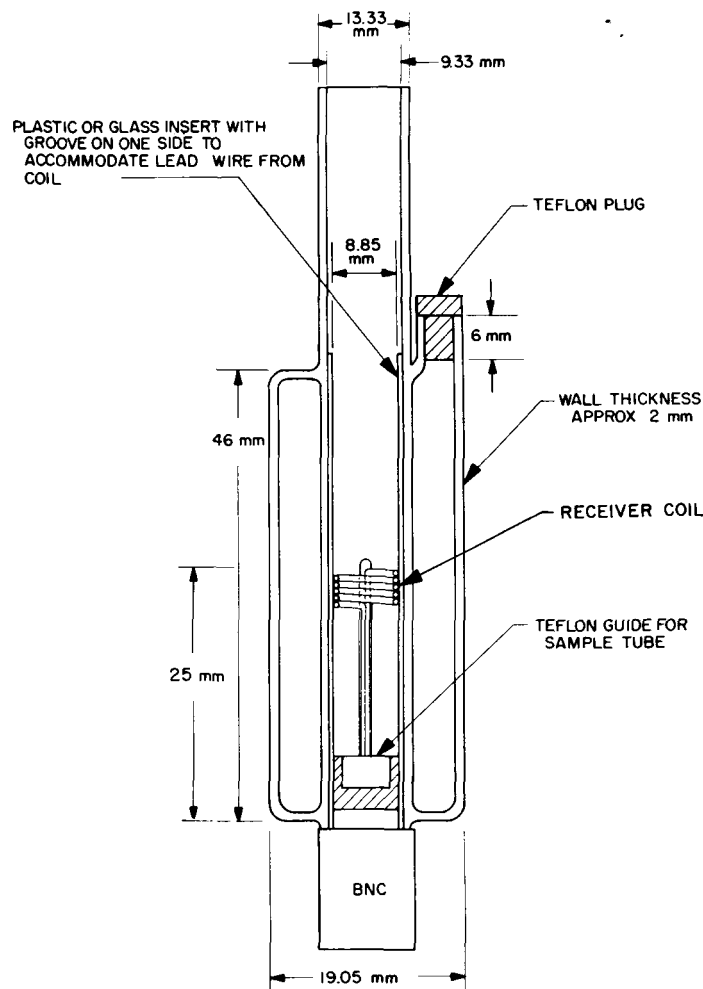
<sup>2</sup>V-4331-5 insert, Varian Associates, Palo Alto, California.

<sup>3</sup>V-4311 RF units and V-4331A probes, Varian Associates, Palo Alto, California.

<sup>4</sup>Some of these problems could no doubt be eliminated by the construction of special probes.



(a) COAXIAL CONTAINER FITTING OVER VARIAN 5-mm INSERT



(b) CONSTRUCTION OF A ONE-PIECE INSERT

**Fig. 1. Coaxial control sample configurations**

increase the field homogeneity at the sample and reference, would be the construction of a one-piece insert with the receiver coil wound inside, as shown in Fig. 1b. The problems concerning the construction of such one-piece inserts are under study<sup>5</sup>.

The placement of a control sample external to the receiver coil, which we have described for nuclear stabilization with nuclei other than  $^1\text{H}$  and  $^{19}\text{F}$ , offers a number of advantages available only with a more complicated NMR system utilizing frequency synthesis (Ref. 4). The spectrometer stays locked when samples are replaced, the study of aqueous solutions and gases is facilitated, the study of chemically reactive systems is made more con-

venient, the use of time-averaging techniques is feasible, the study of certain relaxation effects should be less complicated, the possibility of using NMR for stream analyses appears feasible, and the use of high-resolution NMR in biological studies or kinetic studies requiring a flow system appears practical.

**D. The Signs of Fluorine-Phosphorus Coupling Constants,** S. L. Manatt, D. D. Elleman, A. H. Cowley<sup>6</sup>, and A. B. Burg<sup>7</sup>

Although the magnitudes of a number of fluorine-phosphorus nuclear-magnetic-resonance (NMR) coupling

<sup>6</sup>Department of Chemistry, University of Texas, Austin, Texas.

<sup>7</sup>Department of Chemistry, University of Southern California, Los Angeles, Calif.

<sup>5</sup>The biggest problem at present appears to be the winding and placement of the coil.

constants in fluorine- and phosphorus-containing molecules have been reported (Refs. 11-15), only in a few instances have phosphorus-fluorine coupling constant relative signs been established (Refs. 16 and 17). As part of a general study of the magnitudes and signs of nuclear resonance spin-spin coupling constants, and because the absolute signs of these coupling constants are intimately related to the nature of molecular wave functions (Ref. 18), we report here the signs of certain phosphorus-fluorine spin-spin coupling constants.

We have performed field-sweep double resonance studies on the compounds listed in Table 1 with the results indicated. The relative signs were established from (1) interpretation of changes in the <sup>31</sup>P spectra in transitory selective irradiation experiments (Ref. 19) when either certain <sup>1</sup>H or <sup>19</sup>F lines were saturated, (2) tickling experiments, or (3) partial collapse of multiplet structures with a still larger H<sub>2</sub> field. The interpretation and experimental effort were greatly reduced by simultaneous observation of the <sup>31</sup>P and <sup>19</sup>F spectra or the <sup>31</sup>P and <sup>1</sup>H spectra; this technique will be described subsequently. The <sup>31</sup>P frequency was always held constant and either the <sup>19</sup>F or <sup>1</sup>H frequency was changed.

The absolute signs given in Table 1 are based on the assumption that the sign of the directly bonded phosphorus-proton coupling is absolute positive. The relation of the sign of this coupling to the signs of certain proton-proton couplings has been discussed in detail elsewhere

**Table 1. Relative signs of coupling constants**

Compound	Type of coupling	Sign
CF <sub>3</sub> PH <sub>2</sub>	F-C-P	+
	F-C-P-H	+
	P-H	+
(CH <sub>3</sub> ) <sub>2</sub> PH	F-C-P	+
	F-C-P-H	+
	P-H	+
CF <sub>3</sub> PF <sub>2</sub>	F-C-P	+
	F-C-P-F	-
	P-F	-
(CF <sub>3</sub> ) <sub>2</sub> PF	F-C-P	+
	F-C-P-F	-
	P-F	-
CF <sub>3</sub> -P-P(CH <sub>3</sub> ) <sub>3</sub>	F-C-P	+
	F-C-P-P	+
	P-P	-
	H-C-P	-
	H-C-P-P	-
	H-C-P-P-P	+

(Ref. 20). The results for the compounds CF<sub>3</sub>PH<sub>2</sub> and (CF<sub>3</sub>)<sub>2</sub>PH served to relate the P-H coupling to the P-C-F coupling that was common to many of the fluorophosphine derivatives. A careful scrutiny of the changes of the magnitude of the P-C-F coupling with the nature of the substituents on phosphorus strongly suggests that no inversion of the sign of this coupling is likely for all the molecules reported here. The P-F coupling turns out to be negative, as in the case of the Si-F coupling, and strongly suggests the proposition that any coupling between <sup>19</sup>F and another directly bonded second-row nucleus is negative. Thus Pople and Santry's (Ref. 21) theoretical prediction for coupling between <sup>19</sup>F and another first-row element would seem to be generally true for nuclei of the other rows of the periodic table. The results presented here suggest that, in general, <sup>31</sup>P participates electronically in the coupling to <sup>19</sup>F rather similarly to hydrogen, and phosphorus appears to play a role similar to a carbon atom in a series of atoms in the bonding fragment between coupled nuclei. The F-C-P-F coupling is negative as is the analogous F-C-C-F coupling. The results for CF<sub>3</sub>-P-P(CH<sub>3</sub>)<sub>3</sub> serve to establish that the directly bonded <sup>31</sup>P-<sup>31</sup>P coupling constant is negative even between phosphorus nuclei of widely different valences.

N67-15739

E. Analysis of Mariner II Data for Alfvén Waves,  
T. W. Unti and M. Neugebauer

**1. Introduction**

As indicated by the *Mariner II* magnetometer data<sup>8</sup> (Ref. 22), the solar wind appears to support many large- and small-scale magnetic field fluctuations. The object of the present effort is to determine whether some of these variations are plasma waves (Alfvén and/or acoustic).

**2. Coordinate System**

The satellite measured the interplanetary magnetic field B<sub>k</sub> in a right-handed Cartesian coordinate system x, y, z, where z points radially outward from the Sun, x is in the direction of motion of the satellite and lies in the plane of the ecliptic, and y is normal to the ecliptic (see Fig. 2). The data were first examined for "simple plasma waves"; i.e., linearly polarized waves whose direction of propagation remains essentially constant. For this purpose, 30 sets of data of variable characteristics, length, etc., were chosen on the basis of the apparent presence of quasiperiodic field or plasma variations. In a given coordinate system S, the average value of the magnetic field C<sub>k</sub> is calculated along

<sup>8</sup>Supplied by E. J. Smith and P. J. Coleman, Jr.

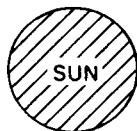
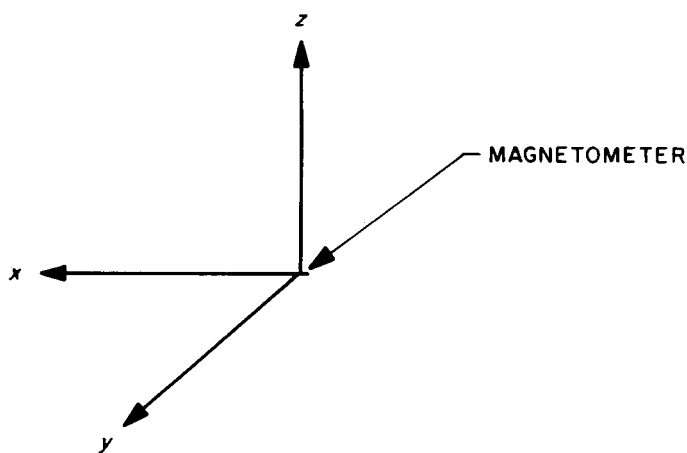


Fig. 2. Mariner II magnetometer coordinate system

each direction  $x, y, z$ . A measure of the fluctuation about that average is

$$D_k = \sum_t |C_k - B_k|$$

where the "sum over time" is a summation over each point of a given set (the 30 sets ranged from about 60 to 580 points).

It is evident that if  $z$  is the direction of the field perturbation of a simple plasma wave, then  $D_3 > D_1$  and  $D_3 > D_2$ . Therefore a coordinate orientation is sought for which  $D = D_1 + D_2$  is minimal. The defect function  $D$  is computed for a given coordinate system; then, as is shown in Fig. 3, the coordinate system is "tilted" via a succession of Euler-angle transformations. After each transformation, the new defect function  $D'$  is computed and compared with  $D$ . After  $D_{min}$  is found, a rotation  $\phi$  is performed in the new  $x, y$  plane, so that  $C_1 = 0$ . The final coordinate system, then, is oriented such that for a given set of magnetometer readings  $C_1 = 0$ , and the field varies primarily along  $z$ .

In seeking a minimal  $D$  coordinate orientation, it was found that, for most of the 30 cases,  $D_3$  was about twice

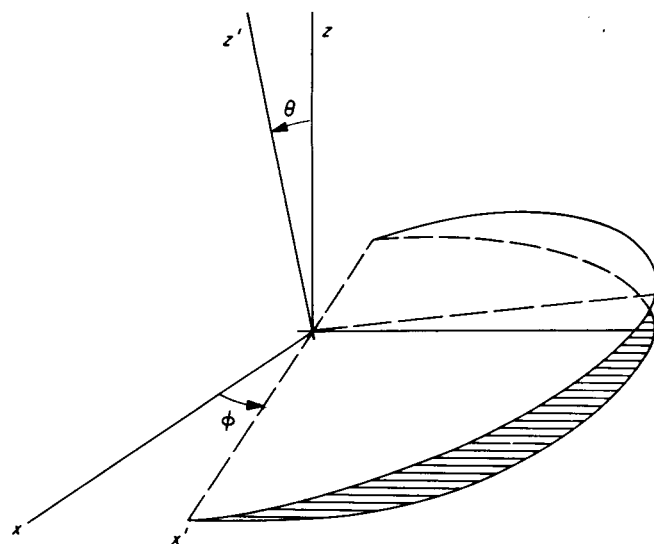


Fig. 3. Euler-angle transformations

as large as  $D_1$  or  $D_2$ . This seems to imply that, in the time intervals represented by the sets of data, the fluctuating "wave" actually does lie in a plane. To proceed with the analysis, it is therefore convenient to consider the fields  $B_1$  and  $B_2$  constant, and equal to  $C_1 = 0$  and  $C_2$ , respectively.

Next, it was observed that in several cases  $C_3 \cong 0$ . For these sets of measurements, the coordinate system is as shown in Fig. 4, where  $b'$  denotes the field fluctuation in the "oriented" coordinate system  $x', y', z'$ .

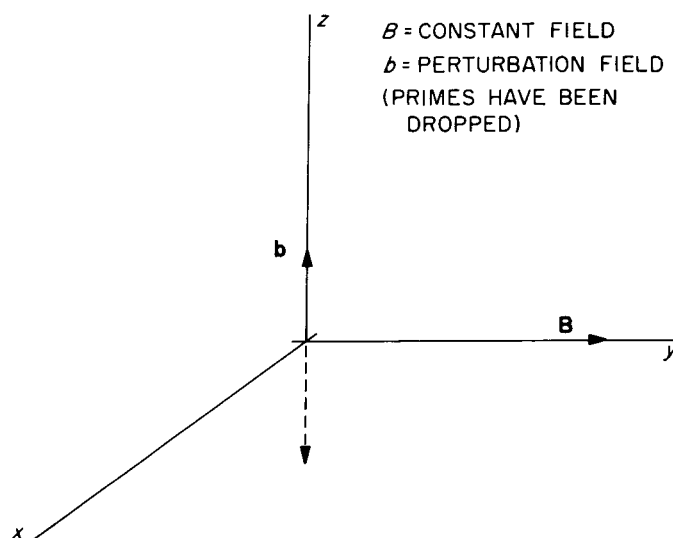


Fig. 4. Final coordinate system and relation of the magnetic field components

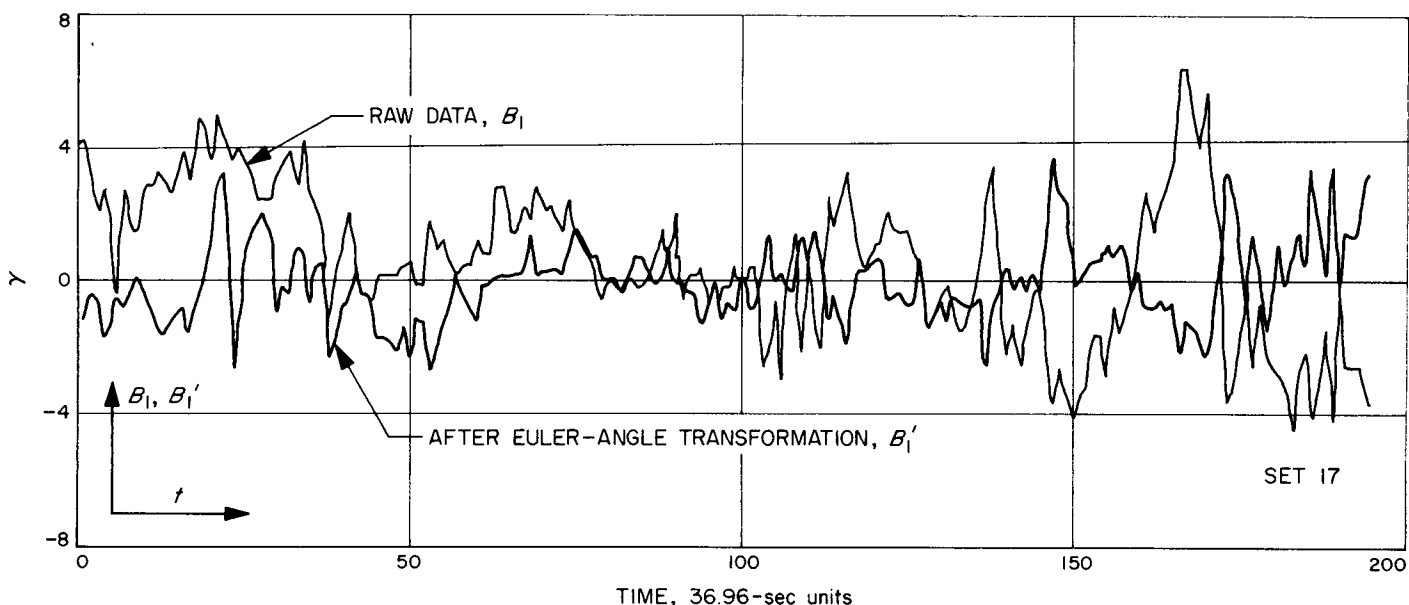


Fig. 5. x-component of magnetic field versus time

Figs. 5, 6, and 7 show the fields before and after the coordinate transformation for set 17. Ignoring the high-frequency oscillations, it is seen that the constant field  $C = B'_2$  has been conveniently extracted via the Euler rotations, and, although there is variation along  $x'$ , the major fluctuation occurs along  $z'$ .

### 3. Analysis

A simplified analysis will be given here. From the linearized hydromagnetic equations for a compressible conducting plasma, one obtains the following mks relations between the constant magnetic field  $B_k$  (the oriented coordinate system of Section 2 is used; primes are dropped), the field perturbations  $b_k$ , the density  $\rho_0$  and its perturbation  $\rho$ , and the plasma velocity perturbation  $v_k$ . (In a more thorough analysis, the velocity of the quiescent solar wind  $V_0$  will be included.) For the equations below, see Ref. 23. Repeated indices are summed:

$$\rho = \bar{\kappa} \rho_0 \alpha_k v_k \quad (1)$$

$$b_k = \bar{\kappa} (B_k \alpha_m - B_n \alpha_n \delta_{km}) v_m \quad (2)$$

$$\left[ \delta_{ij} (1 - \bar{\kappa}^2 A^2 \cos^2 \gamma) - \bar{\kappa}^2 (a^2 + A^2) \alpha_i \alpha_j + \frac{\bar{\kappa}^2}{B} A^2 \cos \gamma (B_i \alpha_j + \alpha_i B_j) \right] v_j = 0 \quad (3)$$

where

$$\bar{\kappa} \equiv k/\omega = (\text{wavelength} \times \text{frequency})^{-1}$$

$$A = (B^2/\mu_0 \rho_0)^{1/2} = \text{Alfvén velocity}$$

$$\alpha_k = \text{unit vector in the direction of propagation}$$

$$\gamma = \text{angle between } \alpha_k \text{ and } B_k$$

$$a = \text{speed of sound in the plasma.}$$

In the oriented coordinate system (Fig. 4), we have

$$\begin{aligned} B_k &= (0, B, 0) \\ b_k &= (0, 0, b) \end{aligned} \quad (4)$$

Hence, by Eq. 2, with  $k = 1, 2, 3$ ,

$$\left. \begin{aligned} 0 &= -\bar{\kappa} B \alpha_2 v_1 \\ 0 &= \bar{\kappa} B (\alpha_1 v_1 + \alpha_3 v_3) \\ b &= -\bar{\kappa} B \alpha_2 v_3 \end{aligned} \right\} \quad (5)$$

If we exclude  $\bar{\kappa} = \infty$ , these three equations imply

$$v_1 = 0, \quad \alpha_3 = 0 \quad (6)$$

so that the vectors bear the relationships shown in Fig. 8, where  $\theta$  and  $\phi$  are as yet undetermined.

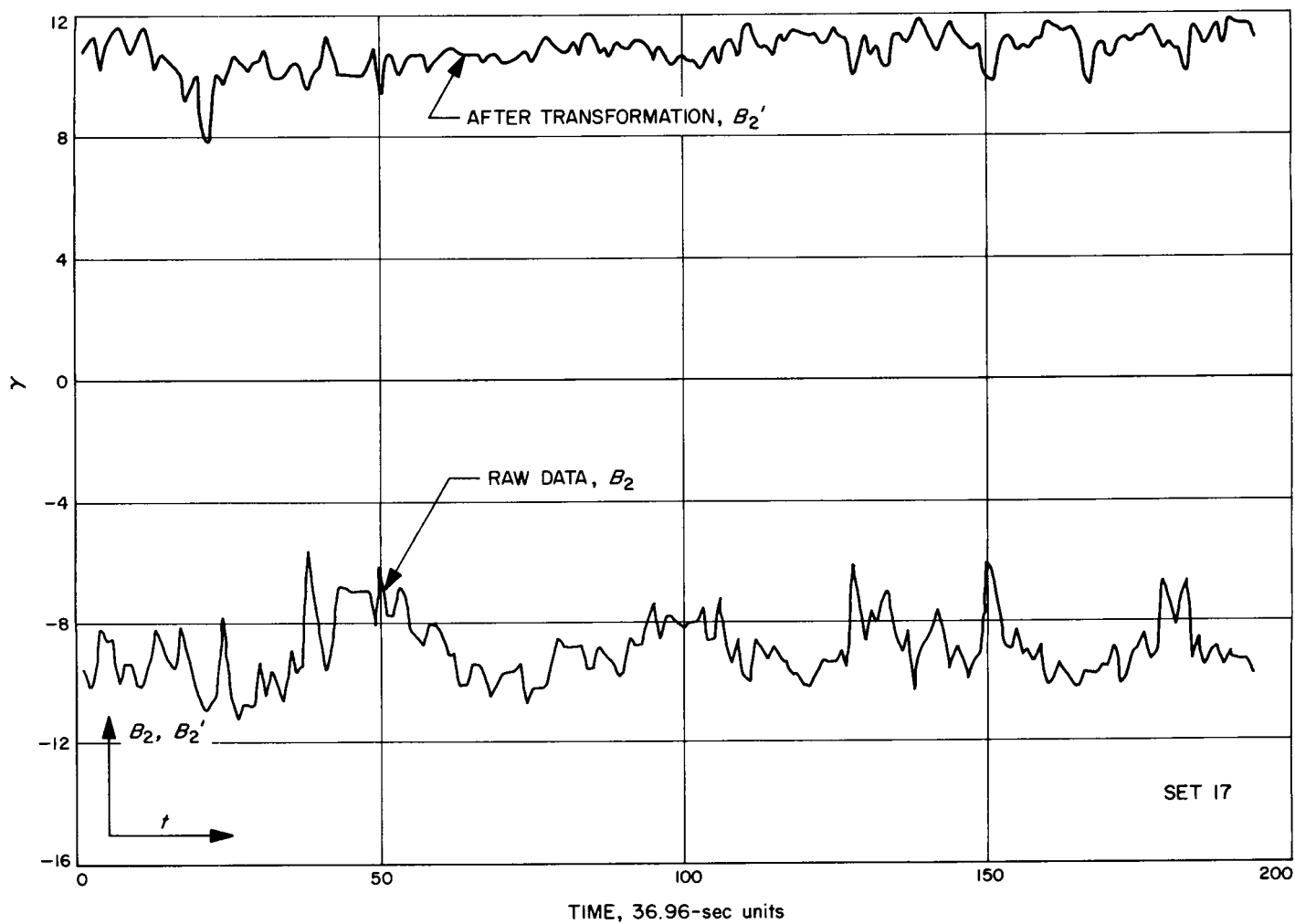


Fig. 6. y-component of magnetic field versus time

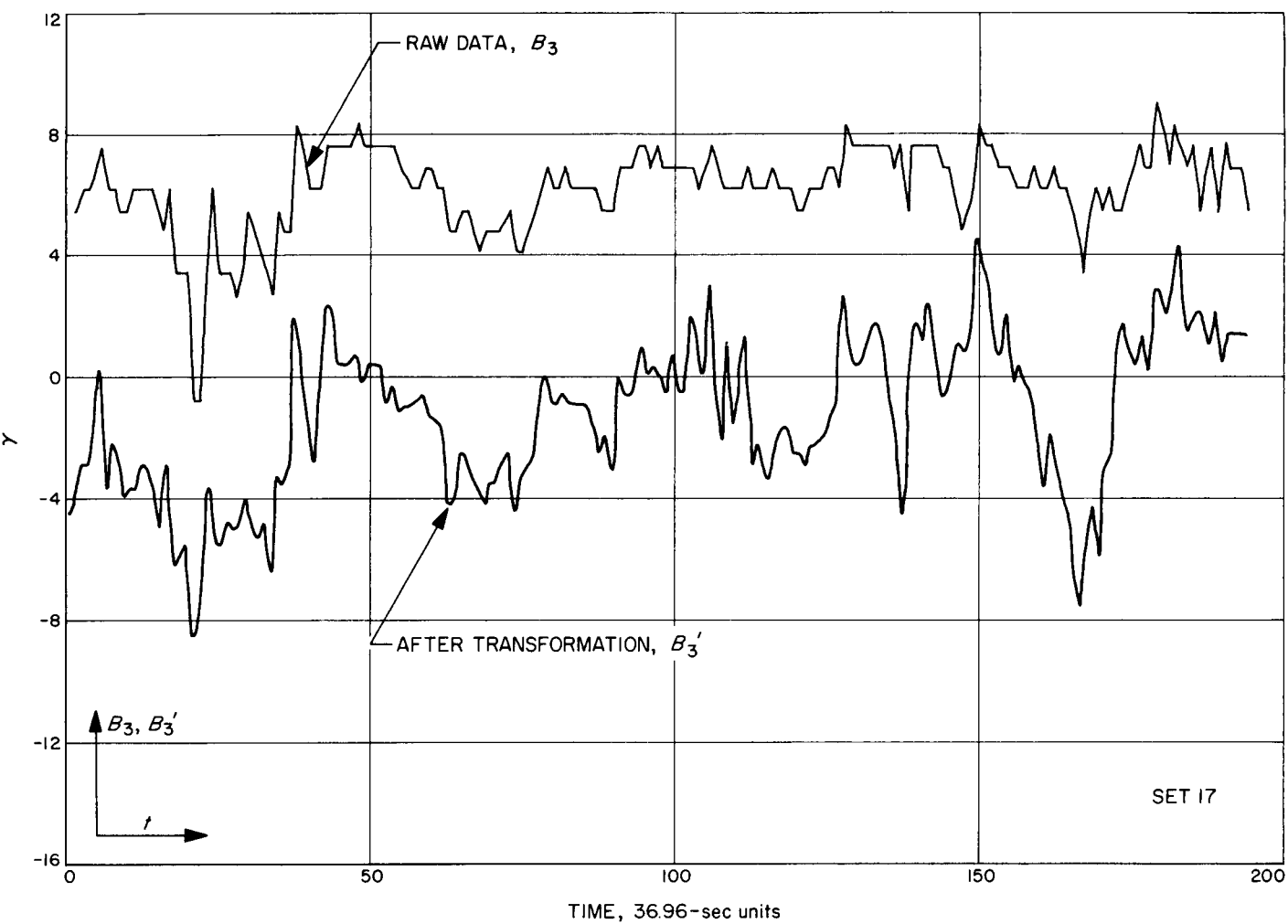


Fig. 7. z-component of magnetic field versus time

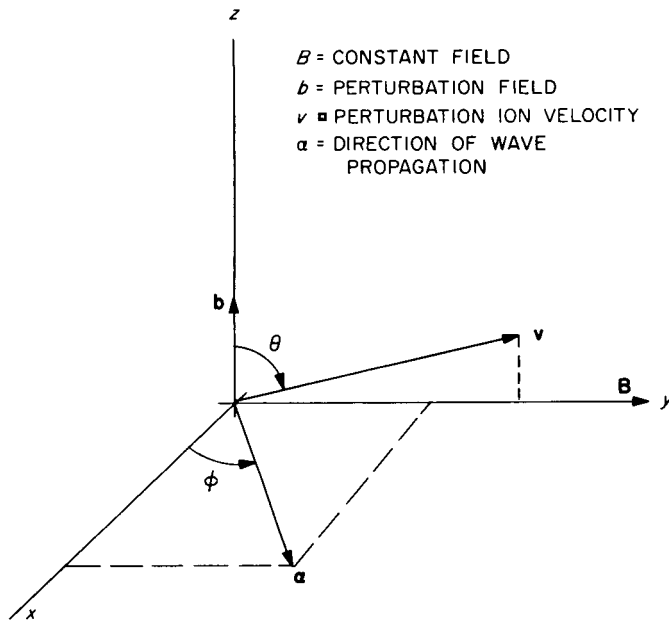


Fig. 8. Relation of parameters to the final coordinate system

We have

$$\left. \begin{aligned} \alpha_1 &= \cos \phi, & v_1 &= 0 \\ \alpha_2 &= \sin \phi, & v_2 &= v \sin \theta \\ \alpha_3 &= 0, & v_3 &= v \cos \theta \end{aligned} \right\} \quad (7)$$

From Eqs. (1) and (2),

$$\rho = \kappa \rho_0 v \sin \phi \sin \theta \quad (8)$$

and

$$b = -\kappa B v \sin \phi \cos \theta \quad (9)$$

so that

$$\tan \theta = -\rho B / b \rho_0 \quad (10)$$

and

$$(\kappa v \sin \phi)^2 = (b/B)^2 + (\rho/\rho_0)^2 \quad (11)$$

By setting the determinant of the matrix multiplying  $v_j$  equal to zero (see Eq. 3), we obtain the "dispersion relation"

$$(\kappa^2 \sin^2 \phi) (\kappa^2 a^2 A^2) - \kappa^2 (a^2 + A^2) + 1 = 0 \quad (12)$$

The measured proton velocity  $|V_k|$  provides the fourth equation in the four unknowns  $\theta, \phi, v, \kappa$ . We have, where  $V_k^0$  is the average (streaming velocity) of the solar wind:

$$V_k = V_k^0 + v_k \quad (13)$$

In polar spherical coordinates (Fig. 9),

$$\left. \begin{aligned} V_1 &= V_0 \cos \phi_V \sin \theta_V \\ V_2 &= V_0 \sin \phi_V \sin \theta_V + v \sin \theta \\ V_3 &= V_0 \cos \theta_V + v \cos \theta \end{aligned} \right\} \quad (14)$$

The measured velocity magnitude of the solar wind protons yields

$$V^2 = V_k V_k = V_0^2 + 2E v + v^2 \quad (15)$$

where  $E = V_0 (\sin \phi_V \sin \theta_V \sin \theta + \cos \theta_V \cos \theta)$ .

Since  $\theta$  is determined by Eq. (10), this may be solved for  $v$ :

$$v = -E + (E^2 + V^2 - V_0^2)^{1/2} \quad (16)$$

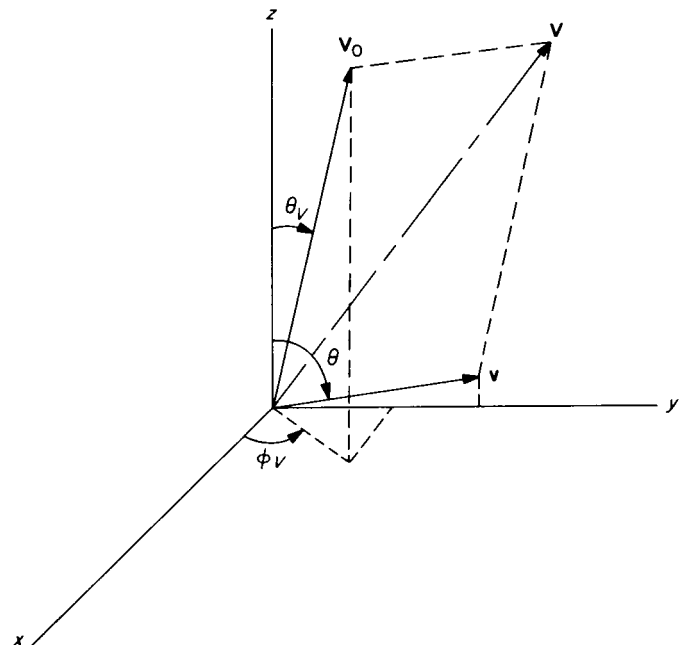


Fig. 9. Relationship of the measured solar wind velocity  $V$  and the perturbation velocity  $v$

By Eq. 11,

$$\kappa^2 \sin^2 \phi = (1/v^2) [(b/B)^2 + (\rho/\rho_0)^2] \equiv Q \tag{17}$$

which defines  $Q$ . Substituting this into Eq. (12) yields the third unknown,

$$\kappa^2 = (a^2 + A^2 - a^2 A^2 Q)^{-1} \tag{18}$$

This, with Eq. (17), yields

$$\sin^2 \phi = Q/\kappa^2 \tag{19}$$

A simple computer program can solve Eqs. (10), (16), (18), and (19), consecutively, for each data point of a given set. Using ordinary statistical criteria, we may determine whether the quantities  $\theta$ ,  $v$ ,  $\kappa$ ,  $\phi$  are constant in time. If so, this may be considered strong evidence for plasma waves. If they are not constant in time, other possibilities must be explored. In particular, the low frequency fluctuations may indicate filamentary structure, hose instability, etc.

#### 4. Future Progress

A least-squares polynomial fit will be used to eliminate the high-frequency oscillations from the  $B_k'$  curves (e.g., see Figs. 5-7). A  $B_3'$  curve which appears to have  $N$  maxima and minima will be least-squares fit by an  $N + 1$  degree polynomial. Usually  $3 \leq N \leq 10$ , so the same degree polynomial would be expected to flatten the  $B_2'$  curve into a nearly straight line. Small variations along the  $x$ -axis will be studied independently.

Preliminary trials suggest that a simple smoothing or averaging process may be more effective for our purposes than a sophisticated minimum-maximum least-squares program. The following "smoothing criterion" may prove useful: The averaging should be just sufficient to reduce the  $B_2'$  to an essentially constant value; this same averaging function would be expected to eliminate only the noise from the  $B_3'$  and  $B_1'$  curves. Identical averaging would also be applied to density, temperature, and velocity fluctuations. The resulting "pure wave forms" can then be studied for phase relationships, etc., to determine whether they satisfy the various interrelationships of Alfvén or acoustic waves. As mentioned in Section 3, it is possible that these large, low-frequency oscillations represent filamentary structure in the interplanetary streaming plasma. If the various wave criteria are not satisfied, this alternative will be carefully considered.

Figs. 10 through 13 show the result of filtering the high frequencies from the  $y$  and  $z$  curves of Figs. 6 and 7. Figs. 10 and 11 are running averages of 12 points, Fig. 10 representing the filtering of the "constant" magnetic field of Fig. 6, and Fig. 11 the perturbation field of Fig. 7. Figs. 12 and 13 are running averages of 18 points. The "proper" degree of filtering must be *ex post facto* adjusted after trial computer results of the analysis outlined in Section 3 (i.e., when we find Alfvén waves, we can stop analyzing).

Finally, the analysis of Section 3 can be carried somewhat further. For example, an equation of state may be determined from the measured temperature and the quantities calculated in Section 3. Various suggestions and hypotheses, such as polarization, rotation of the wave, pressure anisotropy, etc., may also be investigated.

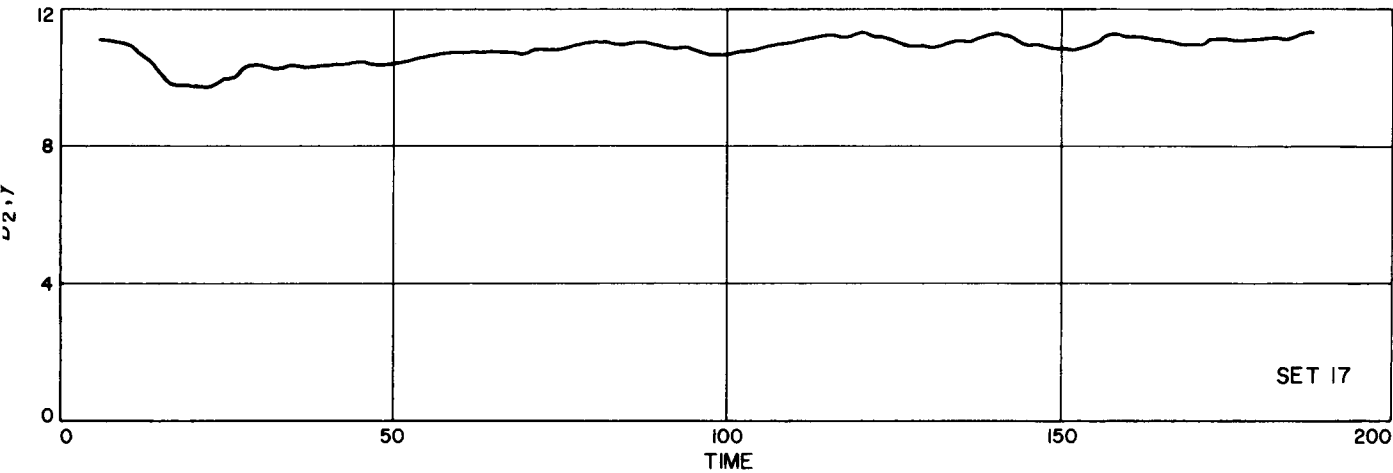


Fig. 10. 12-point running average of  $B_2'$

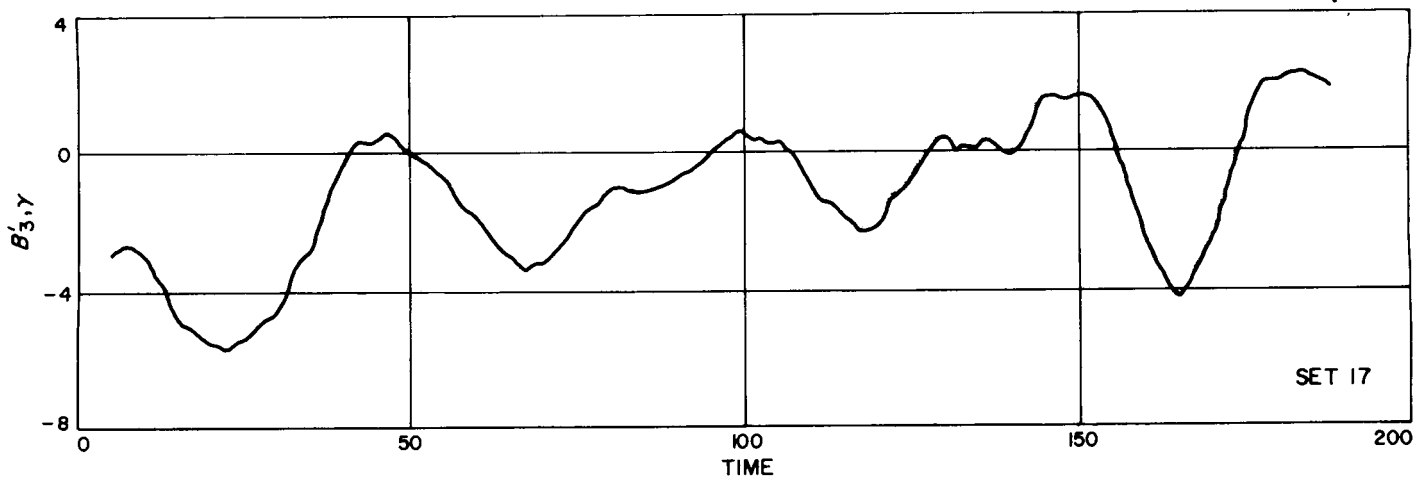


Fig. 11. 12-point running average of  $B'_3$

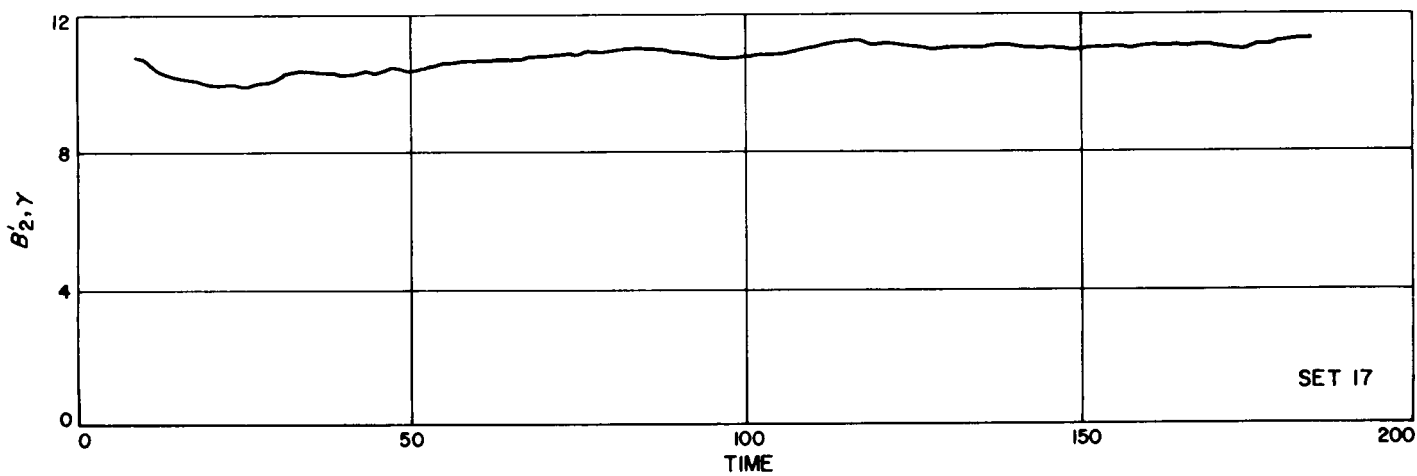


Fig. 12. 18-point running average of  $B'_2$

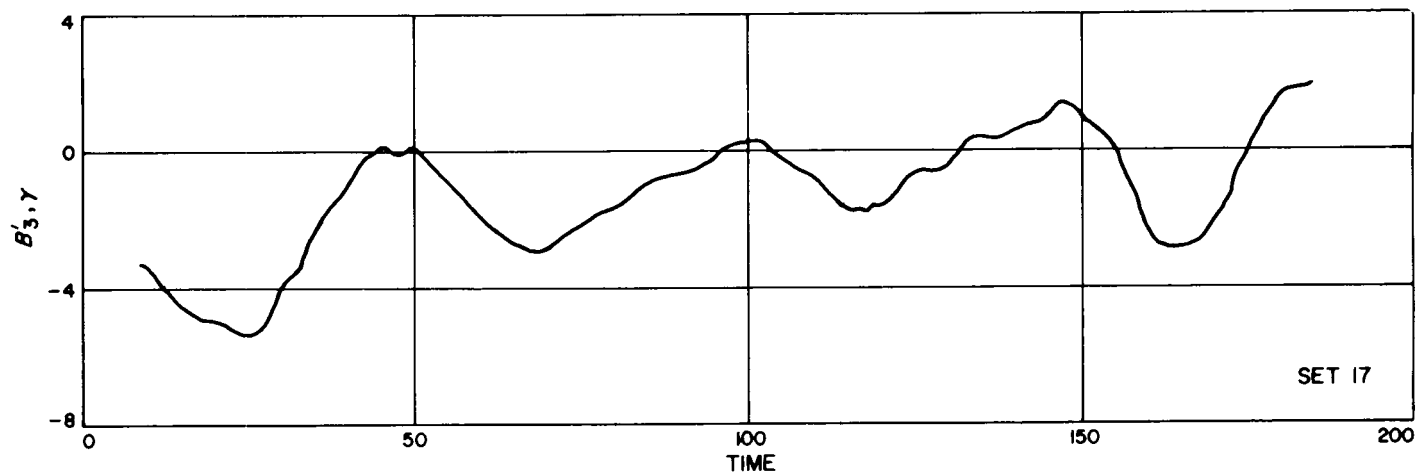


Fig. 13. 18-point running average of  $B'_3$

## F. Junction Conditions in General Relativity, F. B. Estabrook and H. D. Wahlquist

A complete mathematical description of a physical field requires *both* a set of partial differential equations satisfied by the field quantities *and* specification of boundary or junction conditions. For gravity, the field equations are the famous nonlinear Einstein equations of general relativity. The best available formulation of the junction conditions of general relativity has been that of Lichnerowicz (Ref. 24). Having first defined the class of *admissible* coordinates  $\chi^\mu$  in the  $C^2$  differentiable manifold of space-time, Lichnerowicz then asserts that when such a coordinate frame exists in a 4-neighborhood  $N$  (which includes, for example, a 3-surface  $\Sigma$ ):

- (1) the metric tensor  $g_{\mu\nu}(\chi^\nu)$  is, in  $N$ , continuous of class  $C^1$ , and
- (2) the first partials  $g_{\mu\nu,\sigma}$  are, in  $N$ , piecewise continuous of class  $C^2$  (i.e., the higher derivatives  $g_{\mu\nu,\sigma\tau}$ ,  $g_{\mu\nu,\sigma\tau\zeta}$  may jump across a  $\Sigma$  but are continuous tangentially).

O'Brien and Synge (Ref. 25) have shown how the second postulate is physically interpretable in terms of components of the Riemann tensor—in particular, that it includes the relativistic Rankine-Hugoniot relations (Ref. 26). These ensure that no sources of energy and momentum exist as singular distributions on internal boundaries.

We have carefully considered all the physical implications of the junction conditions and reformulated them in a physical tetrad language which does not require the use of admissible coordinates or even the use of a continuous reference tetrad frame. There results a set of 32 scalar conditions of continuity across  $\Sigma$ :

$$({}_R\Lambda_{u,s} + \Gamma_{s'u}^{\prime q} {}_R\Lambda_q)({}_T\Lambda^s - {}_2\Lambda^s \eta_T^2) {}_S\Lambda^u \text{ continuous across } \Sigma$$

$${}_2\Lambda^p {}_R\Lambda^r {}_S\Lambda^s {}_T\Lambda^t {}^*R_{prst} \text{ continuous across } \Sigma$$

Here the  $\Gamma_{s'qu}$  are the Ricci rotation coefficients of the discontinuous tetrad frame, and  ${}^*R_{prst}$  are the tetrad components of the double-dual Riemann tensor. These are all physically interpretable quantities (Ref. 27). The  ${}_R\Lambda^u$  is an implicitly defined orthogonal transformation matrix field on  $\Sigma$ —but different on either side of  $\Sigma$ .

These 32 conditions may be specialized to 29 conditions, by taking  ${}_2\Lambda^r$  to be the tetrad components of the unit normal to  $\Sigma$ . These 29 conditions may be divided into

sets: 14 conditions on the Riemann components, 9 conditions requiring the intrinsic metric description of  $\Sigma$  to be the same from either side, and 6 conditions requiring the second fundamental form of  $\Sigma$  to be the same from either side. The last two sets mix when  $\Sigma$  is null.

We have preferred, however, to calculate the explicit conditions in a dyadic notation (Ref. 27) for the case of normal boundary motion; namely, when the reference frame on either side of  $\Sigma$  is seen, in the reference frame on the other side of  $\Sigma$ , to be moving with 3-velocity normal to the instantaneous bounding 2-surface, or shock front. There results a set of dyadic conditions which may be used with great convenience to formulate exact, but discontinuous, solutions of the Einstein field equations. Such exact solutions are extremely rare in the literature of relativity theory, no doubt because of the unnecessary restriction to admissible, or at least continuous, coordinate systems.

A complete account of the tetrad and dyadic formulations of the junction conditions has been submitted for publication in the open literature. As a first application, an interesting set of discontinuous, spherically symmetric, nonstatic exact solutions has been found, which will be described in a subsequent *Space Programs Summary*.

## G. Molar Extinction Coefficients of Hydrogen Iodide in the Schumann Region, O. F. Raper and W. B. DeMore

### 1. Introduction

Since the early work of Warburg, gaseous hydrogen iodide has proven to be a useful chemical actinometer for radiation in the Schumann region of the ultraviolet (Ref. 28). HI absorbs continuously in the wavelength region from about 3300 Å to below 2000 Å, with an observed loss of two HI molecules per quantum absorbed, the net reaction being  $2\text{HI} + h\nu \rightarrow \text{H}_2 + \text{I}_2$ . While the quantum yield of two and the limiting range of experimental conditions over which this quantum yield is realized have been fairly well established (Ref. 29), there appear to be no published values for the extinction coefficients of HI in this region later than those of Romand (Ref. 30) and Goodeve and Taylor (Ref. 31), with those of Romand covering the widest spectral range.

Cursory examination of the spectrum of HI in the Schumann region which can be obtained with presently available instruments shows a general lack of agreement with that reported earlier by Romand. Since accurate

values for the extinction coefficients are necessary for actinometric determinations and for theoretical consideration of the electronic states of HI involved in the absorption, it was deemed advisable to reinvestigate the spectral characteristics of HI in the 2000– to 3000-Å region. Such an investigation has now been made, and the results are presented here.

## 2. Experimental

The experimental apparatus used is shown in Fig. 14. The hydrogen iodide was obtained from Matheson and contained about 2%  $H_2$  and  $I_2$  as major impurities. These were removed by collecting the HI and  $I_2$  in U-tube 1 at liquid  $N_2$  temperature, while pumping (thus removing the  $H_2$ ), and subsequently distilling the HI from a dry ice-acetone bath (which retained the  $I_2$ ) into U-tube 2, where it was again collected at liquid nitrogen temperature. The resultant product was a pure-white powder which, when evaporated for a short period of time and then recondensed, showed no trace of color and left no residual pressure. These properties indicated it to be an HI sample that was free of  $I_2$  and  $H_2$  and was not decomposing rapidly in the system. Prolonged periods of standing in the gas phase did produce some decomposition of the HI, but these periods were long compared with the time necessary to measure the HI pressure on the sulfuric acid manometer and to isolate the sample in the absorption cell. Once in the cell, the HI could be kept indefinitely with no apparent decomposition.

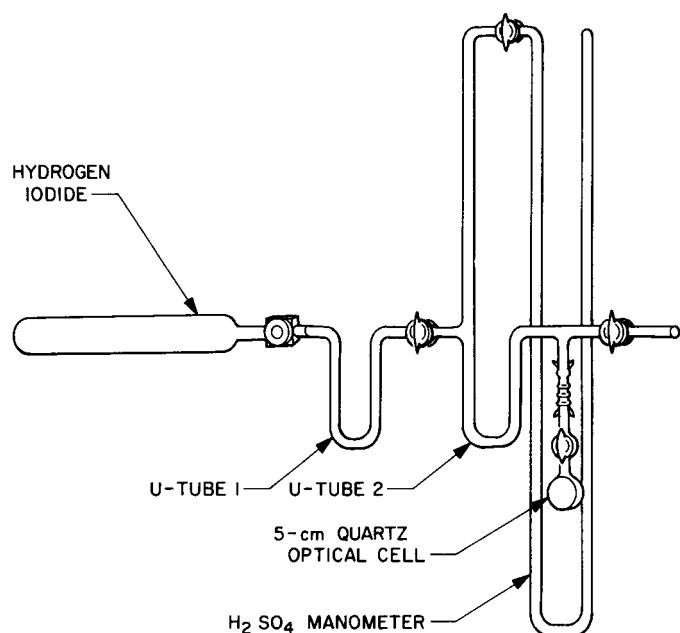


Fig. 14. Experimental apparatus

The density of the  $H_2SO_4$  used in the manometer was determined both gravimetrically and by comparison with a mercury manometer, the results agreeing to within 0.5%. The optical density versus wavelength curves in the region of interest for HI samples at various pressures were obtained directly by means of a Cary Model 11 recording spectrophotometer. The wavelength scale of the Cary spectrophotometer was calibrated with a low-pressure mercury arc and was accurate to  $\pm 0.5$  Å.

## 3. Results and Discussion

Fig. 15 is a plot of optical density versus HI concentration at a wavelength near the maximum for HI absorption in this region (2220 Å). This plot shows no deviation from Beer's law in the HI absorption over the concentration range studied, and also tends to confirm that only pure HI is present in the cell. Any impurities other than those proportional to the HI would cause more scatter in these results than is observed in Fig. 15. Since the only likely impurities are the HI decomposition products  $H_2$  and  $I_2$ , and since the histories of the individual samples prior to the optical density determinations varied widely, it is unlikely that these impurities would be present in constant proportion to the HI.

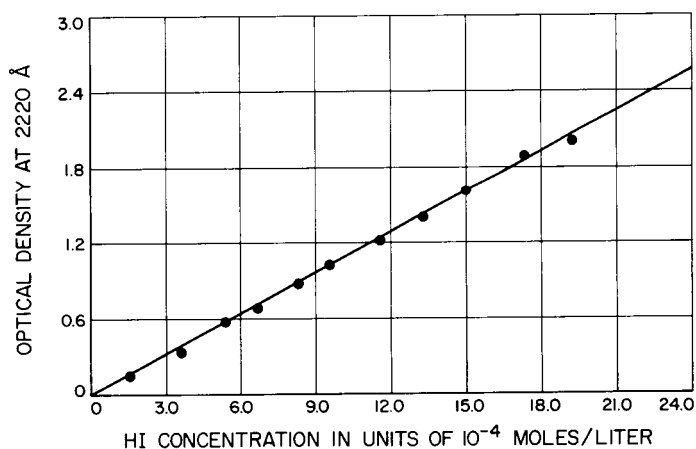
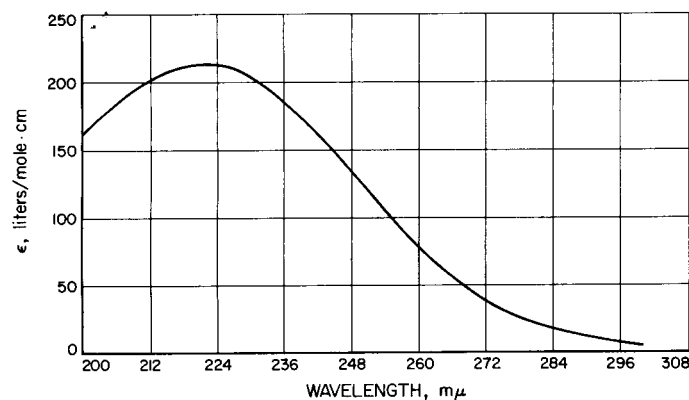


Fig. 15. Observed optical density of HI at 2220 Å as a function of concentration

The molar extinction coefficients for HI between 2000 and 3000 Å are shown graphically in Fig. 16. The coefficient  $\epsilon$  is defined by the equation

$$\log_{10} I_0/I = \epsilon \times c \times l$$

where  $c$  represents the concentration in moles/liter and  $l$  the path length in centimeters. Table 2 is a numerical compilation of the data from Fig. 16. In addition, it lists some



**Fig. 16. Molar extinction coefficients for HI (2000 to 3000 Å)**

of the results of two similar studies, not yet published, made by A. A. Gordus of the University of Michigan<sup>9</sup> and J. M. White of the California Institute of Technology<sup>10</sup>. In the study by Gordus, the  $\epsilon$  values were obtained by averaging several determinations at fixed wavelengths, and since these wavelengths did not correspond exactly to those used in Table 2, the values shown are interpolations of the original data.

While some discrepancies are apparent among the results shown in the table, agreement is, in general, quite good for this type of determination. White's values at the longer wavelengths are slightly higher than those of the authors and may represent somewhat more reliable results in this region. Wavelengths below 2600 Å were of primary interest in the present study, and the lower concentrations used tended to decrease the accuracy of the determinations in the regions of weaker absorption. Gordus' values at the shorter wavelengths agree quite well with those of the present work, except at the maximum, where his appear to be about 1½% lower.

None of the values reported here are in agreement with those reported earlier by Romand, nor is his figure for the wavelength at the absorption maximum consistent with that shown in Fig. 16. While no specific reasons can be given for these discrepancies, the present availability of accurate scanning spectrophotometers and high purity research gases eliminates many of the experimental difficulties encountered in the past. Thus, measurements can, in general, be made with more accuracy than was previously possible. This fact and the excellent agreement

**Table 2. Extinction coefficient, liters/mole-cm**

Wavelength, Å	Present work	White	Gordus
3000	5.42	5.63	—
2980	6.44	6.51	—
2960	7.46	7.44	—
2940	8.48	8.74	—
2920	9.61	10.04	—
2900	11.5	11.53	—
2880	13.2	13.58	—
2860	15.1	15.44	—
2840	17.3	17.86	—
2820	20.0	20.60	—
2800	23.0	23.4	—
2780	26.4	26.78	—
2760	30.3	30.69	—
2740	34.0	35.15	34.2
2720	39.7	39.99	40.18
2700	44.8	45.6	45.58
2680	50.7	51.52	51.39
2660	57.0	58.22	57.74
2640	64.3	65.10	64.71
2620	71.5	72.73	72.38
2600	79.2	80.9	80.32
2580	88.2	89.65	88.8
2560	97.1	98.39	97.5
2540	106.5	108.3	106.8
2520	116.1	117.6	116.1
2500	125.2	127.7	125.7
2480	135.4	137.5	135.0
2460	144.8	146.8	145.1
2440	154.1	156.4	154.0
2420	163.5	—	163.2
2400	172.9	—	172.3
2380	181.8	—	180.6
2360	190.4	—	187.8
2340	196.3	—	194.0
2320	202.2	—	200.2
2300	208.3	—	205.6
2280	212.1	—	209.2
2260	215.4	—	212.4
2240	217.0	—	214.1
2220	217.8	—	214.6
2200	217.6	—	213.9
2180	215.9	—	212.1
2160	213.8	—	209.4
2140	209.9	—	206.6
2120	205.2	—	203.5
2100	199.9	—	—
2080	193.4	—	—
2060	187.8	—	—
2040	180.6	—	—
2020	173.3	—	—
2000	166.1	—	—

between these results and those of Gordus and White tend to indicate that the present values for the HI extinction coefficients can be used with some confidence. Error estimates place a limit of  $\pm 1$  Å on the wavelength accuracy and a limit of  $\pm 2\%$  on the absolute values of the extinction coefficients.

<sup>9</sup>Gordus, A. A., Personal communication to A. Kuppennann, California Institute of Technology, 1966.

<sup>10</sup>White, J. M., Personal communication to O. F. Raper, Jet Propulsion Laboratory, 1966.

# H. Four-Fermion Interaction Lagrangians, J. S. Zmuidzinas

In this note, we show how the combination of the Pauli exclusion principle and the Fierz rearrangement theorem limits the arbitrariness of a Lorentz-invariant interaction Lagrangian (density)  $L_1$  for a self-coupled Dirac field  $\psi$ . Our considerations are restricted to quartic Lagrangians; higher-order Lagrangians will be discussed in a paper now in preparation. Moreover, we limit ourselves to gradient-free and local expressions for  $L_1$ . No restrictions are imposed on the discrete space-time properties of  $L_1$ .

The most general form  $L_1$ , subject to the restrictions of the preceding paragraph, is

$$L_1 = \bar{\psi}_\alpha \bar{\psi}_\beta A_{\alpha\beta, \gamma\delta} \psi_\gamma \psi_\delta \equiv \bar{\psi} \bar{\psi} A \psi \psi \quad (1)$$

where the Greek (spinor) indices are summed from 1 to 4,  $\bar{\psi} = \psi^\dagger \gamma_0$ , and

$$A_{\alpha\beta, \gamma\delta} = \sum_{A, B} h_{AB} \Gamma_{\alpha\beta}^A \Gamma_{\gamma\delta}^B \quad (2)$$

or simply

$$A = \sum_{A, B} h_{AB} \Gamma^A \otimes \Gamma^B \quad (3)$$

Here the  $\Gamma^A$  are the sixteen Dirac matrices, explicitly given by

$$\begin{aligned} \Gamma^1, \dots, \Gamma^5 &= \gamma^0, i\gamma^1, i\gamma^2, i\gamma^3, i\gamma^4 \\ \Gamma^6, \dots, \Gamma^9 &= i\sigma^{05}, \sigma^{15}, \sigma^{25}, \sigma^{35} \\ \Gamma^{10}, \dots, \Gamma^{12} &= i\sigma^{01}, i\sigma^{02}, i\sigma^{03} \\ \Gamma^{13}, \dots, \Gamma^{15} &= \sigma^{23}, \sigma^{31}, \sigma^{12} \\ \Gamma^{16} &= 1 \end{aligned}$$

We use the conventions

$$\begin{aligned} (\gamma^j) &= (\gamma^0, \gamma^1, \gamma^2, \gamma^3, \gamma^5) \\ \gamma^5 &= \gamma^0 \gamma^1 \gamma^2 \gamma^3 \\ \sigma^{JK} &= \frac{i}{2} (\gamma^J \gamma^K - \gamma^K \gamma^J) \\ \gamma^J \gamma^K + \gamma^K \gamma^J &= 2g^{JK} \\ (g^{JK}) &= \text{diag}(1, -1, -1, -1, -1) \\ \gamma^{J\dagger} &= \gamma_0 \gamma^J \gamma_0 \end{aligned}$$

The completeness relation for the  $\Gamma$  matrices is

$$\begin{aligned} \sum_A \Gamma_{\alpha\beta}^A \Gamma_{\gamma\delta}^A &= \delta_{\alpha\beta} \delta_{\gamma\delta} + (\gamma_J)_{\alpha\beta} (\gamma^J)_{\gamma\delta} + \frac{1}{2} (\sigma_{JK})_{\alpha\beta} (\sigma^{JK})_{\gamma\delta} \\ &= 4\delta_{\alpha\delta} \delta_{\beta\gamma} \end{aligned} \quad (4)$$

Using this relation, it is easy to see that

$$X \otimes Y = \frac{1}{4} \sum_A \Gamma^A \otimes (X \Gamma^A Y) \quad (5)$$

for any two matrices  $X$  and  $Y$  in the Dirac algebra. Using this result and the Pauli exclusion principle in the form  $\bar{\psi}_\alpha \bar{\psi}_\beta = -\bar{\psi}_\beta \bar{\psi}_\alpha$  (remembering that  $\bar{\psi}$ 's are at the same space-time point), we find that

$$\begin{aligned} \bar{\psi} \bar{\psi} \left( \sum_{A, B} h_{AB} \Gamma^A \otimes \Gamma^B \right) \psi \psi &= \\ \bar{\psi} \bar{\psi} \left[ -\frac{1}{4} \sum_{A, B, C} h_{AB} \Gamma^C \otimes (\Gamma^A \Gamma^C \Gamma^B) \right] \psi \psi \end{aligned}$$

Taking matrix elements of the two sides of this equation between arbitrary states, we conclude that

$$\sum_{A, B} h_{AB} \Gamma^A \otimes \Gamma^B = -\frac{1}{4} \sum_{A, B, C} h_{AB} \Gamma^A \otimes (\Gamma^A \Gamma^C \Gamma^B) \quad (6)$$

This is a restriction on the constants  $h_{AB}$ . Another obvious (from Eq. 1) restriction on these constants is their symmetry:

$$h_{AB} = h_{BA} \quad (7)$$

Taking into account Eq. (7), the explicit form of Eq. (3) is

$$A = \sum_{k=1}^8 h_k A_k \quad (8)$$

where  $h_k$  are real constants, and

$$\begin{aligned}
A_1 &= 1 \otimes 1 \\
A_2 &= \frac{1}{2} (1 \otimes \gamma^5 + \gamma^5 \otimes 1) \\
A_3 &= \gamma^5 \otimes \gamma^5 \\
A_4 &= \gamma^\mu \otimes \gamma^\mu \\
A_5 &= \frac{1}{2} (\gamma^\mu \otimes i\gamma^\mu \gamma^5 + i\gamma^\mu \gamma^5 \otimes \gamma^\mu) \\
A_6 &= i\gamma^\mu \gamma^5 \otimes i\gamma^\mu \gamma^5 \\
A_7 &= \frac{1}{2} \sigma_{\mu\nu} \otimes \sigma^{\mu\nu} \\
A_8 &= \frac{1}{2} \sigma_{\mu\nu} \otimes \sigma^{\mu\nu} \gamma^5
\end{aligned}$$

In terms of Eq. (8), Eq. (6) reads

$$\sum_{k=1}^8 h_k A_k = \sum_{k=1}^8 h_k A'_k \quad (9)$$

where  $A'_k$  denotes the Fierz-transformed  $A_k$  (computed by Eq. 6). We find after some computation that

$$\left. \begin{aligned}
-4A'_1 &= A_1 + A_3 + A_4 + A_6 + A_7 \\
-4A'_2 &= 2A_2 + A_8 \\
-4A'_3 &= A_1 + A_3 - A_4 - A_6 + A_7 \\
-4A'_4 &= 4A_1 - 4A_3 - 2A_4 + 2A_6 \\
-4A'_5 &= -4A_5 \\
-4A'_6 &= 4A_1 - 4A_3 + 2A_4 - 2A_6 \\
-4A'_7 &= 6A_1 + 6A_3 - 2A_7 \\
-4A'_8 &= 12A_2 - 2A_8
\end{aligned} \right\} \quad (10)$$

It can be readily verified that Eq. (9) is satisfied by arbitrary  $h_1, h_2, h_3, h_4, h_5$ , and by

$$\begin{aligned}
h_6 &= -\frac{1}{2} (h_1 - h_3) - h_4 \\
h_7 &= -\frac{1}{2} (h_1 + h_3) \\
h_8 &= -\frac{1}{2} h_2
\end{aligned}$$

Thus, there are only five, rather than the eight *a priori*, arbitrary coupling constants in  $L_1$ :

$$\begin{aligned}
L_1 &= h_1 \left( A_1 - \frac{1}{2} A_6 - \frac{1}{2} A_7 \right) \\
&\quad + h_2 \left( A_2 - \frac{1}{2} A_8 \right) \\
&\quad + h_3 \left( A_3 + \frac{1}{2} A_6 - \frac{1}{2} A_7 \right) \\
&\quad + h_4 (A_4 - A_6) \\
&\quad + h_5 A_5 \\
&\equiv \sum_{k=1}^5 h_k B_k
\end{aligned}$$

We now briefly discuss the chiral transformation properties of  $L_1$ . Under the chirality transformation

$$\psi \rightarrow \exp(\alpha\gamma_5/4) \psi, \quad \bar{\psi} \rightarrow \bar{\psi} \exp(\alpha\gamma_5/4)$$

we find that  $B_5$  and  $B_6$  are separately invariant, while  $B_1, B_2$ , and  $B_3$  are not. However, one can show that the combinations

$$C_1 = B_1 + B_2 + B_3 \equiv A_1 + A_2 + A_3 - A_7 - \frac{1}{2} A_8$$

$$C_2 = \frac{1}{2} (B_1 + B_3) - 2B_2 \equiv \frac{1}{2} (A_1 + A_3 - A_7) - 2A_2 + A_8$$

$$C_3 = B_1 - B_3 \equiv A_1 - A_3 - A_6$$

have simple chiral transformation properties:

$$\begin{aligned}
C_1 &\rightarrow C_1 \cos \alpha + C_2 \sin \alpha \\
C_2 &\rightarrow -C_1 \sin \alpha + C_2 \cos \alpha \\
C_3 &\rightarrow C_3
\end{aligned}$$

Inasmuch as the  $h_k$  are arbitrary, we may redefine them and write  $L_1$  in terms of the  $C_k$ :

$$L_1 = \sum_{k=1}^5 h_k C_k$$

In this form,  $L_1$  is Fierz-invariant (i.e., invariant under substitutions  $A_k \rightarrow A'_k$  given by Eqs. 10) and, moreover, its 3, 4, 5 terms are chiral-invariant. Furthermore, it is rather interesting to note that *the whole of  $L_1$  is invariant under the discrete chiral transformation  $\psi \rightarrow \exp(\pi\gamma_5/2) \psi \equiv \gamma_5 \psi$ , corresponding to  $\alpha = 2\pi$ .*

## References

1. King, J., Jr., and Benson, S. W., *Journal of Chemical Physics*, Vol. 44, p. 1007, 1966.
2. Lennard-Jones, J. E., and Dent, B. M., *Transactions of the Faraday Society*, Vol. 24, p. 92, 1928.
3. King, J., Jr., and Benson, S. W., *Analytical Chemistry*, Vol. 38, p. 261, 1966.
4. Baker, E. B., and Burd, L. W., *Review of Scientific Instruments*, Vol. 34, p. 238, 1963.
5. Allen, L. C., and Johnson, L. F., *Journal of the American Chemical Society*, Vol. 85, p. 2668, 1963.
6. Allen, L. C., Gladney, H. M. and Glarum, S. H., *Journal of Chemical Physics*, Vol. 40, p. 3135, 1964.
7. Freeman, R., and Anderson, W., *Journal of Chemical Physics*, Vol. 37, p. 2053, 1962.
8. Manatt, S. L., and Elleman, D. D., Paper presented at the 4th Omnibus Conference on Experimental Aspects of NMR Spectroscopy, Mellon Institute, Pittsburgh, Pa., February 25–March 1, 1963, and at the 5th Experimental NMR Conference, Mellon Institute, Pittsburgh, Pa., February 1964.
9. Servis, K. L., and Roberts, J. D., *Journal of the American Chemical Society*, Vol. 87, p. 1339, 1965.
10. Elleman, D. D., Manatt, S. L., and Pearce, C. D., *Journal of Chemical Physics*, Vol. 42, p. 650, 1965.
11. Nixon, J. F., *Journal of the Chemical Society*, Vol. 1965, p. 777, 1965.
12. Nixon, J. F., and Schmutzler, R., *Spectrochimica Acta*, Vol. 20, p. 1835, 1964.
13. Schmutzler, R., and Reddy, G. S., *Inorganic Chemistry*, Vol. 4, p. 191, 1965.
14. Muetterties, E. L., Mahler, W., and Schmutzler, R., *Inorganic Chemistry*, Vol. 2, p. 613, 1963.
15. Holmes, R. R., Carter, R. F., Jr., and Peterson, G. E., *Inorganic Chemistry*, Vol. 3, p. 1748, 1964.
16. Mahler, W., *Journal of the American Chemical Society*, Vol. 86, p. 2306, 1964.
17. Harris, K., and Woodman, C. M., *Molecular Physics*, Vol. 10, p. 437, 1966.
18. Barfield, M., and Grant, D. M., *Advances in Magnetic Resonance*, pp. 149–193 (and references cited therein). Edited by J. S. Waugh, Academic Press, New York, 1965.
19. Forsen, S., and Hoffman, R., *Acta Chemica Scandinavica*, Vol. 18, p. 249, 1964.
20. Manatt, S. L., Juvinall, G. L., Wagner, R. I., and Elleman, D. D., *Journal of the American Chemical Society*, Vol. 88, p. 2689, 1966.

## References (contd)

21. Pople, J. A., and Santry, D. P., *Molecular Physics*, Vol. 8, p. 1, 1964.
22. Davis, L., Jr., Smith, E. J., Coleman, P. J., Jr., and Sonett, C. P., "Interplanetary Magnetic Measurements," in *The Solar Wind*, pp. 35-52. Edited by R. J. Mackin, Jr. and M. Neugebauer, Pergamon Press, New York, 1966.
23. Holt, E., and R. Haskell, *Plasma Dynamics*, Chapter 14.5, The Macmillan Company, New York, 1965.
24. Lichnerowicz, A., *Théories Relativistes de la Gravitation et de l'Électromagnétisme*, Masson et Cie., Paris, 1955.
25. O'Brien, S., and Synge, J. L., "Jump Conditions at Discontinuities in General Relativity," *Communications of the Dublin Institute of Advanced Studies, Series A*, No. 9, 1953.
26. Taub, A. H., "Relativistic Rankine-Hugoniot Equations," *Physical Review*, Vol. 74, pp. 328-334, 1948.
27. Estabrook, F. B., and Wahlquist, H. D., "Dyadic Analysis of Space-Time Congruences," *Journal of Mathematical Physics*, Vol. 5, pp. 1629-1644, 1964.
28. Warburg, E., *Sitzungsberichte der K. Preussischen Akademie der Wissenschaften zu Berlin*, p. 314, 1916.
29. Rollefson, G. K., and Burton M., *Photochemistry and the Mechanism of Chemical Reactions*, pp. 190 ff., Prentice-Hall, Inc., New York, 1939.
30. Romand, J., *Annales de Physique* (Paris), Vol. 4, p. 527, 1949.
31. Goodeve, C. F., and Taylor, A. W. C., *Proceedings of the Royal Society* (London), Vol. 154A, p. 181, 1936.

## XVI. Fluid Physics

### SPACE SCIENCES DIVISION

N67-15743

#### **A) Rotational Temperature Measurement in a Free Jet and in a Static Gas, H. Ashkenas**

Rotational temperatures given by a spectrographic examination of the rotational fine-structure of the band spectra of electron-beam excited nitrogen have been determined for a variety of free-jet flow conditions. Center-line temperature distributions have been made for Reynolds numbers (based on sonic conditions and sonic source radius) varying between 100 and 5,000. This range encompasses flows which should be wholly isentropic (up to the Mach disk) and flows where viscous dissipation effects and/or rotational freezing might be expected. Preliminary data are shown to have the expected qualitative behavior at the extrema of the Reynolds number range. The absolute magnitude of the rotational temperature is in doubt.

The experiments were conducted in leg I of the JPL low density wind tunnels. Recent piping and pumping additions have increased the total plant capacity to some 18,000 l/sec at 15  $\mu$ . The additional pumping capacity has allowed the study of free jet flows from relatively large diameter orifices; the accompanying reduction of axial and radial gradients has made detailed studies of free jet structure possible.

The experimental setup has been described SPS 37-37, Vol. IV, p. 182. The spectral data were reduced using a modification of a computer program developed by Prof. R. S. Hickman<sup>1</sup> of the University of Southern California. The data reduction scheme is based on Muntz' (Ref. 1) model of the excitation and de-excitation of electron-beam excited nitrogen and fits a least squares straight line to the spectral intensity distribution, after making the proper temperature dependent modifications to the data. Final temperatures are deduced after several iterations from the slope of the resulting straight line.

Some preliminary results of the rotational temperature distribution along the jet axis are shown in Fig. 1. For comparison, the curve of translational temperature for isentropic flow, calculated from the method of characteristics solution of Owen and Thornhill (Ref. 2), is shown. With very few exceptions, the measured rotational temperatures lie above the calculated translational values. Tabulated on the figure are various pertinent parameters of the free-jet flows studied.  $Re_r^*$ , the Reynolds number based on sonic conditions and the sonic sphere radius, as defined by Sherman (Ref. 3), serves to delineate the regions where viscous dissipation along the jet axis may

<sup>1</sup>Private communication, May, 1966.

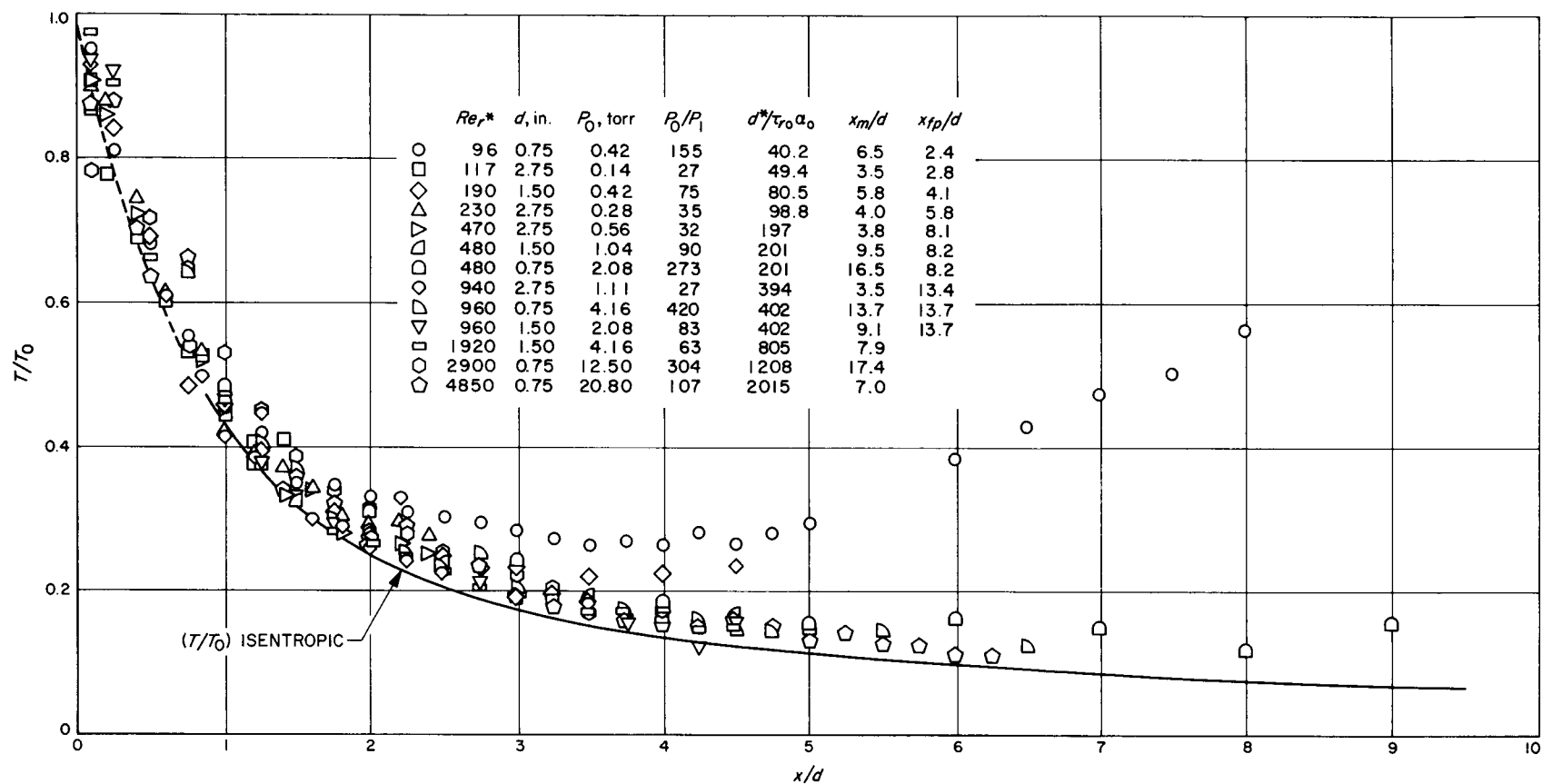


Fig. 1. Axial rotational temperature distributions in the free jet

be expected.  $d^*/\tau_{r_0 a_0}$  is the rotational freezing point parameter defined by Knuth in Ref. 4 and defines the  $x_{fp}/d$  where rotational freezing may take place.  $x_m/d$  locates the Mach disk in the flow field and is taken from Ashkenas and Sherman (Ref. 5), where  $x_m/d = 0.67 (p_0/p_1)^{1/2}$ .

Returning to the rotational temperature data, it is evident that an explanation for the disparity between rotational and translational temperatures may be found for some of the data shown, e.g.:

- (1) Near the orifice exit, the method of characteristics solution is not well defined (hence the dashed curve for translational temperature); gradients are steep, and the resolution of the optical system may give rise to errors.
- (2) For the low Reynolds numbers, rotational freezing has obviously occurred in some instances; in others, dissipative effects which tend to reduce the value of the local Mach number may be present.
- (3) The rise in temperature shown is due to the presence of the Mach disk and represents the increase in temperature found in the diffuse compression ahead of the shock wave.

The failure of the spectroscopic rotational temperature data to agree with the calculated translational data has been noted previously by Robben and Talbot (Ref. 6). They were unable to explain the disparity between rotational and translational temperatures in flows where equilibrium is expected, except on the basis of a single spectrum, taken with a narrower than normal slit, which

did give a rotational temperature close to the translational value. The temperature distribution through the entire fluorescent region surrounding the beam was investigated in the present work. Fig. 2 shows the result of one such set of data. There appears to be no evidence that the temperature varies through the halo or that slit height (or width) should affect the measured rotational temperature.

A further source of possible error in the present investigation lies in the particular orientation chosen for the electron beam, viz., along the axis of the jet. The possibility of beam heating of the gas must be considered. To test this possibility, the beam current was varied over a wide range and the rotational temperature measured. The result, given in Fig. 3, shows that the measured temperature is independent of beam current, and we infer that the orientation of the beam should not affect the measured rotational temperature.

It should be noted, at this point, that the temperatures presented in Figs. 1-3 were not calculated using the entire 0-0 band of the rotational spectrum; only R-branch intensities were used, and of these it has been found that, depending on the temperature, the rotational lines at high rotational quantum numbers must be discarded in order to obtain good straight lines. At room temperature, for example, all 22 lines that are available in the R-branch may be used to define the straight line. (Although there is some P-branch overlap, their contribution to the entire straight line is not significant.) At 78°K, however, it is found that at best only the first five lines may be fitted to obtain nearly the correct temperature. The fact that the

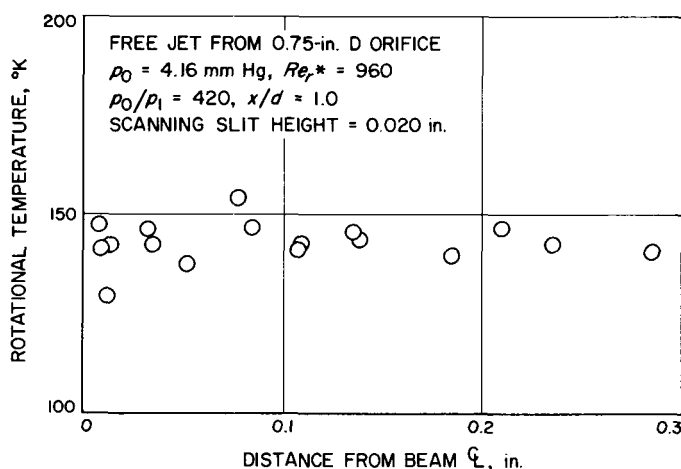


Fig. 2. Temperature distribution through the beam halo

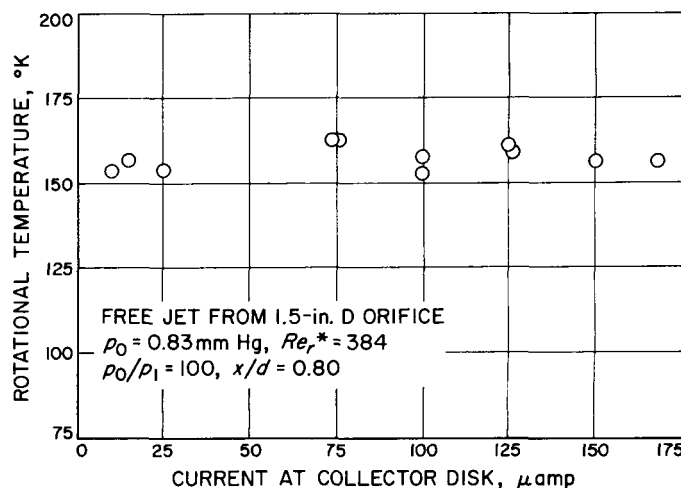


Fig. 3. Temperature dependence on beam current intensity

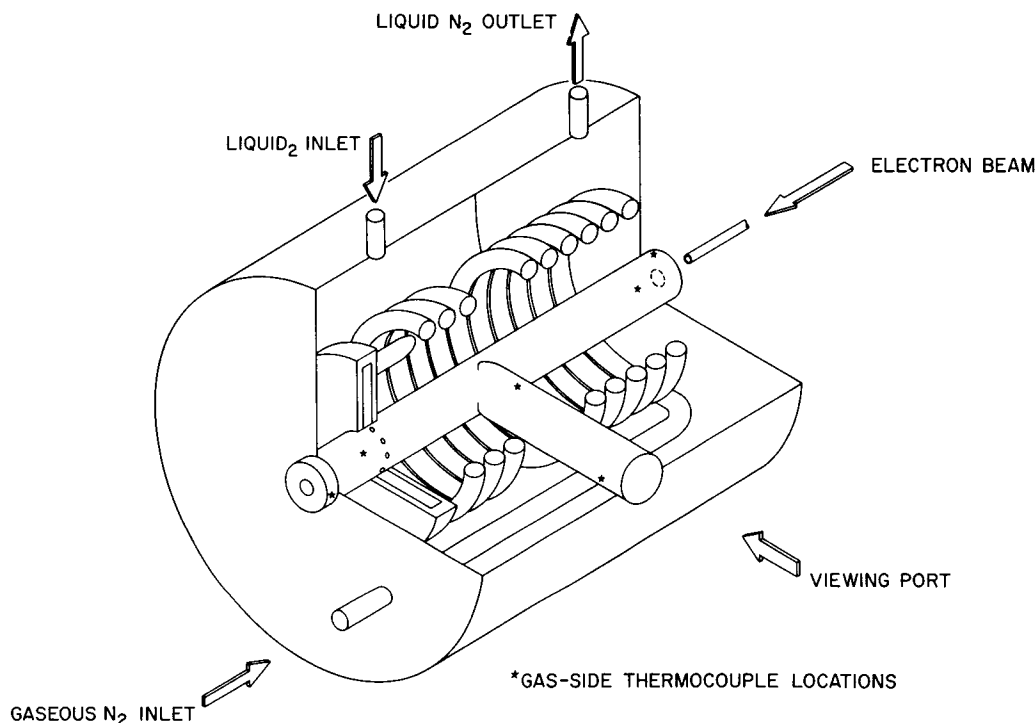


Fig 4. Static gas heat exchanger

data do not fall on a straight line may be interpreted as an indication that the gas is no longer in thermodynamic equilibrium, and the idea of a given rotational temperature being associated with such a gas becomes moot.

In order to test the Muntz model under conditions where both thermodynamic equilibrium and low temperatures prevail, the static gas heat exchanger sketched in Fig. 4 was constructed. The test chamber is mounted inside the low density wind tunnel; dry nitrogen enters the copper coil and is discharged into the "tee" tube where electron beam excitation occurs. The copper coil and tee tube are immersed in liquid nitrogen, generally at atmospheric pressure; the entire chamber is insulated with a 2-in. layer of glass fiber mat. Copper-constantan thermocouples, located as noted, are read out by a sequential recorder so that a record of the thermal history of the heat exchanger is available for each spectrum. The spectrometer is retained in the same position as for the jet spectra, although the internal traversing optical system referenced in SPS 37-37, Vol. IV, p. 182, is not used.

Fig. 5 is a sample spectrum of electron-beam excited nitrogen cooled in the heat exchanger. The temperatures measured by the three innermost thermocouples shown in Fig. 2 were averaged to give a measured gas temperature of 78.5°K. These three thermocouples agreed with

each other within 0.6°K and the change in each of them in the 6 min required to complete the spectrum scan was less than 0.1°K. As a further check on the thermocouples, the pressure on the liquid nitrogen in the heat exchanger was monitored during the spectrum scan; the liquid nitrogen temperature (from vapor pressure-temperature data)

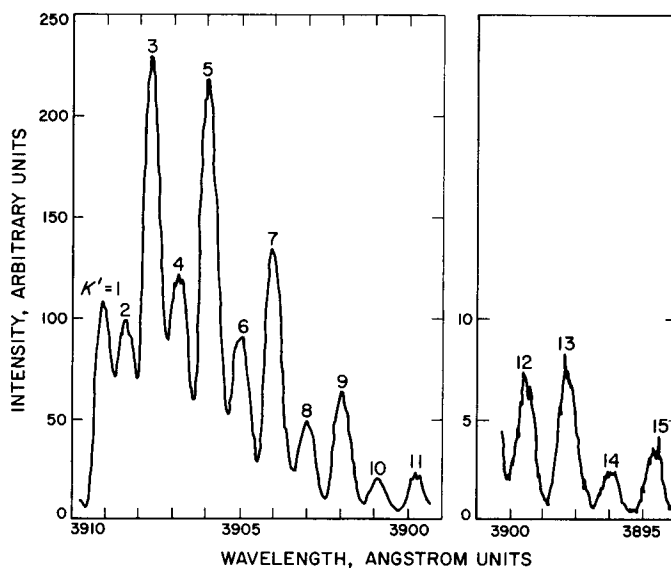


Fig. 5. Sample spectrum; static gas heat exchanger

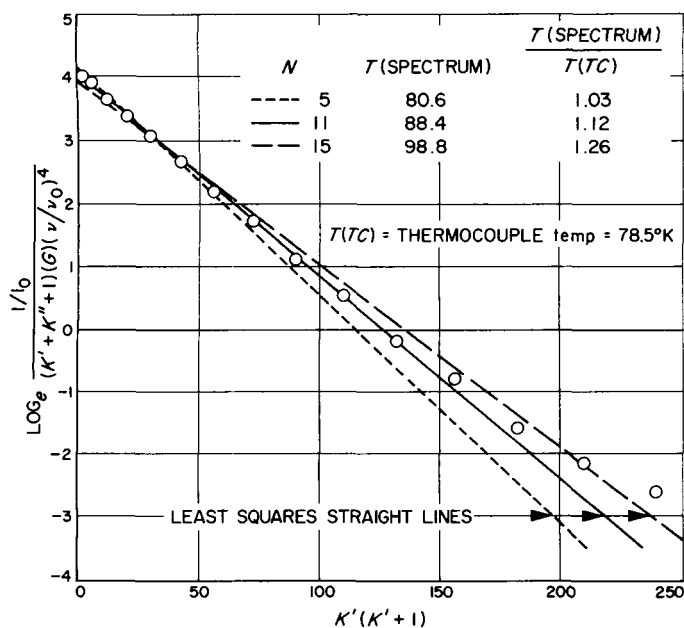


Fig. 6. Intensity plot of spectrum of Fig. 5

was 77°K. Thus, it seems evident that the entire apparatus was at a constant temperature during the spectrum scan, and that the dry nitrogen in the tee tube was in thermodynamic equilibrium at the measured temperature.

The results of the spectral temperature determination are shown in Fig. 6. The circles represent the peaks of the spectrum reduced according to Muntz's (Ref. 1) model. The magnitudes of the even-numbered peaks have been doubled in the data reduction. It is seen that the fifteen peaks (representing fifteen rotational quantum levels), read from the spectrum, do not define a single straight line. Three least squares straight lines are shown. One, using all fifteen peaks represents a temperature 26% in excess of the thermocouple value. If eleven peaks are used, somewhat better agreement is found. The spectral temperature is only 12% higher than that given by the thermocouples. Not until only five peaks are used to determine the temperature does the agreement reach an acceptable value, viz., 3% too high.

It should be noted that the number of spectral peaks required to give the correct temperature varies with the temperature. Fig. 7 presents the averaged results of 66 spectra at liquid nitrogen temperature and 18 at room temperature. It is evident that an unambiguous evaluation of the rotational temperature is not possible.

The conclusion at this point is inescapable; the excitation-de-excitation model suggested by Muntz is in-

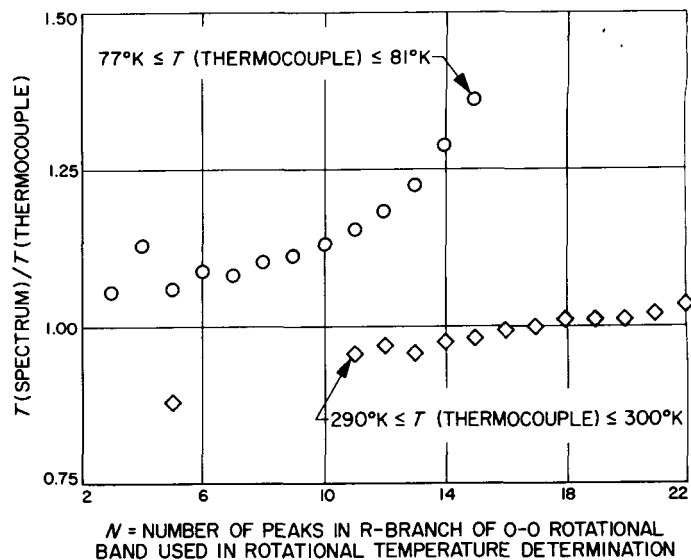


Fig. 7. Effect of number of peaks on calculated rotational temperature

correct. The failure of the model to reduce the spectral intensity distribution to a straight line for the equilibrium situation must be regarded as a major shortcoming. The Muntz model gives good results at temperatures greater than or equal to room temperatures, but its application to cases where the temperature is below 200°K must surely lead to questionable results.

N67-15744

## B. The Scale Depth of the Main Ocean Thermocline, R. C. Alexander

### 1. Introduction

Just how the physical parameters determine the ocean thermocline depth does not seem to have been clarified. The pioneering work of Lineykin (Ref. 7), having to do with inland seas and lakes, when applied to the ocean, as by Stommel and Veronis (Ref. 8), gives a thermocline depth of about 45 km, a factor of 10 greater than the depth of the ocean itself! While the latter authors show that the variation of the Coriolis parameter with latitude is capable of reducing the Lineykin depth by a factor of  $10^{-2}$ , the major weakness of the earlier theories is, admittedly, the assumption of a known constant potential temperature gradient, which is then perturbed.

One theoretical difficulty from the beginning seems to be that the known scale depth of the thermocline ( $\approx 1$  km) does not differ greatly from either the total depth of the ocean ( $\approx 5$  km) or from the Ekman depth ( $\approx 100$  m), where eddy viscosity is important. Consequently, the

regimes of primary influence, i.e., viscous, diffusive, and inviscid-nonconducting, do not separate easily. In fact, they seem to overlap in an essential way.

The author, benefitting partly from the analytical results of other applied mathematicians and partly from the observational results and intuition of physical oceanographers who know the oceans better, attempts here to show what physical parameters might govern the scale depth of the thermocline. If the diagnosis is correct, some of the analytical models may begin to fit together as the treatment of the patient continues.

## 2. Governing Equations

The governing equations are well known:

$$\begin{aligned} -\rho_0 f v &= -p_x + \tau_z^1 \\ \rho_0 f u &= -p_y + \tau_z^2 \\ \rho_0 \alpha T g &= p_z \\ w_z &= -\nabla \cdot \mathbf{u} \\ \mathbf{u} \cdot \nabla T + w T_z &= \kappa T_{zz} \end{aligned} \quad (1)$$

subject to the boundary conditions

$$\begin{aligned} T(x, y, 0) &= T_0 S(x, y) \\ p(x, y, 0) &= p_0(x, y) \\ \tau(x, y, 0) &= \tau_0 \sigma(x, y) \\ w(x, y, 0) &= w_0(x, y) \end{aligned} \quad (2)$$

The notation of Cartesian coordinates is simpler than the spherical counterparts but is not essential; subscripts are partial derivatives:  $x$  is positive eastward (velocity  $u$ ),  $y$  northward (velocity  $v$ ), and  $z$  upward (velocity  $w$ ), with the origin taken at mean sea level and far from continental coasts. The only important eddy viscous stress is taken to be  $\tau = \mu \mathbf{u}_z$ ;  $\rho_0$  is a constant mean density, with departures from the mean given by  $\rho_0 \alpha T$ , where  $\alpha$  is a constant and  $T$  is the potential temperature;  $p$  is the total pressure minus the hydrostatic pressure which would occur if  $T \equiv 0$ ;  $g$  is gravity;  $f$  is the Coriolis parameter,  $2\Omega \sin \theta$ , where  $\Omega$  is Earth's angular velocity; and  $\theta$  is the latitude;  $\nabla$  is the horizontal vector operator; and  $\kappa$  is a coefficient of vertical eddy diffusion. Horizontal diffusion is assumed to be negligible.

## 3. Scale Analysis and Thermocline Depth

For dimensionless equations, replacing

$x, y$	with	$Lx, Ly$
$z$	with	$Dz$
$T$	with	$T_0 T$
$p$	with	$\rho_0 \alpha T_0 g D p = \rho_0 g' D p$
$f$	with	$2\Omega f$
$u, v$	with	$g' D (2\Omega L)^{-1} u, v$
$w$	with	$g' D^2 (2\Omega L^2)^{-1} w$
$\tau$	with	$\tau_0 \tau$

one finds that the constant coefficients  $\rho_0$  and  $\rho_0 \alpha g$  disappear from Eq. (1), and  $T_0$  and  $\tau_0$  from the boundary conditions, Eq. (2). As is well known, two important dimensionless coefficients now appear in Eq. (1): the Ekman number,

$$E = (\rho_0 g' D^2)^{-1} \tau_0 L,$$

which multiplies the wind stresses, and the dimensionless diffusion coefficient,

$$\epsilon = (g' D^3)^{-1} 2\Omega L^2 \kappa,$$

which appears in place of  $\kappa$  in the heat equation. Current estimates seem to indicate that  $\tau_0 \approx 1$  dyne  $\text{cm}^{-2}$  and  $\kappa \approx 1$   $\text{cm}^2 \text{sec}^{-1}$  (Robinson and Stommel, Ref. 9). Using cgs units, and putting  $\tau_0 = 1$ ,  $\kappa = 1$ ,  $\rho_0 = 1$ ,  $g' = 2.5$ ,  $L = 5 \times 10^8$ ,  $D = 5 \times 10^5$ , and  $\Omega = 10^{-4}$ , one finds

$$E = 0.8 \times 10^{-3}, \quad \epsilon = 1.6 \times 10^{-4}$$

The neglected horizontal accelerations are of the order of the Rossby number,

$$R_0 = (2\Omega L)^{-2} g' D = 1.25 \times 10^{-4}$$

so that, to be consistent, the viscous stresses should be dropped wherever  $z$ -derivatives are not of particular importance, e.g., below the surface Ekman layer of depth  $E^{1/2}$ . One can integrate, formally, the continuity equation from the surface  $z = 0$  to a depth  $z = z' < -E^{1/2}$ . Eliminating  $\nabla \cdot \mathbf{u}$  by differentiating the horizontal momentum equations, and applying the surface boundary conditions on  $w$  and  $\tau$ , one finds the well-known relation

$$w(x, y, z') = w_0(x, y) + f^{-2} \beta \int_0^{z'} p_x dz + E \mathbf{k} \cdot \text{curl}(f^{-1} \sigma)$$

where  $\beta = df/dy$  is not necessarily constant and  $\mathbf{k}$  is the unit vertical vector.

A nonzero velocity  $w_0$ , at the surface, is intended to account for such effects as sloping sea surface, evaporation, and precipitation. These cannot be order one effects. Supposing they are of order  $E$  or less, one sets  $w_0(x, y) = EQ(x, y)$ . With the stress terms absent from the first two of Eq. (1), elimination of the velocities in the heat equation gives

$$f^{-1} \left\{ -p_y T_x + p_x T_y + f^{-1} \beta \int_0^z p_x dz' T_z \right\} + E \{ Q(x, y) + \mathbf{k} \cdot \text{curl}(f^{-1} \boldsymbol{\sigma}) \} T_z = \epsilon T_{zz} \quad (3)$$

Eq. (3) is presumably valid at any depth below the surface Ekman layer except, of course, at the very bottom, where viscous stresses again come into play. For depths above the thermocline, diffusion is important and must balance something. This requires a new scale on the  $z$ -derivative. Robinson and Stommel (Ref. 9) suggested intuitively that the existence of a thermocline requires a deep up-welling velocity to balance diffusion of heat downward. Robinson and Welander (Ref. 10), within the framework of a similarity transformation, found that a deep up-welling is a necessary condition, and suggested that the (horizontal) advection of heat is relatively negligible, and that a strong relation exists between boundary layer depth and surface forcing function. A deep vertical velocity was found by Blandford (Ref. 11) in the first analytical solution to the inviscid equations with diffusion. Blandford showed that under certain circumstances the hypothesis of zero advection of heat is valid and that, under those conditions, Stommel and Webster's (Ref. 12) calculations based on a zero-advection model are exact.

Actually, if the scaling which resulted in Eq. (3) is correct, the ultimate answer to the question of the importance of advection and the roll of (vertical) convection with respect to diffusion may lie somewhere in the middle. There appear to be two convection quantities to choose from:

$$\left\{ f^{-2} \beta \int_0^z p_x dz' \right\} T_z \sim \epsilon T_{zz}$$

or

$$E \{ Q + \mathbf{k} \cdot \text{curl}(f^{-1} \boldsymbol{\sigma}) \} T_z \sim \epsilon T_{zz}$$

The former gives a new  $z$ -scale,  $z \sim \epsilon^{1/2}$ , which is too small. It would be imbedded in the Ekman layer at the surface. The latter seems to be the correct balance. Adopting the notation  $\delta^*$  for the thermocline depth scale, one finds

$$\delta^* = E^{-1} \epsilon = 1/5$$

Dimensionally, it is

$$D^* = D\delta^* = \tau_0^{-1} 2\Omega L \rho_0 \kappa = 1 \text{ km}$$

One can, of course, argue about the precise numerical value of  $D^*$ , but the order of magnitude should be correct. This kind of balance may well bring up a number of controversies which can only be resolved after further study. First, one notices that while the Coriolis parameter is important, its variation with latitude may not be, in a qualitative way. Moreover, the up-welling-diffusion balance is homogeneous in  $T$  and  $T_z$ , so that  $D^*$  should be independent of these quantities. There seems to be some conflict here with the results of Stommel and Veronis (Ref. 8) and with those of Blandford (Ref. 11). The latter found that the thermocline depth decreases with increasing surface temperature. The balance envisaged here requires only that there be some nonvanishing temperature and its  $z$ -derivatives, since  $T \equiv 0$  satisfies the full heat equation. What the balance does suggest is that  $D^*$  decreases as the mean density  $\rho_0$  decreases. That the depth increases with  $\Omega$  is in qualitative agreement with Stommel and Veronis (Ref. 8), as well as everyone else since their early work, and that it decreases inversely as the surface wind stress increases appears to be reasonable.  $D^*$  increasing with  $\kappa$  is certainly reasonable. It would be interesting to perform a laboratory experiment somewhat as envisaged by Stommel and Veronis to see if there is any validity at all to the proposition that the product of surface stress and height of convective cells divided by rotation rate, horizontal scale, mean density, and molecular diffusivity is a constant, for sufficiently small  $R_\omega$  and  $E$ .

Admittedly, an argument which starts with the smallest quantities in an equation is rather like putting the cart before the horse. Formally, one can define  $\delta^* = \epsilon^{-1} E$  and set  $z = \delta^* \zeta$ . Then Eq. (3) becomes

$$f^{-1} \left\{ -p_y T_x + p_x T_y + \left( f^{-1} \beta \int_0^\zeta p_x d\zeta' \right) T_\zeta \right\} + (\delta^*)^{-1} E \{ [Q(x, y) + \mathbf{k} \cdot \text{curl}(f^{-1} \boldsymbol{\sigma})] T_\zeta - T_{\zeta\zeta} \} = 0 \quad (4)$$

The single governing parameter below the Ekman layer appears to be  $E/\delta^*$ , which can be written as the product  $ER_0P_r$ , where  $P_r$  is the eddy Prandtl number. Below the thermocline the first expression in curly brackets vanishes separately. This part is essentially the purely advective model posed by Welander (Ref. 15) in a magnificent piece of work. His solution,  $p = k^{-1}fS(x, y) \exp(f^{-1}kz)$ , where  $k$  is a constant, represents the first known analytical solution having to do with the ocean thermocline problem. It predicted correctly the thinning of the thermocline toward the equator, proportional to  $f = \sin \theta$ . Moreover, with the surface temperature  $S = \cos^2 \theta$  it seemed to indicate correctly the subpolar westerlies and midlatitude easterlies and give a reasonable approximation to the actual meridional density distribution. From a theoretical point of view, however, it was not clear how this model, which neglects diffusion as well as viscosity, could predict a thermocline at all. In fact it did, of course.

If the scaling is correct, Eq. (4) says that Welander's model is valid, to order  $E/\delta^*$ , well up into the thermocline region to the very base of the Ekman layer! The formal expansion,  $p = p_0 + (E/\delta^*)p_1 + (E/\delta^*)^2p_2 + \dots$ , and a similar one for  $T$ , assuming convergence, when substituted into Eq. (4) gives Welander's problem for  $p_0$  and  $T_0$ . It is essential, of course, to go at least to the next step, the order  $E/\delta^*$  problem, but this has not been investigated yet. Nonconstant coefficients appear which come from the solution to Welander's problem.

#### 4. A Family of Solutions to the Advective Problem

The purely advective model, then, seems to be a proper starting point, and finding its general solution would appear to be one of the half-dozen or so most fundamental problems in dynamical oceanography. During the course of the writer's unsuccessful attempts to come up with the general solution, he found that any solution of the form

$$T = G(p/f) \quad (5)$$

is a solution to Welander's problem, the latter's solution being a special case of this for  $G = kp/f$ . Indeed, Blandford's solution with diffusion is identical to this, the upwelling velocity being a function of integration of order  $\epsilon$ . The above family with  $f \neq \text{constant}$  might be thought of as the "baroclinic equation of state" for the fluid. That any member of this family is a solution can, of course, be verified by direct substitution. With  $p_z = T$ , the essential thing to show is that  $pp_r - p_z \int_0^z p_r dz' = 0$ , which can be shown to be true since  $(p_r/p_z)_z = 0$ .

However, even the general solution would not be worth very much without an adequate knowledge of boundary conditions. In the present case, the function  $G$  might be determined at the base of the Ekman layer where  $T = T_b$  and  $p = p_b$ . Finding the latter in terms of the surface conditions should present no major difficulty by means of an  $E^{1/2}$  expansion through the layer. To a first approximation, the pressure is independent of depth. The velocities are then given by the Ekman solution so that the heat equation is linear, although with nonconstant coefficients. The integrated heat equation then gives the temperature  $T_b$ . In this way  $G$  is determined. But the accuracy with which it is determined depends on how accurately the surface pressure and temperature are known. One word of caution: at the risk of being repetitious, the family of solutions found is not the most general solution. Obviously the boundary conditions cannot be applied arbitrarily and independently of each other.

More promising for the present might be to take Welander's solution and go to the next step, solving the  $E/\delta^*$  problem in which the upwelling is involved. Here too is the connection with surface wind-stress and evaporation-precipitation. Again, accuracy is limited by how well the boundary conditions are known. The work to be done seems to stretch out ahead.

#### 5. Relationship Between the Welander-Blandford Solution and Surface Boundary Conditions

As a final note, it is perhaps worthwhile to investigate the consequences of splitting the heat equation into two identities, requiring that each curly bracket of Eq. (4) vanish separately. This is actually what the author originally had in mind intuitively (more precisely, with the benefit of the intuition and results of others). Splitting a physical law into two independent equations is a dangerous game which, unless one is very fortunate, or can introduce an additional dependent variable, generally leads to a contradiction. It turns out in this case that the splitting is fortunate, but at the price of losing precious degrees of freedom in the boundary conditions. Solution Eq. (5), of course, satisfies the first curly bracket. The second curly bracket is a linear equation with coefficients independent of  $\zeta$ , but it turns out that the only solution having the required form is

$$\begin{aligned} p &= \delta^* b^{-1} f S(x, y) \exp(f^{-1} b \zeta) \\ T &= S(x, y) \exp(f^{-1} b \zeta) \\ f^{-1} b &= Q(x, y) + \mathbf{k} \cdot \text{curl}(f^{-1} \boldsymbol{\sigma}) \\ \zeta &= z/\delta^* \end{aligned} \quad (6)$$

where  $b$  is a constant of order one, plus one in the northern hemisphere and minus one in the southern, if the solution is to decay with depth. Eqs. (6) is essentially Welander's (Ref. 13) solution, but with diffusion and consequent up-welling, or Blandford's (Ref. 11) with extra freedom in determining the surface temperature distribution,  $S(x, y)$ . The latter found that  $S$  must be proportional to  $xf^{-1}(\phi \sin^{-1} \theta$ , where  $\phi$  is the longitude); but this was, perhaps, a consequence of his having used a similarity formulation developed by Robinson and Stommel (Ref. 9) and by Robinson and Welander (Ref. 10), pioneering efforts, which went far in pointing the way.

The present effort has apparently set the scale  $\delta^*$  in Eqs. (6) and shown how the Welander-Blandford solutions are related. Moreover, the up-welling velocity  $f^{-1}b$  is now identifiable with the surface conditions. Eqs. (6) might be regarded as the total solution for an ocean in which the sum of evaporation-precipitation and surface wind stress curl have the required form. It is hoped that the scale  $\delta^*$  and solutions to Eq. (4) might ultimately find wider applicability.

## 6. Addendum

Any function of the form  $T = G(p/f)$  Eq. (5), appears to be a solution to the purely advective problem *provided*  $p_r = 0$  at the sea surface. Otherwise there would be an order one vertical velocity there. The appearance of the definite integral from zero to  $z$  in the last term of the first curly bracket of the heat Eqs. (3) or (4) provides what amounts to a function of integration which, one has the uneasy feeling, may have been lost in the pioneering works which used an integro-potential function to define all dependent variables. Thus, the surface temperature distribution,  $S$ , in the Welander-Blandford solution Eq. (6) should be a function of latitude,  $y$ , only. This gives order one zonal velocity, zero meridional velocity, and order  $E$  up-welling. Welander's particular example (Ref. 13), which he uses for calculating the zonal velocity and meridional density distributions, is of this type. His apparent success encourages one to pursue the separate-identity game further for situations in which pressure is a function of latitude and depth only. For such cases, each term of the first curly bracket, the order one heat advections, vanishes separately, and one need not be concerned with the form of solution Eq. (5).

One can perhaps envisage a central oceanic region which, in the case of the North Atlantic, begins well to the north of the Equatorial Counter Current and extends

northward over a (hopefully) very flat Bermuda High, elongated in the east-west directions, but not extending so far north as to include the more complicated North Atlantic Current. The North Equatorial Current is excluded to the east as is the Gulf Stream and its meanders to the west. For such a situation, solutions  $p = p(y, z)$  only might be looked for. Then, using the nondimensionalization defined earlier, the governing equations below the Ekman layer become

$$\begin{aligned} p_r &= 0 \\ p_{\theta} &= -fu \\ p_z &= T \\ w &= E [Q(y) - (f^{-1}\sigma)'] \\ wT_z &= \epsilon T_{zz} \end{aligned} \quad (7)$$

subject to the boundary conditions

$$\begin{aligned} p(y, 0) &= \phi(y) \\ T(y, 0) &= S(y) \end{aligned} \quad (8)$$

where  $z = 0$  is a horizontal surface immediately below the Ekman layer, the surface stress has only the  $x$ -component  $\sigma(y)$ , and a prime indicates differentiation with respect to  $y$ . The system Eq. (7) is obviously linear and the author can dispense with his complicated rationalizations leading up to the preceding definition of the thermocline depth. The substitution of  $w$  into the heat equation gives an exponential solution for  $T$ . The  $\exp(-1)$  depth is, dimensionally, that given previously multiplied by  $[Q - (f^{-1}\sigma)']^{-1}$ . For the case  $\sigma = -\cos 3\theta$ , with  $dy = a d\theta$  and  $f = \sin \theta$ , this becomes

$$D^* = \frac{2\Omega L \rho_0 \kappa}{\tau_{0\theta}} \cdot \frac{\sin \theta}{\sin \theta Q(\theta) - a^{-1} [3 \sin 3\theta - \cot \theta \cos 3\theta]} \quad (9)$$

where  $a = R/L \approx 2$ ,  $R$  being the radius of the Earth. Apparently the exponential solution will be valid wherever  $D^* > 0$ . One recalls that when  $D^* < 0$ ,  $T = S \equiv 0$  is a solution. The singularities of  $D^*$  may bring in higher order dynamics. The matter is being investigated further.

## References

1. Muntz, E. P., "Static Temperature Measurements in a Flowing Gas," *Phys. Fluids*, Vol. 5, No. 80, 1962.
2. Owen, P. L. and Thornhill, C. K., "The Flow in Axially Symmetric Supersonic Jets from a Nearly Sonic Orifice into a Vacuum," *Reports and Memoranda*, No. 2616, Ministry of Supply, 1948.
3. Sherman, F. S., "A Sourceflow Model of Viscous Effects in Hypersonic Axisymmetric Free Jets," *Archiwum Mechaniki Stojwanej*, Vol. 16, No. 2, 1964.
4. Knuth, E., *Rotational and Translational Relaxation Effects In Low Density Hypersonic Free Jets*, University of California at Los Angeles, Dept. of Engineering Report No. 64-53, 1964.
5. Ashkenas, H., and Sherman, F. S., *The Structure and Utilization of Supersonic Free Jets in Low Density Wind Tunnels*, Rarefied Gas Dynamics, Supplement 3, Academic Press, N. Y., 1966.
6. Robben, F., and Talbot, L., "Measurement of Rotational Temperature in a Low Density Wind Tunnel," *Phys. Fluids*, Vol. 9, No. 4, April 1966.
7. Lineykin, P. S., "On the Determination of the Thickness of the Baroclinic Layer in the Sea," *Dokl. Akad. Nauk SSSR*, Vol. 101, p. 461, 1955.
8. Stommel, H., and Veronis, G., "Steady Convective Motion in a Horizontal Layer of Fluid Heated Uniformly from above and Cooled Nonuniformly from Below," *Tellus*, Vol. 9, pp. 401-407, 1957.
9. Robinson, A., and Stommel, H., "The Oceanic Thermocline and the Associated Thermohaline Circulation," *Tellus*, Vol. 11, pp. 295-307, 1959.
10. Robinson, A., and Welander, P., "Thermal Circulation on a Rotating Sphere, with Application to the Oceanic Thermocline," *J. Marine Res.*, Vol. 21, pp. 25-37, 1963.
11. Blandford, R., "Notes on the Theory of the Thermocline," *J. Marine Res.*, Vol. 23, No. 1, pp. 19-29, 1965.
12. Stommel, H., and Webster, J., "Some Properties of Thermocline Equations in a Subtropical Gyre," *J. Marine Res.*, Vol. 20, No. 1, pp. 42-56, 1962.
13. Welander, P., "An Advective Model of the Ocean Thermocline," *Tellus*, Vol. 11, No. 3, pp. 309-318, 1959.

**Page intentionally left blank**

## XVII. Communications Elements Research

### TELECOMMUNICATIONS DIVISION

N67-15745

#### A Multipactor Effects: Secondary Electron Emission, H. Erpenbach

Investigation of reduced secondary electron emission from copper surfaces is continuing. In SPS 37-39, Vol. IV, we reported a modified cathode etching technique for generating surfaces on copper which show low secondary yield. The technique employs two gases: the first cleans and etches the surface; the second, a hydrocarbon gas, dissociates to free carbon in a 5-kv discharge to form a thin carbon film of high density on the target surface. We noted that a thin carbon film deposited from cyclopropane yielded fewer secondaries than other hydrocarbons in the series. Further tests indicate that the purity of the hydrocarbons has a direct effect on secondary yield. Table 1 is a list of gases used, the impurity content, and their effect on  $\delta_{\max}$ , the peak in the curve of secondary emission coefficient versus voltage.

As noted in Table 1, cyclopropane has negligible sulfur and oxygen impurities, and the corresponding secondary electron emission is low. The next gas listed in the table is ethane. It is also free of sulfur or oxygen, and the secondary emission is again low. Propane has no oxygen content, but does have a small amount of sulfur, and the secondary emission is correspondingly higher. The last three gases in Table 1, namely methane, butane, and isobutane, have oxygen or sulfur impurities. Tests made with these yielded significantly more secondaries.

The small traces of other impurities contain mostly carbon and hydrogen and are probably not detrimental. Tests will be made on "research grade" of gases in which the impurity content is extremely low.

A recent improvement in the technique for processing copper surfaces was made by allowing the temperature

Table 1. Compiled data

Gas	Formula	Purity mole, %	Grade	Oxygen	Sulfur	Traces of other impurities	$\delta_{\max}$
Cyclopropane	$C_3H_6$	99.50	CP	0	0	Propyl chloride, nitrogen	1.05
Ethane	$C_2H_6$	99.75	CP	0	0	Ethylene, methane, propylene	1.10
Propane	$C_3H_8$	99.00	Instrument	0	0.005	Ethane, butane	1.22
Methane	$CH_4$	99.05	CP	0.3	0	Ethane, carbon dioxide, nitrogen	1.26
Butane	$C_4H_{10}$	99.00	Instrument	0	0.003	Isobutane, propane	1.24
Isobutane	$CH(CH_3)_2$	99.50	Instrument	0	0.004	n-butane	1.28

of the copper target to rise to 500–600°C during the argon etching cycle, instead of maintaining tap water temperature used previously. Fig. 1 is a drawing of a cathode etching table used for processing the copper targets. It is water cooled and capable of handling power of 2500 w. The copper cooling tubes are electrically isolated from the ground with tygon tubing that limits current leakage to 3 ma. A copper target is shown in place on the etching table, and is thermally isolated from the table by three steel balls. The contact area of the spherical surfaces is

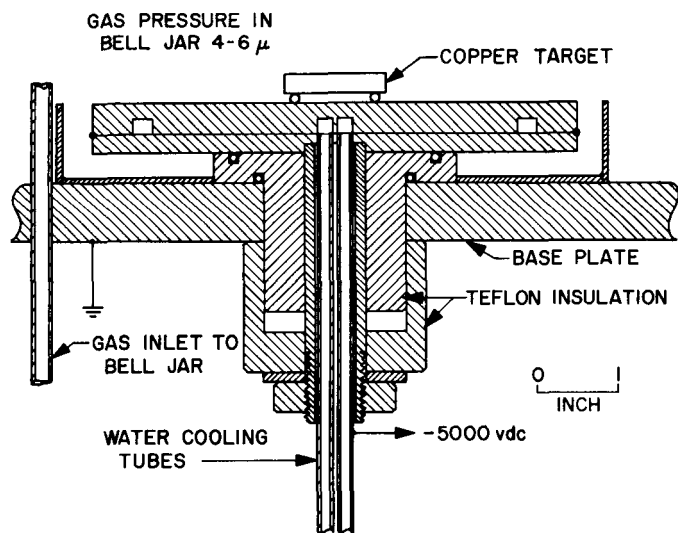


Fig. 1. Cathode etching table

small and allows a steep thermal gradient to develop during the 50-w argon electrical discharge. This power heats the copper target to 600°C in 15 min, at which time hydrocarbon (ethane) is admitted for the second treatment, lasting 1 min.

Fig. 2 shows the secondary electron emission coefficient versus voltage for a surface processed by the above technique. The yield is the lowest yet obtained for a surface that has been exposed to atmosphere for an extended period. Presently we do not understand why the higher temperature of the copper target helps lower the secondary yield; however, it is well known that raising the temperature of a substrate during deposition of an evaporated film produces a more agglomerated film structure. Optical measurements with an interferometer show the thickness of the carbon film to be approximately 250 Å, a thickness greater than the penetration depth of 1000-v electrons.

Electrical resistance measurements on the target surfaces, using a four terminal network, show no differences between a freshly polished copper target and one that was carbonized.

The results on the reduction of secondary electron emission from copper surfaces have been encouraging. The  $\delta_{\max}$  is now practically at unity, a borderline value that should be reduced to 0.85, if possible. Now our plans

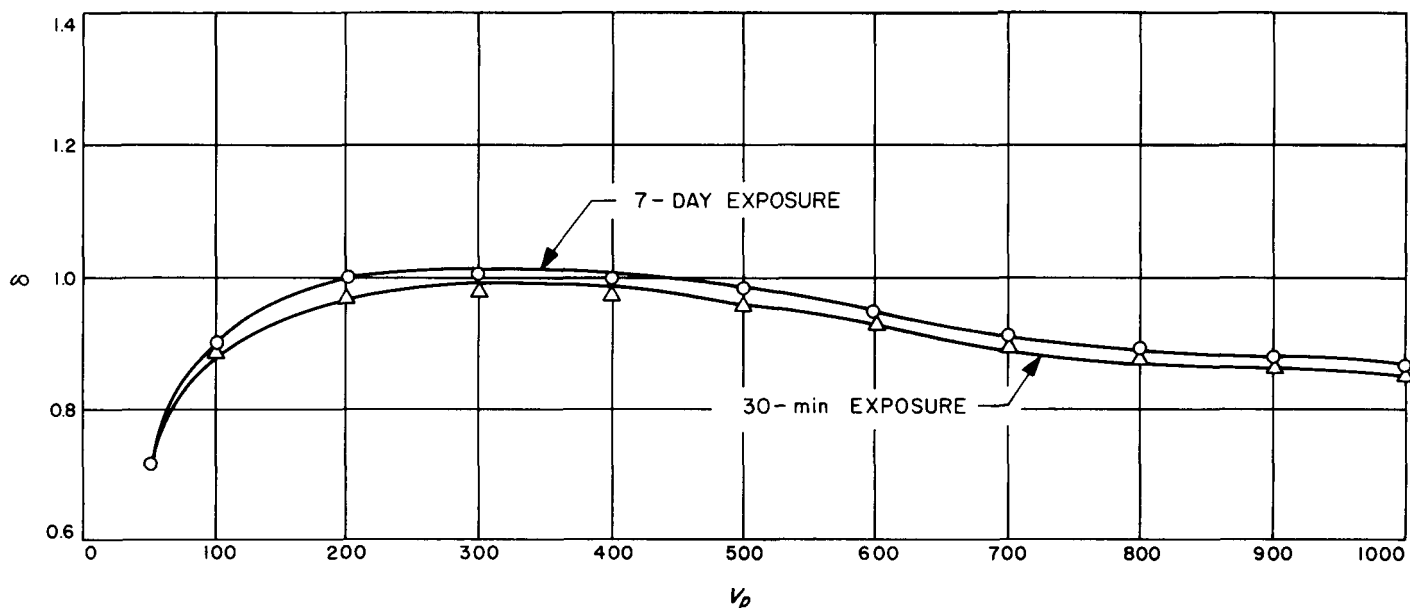


Fig. 2. Ratio  $\delta$  of copper

are to use gases with less impurity and greater flow rate and to use higher temperatures of the copper substrates.

**N67-15746**

## **B. Optical Communications Elements:**

**Simulated Atmosphere, W. H. Wells**

### **1. Introduction**

Little is known about seeing conditions at a possible communications wavelength of  $10\ \mu$ . After passage through the atmosphere, the coherence along a wavefront extends to distances that are comparable to, but typically less than, large telescope apertures. We have used very simple statistical models in a computer program to simulate loss of coherence to estimate the effect of the atmosphere on one form of laser receiver. The random variable of interest here is the peak light intensity at any point in the blurred focal point of a large aperture telescope. Specifically we ask for the greatest intensity that can be found somewhere in the blur circle with some specified high probability.

This particular statistic applies to an optical receiver that consists of a laser preamplifier followed by filters, a field stop, and a detector. In the limit of high preamplifier gain, the fundamental noise is not caused by statistics of the signal photons, but rather, is caused by spontaneous emission in the active laser medium, and it may be specified as a fixed spectral radiance (power per unit area per unit solid angle per unit frequency or wavelength). The perfect receiver would have an SNR of  $S/hfB$  (Planck's constant, frequency, bandwidth), but in practice these are degraded by the noise in the excess solid angle which the detector sees when the field stop is opened to admit a blurred image, and by imperfect population inversion of the amplifying molecules in the laser.

The dependence of noise on solid angle indicates that the SNR may be increased by using only the most intense portion (resolution element) of the blurred image. The location of the peak intensity would have to be redetermined about every 10 msec, because of air movement. Ways to implement such a receiver system seem plausible, but we shall omit this topic since results of this study suggest abandoning the approach. We may modify the study to apply to a system that substitutes heterodyne conversion gain for the laser preamplifier. However, the results here suggest that nothing is gained by dissecting the image as opposed to dissecting the aperture (arraying).

### **2. Mathematical Model**

We have not attempted to select statistical models that closely simulate real conditions in particular sites, since these conditions are very complex and depend heavily on weather. Instead, we chose two quite arbitrary models that are simple and qualitatively very different. This serves as a preliminary study to see if the results depend heavily on the choice of model. It turns out that they do, but are discouraging in either case. The severity and scale size of the turbulence are represented by  $N$ , the minimum number of patches of approximately coherent light that form the wavefront entering the receiving telescope aperture. It is convenient to represent the patches as hexagons that fit into arrays which approximate the circular telescope aperture as shown in Fig. 3 for  $N = 3, 7$ , and  $12$ .

We represent the light distribution in the aperture plane as a sum of  $N$  distributions, one centered on each hexagon, and each having fixed random phase. In one case, which we shall call C for circle, the hexagons were replaced by circles of equal area, and the  $N$  amplitude distributions were taken to be step functions of unit value inside and zero value outside their respective circles. This representation of a distorted wavefront has an unrealistic quality of sudden phase jumps from one circle to the next. Another case, G for gaussian, has smooth phase changes, but the amplitude falls off smoothly at the aperture edge where it should drop abruptly. For case G the amplitude distribution for each hexagon is  $\exp[-(r-r_i)^2]$ , where  $r_i$  is the vector position of its center, and hexagons have sides of unit length. We treat cases C and G for  $N = 3, 7$  and  $12$  for a total of six cases: C3, C7, C12, G3, G7, and G12. Fig. 4 shows an example of amplitude distribution in the aperture plane for case G7 with all phase shifts zero. These are radial plots along perpendicular symmetry axes of Fig. 3(b).

We omit the routine mathematics (diffraction integrals) used to find the intensity distribution in the focal plane. Expressed in terms of focal plane rectangular coordinates,  $u, v$  the intensity function is

$$I(u, v) = E(r) \left[ \frac{N}{2} + \sum_{\substack{n=1 \\ n > m}}^N \cos(\phi_n - \phi_m) \right],$$

where  $\phi_n = \delta_n + 2x_n u + 2y_n v$ ,  $n = 1, 2, \dots, N$ ,  $N = 3, 7$ , and  $12$ ,

$x_n, y_n$  are the coordinates of the centers of the unit hexagons in the aperture plane,

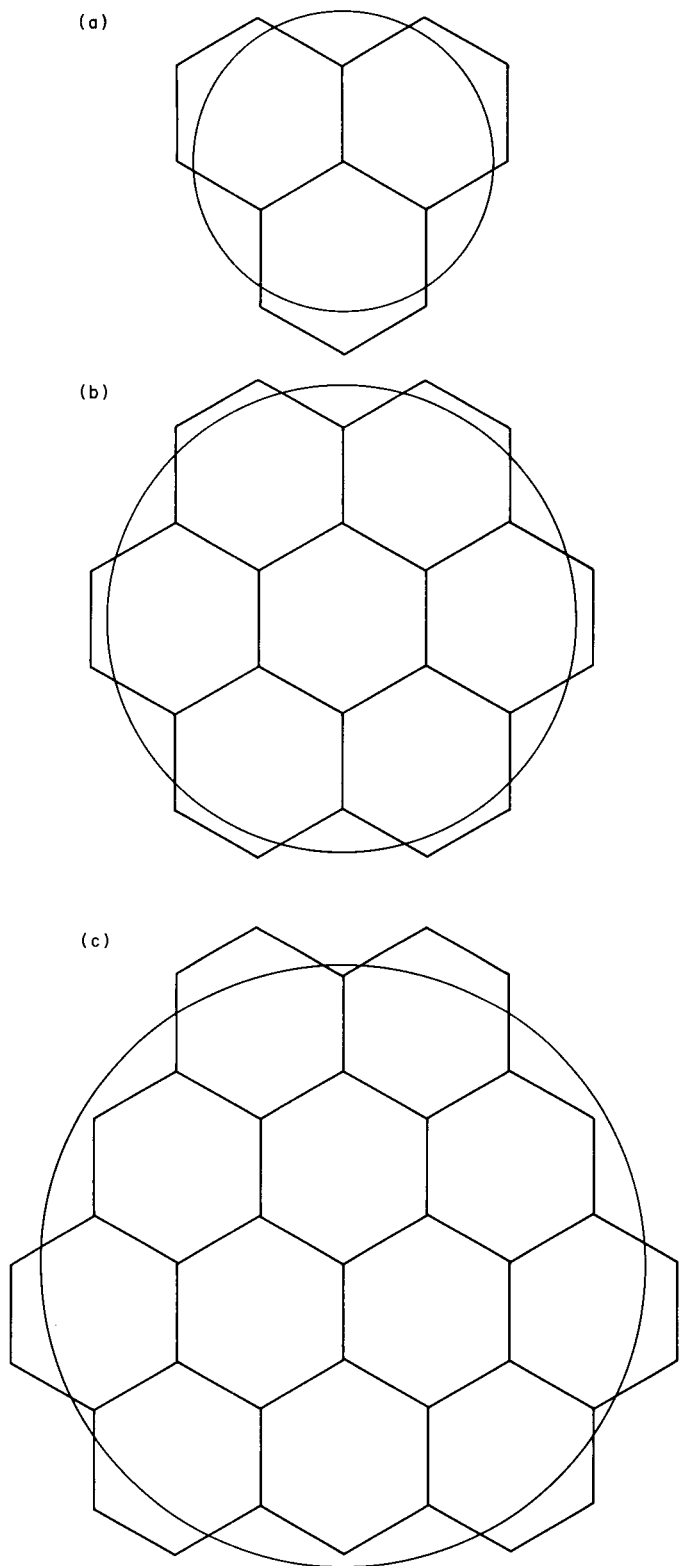


**Fig. 3. Hexagon arrays to approximate coherent patches of a circular aperture: (a)  $N = 3$ ; (b)  $N = 7$ ; (c)  $N = 12$**

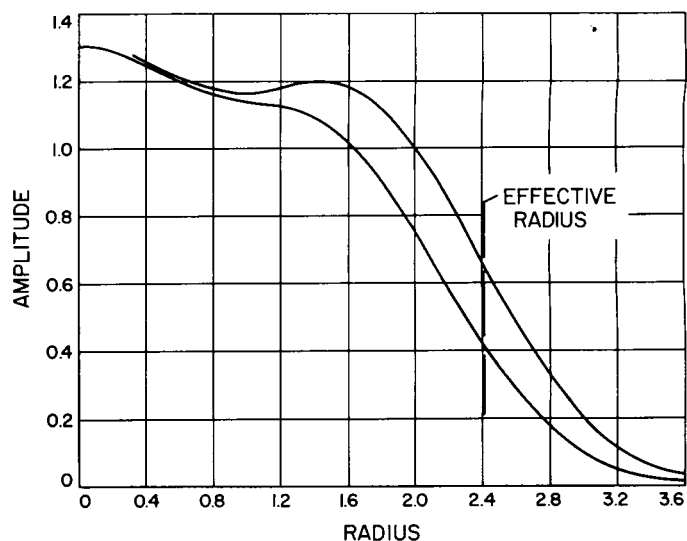


**Fig. 4. Amplitude distribution in the focal plane, case G7, all  $\delta_n = 0$**

$\delta_n$  are independent random phases of the coherent patches in the aperture plane (uniformly distributed 0 to  $2\pi$ ),

$$E(r) = \begin{cases} \exp(-2r^2) & \text{for case G} \\ [2J_1(\rho)/\rho]^2 & \text{for case C, and} \end{cases}$$

$$r = (u^2 + v^2)^{1/2}, \quad \rho = 1.8188 r$$

Note that the choice of case G or C determines an envelope function  $E$  which equals one at the origin. The cosine terms in the bracket represent interference among the various phases. Some numerical constants and scale factors are omitted from the above expressions, because they drop out of the final results. The two envelope functions are quite similar in shape, but the case C function is about 54% wider than the gaussian owing to the increased spread of a diffraction pattern from a sharp-edged aperture.

We checked the mathematical model to see how well it represents the diffraction limited focal pattern caused by a plane wave incident on a circular aperture. This is approximated in our cases by setting all the  $\delta_n = 0$ . The patterns for cases C and G were plotted and compared to a plot for a true circular aperture having the same area as the hexagonal array. The fit was exceedingly close for case C, but the central peak for case G was about 6% narrower.

### 3. Computation and Results

The computer was instructed to generate random values of  $\delta_n$ , evaluate  $I(u, v)$ , and find and remember the function's peak value. This was repeated 150 to 250 times for

each of the six cases to collect the peak value statistics. Successive iterations are statistically independent; hence, they simulate focal patterns at widely spaced intervals of time. No attempt was made to simulate the temporal changes in focal patterns. During the initial runs extra

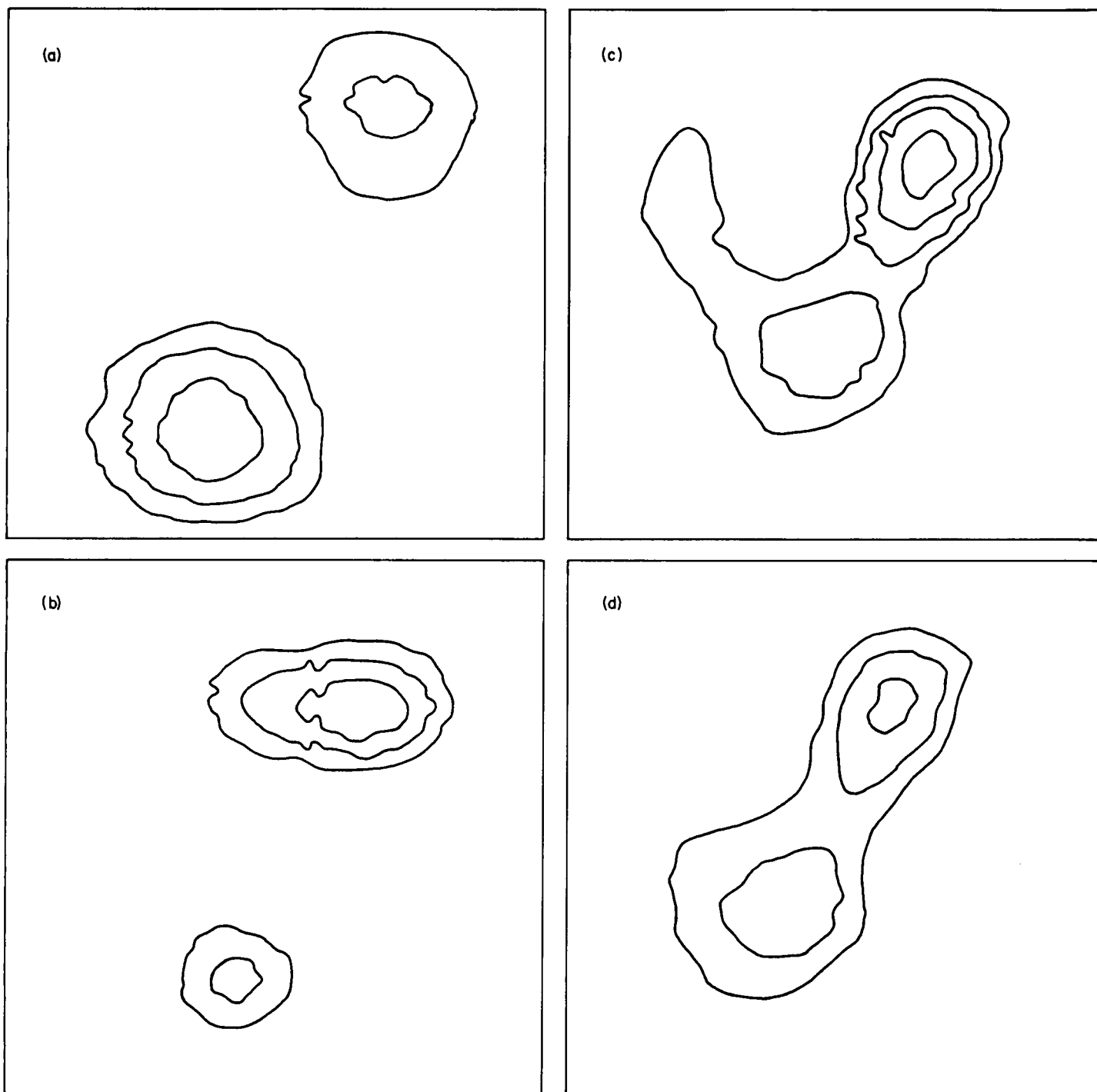


Fig. 5. Contour maps of focal patterns: (a) case C3; (b) case C7; (c) case C12; (d) case G12

data were saved to plot contour maps of the focal patterns; a few having somewhat more structure than typical ones are shown in Fig. 5. The contours are drawn for arbitrary but equally spaced units of intensity near the peak values. Low intensity portions of the patterns are omitted.

The absolute maximum of  $I(u, v)$  is  $N^2/2$  (convenient arbitrary normalization) which occurs at the origin when all  $\delta_n = 0$ . The peaks for random phase shifts were expressed as percentages of this value. These percentages may be regarded as an effective weather-dependent (through  $N$ ) aperture efficiency for the receiver scheme.

The reduced results are shown in Fig. 6. Here the expected peak intensity is plotted as efficiency versus  $N$ , the number of coherent patches in the aperture, which increases as seeing conditions deteriorate. The parameter that labels the graphs is the probability with which we expect to find a peak intensity at least as great as the value plotted. The exact shapes of these curves are not accurate since each was plotted from only four points ( $N = 1, 3, 7$ , and  $12$ ). Nevertheless, the curves show that efficiency drops precipitously for  $N$  greater than 2 or 3; hence, image dissection does not appear to offer a superior solution to the atmospheric problem.

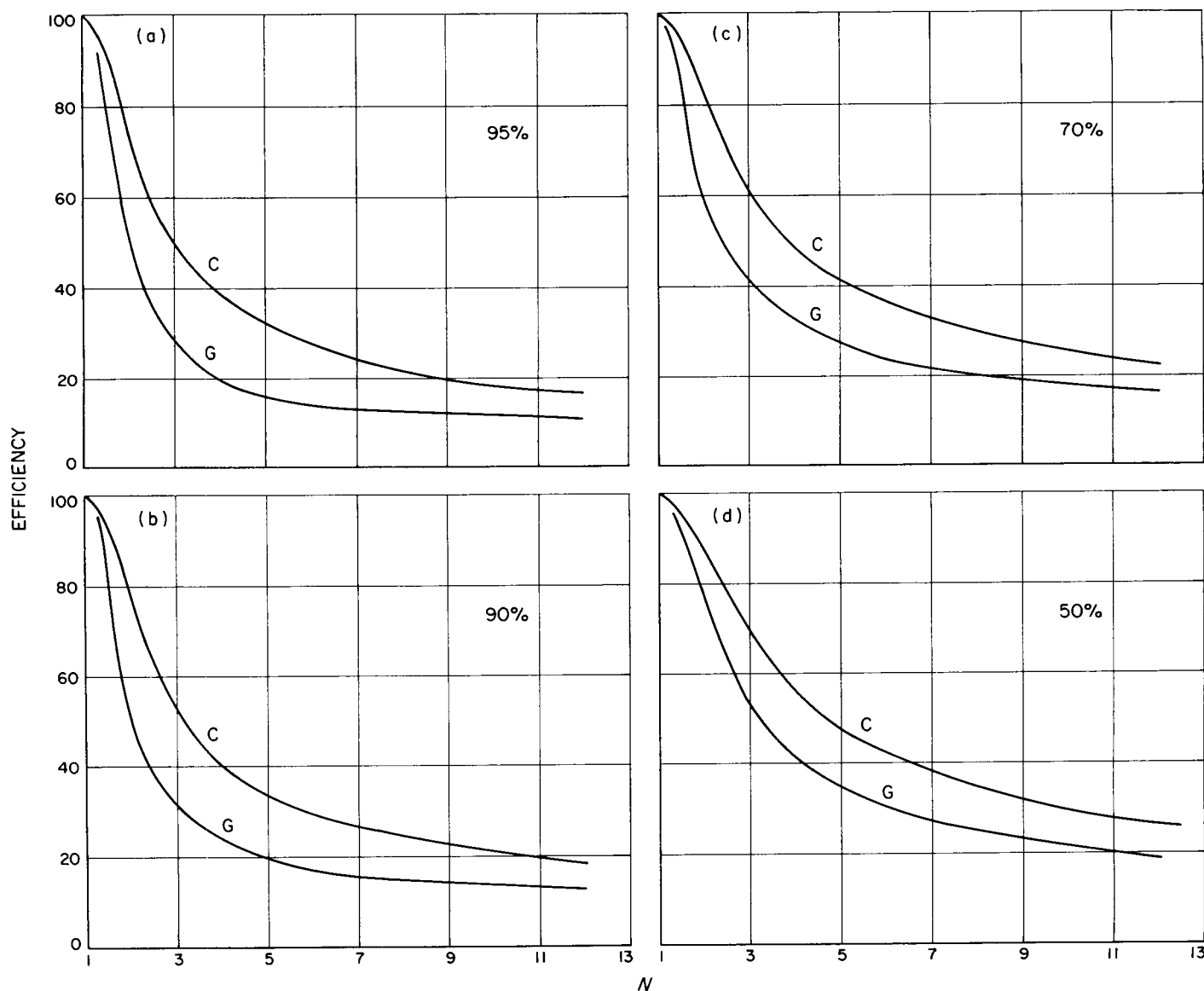


Fig. 6. Weather dependent efficiency as a function of  $N$ , number of coherent patches in aperture. Parameter is probability threshold: (a) 95%; (b) 90%; (c) 70%; (d) 50%

The following pages are missing from this document

213 - 216

The investigation was prompted by the failure of a representative tape transport, which was designed to be sterilizable, to perform satisfactorily during a life test subsequent to exposure to the sterilization cycle (3-cycle exposures of 36 hr each at 145°C sealed with dry nitrogen at a pressure of approximately 21 psi). The subject transport was designed and fabricated under contract with Raymond Engineering Laboratory (REL), Middletown, Connecticut. A complete definition of that program, including a discussion of the design considerations, and preliminary examination and failure analysis, may be found beginning on page 236 of SPS 37-37, Vol. IV.

Each component used in the transport had been individually exposed to, and had survived, the specified sterilization environment prior to transport assembly. However, the preliminary analysis of the failed system led to the suspicion that the assembled and sealed transport, when sterilized, is as adversely affected by the creation of depositions and debris resulting from chemical interaction of outgassing products as it is by the physical and mechanical degradation of certain components. Thus, an investigation into the nature and effects of these relationships was launched. A dimensional analysis of all critical components used in the test transport was performed by the JPL Meteorology Laboratory. Failed shaft bearings were analyzed by Bearing Inspection, Incorporated, a laboratory specializing in this type of work and located in Huntington Park, California.

The services of the JPL Polymer Research Group, Section 382, and the Analytical Chemistry Group, Section 326, were enlisted to investigate the effects of the thermal treatment on the nonmetallic materials and their compatibility with the various metals used. This article is primarily a summary of the investigations conducted by these two groups. The results of the subject investigation reveal the nature and significance of the effects of thermal sterilization on the thirty-two different materials used in the construction of the transport.

## 2. Equipment and Procedures

Samples of the various materials were first classified into categories according to function, such as adhesives, encapsulants, elastomers, lubricants, etc. Pertinent tests were then assigned to each category. The tests were performed on individual samples both before and after thermal sterilization to facilitate a comparison of before and after values. The degree of change in the measured properties was then assessed, and compatibility ratings were assigned.

**a. Test equipment.** The thermal cycling was performed in 1.5-ft<sup>3</sup> capacity National Appliance vacuum ovens with temperatures controlled to  $\pm 2^\circ\text{F}$ . Weight losses were measured within an accuracy of  $\pm 0.1$  mg, using a Mettler balance. An Ames micrometer dial gauge accurate to within  $\pm 0.1$  mil was used to measure volumes.

**b. Materials and preparation of test samples.** All materials tested were proprietary products. Each sample was obtained directly from its manufacturer, and the basic polymeric constituent was known. The manufacturer's recommendations for preparation and handling were followed closely. Test samples were prepared in accordance with the applicable ASTM specification requirements.

**c. Materials testing.** Specific tests, as applicable, were imposed on each material sample to determine its physical and mechanical properties prior to sterilization. These same tests were repeated after the sample had been subjected to thermal cycling.

In addition to the mechanical, physical and thermal tests mentioned in Tables 1-3, the effect of outgassing materials from the polymeric products on some of the metals used in the tape transport was also studied to determine indications of any corrosive action. A sample of each of the materials was sealed, along with strips of selected metals, in a glass tube containing a nitrogen atmosphere. The tubes were then subjected to the thermal sterilization treatment, and the metal strips were then examined for signs of corrosion.

**d. Thermal sterilization procedure.** The test samples were placed on clean metal racks in the ovens at room temperature. Evacuation of each oven to 28.5 in. of mercury gage reading was followed by purging with pure nitrogen. This process was repeated twice more. The oven temperature was then raised to the specified level for sterilization ( $293 \pm 2^\circ\text{F}$ ). A minimum flow of dry nitrogen (about 10 ml/min) was continued to maintain oven pressure at the required 17.5 to 18.0 psi during the entire sterilization cycle (3-cycle exposures of 36 hr each). This pressure level was established to simulate, as closely as possible, the conditions surrounding the tape transport assembly during the system sterilization test program.

## 3. Test Results and Evaluation

To facilitate evaluation of the results of thermal expo-

**Table 1. Summary of test results for the thermal sterilization procedure<sup>a</sup> on adhesives, encapsulants, and adhesive tapes used in the REL tape recorder**

Category	Commercial designation	Material type	Mechanical properties				Physical and thermal properties		Comments	Compati- bility rating
			Hardness, Shore or Rockwell		shear strength, psi		Weight loss, %	Volume change, %		
			Control	After thermal exposure	Control	After thermal exposure				
Adhesives	Bondmaster E645	Epoxy	64.3D	85D	517	1062	42	—	Needs longer cure cycle than recommended by manu- facturer.	NC
	Cycleweld 55-9	Polyvinyl butyral- phenolic resin	Sample not adaptable		495	1146	40.8	—	Same as above. Slight darken- ing of color.	NC
	DuPont PI-1200	Polyimide	Sample too brittle		—	—	0.58	—	Very brittle substance.	M
	EC 826	Buna N	Sample not adaptable		60	894	10.38	—	Needs longer cure cycle than recommended by manu- facturer.	NC
Encapsulants	Number A2 adhesive/A	Epoxy/aluminum	H73.7	H90	502	736	1.63	—		M
	Hysol R9-2039/ HG 3615	Epoxy	R24.2	R25.2	685	685	0.286		No observable color changes.	M
	RTV 60/T-12	Silicone	56.8A	55.7A	36	82	0.996	3.79	No observable color changes.	M
	Silastic RTV 3116	Silicone	38.3A	29.3A	37	66	0.813	3.88	No observable color changes.	M
	Stycast 2651MM/ Cat. No. 11	Epoxy	H74.5	H91	344	929	0.584	0.26	No observable color changes.	M
Adhesive tapes	Scotch electrical tape No. 56	Mylar polyester	Sample not adaptable		43.6 <sup>b</sup>	62.7 <sup>b</sup>	1.149	—	Slight darkening of color.	M
	Scotch video slicing tape No. 390	Polyester- aluminized	Sample not adaptable		12.16 <sup>b</sup>	20.20 <sup>b</sup>	1.955	—	Tendency to blister.	M

<sup>a</sup>3 cycles of 36 hr each at 293°F in a nitrogen atmosphere.  
<sup>b</sup>Adhesion, oz/in. width

**Table 2. Summary of test results for the thermal sterilization procedure<sup>a</sup> on coatings, greases and wire insulation used in REL tape recorder**

Category	Commercial designation	Materials type	Weight loss, %	Comments	Compatibility rating
Coatings	Loctite grade C	Polyester	28.28		NC
	Metaseal 19V5	Polyester	0.23	No change in color or hardness.	M
Greases	DC grease No. 55M	Silicone	5.70	Partial liquefaction, slight darkening of color.	NC
Solder	Alpha solder — Cen-Tri-Core	Contains rosin	1.557	Remaining rosin flux darkens.	M
Wire insulations	Pigtail wire class 105	PVC and nylon insulation	0.479	Darkening and some embrittlement.	NC
	Magnet wire, REA (Mil W-583, type t)	Formvar coating	0.000	No observable changes.	C
	No. 24 AWG type ET (unetched)	TFE teflon coating	0.000	No observable changes.	C
	No. 24 AWG type ET (etched)	TFE teflon coating	0.000	No observable changes.	C

<sup>a</sup>3 cycles of 36 hr each at 293°F in a nitrogen atmosphere.

sure, a compatibility rating was assigned to each product tested based on the following criteria:

Item<sup>1</sup> considered compatible (C) when any of the following occurred:

- (1) Product retained 80% or more of its original mechanical properties.
- (2) Its volume change was less than 4%.
- (3) Its weight loss was less than 0.2%.
- (4) It showed no corrosive action on the metals tested.

Item considered marginal (M) when any of the following occurred:

- (1) Product retained 70–80% of its original mechanical properties.
- (2) Its volume change was 4–6%.
- (3) Its weight loss was 0.2–2.0%.

Item considered not compatible (NC) when any of the following occurred:

- (1) Product retained less than 70% of its original mechanical properties.
- (2) Its volume change was more than 6%.
- (3) Its weight loss was more than 2%.
- (4) It exhibited corrosive action on any of the metals tested.

<sup>1</sup>Compatible itself with the sterilization environment, and with those other materials with which it would be associated in that environment.

Acceptance levels established for the above criteria, selected empirically, were based on practical experience and on a best judgment of their significance relative to the application involved. For example, the 80% level for retention of mechanical properties takes into account the inherent variations in properties of supposedly identical material samples, as well as the unavoidable tolerances imposed on repeatability of experiments due to human and instrument error. Also, in a tape transport for flight application, a permanent reduction of 20% in the strength or hardness of any specific component might very well result in a marginal, if not unacceptable, design condition. Similar considerations apply with respect to volume change. Experience indicated that a 4% reduction in volume of an encapsulated item, for example, can cause serious damage to those components within. The low tolerance of 0.2% for weight loss was established, based on the captive nature of the tape transport environment. In a closed, pressurized atmosphere, particularly when subjected to high temperature, small amounts of potentially harmful outgassing and degradation products can combine to cause serious damage to vital components. That this did in fact occur in the sterilized tape transport unit was indicated by the serious corrosion and degradation found in certain areas upon disassembly of the recorder (SPS 37-37, Vol. IV, p. 236), and was verified by the findings of the subject analysis.

*a. Adhesives, encapsulants, and adhesive tapes.* The summary of thermal exposure data for adhesives, encapsulants, and adhesive tapes is given in Table 1. Among the adhesives, Bondmaster E 645, Cycleweld 55-9, and EC 826 were rated NC because of high weight losses. These are solvent-based adhesives, and the very high weight losses encountered are doubtlessly due to residual solvent

**Table 3. Summary of test results for the thermal sterilization procedure<sup>a</sup> on elastomers, reinforced plastics, films, and heat shrinkable tubing used in the REL tape recorder**

Category	Commercial designation	Material type	Mechanical properties						Physical and thermal properties		Comments	Compati- bility rating
			Hardness		Tensile strength		Elongation		Weight loss %	Volume change %		
			Control	After thermal exposure	Control	After thermal exposure	Control	After thermal exposure				
Elastomers	EPR rubber (E 515-8)	Poly(ethylene- propylene)	76.5A	76.5A	2030	2043	160	152	1.023	0.372	No change in appearance.	M
Reinforced plastics	Viton B 77-545	Fluorocarbon	72.8A	72.5A	2175	1975	240	205	0.131		No change in appearance.	C
	Viton B-95	Fluorocarbon	92.8A	92.7A	2440	1990	120	100	0.150	0.000	No change in appearance.	C
	Micarta 8457 G-10 (Mil P-18177- GEE)	Epoxy/glass	E83.3	E82.0	42925	42100	3.4	3.2	0.205	0.000	Slight darkening of color.	C
	Micarta LE- 221 (Mil P-15035, Type FBE)	Phenolic/linen	F56.5	F65.5	7972	7892	1.7	1.9	3.439	1.71	Darkens.	NC
Film	Rulon, type A	TFE fluoro- carbon	57.3D	59.7D	285	275	295	308	0.008	0.71	No change in appearance.	C
Heat shrinkable	H-Film and electrofilm	Polyimide	Not adaptable		14300	13400	56	40	0.427	None	Tendency to break during elongation after exposure.	M
	Thermofil, RNF 100, type 1, red	Polyolefin/ fire retardant	Not adaptable		1867	1823	403	373	0.341		No change in appearance.	M
	Thermofil, RNF 100, type 1, clear	Polyolefin	Not adaptable		1548	1880	28	25	0.376		Yellowing.	M

<sup>a</sup>3 cycles of 36 hr each at 293°F in a nitrogen atmosphere.

present, even after being cured according to the manufacturer's recommendations. The other two adhesives were considered marginal on the basis of the criteria set for weight loss. It is interesting to note, however, that the tensile shear strength of the adhesives and adhesive tapes was improved after thermal exposure.

**b. Coatings, grease, and wire insulations.** Summary of weight losses and visual observations on physical changes after thermal exposure for coatings, a grease, a solder, and wire insulations are reported in Table 2.

Loctite C, DC grease 55M, and the insulation on pigtail wire were rated NC, the first two because of excessive weight losses and the third because of the corrosive action of its outgassing material on some of the metals used in the tape recorder construction.

Based on the criteria for weight loss, both alpha solder and Metaseal 19V5 were rated M. The weight loss from the solder was due to the rosin flux present. In application, most of the flux would normally be removed by appropriate solvents. This, of course, would result in a weight loss lower than reported here, although most likely still significant.

The Formvar and Teflon insulations were considered C, because neither measurable weight loss, nor corrosive effects on the metals were encountered.

**c. Elastomers, reinforced plastics, film and heat shrinkable tubing (Table 3).** The two fluorocarbon elastomeric products, Viton B77-545 and Viton B-95, as well as the two reinforced plastics, Micarta 8457 G-10 and Rulon, Type A, were rated C. Micarta LE-221 was considered NC because of high weight loss and possible corrosive action of the outgassing products on the metals tested.

Weight losses again were the reason for giving M ratings to the EPR rubber, the H-film (Kapton) backed magnetic tape coated with electrofilm, and the heat shrinkable tubings. Previous testing of the film tape revealed that the polyvinyl-polyacetate adhesive, used to bind the oxide, decomposed under thermal sterilization cycling, giving off highly corrosive HCl. Corrosive action was verified on strips of copper and zinc. All of the products listed in Table 3 retained 80% or more of their original mechanical properties. An exception to this is the H-film which retained only 72% of its original elongation capability after thermal exposure.

As previously pointed out in SPS 37-37, Vol. IV, p. 236, the slight deterioration of mechanical properties exhibited by H-film, though undesirable, is not presently considered a serious problem since it appears that it can be estimated and compensated for in design.

The physical and mechanical characteristics of H-film relative to its applications in spacecraft tape recorders will be investigated more thoroughly in a subsequent study program.

**d. Critical hardware.** A dimensional examination of shafts, pulleys, and critical mounting components revealed that no permanent deformation had taken place during the sterilization cycle. Significant dimensions, checked and compared with those specified in the documentation, showed agreement within the design tolerances specified.

Since some shaft misalignment had been observed during examination of the transport subsequent to thermal sterilization and life testing, the remaining source of misalignment was considered to be the ball bearing assemblies. This theory was supported by disassembly and analysis of two of the failed bearings. Examination revealed that the primary cause of bearing failure was inadequate lubrication resulting from evaporation during the sterilization process. Though there was no indication of corrosive activity on the part of the lubricant, its loss from the contact surfaces resulted in higher operating temperatures, accelerating the bearing wear and oxidation process in the presence of the contaminated atmosphere. The gradual physical deterioration of the bearings and attendant loss of preload accounts for the increase in torque and dimensional instability previously noted.

Further evaluation of lubricants and lubrication techniques for instrument bearings subjected to extreme environments is being conducted as part of another study program.

**e. Outgassing characteristics.** The volatile condensable material (VCM) and the total percent weight loss at 110°C and  $2 \times 10^{-6}$  torr of the polymeric product was determined. These data are summarized in Table 4. It will be noticed that the outgassing test conditions are not a simulation of those actually existing during the thermal sterilization of the REL tape transport. They do serve, however, to indicate how much material could be outgassed if the polymeric products were heated to higher temperatures or for longer periods and under higher pressure, say 1 to 1½ atm.

Table 4. Outgassing at 110°C and  $2 \times 10^{-6}$  torr<sup>a</sup>

Commercial designation	VCM <sup>b</sup> , %	Total volatiles, %	Identity of VCM <sup>b</sup> by infrared (IR)	Identity of VNCM <sup>c</sup> by IR
Bearing residue			Benzene soluble material-acrylate (metallic residue 45% iron, originated elsewhere)	
Bondmaster E 645	0.15	6.73	Opaque deposit. Diisocyanate	No IR
Cycleweld 55-9	0.43	12.83	White crystals. Bisphenol	Bisphenol
DC 55M grease	12.11	13.28	Oleate ester + silicone	Aliphatic hydrocarbon + silicone
DuPont PI-1200	0.11	0.21	No visible deposit. Hydrocarbon	Hydrocarbon
EC 826	2.88	13.14	Yellow liquid and solid. Liquid seemed to be bisphenol or cresol. Solid was naphthyl amine or bisphenol.	Naphthyl amine or bisphenol
EPR rubber	0.46	1.00	Light yellow liquid. Dioctyl phthalate	Aliphatic + aromatic
Felt pad deposit			Epoxy + ester	
H-Film + electrofilm			Graphite particles (identified by microscopy)	
Hysol R9-2039/HG 3615	0.26	0.37	Opaque deposit. Epoxy and ester	Hydrocarbon
Metaseal 19V5	0.22	0.69	Nothing visible.	Hydrocarbon
Micarta 8457 G-10	0.00	0.41	Nothing visible. No IR	Hydrocarbon
Micarta LE-221	1.52	2.72	Nothing visible. No IR	Hydrocarbon and water Phenolic odor
Number A2 adhesive/A	0.17	0.39	Liquid. Epoxy	Hydrocarbon
RTV 60/T-12	1.32	1.60	Clear liquid. Silicone.	Silicone
Rulon, type A	0.00	0.03	Nothing visible. No IR	No IR
Scotch electrical tape No. 56	2.73	2.93	Opaque deposit. Aliphatic acid	Hydrocarbon
Scotch video splicing tape No. 390	1.72	1.84	Opaque deposit. Polyester. Possibly urethane	Hexamethylene diamine
Silastic RTV 3116	0.48	1.00	Liquid. Silicone	Silicone
Stycast 2651/Catalyst No. 11	0.44	0.48	Opaque deposit. Epoxy and ester	No IR
Thermofit RNF 100, type 1, red	0.78	1.09	Light yellow opaque deposit. Phthalate ester	Hydrocarbon
Thermofit RNF 100, type 1, clear	0.32	0.70	Opaque deposit. Phthalate	Hydrocarbon
Viton B 77-545	0.16	0.31	Opaque deposit. Ester	Water apparently
Viton B 95	0.01	0.48	Nothing visible. Nothing detected	Water apparently
Wire insulation on				
Magnet wire REA	0.00	12.68	Nothing visible. No IR	Hydrocarbon
A 24 AWG type E-T unetched	0.00	0.04	Nothing visible. No IR	No IR
A 24 AWG type E-T etched	0.00	0.05	Nothing visible. No IR	No IR
Pigtail wire class 105				
Outer jacket	3.62	4.10	Liquid. Ester and tricresyl phosphate	Carboxylic acid
Wire insulation	0.16	0.28	Liquid Hydrocarbon (polyether) possibly	Hydrocarbon
Metalized inner jacket	0.00	0.47	Nothing visible. No IR	No IR

<sup>a</sup>Courtesy of JPL analytical laboratory, Mr. Stephen P. Vango.

<sup>b</sup>VCM = volatile condensable material.

<sup>c</sup>VNCM = volatile noncondensable material.

*f. Effect of outgassed material on metals.* Table 5 summarizes the results of the experiments performed to determine the effects of materials released from each product during thermal sterilization on metals used in the recorder, i.e., copper, brass, magnesium, Mu metal, and stainless steel.

The metals were represented by sample strips, except for the stainless steel samples which were rods. The magnesium strips were cut from plates having the two types of surface finish that were used in the recorder application. The bare metal, exposed by cutting, was noticeably affected by the outgassing materials from many of the products. Seven of the products listed in Table 5 showed

an indication of possible corrosive effect on the metal surfaces. The metals most affected were copper, brass, and untreated magnesium. Unfinished magnesium, of course, was not, and would not be, used in a tape recorder application. However, serious corrosive action could be expected at faying surfaces, such as mounting points and points of contact with other components, where abrasive action is likely to wear off the protective finish. This would occur also at points of imperfection in the surface finish, or where it was relatively thin. Such action was notably observed on magnesium components in the tape transport.

Examination of Table 4 reveals why some of the outgassing products would have corrosive action on the

**Table 5. Effect of outgassed material on some metals used in the REL tape recorder**

Polymeric product	Effect of outgassed material
Alpha solder cen-tri-core	Corrosion on Mg, extensive discoloration of Cu and brass
Bondmaster E645	Discoloration of Cu and brass
Cycleweld 55-9	Discoloration of Cu and brass Slight discoloration of Mg
DC 55M grease	Discoloration of Cu and brass
DuPont PI-1200	Discoloration of Cu and brass
EC 826	Discoloration of Cu, brass, and Mg. Possible corrosion
EPR rubber	Discoloration of Cu and brass
H-film + electrofilm	Discoloration of Cu and brass
Hysol R9-2039/HG 3615	Very slight discoloration of Cu and brass
Loctite grade C	Not performed—requires anaerobic cure
Metaseal 19V5	Discoloration of brass and Cu. Possible corrosion
Micarta 8457 G-10	Slight discoloration of Cu and brass
Micarta LE 221	Discoloration of Cu and brass. Possible corrosion
Number A2 adhesive/A	Very slight discoloration of Cu and brass
RTV 60/T-12	Very slight discoloration of Cu and brass
Rulon, type A	Very slight discoloration of Cu and brass
Scotch electrical tape No. 56	Extensive discoloration of Cu and brass. Possible corrosion
Scotch video splicing tape No. 390	Discoloration of Cu and brass
Silastic RTV 3116	Very slight discoloration of Cu and brass
Stycast 2651MM/catalyst No. 11	Slight discoloration of Cu and brass
Thermofit RNF 100, type 1, red	Discoloration of Cu, brass and Mg. Pot marks indicating corrosion
Thermofit RNF 100, type 1, clear	Discoloration of Cu, brass and Mg
Viton B 77-545	Discoloration of Cu, brass and Mg
Viton B 90	Discoloration of Cu, brass and Mg
Wire insulation on Magnet wire REA	None
A 24 AWG type E-T unetched	None
A 24 AWG type E-T etched	None
Pigtail wire, class 105	Corrosion of Cu and brass

metals. For example, the VCM from Scotch electrical tape No. 56 is identified as an aliphatic acid. Similarly, a phenol, possibly bisphenol A, is identified among the VCM obtained from EC 826. In the presence of moisture and air desorbed from the materials used in the recorder during the heating process, the outgassed products such as acid, phenols, organic halides, etc., become potential corrosive agents.

*g. Observations on thermal-vacuum pretreatment.* Examination of the poststerilization data on mechanical properties relative to physical and thermal properties suggests that the damage resulting from outgassed materials

could be substantially reduced if the products could be outgassed or cleaned prior to use.

A series of weight loss determinations on two of the encapsulants, RTV 60 and Silastic 3116, were made at various temperatures and time intervals under vacuum. Fig. 7 shows the percent weight loss after 6 hr at 28.5 in. of mercury vacuum and at three different temperatures. Fig. 8 shows the percent weight loss at 293°F and the same vacuum at various time intervals. Table 1 shows the weight losses of the two subject products to be slightly under 1%, resulting from thermal sterilization. It can be seen from examination of the data presented in Figs. 7 and 8 that 24 hr of outgassing in vacuum at 293°F is

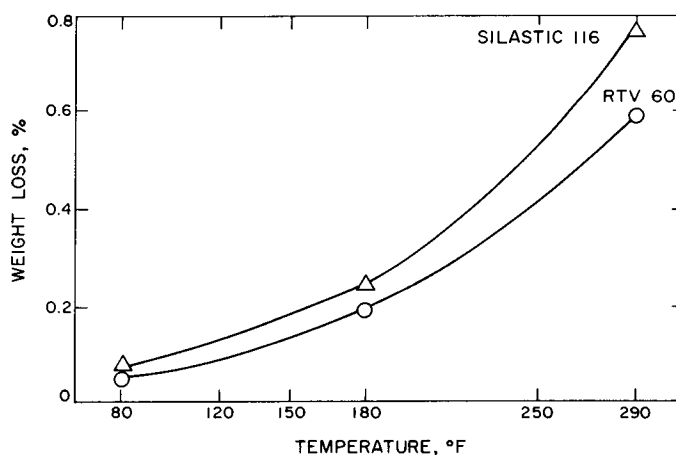


**Fig. 7. Percent weight loss of silicone encapsulants at various temperatures after 6 hrs outgassing at 28.5 in. of mercury vacuum (gage reading)**

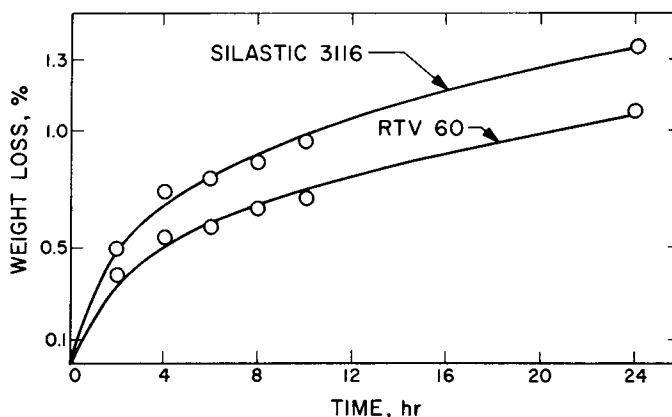


**Fig. 8. Percent weight loss of silicone encapsulants at 293°F and 28.5 in. of mercury vacuum (gage reading)**

adequate to preclean these two products. It is reasonable to assume that similar procedures could be applied to pretreat other polymeric materials used in tape recorder construction.

#### **4. Summary and Conclusions**

Based on the criteria established herein, 25% of the products tested were rated compatible, and were recommended as satisfactory for use in a thermally sterilized tape recorder. Another 25% were found to be not compatible, and suitable substitutes that have been proven sterilizable should be employed. 50% of the products are considered marginal. Those so rated on the basis of percent weight loss can, in many instances, be rid of harmful outgassing materials by thermal-vacuum pretreatments, and thereby be rendered acceptable.

From the estimated quantities of each of the polymeric materials used in the tape transport, and the total percent weight losses, it is determined that 3.5 to 4.0 g of volatile material was floating in the airtight transport housing after thermal sterilization. The volatile material was composed of water vapor and carbon dioxide, phenols, hydrocarbons, organic acids, esters, amines, and silicones. It is apparent that these chemicals acted deleteriously on both metallic and nonmetallic components of the tape transport, particularly in the sealed atmosphere during the elevated temperature cycle. This emphasizes the importance of selecting materials of fabrication having minimum weight loss and/or those that can be precleaned prior to use, as well as the necessity of proper handling techniques (curing procedures, surface treatments, etc.) that affect the preparation of materials for use in spacecraft tape recorder applications.

## XIX. Spacecraft Radio

### TELECOMMUNICATIONS DIVISION

N67-15749

#### **A. Radar Altimeter and Doppler Velocity Sensor, Frequency Discriminator Analysis, R. L. Horner**

##### **1. Introduction**

The *Surveyor* radar altimeter and doppler velocity sensor (RADVS) was described in SPS 37-38, Vol. IV, pp. 212-217. In that analysis the input signal was a constant amplitude sinusoidal wave in a gaussian random noise process. This article treats the more realistic case, assuming both signal and noise are gaussian. In addition, the processes need not be narrowband, and the noise processes may or may not be correlated.

##### **2. Operation of the RADVS Discriminator**

Fig. 1 will help to explain the operation of the discriminator. Pulses generated by the positive-going zero crossings in one channel are used to sample the hard-limited quadrature component in the other. The output, then, is a train of pulses, positive or negative, depending on the phase relationship between the two input channels.

Eq. (1) shows the input model used in this analysis. Both signal and noise are sample functions from stationary gaussian random processes. The parameter  $\omega_D$  is the magnitude of the doppler shift from the carrier, and its sign

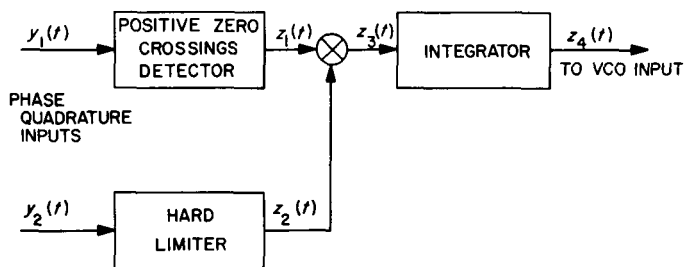


**Fig. 1. Block diagram of RADVS discriminator**

depends on whether the relative velocity is closing or opening. (Note how its sign determines the phase relationship between the two channels.)

$$\begin{aligned}
 y_1(t) &= (s_1(t) + n_1(t)) \sin(\pm\omega_D t + \theta) \\
 &\quad + (s_2(t) + n_2(t)) \cos(\pm\omega_D t + \theta) \\
 y_2(t) &= (s_1(t) + n_1(t)) \cos(\pm\omega_D t + \theta) \\
 &\quad - (s_2(t) + n_2(t)) \sin(\pm\omega_D t + \theta) \quad (1)
 \end{aligned}$$

##### **3. Analysis**

The operations indicated in the block diagram must be described mathematically. A counting functional, shown

in Eq. (2), locates positive-going zero crossings. The term  $u_0(y_1(t))\dot{y}_1(t)$  is a unit impulse on the time axis whenever  $y_1(t)$  is zero. Since this term locates both positive and negative crossings, the unit step  $u_{-1}(\dot{y}_1(t))$  is used to eliminate negative-going crossings. Thus,

$$z_1(t) = [u_0(y_1(t))\dot{y}_1(t)][u_{-1}(\dot{y}_1(t))] \quad (2)$$

where

$$u_0(t) = \text{unit impulse}$$

$$u_{-1}(t) = \text{unit step}$$

$$\dot{y}_1(t) = \frac{d}{dt}y_1(t)$$

The integral of  $z_1(t)$  across the neighborhood of a positive zero crossing is one. Therefore, the time average of  $z_1(t)$  yields the average number of positive zero crossings per unit time. This should be a measure of the frequency of  $y_1(t)$ .

The limiter is defined as follows: Let

$$z_2(t) = g(y_2(t)) \quad (3)$$

where

$$g(x) = \begin{cases} 1 & x > 0 \\ 0 & x = 0 \\ -1 & x < 0 \end{cases}$$

The system output before filtering is expressed by the product of  $z_1$  and  $z_2$ .

$$z_3(t) = z_1(t) \cdot z_2(t) \quad (4)$$

The time average of  $z_3(t)$  will yield the average frequency (and sign) of the total input process  $y(t)$ .

$$z_4(t) = \langle z_3(t) \rangle$$

$$= \lim_{T \rightarrow \infty} \frac{1}{2T} \int_{-T}^T g(y_2(t)) u_0(y_1(t)) \dot{y}_1(t) u_{-1}(\dot{y}_1(t)) dt \quad (5)$$

Since the input processes are covariance stationary, an ensemble average may be used to calculate the time average indicated in Eq. (5). Thus,

$$\begin{aligned} \overline{z_4(t)} &= \int_{-\infty}^{\infty} dy_1 \int_{-\infty}^{\infty} d\dot{y}_1 \\ &\times \int_{-\infty}^{\infty} dy_2 g(y_2) u_0(y_1) \dot{y}_1 u_{-1}(\dot{y}_1) p_{y_1 \dot{y}_1 y_2}(y_1, \dot{y}_1, y_2) \end{aligned} \quad (6)$$

where  $p_{y_1 \dot{y}_1 y_2}(y_1, \dot{y}_1, y_2)$  is a joint probability density function. Since the processes are gaussian, the density function may be written by inspection, using the following parameters

$$\sigma_1^2 = E\{y_1^2\}$$

$$\sigma_3^2 = E\{y_2^2\}$$

$$\sigma_2^2 = E\{\dot{y}_1^2\}$$

$$\rho_{\dot{y}_1 y_2} \sigma_2 \sigma_3 = E\{\dot{y}_1 y_2\} = \rho \sigma_2 \sigma_3$$

$$E\{y_1 \dot{y}_1\} = \frac{d}{d\tau} E\{y_1 y_1\} \Big|_{\tau=0} = \frac{d}{d\tau} R_{y_1}(\tau) \Big|_{\tau=0} = 0$$

$$E\{y_1 y_2\} = R_{y_1 y_2}(\tau) \Big|_{\tau=0} = 0$$

The density function becomes

$$p_{y_1 \dot{y}_1 y_2}(y_1, \dot{y}_1, y_2) = \frac{1}{(2\pi)^{3/2} (1 - \rho^2)^{1/2} \sigma_1 \sigma_2 \sigma_3} \exp \left[ -\frac{y_1^2}{2\sigma_1^2} - \frac{\sigma_2^2 \dot{y}_1^2 - 2\rho \sigma_2 \sigma_3 \dot{y}_1 y_2 + \sigma_3^2 y_2^2}{2\sigma_2^2 \sigma_3^2 (1 - \rho^2)} \right] \quad (7)$$

Substituting into Eq. (6) gives

$$\begin{aligned} \overline{z_4(t)} &= \int_{-\infty}^{\infty} dy_1 \int_{-\infty}^{\infty} d\dot{y}_1 \int_{-\infty}^{\infty} dy_2 u_0(y_1) \dot{y}_1 u_{-1}(\dot{y}_1) g(y_2) \\ &\times \frac{1}{(2\pi)^{3/2} (1 - \rho^2)^{1/2} \sigma_1 \sigma_2 \sigma_3} \exp \left[ -\frac{y_1^2}{2\sigma_1^2} - \frac{\sigma_2^2 \dot{y}_1^2 - 2\rho \sigma_2 \sigma_3 \dot{y}_1 y_2 + \sigma_3^2 y_2^2}{2\sigma_2^2 \sigma_3^2 (1 - \rho^2)} \right] \end{aligned} \quad (8)$$

The integration over  $y_1$  is trivial.

$$\overline{z_4(t)} = \frac{1}{(2\pi)^{1/2} \sigma_1} \int_{-\infty}^{\infty} d\dot{y}_1 \int_{-\infty}^{\infty} dy_2 g(y_2) \dot{y}_1 u_{-1}(\dot{y}_1) \cdot \frac{1}{2\pi (1 - \rho^2)^{1/2} \sigma_2 \sigma_3} \exp \left[ - \frac{\sigma_3^2 \dot{y}_1^2 - 2\rho \sigma_2 \sigma_3 \dot{y}_1 y_2 + \sigma_2^2 y_2^2}{2\sigma_2^2 \sigma_3^2 (1 - \rho^2)} \right]$$

Further simplification results from the properties of  $u_{-1}(\dot{y}_1)$  and  $g(y_2)$ .

$$\begin{aligned} \overline{z_4(t)} = \frac{1}{(2\pi)^{1/2} \sigma_1} \frac{1}{2\pi \sigma_2 \sigma_3 (1 - \rho^2)^{1/2}} \int_0^{\infty} d\dot{y}_1 \dot{y}_1 \int_0^{\infty} dy_2 \cdot \left\{ \exp \left[ - \frac{\sigma_3^2 \dot{y}_1^2 - 2\rho \sigma_2 \sigma_3 \dot{y}_1 y_2 + \sigma_2^2 y_2^2}{2\sigma_2^2 \sigma_3^2 (1 - \rho^2)} \right] \right. \\ \left. - \exp \left[ - \frac{\sigma_3^2 \dot{y}_1^2 + 2\rho \sigma_2 \sigma_3 \dot{y}_1 y_2 + \sigma_2^2 y_2^2}{2\sigma_2^2 \sigma_3^2 (1 - \rho^2)} \right] \right\} \end{aligned} \quad (9)$$

Introducing the change of variables

$$x_1 = \frac{\dot{y}_1}{(2)^{1/2} \sigma_2 (1 - \rho^2)^{1/2}} \quad x_2 = \frac{y_2}{(2)^{1/2} \sigma_3 (1 - \rho^2)^{1/2}}$$

the double integral in Eq. (9) becomes

$$\overline{z_4(t)} = \frac{\sigma_2 (1 - \rho^2)^{1/2}}{\pi^{3/2} \sigma_1} \int_0^{\infty} dx_1 x_1 \times \int_0^{\infty} dx_2 \{ \exp [ - (x_1^2 - 2\rho x_1 x_2 + x_2^2) ] - \exp [ - (x_1^2 + 2\rho x_1 x_2 + x_2^2) ] \} \quad (10)$$

This particular integral is performed in Middleton (Ref. 1).

$$\int_0^{\infty} dx_1 x_1 \int_0^{\infty} dx_2 \exp [ - (x_1^2 + 2\rho x_1 x_2 + x_2^2) ] = \frac{(\pi)^{1/2}}{4} \frac{1}{1 + \rho}$$

Substituting this result into Eq. (10) yields

$$\begin{aligned} \overline{z_4(t)} &= \frac{\sigma_2 (1 - \rho^2)}{\pi^{3/2} \sigma_1} \frac{(\pi)^{1/2}}{4} \left[ \frac{1}{1 - \rho} - \frac{1}{1 + \rho} \right] \\ &= \frac{1}{2\pi} \frac{\sigma_2}{\sigma_1} \rho \end{aligned} \quad (11)$$

The terms in Eq. (11) have already been defined.

$$\rho = \frac{E \{ \dot{y}_1 y_2 \}}{\sigma_2 \sigma_3}$$

So

$$\overline{z_4(t)} = \frac{1}{2\pi} \frac{E \{ \dot{y}_1 y_2 \}}{\sigma_1 \sigma_3}$$

The processes  $y_1(t)$  and  $y_2(t)$  are quadrature components, hence

$$E \{ y_1^2 \} = \sigma_1^2 = E \{ y_2^2 \} = \sigma_2^2 = R_y(0)$$

$$E \{ \dot{y}_1 y_2 \} = - \frac{d}{d\tau} E \{ \dot{y}_1 y_2 \} \Big|_{\tau=0} = - \dot{R}_{y_1 y_2}(0)$$

The discriminator output is, then

$$\overline{z_4(t)} = \frac{1}{2\pi} \frac{-\dot{R}_{y_1 y_2}(0)}{R_y(0)} = \frac{1}{2\pi} \frac{- \int_{-\infty}^{\infty} d\omega \omega S_{y_1 y_2}(\omega)}{\int_{-\infty}^{\infty} d\omega S_y(\omega)} \quad (12)$$

Note that if  $y_1(t)$  and  $y_2(t)$  are independent instead of quadrature components, the discriminator average output would be zero.

With the signal model chosen in Eq. (1) and the correlation properties of the signal and noise functions

$$E \{s_1(t) s_1(t + \tau)\} = E \{s_2(t) s_2(t + \tau)\} = R_s(\tau)$$

$$E \{s_1(t) s_2(t + \tau)\} = R_{s_1 s_2}(\tau)$$

$$E \{n_1(t) n_1(t + \tau)\} = E \{n_2(t) n_2(t + \tau)\} = R_n(\tau)$$

$$E \{n_1(t) n_2(t + \tau)\} = R_{n_1 n_2}(\tau)$$

$$E \{s_i(t) n_j(t + \tau)\} = 0 \quad i, j = 1, 2$$

the correlation functions of  $y_1(t)$  and  $y_2(t)$  are

$$\begin{aligned} R_{y_1}(\tau) &= (R_s(\tau) + R_n(\tau)) \cos(\pm \omega_D \tau) \\ &\quad - (R_{s_1 s_2}(\tau) + R_{n_1 n_2}(\tau)) \sin(\pm \omega_D \tau) \\ R_{y_1 y_2}(\tau) &= - (R_s(\tau) + R_n(\tau)) \sin(\pm \omega_D \tau) \\ &\quad - (R_{s_1 s_2}(\tau) + R_{n_1 n_2}(\tau)) \cos(\pm \omega_D \tau) \end{aligned} \quad (13)$$

Thus,

$$R_y(0) = R_s(0) + R_n(0)$$

and

$$\begin{aligned} R_{y_1 y_2}(\tau) &= - (\dot{R}_s(\tau) + \dot{R}_n(\tau)) \sin(\pm \omega_D \tau) \\ &\quad \mp (R_s(\tau) + R_n(\tau)) \omega_D \cos(\pm \omega_D \tau) \\ &\quad - (\dot{R}_{s_1 s_2}(\tau) + \dot{R}_{n_1 n_2}(\tau)) \cos(\pm \omega_D \tau) \\ &\quad \mp (R_{s_1 s_2}(\tau) + R_{n_1 n_2}(\tau)) \omega_D \sin(\pm \omega_D \tau) \\ - \dot{R}_{y_1 y_2}(0) &= \pm \omega_D (R_s(0) + R_n(0)) \\ &\quad + (\dot{R}_{s_1 s_2}(0) + \dot{R}_{n_1 n_2}(0)) \end{aligned}$$

In terms of the input processes, the discriminator output is

$$\begin{aligned} \overline{z_4(t)} &= \frac{1}{2\pi} \frac{-\dot{R}_{y_1 y_2}(0)}{R_y(0)} \\ &= \frac{1}{2\pi} \left[ \pm \omega_D + \frac{(\dot{R}_{s_1 s_2}(0) + \dot{R}_{n_1 n_2}(0))}{R_s(0) + R_n(0)} \right] \end{aligned}$$

By rearranging terms, the relative contributions to the bias by the signal and noise asymmetries become more apparent. Thus

$$z_4(t) = \frac{1}{2\pi} \left[ \pm \omega_D + \frac{\frac{\dot{R}_{n_1 n_2}(0)}{R_n(0)} + \text{SNR} \frac{\dot{R}_{s_1 s_2}(0)}{R_s(0)}}{1 + \text{SNR}} \right]$$

where

$$\text{SNR} = \frac{R_s(0)}{R_n(0)}$$

$$\frac{\dot{R}_{n_1 n_2}(0)}{R_n(0)} = \text{noise frequency bias}$$

$$\frac{\dot{R}_{s_1 s_2}(0)}{R_s(0)} = \text{signal frequency bias}$$

The total bias may be positive or negative, thereby increasing or decreasing the magnitude of the discriminator output.

#### 4. Conclusions

The analysis in this article shows explicitly that the RADVS discriminator responds to the centroid of the input cross power spectrum. Therefore, if the spectrum is unsymmetric, as caused by terrain biasing or mixer flicker noise, the output will be biased away from the true doppler frequency. Whether the error is sufficient to cause difficulty depends on the application.

**N67-15750**

**B. Electron Tube Filament Study, L. J. Derr**

#### 1. Introduction

A study program has been conducted by the Machlett Laboratories at Stamford, Connecticut, to develop methods which would enhance the efficiency of heat transfer between the filament and cathode of electron tubes (JPL Contract No. B4-226592). This advanced development study was initiated in October 1963 and was terminated in June 1966. During this period, the contractor originated and tested numerous designs; but because of limited resources, it was not possible to explore any one technique extensively. Some of the designs required rather advanced

fabricating techniques. Consequently, a percentage of the designs failed simply because they could not be made. In the end, the program successfully produced at least two assemblies which met requirements.

The goal of this study was to accomplish a 30% improvement in filament efficiency over standard design assemblies.

The function of the filament in electron tubes is to provide the necessary heating power to raise the oxidized emitting surface of the cathode to a temperature at which it freely releases electrons. These electrons are necessary for the proper operation of a thermionic amplifying device. The temperature at which sufficient emission can be obtained lies within the range of 800–900°C. Heating the cathode element via the independent filament consumes a sizeable percentage of the total electrical power furnished to the tube and is thus detrimental to its over-all efficiency. By improving the efficiency of the heating system, there is a direct improvement in the total tube efficiency.

In order to establish a standard from which improvements can be measured, a modern electron tube (Machlett ML-8534) was selected as a reference (Fig. 2). Thermal

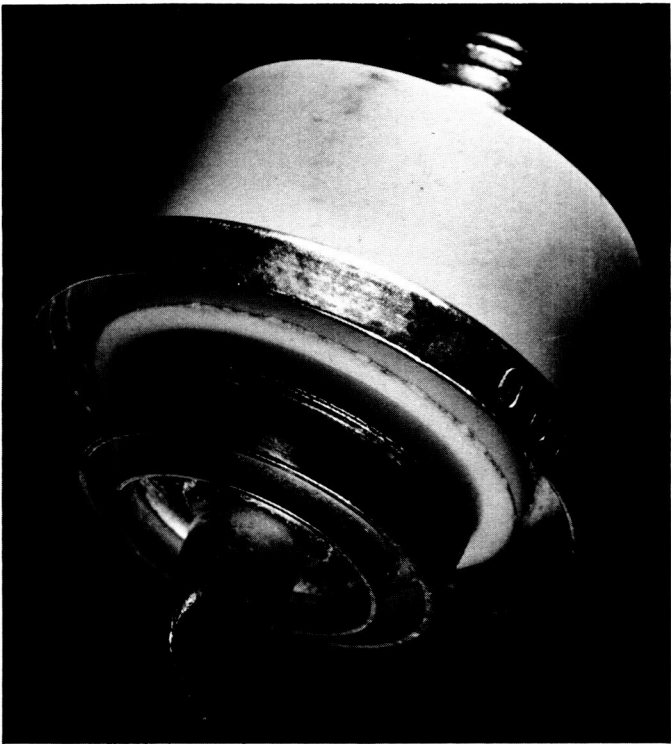


Fig. 2. ML-8534 electron tube

measurements were pyrometrically made in glass envelopes. The electronic performance of completed assemblies was evaluated in a modified P-21-H cavity amplifier, manufactured by Resdel Engineering, Inc.

## 2. Study Program

At the time when the contract was first initiated it was standard practice to mechanically suspend the filament near the back side of the cathode disc. Heat was transferred from the electrically-excited filament to the cathode-emitting surface by a combination of radiative and conductive paths. Since the assembly operated within a vacuum, the third means, convection, was not a factor.

The conventional design can be seen in Fig. 3 showing that heat was first radiated from the filament to the back of the cathode, then conducted through the cathode to its emitting surface on the opposite side. The efficiency at which such a system can operate is determined by the inherent losses. From Fig. 3 it is seen that the losses are both radiative and conductive. Only the heat reaching the cathode disc can be considered as useful; the rest constitutes the system losses. The filament winding, being flat, tends to concentrate its heat in an upward and downward dipole pattern. The upward heat reaches the cathode and becomes its sole thermal excitement. The downward and sideward radiation is lost to the cathode support and other nearby elements of the tube where it is conducted away by their heavy external connections. Conduction heat losses of the filament are unavoidably made through its electrical connections. Usually one connection is made at

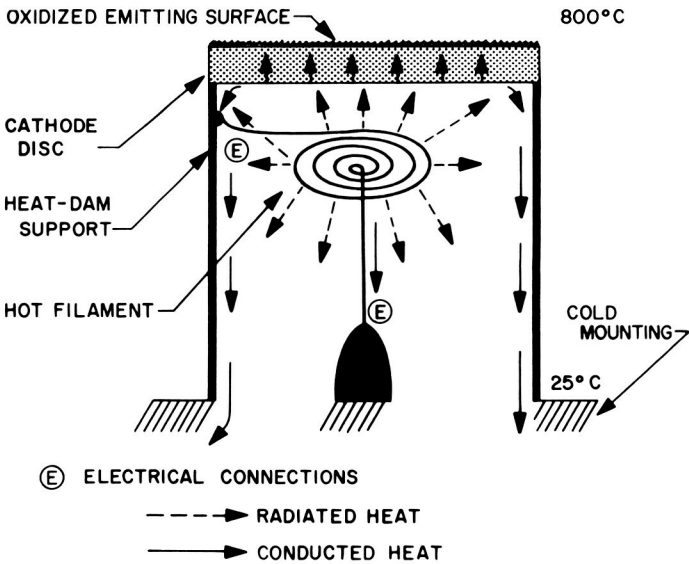


Fig. 3. Standard cathode assembly

a high temperature spot on the cathode heat-dam support, minimizing the conduction losses in that direction; but the other electrical connection must be made to a cold, heat-consuming attachment.

It is evident, when considering the system as a whole, that filament efficiency can be increased by either improving the heat transfer mechanism or reducing the loss. This would allow the filament to operate at a lower exciting temperature, which would, in turn, further reduce the radiative and conductive loss.

The vendor's attempt to improve efficiency was to imbed an insulated filament directly within the metal cathode itself, changing the filament to cathode heat transfer from radiative to conductive. To this end, the contractor experimented with various methods of mechanically potting the two together as well as a rather involved way of forming a monolithic structure by the use of metal vapor deposition, flame spraying, grinding, and plating techniques.

### 3. Experimental Results

**Nickel imbedding.** The contractor first attempted to imbed the insulated filament in a conductive nickel powder. The spiral filament was first placed in the recessed back of the cathode disc. Then the recess was filled with pure Ni powder, which completely covered the filament spiral. This assembly was then placed in a press, where it was raised to nickel-sintering temperatures (1100–1300°C) in a hydrogen atmosphere. Problems encountered were improper adhesion of the sintered Ni powder (Fig. 4) and flaking of the filament insulation (Fig. 5). Thermal shrinkage could not be avoided, although numerous sinter temperatures were used and sintering pressure was varied from 1000 to 2000 lbs.

At that time the problem of nickel potting had not been solved by industry. In his search for a solution, the vendor turned to other materials but continued work on the nickel process. Later he deduced that the sintering pressure should be eliminated, thereby allowing greater molecular freedom during the cooling period. This would, in turn, relieve the cracking stresses. Further, he nickelated (sintered a thin coating of nickel powder) the inside surface of the cathode recess for greater adherence. By these means the vendor made several satisfactory models, which were thermally tested and showed a heat transfer improvement of greater than 30%. One test, to see if the filament heat itself could accomplish the sintering process, was unsuccessful, and the approach was discarded.

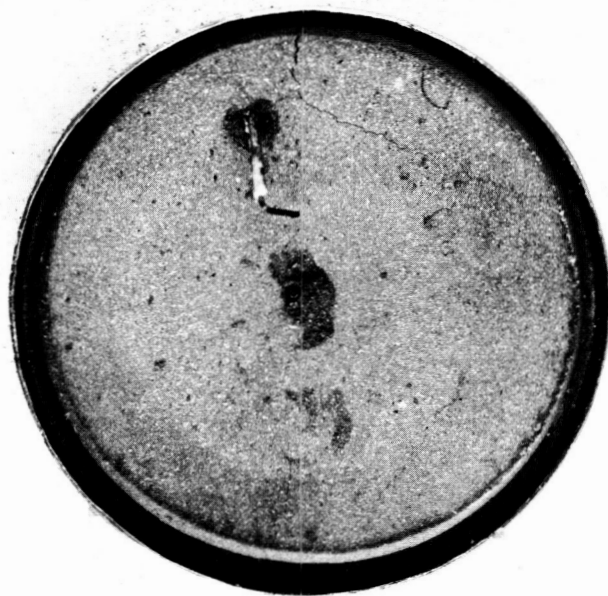


Fig. 4. Pressure-sintering nickel imbedding

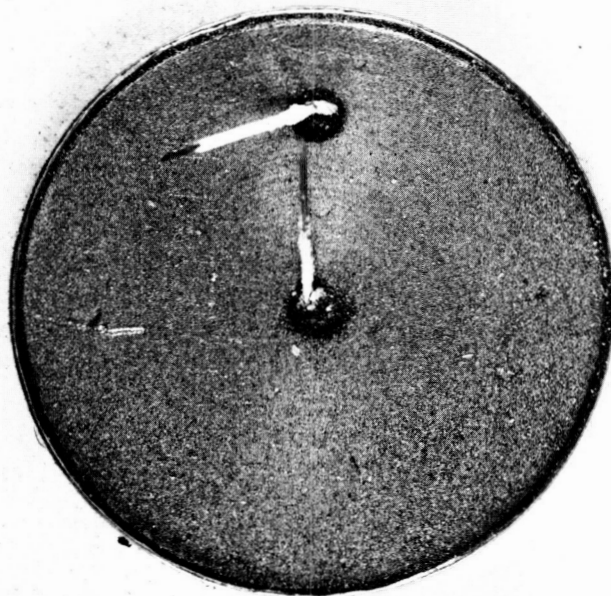
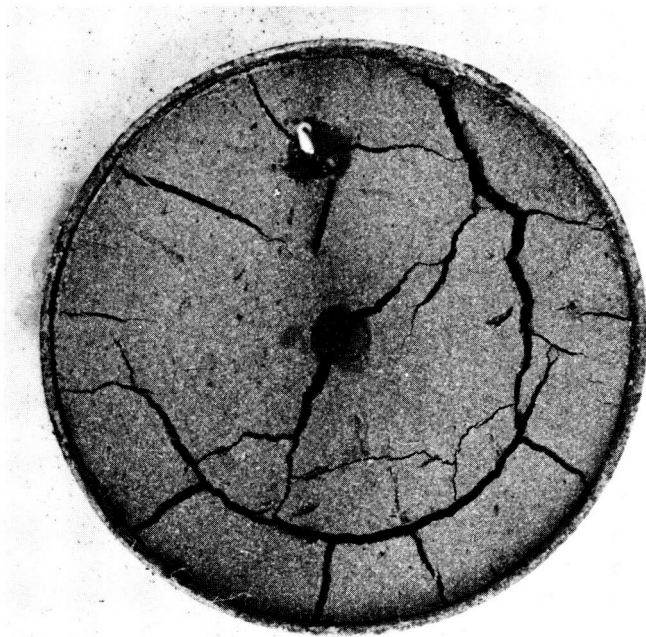


Fig. 5. Defective filament insulation

**Molybdenum-nickel imbedding.** A molybdenum-nickel powder was next investigated as a metal potting. Several compounds with Ni content ranging from 2 to 10% were tested using the pressure-sintering technique designed



**Fig. 6. Molybdenum-nickel imbedding**

for the nickel powder. In spite of their good theoretical heat conduction capabilities, none of these compounds was found to be satisfactory for potting. Severe cracking occurred during cooling, as illustrated in Fig. 6.

**Flat spiral heaters.** To reduce the filament to cathode spacing and to increase the filament surface for better heat transfer, the contractor designed a flat spiral heater. This was made by photoetching the pattern from a sheet of rhenium tungsten (Fig. 7). It was then found that aluminum oxide insulation would not adhere to the sharp corners of the etched spiral. Further, the rhenium tungsten became extremely brittle after exposure to the coating firing temperature of 1700°C. Consequently, no thermal evaluation of this configuration was possible.

**Sauereisen imbedding.** The contractor next explored the possibility of ceramic potting. Several of these were known to be thermally conductive from prior experience. The first one tried was a cement, Sauereisen Insia-lute, Hi temperature cement No. 7 (Fig. 8). This material worked quite well as an imbedding means, and ensuing tests indicated a thermal improvement of approximately 25%. However, further investigation was discontinued because rare-earth elements known to poison the cathode emitting surface were discovered in the cement. Since the rare-earths are essential for achieving the proper characteristics of the cement, they could not be eliminated.

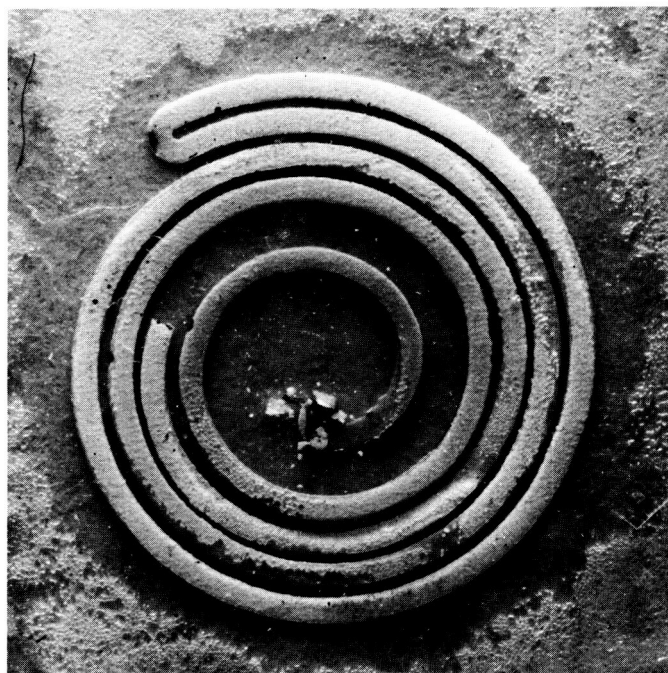


**Fig. 7. Photoetched heater**

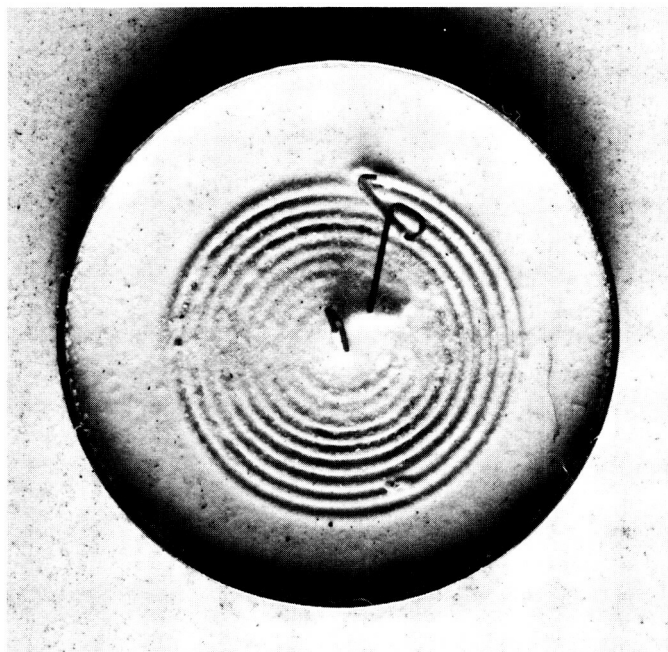


**Fig. 8. Sauereisen cement imbedding**

**Ceramabond imbedding.** Another ceramic cement, Ceramabond 503, manufactured by Areenco Products, was investigated. Although this material bonds at temperatures below 500°C, it also decomposes in a vacuum. Several test

vehicles were assembled using this material, and a heat transfer improvement of 10% was measured. Electronic tests which followed indicated that the rapid decomposition of the bonding material destroyed the emitting capabilities of the cathode.

**Flame-spray imbedding.** The next imbedding process involved the evaluation of flame-spray techniques for pure aluminum oxide ceramic. This process was explored with the help of Linde Ceramic Laboratories. In this method, the oxide is vaporized by an extremely hot flame. The evaporated particles cool as they approach the potting target. In spite of the "less than sintering" temperature of the particles, they adhere strongly to the target.

Numerous attempts were made by Linde to flame spray the Machlett filament/cathode assembly. Early tests consistently resulted in burning off the heater legs. In a final attempt, Linde shielded these legs from the flame, which resulted in a large area not being potted (Fig. 9). Subsequent tests showed a 25% decrease in efficiency, rather than a hoped-for increase. Further work was discontinued on this method.

**Monolithic structures.** During the final phase of the program, the contractor designed a monolithic, one-piece, filament/cathode structure consisting of a thin BeO or

$\text{Al}_2\text{O}_3$  ceramic disc on which a single spiral groove was etched by the Coors Laboratory (Fig. 10). This ceramic blank was then processed by the Sylvania Co., who deposited tungsten on the substrate by a hexachloride process. Excess tungsten was then removed by grinding (Machlett). This process cleared both sides of the disc except for the tungsten in the spiral groove. Further grinding reduced the tungsten thickness to the correct value of resistance for heater operation. A gas analysis of the assembly proved that the Machlett cleaning methods were adequate to remove all traces of chlorine, which is detrimental to cathode emission.

Next, it was necessary to deposit the activator coating (nickel) on the opposite side of the blank. This was accomplished by sintering. The process was not successful due to the wide disagreement between the expansion coefficients of aluminum oxide and nickel. The blank became a saucer as it cooled and then eventually fractured. To eliminate this, a tungsten activator was used, allowing the assembly to remain flat during the sintering-cooling cycle.

Next, the edge of the blank was metalized so that a Kovar heat-dam (tube) could be attached for proper mounting in the electron tube. Present filament electrical connections are made through the Kovar heat-dam and a center post, which contacts the opposite end of the

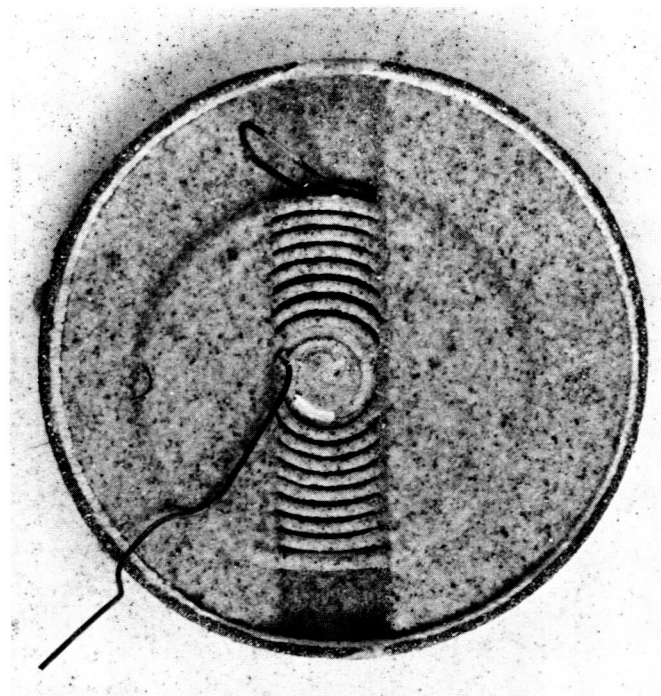


Fig. 9. Flame-spray imbedding

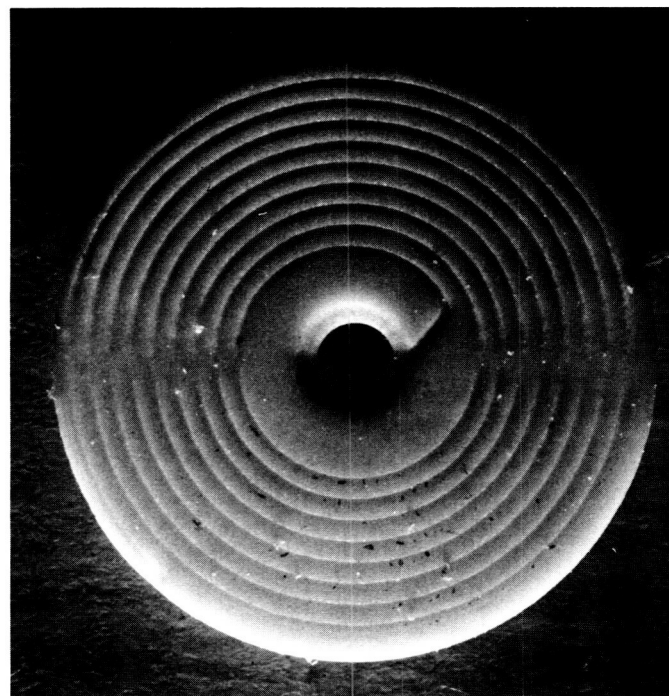
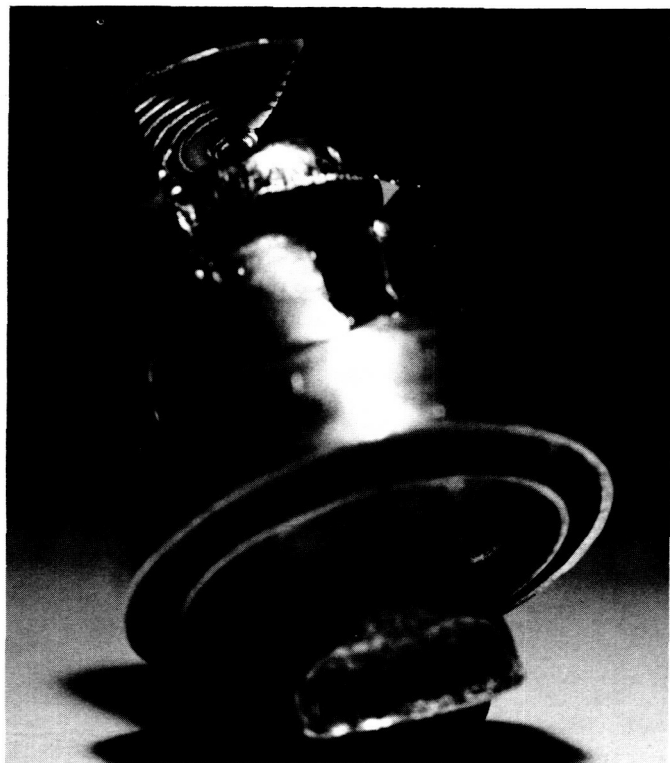


Fig. 10. Grooved ceramic substrate



**Fig. 11. Monolithic cathode structure**

tungsten spiral. (Fig. 11 shows a partially destroyed assembly.)

Several electron tubes employing the monolithic cathode structure were assembled and tested. A heat transfer efficiency improvement of 30% was measured on the test units. Electronic tests, however, showed that tungsten as an activator (emitter base) is far too active. This in turn would lead to short average life capability. Some remedial possibilities appear to exist by nickel plating over the tungsten. This was not tried during the course of this work.

#### 4. Conclusions

The actual performance data on each assembly tested are summarized in Fig. 12, which shows the heating power needed for each unit to reach the brightness temperature of the reference tube. Only approximate efficiency figures have been quoted in the text, since it is evident from the various slopes of the lines that these figures would change somewhat for other temperature levels.

During the course of this lengthy program, the technique of sintering nickel potting powders was perfected independently by several other tube manufacturers and

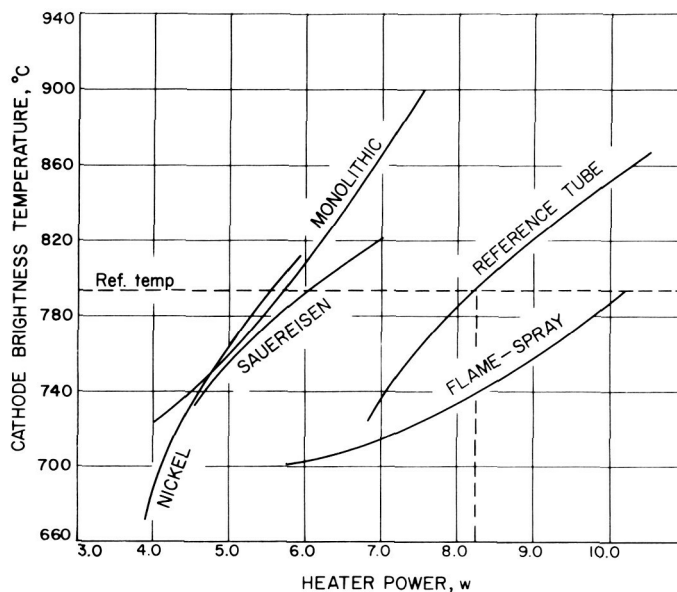


**Fig. 12. Thermal characteristics of test vehicles**

is now commonly used throughout the industry. There is, therefore, no necessity to investigate this process further.

A study of Fig. 12 shows the excellent characteristics of the monolithic structure. While inherently as efficient as the nickel potting, it also lends itself well to compact, rugged electron tube construction, which feasibly could be used for high impact applications. Some development work remains to be done in the mounting scheme and activator application. There are, however, unexplored techniques which show promise in this area (electron deposition, Hiel Scientific Laboratories). Should the requirement for such a solid assembly arise, this program will have laid the groundwork for its perfection.

Keeping within the nature of a true advanced development effort, this project was beneficial not only in uncovering new, interesting, and useful designs, but also in cataloging some apparently promising materials, which can not now be considered reliable tube components. This study was ably managed and conducted by Mr. Werner Brunhart, Chief Engineer, Tube Division, Machlett Laboratories.

**N67-15751**

**C. Approximate Analysis of a Frequency-Shift Keyed System With Uncertainty in the Carrier Frequency, D. W. Boyd**

#### 1. Introduction

In some applications it is desirable to have simple communications systems. In these cases, it is usually possible

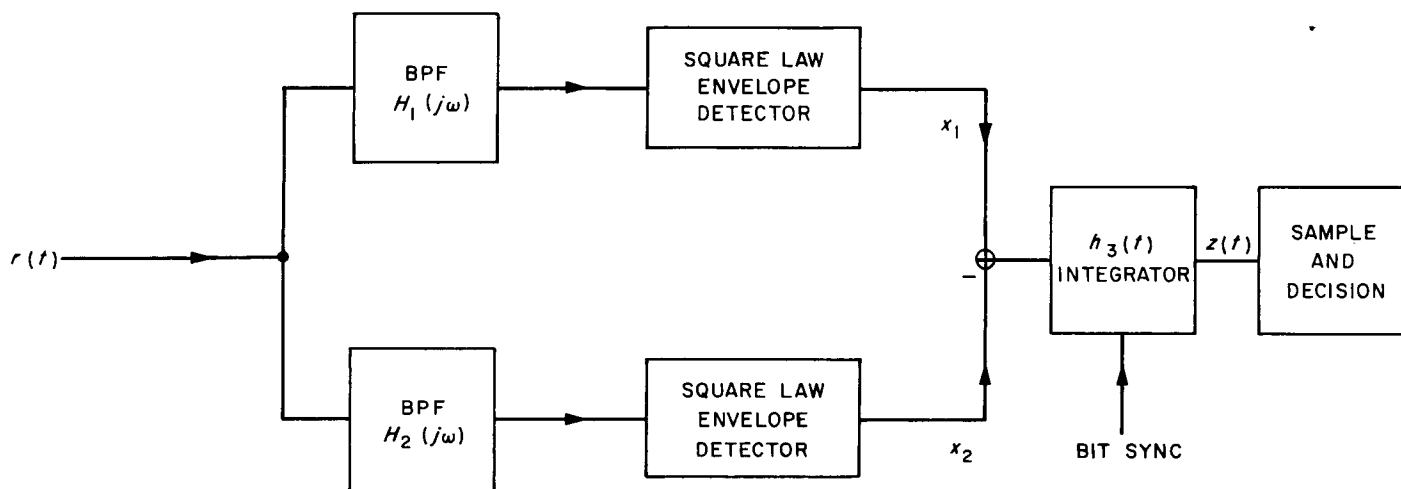


Fig. 13. Block diagram of an FSK system

to trade performance for simplicity. An example of such a system is the frequency-shift keyed (FSK) telemetry receiver shown in Fig. 13. The received signal is

$$r(t) = (2S)^{1/2} \cos(\omega_1 t + \psi) + n(t) \quad \text{hypothesis 1, } H_1 \quad (1)$$

if a mark (hypothesis 1) is sent and

$$r(t) = (2S)^{1/2} \cos(\omega_2 t + \psi) + n(t) \quad \text{hypothesis 2, } H_2 \quad (2)$$

if a space (hypothesis 2) is sent. The phase angle  $\psi$  has a probability density function (pdf)

$$p_\psi(\psi) = \frac{1}{2\pi} \quad 0 \leq \psi < 2\pi \quad (3)$$

and the noise is zero-mean gaussian with a two-sided power density spectrum of height  $N_0/2$  over the range of frequencies of interest where

$$N_0 = kT_s$$

$k$  = Boltzmann's constant

$T_s$  = system equivalent noise temperature

The bandpass filters have the characteristics shown in Fig. 14. So that the system will not have to have carrier

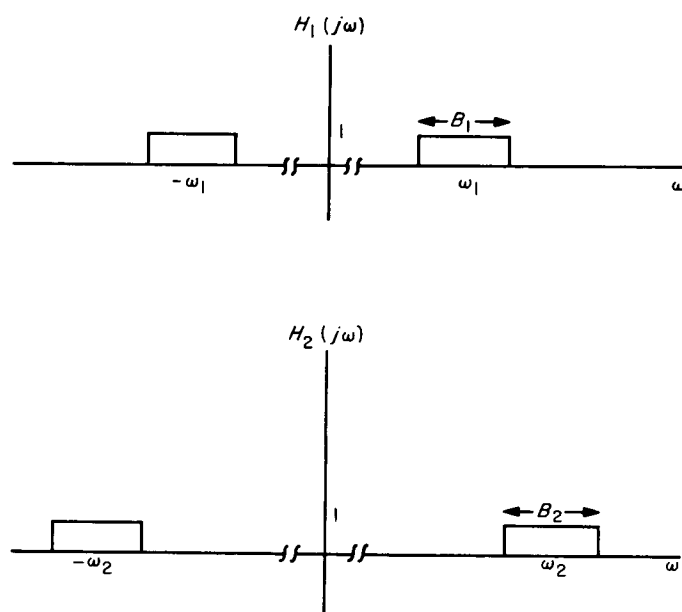


Fig. 14. Bandpass filter transfer functions

synchronization, the bandwidths of the filters are chosen so that

$$B = B_1 = B_2 = Cf_{\text{BIT}} + f_{\text{DRT}} + f_{\text{DOP}} \quad (4)$$

where

$f_{\text{BIT}} \equiv$  bit rate of telemetry system

$C \equiv$  constant chosen according to practical considerations; its minimum value = 2

$f_{\text{DRT}} \equiv$  frequency uncertainty caused by component inaccuracies

$f_{\text{DOP}} \equiv$  frequency uncertainty caused by doppler shift

In addition, the filters are chosen so that they do not overlap. The price we are paying for simplicity is clearly evident since the filters pass more noise than they do for an FSK system in which the carrier frequency is known. In fact, with the receiver implementation in Fig. 13, even if  $f_{\text{DRT}}$  and  $f_{\text{DOP}}$  are zero, the equivalent noise bandwidth of the bandpass filters is at least twice that of the matched filters in an FSK system with known carrier frequency.

In this note, we will assume that bit synchronization is available at the receiver and will calculate the probability of error for the system, using an approximation for the square law output. As an incidental result, we will calculate the signal-to-noise ratio (SNR) at the output of the integrator.

## 2. Probability Density Function of the Output of the Square Law Device

As a first step in analyzing the performance of the receiver, we will determine the pdfs of the random variables  $x_1$  and  $x_2$ , where

$x_n \equiv$  normalized amplitude of output of square law device in channel  $n$

These pdfs can be found in a straightforward way from the pdfs of  $y_1$  and  $y_2$ , where

$y_n \equiv$  amplitude of the signal envelope in channel  $n$

For purposes of analysis we will assume that  $r(t)$  is given by

$$r(t) = (2S)^{1/2} \cos(\omega_1 t + \psi) + n(t) \quad (5)$$

Since the channels are symmetric, the results do not depend on whether we assume  $H_1$  or  $H_2$  is true, if  $H_1$  and  $H_2$  are equally likely. If  $B$  is much less than  $\omega_1$  or  $\omega_2$ , it is well known (Ref. 2) that  $p_{y_1}(y_1)$  and  $p_{y_2}(y_2)$  are given

$$p_{y_1}(y_1) = \begin{cases} \frac{y_1}{\sigma^2} \exp - \left( \frac{y_1^2 + 2S}{2\sigma^2} \right) I_0 \left( \frac{(2S)^{1/2} y_1}{\sigma^2} \right) & y_1 \geq 0 \\ 0 & \text{elsewhere} \end{cases} \quad (6)$$

and

$$p_{y_2}(y_2) = \begin{cases} \frac{y_2}{\sigma^2} \exp - \frac{y_2^2}{2\sigma^2} & y_2 \geq 0 \\ 0 & \text{elsewhere} \end{cases} \quad (7)$$

where

$$\sigma^2 = N_0 B$$

Since we have assumed that the bandpasses of the two filters do not overlap,  $y_1$  and  $y_2$  are independent random variables.

Using Eqs. (6) and (7), we can easily find  $p_{x_1}(x_1)$  and  $p_{x_2}(x_2)$ . Since

$$x_1 \equiv \frac{y_1^2}{2\sigma^2}$$

and  $y_1 \geq 0$ , we know that

$$\begin{aligned} pr[x_1 \leq x_{10}] &= pr[y_1 \leq (2)^{1/2} \sigma x_{10}^{1/2}] \\ &= \int_0^{(2)^{1/2} \sigma x_{10}^{1/2}} p_{y_1}(y_1) dy_1 \end{aligned}$$

Differentiating, we obtain

$$p_{x_1}(x_1) = \frac{(2)^{1/2} \sigma}{2} x_1^{-1/2} p_{y_1}[(2)^{1/2} \sigma x_1^{1/2}] \quad (8)$$

so that

$$p_{x_1}(x_1) = \begin{cases} e^{-(x_1 + P)} I_0[2P^{1/2} x_1^{1/2}] & x_1 \geq 0 \\ 0 & \text{elsewhere} \end{cases} \quad (9)$$

where

$$P \equiv \frac{S}{N_0 B} = \text{input SNR in the bandwidth } B$$

In a similar fashion, we find

$$p_{x_2}(x_2) = \begin{cases} e^{-x_2} & x_2 \geq 0 \\ 0 & \text{elsewhere} \end{cases} \quad (10)$$

We are now ready to investigate the output of the integrator  $z(t)$ .

### 3. Output of Integrator

Ideally we would like a complete statistical description of the continuous time function  $z(t)$ . Unfortunately, because of the nonlinearities of the system, this is a difficult task, although some limited results are available (Ref. 3). We will use an approximate approach.

Ruina and Maximon (Ref. 4) have shown that the input to the integrator  $x_1(t) - x_2(t)$ , can be approximated by

$$x_1(t) - x_2(t) \approx \sum_{k=-\infty}^{\infty} [x_1(kT) - x_2(kT)] f(t - kT) \quad (11)$$

where

$$f(t) \equiv \begin{cases} 1 & 0 \leq t < T \\ 0 & \text{elsewhere} \end{cases} \quad (12)$$

The validity of the approximation can be measured in terms of how closely the statistics at the output of the integrator, using the approximation, correspond to the actual statistics. Determining this correspondence is naturally a formidable problem, but the calculations in Ref. 4 indicate that the approximation is valid at least through the second moment of the output. Determining further correspondence is probably best left to experiment. In Eq. (11) the random variables  $x_1(kT)$  and  $x_2(kT)$  are independent and have the pdfs given in Eqs. (9) and (10). The sketch in Fig. 15 indicates how the approximate

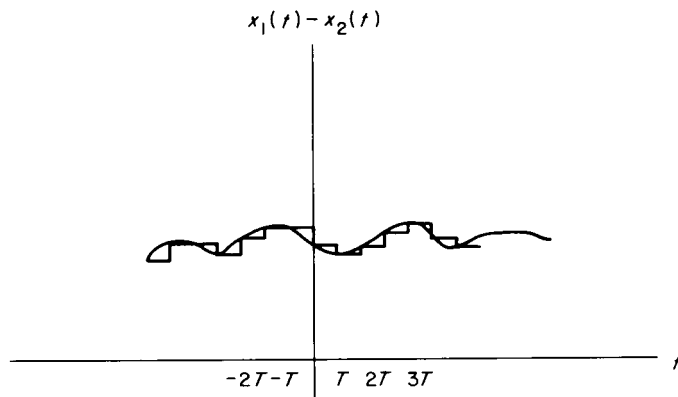


Fig. 15. Approximation for  $x_1(t) - x_2(t)$

waveform is formed:  $[x_1(kT) - x_2(kT)]$  is modeled as being independent from  $[x_1(mT) - x_2(mT)]$  for  $k \neq m$ .

Since  $h_3(t)$  has the impulse response

$$h_3(t) = \begin{cases} 1 & 0 \leq t < T_3 \\ 0 & \text{elsewhere} \end{cases} \quad (13)$$

where

$$T_3 \equiv 1/f_{\text{BIT}} = \text{bit period}$$

we write  $z(t)$  at the sampling instant as

$$z(T_3) = \int_0^{T_3} (x_1(t) - x_2(t)) dt \quad (14)$$

If we assume  $N = T_3/T$  and use Eq. (11), we have

$$z(T_3) = T \sum_{k=0}^{N-1} [x_1(kT) - x_2(kT)] \quad (15)$$

The constant  $N$  is most conveniently interpreted as the ratio of the input bandwidth to the bit rate. Larger uncertainties in the received frequency necessitate a larger  $B$  and increased  $N$ . By using the approximation of Eq. (11), we have reduced the problem to that of describing the random variable

$$z(T_3) = T [z_1(T_3) - z_2(T_3)] \quad (16)$$

where

$$\begin{aligned} z_1(T_3) &\equiv z_1 = \sum_{k=0}^{N-1} x_1(kT) \\ z_2(T_3) &\equiv z_2 = \sum_{k=0}^{N-1} x_2(kT) \end{aligned} \quad (17)$$

To find the probability of error, it will be sufficient to find the pdfs of  $z_1$  and  $z_2$ .

The most convenient way to find  $p_{z_1}(z_1)$  is to use transform techniques. The characteristic function of  $x_1$  is defined as

$$M_{x_1}(jv) = \int_{-\infty}^{\infty} p_{x_1}(x_1) e^{jvx_1} dx_1 \quad (18)$$

Using the tables in Ref. 5, and letting  $s = jv$ , we obtain

$$M_{x_1}(s) = e^{-P} \frac{1}{-s+1} e^{P/-s+1} \quad (19)$$

Since  $z_1$  is the sum of  $N$  identically distributed, independent random variables, we have

$$\begin{aligned} M_{z_1}(s) &= [M_{x_1}(s)]^N \\ &= e^{-NP} \frac{1}{(-s+1)^N} e^{NP/-s+1} \end{aligned} \quad (20)$$

Using Ref. 5 again, we can invert Eq. (15) to yield

$$p_{z_1}(z_1) = \begin{cases} \left(\frac{z_1}{NP}\right)^{\frac{N-1}{2}} e^{-z_1-NP} I_{N-1}[2(NPz_1)^{1/2}] & z_1 \geq 0 \\ 0 & \text{elsewhere} \end{cases} \quad (21)$$

By following a similar approach we find  $p_{z_2}(z_2)$  to be given by

$$p_{z_2}(z_2) = \frac{z_2^{N-1}}{(N-1)!} e^{-z_2} \quad (22)$$

These calculations are analogous to those performed by Marcum (Ref. 6) for the radar detection problem. With the two densities given in Eqs. (21) and (22), we are now able to calculate the probability of error.

#### 4. Probability of Error

If  $H_1$  is true, the system will make a correct decision if  $z_1 > z_2$ . Thus

$$P_c = 1 - P_E = p_r[z_1 > z_2] \quad (23)$$

where

$$P_c \equiv \text{probability of correct decision}$$

Since  $z_1$  and  $z_2$  are independent, we can write

$$P_c = \int_0^\infty dz_1 p_{z_1}(z_1) \int_0^{z_1} dz_2 p_{z_2}(z_2) \quad (24)$$

Evaluating the  $z_2$  integral first, we obtain

$$\int_0^{z_1} \frac{z_2^{N-1}}{(N-1)!} e^{-z_2} dz_2 = F(N, z_1) \quad (25)$$

Integrating by parts, we can show that

$$F(N, z_1) = 1 - e^{-z_1} \sum_{k=0}^{N-1} \frac{z_1^k}{k!} \quad (26)$$

so that

$$P_c = \int_0^\infty p_{z_1}(z_1) \left(1 - e^{-z_1} \sum_{k=0}^{N-1} \frac{z_1^k}{k!}\right) dz_1 \quad (27)$$

Since the first integral equals 1, the probability of error is

$$P_E = \int_0^\infty e^{-z_1} \sum_{k=0}^{N-1} \frac{z_1^k}{k!} \left(\frac{z_1}{NP}\right)^{\frac{N-1}{2}} e^{-z_1-NP} I_{N-1}[2(NPz_1)^{1/2}] dz_1 \quad (28)$$

Making the substitution

$$(z_1)^{1/2} = \eta \quad (29)$$

we have

$$\begin{aligned} P_E &= 2 \left(\frac{1}{NP}\right)^{\frac{N-1}{2}} e^{-NP} \sum_{k=0}^{N-1} \frac{1}{k!} \\ &\quad \times \int_0^\infty \eta^{2k+N} e^{-2\eta^2} I_{N-1}[2(NP)^{1/2} \eta] d\eta \end{aligned} \quad (30)$$

Using the identity

$$I_{N-1}[2(NP)^{1/2} \eta] = (-j)^{N-1} I_{N-1}[2(NP)^{1/2} e^{j\pi/2} \eta] \quad (31)$$

and Eq. 11.4.28 of Ref. 7, we have finally

$$P_E = e^{-NP} \sum_{k=0}^{N-1} \frac{\Gamma(N+k)}{k! 2^{N+k} \Gamma(N)} M\left(N+k, N, \frac{NP}{2}\right) \quad (32)$$

where

$$M(a, b, z) \equiv \text{confluent hypergeometric function}$$

This expression can be simplified somewhat by using Kummer's transformation,

$$M(a, b, z) = e^z M(b - a, b, -z) \quad (33)$$

to rewrite the confluent hypergeometric function as

$$M\left(N + k, N, \frac{NP}{2}\right) = e^{NP/2} M\left(-k, N, -\frac{NP}{2}\right) \quad (34)$$

and then observing (Ref. 6) that the hypergeometric function can be written in terms of a generalized Laguerre polynomial,

$$M\left(-k, N, -\frac{NP}{2}\right) = L_k^{(N-1)}\left(-\frac{NP}{2}\right) \quad (35)$$

Thus Eq. (32) can be written

$$P_E = \frac{e^{-NP/2}}{2^N} \sum_{k=0}^{N-1} \frac{1}{2^k} L_k^{(N-1)}\left(-\frac{NP}{2}\right) \quad (36)$$

where

$$= (z)_{(u)} I \frac{e^z z^{-n}}{k!} \frac{d^k}{dz^k} (e^{-z} z^{k+n}) \quad (37)$$

or

$$\begin{aligned} L_k^{(n)}(z) = & \frac{(-1)^k}{k!} \left[ x^k - \frac{k}{1} (n+k) x^{k-1} \right. \\ & + \frac{k(k-1)}{2!} (n+k)(n+k-1) x^{k-2} + \dots \\ & \left. + (-1)^k (n+k)(n+k-1) \dots (n+1) \right] \end{aligned} \quad (38)$$

If we define the input SNR per bit period as

$$P_3 = \frac{ST_3}{N_0} \quad (39)$$

we can write

$$P = \frac{1}{N} P_3 \quad (40)$$

and write the probability of error in terms of the SNR per bit period as

$$P_E = \frac{e^{-P_3/2}}{2^N} \sum_{k=0}^{N-1} \frac{1}{2^k} L_k^{(N-1)}\left(-\frac{P_3}{2}\right) \quad (41)$$

For a fixed  $P_3$ ,  $P_E$  is found to be an increasing function of  $N$ , as expected, since increasing  $N$  corresponds to passing more noise in the front end. From Eq. (4) and the definition of  $N$ , we see that the minimum value of  $N$  is 2. Substituting for the Laguerre polynomial in Eq. (41), we obtain the following results for  $N = 2, 3$ , and 4

$$P_E(N=2) = \frac{1}{2} e^{-P_3/2} (1 + P_{3/8}) \quad (42)$$

$$P_E(N=3) = \frac{1}{2} e^{-P_3/2} \left(1 + \frac{3}{16} P_3 + \frac{1}{128} P_3^2\right) \quad (43)$$

$$P_E(N=4) = \frac{1}{2} e^{-P_3/2} \left(1 + \frac{29}{128} P_3 + \frac{1}{64} P_3^2 + \frac{1}{3072} P_3^3\right) \quad (44)$$

Eqs. (42), (43), and (44) show very clearly the degradation from the probability of error for a standard FSK receiver, which is given by (Ref. 8)

$$P_E = \frac{1}{2} e^{-P_3/2} \quad (45)$$

An interesting observation is that for  $N = 1$ , Eq. (41) yields Eq. (45). These results correspond mathematically, since for  $N = 1$ , the bandpass filters pass an equivalent amount of noise to the matched filters in a standard FSK configuration. However, the result is not strictly valid, since  $N = 1$  requires  $B = f_{\text{BIT}}$ , which would severely distort the input signal and make invalid the use of Eqs. (6) and (7). Fig. 16 gives plots of Eqs. (42), (43), (44), and (45) versus  $P_3$ . The degradation caused by having the larger input bandwidth is apparent.

## 5. Signal-To-Noise Ratio

Another parameter of interest is the SNR at the integrator output, defined as

$$P_0 = \frac{\{E[z_1 - z_2]\}^2}{\text{Var}[z_1] + \text{Var}[z_2]} \quad (46)$$

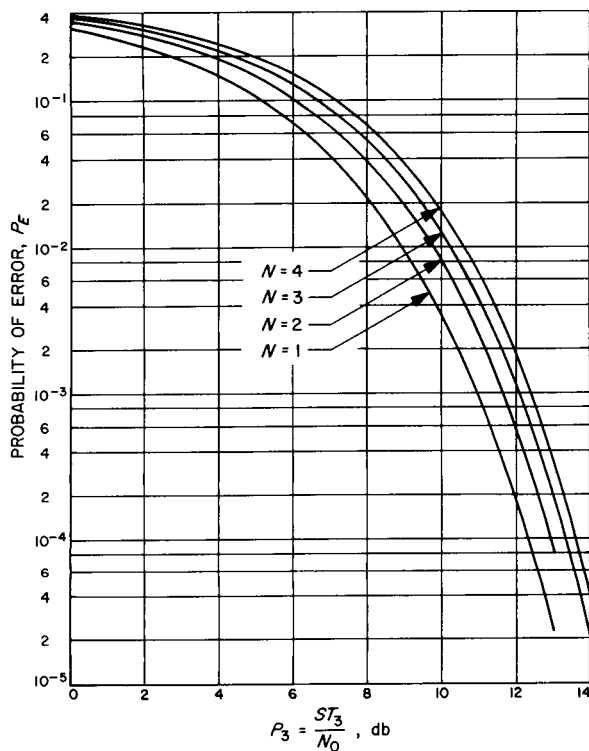


Fig. 16. Probability of error versus  $p_3 = ST_3/N_0$

This parameter is a measure of how large the mean value of the output caused by the signal is compared to the system noise. The necessary integrals are evaluated similarly to Eq. (28) and yield

$$P_0 = \frac{N}{2} \frac{P^2}{1+P} \quad (47)$$

In terms of  $P_3$ ,  $P_0$  can be written as

$$P_0 = \frac{1}{2} \frac{P_3^2}{N + P_3} \quad (48)$$

Eq. (48) behaves as expected. For small  $N$  there is a 3-db loss at high  $P_3$ , and there is small signal suppression at low  $P_3$ . Both of these properties would be expected for a square law system. In addition, there is a degradation caused by the  $N$ . As  $N$  is increased, more noise is passed in the front end, and the output SNR  $P_0$  is correspondingly degraded.

## 6. Discussion

When applying these results, remember that they have not been checked practically. Although the approximation employed appears to be well grounded, its final verifica-

tion rests in the testing of a system built as described in Fig. 13.

**N67-15752**

## D. High Impact Antenna Study: Cavity-Backed Spiral Antenna, K. Woo

### 1. Introduction

In SPS 37-40, Vol. IV, p. 201, the mechanical and electrical requirements for direct and indirect high impact antennas were discussed. The preliminary test results of a direct impact antenna, a coaxial cavity type radiator, were also presented. In this SPS, the progress made in developing an indirect impact antenna, a cavity-backed planar spiral, is described.

The cavity-backed spiral antenna has been chosen for development in that it is compact, lightweight, and broadband. Indirect impact tests of a commercial model (Ref. 9) showed survival at 4,000 g imparted into its mounting structure but complete failure at 5,600 g, due to breakage of spiral feed connections (soldering joints) and deformation of cavity walls. An indirect impact test of the present model showed that the antenna sustained a 10,000-g shock without visible physical damage or marked degradation in electrical performance.

### 2. Experimental Model

The experimental model under development is shown in Figs. 17 and 18. It is made up of a pair of closely wound copper Archimedean spirals printed on a fiberglass board (0.135 in. thick) and backed by an aluminum cavity (2.771 in. in dia, 0.861 in. deep). In order to facilitate the development of a reliable feed system for the spirals, without the complication introduced by cavity deformation, the cavity walls have been made extremely rugged. The wall thickness will be carefully trimmed, after the feed is perfected, so that the finished antenna will be not only impact proof but also of minimum weight. The input arms of the spirals, symmetrically located in the center of the board, are fed by a coaxial transmission line protruding into the cavity from the rear, as shown. The center conductor (0.077 in. in dia) and the ground stud (0.077 in. in dia) of the feeding line are respectively connected to the input arms by means of a self-locking nut (2-56 thread). Each locking nut is tightened respectively against another nut (not shown) countersunk into the back of the circuit board to produce good pressure contacts with the spiral arms. As is, the antenna will radiate predominantly left circularly polarized (LCP) waves in the forward direction. It may easily be modified to radiate predominately right circularly polarized (RCP) waves when required.

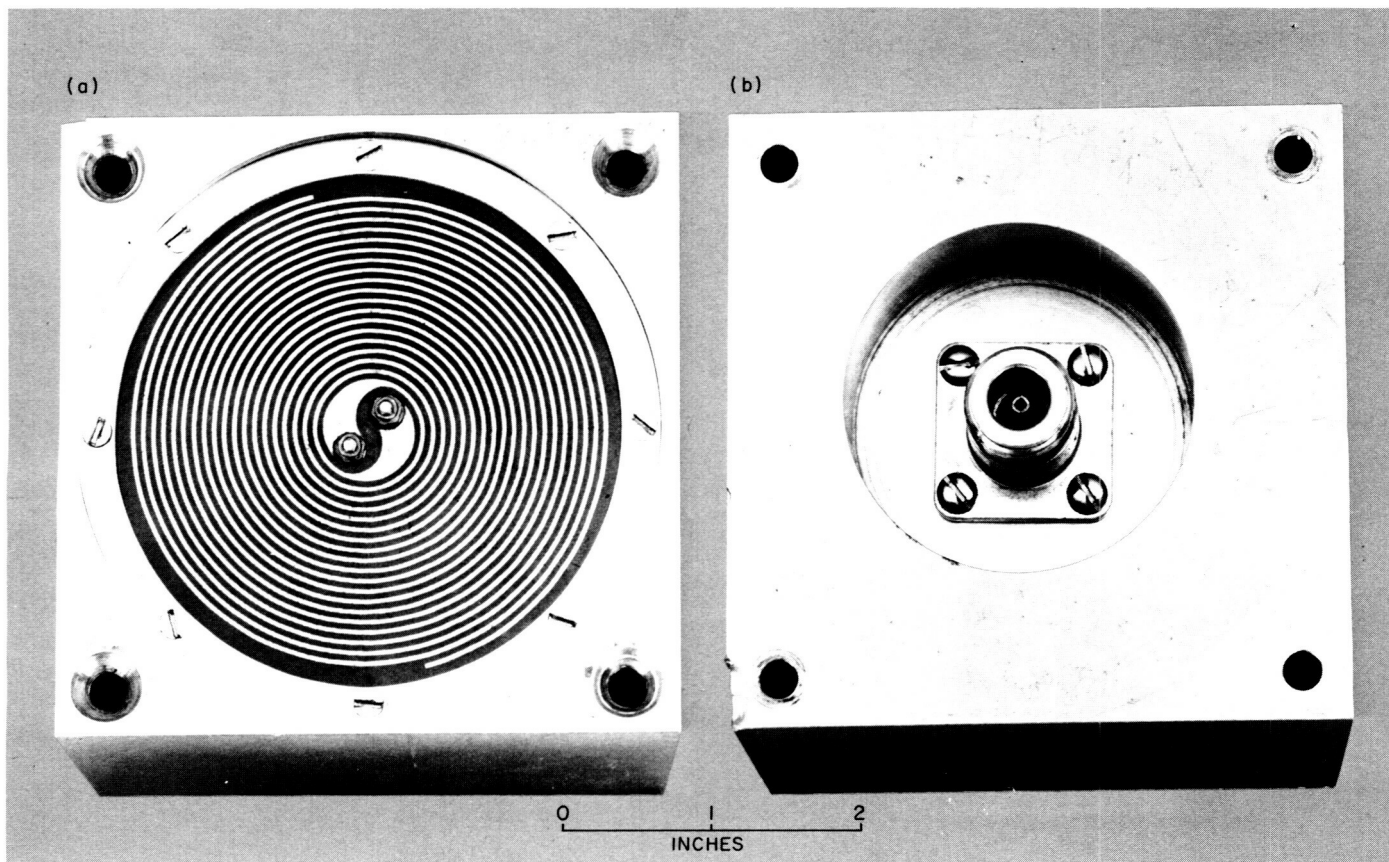


**Fig. 17. Exterior of spiral antenna: (a) front view; (b) rear view**

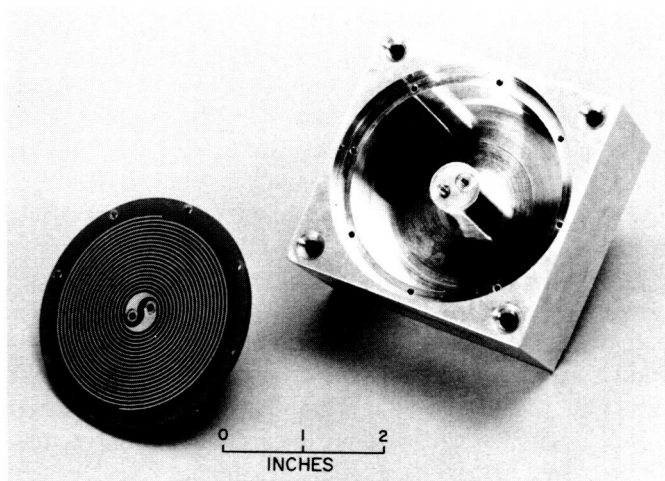


**Fig. 18. Interior of spiral antenna**

### 3. Results

Indirect impact test of the antenna at the 10,000-*g* level was carried out with a special horizontal shock tester

(Ref. 10). The antenna was attached to the specimen carriage of the tester, and the carriage was then impacted against an annealed copper target. A postimpact examination of the antenna revealed no visible physical damage, except that at the ground connection the contact between the locking nut and the spiral arm was loosened for about one quarter of a turn. The loosening was probably due to some thread yielding or inadequate support in the ground feed. Electrically, there has been some degradation in antenna performance as the result of the impact. Fig. 19 shows the LCP and RCP radiation patterns taken before and after the impact at 2298 MHz. The decrease in gain (from 4.8 to 4.2 db) and a corresponding increase in input VSWR (from 1.87 to 2.70) were attributed to the loosening of the ground contact.

On the basis of the above results, it can be said that with improvements this type of antenna can be used as an indirect impact survival antenna. Further work to strengthen the feed contacts and to refine the electrical performance is in progress.

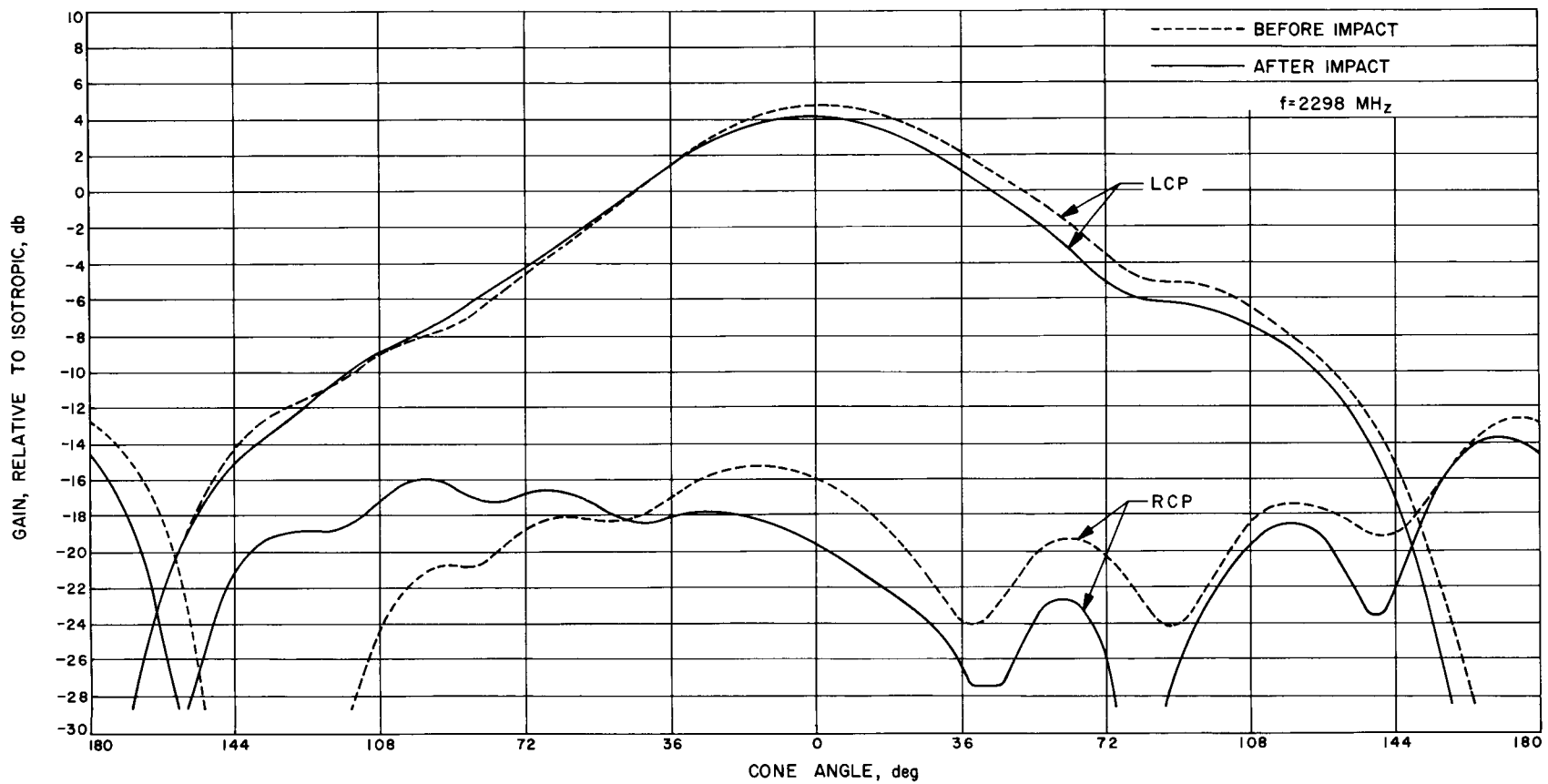


Fig. 19. Radiation patterns before and after impact

## E. Experimental Study of Multipacting Between Coaxial Electrodes, R. Woo

### 1. Introduction

The case of multipacting in the parallel plates geometry has been studied in detail both analytically and experimentally (Ref. 11). There have been some experiments conducted for the coaxial geometry (Refs. 12 and 13). However, these have not been supported by any analysis. In addition, these experiments do not provide sufficient data for coaxial electrodes to check either the results of the similarity principle described in SPS 37-35 and 37-36, Vol. IV, pp. 282-287 and 278-283, respectively, or the computer study results predicted in SPS 37-38, Vol. IV, pp. 217-223. Therefore, an experimental study on multipacting between coaxial electrodes is being conducted at JPL. This article covers the initial phase of this study.

The frequency range of 10-150 MHz has been chosen for these multipacting experiments. At these frequencies, open electrodes may be used, and the separation distance for the electrodes is of the order of a few centimeters for the  $\frac{1}{2}$ -cycle multipacting mode. Consequently, pressure levels between the electrodes can be readily controlled. Reliable voltage measurements can also be made employing a high frequency vacuum tube voltmeter. In contrast, at S-band frequencies, a closed geometry has to be used, e.g., waveguide, coaxial line, cavity resonator, etc. As a result of these closed and smaller geometries, it becomes more difficult to assure that the pressure levels within these multipacting components remain sufficiently low and constant because of trapped gases, outgassing, and heating. In addition, precise voltage measurements are more difficult. If the scaling laws predicted by the similarity principle are demonstrated in these experiments,

then the normalized data would be valid for S-band frequencies as well.

### 2. Experimental Apparatus

In order to arrive at voltages sufficiently high for multipacting in the 10-150 MHz frequency range, the set-up in Fig. 20 was used. The schematic is shown in Fig. 21. Hewlett-Packard's 608D signal generator and 230A power amplifier were used to drive a Millen 90811 100-w RF amplifier. Power was coupled through the impedance

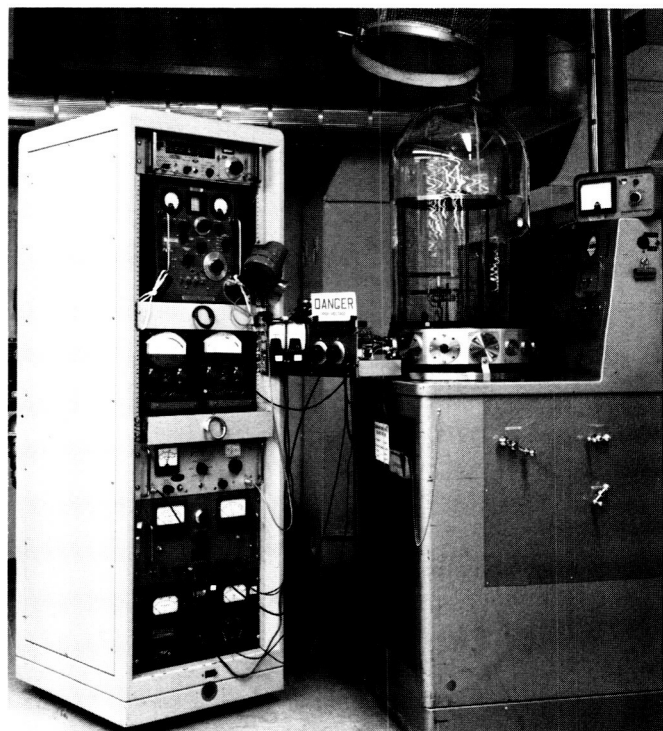


Fig. 20. Experimental setup

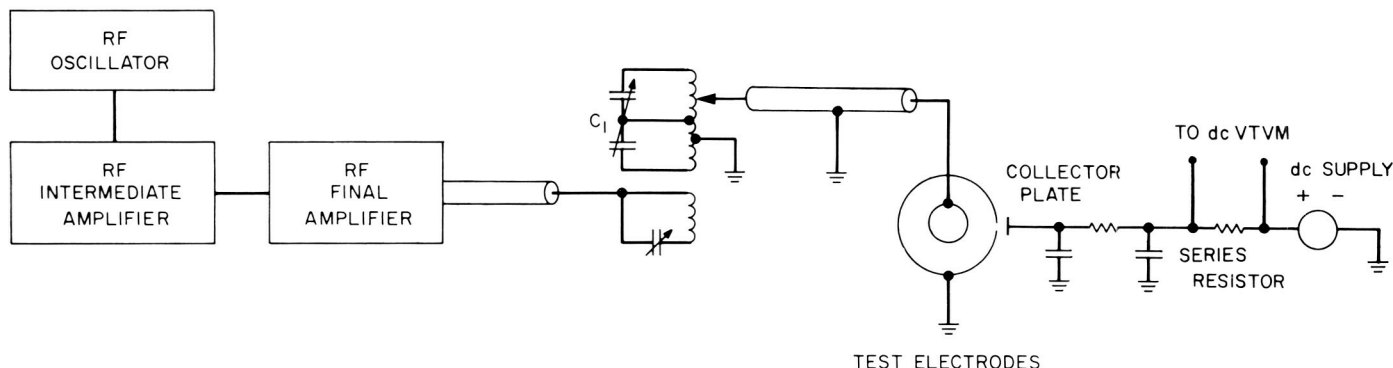
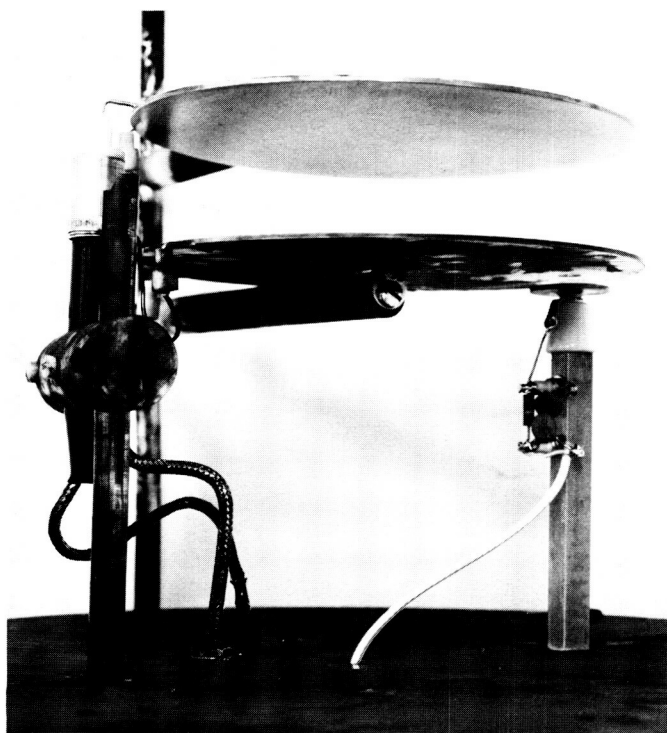


Fig. 21. Schematic diagram of experimental setup

matching network to the LC resonant circuit. The electrodes formed part of the capacitance of this resonant circuit which was tuned by various plug-in coils and the variable capacitor  $C_1$ . RF voltage was measured with a General Radio 1860A vacuum tube voltmeter. The voltmeter probe was modified to allow it to be placed in the vacuum chamber. Frequency was measured with a Hewlett-Packard 5245L frequency counter.

Because of the difficulty in some cases of detecting multipacting either visually or by its loading on the RF circuit, a positively-biased collector plate was set up behind a  $\frac{1}{8}$ -in.-diameter hole in the outer electrode. When multipacting occurred, a voltage was detected across the series resistor. Figs. 22 and 23 show the parallel and coaxial electrode set-ups, respectively. All electrodes were made of commercial copper, and the parallel plates were 5 in. in diameter while the coaxial electrodes were 3 in. long. A plexiglas table with precise grooves cut in it was used to support the coaxial electrodes. As a result, the concentricity of the coaxial electrodes was within 0.005 in. The electrodes themselves were machined to within a 0.002-in. tolerance.

All experiments were conducted in a vacuum at a pressure  $< 0.1\mu$  of Hg. The vacuum system consisted of an



**Fig. 22. Parallel electrodes setup**

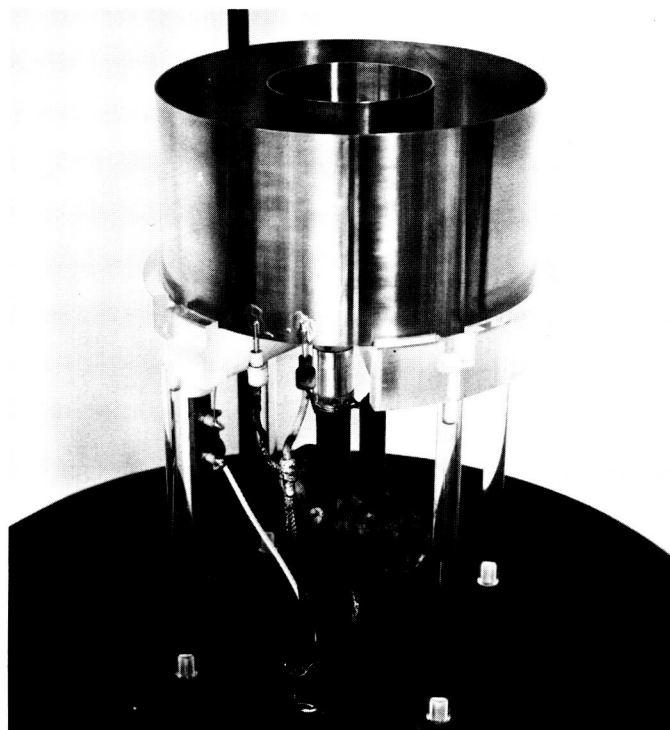


**Fig. 23. Coaxial electrodes setup**

18-in. bell jar equipped with a CVC PMC 1440 oil diffusion pump and a Welch 1397 roughing pump. A CVC BC-61 liquid nitrogen cold trap was also used. Pressure was measured with a CVC GPH 140 pirani gauge, which was calibrated periodically against a McLeod gauge.

### 3. Experimental Procedure

The strong dependence of multipacting on electrode surface conditions and the length of time of outgassing the electrodes by burning the discharge has been reported in the literature (Refs. 14-17) and is well known. In our experiments such behavior was also evidenced. To minimize these effects on the threshold voltage, and in order to achieve a fair amount of consistency and reproducibility in the multipacting data, the following procedure was established. The copper electrodes were abrasively cleaned immediately before pump-down for each test. When the pressure reached  $5 \times 10^{-4}$  mm of Hg, the experiments were initiated.

Minimum breakdown voltage was measured by slowly increasing the plate voltage of the final RF amplifier until the instant when electrons were collected by the collector plate. The voltage observed at this instant was recorded as the minimum breakdown voltage. Normally this would

be accompanied by a decrease in the RF voltmeter reading, due to detuning of the resonant circuit and the appearance of a very faint blue glow between the electrodes. Data for the minimum breakdown voltage curve were obtained in the order of increasing frequency starting at the cut-off frequency. Throughout the experiments, the amount of multipacting discharge time was kept to a minimum.

When the minimum breakdown data were completed, the electrodes were removed from the chamber, and the cleaning and pumpdown procedure was repeated to prepare for recording the maximum breakdown voltage curve. In order to raise the RF voltage above the maximum breakdown voltage without multipacting occurring, a dc voltage of a few hundred volts was applied to the electrodes, the full plate voltage of the final RF amplifier was applied, and the dc voltage was then removed. In this way, unnecessary discharge time was kept to a minimum. To measure the maximum breakdown voltage, the plate voltage of the final RF amplifier would be gradually reduced until the instant electrons were collected by the collector plate when the plate voltage would be immediately turned off. The RF voltage observed at this instant was recorded as the maximum breakdown voltage. As in the case of the lower breakdown curve, data were taken in the order of increasing frequency, starting at the cut-off frequency.

#### 4. Experimental Results and Discussion

Before the experimental data are presented, let us briefly review what is to be expected from our previous studies of coaxial multipacting. (See Section 1.) If we assume the electrode separation distance  $d$  to be the characteristic length of the coaxial configuration, then, according to the similarity principle, the multipacting breakdown voltage for similar coaxial electrodes is a function of  $fd$ , where  $f$  is the frequency of the RF voltage. For the phase-controlled boundaries, this function varies as  $(fd)^2$  for similar coaxial electrodes. In effect, the similarity principle extends the simple theory of Hatch and Williams (Ref. 14) to the case of similar coaxial electrodes.

In addition to the scaling studies, a computer program was written to solve the equation of electron motion between coaxial electrodes. The solutions of the 50-ohm impedance coaxial case were compared with those of the parallel plates geometry, where the electrode separation distance and initial boundary conditions were identical, and it was predicted that the multipacting regions would be approximately the same, with one exception. The minimum energy boundary of the coaxial case would be higher than that of the parallel plates case.

Experiments were conducted with 50-ohm impedance coaxial electrodes having electrode separation distances of 2, 3, and 4 cms. The 50-ohm impedance corresponds to cases where the ratio of outer to inner radii is equal to 2.3. Shown in Fig. 24 is the breakdown voltage plotted as a function of frequency for the 4 cms electrode separation distance case. The three sets of data were taken on separate days, and the reproducibility is quite typical of all experiments conducted.

In general, the breakdown voltage was reproducible to within 15% for the minimum energy boundary (BC in Fig. 24) and to within 4% for the phase-controlled boundaries (AB and CD in Fig. 24). The high variation in the

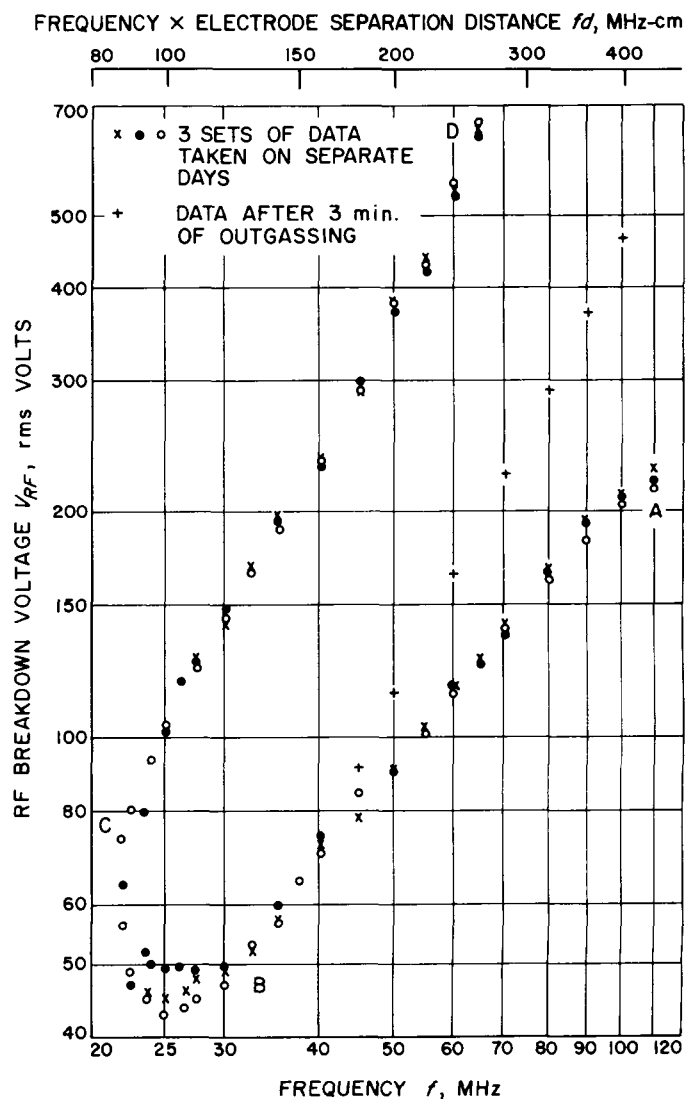


Fig. 24. Reproducibility of multipacting region for coaxial electrodes  $d = 4$  cms,  $b/a = 2.3$

minimum energy boundary is to be expected since the breakdown voltage in this region is highly sensitive to electrode surface conditions. Also shown in Fig. 24 is the effect on the lower phase-controlled boundary if the electrodes are outgassed by burning the discharge for 2 min prior to making the voltage measurements. The upper phase-controlled boundary is less sensitive and is not significantly affected by a discharge of this short a duration. However, if any further outgassing is carried out, the overall multipacting region shrinks with the shape of the multipacting region remaining the same. This type of behavior is similar to that noted in the parallel plates case (Refs. 15 and 16). Data are not presented since the threshold voltages in the absence of outgassing are of prime concern. Moreover, the measurement of outgassing time and surface preservation are quite arbitrary.

It suffices here to show that cleaning the surfaces by a slight amount of outgassing produces a lower phase-controlled boundary that is proportional to  $(fd)^2$ , as predicted by the similarity principle. On the other hand, the upper phase-controlled boundary is proportional to  $(fd)^2$ , as predicted by the similarity principle without any outgassing.

In Fig. 25 we have plotted the breakdown voltage for the three cases of 2-, 3-, and 4-cms coaxial electrode separation distances as a function of  $fd$ . The similarity principle predicts that these three cases should coincide. As can be seen, the agreement is within experimental and reproducibility error except for the minimum energy boundary which is seen to decrease with a decrease in electrode size. This behavior of the minimum energy boundary is being investigated further. For comparison we show in Fig. 26 the parallel plates data obtained for 2-, 3-, and 4-cms coaxial electrode separation distances. The similarity principle for this geometry is demonstrated for the minimum energy boundary as well. The discontinuity in the data corresponds to the transition region between the  $\frac{1}{2}$ - and  $\frac{3}{2}$ -cycle multipacting modes (Ref. 15).

Last of all, we wish to compare a coaxial case and a parallel case where the electrode separation distance is the same. Shown in Fig. 27 are data of these two geometries, where the electrode separation distance is 3 cms. As predicted, the minimum energy boundary of the coaxial case is higher than that of the parallel plates case while elsewhere the correspondence is close. It is unfortunate that with our present setup, data for higher values of  $fd$  for the coaxial electrodes could not be obtained. Other-

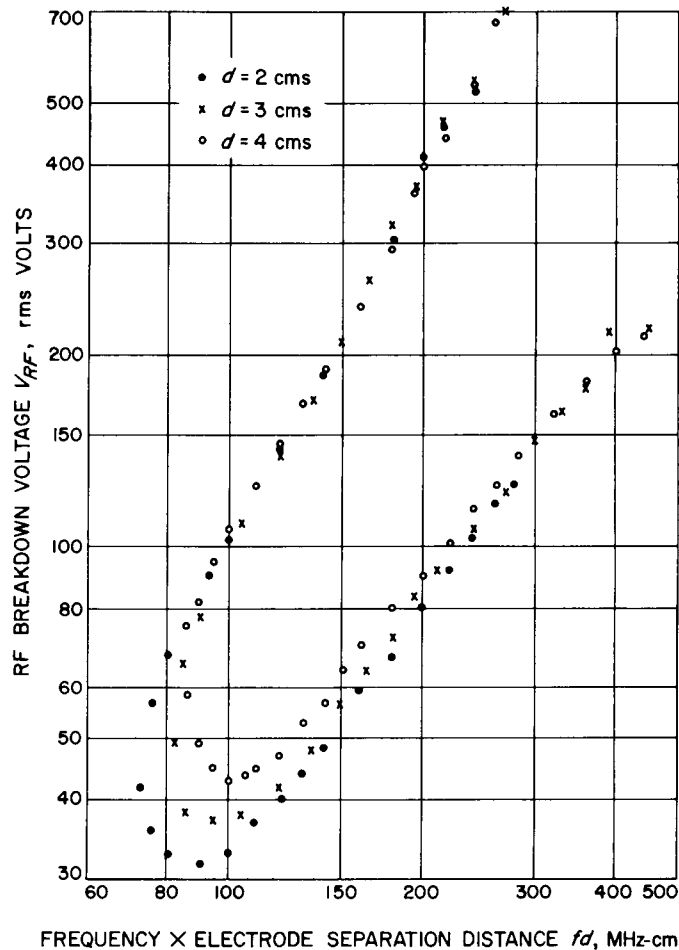


**Fig. 25. Multipacting region for coaxial electrodes**  
 **$d = 2, 3, \text{ and } 4 \text{ cms, } b/a = 2.3$**

wise, the  $\frac{3}{2}$ -cycle multipacting mode, whose presence is evidenced in the parallel plates cases, could have been checked. It would be expected that the discontinuity for the coaxial case would occur at a higher value of  $fd$  than for the parallel plates case. This is because the minimum energy boundary for the  $\frac{3}{2}$ -cycle multipacting mode would be higher in the coaxial case than in the parallel case in the same way as it was for the  $\frac{1}{2}$ -cycle multipacting mode.

## 5. Conclusions

Experimental results bear out the predictions made by the similarity principle and the computer studies reported in previous issues of the SPS. These experiments were conducted with coaxial electrodes where the ratio of outer to inner radii was 2.3. Further experiments with higher ratios of outer to inner radii are being conducted.

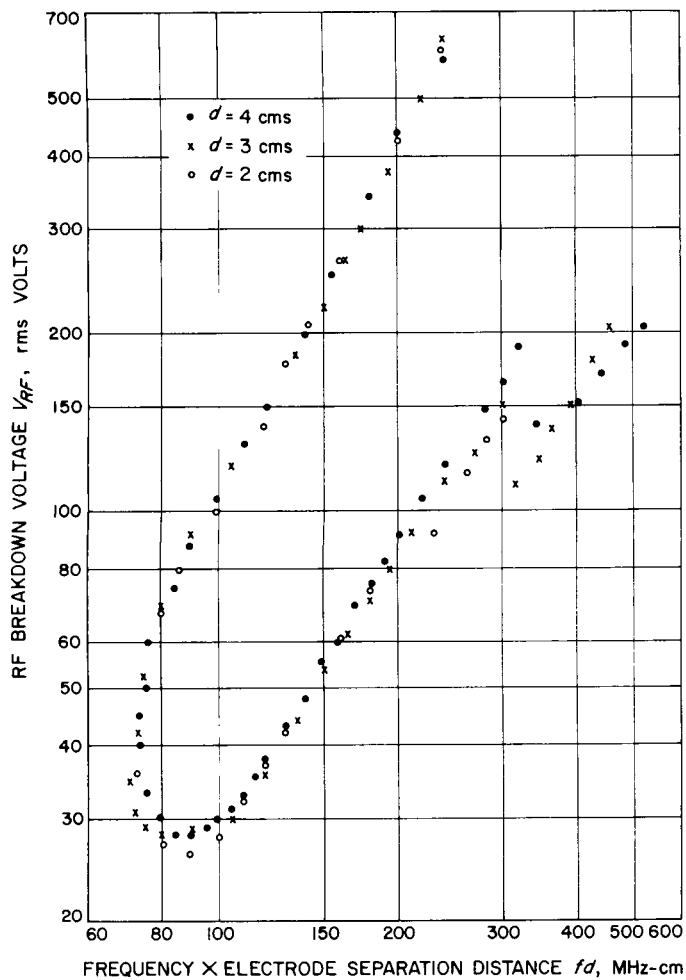


Fig. 26. Multipacting region for parallel plates  $d = 2, 3$ , and  $4$  cms

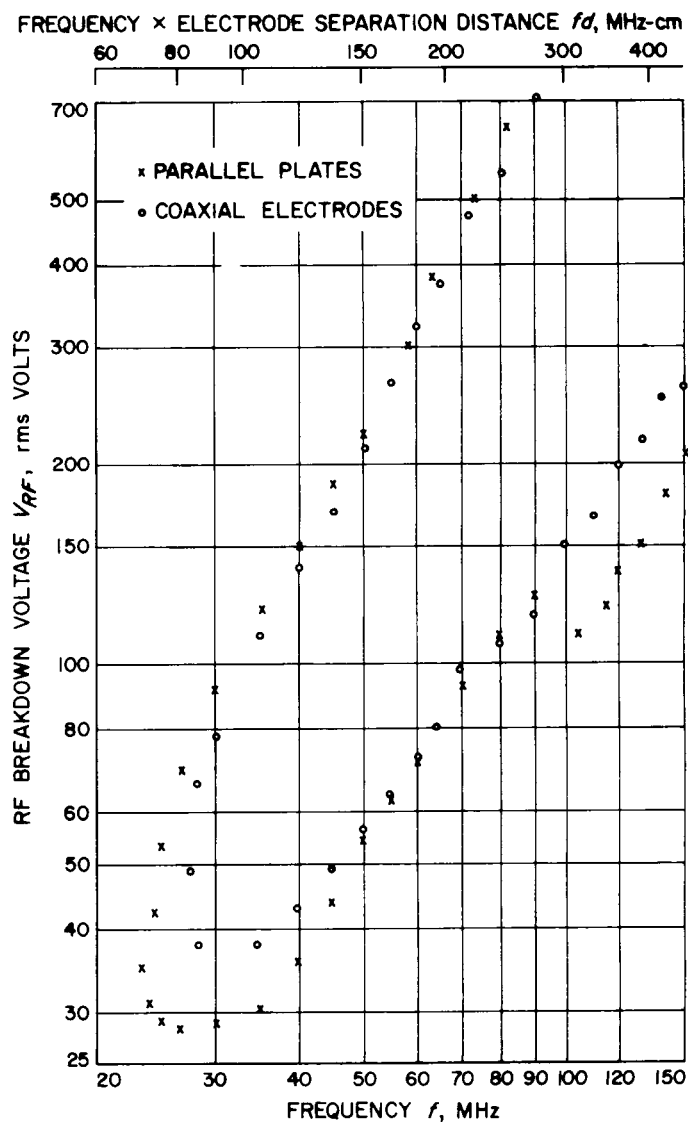


Fig. 27. Multipacting region for coaxial electrodes and parallel plates  $d = 3$  cms

## References

1. Middleton, David, *Introduction to Statistical Communication Theory*, McGraw-Hill Book Co., New York, N.Y., p. 340, 1960.
2. Rice, S. O., "Mathematical Analysis of Random Noise," *Bell System Technical Journal*, Vol. 24, 1945.
3. Steenson, B. O., and Stirling, N. C., "The Amplitude Distribution and False-Alarm Rate of Filtered Noise," *Proceedings of the IEEE*, Vol. 53, No. 1, January, 1965. (Also, see references listed in the article.)
4. Maximon, L. C., and Ruina, J. P., "Some Statistical Properties of Signal Plus Narrow Band Noise Integrated Over a Finite Time Interval," *J. Appl. Phys.*, Vol. 27, pp. 1442-1448, December, 1956.
5. Erdelyi, A., Ed., *Tables of Integral Transforms*, Vol. I, McGraw-Hill, 1954.
6. Marcum, J. I., *A Statistical Theory of Target Detection by Pulsed Radar*, Rand Corp. Report RM-754, December 1, 1947. Mathematical Appendix, R113, July 1, 1948.
7. Abramowitz, M., and Stegun, I. A., Ed., *Handbook of Mathematical Functions*, National Bureau of Standards, Applied Mathematical Series.
8. Lawton, J. G., and Becker, H. D., *Theoretical Comparison of Binary Data Transmission Systems*, Report No. CA-1172-S-1, Cornell Aeronautical Laboratory, Inc., May 1958.
9. Boreham, J. F., *Capsule Antenna Study*, Technical Memorandum No. 33-272, Vol. I, pp. 215-218, Jet Propulsion Laboratory, Pasadena, California, January 31, 1966.
10. Lonborg, J. O., *High Impact Survival*, Technical Report No. 32-647, Jet Propulsion Laboratory, Pasadena, California, September 30, 1964.
11. Francis, G., *Ionization Phenomena in Gases*, Butterworths Scientific Publications, London, 1960.
12. Vance, E. F., and Navevich, J. E., "RF Breakdown in Space Environment," *14th Annual Symposium of Air Force Antenna Research and Development*, University of Illinois, 1964.
13. *The Study of Multipactor Breakdown in Space Electronics Systems*, Report P65-45, Hughes Aircraft Company, Culver City, California, April, 1965.
14. Hatch, A. J., and Williams, H. B., "The Secondary Electron Resonance Mechanism of Low Pressure High Frequency Breakdown," *Journal of Applied Physics*, Vol. 25, pp. 417-423, 1954.
15. Hatch, A. J., and Williams, H. B., "Multipacting Modes of High Frequency Gaseous Breakdown," *Physical Review*, Vol. 112, pp. 681-685, 1958.
16. Tamagawa, H., "On the Mechanism of the High Frequency Vacuum Discharge," *Electrotechnical Journal of Japan*, Vol. 3, pp. 42-46, 1957.
17. Zager, B. A., and Tishin, V. G., "Multipactor Discharge and Ways of Suppressing It," *Soviet Physics - Technical Physics*, Vol. 9, No. 2, p. 234, August 1964.

## XX. Communications Systems Research

### TELECOMMUNICATIONS DIVISION

N67-15754

#### A. Combinatorial Communications: The Target Lemma, E. Rodemich

##### 1. Summary

A geometric property of the multivariate Gaussian distribution is proved, in a quite general setting. This result is needed in detection theory and data compression.

##### 2. Introduction

If  $C$  is a region in  $n$ -dimensional space, we mean by  $C + t$  the region into which  $C$  is transformed when each point is translated by the vector  $t$ .  $C$  is said to be *symmetric* about the point  $P$  if it is invariant under the transformation  $x \rightarrow 2x(P) - x$ , where  $x$  denotes the coordinate vector of a general point. The following lemma will be proved:

**a. Target Lemma.** Let the random variable  $X$  in  $n$ -dimensional space have a probability density  $p(x)$  with the property that for any  $\lambda > 0$ , the region

$$\{x : p(x) \geq \lambda\}$$

is convex and symmetric about the origin. Let  $C$  be a

convex region symmetric about the origin. Then the probability

$$P(t) = \Pr \{X \in C + t\}$$

is a maximum when  $t = 0$ .

This lemma was needed for an application in which  $X$  had an  $n$ -variate Gaussian distribution and  $C$  was a coordinate hypercube.<sup>1</sup> The result then proved was that a Gaussian process has a positive probability of being as small as we please on a given finite interval. In detection theory, the lemma proves that a symmetric detection region is best, even in the presence of correlated noise.

##### 3. Auxiliary Lemmas

**Lemma 1:** Let  $A$  and  $B$  be convex regions in  $n$ -space. Then the volume of the intersection of  $A$  and  $B + t$ :

$$F(t) = \text{Vol} \{A \cap (B + t)\}$$

<sup>1</sup>Garcia, E., Posner, E. C., and Rodemich, E., "Some Properties of the Sample Functions of a Gaussian Process," *J. Math. Anal. Appl.* (to be published).

has the property that for any  $\lambda > 0$  the set

$$\{t : F(t) \geq \lambda\} \quad (1)$$

is convex.

**Proof:** Define

$$C(t) = A \cap (B + t).$$

Then for  $0 < \alpha < 1$ ,

$$\alpha C(t) + (1 - \alpha) C(t^1) \subset C(\alpha t + (1 - \alpha) t^1) \quad (2)$$

where the set on the left is the set of all points of the form  $\alpha x + (1 - \alpha) x^1$ , with  $x \in C(t)$  and  $x^1 \in C(t^1)$ . To see that this is true, we have

$$C(t), C(t^1) \subset A,$$

hence

$$\alpha C(t) + (1 - \alpha) C(t^1) \subset A$$

and

$$C(t) - t, C(t^1) - t^1 \subset B,$$

hence

$$\alpha(C(t) - t) + (1 - \alpha)(C(t^1) - t^1) \subset B$$

But the last inclusion is equivalent to

$$\alpha C(t) + (1 - \alpha) C(t^1) \subset B + \alpha t + (1 - \alpha) t^1$$

Hence

$$\alpha C(t) + (1 - \alpha) C(t^1) \subset A \cap [B + \alpha t + (1 - \alpha) t^1]$$

which verifies (2).

The Brün-Minkowsky inequality (Ref. 1) for the special case of two convex bodies of equal volume, implies that if  $F(t) \geq \lambda$  and  $F(t^1) \geq \lambda$ , then

$$\text{Vol}[\alpha C(t) + (1 - \alpha) C(t^1)] \geq \lambda$$

Hence by (2),  $F(\alpha t + (1 - \alpha) t^1) \geq \lambda$ . This shows that the region (1) is convex.

**Lemma 2:** If  $A$  and  $B$  are convex regions, symmetric about the origin, then the function

$$F(t) = \text{Vol}[A \cap (B + t)]$$

assumes its maximum value at  $t = 0$ .

**Proof:** Let  $\lambda$  be any number less than the supremum of  $F(t)$ . Then

$$\{x : F(t) \geq \lambda\}$$

is non-empty. By lemma 1, this is a convex set. Also, it is symmetric about 0, for the symmetry of  $A$  and  $B$  implies that  $F(-t) = F(t)$ . Hence 0 lies in the set; that is to say

$$F(0) \geq \lambda$$

Letting  $\lambda \rightarrow \sup F(t)$  completes the proof.

#### 4. Proof of the Target Lemma

For any positive integer  $k$ , let  $p_k(x)$  be the following approximation to  $p(x)$ :

$$P_k(x) =$$

$$\begin{cases} k, p(x) \geq k \\ \frac{l}{k}, \frac{l}{k} \leq p(x) < \frac{l+1}{k}, \quad l = 0, 1, \dots, k^2 - 1 \end{cases}$$

If  $E_{kl}$  is the region

$$\{x : p(x) \geq l/k\}$$

and  $X_{kl}(x)$  is its characteristic function,

$$p_k(x) = \frac{1}{k} \sum_{l=1}^{k^2} X_{kl}(x)$$

Each of the regions  $E_{kl}$  is convex and symmetric about 0. By lemma 2,

$$\text{Vol}[E_{kl} \cap (C + t)] \leq \text{Vol}[E_{kl} \cap C]$$

which can be put in the form

$$\int_{c+t} X_{k\ell}(x) dx \leq \int_c X_{k\ell}(x) dx$$

Sum over  $\ell$  and divide by  $k$ :

$$\int_{c+t} p_k(x) dx \leq \int_c p_k(x) dx$$

$p_k(x)$  increases to  $p(x)$  as  $k \rightarrow \infty$  through a sequence of powers of 2. Hence, taking the limit,

$$\int_{c+t} p(x) dx \leq \int_c p(x) dx$$

which was to be proved. The lemma is called the Target Lemma because it says that if an archer has to hit a convex symmetric target, and his error distribution is also convex and symmetric about his aiming point, he should aim for the center of the target to maximize his probability of hitting it.

N67-15755

## B. Combinatorial Communications: Primitive Trinomials of High Degree, E. Rodemich and Howard Rumsey, Jr.

### 1. Summary

New primitive polynomials of high degree were found by the methods described here. The polynomials are all trinomials; such trinomials are useful for generating pseudorandom sequences of 0's and 1's of long length (Ref. 2).

### 2. Introduction

An irreducible polynomial of degree  $n$  over  $GF(2)$  has the form

$$P(x) = x^n + \sum_{k=1}^n a_k x^{n-k}$$

where  $a_k = 0$  or  $1$ ,  $k = 1, \dots, n$ . It is easily shown that the roots of  $P(x)$  lie in  $GF(2^n)$ ; accordingly, they satisfy the equation

$$x^{2^n-1} = 1 \quad (1)$$

$P(x)$  is said to be *primitive* if its roots do not satisfy  $x^m = 1$  for any positive  $m$  less than  $2^n - 1$ . Then, for any root of  $P(x)$ , the numbers  $x, x^2, \dots, x^{2^n-1}$  are all the non-zero elements of  $GF(2^n)$  (Ref. 3).

There is a linear recurrence relation associated with  $P(x)$ . Let  $y_1, y_2, \dots, y_n$  have values zero and one, and define  $y_j = 0$  or  $1$ , for  $j \geq n+1$ , by

$$y_j = \sum_{k=1}^n a_k y_{j-k}$$

If  $P(x)$  is primitive, and  $n$  and  $2^n - 1$  are relatively prime, consecutive sets of  $n$ -tuples  $(y_{\ell n+1}, y_{\ell n+2}, \dots, y_{\ell n+n})$ ,  $\ell = 0, 1, 2, \dots$  have many statistical properties which approximate those of a sequence of independent random  $n$ -tuples of zeros and ones (see Ref. 2). Thus a primitive polynomial of degree  $n$  is useful for generating a pseudorandom sequence of  $n$ -tuples of zeros and ones. In this application, trinomials are better than polynomials with more non-zero coefficients, because the complexity of the hardware needed grows with the number of coefficients.

### 3. Method

In general, to determine whether a given trinomial  $P(x)$  of high degree  $n$  is primitive is no simple task. If the trinomial is known to be irreducible, it is a factor of  $x^{2^n-1} + 1$ . Then  $P(x)$  is primitive if it is not a factor of  $x^m + 1$  for any  $m$  which is a proper factor of  $2^n - 1$ . If  $P(x)$  is not known to be irreducible, then instead of divisibility of these binomials by  $P(x)$ , we must check for the presence of a common factor. This procedure is complicated by the fact that with rare exceptions, the factorization of  $2^n - 1$  is unknown, and difficult to find.

The test for irreducibility is simplified, if  $2^n - 1$  is known to be prime. The sequence of prime numbers of this form is called the sequence of *Mersenne primes*;  $n$  is called a *Mersenne exponent*. Many large Mersenne primes have been found in recent years (Ref. 4). (Until the application of modern digital computers, the largest known Mersenne prime was  $2^{127} - 1$ .) For such values of  $n$ , the following lemma can be used:

**Lemma:** If  $2^n - 1$  is prime, a trinomial of degree  $n$  is primitive if, and only if, it is a factor of  $x^{2^n-1} + 1$ .

**Proof:** Let  $x_1$  be any root of the trinomial  $P(x)$ , and let  $m$  be the smallest positive number such that  $x_1^m = 1$ . Then  $m$  is a factor of  $2^n - 1$ . By hypothesis,  $2^n - 1$  is prime; hence  $m = 2^n - 1$ .  $P(x)$  must be irreducible, for,

if  $x_1$  were a root of an irreducible factor of  $P(x)$  of degree  $d < n$ ,  $m$  would divide  $2^d - 1$ .

This lemma can be applied in the following way. For a general root  $x$  of  $P(x)$ , any power of  $x$  can be written as a polynomial of degree less than  $n$ , reducing the degree by application of the relation

$$x^N = \sum_{k=1}^n a_k x^{N-k}, \qquad N \geq n$$

In particular,

$$x^{2^j} = Q_j(x), \qquad j = 1, 2, \cdots$$

where  $Q_j(x)$  has degree less than  $n$ .  $Q_j(x)$  can be determined from  $Q_{j-1}(x)$  by squaring and reducing the degree. By the lemma, if  $2^n - 1$  is prime,  $P(x)$  is irreducible if, and only if,  $Q_n(x) = x$ .

Using various Mersenne exponents  $n$ , the trinomials

$$P(x) = x^n + x^p + 1, \qquad 1 \leq p < \frac{n}{2}$$

were tested for primitivity. Only values of  $p < n/2$  were used, because if  $P(x)$  is primitive, then

$$x^n P(1/x) = x^n + x^{n-p} + 1$$

is also primitive. To speed up the work, a simpler test than the one described above was used to eliminate about 80% of the possible values of  $p$ .

This simpler test checked  $P(x)$  for factors in common with the polynomials  $x^{2^j-1} + 1, j = 2, 3, \cdots 10$ .  $P(x)$  has a factor in common with  $x^{2^j-1} + 1$  if  $p$  belongs to certain residue classes modulo  $2^j - 1$  (depending on  $n$ ). For example,  $P(x)$  and  $x^3 + 1$  have a common factor if

$$n + p \equiv 0 \pmod{3}$$

For each value of  $n$ , these prohibited residue classes were computed at the beginning by running through the values of  $p \pmod{2^j - 1}$  and applying Euclid's algorithm for finding a common factor. Then for  $p = 1, 2, \cdots (n-1)/2$ , if  $p$  did not belong to any of these residue classes, the coefficients of  $Q_n(x)$  were computed.

#### 4. Results

In the following table, all Mersenne exponents  $n$  from 127 to 2281 are listed. The values given for  $p$  are all choices of the second exponent which are less than  $n/2$ , such that  $P(x)$  is primitive. In particular, primitive polynomials of high degree are now known; the previous high was degree 127 with  $x^{127} + x + 1$ . There are no primitive trinomials for the Mersenne exponent 2203.

Table 1. Exponents for primitive trinomials

$n$	$p$
127	1, 7, 15, 30, 63
521	32
607	105, 147, 273
1279	418
2203	none
2281	715, 915, 1029

N67-15756

C. Combinatorial Communications: Note on Existence Criteria for Cyclic Difference Sets, L. D. Baumert and Howard Rumsey, Jr.

#### 1. Introduction

Many of the codes used in digital communications are derived from cyclic difference sets (see Ref. 8 for a detailed discussion). Hence, questions regarding the existence of cyclic difference sets are of some interest. The purpose of this note is to point out that the criterion given by Yamamoto (Ref. 11, Theorem 2) includes several of the more well-known existence tests for cyclic difference sets.

#### 2. Preliminaries

A symmetric balanced incomplete block design is an arrangement of  $v$  objects into  $v$  sets (called blocks) such that:

- (1) each block contains exactly  $k$  objects
- (2) each object occurs in exactly  $k$  blocks
- (3) every pair of objects occurs in exactly  $\lambda$  distinct blocks.

Any mapping of the objects onto themselves which also takes the collection of blocks into itself is called an *automorphism* of the block design. The set of all automorphisms of a block design forms a group, the *automorphism group* of the design. Below we shall be interested (for the most part) with subgroups of this automorphism group and thus shall speak of an automorphism group of the

design, meaning thereby any collection of automorphisms of the design which is also a group.

A block design is called regular of degree  $m$  if:

- (1) it possesses an automorphism group which contains precisely  $m$  mappings and
- (2) the identity mapping is the only member of this group which fixes any of the objects.

In particular, if an automorphism group is generated by one mapping, and if this mapping merely permutes cyclically all the objects, then the associated block design is clearly regular of degree  $v$ .

A cyclic difference set  $D = \{d_1, \dots, d_k\}$  is a collection of  $k$  residues modulo  $v$  for which the congruence

$$d_i - d_j \equiv \alpha \pmod{v}$$

has exactly  $\lambda$  solution pairs  $(d_i, d_j)$  for each  $\alpha = 1, \dots, v-1$ . (All difference sets mentioned below are cyclic.) From the definition it follows that the relation (letting  $n = k - \lambda$  as usual)

$$k(k-1) = \lambda(v-1) \text{ or equivalently } k^2 = n + \lambda v \quad (1)$$

holds among the parameters  $v, k$  and  $\lambda$ ; a relation which is also satisfied by symmetric balanced incomplete block designs. In fact, any such block design which has an automorphism  $\sigma$  such that  $\sigma$  permutes the  $v$  objects cyclically can be identified with a cyclic difference set (see Ref. 8, p. 58 for a proof of this fact).

### 3. The Existence Criteria

In Refs. 6 and 7 the following criterion (the so-called *Bruck-Ryser-Chowla Theorem*) was developed:

**Criterion A:** A symmetric balanced incomplete block design with parameters  $v, k, \lambda$  ( $v$  odd) exists only if the diophantine equation

$$x^2 = ny^2 + (-1)^{(v-1)/2} \lambda z^2$$

has a solution  $(x, y, z) \neq (0, 0, 0)$ .

As pointed out in the previous section, cyclic difference sets can be considered as special kinds of such block designs, thus this test applies to cyclic difference sets.

**Criterion B:** (Ref. 9) A cyclic difference set with parameters  $v, k, \lambda$  ( $v$  odd) exists only if the diophantine equations

$$x^2 = ny^2 + (-1)^{(s-1)/2} sz^2$$

(all divisors  $s$  of  $v$ ) have solutions  $(x, y, z) \neq (0, 0, 0)$ .

**Criterion C:** (Ref. 10) A symmetric balanced incomplete block design which is regular of degree  $m = (v/s)$ , ( $s$  odd) exists only if the diophantine equation

$$x^2 = ny^2 + (-1)^{(s-1)/2} (v/s) \lambda z^2$$

has a solution  $(x, y, z) \neq (0, 0, 0)$ .

As pointed out in the previous section, a cyclic difference set can be identified with a block design regular of degree  $v$ . By the nature of the regularity in this case, it follows that the block design is regular of degree  $m$ , for every  $m$  dividing  $v$ . Thus, this criterion applies to cyclic difference sets, for all  $s$  dividing  $v$  ( $v$  odd).

**Criterion D:** (Ref. 11) A cyclic difference set exists only if the diophantine equations

$$x^2 = p^e y^2 + (-1)^{(s-1)/2} sz^2$$

(for all odd  $s$  dividing  $v$  and all primes  $p$  such that  $p^e$  divides  $n$  where  $p^{e+1}$  does not divide  $n$ ) possess solutions  $(x, y, z) \neq (0, 0, 0)$ .

The following criterion (Theorem 2, Ref. 11) includes A, B, C, D insofar as cyclic difference sets are concerned. That is, if one is interested in cyclic difference sets, and not in more general block designs, this criterion is the only one that needs to be investigated.

**Yamamoto's Criterion:** Assume a cyclic difference set exists with parameters  $v, k, \lambda$ . Then for all prime divisors  $p$  of  $n$  and prime divisors  $q$  of  $v$ , if  $p' \equiv -1 \pmod{q}$  for any integer  $f > 0$  then the integer  $e$  is even, where  $p^e$  divides  $n$  and  $p^{e+1}$  does not divide  $n$ .

### 4. Diophantine Equations and the Hilbert Norm Residue Symbol

In order to establish the dependence of criteria A, B, C, D, on Yamamoto's test, it is necessary to know the connection between diophantine equations of the type encountered above and the so-called *Hilbert norm residue symbol* (see Ref. 5 for more information and proofs).

The basic fact is that the diophantine equation

$$x^2 = \alpha y^2 + \beta z^2 \quad \alpha, \beta \text{ integers}$$

has a solution  $(x, y, z) \neq (0, 0, 0)$  if, and only if, the Hilbert norm residue symbol

$$\left( \frac{\alpha, \beta}{t} \right) = 1$$

for all primes  $t$  (including the so-called infinite prime  $t = \infty$ ). The norm residue symbol is defined in Ref. 5 and many of its properties are discussed. Those of interest here are (for all integers  $\alpha, \alpha_1, \alpha_2, \beta$  and all primes  $t$ ):

$$(1) \left( \frac{\alpha, \beta}{t} \right) = \pm 1$$

$$(2) \left( \frac{\alpha_1 \alpha_2, \beta}{t} \right) = \left( \frac{\alpha_1, \beta}{t} \right) \left( \frac{\alpha_2, \beta}{t} \right)$$

$$(3) \left( \frac{\alpha, \beta}{t} \right) = \left( \frac{\beta, \alpha}{t} \right)$$

## 5. Proofs

Corollary 2 of Ref. 11 establishes that criterion  $D$  is a consequence of Yamamoto's test. So assume  $D$ , i.e., assume that the diophantine equation

$$x^2 = p^e y^2 + (-1)^{(s-1)/2} s z^2$$

has a solution  $(x, y, z) \neq (0, 0, 0)$  for each divisor  $s$  of  $v$  and for each prime  $p$  dividing  $n$  (where  $p^e$  divides  $n$  but  $p^{e+1}$  does not divide  $n$ ). That is (see above), assume that

$$\left[ \frac{p^e, (-1)^{(s-1)/2} s}{t} \right] = 1$$

for all such  $p^e, s$  and primes  $t$ . From this and property (2) of the norm residue symbol it follows that

$$\left[ \frac{n, (-1)^{(s-1)/2} s}{t} \right] = 1$$

for all such  $s, t$ . But this is equivalent to criterion  $B$ .

The proofs of  $A$  and  $C$  are only slightly more complicated. For  $A$  consider Eq. (1): it translates as

$$1 = \left( \frac{n, \lambda v}{t} \right) = \left( \frac{n, \lambda}{t} \right) \left( \frac{n, v}{t} \right)$$

for all primes  $t$ , i.e.

$$\left( \frac{n, \lambda}{t} \right) = \left( \frac{n, v}{t} \right) \text{ for all primes } t. \quad (2)$$

Let  $s = v$  in  $B$ ; this yields

$$1 = \left[ \frac{n, (-1)^{(v-1)/2} v}{t} \right] = \left( \frac{n, v}{t} \right) \left[ \frac{n, (-1)^{(v-1)/2}}{t} \right]$$

So

$$\left( \frac{n, \lambda}{t} \right) = \left( \frac{n, v}{t} \right) = \left[ \frac{n, (-1)^{(v-1)/2}}{t} \right]$$

Thus

$$\left( \frac{n, \lambda}{t} \right) \left[ \frac{n, (-1)^{(v-1)/2}}{t} \right] = \left[ \frac{n, (-1)^{(v-1)/2} \lambda}{t} \right] = 1$$

which is equivalent to criterion  $A$ .

As for  $C$  start with

$$\left( \frac{n, v}{t} \right) \left( \frac{n, v}{t} \right) = 1 = \left( \frac{n, v}{t} \right) \left( \frac{n, s}{t} \right) \left( \frac{n, v/s}{t} \right)$$

then use Eq. (2) on  $\frac{n, v}{t}$  and criterion  $B$  for  $\frac{n, s}{t}$ . This yields

$$\begin{aligned} 1 &= \left( \frac{n, \lambda}{t} \right) \left[ \frac{n, (-1)^{(s-1)/2}}{t} \right] \left( \frac{n, v/s}{t} \right) \\ &= \left[ \frac{n, (-1)^{(s-1)/2} \lambda (v/s)}{t} \right] \end{aligned}$$

which is equivalent to criterion  $C$ .

## D. Propagation Studies: On Decision-Directed Subcarrier Phase Estimation, J. W. Layland

### 1. Introduction

Many communications systems transmit signals in the form  $S(t) = m(t) \cos(\omega_0 t + \phi)$  where  $m(t)$  is the modulating data signal, and  $\phi$  is a slowly-varying random process which must be estimated in order to detect the signal coherently. If  $m(t)$  contains a DC component,  $S(t)$  contains a component at  $\omega_0$  which can be tracked by a phase-locked loop to provide the desired coherent reference. If  $m(t)$  does not contain a DC component, some method must be employed to produce a signal from which the sub-carrier phase may be estimated.

The squaring loop (Ref. 12 and SPS 37-37, Vol. IV, pp. 290-293) is one such method. For any real  $m(t)$ ,  $m^2(t)$  contains a DC component, and  $S^2(t)$  contains a component at  $2\omega_0$  which is coherent (except for a sign ambiguity) with the received signal. This component may be tracked by a phase-locked loop, and the output of the loop frequency-divided and used to demodulate the received signal. The non-linearity of the squaring operation results in enhancing noise at the expense of signal to an extent governed by the filtered-signal bandwidth just prior to the squaring operation. If a steep-sided filter with bandwidth equal to  $h$  times the code bandwidth is used ahead of the squaring operation, the signal-power-to-noise-spectral-density ratio at the phase-locked loop input is reduced by a factor  $\eta$ :

$$\eta = \frac{r(h)}{1 + \frac{h}{r(h)} \frac{N_0}{ST_s}} \quad (1)$$

where  $r(h)$  is the fraction of the signal power passed by the filter,  $S$  is received signal power;  $T_s$  is symbol duration, and  $N_0$  is single-sided noise spectral density. A steep-sided filter with  $h = 0.75$  ( $r(h) = 0.9$ ) gives

$$\eta = \frac{0.9}{1 + 0.83 \frac{N_0}{ST_s}} \quad (2)$$

which seems to be a good approximation to the optimal filter. The efficiency ( $\eta$ ) can be quite small whenever  $ST_s/N_0$  is small (as it is if a long code is used).

One alternative to the squaring loop might be termed a decision-directed loop, and is the main subject of this

article. In this system the modulation on the incoming signal is first estimated using the partial-word correlations; then this estimate is multiplied with the incoming signal and the resultant fed to a phase-locked loop. With PSK modulation, the effective signal power at loop input is  $(1 - 2P_e)^2 S$ , where  $S$  is gross signal power, and  $P_e$  is the fraction of time that the modulation estimate is in error. If the noise on  $S(t)$  is white, Gaussian, and of spectral density  $N_0$ , the noise input to the phase-locked loop is also white, Gaussian, and of spectral density  $N_0$ , since the modulation estimate is  $+1/-1$  and is independent of the current  $n(t)$ . Stiffler (SPS 37-37, Vol. IV, pp. 268-275) has compared the squaring loop and decision-directed loop in an uncoded binary PSK environment and found them to be roughly equivalent. The work presented here was initiated in the expectation that a decision-directed loop would be degraded little or not at all by coding. While this is not exactly the case, Monte Carlo evaluation of  $(1 - 2P_e)$  for trans-orthogonal (T-O) codes of up to 6 bits shows only slight decrease of efficiency with increasing code length. A lower bound has been found which guarantees a non-zero efficiency for the decision-directed loop as code-length approaches infinity.

### 2. The Decision-Directed Loop

The decision-directed loop may be motivated by the following adaptive-controls approach: Suppose that it is desired to control a process in such a way that some measure of its performance is maximized. This measure of performance is a function of one controllable variable and at least one process variable which cannot be directly measured. (The performance measure is assumed to be available. Everything may be time-varying.) Denote by  $\phi(t)$  the truly maximizing value of the control variable, and by  $\theta(t)$  the value actually used. Then, if one can measure (or compute) some performance index (PI) which is monotonically increasing in the desired measure of performance and which is quadratic in  $\theta(t)$  about  $\phi(t)$ , the signal

$$\epsilon(t) = \frac{\partial PI(\phi(t), \theta(t))}{\partial \theta(t)} \quad (3)$$

is proportional to  $\phi(t) - \theta(t)$ , and is the optimum controller error input for modifying  $\theta(t)$ , (Ref. 13). Knowledge about  $\phi(t)$  must be used to design the controller.

In sub-carrier phase estimation, the control variable in question is the phase of the locally-generated subcarrier reference; the performance measure is the *a posteriori*

probability of that phase given the received signal prior to current time; and the truly maximizing control variable is the phase of the received subcarrier. A quadratic performance index is the log of the *a posteriori* probability.

$$\begin{aligned}
 PI(\hat{\theta}, \theta) = & \ln [P(\hat{\theta}(t))] \\
 & + \sum_{\text{Past } T} \log \left\{ \sum_{\text{Code wd}_j} \exp \left[ \frac{(2S)^{1/2}}{N_0} \int_{T-1}^T C_{Tj}(\tau) y(\tau) \cos(\omega_0 \tau + \hat{\theta}(\tau)) d\tau \right] \right\} \\
 & + \log \left\{ \sum_{\text{Code wd}_j} \exp \left[ \frac{(2S)^{1/2}}{N_0} \int_{T_L}^t C_j(\tau) y(\tau) \cos(\omega_0 \tau + \hat{\theta}(\tau)) d\tau \right] \right\}
 \end{aligned} \quad (4)$$

where  $y(t)$  is the received signal,  $N_0$  is the one-sided noise spectral density, and  $S$  is signal power. The first term of Eq. (4) is the prior probability weighting and is usually constant. The second term is a measure of how accurate  $\hat{\theta}(t)$  has been throughout past received words, while the third term indicates how accurate  $\hat{\theta}(t)$  has been throughout the current word. If the *a priori* distribution is uniform, only the third term of  $PI$  is a function of the current value of  $\hat{\theta}(t)$ , and the controller error signal,  $e(t)$  is

$$\begin{aligned}
 e(t) = & \frac{\partial PI(\hat{\theta}, \theta)}{\partial \theta} = \\
 & \frac{y(t) \frac{(2S)^{1/2}}{N_0} \sin(\omega_0 t + \hat{\theta}) \sum_{\text{code } j} C_j(t) \exp \left[ \frac{(2S)^{1/2}}{N_0} \int_{T_L}^t C_j(\tau) y(\tau) \cos(\omega_0 \tau + \hat{\theta}(\tau)) d\tau \right]}{\sum_{\text{code } j} \exp \left[ \frac{(2S)^{1/2}}{N_0} \int_{T_L}^t C_j(\tau) y(\tau) \cos(\omega_0 \tau + \hat{\theta}(\tau)) d\tau \right]}
 \end{aligned} \quad (5)$$

Examination of Eq. (5) reveals that  $e(t)$  is exactly the error signal of a phase-locked loop whose input is modified by an estimate of the current modulation sign and signal strength derived from the likelihood functions of the code words. The device is illustrated in Fig. 1. For an uncoded signal this device is identical to Fig. 7 (SPS 37-37, Vol. IV, p. 272). Unfortunately, both the analysis and construction of such a device are nearly impossible.

An alternative is the decision-directed feedback shown in Fig. 2, where  $W(t)$  takes values  $+1/-1$ . In the succeeding work,  $W(t)$  takes two forms:

$$\text{A: } w(t) = \left\{ C_j(t) \left| \int_{T_L}^t C_j(\tau) y(\tau) \cos(\omega_0 \tau + \hat{\theta}(\tau)) d\tau \right| > \left[ \int_{T_L}^t C_i(\tau) y(\tau) \cos(\omega_0 \tau + \hat{\theta}(\tau)) d\tau \right] i \neq j \right\}$$

i.e.,  $w(t)$  is at any time identical to the currently most likely word.

$$\text{B: } w(t) = \text{Sign} \left\{ \sum_j C_j(t) \exp \left[ \frac{2S}{N_0} \int_{T_L}^t C_j(\tau) y(\tau) \cos(\omega_0 \tau + \hat{\theta}(\tau)) d\tau \right] \right\}$$

or essentially the maximum-likelihood estimate of the current modulation sign.

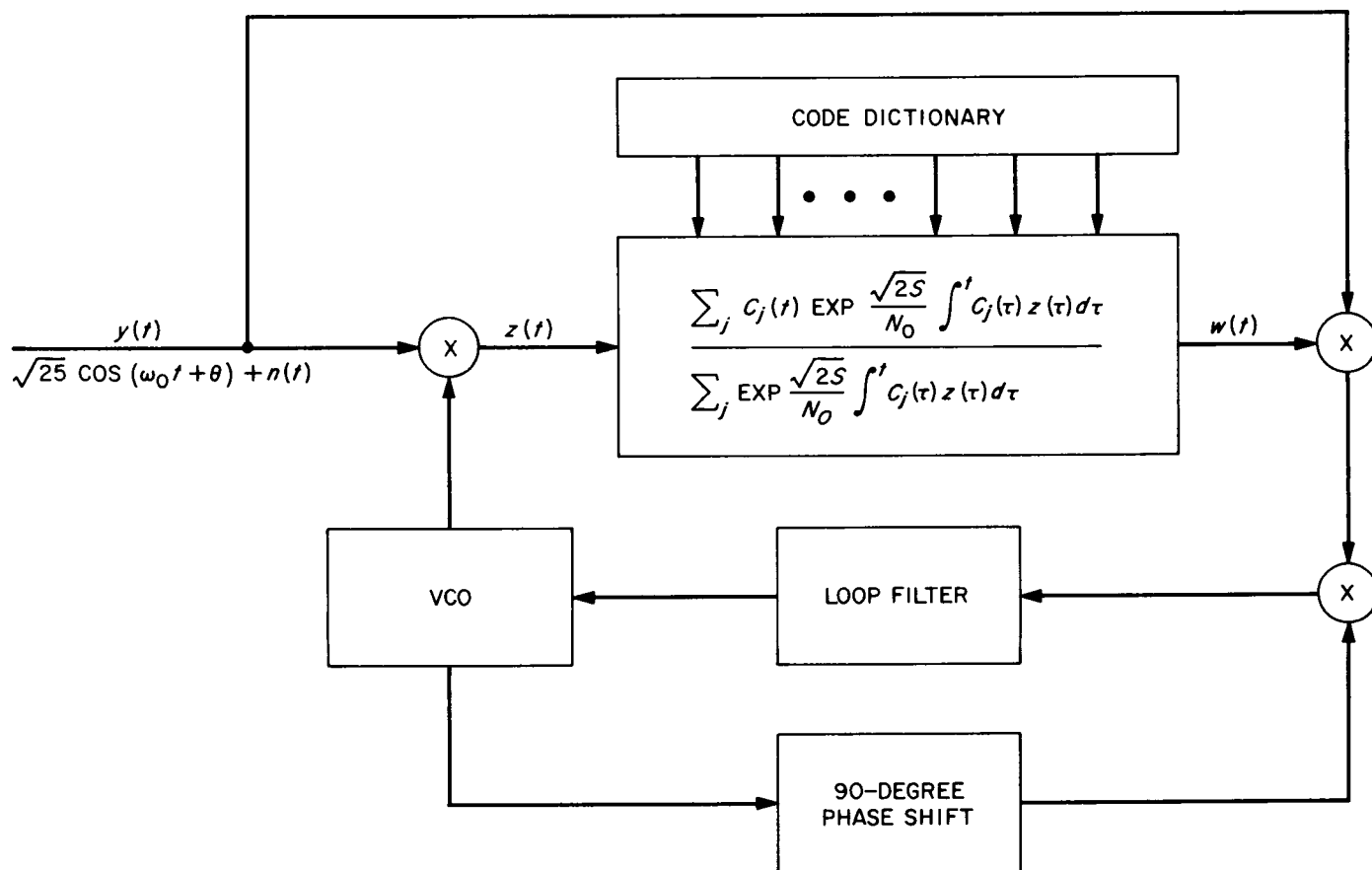


Fig. 1. A decision-variable loop with coding

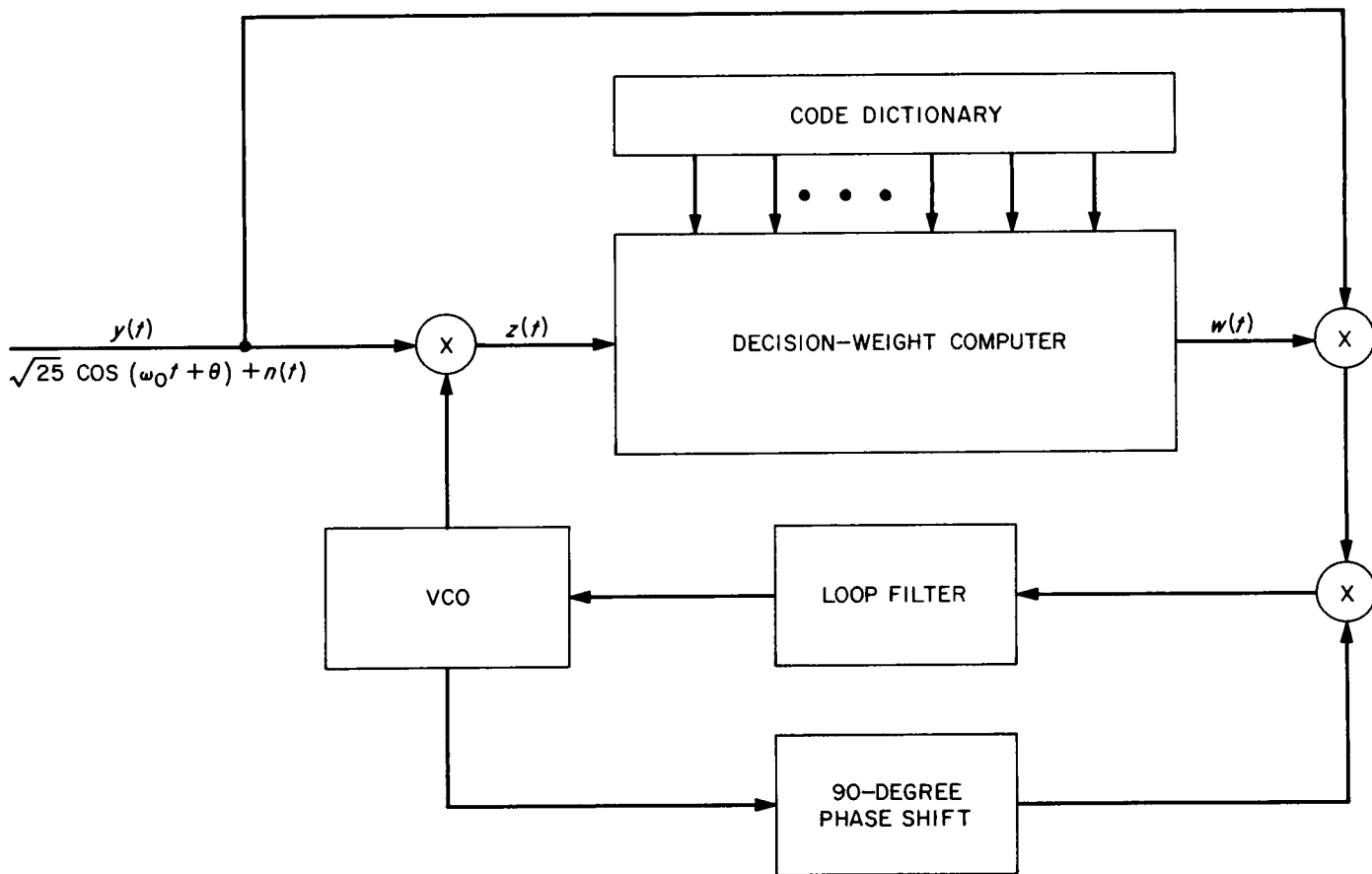


Fig. 2. A decision-directed loop  $\omega(t) = +1/-1$

For either case, define the signal transfer coefficient (STC) to be the expected value of the fraction of time that  $w(t)$  has the correct sign less the fraction of time that  $w(t)$  has the incorrect sign. The noise statistics are unchanged by either  $w(t)$ , and the efficiency of the non-linear pre-loop processing is just  $(\text{STC})^2$ . While not amenable to analysis, the STC is easy to evaluate by Monte Carlo techniques, and the results of this evaluation are presented in the next section.

### 3. Monte Carlo Evaluation of STC For Transorthogonal K-Bit Codes, $1 \leq K \leq 6$

The behavior of both the maximum-likelihood and most-likely-word decision-feedback computers has been computer-simulated. Correlation detection in white Gaussian noise is assumed, as is known word sync. Uncorrelated Gaussian noise is simulated via a Gaussianizing transform (Ref. 14) of pairs of independent 23-bit uniform (0, 1) random numbers (SPS 37-34, Vol. IV, p. 296).

The averaging over the code-words of the time that the decision feed-back is correct less the time that is incorrect is performed by a non-linear, 12-point-per-symbol, numerical integration. (The method was chosen to give good agreement between analytical and numerical integration of STC for a one-bit trans-orthogonal code with the least possible number of function evaluations.) The mean and variance of the individual STC evaluations are estimated by repeated sampling, and for each case, enough samples are taken to reduce the standard deviation of the resultant  $\overline{\text{STC}}$  to below 0.02 for all codes and all SNR for which STC was computed. Evaluation of the  $\overline{\text{STC}}$  for a one-bit trans-orthogonal code was concluded with  $\sigma < 0.007$ . The simulated results agree to better than two significant figures with the analytical results which are available for this case (SPS 37-37, Vol. IV, pp. 268-275).

Fig. 3 summarizes the simulation results for trans-orthogonal (T-O) codes using maximum likelihood sign

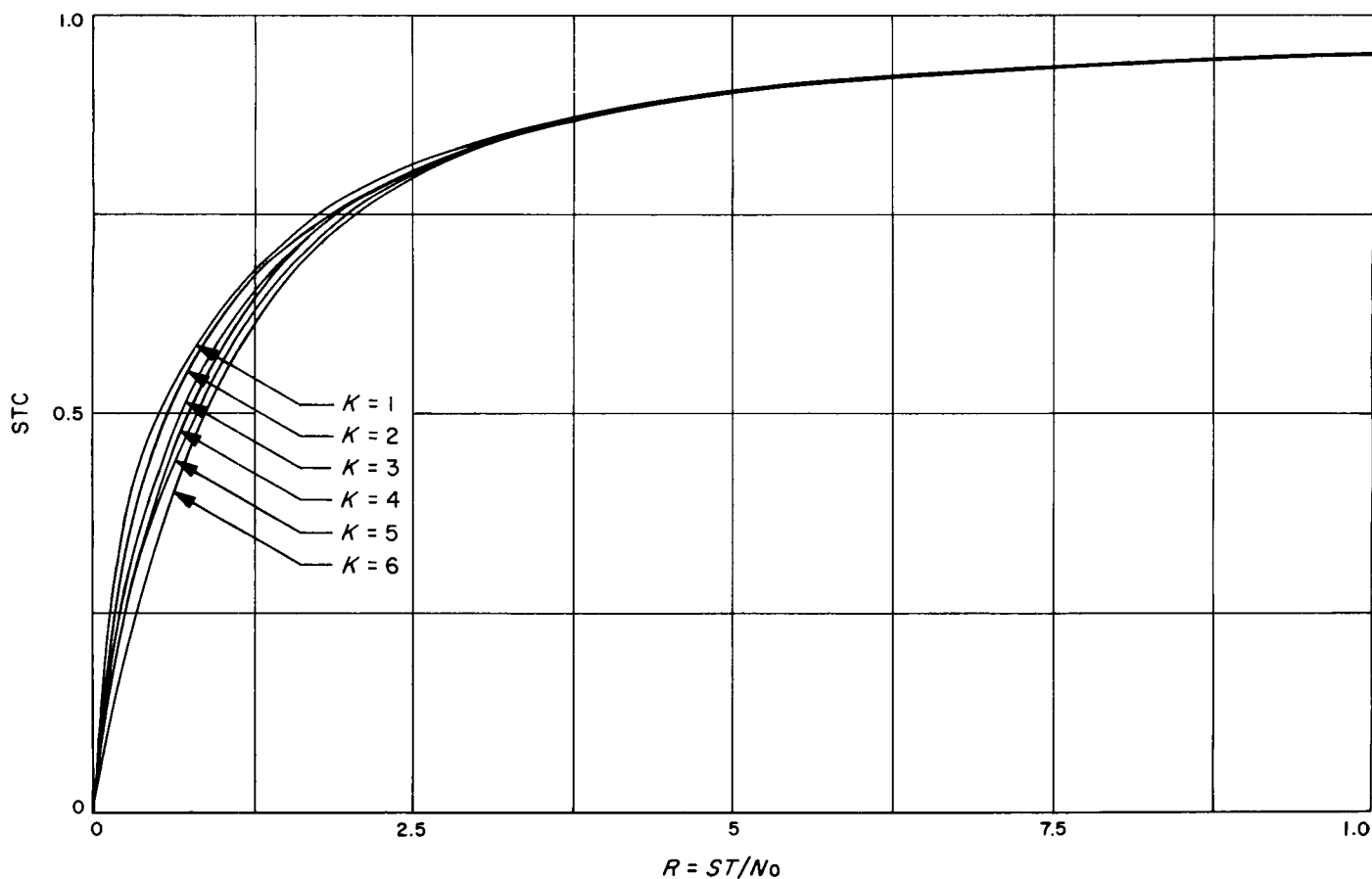


Fig. 3. Effective signal-transfer coefficient for maximum-likelihood sign estimation

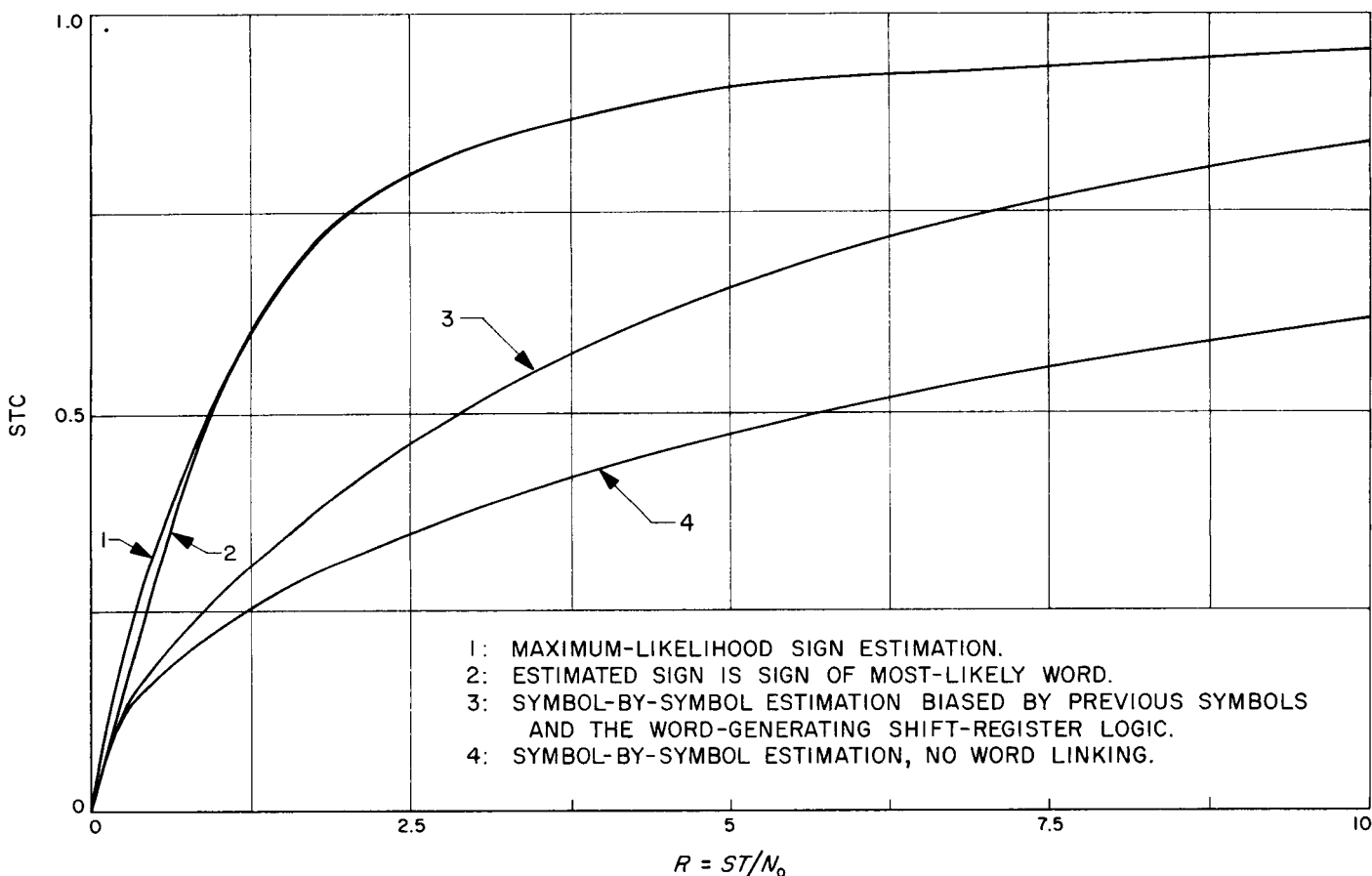


Fig. 4. Effective signal-transfer coefficient for four modes of sign estimation

estimation. The most-likely-word sign estimation was evaluated for 4-, 5-, and 6-bit codes and found to be only slightly poorer than the much harder to implement maximum-likelihood estimation. Fig. 4 shows the STC available with 6-bit T-O codes and four possible modes of decision feedback. Line 1 is STC for maximum-likelihood feedback, while line 2 represents most-likely-word feedback. The methods represented by lines 3 and 4 avoid the accumulation of the word-decision variables in parallel, but at considerable reduction in efficiency. Line 4 represents a decision-directed feedback which treats each symbol as an independent bit. Since a squaring-loop pre-squaring bandwidth must be proportional to the reciprocal of the symbol rate, line 4 is indicative of the efficiency of a squaring-loop-tracking subcarrier in a 6-bit T-O code. The scheme represented by line 3 generated an estimate of the current symbol sign which is a weighted average of a current-symbol sign estimate and weighted of previously received symbol signs. Previous symbols contribute to the current estimate sign-weighted by the logical equations of code word generation. The

STC for both of the symbol-by-symbol schemes decreases to zero as the code length grows large.

The STC for a 6-bit bi-orthogonal code has been Monte-Carlo evaluated to a standard deviation of less than 0.02 with results similar to the T-O codes: i.e., the STC values for a maximum likelihood estimated feedback and a most-likely-word feedback differ only slightly from each other and from the STC of the decision feedback with no coding.

#### 4. A Lower Bound on STC

The STC was defined in Section 2 to be

$$\text{STC} = E \left\{ \frac{\text{Fraction of time word-sign-estimate correct}}{\text{fraction of time word-sign-estimate false}} \right\} \quad (6)$$

Let  $\theta$  denote the fraction of a word length upon which the feedback sign estimator operates. Then taking the

expectation of Eq. 6 produces (for most-likely word feed-back)

$$\begin{aligned} \text{STC} &= 1 - 2 \int_0^1 \Pr \left\{ \text{word error} | \theta \right\} \times \Pr \left\{ \text{sign error} | \text{word error}, \theta \right\} d\theta \\ &\geq 1 - 2 \int_0^1 \Pr \left\{ \text{word error} | \theta \right\} d\theta \end{aligned} \quad (7)$$

Although the dictionary is trans-orthogonal at  $\theta = 1$ , its structure at  $\theta < 1$  is difficult to determine, and further bounding is necessary.

Let  $\Phi(\theta)$  denote the minimum distance (normalized by the code-word length) between the true code word and any contender, and let  $\Psi(\theta)$  denote the maximum distance between any code words, given the fraction  $\theta$  of the code word received [for  $k$ -bit T-O codes,  $\Phi(1) = \Psi(1) = 2^{k-1}/2^k - 1$ ]. The probability of picking a contender instead of the true word is less than it would be if all contenders were at distance  $\Phi(\theta)$  from the true word. The covariance between the noise on any two word-decision variables ( $w_i$  and  $w_j$ ) is equal to  $[\theta - 2 \times D_{ij}(\theta)] \text{VAR}$  where  $D_{ij}$  represents the distance between the two code words, and  $\text{VAR}$  represents total noise variance. The covariance between any pair of words is thus at least  $\text{VAR} \times [\theta - 2\Psi(\theta)]$ . Adding identical noises with variance  $= \text{VAR} \times \max\{0, 2\Psi(\theta) - \theta\}$  will not change the error probability, but it will make the covariance between the noises on all code-word decision variables non-negative. But the probability that one of a set of random variables with zero mean exceeds the one random variable of that set with positive mean, when all have the same variance and non-negative covariances is less than, or equal to, that probability when covariances are all zero.

Hence, for a  $k$ -bit code with signal power  $S$ , bit duration  $T$ , and noise density  $N_0$ , the probability of word-detection error at  $\theta$  is bounded above by the probability of word detection error of a  $k$ -bit orthogonal signal set with

$$\mu_{\text{true}} = 2 \frac{SkT_b}{N_0} \times 2\Phi(0)$$

$$\mu_{\text{false}} = 0$$

$$V_{\text{all}} = 2 \frac{SkT_b}{N_0} (\theta + \text{Max}\{0, 2\Psi(\theta) - \theta\})$$

The orthogonal code-set error probability has been tabulated for  $k \leq 20$  (Ref. 15), and  $\Phi(\theta)$  and  $\Psi(\theta)$  can easily be determined by counting for any given code dictionary.

Numerical integration could then be used to place a lower bound upon STC for any particular situation of interest.

A more general (though considerably looser) lower bound upon STC utilizes the run-length property of the trans-orthogonal code-words. Except for the one all-zero word, the  $k$ -bit T-O code words have the following property:

there is one run of length  $k$ , all ones

there is one run of length  $k - 1$ , all zeros

there are  $2^{k-1-j}$  runs of length  $j$ , for  $1 \leq j < k + 1$ , and half of the runs of each length are ones and the other half are zeros.

The T-O code words form a group, so the true code-word may be assumed to be the all-zero's word. A worst-case bound for  $\Phi(\theta)$  assumes that the near contender starts with  $k - 1$  zeros, 1 one,  $k - 2$  zeros, 1 one, etc., leading with the longest runs of zeros and the shortest runs of ones. At

$$\theta_1 = \frac{2^k - 2}{2(2^k - 1)}$$

all of the runs of 1 one are past, as are all runs of zeros of length greater than one;  $\Phi(\theta_1) = 2^{k-3}$  (for  $k > 3$ ). The second half of this hypothetical contender consists mostly of ones. Figs. 5 and 6 compare this run-length bound with the counted minimum  $\Phi(0)$  for  $k = 5$  and  $k = 8$  T-O codes. Two things may be seen from these curves: the run-length bound is quite loose, and the run-length bound itself is bounded by

$$\Phi(\theta) = \Phi(1) \times \theta^2 - \frac{1}{2^k - 1} \quad (9)$$

$\Psi(\theta)$  may be immediately determined from  $\Phi(\theta)$ . Because the contenders are phase-shifts of each other, the most distant word, after  $1 - \theta$  of the word length is considered, is identical to the unconsidered part of the nearest word when only  $\theta$  of the word is considered.

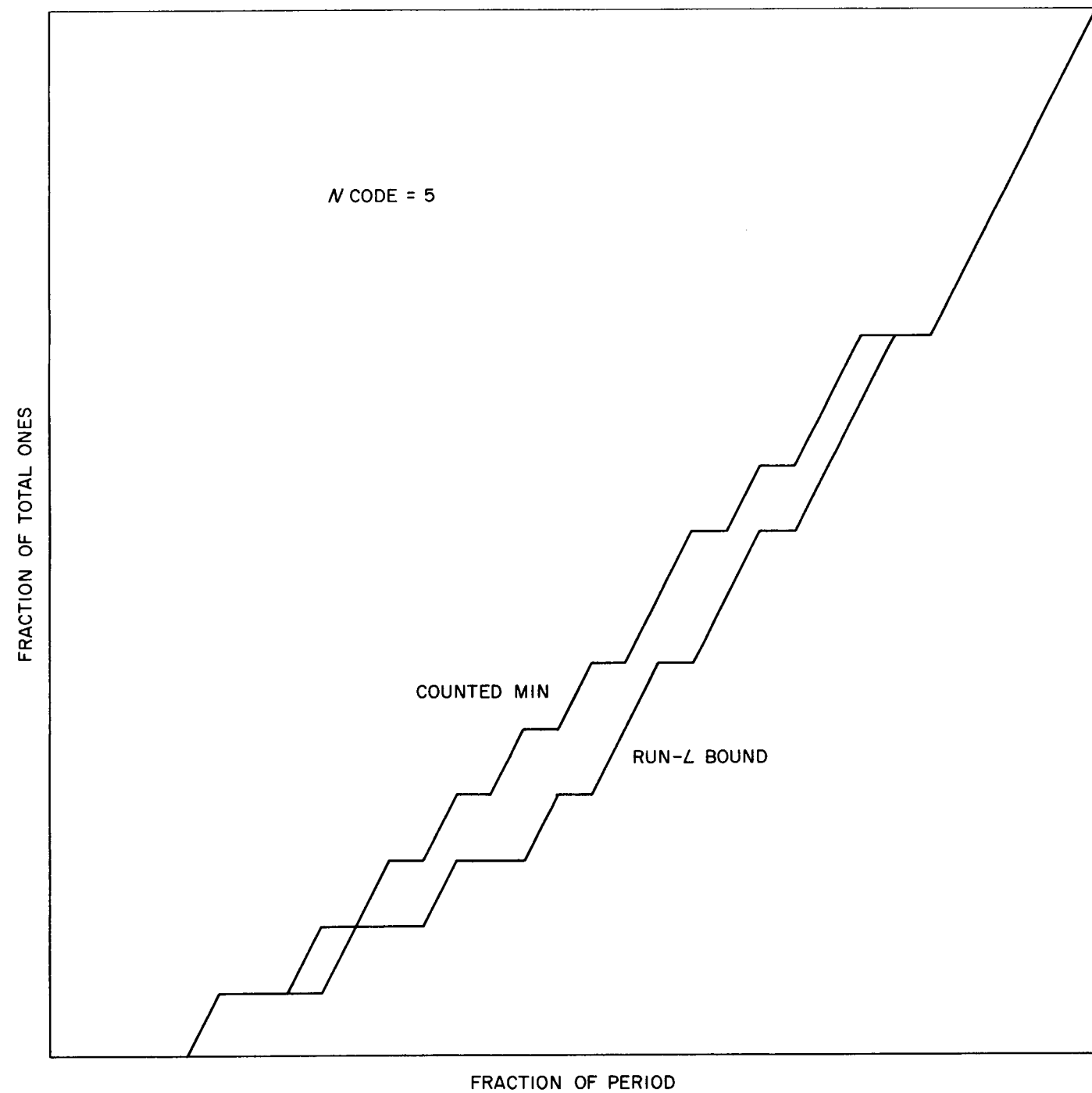


Fig. 5. Bounds for  $\phi(\theta)$ , 5-bit T-O code

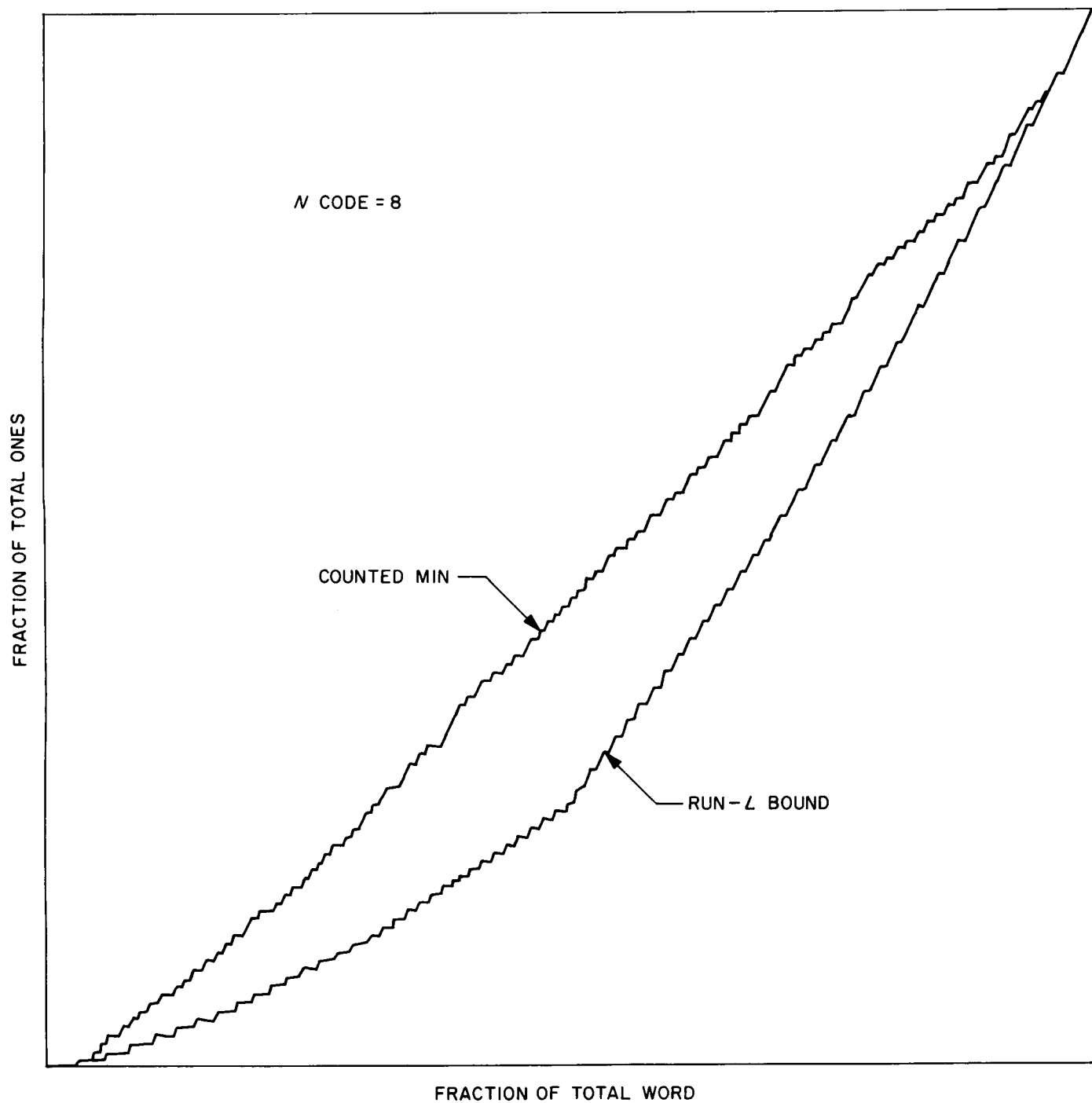


Fig. 6. Bounds for  $\phi(\theta)$ , 8-bit T-O code

$$\text{I.E.: } \Psi(\theta) = \Phi(1) - \Phi(1 - \theta)$$

hence

$$\begin{aligned} \Phi(\theta) &\geq \frac{2^{k-1}}{2^k - 1} \theta^2 - \frac{1}{2^k - 1} \\ \Psi(0) &\leq \frac{2^{k-1}}{2^k - 1} (2\theta - \theta^2) + \frac{1}{2^k - 1} \end{aligned} \quad (10)$$

The word-error probability of the T-O code set after observing  $\theta$  of the code word is therefore bounded above by the word-error probability of an orthogonal code set with

$$\frac{\mu^2}{V} = 2 \frac{ST_b}{N_0} \frac{2^k}{2^k - 1} \frac{\theta^3}{2 - \theta} - 0 \left( \frac{1}{2^k - 1} \right) \quad (11)$$

for any code-length  $k$ .

Consider  $\theta_0$  and the code/signal parameters such that

$$\frac{ST_b}{N_0} \frac{\theta_0^3}{2 - \theta_0} = \ln 2 + \varepsilon$$

where  $\varepsilon$  is an arbitrarily small fixed positive number. Then there is a  $K$  such that  $k > K$  and  $\theta \geq \theta_0$  implies  $\mu^2/V > 2 \ln 2$ . Since the orthogonal word error probability approaches 0 as  $k \rightarrow \infty$  for  $\mu^2/V > 2 \ln 2$  (Ref. 15), the limit as  $k \rightarrow \infty$  of the T-O error probability, given  $\theta$ , approaches 0 for all  $\theta > \theta_0$ .

Similarly, if  $\theta_1$  is such that

$$\frac{ST_b}{N_0} \frac{\theta_1^3}{2 - \theta_1} = \ln 2 - \varepsilon$$

for the same  $\varepsilon$  as before, then there exists a  $K$  such that  $k > K$  implies  $\mu^2/V \leq 2 \ln 2$ , and, for  $\theta < \theta_1$ , the T-O error probability approaches 1 as  $k \rightarrow \infty$ . Furthermore, for  $\theta < \theta_1$ , and infinitely long codes, all words are equally likely, and as half of the words have correct sign and half have incorrect sign,

$$\Pr \{ \text{Sign error} | \text{word error}, \theta \} = \frac{1}{2}, \text{ for } \theta < \theta_1 \quad (12)$$

Using Eq. (7)

$$\text{STC}|_{\text{bound}} = 1 - 2 \left[ \int_0^{\theta_1} \frac{1}{2} \times 1 d\theta + \int_{\theta_1}^{\theta_0} P_0 d\theta + \int_{\theta_0}^1 0 d\theta \right] \quad (13)$$

Since  $\varepsilon$  is arbitrarily small,  $\theta_0 - \theta_1$  is also arbitrarily small, and as  $P_0 \leq 1$ ,

$$\begin{aligned} \text{STC}|_{\text{bound}} &= 1 - \theta_0, \quad \text{if } \theta_0 < 1 \\ &= 0 \text{ otherwise} \end{aligned} \quad (14)$$

Let  $R = ST_b/N_0$ . Then the value of  $\theta$  at which correct word detection begins is the solution to

$$R \frac{\theta^3}{2 - \theta} = \ln 2 \quad (15)$$

or

$$\begin{aligned} \theta^* &= \left( \frac{\ln 2}{R} \right)^{1/3} \left\{ \left[ 1 + \left( 1 + \frac{\ln 2}{27R} \right)^{1/2} \right]^{1/3} \right. \\ &\quad \left. + \left[ 1 - \left( 1 + \frac{\ln 2}{27R} \right)^{1/2} \right]^{1/3} \right\} \end{aligned} \quad (16)$$

and

$$\text{STC}|_{k \rightarrow \infty} \geq \max \{ 1 - \theta^*, 0 \} \quad (17)$$

Fig. 7 shows this bound.

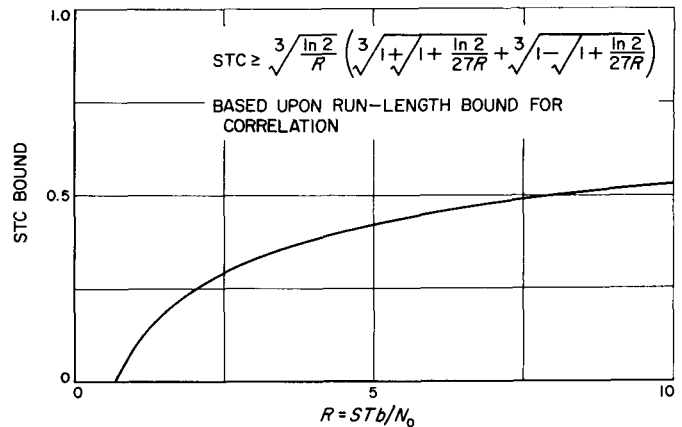


Fig. 7. Lower bound on STC as  $k \rightarrow \infty$

## 5. Summary

The results presented here show that a phase-estimator with decision-directed feedback can perform with relatively high efficiency, when used with a coded PSK telemetry system and an arbitrarily long code. Contrarily, the efficiency of a squaring loop with coded signals decreases monotonically to zero as code-length increases, thus severely limiting its usefulness.

One problem with the decision-directed loop which has been ignored is that word-sync is required for the decision feedback to operate properly. Imperfect word sync will cause a reduction in the STC analogous to that caused in the signal-strength of the word-decision variables. This dependence will either require that the search for word and sub-carrier sync be made simultaneously, or that a special start-up procedure be used (e.g., the less-efficient squaring loop) and, once sync is tentatively acquired, the phase estimate be refined by the more-efficient decision-directed loop.

N67-15758

## E. Information Processing: A Class of Two-Weight Codes, R. J. McEliece

### 1. Introduction

In this report, we shall prove the existence of an infinite number of irreducible cyclic codes in which only two weights occur. These codes will be shown to have essentially the same error-correcting abilities as the well-known single-weight primitive cyclic codes, and considerably larger rates.

### 2. A General Theory

Suppose  $f(x) = x^k + a_1 x^{k-1} + \dots + a_k$  is an irreducible polynomial over a finite field  $GF(q)$ , where  $q$  is a power of a prime  $p$ . Further, suppose that  $n$  is the smallest integer such that  $f(x) | x^n - 1$ . Then, it is well-known that if we associate with  $f$  the linear recurrence  $u_k + a_1 u_{k-1} + \dots + a_k = 0$  over  $GF(q)$ , then all sequences generated in this way are periodic of period  $n$ , and that there are, in fact, exactly  $q^k$  such periodic sequences. We shall now exhibit a 1-1 correspondence between the  $q^k$  periodic sequences (of period  $n$ ) generated by  $f$  and the elements of  $GF(q^k)$ .

Since  $f$  is irreducible, its splitting field over  $F_q$  is (isomorphic to)  $GF(q^k)$ . If  $\theta$  is a root of  $f$  in  $GF(q^k)$ , then our assumptions about  $f$  imply that  $\theta$  is a primitive element of order  $n$  in  $GF(q^k)$ ;  $\theta$  therefore generates a (cyclic) subgroup  $T$  of order  $n$  in  $GF(q^k) - \{0\}$ . To each

element  $x \in GF(q^k)$  we now associate an ordered coset of  $T$ ; viz

$$x \rightarrow \{x, x\theta, \dots, x\theta^{n-1}\}$$

Next we map this  $n$ -tuple of elements of  $GF(q^k)$  onto an  $n$ -tuple of elements of  $GF(q)$  by means of a linear functional  $t$

$$\{x, x\theta, \dots, x\theta^{n-1}\} \rightarrow \{t(x), t(x\theta), \dots, t(x\theta^{n-1})\} = \vec{s}(x)$$

**a. Theorem 1:** The set of sequences generated in this manner is precisely the set of sequences generated by  $f$ .

*Proof:* First, let us show that the sequence  $\vec{s}(x)$  satisfies the recurrence relation determined by  $f$ . In  $GF(q^k)$

$$\theta^k + a_1 \theta^{k-1} + \dots + a_k = 0$$

If we multiply this relation by  $x$  and operate with  $t$ , we obtain

$$t(x\theta^k) + a_1 t(x\theta^{k-1}) + \dots + a_k t(x) = 0$$

But this is precisely the statement that  $\vec{s}(x)$  satisfies the recurrence defined by  $f$ .

Conversely, since the number of elements in  $GF(q^k)$  is the same as the number of periodic sequences generated by  $f$ , if we show that the sequences  $\vec{s}(x)$  are all distinct, we will also have shown that every sequence generated by  $f$  must occur as  $\vec{s}(x)$  for some  $x$ .

Let us, therefore, assume that  $\vec{s}(y) = \vec{s}(z)$  for  $y, z \in GF(q^k)$ . This means that  $t(x\theta^i) = 0$ ,  $i = 0, 1, \dots, k-1$ , with  $x = y - z$ . If  $x\theta^i = y_i$ , we see that the  $y_i$  all lie in the nullspace of  $t$ . But the nullspace has dimension  $k-1$ , and so the  $y_i$  are linearly dependent; i.e., we have a nontrivial relation of the form  $\sum b_i y_i = 0$ , and so, also, a relation of the form

$$x \sum_{i=0}^{k-1} b_i \theta^i = 0$$

But the  $\theta^i$  are linearly independent, and this forces  $x = 0$ , and so  $y = z$ . Thus, the map  $x \rightarrow \vec{s}(x)$  is 1-1 as asserted. This completes the proof of theorem 1.

Although theorem 1 allows us to choose  $t$  to be *any* linear functional of  $GF(q^k)/GF(q)$ , we shall in fact always choose  $t$  to be the *trace*. There is no loss involved in doing this, for it is not difficult to see that every linear functional  $t$  has the form  $t(x) = \text{trace}(ax)$  for some  $a \in GF(q^k)$ .

The 1-1 correspondence exhibited above is particularly well-suited to a discussion of the distribution of the elements of  $GF(q)$  among sequences  $\vec{s}$ . That is, while the sequence  $\vec{s}(x)$  depends upon the ordering of the coset  $\{x, x\theta, \dots, x\theta^{n-1}\}$ , if we are only interested in the number of times a given element of  $GF(q)$  occurs in  $\vec{s}(x)$ , the order is immaterial. Therefore, the question we shall be interested in from now on is:

"What values does the trace take on the cosets of  $T$ ?"

Let us agree to call two elements  $x$  and  $y$  of  $GF(q^k)$  *equivalent* (write  $x \sim y$ ) if  $\vec{s}(x)$  can be permuted to obtain  $\vec{s}(y)$ ; that is, if  $\vec{s}(x)$  and  $\vec{s}(y)$  have the same distribution of elements from  $GF(q)$ . There are two simple sufficient conditions for  $x \sim y$

- (1)  $x \sim y$  if  $y = x\theta^i$  for some  $i$ .
- (2)  $x \sim y$  if  $y = x^{q^i}$  for some  $i$ .

Condition 1 is, of course, obvious, and it shows that the number of equivalence classes is  $\leq N = (q^k - 1)/n$ . Condition 2 follows, if we recall that  $\text{trace}(x) = \text{trace}(x^{q^i})$  for all  $i$ , so that the permutation  $\theta^j \rightarrow \theta^{jq^i}$  exhibits a trace-preserving permutation of  $\vec{s}(x)$  to  $\vec{s}(y)$ . (It turns out, incidentally, that the *only* trace preserving maps of the form  $\theta^j \rightarrow \theta^{jd}$  occur for  $d = q^k$ .)

We shall now obtain an upper bound for the number of equivalence classes by choosing a set of coset representatives for  $T$  which fall into as few classes under condition 2 as possible.

Suppose that  $\psi$  is a primitive root of  $GF(q^k)$ , i.e., that  $\psi$  has multiplicative order  $2^k - 1$ . We may always choose  $\psi$  in such a way that  $\theta = \psi^N$ , so that the subgroup  $T$  is given by  $T = \{1, \psi^N, \psi^{2N}, \dots, \psi^{(n-1)N}\}$ . It is clear that the coset to which an arbitrary element  $\psi^s$  belongs is determined by  $s \pmod{N}$ . If  $\psi^s$  is a coset representative, then the elements of the sequence  $\psi^{sq}, \psi^{sq^2}, \dots$  will all lie in distinct cosets of  $T$ , until  $sq^r \equiv s \pmod{N}$ . This process of mapping the residues  $\pmod{N}$  into themselves by  $i \rightarrow qi$  is a familiar one; it is the one way of determining

the number of irreducible factors of  $x^N - 1$  over  $GF(q)$ , and is perhaps best illustrated by an example:

*Example:*  $N = 21$ ,  $q = 2$ . We operate on the integers  $0, 1, \dots, 20 \pmod{21}$  by  $i \rightarrow 2i$ , and obtain the following six "equivalence" classes. ( $i$  and  $j$  are "equivalent" if  $i = 2^\mu j \pmod{21}$  for some  $\mu$ )

(0)  
(1,2,4,8,16,11)  
(3,6,12)  
(5,10,20,19,17,13)  
(7,14)  
(9,18,15) /

This shows (Ref. 16), among other things, that  $x^{21} - 1$  is the product of 6 irreducible factors  $\pmod{2}$ , 1 of degree 1, 1 of degree 2, 2 of degree 3, and 2 of degree 6.

From now on, let us denote by  $\Phi_q(N)$  the number of irreducible factors of  $x^N - 1$  over  $GF(q)$ .

We have now proved theorem 2: Among all the sequences  $\vec{s}(x)$  described above, there are at most  $\Phi_q(N)$  distributions which can occur.

### 3. Applications

We shall restrict ourselves to  $GF(2)$  here, so that the space of all sequences  $\vec{s}(x)$  becomes a *binary*  $(n, k)$  *irreducible cyclic code*. We observe that for  $N \geq 2$ ,  $\Phi_2(N) \geq 2$  and that  $\Phi_2(N) = 2$  if, and only if,  $N = p$  is a prime and 2 is a *primitive root* of  $p$ . Consequently, whenever  $N = p$  is such a prime, the code in question will have only two possible distributions, and, since the distribution of the elements in  $GF(2)$  in a code word is known if the weights are known, we see that such a code has at most 2 weights. Thus, to get a code with only 2 weights, we need only find  $(n, k)$  such that  $(2^k - 1)/n = p$ , where  $p$  is a prime for which 2 is a primitive root. We claim that

$$n = \frac{2^{t(p-1)} - 1}{p}, \quad k = t(p-1)$$

will do the job. To prove this, it is sufficient to show that  $k$  is the exponent of 2 mod  $n$ ; i.e., that  $n \mid 2^k - 1$  but that  $n \nmid 2^{k'} - 1$  for any  $k' < k$ , for then  $x^n + 1$  will have an irreducible factor of degree  $k$  which will generate a two-weight code.

It is of course clear that  $n|2^k - 1$ . But now suppose that  $n|2^{k'} - 1$  for some  $k' < k$ . Then it follows that  $k'|k$ , and so  $2^{k'} - 1|2^k - 1$ , but since  $n \neq 2^{k'} - 1$ , this means that  $(2^k - 1)/n = [(2^k - 1)/(2^{k'} - 1)] \times [(2^{k'} - 1)/n]$  is the product of at least 2 primes, and we know that this is not the case. We have therefore proved the existence of an irreducible two-weight cyclic code with parameters

$$\left[ \frac{2^{t(p-1)} - 1}{p}, t(p-1) \right]$$

We now proceed to find the exact distribution of weights in these codes, using some recent results of Stanley (SPS 37-40, Vol. IV, pp. 214-216).

If the weights in our  $(n, k)$  code are  $w_1$  and  $w_2$ , then it is clear from what has been said that  $p - 1$  of the cosets will have one of the weights, and the other (the subgroup) will have weight  $w_2$ . Then, according to Stanley's results, we have

$$(p-1)w_1 + w_2 = 2^{k-1}$$

$$(p-1)w_1^2 + w_2^2 = (n+1)2^{k-2}$$

A straightforward manipulation of these equations yields

$$w_1 = \frac{2^{k-1} + (-1)^{t+1} 2^{(k/2)-1}}{p}$$

$$w_2 = \frac{2^{k-1} + (-1)^t (p-1) 2^{(k/2)-1}}{p}$$

It is clear that the *rate* of the two-weight  $(n, k)$  code is  $p$  times as large as the corresponding  $(2^k - 1, k)$  maximal-length shift-register code. But, also, we see that the minimum weight of the two-weight codes is very close to  $n/2$ , so that these codes will correct virtually as large a percentage of errors as will the  $(2^k - 1, k)$  code.

Let us remark finally that, while it is not known whether or not there are infinitely many primes  $p$  for which 2 is a primitive root, there is, nevertheless, no scarcity of such primes. In fact, it has been conjectured (Ref. 17, p. 81) that if  $\pi(x)$  represents the number of primes less than  $x$ , and  $\pi_2(x)$  represents the number of primes less than  $x$  for which 2 is a primitive root, then

$$\frac{\pi_2(x)}{\pi(x)} \rightarrow 0.374$$

The first few primes for which 2 is a primitive root are 3, 5, 11, 13, 19, 29, 37, . . . . Table 2 lists a few of the two-weight codes which have been constructed. The last two columns of Table 2 indicate the number of words of each weight, and the entries are always  $n \cdot (p-1)$  and  $n \cdot 1$ , since each coset corresponds to  $n$  code words under cyclic shift, and, as observed above,  $p-1$  of the cosets have weight  $w_1$ , and 1 has weight  $w_2$ .

Table 2. Two-weight codes

$(p, t)$	$(n, k)$	$w_1$	$w_2$	No. words of wt. $w_1$	No. words of wt. $w_2$
(3, 2)	(5, 4)	2	4	5.2	5.1
(3, 3)	(21, 6)	12	8	21.2	21.1
(3, 4)	(85, 8)	40	48	85.2	85.1
(3, 5)	(341, 10)	176	160	341.2	341.1
(5, 2)	(51, 8)	24	32	51.4	51.1
(5, 3)	(819, 12)	416	384	819.4	819.1
(11, 1)	(93, 10)	48	32	93.10	93.1
(13, 1)	(315, 12)	160	128	315.12	315.1

N67-15759

Information Processing: Tri-Weight Cyclic Codes, G. Solomon

## 1. Summary

We characterize a class of cyclic codes which have three non-zero weights. We give their weight distribution which is the same as for the BCH code of the same dimension. These codes have uniformly low cross-correlation values and thus are useful in spread-spectrum communication systems for multiplexing operations. (Ref. 18) In addition, for large lengths, these codes have asymptotically the same error-correcting properties of maximal-length shift register codes at twice the rate. The code words of different weights are characterized algebraically, and thus non-linear codes with specified weights can be encoded algebraically.

## 2. Theorem

Let  $k$  be odd. Then the  $(2^k - 1, 2k)$  cyclic code generated by the polynomial  $f_1(x)f_{2^{l+1}}(x)$  via linear recursion (Ref. 19) is a tri-weight code with non-zero weights  $2^{k-1}, 2^{k-1} \pm 2^{k-1/2}$ . Here,  $f_1(x)$  is a primitive polynomial over  $GF(2^k)$  with root  $\alpha$ , and  $f_{2^{l+1}}(x)$  is an irreducible polynomial with  $\alpha^{2^{l+1}}$  as a root;  $l$  is prime to  $k$  ( $(l, k) = 1$ ). Furthermore, the weight distribution for these codes is given

below;  $N(w)$  is the number of code words of weight  $w$  in the code:

$w$	$N(w)$
$2^{k-1}$	$(2^k - 1)(2^{k-1})$
$2^{k-1} + 2^{(k-1)/2}$	$(2^k - 1)(2^{k-2} - 2^{(k-3)/2})$
$2^{k-1} - 2^{(k-1)/2}$	$(2^k - 1)(2^{k-2} + 2^{(k-3)/2})$

**Proof:** We prove the theorem with a set of lemmas using recent results of McEliece (SPS 37-40, Vol. IV, pp. 216-218) and Peterson (Ref. 20).

**Lemma 1:** If  $k$  is odd and  $(l, k) = 1$ , then  $(2^l + 1, 2^k - 1) = 1$  and  $f_{2^l+1}(x)$  is primitive (of degree  $k$ ).

**Proof:** A well-known result on greatest common divisors gives  $(2^{2^l} - 1, 2^k - 1) = 2^{(2^l, k)} - 1 = 1$  since  $k$  odd and  $(l, k) = 1$ . It then follows that  $(2^l + 1, 2^k - 1) = 1$  also. Thus  $f_{2^l+1}(x)$  is primitive, since  $\alpha^{2^l+1}$  is primitive if  $\alpha$  is. Herein, we will use lemma 1 often.

Consider the cyclic code  $A$  generated by  $f_{2^l+1}$  via recursion. Each code word  $a = (a_0, a_1, a_2, \dots)$  may be characterized by its Mattson-Solomon (M-S) polynomial (Ref. 19)  $g_a(x) = \text{Tr } cx + \text{Tr } dx^{2^l+1}$  where  $\text{Tr } x = \sum_{i=0}^{k-1} x^{2^i}$ ,  $c, d \in GF(2^k)$ ;  $g_a(\alpha^i) = a_i$ ,  $\alpha$  a root of  $f_1(x)$ . Thus the map  $a \rightarrow (c, d)$  is a linear map of the code  $A$  into  $GF(2^k) \times GF(2^k)$ . A cyclic shift  $T_s$  to the right of length  $S$ , transforms  $a \rightarrow T_s(a)$  and  $(c, d) \rightarrow (\alpha^S c, (\alpha^S)^{2^l+1} d)$ . Obviously, the weight of  $a$ ,  $w(a)$ , is preserved under such a shift. In particular, if we let

$$\alpha^{S(2^l+1)} = d^{-1} \quad \text{or}$$

$$\alpha^S = d^{1/2^l+1} \quad \text{then}$$

$$w(a) = w(T_s(a))$$

We can extract the above root, as  $2^l + 1$  is prime to  $2^k - 1$  (lemma 1).

**Definition:** The tuple  $(c, d)$  is equivalent to  $(e, f)$ ,  $(c, d) \sim (e, f)$  if the corresponding code words have the same weight. Note:  $(c, d) \sim (c\alpha^S, 1)$ . We need only consider code words of type  $(c, 0)$   $(0, d)$  and  $(c, 1)$ . The code words  $(c, 0)$  and  $(0, d)$  correspond to maximal-length shift register code words and are of weight  $2^{k-1}$ . There are clearly  $2(2^{k-1})$  of them.

We now consider code words of type  $(c, 1)$ . Let  $a$  be such a code word with associated polynomial  $g_a(x) = \text{Tr } cx + \text{Tr } x^{2^l+1}$  where  $x$  runs over the  $(2^k - 1)$  roots of unity. If we allow  $x = 0$  as a coordinate, then  $g_a(0) = 0$  and we have in effect the  $(2^k, 2k)$  code word  $a$  of weight  $w(a)$ . The affine map  $x \rightarrow x + \beta$ ,  $\beta \in GF(2^k)$  (Peterson, Ref. 20) is a permutation of the coordinates which leaves  $w(a)$  fixed, but moves the 0 position to  $\beta$  and the  $\beta$  to 0. The "M-S" polynomial of the permuted vector  $\hat{a}$  is given by

$$g_a(x) = \text{Tr}(c\beta + \beta^{2^l+1} - 1) + \text{Tr } x(c + \beta^{2^{-l}} + \beta^{2^l}) + \text{Tr } x^{2^l+1}$$

The restriction  $\hat{a}$  to the non-zero  $x \in GF(2^k)$  gives us a code word in the  $(2^k - 1, 2k + 1)$  code. (This contains the all-one vector). Note: If  $\text{Tr}(c\beta + \beta^{2^l+1}) = 0$ , then  $a$  is in the original code ( $g_a(0) = 0$ ) and the weight is preserved. Thus, under the map  $x \rightarrow x + \beta$

$$(c, 1) \rightarrow (c + \beta^{2^{-l}} + \beta^{2^l}, 1), \quad \text{if } \text{Tr}(c\beta + \beta^{2^l+1}) = 0$$

If  $\text{Tr}(c\beta + \beta^{2^l+1}) = 1$ , then  $g_a(0) = 1$  and  $(c, 1)$  goes into the complement of  $(c + \beta^{2^{-l}} + \beta^{2^l}, 1)$ . Since  $w(a) = w(\hat{a})$ , all  $x \in GF(2^k)$

$$2^k - w(c + \beta^{2^{-l}} + \beta^{2^l}, 1) = w(c, 1)$$

**Lemma 2:** If  $\text{Tr } c = 0$  then  $w(c, 1) = 2^{k-1}$ .

**Proof:** If we can find  $\beta \in GF(2^k)$  such that

$$\beta^{2^l} + c + \beta^{2^{-l}} = 0, \quad \text{then}$$

$$w(c, 1) = w(0, 1) = 2^{k-1} \quad \text{if} \quad \text{Tr}(c\beta + \beta^{2^l+1}) = 0$$

or

$$w(c, 1) = 2^k - w(0, 1) = 2^{k-1} \quad \text{if} \quad \text{Tr}(c\beta + \beta^{2^l+1}) = 1$$

Using a result of McEliece (SPS 37-40, Vol. IV), the equation  $x^{2^{2^l}} + x + c^{2^l} = 0$  for  $(l, k) = 1$  has 2 solutions in  $GF(2^k)$  if  $\text{Tr } c = 0$ . Then there exists such a  $\beta$  and lemma 2 is proved.

Since there are  $(2^{k-1} - 1)$  non-zero elements of trace 0 in  $GF(2^k)$ , we have  $(2^k - 1)(2^{k-1} - 1)$  additional words of weight  $2^{k-1}$  giving us a total of  $(2^k - 1)(2^{k-1} + 1)$  such words. The algebraic characterization of these words in terms of the M-S polynomials is

$$g_a(x) = \text{Tr } cx + \text{Tr } dx^{2^{i+1}}$$

where  $(c, d)$  are of the following forms:

$$(c, 0) \quad c \in GF(2^k)$$

$$(0, d) \quad d \in GF(2^k)$$

$$(c, d) \quad \text{Tr } cd^{(2^{i+1})^{-1}} = 0$$

We now consider  $(c, 1)$  with  $\text{Tr } c = 1$ . For such words, we have two weights occurring. Since  $k$  is odd, and  $\text{Tr } 1 = 1$ , let  $w_1 = w(1, 1)$ . Then the weights that occur are  $w_1$ ,  $2^k - w_1$ .

**Lemma 3:** The number of words of weight  $w_1 = w(1, 1)$ ,  $N(w_1)$ , given by

$$N(w_1) = (2^k - 1) \left( 2^{k-1} - \frac{w_1}{2} \right)$$

**Proof:** The map  $x \rightarrow x + \beta$  takes the vector  $(1, 1)$  into  $(1 + \beta^{2^{-i}} + \beta^{2^i}, 1)$  or its complement. Now for any  $c \in GF(2^k)$  with  $\text{Tr } c = 1$ , there exists a  $\beta$  and  $\beta + 1$  such that  $\beta^{2^{-i}} + \beta^{2^{i+1}} = c$ . Note that this is lemma 1 since  $\text{Tr}(c + 1) = 0$ . Thus  $w(c_1)$  is either  $w(1, 1)$  or  $2^k - w(1)$ . Now  $(c, 1) \sim (1, 1)$  if  $\text{Tr}(\beta + \beta^{2^{i+1}}) = 0$ . But the number of  $\beta$  such that  $\text{Tr}(\beta + \beta^{2^{i+1}}) = 1$  is simply the number of ones of the code word  $\text{Tr } x + \text{Tr } x^{2^{i+1}}$ , which number is by definition  $w_1$ . Since  $\beta$  and  $\beta + 1$  give rise to the same  $c$ , we have that the number of  $\beta$  above is  $w_1/2$ . Thus, there are  $2^{k-1} w_1/2$  vectors of the same weight as  $w_1$ ;  $w_1/2$  words of weight  $2^k - w_1$ . Since  $(c, c^{2^{i+1}}) \sim (1, 1)$  for any  $c \in GF(2^k)$  we have  $(2^k - 1)(2^{k-1} - w_1/2)$  words of weight  $w_1$ . Parenthetically, we note that the Peterson formula for weights of BCH codes is valid here, namely

**Lemma 4:**

$$wN(w) = (2^k - w)N(2^k - w)$$

We may finally compute  $w(1, 1)$  by using the average weight. Since the  $(2^k - 1, 2k)$  code is a group, we have, by adding up the columns of the code words, a total of

$(2^{2k-1})(2^{k-1} - 1)$  ones in the non-zero words. By adding up our code words with their weights, we obtain

$$(2^k - 1)(2^{k-1} + 1)2(2^k - 1)w_1(2^k - w_1)$$

Setting the two numbers equal gives us

$$w_1 = 2^{k-1} + 2^{k-1/2}$$

**Corollary:** Let  $\phi$  be a 1-1 map of the integers mod  $(2^k - 1)$  into itself such that  $\phi(2^i + 1) = 1$ . The code generated by  $f_1(x)f_{\phi(1)}(x)$  is also a cyclic code of the tri-weight type. ( $f_{\phi(1)}$  is the irreducible polynomial with  $\alpha^{\phi(1)}$  as a root.)

**Example:**  $k = 5$ . The  $(31, 10)$  code generated by the polynomials  $f_1 f_3, f_1 f_5, f_1 f_7, f_1 f_{11}$ , all have weights 16, 20 and 12.  $f_1(x) = x^5 + x^2 + 1$ . The BCH code of this dimension and these properties is generated via recursion by  $f_1 f_5$ . The  $(31, 11)$  code has minimum distance 11 and is generated by having  $(x^5 + 1)$  as a multiplying factor.

N67-15760  
**G. Digital Communication and Tracking: Limit-Cycles in Passive-Filter Phase-Locked Loops,**  
R. C. Tausworthe

## 1. Introduction

The way a phase-locked loop reaches its lock-in point is determined by its order, the configuration of its loop filter, and the incoming doppler function. It is possible to show for a doppler polynomial of degree  $n$  that one necessary condition for ultimate lock is that the number of poles at the origin contained in the loop filter be not less than  $n - 1$ . This alone is not sufficient, for some restriction must also be made on the leading doppler coefficient, when the loop filter has exactly  $n - 1$  poles at the origin. For example, the first-order loop must have the frequency offset  $\Omega_0$  less than twice the loop bandwidth,  $\Omega_0 < 2w_L$  in order to lock.

A passive loop filter  $F(s)$  is one having no  $j$ -axis poles. Phase-locked systems with such a filter can thus acquire, at most, the doppler phase function  $\Omega_0 t + \theta_0$ . Viterbi (Ref. 21) developed an approximate upper bound for the largest  $\Omega_0$  possible with a passive second-order loop, asymptotically correct as the ratio  $F(\infty)/F(0)$  tends to zero. This report extends Viterbi's result, to obtain a formula valid over the entire range of  $F(\infty)/F(0)$  and valid for any order passive loop filter, subject to a particular restriction. As a check, the result is not only asymptotically the same as Viterbi's for small  $F(\infty)/F(0)$ , but also gives the exact first-order results (i.e., when  $F(\infty) = F(0)$ ).

## 2. Loop Filters with no Pole at the Origin

Whenever the loop filter  $F(s)$  has no pole at the origin, the highest-order doppler polynomial possible for ultimate lock has the form  $\Omega_0 t + \theta_0$ . The loop phase error  $\phi$  is then governed by the equation

$$\Omega_0 = \dot{\phi} + AKF(p) \sin \phi \quad (1)$$

in which  $A$  is the rms sinusoid input amplitude,  $K$  is the open loop gain (including the DC gain of  $F(s)$ ) so  $F(0) = 1$  and  $p (= d/dt)$  is the Heaviside operator. If we substitute  $y = \sin \theta$ ,

$$\Omega_0 = \frac{\dot{y}}{(1-y^2)^{1/2}} + AKF(p)y \quad (2)$$

Let us suppose that  $\Omega_0$  is so large that there exists a periodic non-constant solution  $y$  to (2), and develop a condition on  $\Omega_0$  whereby this is the case. It will then follow that for  $\Omega_0$  less than some critical value, no periodic solution may exist, thus lock-in is assured.

Since  $y$  is a periodic function by hypothesis, it has some Fourier series representation

$$y = \mu + \sum_{n=1}^{\infty} a_n \cos(\omega_n t + \Psi_n) \quad (3)$$

for which it then follows that

$$F(p)y = F(0)y + \sum_{n=1}^{\infty} a_n |F(j\omega_n)| \cos(\omega_n t + \Psi_n - \delta_n) \quad (4)$$

where  $F(j\omega_n) = |F(j\omega_n)| e^{-j\delta_n}$

The one assumption we shall make concerning the loop filter  $F(s)$  is that all non-zero frequencies in the expansion (Eq. (4)) lie outside the effective bandwidth of  $F(s)$ , and further, that the response is flat<sup>2</sup> over the frequency range containing the significant terms in Eq. (4), as

$$F(j\omega_n) = F \quad (5)$$

where  $F$  is a real number.

<sup>2</sup>This restriction rules out such filters as  $F(s) = 1/(1 + \tau s)$ . However, by putting  $F = F(j\omega_1)$  and  $\delta_1 = \pi/2$ , the ensuing results are again approximate.

Under this restriction, we find that  $y$  satisfies the separable equation

$$\Omega_0 = \frac{\dot{y}}{(1-y^2)^{1/2}} + AK\mu + (y - \mu) AKF \quad (6)$$

By separating variables, we find

$$-AKF dt = \frac{dy}{(y - \alpha)(1 - y^2)^{1/2}} \quad (7)$$

in which we have set

$$\alpha = \frac{\Omega_0 - AK\mu(1 - F)}{AKF} = \frac{\Phi - \mu(1 - F)}{F} \quad (8)$$

with  $\Phi = \Omega_0/AK$ . There is only one case for which Eq. (7) possesses a periodic solution, and this occurs when

$$\alpha^2 > 1 \quad (9)$$

The integral of Eq. (7) then takes the form

$$-AKFt + C = \frac{1}{\beta} \arcsin \frac{\alpha(y - \alpha) + \beta^2}{|y - \alpha|} \quad (10)$$

with the parameter  $\beta$  defined as

$$\beta = (\alpha^2 - 1)^{1/2} \quad (11)$$

Eq. (10) leads straightforwardly to the solution  $y$ :

$$y = \alpha - \frac{\beta^2}{\alpha + \sin(\omega t + \gamma)} \quad (12)$$

in which we have defined

$$\omega = AKF\beta \quad (13)$$

By integrating  $y$  over one cycle, we find that

$$\mu = \alpha - \frac{\beta^2}{(\alpha^2 - 1)^{1/2}} = \alpha - \beta \quad (14)$$

which leads to the condition

$$\mu - \alpha = -\beta = -(\alpha^2 - 1)^{1/2} \quad (15)$$

or, with both sides squared, we find that  $\mu$  must satisfy

$$\mu^2(2 - F) - 2\Phi\mu + F = 0 \quad (16)$$

Of course,  $\mu$  must be a real number, so it follows that

$$\Phi^2 > F(2 - F) \quad (17)$$

We have thus shown in order for  $y$  to be periodic that  $|\Omega_0/AK| > [F(2 - F)]^{1/2}$ . It is also clear when  $|\Omega_0/AK| < [F(2 - F)]^{1/2}$  that  $\mu$  is complex, so there is no periodic solution to Eq. (1). We thus have obtained the following theorem.

**a. Theorem.** If  $F(0) = 1$ , and if there exist real numbers  $\omega_{crit}$ , and  $F$  such that  $F(j\omega) = F$  for  $\omega > \omega_{crit}$ , then the phase-locked loop with filter  $F(s)$  has an oscillatory limit cycle with fundamental  $\omega > \omega_{crit}$  if and only if

$$|\Omega_0/AK| > [F(2 - F)]^{1/2}$$

As an example, let us consider the second-order loop with passive integrator:

$$F(s) = \frac{1 + \tau_2 s}{1 + \tau_1 s} \quad (18)$$

This has  $F \approx \tau_2/\tau_1$  for all frequencies greater than the loop bandwidth. We can thus apply the theorem above to obtain the limit frequency  $\Omega_0$ . For lock, it is necessary and sufficient that

$$\left| \frac{\Omega_0}{AK} \right| < \left[ \frac{\tau_2}{\tau_1} \left( 2 - \frac{\tau_2}{\tau_1} \right) \right]^{1/2} < \left[ 2 \frac{\tau_2}{\tau_1} \right]^{1/2} \quad (19)$$

This is asymptotically the same as Viterbi's result (Ref. 21) as  $F = \tau_2/\tau_1 \rightarrow 0$ , but may be somewhat more useful in

that Eq. (19) also holds in the degenerate case  $F = 1$  (the first-order loop).

In terms more common to this second order loop (Ref. 22), the restriction (Eq. 19) is given as

$$\left| \frac{\Omega_0}{\omega_L} \right| < 2 \left( \frac{r}{r+1} \right) \left( 1 + \frac{\tau_2}{r\tau_1} \right) \left[ 2 \frac{\tau_1}{\tau_2} - 1 \right]^{1/2} \quad (20)$$

where  $r = AK\tau_2/\tau_1 \approx 4\zeta^2$ , with  $\zeta$  the loop damping factor.

N67-15761

## H. Digital Communication and Tracking: The Mean-Square Approximation to the Optimum Cross-Correlation Function, J. J. Stiffler

### 1. Introduction

Consider a device, such as the phase-locked loop, designed to track a null in the cross-correlation between a received and a locally-generated signal. Evidently, the optimum cross-correlation function for such a device would be a square-wave. If the locally-generated signal "leads" the received signal, the maximum possible positive error signal should be available to inform the device of this fact. Similarly, if the local signal "lags" the received signal, the error signal should be maximally negative. The power in both the receiver and the locally-generated signals are limited: the received signal power for obvious reasons, and the local signal power because the performance of the device is independent of this parameter (i.e., increasing the power of the local signal only increases the noise power proportionately). Accordingly, the amplitude of the cross-correlation function is also limited. It is convenient to normalize the received and local signals so that they both have unit power. In this case, the absolute value of the cross-correlation coefficient is evidently limited to unity, and, from the preceding argument, the optimum cross-correlation function is a symmetrical square wave with unit amplitude.

Unfortunately, no such cross-correlation function exists, as is easily demonstrated. In this report, we determine the optimum approximation, in the mean-squared sense, to this ideal function.

### 2. The Mean-Square Optimum Cross-Correlation Function

Without loss of generality, let both the received signal  $y(t)$  and the locally-generated signal  $x(t)$  have equal

periods  $T$ . Then

$$\begin{aligned} x(t) &= \sum_n a_n e^{j\omega_n t} \\ y(t) &= \sum_n b_n e^{j\omega_n t} \end{aligned} \quad \omega_n = \frac{2\pi n}{T} \quad (1)$$

and the cross-correlation function  $R_{xy}(\tau)$  can be written

$$\begin{aligned} R_{xy}(\tau) &= \frac{1}{T} \int_0^T x(t) y(t + \tau) dt \\ &= \frac{1}{T} \sum_n \sum_m a_n b_m \int_0^T e^{j(\omega_n + \omega_m)t} e^{j\omega_m \tau} dt \quad (2) \\ &= \sum_n a_n b_n^* e^{j\omega_n \tau} \end{aligned}$$

where  $b_n^*$  is the complex conjugate of  $b_n$ . The ideal cross-correlation function  $R'_{xy}(\tau)$  can be expressed in the form

$$R'_{xy}(\tau) = \sum_n c_n e^{j\omega_n \tau} = \begin{cases} 1 - \frac{T}{4} < \tau < \frac{T}{4} \\ -1 - \frac{T}{4} < \tau < \frac{3T}{4} \end{cases} \quad (3)$$

where

$$c_n = \begin{cases} (-1)^{|n-1/2|} \frac{2}{\pi} \frac{1}{|n|} & n \text{ odd} \\ 0 & n \text{ even} \end{cases}$$

Thus, we wish to choose  $a_n$  and  $b_n$  so as to minimize the mean-squared difference  $\sigma_c^2$  between  $R_{xy}(\tau)$  and  $R'_{xy}(\tau)$ :

$$\begin{aligned} \sigma_c^2 &= \frac{1}{T} \int_0^T \left( \sum_n a_n b_n^* e^{j\omega_n \tau} - \sum_n c_n e^{j\omega_n \tau} \right)^2 d\tau \\ &= \sum_n \sum_n \frac{1}{T} \int_0^T d_m d_n e^{j(\omega_n \tau + \omega_m \tau)} d\tau = \sum_n |d_n|^2 \quad (4) \end{aligned}$$

where

$$d_n = a_n b_n^* - c_n$$

But

$$\sigma_c^2 = \sum (|a_n|^2 |b_n|^2 - a_n b_n^* c_n - a_n^* b_n c_n^* + |c_n|^2) \quad (5)$$

and letting  $a_n = \alpha_n e^{j\theta_n}$  and  $b_n = \beta_n e^{j\phi_n}$  with  $\alpha_n$  and  $\beta_n$  both real and positive, we have

$$\sigma_c^2 = \sum (\alpha_n^2 \beta_n^2 - 2\alpha_n \beta_n c_n \cos(\theta_n - \phi_n) + c_n^2) \quad (6)$$

Clearly, regardless of the values of  $\alpha_n$  and  $\beta_n$ , the optimum choice of the phase angles  $\theta_n$  and  $\phi_n$  satisfies the relationship

$$\cos(\theta_n - \phi_n) = \begin{cases} 1 & c_n > 0 \\ -1 & c_n < 0 \end{cases} \quad (7)$$

Under this condition

$$\sigma_c^2 = \sum (\alpha_n \beta_n - |c_n|)^2 \quad (8)$$

This expression is obviously minimized by equating the product  $\alpha_n \beta_n$  to  $|c_n|$ . But to do so necessarily violates the condition that  $x(t)$  and  $y(t)$  both represent unit power; i.e., that

$$\sum \alpha_n^2 = \sum \beta_n^2 = 1 \quad (9)$$

In fact, if  $\alpha_n \beta_n = |c_n|$  either  $\sum \alpha_n^2 = \infty$  or  $\sum \beta_n^2 = \infty$  or both. Hence, we must explicitly impose this additional constraint on  $\alpha_n$  and  $\beta_n$ . In particular, we must minimize the quantity

$$\sum (\alpha_n \beta_n - |c_n|)^2 + \lambda_1 \sum \alpha_n^2 + \lambda_2 \sum \beta_n^2 \quad (10)$$

where  $\lambda_1$  and  $\lambda_2$  are defined so as to satisfy the conditions (Eq. 9). This minimization procedure can be simplified by the following observation: first of all, the product  $\alpha_n \beta_n$  will never exceed  $|c_n|$  for any  $n$  when  $\alpha_n$  and  $\beta_n$  are chosen optimally; since, were this the case, the mean-squared error could always be decreased by decreasing that particular product and increasing  $\alpha_{n'} \beta_{n'}$  for some  $n'$  for which  $\alpha_{n'} \beta_{n'} < |c_{n'}|$ . (At least some of the products  $\alpha_n \beta_n$  must be less than  $|c_n|$  because of the conditions (Eq. 9). Now letting  $\alpha_m^2 + \beta_m^2 = K_m$  and differentiating Eq. (8) with respect to  $\alpha_m$  we obtain

$$2(\alpha_m \beta_m - |c_m|)(K_m - \alpha_m^2)^{1/2} [1 - \alpha_m^2 / \beta_m^2] \quad (11)$$

a positive quantity when  $\alpha_m > \beta_m$  and a negative quantity otherwise. Thus, for any  $K_m$  the mean-squared error

is decreased by decreasing  $\alpha_m$  when it exceeds  $\beta_m$  and increasing it when it is smaller than  $\beta_m$ . Evidently, the optimum situation obtains when  $\alpha_m = \beta_m$  for all  $m$ . Thus, we wish to select the set of coefficients  $\{\alpha_m\}$  minimizing the expression

$$E^2 \equiv \sum (\alpha_m^2 - |c_m|)^2 + \lambda \sum \alpha_m^2 \quad (12)$$

Differentiating, we find

$$\frac{\partial E^2}{\partial \alpha_m} = 4\alpha_m \left[ \alpha_m^2 - |c_m| + \frac{\lambda}{2} \right] \quad (13)$$

and  $E^2$  is an increasing function of  $\alpha_m$  for  $\alpha_m^2 > |c_m| - \lambda/2$  and a decreasing function of  $\alpha_m$  otherwise. We conclude therefore, that, since  $\alpha_m$  is real,

$$\alpha_m = \begin{cases} \left( |c_m| - \frac{\lambda}{2} \right)^{1/2} & |c_m| \geq \frac{\lambda}{2} \\ 0 & |c_m| < \frac{\lambda}{2} \end{cases} \quad (14)$$

and, since

$$\begin{aligned} \sum_m \alpha_m^2 &= 1 \\ 2 \sum_{\substack{m=1 \\ m \text{ odd}}}^N \left( |c_m| - \frac{\lambda}{2} \right) &= 1 \end{aligned} \quad (15)$$

where  $N$  is the largest integer for which

$$|c_N| > \frac{\lambda}{2} \quad (16)$$

(Note the  $|c_m|$  terms are monotonically decreasing functions of  $m$ .) Thus

$$\frac{\lambda}{2} = \frac{2}{N+1} \sum_{\substack{m=1 \\ m \text{ odd}}}^N |c_m| - \frac{1}{N+1} \quad (17)$$

Substituting Eq. (17) into the inequality (Eq. 16), we find that  $N = 3$  and that

$$\begin{aligned} \alpha_1 &= \left( \frac{1}{4} + \frac{2}{3\pi} \right)^{1/2} \simeq 0.68 \\ \alpha_3 &= \left( \frac{1}{4} - \frac{2}{3\pi} \right)^{1/2} \simeq 0.2 \end{aligned} \quad (18)$$

and

$$R_{xy}(\tau) = 0.924 \cos \frac{2\pi\tau}{T} - 0.076 \cos \frac{6\pi\tau}{T}$$

This cross-correlation function is plotted in Fig. 8 along with the ideal function  $R'_{xy}(\tau)$  and the function

$$R''_{xy}(\tau) = \cos \frac{2\pi\tau}{T}$$

which results when all of the available power is placed in the fundamental.

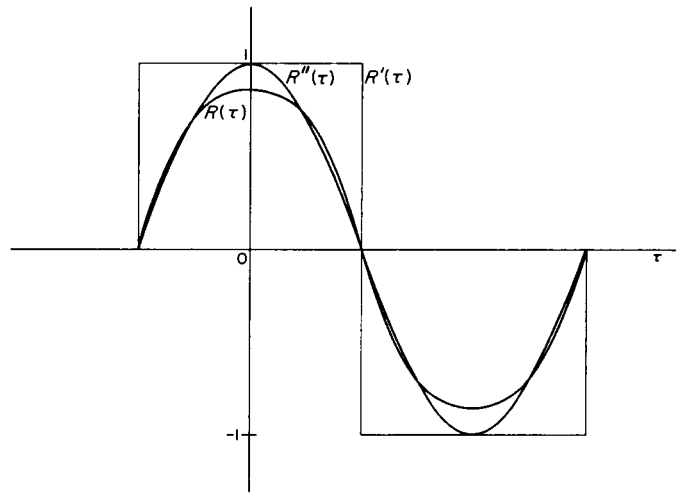


Fig. 8. The optimum mean-square approximation to the ideal cross-correlation function

### 3. Conclusions

It is evident from Eq. (18) and from Fig. 8 that little is to be gained, under the criterion used in this report, in using other than a single sinusoid as a tracking signal. The mean-square criterion, of course, is quite arbitrary, and different conclusions might result from different criteria. If the transmitted and locally-generated signals are chosen for a particular signal-to-noise ratio, decided improvements can be obtained by using other than a single sinusoid. The delay-locked loop, for example, operates on this principle. Nevertheless, as the signal-to-noise ratio changes, the performance of such devices will in general deteriorate more rapidly than those using a sinusoidal signal. The optimal tracking cross-correlation function remains the square wave as discussed here, regardless of the signal-to-noise ratio. It is unfortunate that such a function cannot be approximated more closely.

# 1. Data Compression Development: A Comparison Of Two Floating-Aperture Data Compression Schemes, J. C. Wilson

## 1. Introduction

A number of methods have been suggested for compressing data, such as telemetry records from a spacecraft, into a form that is more economical to transmit. For example, instead of sending back sample readings of temperature every minute or every second, the mean and variance of temperature readings for that hour might be transmitted once each hour. Some recent work has been done at JPL in this area of data compression (Ref. 23).

In most cases, however, the equipment required to compress the data must be as simple as possible; and in some cases, the desired information must approximate the actual waveform of the signal. The methods discussed below have the advantage that they are quite simple. They operate directly on data that would normally be transmitted in an uncompressed mode so that an approximation to the exact waveform is sent.

## 2. Zeroth and First-Order Data Compression

The basic method is the following (Fig. 9). The data are given as samples, taken  $\tau$  seconds apart, of a signal  $f(t)$ . The samples are taken often enough to define the signal, through some interpolation procedure, to the accuracy desired. At  $t = 0$  (arbitrary),  $f(0)$  is transmitted. If  $f(\tau)$  and  $f(0)$  differ by more than some preassigned constant  $K$ , called the (half) aperture, then  $f(\tau)$  is transmitted at  $t = \tau$ . If  $f(\tau)$  and  $f(0)$  differ by less than  $K$ , then  $f(\tau)$  is not transmitted, and the next sample,  $f(2\tau)$ , is compared with  $f(0)$ . It will then be sent or not sent (at  $t = 2\tau$ ), depending on how much it differs from  $f(0)$ .

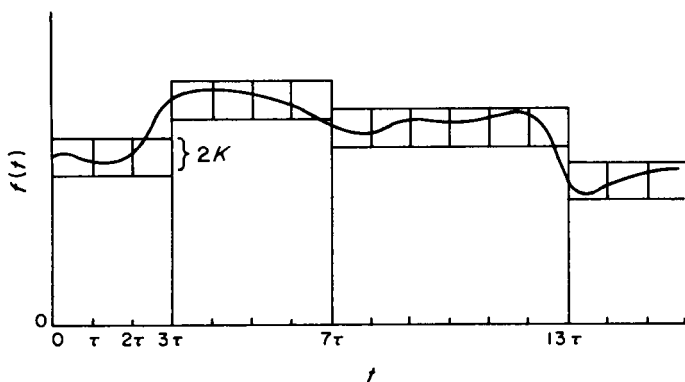


Fig. 9. Zeroth-order compression scheme

Each time a sample, say  $f(j\tau)$ , is transmitted, it becomes the new reference to which succeeding samples are compared. Since the aperture effectively "floats" around the last transmitted sample, this is often called the floating-aperture scheme (SPS 37-17, Vol. IV, pp. 81-84). We shall also refer to it as zeroth-order data compression.

We can readily extend the basic idea to what could be called a first-order compression scheme, where the slope of the function is taken into account. In one possible method,  $f(0)$  is first sent. Then the slope of the curve between  $f(0)$  and  $f(\tau)$  can be found, and a line extended beyond  $f(\tau)$  with that slope. If the next sample,  $f(2\tau)$  differs by more than  $K$  from the line, it is transmitted; otherwise it is not, and the next sample is examined. As before, once a sample value has been transmitted, it becomes the new reference for succeeding samples, with a new slope determination (see Fig. 10).

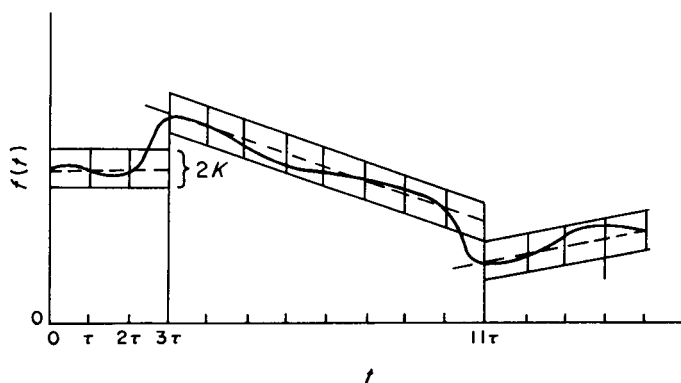


Fig. 10. First-order compression scheme

A variation on this first-order scheme has been suggested by T. O. Anderson (JPL Section 339). This involves storing a small number of slopes for comparison with the actual slope of the function. Whenever a sample  $f(j\tau)$  is transmitted, the slope between it and the next sample is compared with the stored slopes, and the closest stored slope is used as the reference to which succeeding samples are compared.

It is fairly clear that higher compression ratios (the ratio of the total number of samples observed to the number of transmitted samples) would be expected for the first-order compression scheme than for the zeroth-order one. However, we might also ask how much error we will suffer at the receiver when the (compressed) signal is reconstructed.

For the zeroth-order scheme, the error due to compression is bounded by  $\pm K$  about the last transmitted sample. The first-order case is not quite so simple, since we do not know the value of the slope of the curve at the last transmitted sample. If we were to send two values at each transmission, to cover both  $f(j\tau)$  and the slope of

the curve at  $f(j\tau)$ , the (compression) error would be  $\pm K$ , as before. But if only one sample is sent, the error is indeterminate, although the actual error after reconstruction will not differ much from that of the zeroth-order scheme if a simple interpolation procedure is used. Fig. 11 shows the possible errors resulting from the use of these data compression schemes.

### 3. Experimental Setup

A good idea of the range of compression ratios available can be obtained by performing the various compression schemes on a random signal. For this purpose, colored Gaussian noise was generated on a computer by smoothing white Gaussian noise of zero mean and unit variance (also generated on the computer). The two compression schemes were programmed, and various combinations of  $\tau$  (sample spacing) and  $K$  (aperture) tried. In addition, for some choices of these parameters, the computer plotted the uncompressed data and the zeroth-order and first-order approximations.

Here something should be said about subjectiveness in interpreting the data. We can think of many fidelity criteria or metrics that will give us a numerical measure of how well the compressed data approximates the original data. From each of these metrics we can make some kind of comparison between various compression schemes. However, two problems arise. First of all, one scheme may give best results under one metric while another scheme gives best results under another metric. Consequently, there is a subjectiveness in deciding which representation of fidelity is most appropriate for our particular purposes.

There is also the related problem of determining what types of signals are most likely to be received. For example, for certain types of signals, sampling uniformly at a slow rate and using a good interpolation scheme may be preferable to using, say, the first-order data-compression method. However, for signals consisting of long steady periods, with occasional transient bursts, some other method would be more economical. The waveforms used were supposed to be short samples of the latter type of process.

### 4. Results

The experimental results are graphically displayed in Figs. 12–15, which illustrate typical behavior with changes in aperture-width and sample spacing. As mentioned before, the *compression ratio* is the ratio of the number of samples observed to the number actually transmitted after

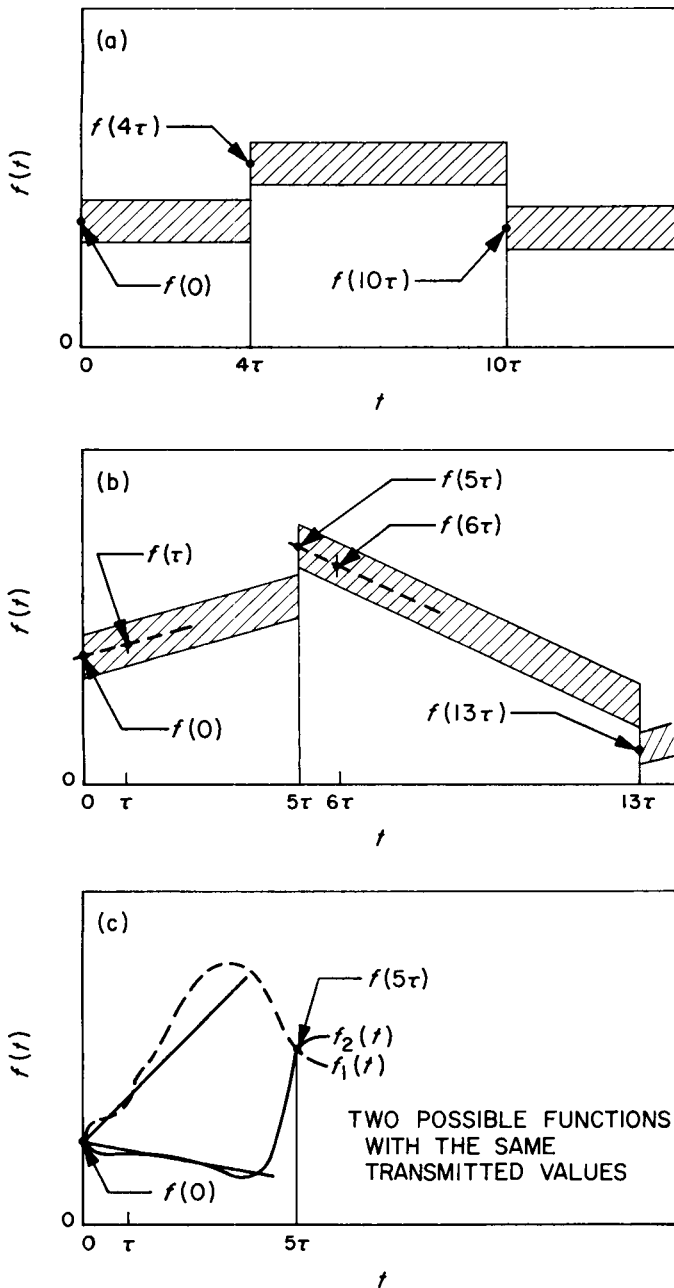


Fig. 11. Bands of possible values for  $f(j\tau)$  at receiver: (a) zeroth-order compression; (b) first-order compression with value of slope given; (c) first-order compression with value of slope not given

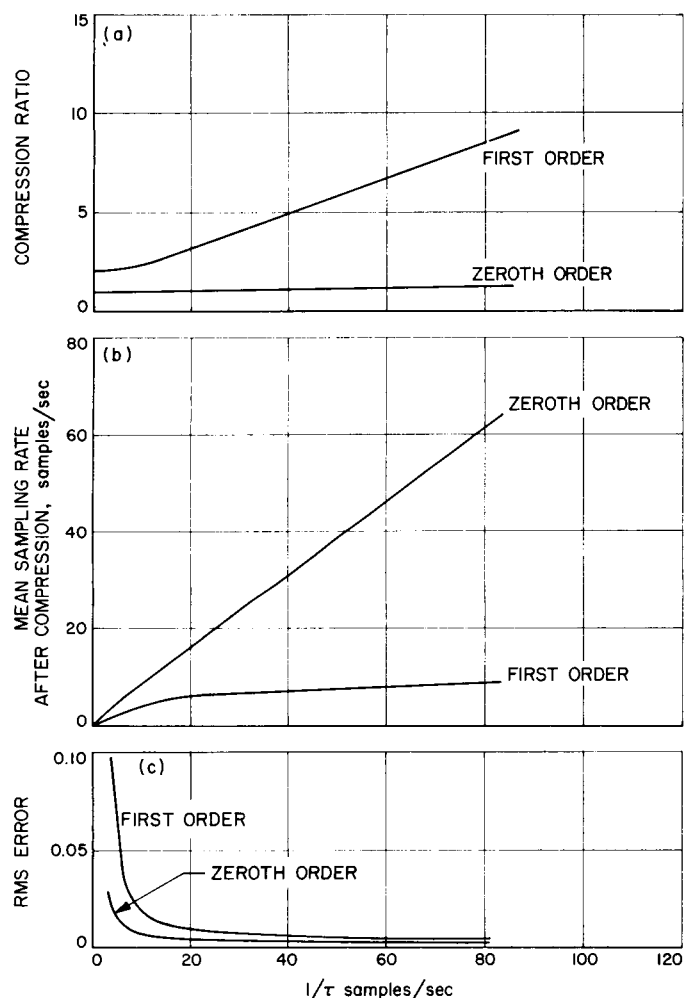


Fig. 12. Compression ratio, mean sampling rate, and rms error vs. sampling rate ( $1/\text{sample spacing}$ ) for a half-aperture of 0.0125

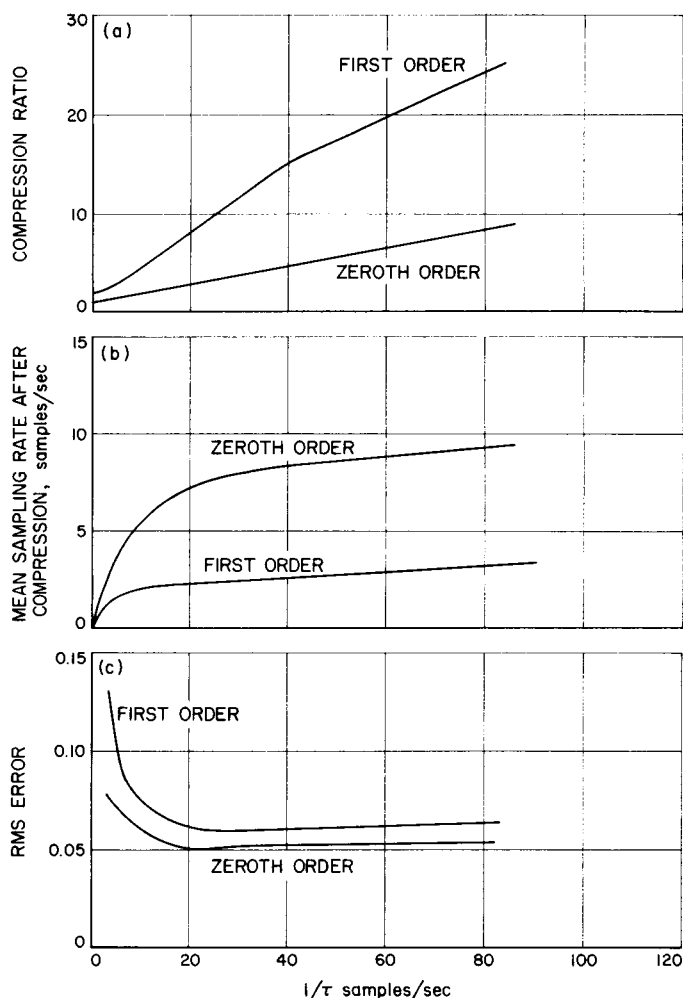


Fig. 13. Compression ratio, mean sampling rate, and rms error vs. sampling rate for a half-aperture of 0.125

compression. Considered alone, the compression ratio is somewhat meaningless, since we can achieve arbitrarily high ratios simply by taking samples closer and closer together. A more meaningful measure of compression is the *mean sampling rate*, which is the average rate at which samples are transmitted after data compression has taken place; it can be derived from the compression ratio as:

Sampling rate before compression  $\div$  compression ratio.

The *efficiency* of the system relative to some theoretical optimum would be a better parameter, but the optimum is not usually known.

Finally, *rms error* refers to the rms value of the difference between the uncompressed data and the compressed

data, after a linear interpolation between compressed points. This, then, is our measure of how well the transmitted samples approximate the original data.

Of primary interest in this report is the comparison between the zeroth-order and first-order compression schemes (slope not transmitted). In all cases, substantially lower mean sampling rates were achieved with the first-order scheme than with the zeroth-order one (Figs. 12(b) and 13(b)). In most cases, this was not at the expense of a larger error (Figs. 12(c) and 13(c)). For small sampling rates in the neighborhood of less than 10 samples/sec, the difference in error became less pronounced as the aperture was increased, as shown in Fig. 14(c), which plots error versus aperture for a rate of 4 samples/sec. In general, then, the first-order scheme is probably to be preferred over the zeroth-order one from the

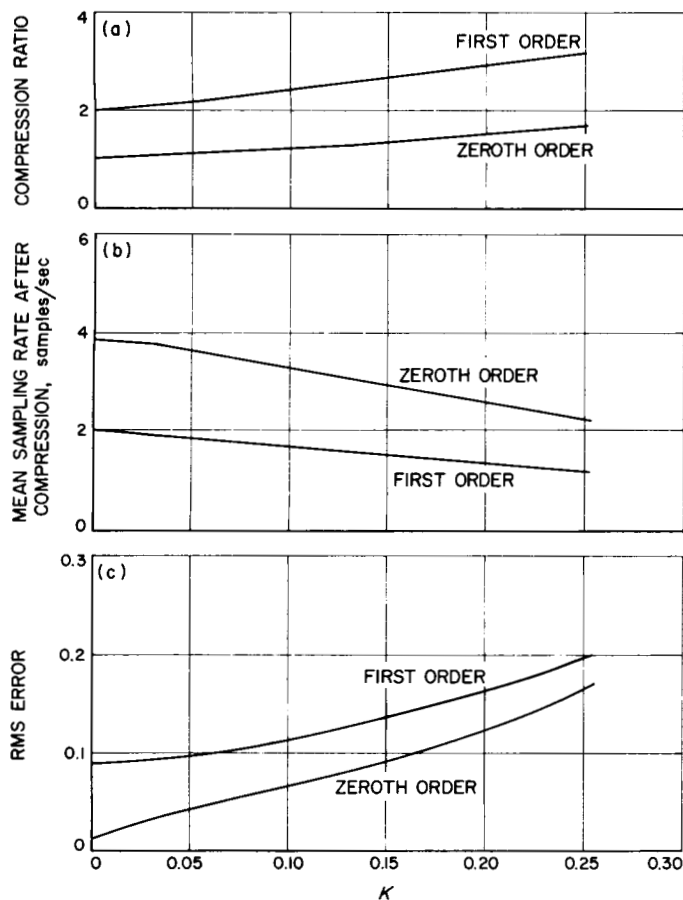


Fig. 14. Compression ratio, mean sampling rate, and rms error vs. half-aperture ( $K$ ) for a sample spacing of 0.25 sec.

standpoint of economy in transmission, disregarding the various hardware requirements of the two methods.

There are some interesting results aside from a comparison of the two schemes. The first relates to the observation made earlier that a high compression ratio, considered by itself, can be misleading. Fig. 12(a) and 12(b) show that, even though the compression ratio increases with the sampling rate, the mean sampling rate is also increasing, which is not desirable.

A second observation is that although the rms error changes sharply with changes in the sampling rate for  $1/\tau < 10$  samples/sec., it levels off above this point. Taking samples closer together does not lessen our error substantially, but it does bring about an increase in the mean sampling rate after compression. There is definitely room in this area for design to achieve a trade-off between small errors and low average sampling rates.

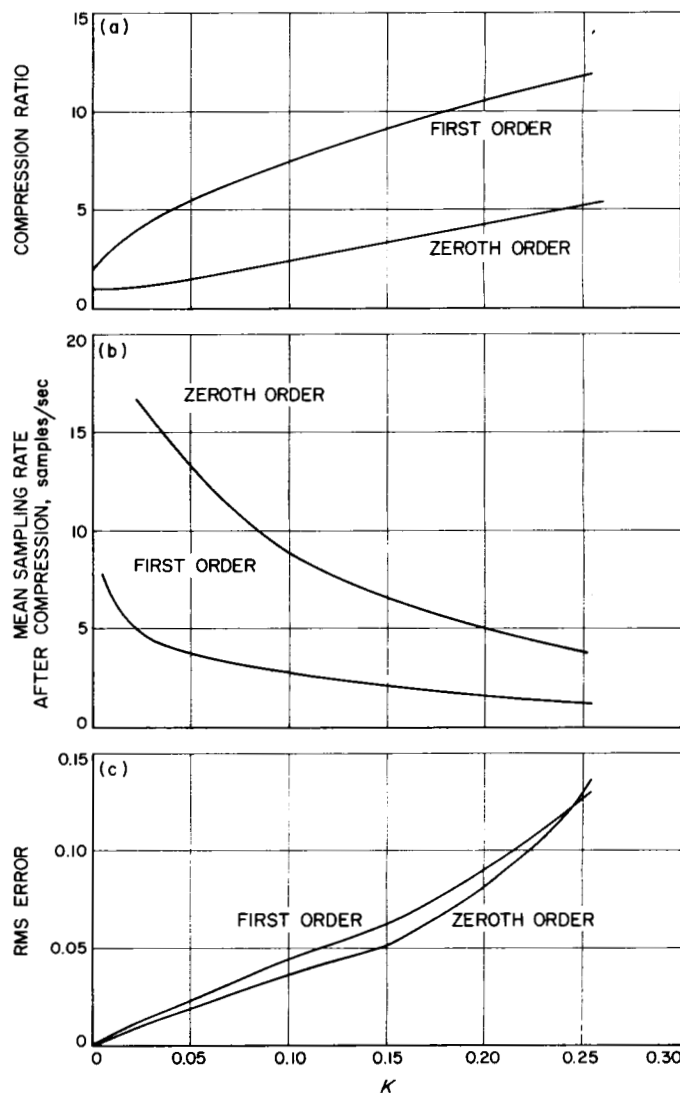


Fig. 15. Compression ratio, mean sampling rate, and rms error vs. half-aperture for a sample spacing of 0.05 sec.

A third observation is that the rms error for the first-order scheme was achieved with no knowledge of the slope of the signal at the receiver. Transmitting the slope will insure that we can reconstruct the signal with a maximum absolute error of  $K$  at each of the original sampling points.

Finally, we can look at some actual waveforms (Figs. 16–18) to compare the compression schemes. In all the plots, a linear interpolation was made between data points. In Fig. 16, it will be seen that even a very small aperture does not necessarily mean good fidelity. Fig. 17, however, illustrates the trend, mentioned above, of a smaller error with a smaller  $\tau$  (higher sampling rate).

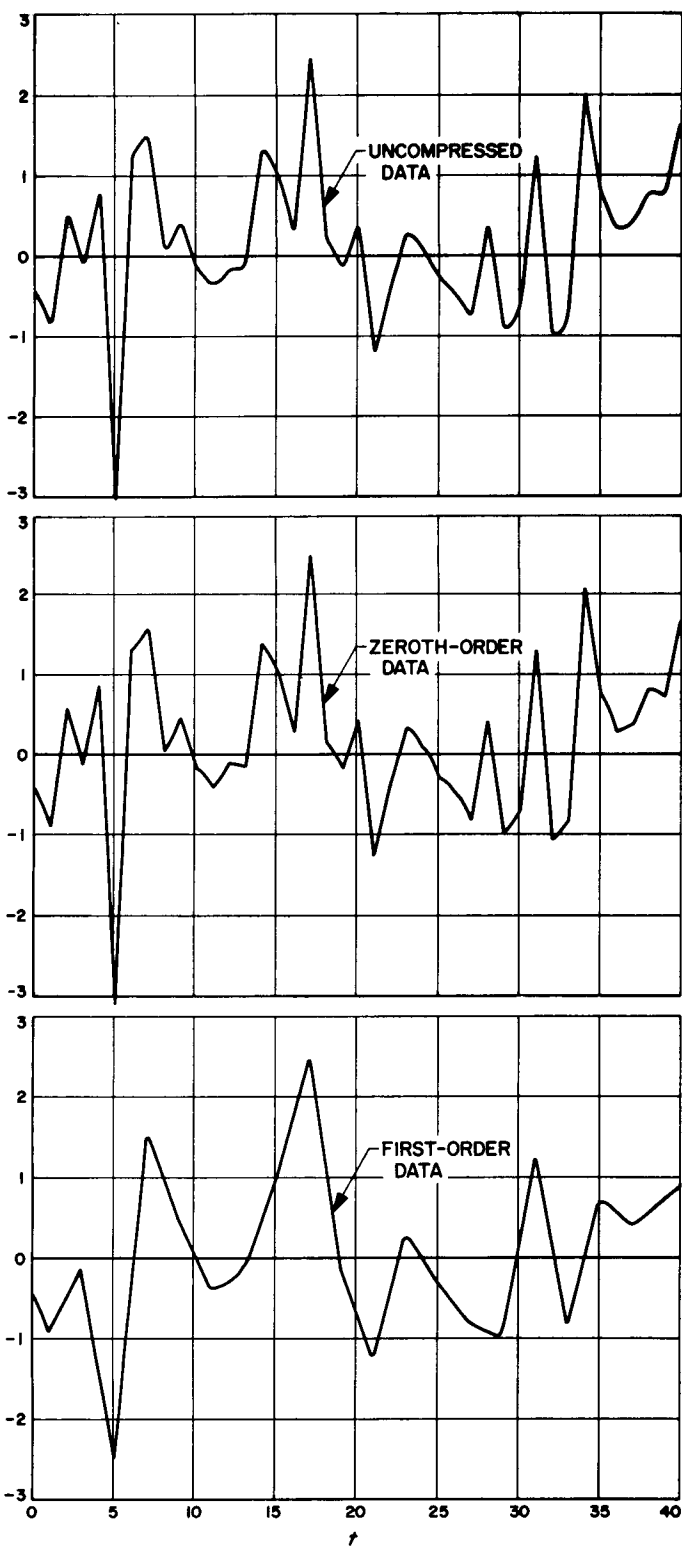


Fig. 16. Plots of uncompressed data, and the zeroth and first-order approximations to them:  
 $\tau = 1.0$ ;  $K = 0.00625$

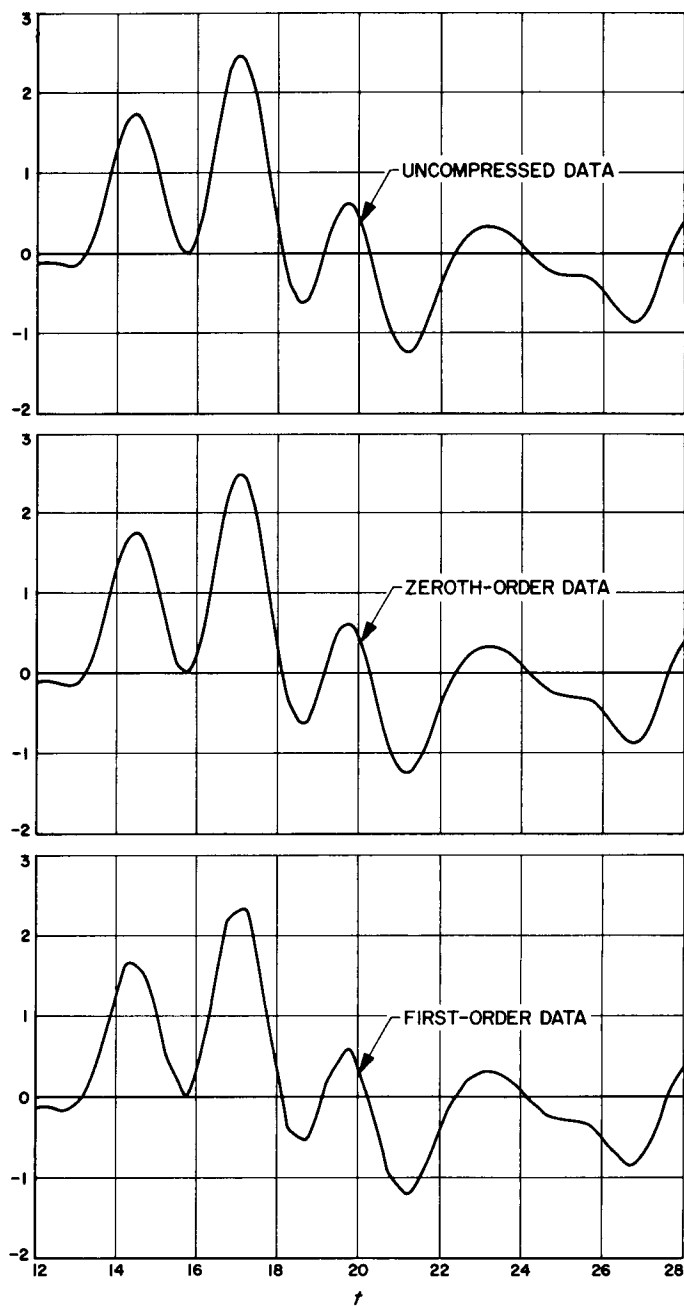
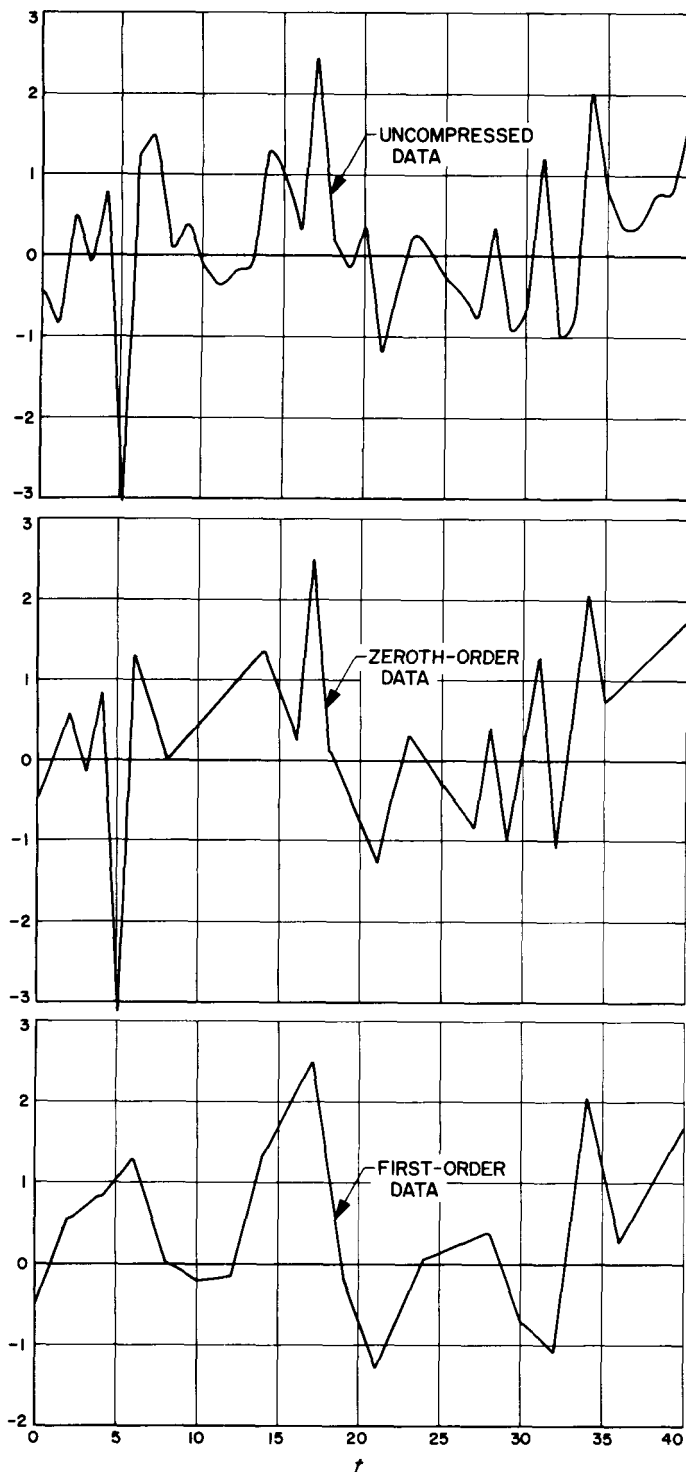


Fig. 17. Plots of uncompressed data, and the zeroth and first-order approximations to them:  
 $\tau = 0.25$ ;  $K = 0.00625$



**Fig. 18. Plots of uncompressed data and the zeroth and first-order approximations to them:**  
 $\tau = 1.0; K = 0.5$

Figures 16 and 18, when compared, illustrate the loss of fidelity when the aperture is increased. Note particularly the zeroth-order case.

We have seen that the first-order data compression scheme is generally superior to the zeroth-order one. A reduction of a factor of 3 to 6 or more in the number of samples sent occurs when the first-order system is chosen over the zeroth-order system, for a wide choice of parameters. Moreover, the first-order system requires fewer timing bits, since samples occur less frequently. It appears safe to say that, for a large class of signal sources, that resemble colored Gaussian sources, a factor of at least 3 can be gained in choosing a first-order system over a zeroth-order one.

One last point; for the purposes of comparing data-compression schemes, instead of sending out the compressed version of the data samples as they are observed, the usual procedure is to store them in a buffer to be sent out at a uniform rate. Consequently, timing information will have to be sent along, decreasing the net transmission rate. Also consider the quantization of the data for coding purposes. The results indicate that there is much room for trade-off design once a scheme has been chosen. For example, a large sample spacing (low rate) may result in a large error, while a very small spacing may yield too much compressed data to transmit economically.

**N67-15763**

**J. Digital Devices Development: Integrated Circuits — Delay Line Interface Circuitry,**

*R. A. Winklestein and E. Lutz*

### 1. Introduction

This article describes a unique and flexible system of interfacing ultrasonic delay lines within digital systems using integrated-circuit logic. To avoid misunderstanding, the term "NRZ" in this document refers only to input-output waveform relations which are similar to those achieved by conventional Non-Return-to-Zero detection schemes. However, all the advantages of the NRZ mode of operation are maintained while certain distinct disadvantages are completely eliminated.

The basic technique is to store digital information of an aperiodic nature in the delay medium and to retrieve an exact replica of that information delayed by a certain amount. The conventional method of detection is shown by the timing diagram in Fig. 19 where the amplified waveform from the delay line is "sliced" by two threshold levels: one level to set and the other to reset a flip-flop. A change of state at the output of the flip-flop takes place only if a "1" follows a "0," or a "0" follows a "1." This method produces an output waveform which is an exact

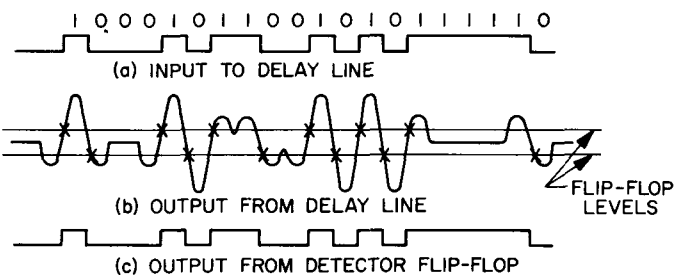


Fig. 19. Typical NRZ mode waveforms

duplicate of the input signal. However, noise transients can upset the sequence of "sets" and "resets," causing a severe distortion of the stored data. Delay lines having large SNRs are therefore recommended when used in this mode of operation. In addition, transients due to mechanical shock and amplitude variations due to change in ambient temperatures must also be taken into account. These severe and unpredictable limitations often force the design engineer to choose an alternative method at the cost of performance. Such a method is shown in Fig. 20 where one threshold slices the amplified signal. The result is an output waveform which is clocked, therefore the presence of a pulse represents a "1" and no pulse represents a "0." This method of operation is called the return-to-zero or RZ mode. When comparing the two modes, it can easily be seen that the NRZ mode allows twice as many bits to be stored as the RZ mode, but with less noise immunity. There is yet another method of operation called phase-reversal mode; however, neither phase-reversal nor RZ modes are discussed in this article.

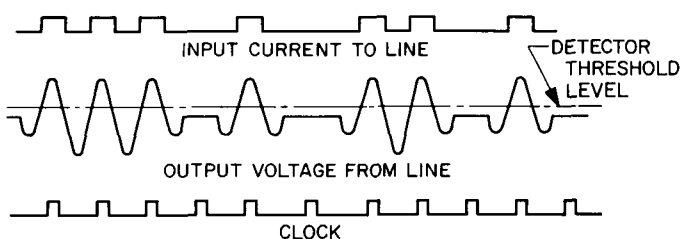


Fig. 20. Typical RZ mode waveforms

## 2. System Description

The developed system operates in the NRZ mode, maintaining the high bit density capability of this mode but with much higher noise immunity than conventional schemes. Typical waveforms inside ultrasonic delay lines, such as those classified as magnetostrictive lines, glass lines or others, are illustrated in Fig. 21 which shows an idealized timing diagram where an input current step is applied

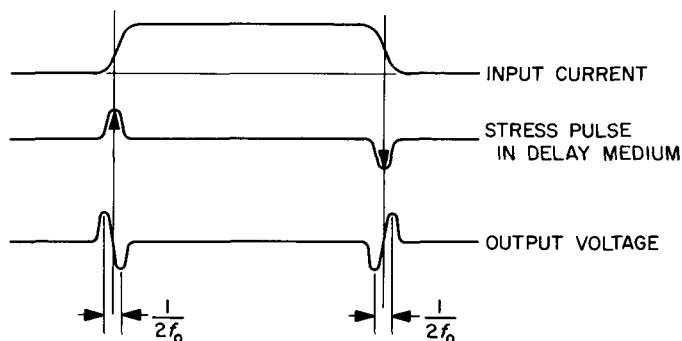


Fig. 21. Delay line response to current step

to the launch coil, causing a mechanical stress pulse in the delay medium to propagate through the line at a certain velocity. It is important to note that the stress pulse is proportional to the first derivative of the input current step. The response of the output pick-up coil to the stress pulse is a voltage waveform which is proportional to the second derivative of the input current step. This voltage is amplified to a suitable level and fed to the detection circuitry for further processing. At this point, it is obvious that the conventional detection scheme mentioned earlier presents certain problems (such as noise transients) and that it is more advantageous and reliable to use a waveform similar and proportional to the mechanical stress pulse itself. To obtain such a waveform, the output signal is *operationally* integrated. The result is a more reliable and predictable system, since sporadic noise transients of appreciable amplitude are attenuated to a large extent. Furthermore, a simpler detection scheme can be used by feeding the positive pulses to the "set" side and the negative pulses to the "reset" side of a bistable device. Alternatively, the signal may be detected by a Schmitt trigger as is done in the present system.

As is shown in Fig. 22, a driver circuit converts input voltage pulses into current pulses of specified magnitude. The output voltage of the line is amplified several hundred times and is then fed to an operational integrator (discussed in detail in the following section). Finally, the integrator output is sensed by the detector circuit.

## 3. Description of Circuits

The circuits developed for this system are not unique (with the possible exception of the operational integrator) and can be replaced by different circuits to suit any particular application. In this case, a magnetostrictive delay line manufactured by Digital Devices, Inc. was selected for the prototype system.

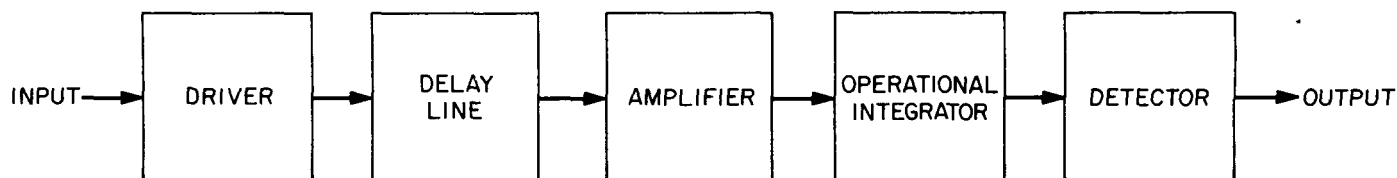


Fig. 22. System block diagram

**a. Driver.** Fig. 23 shows a Darlington pair gated at the input and clamped to limit the voltage swing to +5 v. A voltage step of approximately +2 v developed across the emitter resistor of the driver transistor drives a 40 ma current step into the delay line launch coil which is critically damped by a 300  $\Omega$  resistor. The zener diode across the coil prevents excessive voltage buildup at the collector of the driver and is in series with a regular low-storage diode to minimize capacitive loading.

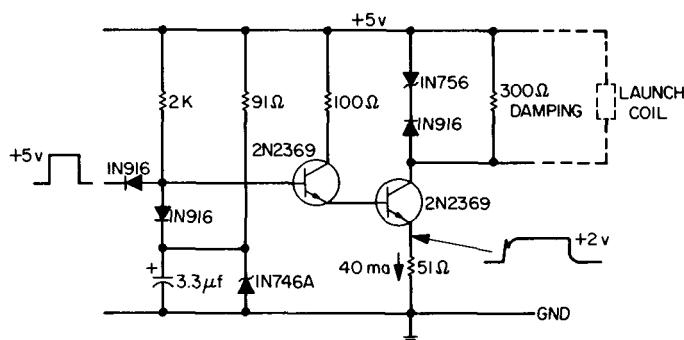


Fig. 23. Driver, schematic diagram

**b. Amplifier.** The amplifier, shown in Fig. 24, is designed to operate between -3 and +5 v and has sufficient bandwidth to allow narrow pulses (0.45  $\mu$ sec/min) to be amplified 100 times. The output is buffered by an emitter follower.

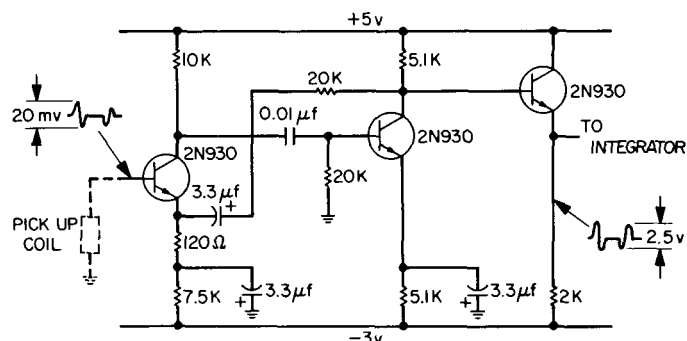


Fig. 24. Amplifier, schematic diagram

**c. Operational integrator.** Early attempts using operational amplifiers in conjunction with external networks to form an operational integrator failed due to limited bandwidth and poor circuit stability (unwanted oscillations). A special circuit was then developed to alleviate the many problems operational amplifiers have at higher frequencies. Such a circuit is shown in Fig. 25(a) with the following transfer function

$$e_2(s) = \frac{K_1}{C} \frac{1}{s + \frac{1}{R_1 C} - \frac{K_2}{C}} e_1(s) \quad (1)$$

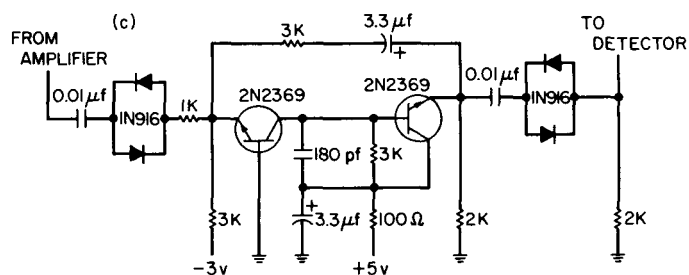
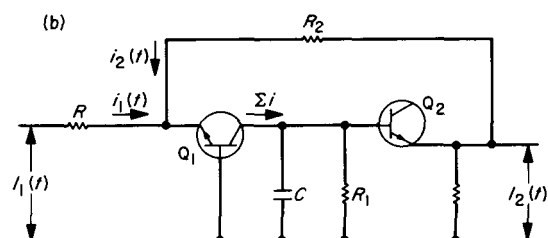
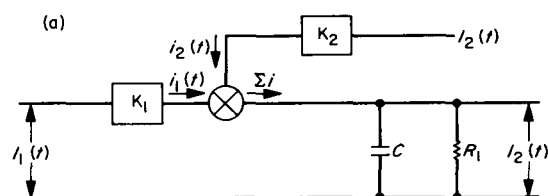


Fig. 25. Operational integrator: (a) basic configuration; (b) shown without biasing; (c) schematic diagram

Assigning a unique value to  $K_2$  namely

$$K_2 = \frac{1}{R_1}$$

Eq. (1) reduces to

$$e_2(s) = \frac{K_1}{C} \frac{1}{s} e_1(s)$$

or, translating back into the  $t$ -domain

$$e_2(t) = \frac{K_1}{C} \int_0^t e_1(t) dt$$

Fig. 25(b) shows the AC representation of this circuit featuring  $Q_1$  as a current summing transistor and  $Q_2$  as a buffer stage. When considering  $R$  and  $R_2$  large with respect to the input impedance of  $Q_1$ ,

$$K_1 = \frac{1}{R} \quad \text{and} \quad K_2 = \frac{1}{R_2} = \frac{1}{R_1}$$

Therefore

$$e_2(t) = \frac{1}{RC} \int_0^t e_1(t) dt \quad (2)$$

The actual circuit used in the system is shown in Fig. 25(c) and features two "dead space" generators at

both input and output for the purpose of removing baseline noise. The baseline noise at the input is primarily caused by the delay line itself, while the output has a baseline signal caused by the dissymmetry of the input signal. This results in an unwanted baseline offset. Filtering of the  $+5$  v supply is necessary to maintain the purity of the integration process.

**d. Detector.** The circuit in Fig. 26 consists of an input amplifier and buffer stage connected to a Schmitt trigger. The Schmitt trigger is designed to have a hysteresis about ground such that the quiescent level from the amplifier is located in the center of the hysteresis band. This results in a bistable condition such that the Schmitt trigger is set when a positive pulse comes along and is reset only on a negative pulse. The centering of the hysteresis band about ground is adjusted by the  $2k \Omega$  potentiometer.

#### 4. Test Results

The photographs in Fig. 27 and 28 show the actual operation. In Fig. 27 the upper trace is the applied input voltage of  $+5$  v, the second trace is the amplified output of the line, the third trace is the amplified integrated output, and the last trace represents the Schmitt trigger output.

Fig. 28 shows the progression of signals through the operational integrator. The upper trace again is the amplified signal from the line, including some unwanted feed-through noise. The second trace is the same waveform (with considerably less noise) after it has passed through the first "dead space" generator. The third trace is the

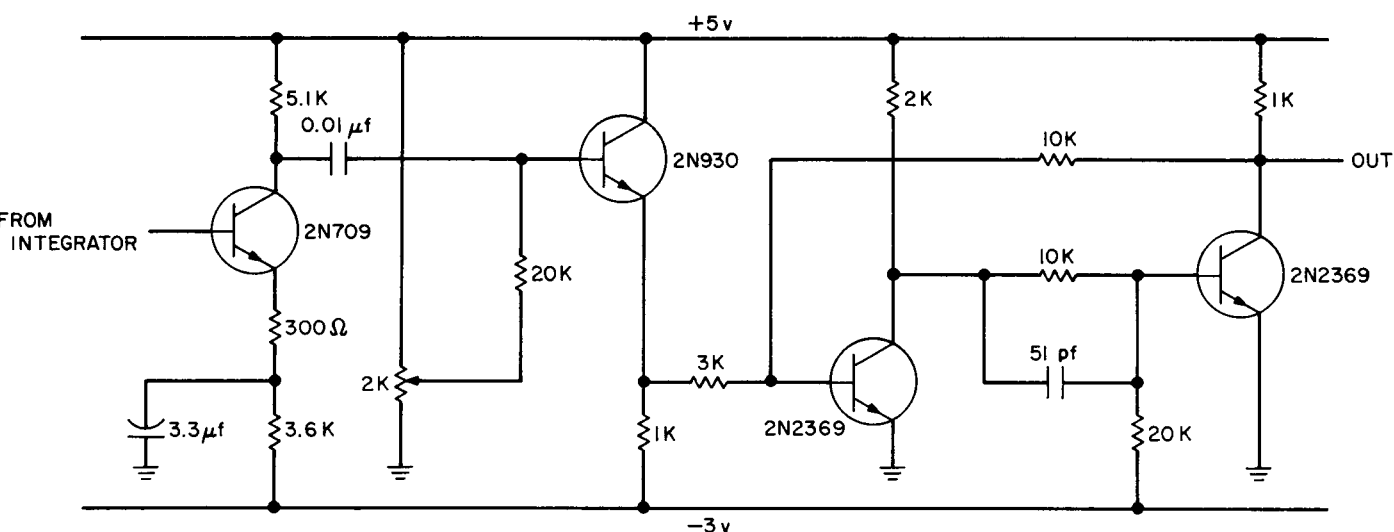


Fig. 26. Detector, schematic diagram

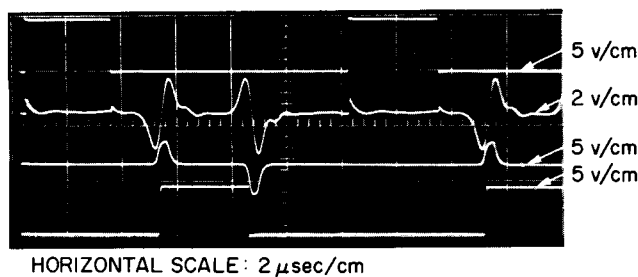


Fig. 27. System operation waveforms

signal directly out of the integrator showing the slight baseline offset caused by signal dissymmetry. This offset is totally removed after the second "dead space" generator (bottom trace).

The delay line used in this application is a Digital Devices, Inc. line specified as follows: 1 MHz with a delay of 100  $\mu$ sec to be operated in the RZ mode. When used in the new system, the line is operated in the NRZ mode at the upper frequency limit to 1 MHz without difficulty. This corresponds to a maximum clock rate of 2 MHz.

Final tests also included power supply variations in excess of  $\pm 10\%$  without deterioration in performance.

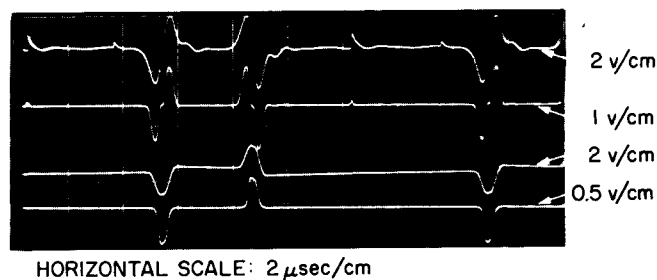


Fig. 28. Integration process waveforms

## 5. Conclusion

The prototype system has proved to be satisfactory and has sufficient flexibility to insure reliable and repeatable operation. Normal construction procedures were observed in building the various circuits on a single board mounted in parallel with the delay line.

The basic system may be used in the development of high-frequency memory systems featuring glass delay lines. The use of integrated components such as amplifiers with bandwidths up to hundreds of MHz can be of great value in such a system. Furthermore, the operational integrator described above can be used at these high frequencies with presently available components.

## References

1. Eggleston, H. G., *Convexity*, Cambridge University Press, Cambridge, England, 1958.
2. Tausworthe, R. C., "Random Numbers Generated by Linear Recurrence Modulo Two," *Mathematics of Computation*, Vol. 19, 1965, pp. 201-209.
3. Albert, A. A., *Fundamental Concepts of Higher Algebra*, University of Chicago Press, Chicago, Ill., 1956.
4. Shanks, D., *Solved and Unsolved Problems in Number Theory*, Spartan Books, Washington, D. C., 1962.
5. Borevich, Z. I., and Shafarevich, I. R., *Number Theory*, Academic Press, New York, 1966.
6. Bruck, R. H. and Ryser, H. J., "The Nonexistence of Certain Finite Projective Planes," *Canad. J. Math.*, Vol. 1, 1949, pp. 88-93.
7. Chowla, S. and Ryser, H. J., "Combinatorial Problems," *Canad. J. Math.*, Vol. 2, 1950, pp. 93-99.

## References (contd)

8. Golomb, S. W., et al., *Digital Communications with Space Applications*, Prentice-Hall Inc., New Jersey, 1964.
9. Hall, M., Jr. and Ryser, H. J., "Cyclic Incidence Matrices," *Canad. J. Math.*, Vol. 3, 1951, pp. 495-502.
10. Hughes, D. R., "Regular Collineation Groups," *Proc. Amer. Math. Soc.*, Vol. 8, 1957, pp. 165-168.
11. Yamamoto, K., "Decomposition Fields of Difference Sets," *Pac. J. Math.*, Vol. 13, 1963, pp. 337-352.
12. Stiffler, J. J., "On the Allocation of Power in a Synchronous Binary PSK Communication System," National Telemetry Conference Paper No. 5-1, 1964.
13. Mastascusa, E. J., "Adaptive Tracking of a Non-Stationary Maximum," PhD Thesis, Carnegie Institute of Technology, 1963.
14. Box, G. E. P., and Muller, M. E., "A Note on the Generation of Random Normal Deviates," *Ann. Math. Stat.*, Vol. 29, p. 610, 1958.
15. Viterbi, A. J., "On Coded Phase-Coherent Communications," IRT Trans. SET, March 1961.
16. Solomon, G., *Introduction to Algebraic Coding Theory*, Inter-University Series, McGraw-Hill, N. Y. (1967).
17. Shanks, D., *Solved and Unsolved Problems in Number Theory*, Vol. 1 Spartan Books, Washington, D. C. (1962).
18. Gold, R., "Optimal Binary Sequences for Spread Spectrum Multiplexing," Digest of Technical Papers, 1966 IEEE Int'l Communications Conf., Philadelphia, June 1966.
19. Mattson, H. F., and Solomon, G., "A New Treatment of Bose-Chaudhuri Codes," *Journal, Soc. Indus. Appl. Math.*, Dec. 1961.
20. Peterson, W. W., "On the Weight Structure and Symmetry of BCH Codes," Air Force Cambridge Research Lab Report 65-515, July 1965.
21. Viterbi, A. J., "Acquisition and Tracking Behavior of Phase-Locked Loops," *Symposium on Active Networks and Feedback Systems*, Polytechnic Inst. of Brooklyn, Apr. 19-21, 1960.
22. Tausworthe, R. C., "Theory and Practiced Design of Phase-Locked Receivers," Technical Report 32-819, Jet Propulsion Laboratory, Pasadena, Calif.
23. Eisenberger, I., "Tests of Hypotheses and Estimation of the Correlation Coefficient Using Quantiles, I," Technical Report 32-718, Jet Propulsion Laboratory, Pasadena, Calif., June 1965.

**Page intentionally left blank**

## XXI. Future Projects

### ADVANCED STUDIES OFFICE

N67-15764

**A. Venus Capsule Science**, R. G. Brereton,<sup>1</sup> R. W. Davies,  
and C. E. Giffin<sup>2</sup>

A number of instruments for measuring the altitude-dependent physical properties of the Cytherean atmosphere from an entry capsule are described. The objective of these measurements is to establish an altitude profile of gas density, temperature, pressure, and composition. Although not designed to survive the ballistic impact on the planet's surface, a probe of this type should carry some kind of accelerometer to distinguish between solid and liquid surfaces (Ref. 1). A method for determining the environmental measurements as a function of altitude should also be included. Means to accomplish this could vary from a lightweight and simple three-axis accelerometer technique, where the capsule altitude would be interpretive as a function of the deceleration curve, to

techniques using radar for precision capsule-altitude measurements (SPS 37-30, Vol. IV, pp. 196-205).

If additional weight, power, and data capabilities are available, it would be advantageous to incorporate an atmospheric aerosol detector, or disdrometer. An instrument commercially available through Bausch and Lomb, used for counting dust particles ranging in size from 0.3 to 10  $\mu$  at concentrations between  $10^3$  and  $10^6$  particles/ft<sup>3</sup>, may be suitably modified for this purpose.

A suggested capsule scientific payload (shown in Table 1) is discussed in the following paragraphs and in Ref. 2. The payload should consist of a thermodynamic variables package, which would include experiments to examine the density, temperature, pressure, and velocity of sound of the atmosphere; an atmospheric composition experiment; an impact accelerometer; a visual or UV photometer to determine the cloud layers and the scattering properties of the atmosphere; and a triaxial accelerometer. The total science payload weight is only about 16 lb.

<sup>1</sup>JPL Section 320.

<sup>2</sup>JPL Section 326.

Table 1. Typical Venus capsule instruments

Instrument	Measurement capabilities	Approx weight	Approx power	Bits/sample & total information (Venus)
Aerometeorometer	Static temperature: 180 to 800°K, accuracy of measurement is $\pm 1\%$ of ambient temperature	10 oz	70 mw	9 bits/sample—measure every 500 m
	Static pressure: 10 mb to 100 atm. The accuracy of measurement is approximately 2%	10 oz	100 mw	15 bits/sample—measure every 500 m
	Density: $2 \times 10^{-4}$ to 30 kg/m <sup>3</sup> , accuracy of measurement is $\pm 1\%$ of ambient	15 oz	250 mw	10 bits/sample—measure every 500 m
	Velocity of sound: 250 to 380 m/sec is 1% of ambient (accuracy of measurement)	10 oz	300 mw	10 bits/sample—measure every 500 m
Mass spectrometer	Determines the composition of the atmosphere in the mass range of 12 to 50 amu	5 lb	6 w	1100 bits/sample, 5500 bits total. This is for complete analog spectra. Bit rate can be reduced to 100 bits/sample
Visual or UV photometer	Determines the cloud tops and cloud base and the optical properties of the Cytherean atmosphere	2 lb	1.0 w	7 bits/sample—measure every 5 sec
Impactometer	Distinguishes between a hard and a soft surface; e.g., unconsolidated sand-like material and any consolidated surface	3 lb	1.0 w	2 $\mu$ sec pulses on the capsule carrier frequency
Three-axis accelerometer	Provides data for determining pressure-density-RT product as a function of altitude	3 lb (includes 5000-bit storage unit)	1.0 w	40 bits/sample—sample every second during supersonic flight and every 500 m during subsonic flight

In considering these capsule instruments, note that:

- (1) In no case has the weight of the ducts or tubing been taken into consideration (assumed to be structure weight).
- (2) The capsule should reach a velocity of Mach 1 as high above the planet's surface as possible, as the experiments were chosen for the subsonic regime of the descent.
- (3) Attitude stabilization of the capsule is required.
- (4) Because of the thermal energy at the time of the measurements as well as the unpredictable aerodynamic behavior subsequent to the loss of the ablative material, the heat shield will be a source of error. Therefore, the shield should be jettisoned, or its effects on the instruments should be clearly understood.

### 1. Thermodynamic Variables

Four instruments—to measure density, temperature, pressure, and velocity of sound—are suggested for the

thermodynamics variables package. Each should have an analog output. Sterilization, if required, does not appear to be a problem with these instruments. The following approach is just one of a variety of instrumental techniques possible for these experiments. Capsule directional stability and a speed of less than Mach 1 are required for most of these instruments. The triaxial accelerometer (discussed later) will provide information toward a better understanding and interpretation of these experiments; also, the aerodynamic properties of the capsule, as recorded in flight by the triaxial accelerometer, will provide basic information about the atmospheric density-pressure-temperature during both the supersonic and subsonic portions of the flight. Thus, the atmospheric density should be interpretive as a function of capsule oscillation and velocity for the complete deceleration profile.

*a. Density.* The proposed instrument would use an absorption technique in which the energy loss between a beta source and a detector would be measured over a known gas path. The beta source should be adequately

shielded and of low intensity to avoid affecting the cruise science radiation experiments; a 1-mC source seems reasonable. The instrument should be located adjacent to the capsule wall, and is expected to perform over a pressure range from 0.1 to 100 atm, with a sensitivity of approximately  $2 \times 10^{-5}$  g/cm<sup>3</sup>. The instrument will weigh less than 15 oz and have a data rate of 10 bits per sample, with a sample interval every 500 m.

**b. Temperature.** A vortex tube or similar device to counteract the effect of speed on the temperature reading may be required. The device must be deployed in free stream or located at a static pressure point at the rear of the capsule, and thus must be calibrated as a part of the total capsule system. A resistance-type thermometer, or other temperature sensor, with a dynamic range from 100 to 800°K is also necessary. This experimental package would weigh about 10 oz.

**c. Pressure.** The pressure readings should begin at as great an altitude as possible above the planetary surface, and these data should continue in an uninterrupted profile to the surface. Sample readings at intervals of 500 m are suggested. The accuracy of the pressure reading should be about 2% of the ambient pressure, with a response time of 0.5 sec. The instrument sensors will require a static pressure point and calibration as part of the total capsule system. The proposed instrument package would consist of two sensors — an aneroid barometer for measuring the low pressures at the higher portions of the Cytherean atmosphere, and a Statham-type gauge for measuring the higher pressures that might prevail near the bottom of the atmosphere. The instrument package will weigh about 12 oz and will measure 4 in. in diameter and 3 in. in length. The data rate will be 15 bits per sample, with sample intervals every 500 m.

**d Velocity of sound.** The velocity of sound in the Cytherean atmosphere will be a function of both the density and temperature of the atmospheric medium, and to a lesser extent, the wind velocity; therefore, this experiment is expected to provide useful information for interpreting the density and temperature experiments discussed. It would be most desirable to conduct this experiment after the fashion of a so-called "grenade experiment," where the capsule would eject small charges at specified points in its traverse through the atmosphere, and the acoustical properties of the atmospheric medium between the individual point sources and the detector or geophone on the capsule could be determined. However, sufficient weight, power, and instrument sophistication for an experiment of this type appears unlikely for

this mission. A simple, lightweight, practical experiment for determining the acoustical properties of the Cytherean atmosphere could be composed from two acoustic detectors separated orthogonally from a point sound source. The detector-source spread should be at least 5 cm, and physically located where least affected by the airflow about the capsule; a short boom position would be best. If this proves practical, the experiment might possibly provide some information on the atmospheric wind velocity.

A minimum experiment is listed in Table 1. It would consist of an acoustic source and one detector, separated by a distance of 5 cm. Only the time of travel between the source and detector would be measured; thus, the data rate would be low, on the order of 10 bits per sample. The experiment would weigh about 10 oz, not including the boom or pickup point.

## 2. Atmospheric Composition

Atmospheric composition can be determined by either a mass spectrometer, gas chromatograph, or a series of simple composition instruments. The elements and compounds of major interest are: H<sub>2</sub>O, O<sub>2</sub>, A, N<sub>2</sub>, CO<sub>2</sub>, hydrocarbons, and O<sub>3</sub>.

In the case of O<sub>2</sub>, A, the hydrocarbons, and O<sub>3</sub>, it would be useful to know the percentage or amount present to a few parts per million. For CO<sub>2</sub> and N<sub>2</sub>, a 1% accuracy is sufficient.

A 60-deg magnetic sector mass spectrometer could be considered for this experiment. This instrument, presently in breadboard stage, uses a permanent magnet weighing about 2 lb. It has a dynamic range of 10<sup>5</sup>, which would allow 0.01% components to be measured, if one assumes a factor of 10 padding in the Cytherean atmospheric pressure estimate. Gaseous constituents will be detectable within the mass range at 12 to 50. A few of these are: CH<sub>4</sub>, H<sub>2</sub>O, Ne, N<sub>2</sub>, O<sub>2</sub>, A, and CO<sub>2</sub>.

In the present system, all of these constituents can be determined to as low as 0.1% by volume. The present input pressure sampling limit of the system without special purging is 0.5 atm or less; however, by means of a lightweight (less than 1 lb) Bernoulli tube, the sample in the examining chamber could be easily exchanged. The mass spectrometer with the present all-solid-state electrometer can maintain its dynamic range with a 60-sec scan between masses 12 and 50. If the dynamic range were reduced to 10<sup>4</sup>, a single scan could be made in 2 sec.

The number of data bits required by this experiment is difficult to assess without specific telemetry ground rules. Complete analog spectra would require 2500 bits. If peak detector methods were used, the absolute partial pressures of the three major components could be determined for less than 100 bits. The data requirements of the mass spectrometer depend entirely upon the sophistication of the scientific data required. Many tradeoffs occur between this lower limit of 100 bits and the upper limit of 2500 bits per sample.

### 3. Visual and/or UV Photometer

The purpose of this experiment is to ascertain the altitude of the cloud tops and to determine if a layered structure exists in the Cytherean atmosphere that would indicate separate cloud decks. This information will be interesting in terms of the experiments discussed.

The instrument to be used will weigh about 2 lb, have a data rate of less than 10 bits per sample, a look direction back along the trajectory, and should begin to operate before Mach 1, or at a pressure of approximately 10 mb. It should have a sensitivity to most of the visible spectrum—in the range of 4000 to 6000 Å. If additional weight, power, and data rate are available, it would be practicable to include a narrow-band sensor, tuned for about 3000 Å, to examine the scattering properties of the atmosphere.

### 4. Impact Accelerometer

Instrumentation to indicate the hardness/density of the Cytherean surface from the ballistic impact of the capsule is limited by capsule weight, power, data rate, and, finally, by destruction upon impact. The device suggested is an impact accelerometer designed to provide an order-of-magnitude measurement of the hardness/density of the surface which it impacts by indicating the rate of change of velocity measured between the discharge of one electrode in the outer skin of the capsule and a second electrode in the inner skin of the capsule. The capsule would be acting as a hollow-shell-type accelerometer.

At impact, the outer electrode begins to collapse or flatten out. The inner electrode, not physically connected to the outer shell, feels no forces; hence, it continues forward with its velocity unchanged. If the target surface is completely unyielding, as is somewhat the case with solid rock, the outside capsule surface will flatten on the

impact surface, and the original distance between the two electrodes will close at the impact velocity. If, on the other hand, the impact surface is of very low density, or yielding, such as water, the flattening of the outer surface and the time between pulses from the discharges of each electrode will be longer. The entire capsule would be destroyed upon impact, or a few  $\mu$ sec after the impact accelerometer had passed its two pulses to the capsule transmitter.

### 5. Three-Axis Accelerometer

This instrument will be an integral part of the complete capsule system. It is expected to provide (1) the primary science data for the supersonic portion of the capsule flight, and (2) information that will be useful in the interpretation of the other capsule instruments.

During the supersonic portion of the flight, known aerodynamic properties of the capsule will cause it to react to the Cytherean atmosphere by deceleration and oscillation thus providing information interpretive in terms of atmospheric density–pressure–temperature. For the subsonic portion of the flight, and to the terminal velocity point, the 3-axis accelerometer will provide information interpretive in terms of atmospheric density–pressure–temperature, and will also provide relative altitude information for interpreting the data from the other capsule science instruments.

During the supersonic entry portion of the capsule descent, an ionization sheath will likely form to interfere with communications; therefore, data storage capabilities will be required to preserve these data for later transmission. The data rate for the 3-axis accelerometer will be less than 40 bits per sample, and, if possible, the high-speed portion of the flight should be recorded at intervals of 1 sec, to a total recorder capacity of 5000 bits or 2 min. The total duration of the supersonic portion of the flight will be a function of entry velocity, entry angle, atmospheric density, capsule shape, capsule density, and other considerations; therefore, it is unknown at this time. If it is anticipated that the supersonic portion of the flight will continue beyond the data storage capabilities of the recorder, a 2-sec sample interval is recommended or data logic must be used to control the sampling rate.

During the subsonic portion of the descent, the 3-axis accelerometer should be sampled every 500 m, or as frequently as the data link will allow. This instrument, including the data recorder, will weigh approximately 3 lb.

## References

1. *Space Research, Direction For The Future: Part One*, p. 36, Space Science Board, National Academy of Sciences, National Research Council, Washington, D.C., December, 1965.
2. Brereton, R. G., et al., *Venus: Preliminary Science Objectives and Experiments for Use in Advanced Mission Studies*, Technical Memorandum 33-282, Revision No. 1, pp. 14-17, Jet Propulsion Laboratory, Pasadena, California, August 1, 1966.